UNIVERSITÀ DEGLI STUDI DI TRIESTE

Università Ca'Foscari Venezia

UNIVERSITÀ DEGLI STUDI DI TRIESTE

e

UNIVERSITÀ CA' FOSCARI DI VENEZIA

XXXV CICLO DEL DOTTORATO DI RICERCA IN CHIMICA

CHEMICAL BIOWASTE UPGRADING: CARBON DOTS, BIOPOLYMERS AND ACTIVES

Settore scientifico-disciplinare: **CHIM/06**

DOTTORANDA
CARLOTTA CAMPALANI Carlotta Campalani

COORDINATORE
PROF. ENZO ALESSIO

SUPERVISORE DI TESI
PROF. ALVISE PEROSA

ANNO ACCADEMICO 2021/2022

To all curious people

“A scientist in his laboratory is not a mere technician: he is also a child confronting natural phenomena that impress him as though they were fairy tales.” - *Marie Skłodowska Curie*

Abstract

The herein reported thesis finds its roots in the concepts of sustainability and circular economy and has as purpose the valorisation of agro- and fishery-waste for the production of added-value products. In particular, different types of waste biomass were used as starting material for the synthesis of carbon dots (CDs) used as photocatalysts, for the obtainment of biopolymers, namely collagen and chitin, and for the extraction of valuable compounds using supercritical CO_2.

The investigation started studying the dependence of structure and photocatalytic behaviour of CDs on the carbon source. Six different types of carbon nanoparticles were synthesized from citric acid, glucose and fructose and compared from the morphological and optical point of view revealing a strong correlation of their properties with the starting material and the synthetic method. The citric acid-derived CDs were then employed to photoactivate the atom transfer radical polymerization of a methacrylate leading to the obtainment of the polymer in high conversions (89%) and narrow dispersity (1.4). The study on CDs proceeded then with the employment of more complex starting material, namely fish scales. Naturally nitrogen doped carbon dots were successfully synthesized starting from bass scales, fully characterized and employed as photocatalyst for the reduction of methyl viologen. The bass-CDs were compared with classic citric acid-derived CDs resulting in lower lifetime of the excited state (7.0 ns vs 13.0 ns of a-N-CDs), mass absorption coefficient (0.37 $L{\cdot}g^{-1}\ cm^{-1}$ vs 10.93) and quantum yields (6.0% vs 17.3%), but higher initial photoreduction rate ($7.5{\cdot}10^{-8}\ M{\cdot}s^{-1}$ vs $4.9{\cdot}10^{-8}\ M{\cdot}s^{-1}$ for absorption normalized experiment). The fishery waste-derived nanoparticles were then applied as photocatalyst for the continuous flow degradation of azo dyes highlighting a quantitative degradation of five model dyes in only 2 min. This study was conducted during a research period abroad (September 2021-April 2022) in the laboratories of the Université de Liège under the supervision of Professor Jean-Christophe Monbaliu.

The interest on the upgrading of fishery waste was then developed more during the second part of this thesis where studies on the possibility to extract biopolymers from fish scales or crab carapaces were conducted. After a review study on the production of UV-shields using biopolymers, an investigation on the preparation of UV-blocking films from mullet scales-derived gelatin and bass-CDs was conducted. The obtained materials were fully characterized from the morphological, mechanical and optical point of view; by adding just 5% of CDs the films blocked almost 70% of the UV radiation with negligible change in opacity (1.32 for non-loaded vs 1.61 for 5% CDs) and in transparency (88.6% for the non-loaded vs 84.4% for 5% CDs). A further study on the possibility to obtain chitin from crab shells using a one-step protocol using ionic liquids was then conducted. All characterization data confirmed that in the conditions tested, ammonium formate prepared in situ seems to be a promising candidate for one-pot chitin pulping process, allowing quantitative isolation, high purity and a high degree of acetylation (DA > 90%).

To have a complete overview on the possibility to exploit waste biomass for the production of added-value products, an investigation on the valorisation of agro-waste was then conducted. In this frame, a supercritical CO_2 extraction method was developed to obtain natural preservatives from hops and jimsonweed. $scCO_2$ extracts were compared to ethanolic ones (Soxhlet technique): the supercritical fluid led to the selective extraction of volatile compounds, such as terpenes, terpenoids, bitter acids and fatty acids, resulting in a better recovery for preservatives. The $scCO_2$ technique was then applied to obtain fatty acids for cosmetic formulations from fruit pomace, resulting again more selective when compared to classical organic solvents. This part of the thesis was developed in collaboration with Università degli studi di Padova for the analytical characterization of the extracts, and two industries, namely Rigoni di Asiago Srl (for the supplying of fruit pomace) and Unifarco SpA (for the possible cosmetic and nutraceutical application).

List of abbreviations

In alphabetical order

AA	Ammonium Acetate
AF	Ammonium Formate
AFM	Atomic Force Microscopy
AM	Amaranth
AOP	Advanced Oxidation Process
AR	Acid Red
ATRP	Atom Transfer Radical Polymerization
BE	Binding Energy
BPR	Back Pressure Regulator
CB	Conduction Band
CDs	Carbon Dots
CE	Circular Economy
CF	Continuous Flow
CH	Chromotrope
DA	Degree of Acetylation
DD	Deacetylation Degree
DM	Demineralization
DP	Deproteinization
DSC	Differential Scanning Calorimetry
EDTA	Ethylenediaminetetraacetate
FAs	Fatty Acids
FAMEs	Fatty Acids Methyl Esters
FT-IR	Fourier Transform Infrared spectroscopy
FRET	Fluorescence Resonance Energy Transfer
GC-FID	Gas Chromatography – Flame Ionization Detector
GC-MS	Gas Chromatography – Mass Spectroscopy
GPC	Gel Permeation Chromatography
HA	Hydroxylammonium Acetate
HOMO	Highest Occupied Molecular Orbital
HR-TEM	High Resolution Transmission Electron Microscopy
ICP-OES	Inductively Coupled Plasma Optical Emission Spectrometry

IL	Ionic Liquid
LED	Light Emitting Diode
LUMO	Lowest Unoccupied Molecular Orbital
MFC	Mass Flow Controller
MO	Methyl Orange
MUFAs	Monounsaturated Fatty Acids
MV	Methyl Viologen
MW	Molecular Weight
MWNTs	Multi Walled NanoTubes
NMR	Nuclear Magnetic Resonance
NPs	Nanoparticles
PET	Photoinduced Electron Transfer
PL	Photoluminescence
PLE	Photoluminescence Emission
PUFAs	Polyunsaturated Fatty Acids
QY	Quantum Yields
SAED	Selected Area Electron Diffraction
SAFAs	Saturated Fatty Acids
SAXS	Small Angle X-ray Scattering
$scCO_2$	Supercritical Carbon Dioxide
SEM	Scanning Electron Microscopy
SF	Supercritical Fluid
SFE	Supercritical Fluid Extractions
SLS	Static Light Scattering
SWNTs	Single Walled NanoTubes
SY	Sunset Yellow
TEM	Transmission Electron Microscopy
TGA	Thermogravimetric Analysis
UV	Ultraviolet
WS	Water Solubility
WVP	Water Vapour Permeability
VB	Valence Band
XPS	X-ray Photoelectron Spectroscopy

Table of Contents

1. Introduction

This thesis focuses on the chemical valorisation of waste biomass for the obtainment of added-value products. In particular, two types of waste, fishery and agricultural, were used for the preparation of different products: carbon dots further used for photocatalysis; biopolymers, in particular collagen and chitin; and active chemical products, namely preservatives and fatty acids for the cosmetic industry. The two crucial concepts that inspired this investigation are *Sustainability* and *Circular Economy*. These two models will be discussed in the introductive chapter, followed by a more detailed analysis on the type of waste used as starting materials during this study (fishery waste and agro waste see **Sections 1.2** and **1.3**), and by a chapter for each of the different processes and applications studied in this thesis. Each of them will be explained and examined at the beginning of every section (Carbon Dots in **Chapter 3**, Biopolymers in **Chapter 4** and supercritical CO_2 extractions of actives in **Chapter 5**).

1.1 Sustainability and Circular Economy

SUSTAINABILITY

> *"Sustainability is becoming a key business imperative, as the eternal search for domination over nature is replaced by the challenge of achieving environmental balance".*[1]

The first pillar on which this thesis is founded and that inspired our investigations is sustainability.

The concept of sustainability finds its roots on the silvicultural principle of the 18th century that the amount of harvested wood should not exceed the volume that is able to grow again.[2] Later on, this idea has been transferred to other contexts, such as ecology, as the respect of the ability of nature to regenerate itself. Sustainable development has then been defined in 1987 by the World Commission on Environment and Development, aka Brundtland commission, as the "development that meets the needs of the present without compromising the ability of future generations to meet their own needs".[3,4] Anyway, around 300 different definitions of sustainability are estimated to exist.[5] To cite some others, it can be defined as a situation in which human activity is conducted in a way that conserves the functions of the earth's ecosystems,[6] a transformation of human lifestyle that optimises the likelihood that living conditions will continuously support security, well-being, and health, particularly by maintaining the supply of non-replaceable goods and services,[7] or an indefinite perpetuation of all life forms.[8] However, the most accepted definition remains the one given by the Brundtland Commission. To be meaningful, however, this concept must include the maintenance, renovation or restoration of something specific, but it also has to include a more ethical dimension based on fairness of trade-off between the current economy and the future needs of the environment. Sustainability is, indeed, more and more incorporated into both agendas of policymakers and into companies' strategies. The spread of interest on sustainability can be tracked back to when increasing evidence on global-scale environmental risks (e.g. climate change, biodiversity loss, ozone depletion or alteration of the nitrogen cycle, pollution just to name a few) started to be noticed. The investigation on these threats is ongoing since the 60s and it never stops raising questions about whether the present prosperity trends will be able to be maintained in the future.[9] The term "sustainable development" was initially driven by environmental concerns but then started to comprise a plethora of expectations for desirable progress becoming more and more wide and heterogenous.[10] The three pillars of sustainability are called the "triple bottom line" and are considered to be people, profit and planet[11] and, more specifically after the World Summit in 2002, they refer to the balanced integration of economic, social and environmental performances. These three spheres, indeed, are intimately connected and continuously affect one another[12] acting as three pillars that are interdependent, that can mutually reinforce themselves and that can be adapted to a wide range of contexts.[13] During the last decade, sustainability has been more and more institutionalised into policymakers' agendas and into strategies of large organizations becoming more embedded into the rules that structure social interventions and shape behaviours. Among them, the most recent and famous is certainly the 2030 Agenda for Sustainable Development, adopted by all United Nations Member States in 2015. This action plan provides a shared proposal for peace and prosperity for both the people and the planted. The core of Agenda 2030 is composed by its 17 Sustainable Development Goals (**Figure 1.1.1**) which represent a call for action by all countries in a global partnership. The central idea at the base of the Goals is that the end of poverty and other deprivations must go together with strategies that improve health and education, reduce inequalities, and spur economic growth while tackling climate change and working to preserve oceans and forests.[14]

Figure 1.1.1. Sustainable Development Goals of the 2030 Agenda for Sustainable Development from the United Nations.[14]

In particular, the idea at the base of this thesis is inspired principally by Goals 12, 13 and 14 (**Figure 1.1.2**). Goal 12 is focused on ensuring sustainable consumption and production patterns. The economic development during the last decades, indeed, has been accompanied by environmental degradation and there is a need to reverse this trend and shift the consumption and production patterns towards a more sustainable course. For a successful transition different hurdles must be overcome, such as in resource efficiency, consideration of the entire life cycle of economic activities and active engagement in multilateral environmental agreements. The reduction of food loss and waste, indeed, can contribute to environmental sustainability by lowering the impact and cost of production and by increasing food chain efficiency. Nowadays almost 14% of the food is lost after harvesting, during transport, storage and processing, with blatant ethical implications but also amounting to a cost of over 400 billion dollars every year. In addition, we are polluting water faster than nature's ability to recover and purify it in rivers and lakes. The purpose of Goal 13 is to take actions to tackle climate change and its impacts. Climate change is affecting every country in the world and, this last decade has been the warmest ever on record, bringing to a plethora of climate disasters across continents. Efforts must be increased to overcome this problem: the world must transform its energy, industry, food, transport and agriculture sectors to limit the global temperature rise. Joining the aim of this goal, many companies are committing to lowering their emissions, but we still need a much greater scale of annual investment in order to achieve a low-carbon and climate-resilient transition. The last of the three goals that inspired this thesis, is Goal 14. This aims to preserve and exploit in a sustainable way oceans, seas and all marine resources. Oceans absorbs around 23% of the annual carbon dioxide emissions and helps to mitigate the impacts of climate change absorbing more than 90% of the excess heat. Despite the importance of water habitats form economic, social and environmental point of view, decades of irresponsible exploitation have led to an alarming level of degradation. Every year, an estimated 5 to 12 million metric tonnes of plastic enters the ocean and circa 89% of plastic litter found on the ocean floor are single-use items like plastic bags.

Figure 1.1.2. Focus on Agenda 2030 Goals 12, 13 and 14 on which this thesis is based.[14]

CIRCULAR ECONOMY

"As it is in nature, the concept of "waste" must disappear from our design frameworks, such that we instead think in terms of material and energy flows".[15]

The second concept on which this investigation was built is Circular Economy.

Despite the abundant presence of cycles in nature, such as the one of water or nutrients, humans continue to "produce, use, dispose". One of the main examples is given by plastic: one third of plastic waste is not collected or managed but simply discarded increasing enormously the amount of non-treated waste worldwide.[16] A "circular economy" (CE), instead, would turn goods that are at the end of their lives and waste into valuable resources, closing loops in industrial ecosystems and minimizing waste (**Figure 1.1.3**). In other words, the current economic pathway comprises taking of materials form the Earth, the production of goods and discarding them as wastes, in a linear process. In circular economy, by contrast, the aim is to stop waste from being produced in the first place. CE is mainly based on three principles: the elimination/reduction of waste and pollutants, the circulation of products and materials, and their regeneration.[17] This concept is supported by the transition to renewable energy and materials, it can decouple economic activities from the consumption of finite resources, and it represents a system that is good for people, business and the environment. A complete shift to CE would reduce each nation's greenhouse-gas emission up to 70%.

To better explain, in a linear economy, natural resources are turned into base materials and products for sale through a series of value-adding steps. After sale, the owner decides whether to reuse, recycle or discard the goods after their usage. Linear economy is therefore driven by "bigger, better, faster, safer" concept and is based on economic growth (profit), in turn fuelled by fashions, emotions and progress. Companies, indeed, increase their profits by selling the highest possible volumes of the most economically convenient and appealing products. In CE, instead, the reprocessing of goods and materials can generate new jobs and save energy while reducing the consumption of resources and the generation of waste. The final aim of CE is to maximize value at each point in a product's life and avoid production of non-useable waste. To realize a circular economy research and innovations are needed at all levels: commercial, social, scientific and technological. Obviously, this issue concerns also the chemical sector which is asked to understand what kind, nature and production processes of synthetic chemicals will be needed for a sustainable civilization. Today's chemical sector follows a linear path: feedstocks (often fossil ones) are exploited through the production chain that usually relies on highly reactive, toxic and persistent reagents. The majority of these processes, in addition, generate waste with rates higher than the products of interest (e.g., 5 to 50 times for specialty chemicals and 25 to 100 times for pharmaceuticals).[18] Thanks to the advances in *Green Chemistry* and *Green Engineering* it has been demonstrated that more performances and functionalities from chemicals and processes can be realized. Conditions and circumstances by which we produce and use chemicals must be changed together with the nature of chemicals and reagents themselves.[19,20]

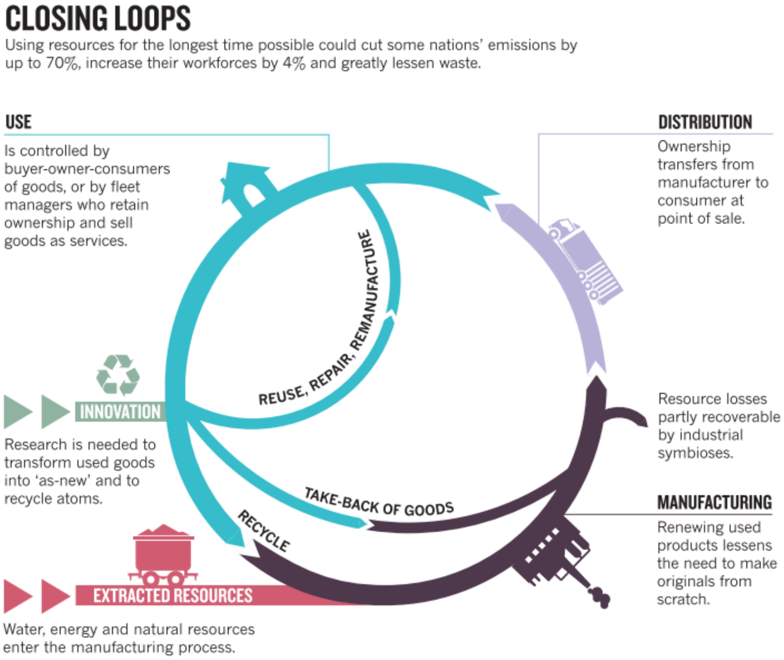

Figure 1.1.3. Pictorial representation of Circular Economy from reference.[16]

As for sustainability, also CE is becoming part of action plans of different countries, associations and companies. One example is given by the new Circular Economy Action Plan of the European Commission (**Figure 1.1.4**). This plan has been adopted in March 2020 and it is one of the main building blocks of the European Green Deal: the new European Agenda for sustainable growth. The transition of the European Union to circular economy will reduce the pressure on natural resources and it is one of the prerequisites to achieve the EU's 2050 climate neutrality target and halt biodiversity loss. A plethora of different initiatives concerning the entire life cycle of products are comprised in the plan. In particular, it aims to a more conscious production and design of products, together with an encouragement in sustainable consumption and prevention of waste.[21]

Figure 1.1.4. European Green Deal 2050 goals.[21]

1.2 Fishery Waste

The fishery and aquaculture production has seen a massive increase in the last seven decades, led by the growth of global population, urbanization, industrialization and fishing technologies. Indeed, in 1950 the production was around 19 million tonnes (live weight equivalent) and it reached an all-time record of 179 million tonnes in 2018 following an annual growth rate of 3.3%.[22] In particular, the main driver of growth total production since late 1980s has been the aquaculture production: in 2020 51% of fish production derived from capture fisheries and 49% from aquaculture, while in the past capture represented always the main source (**Figure 1.2.1**). On the basis of these data, total fisheries and aquaculture production is expected to expand further and reach 202 million tonnes in 2030 (**Figure 1.2.1**, b).

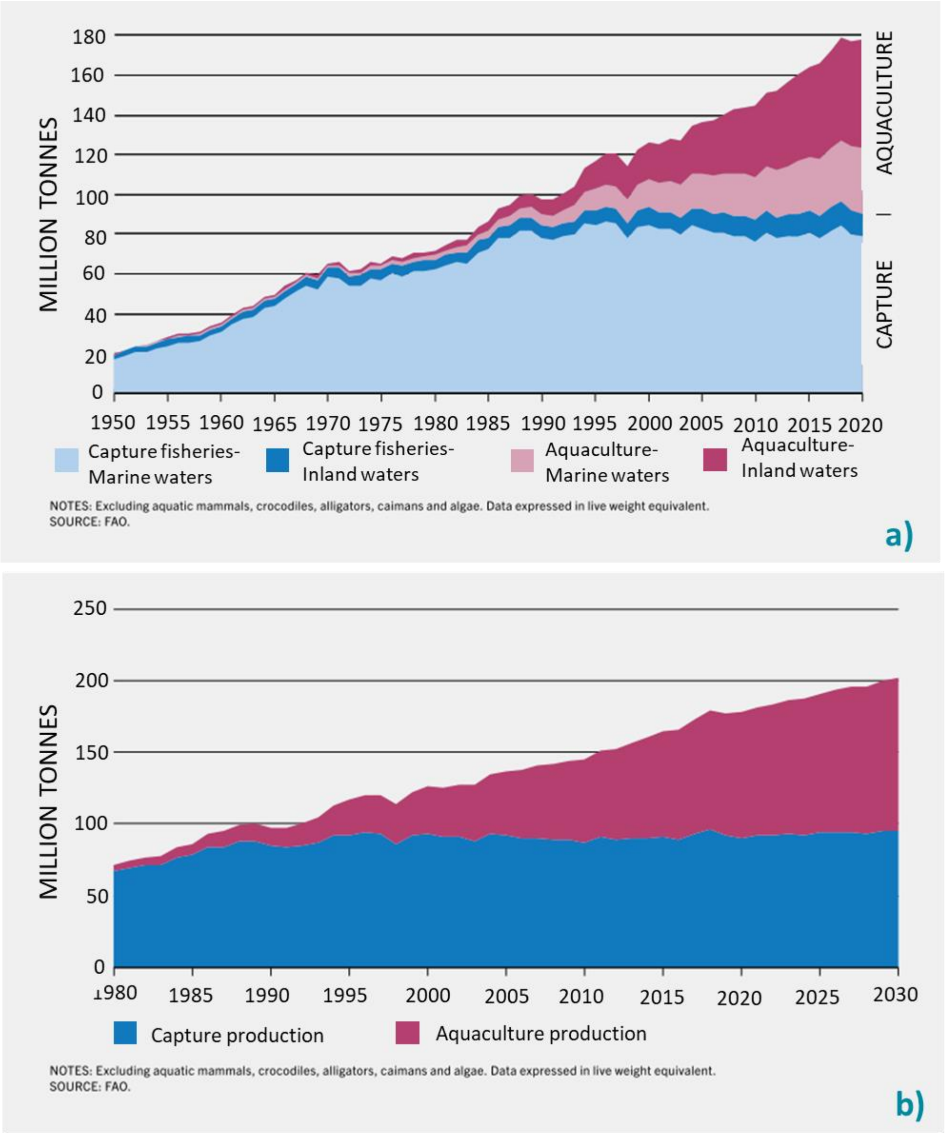

NOTES: Excluding aquatic mammals, crocodiles, alligators, caimans and algae. Data expressed in live weight equivalent.
SOURCE: FAO.

NOTES: Excluding aquatic mammals, crocodiles, alligators, caimans and algae. Data expressed in live weight equivalent.
SOURCE: FAO.

Figure 1.2.1. World capture fisheries and aquaculture production a) from 1950 to 2020; b) from 1980 and previsions until 2030.[22]

Asian countries produced 70% of the total fish in 2020, followed by the Americas (12%), Europe (10%), Africa (7%) and lastly Oceania (1%). In particular, China is the major producer (35% of total world fish), followed by India (8%), Indonesia (7%), Viet Nam (5%) and Peru (3%): these five countries were responsible of 58% of the world fisheries and aquaculture production in 2020.

A plethora of different species are harvested every year, with different numbers and species according to the fishing region. Together with the production, also the global consumption of fish is increasing significantly: nowadays we consume more than five times the quantity that was consumed 60 years ago. In 2019, global aquatic food consumption was estimated at 158 million tonnes, up from 28 million tonnes in 1961.[22] Per capita consumption was influenced most strongly by increased supplies, changing consumer preferences, advancements in technology and income growth. Overall, by 2030, the amount of aquatic food for human consumption is projected to increase by 24 million tonnes compared with 2020, reaching 182 million tonnes.

Obviously, together with the increase of consumption and production of fish, the amount of fish waste also increased: it has been estimated that about two-thirds of the total amount of fish is discarded as a waste, leading to huge economic and environmental issues.[23] Thanks to the growing attention on sustainability and circular economy, it has been understood that the use of discarded marine materials can be a strategy to achieve a circular bioeconomy.

Composition and current use

Although the data on the amount of fish waste are not clearly defined, it can be estimated in the order of dozens of million tons per year, representing a resource of an extraordinary chemical richness.[24] Nowadays, fishery waste is commonly used for the production of fertilizers, fishmeal or fish oil, used for direct feeding in aquaculture[25,26] or partly discarded.[27] However, in order to overcome environmental issues, a better management of the fish biowaste is needed, in particular for a complete use of biomass for high-commercial value purposes. Recently, indeed, several studies reported the possible use of this type of waste as a natural source of interesting compounds such as biopolymers (like collagen and chitin), enzymes and peptides, minerals and polyunsaturated fatty acids (PUFAs) that can be suitable in different fields from biotechnological or pharmaceutical applications.[28,29,30,31]

Collagen is an abundant and structural protein with a triple helix structure that can be used in a plethora of different fields: pharmaceutical, biomaterial, food and nutraceutical[32,33] (see **Chapter 4.2.1** for further details). Collagen, indeed, is one of the most promising biopolymers for the construction of scaffolds in tissue engineering thanks to its ability to promote cell regeneration,[34] its biosafety and biocompatibility and weak antigenicity. Another interesting aspect is the use of collagen as biomaterial in wet wound dressing.[35] To date different part of fish biowaste, from skin to scales, have been used to produce collagen finding applications ranging from food packaging,[36,37] wound healing[38,39] and for antioxidant purposed.[40,41]

Chitin is a long chain polysaccharide composed of N-acetyl-β-D-glucosamine units[42] and it is the second most abundant biopolymer in nature after cellulose (see **Chapter 4.3** for further details). Chitin can be easily transformed in its more soluble form, chitosan, via deacetylation. The properties of chitosan and chitin make them suitable for a great number of applications ranging from medical, pharmaceutical and cosmetic.[28,43,44] Chitosan, in particular, is used for the production of several consumer products such as antiseptics, food, textiles, cosmetics and so on, and it is becoming more and more attractive also as therapeutic agent due to its antibacterial and antifungal characteristics.

Different studies describe marine organisms as sources of bioactive proteins/peptides[45] and several among them have been isolated from fish waste such as scales, bones, heads, gonads and viscera.[30,46] Also fish oil is one of the main products that can be obtained from fish biowaste and it is principally used as ingredient in the aquaculture industry.[47] Fish oil is mainly composed by triglycerides, phospholipids, wax esters and glycerol ethers being one of the most nutrient and digestible ingredients derived from fish. The fatty acid profile is composed mainly from PUFAs, also known as omega-3, essential fatty acids that cover a wide range of important functions in the human body.[48]

According to the report "The state of world fisheries and aquaculture 2022" published by the Food and Agriculture Organization of the United Nations (FAO),[22] fishery by-products may represent up to the residual 70% of processed fish. These by-products are composed by heads (9-12% of total weight), viscera (12-18%), skin (1-3%), bones (9-15%) and scales (around 5%). The processing of fish waste involves, however, some environmental and technical challenges due to the high microbial and enzyme content and to the rapid degradation of the raw materials. The development of new materials based on fish biowaste can, anyway, provide an interesting alternative useful to reduce environmental impact of this sector.

Perspectives and use in this work of thesis

Different initiatives are being implemented in order to create a more sustainable fishery sector. The Roadmap for Blue Transformation, for example, aligns with the 2021 Declaration for Sustainable Fisheries and Aquaculture of the Committee on Fisheries of FAO[49] and it is focused on maximizing the contribution of aquatic food systems to the Sustainable Development Goals (see **Section 1.1**). The Blue Transformation Roadmap, indeed, recognizes the need to support Agenda 2030 principles for a more sustainable society. In fact, it supports an evolving and positive vision for fisheries and aquaculture in the 21st century to contribute to fight poverty and malnutrition together with a quick response to climate change, ocean conditions and a commitment to sustainability. Among the goals set by the FAO, there are the recognition of the importance of the integration of conservation and sustainable utilization of the ecosystems together with a reduction of the impact of marine litter and of discards and by-catch issues. In addition, another key point, is the reduction of pre- and post-harvest loss and waste together with an increase in the value of fish products in support of a more sustainable and inclusive ocean economy (**Figure 1.2.2**).

Objective

Upgraded value chains ensure the social, economic and environmental viability of aquatic food systems

Outcomes

- Significantly increase in global per capita fish consumption, especially across Global South.
- Reduce global fish loss and waste by half by 2030.[8]
- Current and potential exporters in developing countries can comply fully with import market requirements of major import countries.
- All forms of discrimination and abuse against women throughout the value-chain phased out.[9]

Figure 1.2.2. Target V1 of the Roadmap for Blue Transformation: Efficient value chains that increase profitability and reduce food loss and creation of waste.[49]

Innovative ways of enhancing economic returns for the fishery sector can offer valuable alternatives useful to maximize value beyond the conventional options, paving the way for improved sustainability.

In this thesis fishery wastes, in particular scales of sea bass and mullet and spider crab shells, have been used to produce high added-value materials with a view for Green Chemistry and Circular Economy. In summary:

- Sea bass scales have been used as starting material for the preparation of luminescent Carbon Dots (bass-CDs) further used as photocatalyst in the purification of wastewaters from pollutants.
- Mullet scales have been exploited for the preparation of biodegradable collagen based- films that act as UV-shields thanks to the action of the above-cited bass-CDs.
- Spider crab shells have been used for the green extraction of chitin using ionic liquids (ILs) as greener pulping agents instead of conventional chemical techniques.

1.3 Agro waste

Even though definitions of food loss and waste vary,[50,51,52] the United Nations defined agricultural waste as the waste produced as a result of various agricultural operations.[53] In detail, agro waste are the residues derived from the growing and processing of raw agricultural good: vegetables, fruits, meat, poultry, dairy products and crops. They can be seen as the “non-product” output of agricultural processing, and they can contain valuable materials. Depending on the agricultural activity and on the geographical area, the composition of these waste can be very different. Among agricultural waste we can find animal waste (manure, animal carcasses), food processing waste (e.g. only 20% of maize is used while 80% is wasted), crop waste (sugarcane bagasse, corn stalks…) and toxic and hazardous agricultural waste (insecticides, herbicides, pesticides…) (**Figure 1.3.1**).[54]

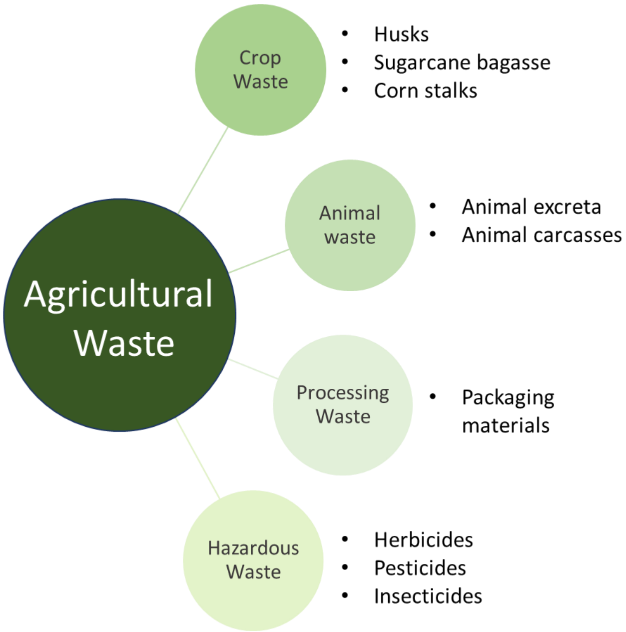

Figure 1.3.1. Types of agricultural waste.

Agricultural production increased more than three times over the last 50 years, reaching around 23.7 million tons of food every day (**Figure 1.3.2**).[55] This great expansion is due to the technological progress, the extension of agricultural soils and the growth of population and it is creating a great pressure on the environment with a negative impact on soil, air and water resources.[56] The agricultural sector, indeed, is responsible for the 21% of the greenhouse gases emissions. Being one of the largest sectors, agriculture has also the highest production of biomass, an essential input for bioeconomy.[57] The recovery and reuse of agro-waste represents therefore an opportunity; going from the replacement of fossil fuels, and consequent reduction of greenhouse effect,[58] on to the development of new green markets and jobs promoting the conversion of this waste into value-added products.[59,60]

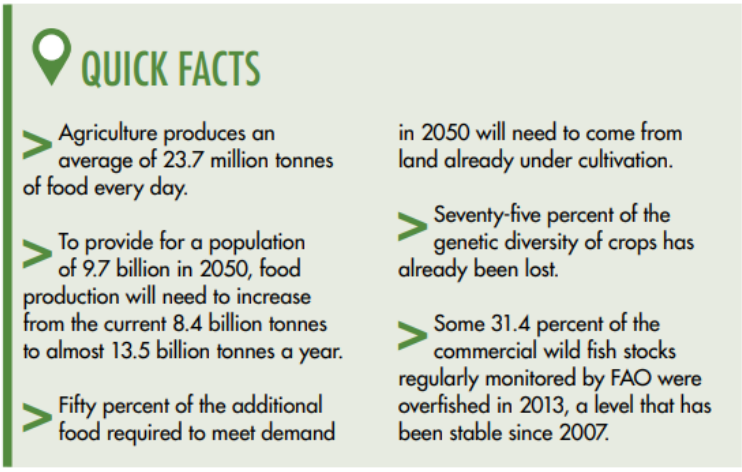

QUICK FACTS

- Agriculture produces an average of 23.7 million tonnes of food every day.
- To provide for a population of 9.7 billion in 2050, food production will need to increase from the current 8.4 billion tonnes to almost 13.5 billion tonnes a year.
- Fifty percent of the additional food required to meet demand in 2050 will need to come from land already under cultivation.
- Seventy-five percent of the genetic diversity of crops has already been lost.
- Some 31.4 percent of the commercial wild fish stocks regularly monitored by FAO were overfished in 2013, a level that has been stable since 2007.

Figure 1.3.2. Facts and data about agriculture and food industry nowadays, from reference.[55]

The expansion of agriculture, obviously, leads to increased crop residues, livestock waste and agro-industrial by-products and, the continuous intensification of the farming system will imply a continuous increase in this type of waste. It is estimated that about 998 million tonnes of agricultural waste are produced every year[54] and this often creates environmental and economic burdens. In **Table 1.3.1** the most common type of agricultural waste and their sources are listed.[61]

Table 1.3.1. Source, composition major producer and yearly amount of the most common agro waste.

Entry	Source	Composition	Major Producer [a]	Yearly amount in 2020 (millions of tonnes) [a]
1	Sugarcane	Sugarcane tops, bagasse and molasses	Brazil	>750
2	Maize	Stover, husk, skin trimming, cobs	United States	>350
3	Rice	Husk, bran	China and India	>300
4	Wheat	Bran, straw	China	>130
5	Millet	Stover	India	>12
6	Oat	Straw	Russia	>5
7	Pineapple	Outer peel, crown, bud ends, trimming	Philippines	>2.5

[a] Source: Food and Agriculture Organization Corporate Statistical Database (FAOSTAT).[62]

As already stated, agro waste can be turned into valuable resources such as bioenergy, biomaterials, bio-fertilizers and biomolecules.[63,64] This exploitation is a complex and multi-disciplinary problem that is being widely approached from the technological point of view.[65,66,67,68]

Composition and current use

In this thesis, agro waste from selected crops, weeds and fruit, in particular hops, jimsonweed and berry pomaces, have been used.

Waste derived from fruit and vegetable processing has a similar nature to the food itself; they are, indeed, derived from trimming, culling, juicing and blanching of the raw materials. Generally, the main components of fruit and vegetables waste are starch/cellulose and sugars, but the fine composition can change enormously depending on the type of biomass (regarding the profile of fatty acids, terpenes, vitamins…).
Many processes are used to provide bioenergy or valuable chemicals starting from this type of waste, while helping pollution control and circular economy. Agro-waste from food industry is, indeed, ideal candidates for bioprocessing thanks to their high amount of easily degradable organic materials that can make it a potential commodity for the production of bioenergy and biochemicals, possibly reducing our dependence on fossil fuels.[69] Among the transformation procedures we can find pyrolysis, methane recovery, gasification, bacterial digestion for hydrogen production and bioethanol production. In 2006 the 10% of the world energy

was represented by bioenergy[70] and, in last years the biofuel production significantly increased the crop demand.[71] Anyway, bioenergy production cannot entirely satisfy the energy demand of our society making the production of high-value chemicals from waste more feasible.

The most widespread uses of agro waste include anaerobic digestion, pyrolysis, as metal absorbers and direct combustion and some others.[54] With anaerobic digestion it is possible to obtain methane from wastes and it is performed with a two-step microbial fermentation. One of the most used fermentation process from food and agro waste is the lactic acid fermentation from which lactic acid is produced and subsequently used for polylactic acid preparation.[69] In recent year, agro waste was proven to be also a cheap alternative for the treatment of heavy metals containing wastewater. In particular different researchers demonstrate the ability of sugarcane bagasse[72] and rice husk,[73] among others, to absorb metallic pollutants. Another common waste treatment is pyrolysis in which biomass is heated at high temperature (400-600° C) in absence of oxygen to produce char together with oil and low heating value gas. Pyrolysis is considered a high-technology process for the treatment of agricultural waste together with hydrogenation and hydro-gasification that are used for the production of chemicals and for energy recovery. However, of all processes that can be used to convert agricultural waste, combustion is still the dominant technology accounting more than 95% of all biomass energy utilized today.[74] Complete combustion of agro waste release energy with the simultaneous formation of carbon dioxide and water.

Considering the enormous amount of interesting compounds present in agro-waste matrixes (i.e. terpenes, fatty acids, polyphenols), different types of extractive methods to retrieve them are nowadays gaining interest. In order to obtain active molecules, traditional extraction procedures use chemicals or solvents able to disrupt the cells or the tissues of the matrix; among these acid or alkali extraction and solvent extraction can be named. However, the majority of these techniques necessitate high temperatures, a considerable amount of time and the use of hazardous solvents that can leave traces in the final products.[75] More modern extractive techniques try to solve these problems maximizing the selectivity towards the desired compounds and avoiding the use of environmental unfriendly dangerous solvents. The so called “green extractions” are based on the discovery and design of extraction processes which reduces energy consumption, allows the use of alternative solvents, produces renewable natural products, and ensures a safe and high-quality extract and or products; among these it is possible to find microwave or ultrasound assisted extractions and extractions performed using supercritical fluids.[76] In particular, the possibility to use supercritical CO_2 ($scCO_2$) as an alternative to classical extractive technique for the generation of high added value products is receiving widespread interest thanks to the direct application in industries, such as food and pharmaceutical. Moreover, the possibility to work at lower temperatures, that can be responsible for the destruction of valuable substances, and the avoidance of product contamination with solvent residues[77] are contributing to candidate supercritical fluids extraction as a promising alternative to conventional extraction techniques.

Perspectives and use in this work of thesis

From this analysis it came out that agriculture seems to be posing new challenges with a need to create a more sustainable sector. This situation has driven a model with a more balanced development that would imply severe changes in the agricultural production system.[78] The warn of the World Commission on Environment and Development about the environmental crisis due to fast population growth that implied an increased demand of natural resources,[79] lead to the articulation and coordination of political actions worldwide for a better management of these resources to ensure durable human progress.[80] From 1992 Rio Declaration on Environment and Development, indeed, new models of sustainable development, that comprise environmental, economic and social factors, were consolidated.[81] Those guidelines were oriented since then to global development objectives such as the Millennium Development Goals in 2010 and the Agenda 2030 Sustainable Development Goals in 2015, that reflect the desire of world leaders to implement strategies for the preservation of natural resources to guarantee environmental sustainability.[82,83] These goals pose the need for real reforms where the transformation of biowaste to valuable products plays a crucial role.

In this thesis different types of agro waste were used to perform $scCO_2$ extractions to obtain high added-value compounds. In particular:

- Hops leaves and jimsonweed were used for the obtainment of natural preservatives that can be exploited, for example, in the cosmetic industry.
- Different fruit pomaces (raspberry, blueberry, pomegranate, wild strawberry, blackberry and blackcurrant) obtained as waste from the food industry were used as starting material to obtain interesting fatty acids used in cosmetic and nutraceutical formulations.

1.4 Bibliography

(1) Clarke, T.; Clegg, S. R. *Changing Paradigms: The Transformation of Management for the 21st Century - Ed. Haprer Collins Businness*; 2000.

(2) Geissdoerfer, M.; Savaget, P.; Bocken, N. M. P.; Hultink, E. J. The Circular Economy – A New Sustainability Paradigm? *J Clean Prod* **2017**, *143*, 757–768. https://doi.org/10.1016/j.jclepro.2016.12.048.

(3) Wilkinson, A.; Hill, M. The Sustainability Debate. *International Journal of Operations & Production Managment* **2001**, *21* (12), 1492–1502. https://doi.org/https://doi.org/10.1108/01443570110410865.

(4) Brundtland, G. H. Our Common Future: Report of the World Commision on Environment and Development. *Med. Confl. Surviv.* **1987**, *4* (1), 300. https://doi.org/http://dx.doi.org/ 10.1080/07488008808408783.

(5) Johnston, P.; Everard, M.; Santillo, D.; Robèrt, K. Reclaiming the Definition of Sustainability. *Environmental Science and Pollution Research* **2007**, *14* (1), 60–66.

(6) Sustainability in Building Construction—General Principles; ISO 15392; Geneva, Switzerland. *International Organization for Standardization (ISO).* **2008**.

(7) McMichael, A. J.; Butler, C. D.; Folke, C. New Visions for Addressing Sustainability. *Science (1979)* **2003**, *302* (5652), 1919–1920. https://doi.org/10.1126/science.1090001.

(8) Ehrenfeld, J. R. The Roots of Sustainability. *MIT Sloan Manag Rev* **2005**, *46*, 23–25. https://doi.org/10.1007/s12129-009-9151-5.

(9) Clark, W. C.; Crutzen, P. J.; Schellnhuber, H. J. Science for Global Sustainability: Toward a New Paradigm. *SSRN Electronic Journal* **2011**, *120*. https://doi.org/10.2139/ssrn.702501.

(10) Kates, R. W.; Parris, T. M.; Leiserowitz, A. A. What Is Sustainable Development? Goals, Indicators, Values, and Practice. *Environ. Sci. Policy* **2005**, *47*, 8–21. https://doi.org/https://doi.org/10.1080/00139157.2005.10524444.

(11) Elkington, J.; Rowlands, I. H. Cannibals with Forks: The Triple Bottom Line for 21st Century Businness. *Alternatives Journal, Waterloo* **1999**, *25*, 42–43.

(12) McKelvey, B. Managing Coevolutionary Dynamics. *18th EGOS Colloquium* **2002**, No. 4-6 July, 1–20.

(13) Wise, N. Outlining Triple Bottom Line Contexts in Urban Tourism Regeneration. *Cities* **2016**, *53*, 30–34. https://doi.org/10.1016/j.cities.2016.01.003.

(14) *17 Goals to Transform Our World (accessed 19 July 2022)*. http://www.un.org/sustainabledevelopment.

(15) Zimmerman, J. B.; Anastas, P. T.; Erythropel, H. C.; Leitner, W. Designing for a Green Chemistry Future. *Science (1979)* **2020**, *367* (6476), 397–400. https://doi.org/10.1126/science.aay3060.

(16) Stahel, W. R. Circular Economy. *Nature* **2016**, *531*, 435–438. https://doi.org/10.4324/9781315270326-38.

(17) Ellen MacArthur Foundation World Economic Forum AndMcKinsey & Company. The New Plastics Economy: Rethinking the Future of Plastics. *Ellen MacArthur Foundation* **2016**.

(18) Sheldon, R. A. The: E Factor 25 Years on: The Rise of Green Chemistry and Sustainability. *Green Chemistry* **2017**, *19* (1), 18–43. https://doi.org/10.1039/c6gc02157c.

(19) Anastas, P. T.; Zimmerman, J. B. Design through the 12 Principles of Green Engineering. *Environ Sci Technol* **2003**, *37*, 94–101. https://doi.org/10.1109/EMR.2007.4296421.

(20) Erythropel, H. C.; Zimmerman, J. B.; De Winter, T. M.; Petitjean, L.; Melnikov, F.; Lam, C. H.; Lounsbury, A. W.; Mellor, K. E.; Janković, N. Z.; Tu, Q.; Pincus, L. N.; Falinski, M. M.; Shi, W.; Coish, P.; Plata, D. L.; Anastas, P. T. The Green ChemisTREE: 20 Years after Taking Root with the 12 Principles. *Green Chemistry* **2018**, *20* (9), 1929–1961. https://doi.org/10.1039/c8gc00482j.

(21) A European Green Deal (Accessed 19 July 2022).

(22) FAO. *The State of World Fisheries and Aquaculture 2022. Towards Blue Transformation. Rome*; 2022. https://doi.org/https://doi.org/10.4060/cc0461en.

(23) Coppola, D.; Lauritano, C.; Palma Esposito, F.; Riccio, G.; Rizzo, C.; de Pascale, D. Fish Waste: From Problem to Valuable Resource. *Mar Drugs* **2021**, *19* (2), 1–39. https://doi.org/10.3390/md19020116.

(24) Maschmeyer, T.; Luque, R.; Selva, M. Upgrading of Marine (Fish and Crustaceans) Biowaste for High Added-Value Molecules and Bio(Nano)-Materials. *Chem Soc Rev* **2020**, *49* (13), 4527–4563. https://doi.org/10.1039/c9cs00653b.

(25) Mo, W. Y.; Man, Y. B.; Wong, M. H. Use of Food Waste, Fish Waste and Food Processing Waste for China's Aquaculture Industry: Needs and Challenge. *Science of the Total Environment* **2018**, *613–614*, 635–643. https://doi.org/10.1016/j.scitotenv.2017.08.321.

(26) Ahuja, I.; Dauksas, E.; Remme, J. F.; Richardsen, R.; Løes, A. K. Fish and Fish Waste-Based Fertilizers in Organic Farming – With Status in Norway: A Review. *Waste Management* **2020**, *115*, 95–112. https://doi.org/10.1016/j.wasman.2020.07.025.

(27) Guillen, J.; Holmes, S. J.; Carvalho, N.; Casey, J.; Dörner, H.; Gibin, M.; Mannini, A.; Vasilakopoulos, P.; Zanzi, A. A Review of the European Union Landing Obligation Focusing on Its Implications for Fisheries and the Environment. *Sustainability* **2018**, *10* (4), 900. https://doi.org/10.3390/su10040900.

(28) Shahidi, F.; Varatharajan, V.; Peng, H.; Senadheera, R. Utilization of Marine By-Products for the Recovery of Value-Added Products. *Journal of Food Bioactives* **2019**, *6*, 10–61. https://doi.org/10.31665/jfb.2019.6184.

(29) Coppola, D.; Oliviero, M.; Vitale, G. A.; Lauritano, C.; D'Ambra, I.; Iannace, S.; de Pascale, D. Marine Collagen from Alternative and Sustainable Sources: Extraction, Processing and Applications. *Mar Drugs* **2020**, *18* (4), 214. https://doi.org/10.3390/md18040214.

(30) Abuine, R.; Rathnayake, A. U.; Byun, H. G. Biological Activity of Peptides Purified from Fish Skin Hydrolysates. *Fish Aquatic Sci* **2019**, *22* (1), 1–14. https://doi.org/10.1186/s41240-019-0125-4.

(31) Karkal, S. S.; Kudre, T. G. Valorization of Fish Discards for the Sustainable Production of Renewable Fuels. *J Clean Prod* **2020**, *275*, 122985. https://doi.org/10.1016/j.jclepro.2020.122985.

(32) Alves, A. L.; Marques, A. L. P.; Martins, E.; Silva, T. H.; Reis, R. L. Cosmetic Potential of Marine Fish Skin Collagen. *Cosmetics* **2017**, *4* (4), 1–16. https://doi.org/10.3390/cosmetics4040039.

(33) Leòn-Lòpez, A.; Morales-Penaloza, A.; Martìnez-Juàrez, V. M.; Vargas-Torres, A.; Zeugolis, D. I.; Aguirre-Alvarez, G. Hydrolyzed Collagen - Sources and Applications. *Molecules* **2019**, *24*, 4031. https://doi.org/doi:10.3390/molecules24224031.

(34) Xu, Y.; Duan, L.; Li, Y.; She, Y.; Zhu, J.; Zhou, G.; Jiang, G.; Yang, Y. Nanofibrillar Decellularized Wharton's Jelly Matrix for Segmental Tracheal Repair. *Adv Funct Mater* **2020**, *30*, 1910067. https://doi.org/10.1002/adfm.201910067.

(35) Parenteau-Bareil, R.; Gauvin, R.; Berthod, F. Collagen-Based Biomaterials for Tissue Engineering Applications. *Materials* **2010**, *3* (3), 1863–1887. https://doi.org/10.3390/ma3031863.

(36) Liu, J.; Shibata, M.; Ma, Q.; Liu, F.; Lu, Q.; Shan, Q.; Hagiwara, T.; Bao, J. Characterization of Fish Collagen from Blue Shark Skin and Its Application for Chitosan- Collagen Composite Coating to Preserve Red Porgy (Pagrus Major) Meat. *J Food Biochem* **2020**, *44* (8), 1–14. https://doi.org/10.1111/jfbc.13265.

(37) Slimane, E. Ben; Sadok, S. Collagen from Cartilaginous Fish By-Products for a Potential Application in Bioactive Film Composite. *Mar Drugs* **2018**, *16*, 211. https://doi.org/10.3390/md16060211.

(38) Shi, Y.; Zhang, H.; Zhang, X.; Chen, Z.; Zhao, D.; Ma, J. A Comparative Study of Two Porous Sponge Scaffolds Prepared by Collagen Derived from Porcine Skin and Fish Scales as Burn Wound Dressings in a Rabbit Model. *Regen Biomater* **2019**, *7* (1), 63–70. https://doi.org/10.1093/rb/rbz036.

(39) Ibrahim, A.; Soliman, M.; Kotb, S.; Ali, M. M. Evaluation of Fish Skin as a Biological Dressing for Metacarpal Wounds in Donkeys. *BMC Vet Res* **2020**, *16* (1), 1–10. https://doi.org/10.1186/s12917-020-02693-w.

(40) Hua, Y.; Ma, C.; Wei, T.; Zhang, L.; Shen, J. Collagen/Chitosan Complexes: Preparation, Antioxidant Activity, Tyrosinase Inhibition Activity, and Melanin Synthesis. *Int J Mol Sci* **2020**, *21*, 313. https://doi.org/10.3390/ijms21010313.

(41) Asaduzzaman, A. K. M.; Getachew, A. T.; Cho, Y. J.; Park, J. S.; Haq, M.; Chun, B. S. Characterization of Pepsin-Solubilised Collagen Recovered from Mackerel (Scomber Japonicus) Bone and Skin Using Subcritical Water Hydrolysis. *Int J Biol Macromol* **2020**, *148*, 1290–1297. https://doi.org/10.1016/j.ijbiomac.2019.10.104.

(42) Cheba, B. A. Chitin and Chitosan: Marine Biopolymers with Unique Properties and Versatile Applications. *Global Journal of Biotechnology & Biochemistry* **2011**, *6* (3), 149–153.

(43) Yadav, M.; Goswami, P.; Paritosh, K.; Kumar, M.; Pareek, N.; Vivekanand, V. Seafood Waste: A Source for Preparation of Commercially Employable Chitin/Chitosan Materials. *Bioresour Bioprocess* **2019**, *6* (8). https://doi.org/10.1186/s40643-019-0243-y.

(44) Younes, I.; Rinaudo, M. Chitin and Chitosan Preparation from Marine Sources. Structure, Properties and Applications. *Mar Drugs* **2015**, *13* (3), 1133–1174. https://doi.org/10.3390/md13031133.

(45) Giordano, D.; Costantini, M.; Coppola, D.; Lauritano, C.; Núñez Pons, L.; Ruocco, N.; di Prisco, G.; Ianora, A.; Verde, C. Biotechnological Applications of Bioactive Peptides From Marine Sources. *Adv Microb Physiol* **2018**, *73*, 171–220. https://doi.org/10.1016/bs.ampbs.2018.05.002.

(46) Harnedy, P. A.; FitzGerald, R. J. Bioactive Peptides from Marine Processing Waste and Shellfish: A Review. *J Funct Foods* **2012**, *4* (1), 6–24. https://doi.org/10.1016/j.jff.2011.09.001.

(47) Wijesundera, C.; Kitessa, S.; Abeywardena, M.; Bignell, W.; Nichols, P. D. Long-Chain Omega-3 Oils: Current and Future Supplies, Food and Feed Applications, and Stability. *Lipid Technol* **2011**, *23* (3), 55–58. https://doi.org/10.1002/lite.201100091.

(48) Kim, S. K.; Mendis, E. Bioactive Compounds from Marine Processing Byproducts - A Review. *Food Research International* **2006**, *39* (4), 383–393. https://doi.org/10.1016/j.foodres.2005.10.010.

(49) FAO. *Blue Transformation - Roadmap 2022–2030: A Vision for FAo's Work on Aquatic Food Systems. Rome*; 2022. https://doi.org/https://doi.org/10.4060/cc0459en.

(50) Bellemare, M. F.; Çakir, M.; Peterson, H. H.; Novak, L.; Rudi, J. On the Measurement of Food Waste. *Am J Agric Econ* **2017**, *99* (5), 1148–1158. https://doi.org/10.1093/ajae/aax034.

(51) Chaboud, G.; Daviron, B. Food Losses and Waste: Navigating the Inconsistencies. *Glob Food Sec* **2017**, *12* (November 2016), 1–7. https://doi.org/10.1016/j.gfs.2016.11.004.

(52) Teigiserova, D. A.; Hamelin, L.; Thomsen, M. Towards Transparent Valorization of Food Surplus, Waste and Loss: Clarifying Definitions, Food Waste Hierarchy, and Role in the Circular Economy. *Science of the Total Environment* **2020**, *706*, 136033. https://doi.org/10.1016/j.scitotenv.2019.136033.

(53) United Nations. Glossary of Environment Statistics, Studies in Methods, Series F, 67, Department for Economic and Social Information and Policy Analysis, Statistic Division, New York, USA. **1997**.

(54) Obi, F. O.; Ugwuishiwu, B. O.; Nwakaire, J. N. Agricultural Waste Concept, Generation, Utilization and Management. *Nigerian Journal of Technology* **2016**, *35* (4), 957–964. https://doi.org/10.4314/njt.v35i4.34.

(55) FAO. Strategic Work of FAO for Sustainable Food and Agriculture. **2017**. https://doi.org/https://www.fao.org/3/i6488e/i6488e.pdf.

(56) FAO. The State of Food and Agrivulture Leveraging Food Systems for Inclusive Rural Transformation. **2017**. https://doi.org/http://www.fao.org/3/a-i7658e.pdf.

(57) Bracco, S.; Calicioglu, O.; Juan, M. G. S.; Flammini, A. Assessing the Contribution of Bioeconomy to the Total Economy: A Review of National Frameworks. *Sustainability* **2018**, *10*, 1698. https://doi.org/10.3390/su10061698.

(58) McCormick, K.; Kautto, N. The Bioeconomy in Europe: An Overview. *Sustainability (Switzerland)* **2013**, *5* (6), 2589–2608. https://doi.org/10.3390/su5062589.

(59) Scarlat, N.; Dallemand, J. F.; Monforti-Ferrario, F.; Nita, V. The Role of Biomass and Bioenergy in a Future Bioeconomy: Policies and Facts. *Environ Dev* **2015**, *15* (2015), 3–34. https://doi.org/10.1016/j.envdev.2015.03.006.

(60) Mohanty, A. K.; Misra, M.; Drzal, L. T. Sustainable Bio-Composites from Renewable Resources: Opportunities and Challenges in the Green Materials World. *J Polym Environ* **2002**, *10* (1–2), 19–26. https://doi.org/10.1023/A:1021013921916.

(61) Nagendran, R. Agricultural Waste and Pollution. In *Waste*; Elsevier Inc., 2011; pp 341–355. https://doi.org/10.1016/B978-0-12-381475-3.10024-5.

(62) Food and Agriculture Organization Corporate Statistical Database (FAOSTAT) Https://Www.Fao.Org/Faostat/En/#home (Accessed17/01/2023).

(63) Vea, E. B.; Romeo, D.; Thomsen, M. Biowaste Valorisation in a Future Circular Bioeconomy. *Procedia CIRP* **2018**, *69* (May), 591–596. https://doi.org/10.1016/j.procir.2017.11.062.

(64) Dahiya, S.; Kumar, A. N.; Shanthi Sravan, J.; Chatterjee, S.; Sarkar, O.; Mohan, S. V. Food Waste Biorefinery: Sustainable Strategy for Circular Bioeconomy. *Bioresour Technol* **2018**, *248* (July 2017), 2–12. https://doi.org/10.1016/j.biortech.2017.07.176.

(65) Duque-Acevedo, M.; Belmonte-Ureña, L. J.; Cortés-García, F. J.; Camacho-Ferre, F. Agricultural Waste: Review of the Evolution, Approaches and Perspectives on Alternative Uses. *Glob Ecol Conserv* **2020**, *22*. https://doi.org/10.1016/j.gecco.2020.e00902.

(66) Donner, M.; Verniquet, A.; Broeze, J.; Kayser, K.; De Vries, H. Critical Success and Risk Factors for Circular Business Models Valorising Agricultural Waste and By-Products. *Resour Conserv Recycl* **2021**, *165*, 105236. https://doi.org/10.1016/j.resconrec.2020.105236.

(67) Batstone, D. J.; Virdis, B. The Role of Anaerobic Digestion in the Emerging Energy Economy. *Curr Opin Biotechnol* **2014**, *27*, 142–149. https://doi.org/10.1016/j.copbio.2014.01.013.

(68) Pellis, A.; Cantone, S.; Ebert, C.; Gardossi, L. Evolving Biocatalysis to Meet Bioeconomy Challenges and Opportunities. *N Biotechnol* **2018**, *40*, 154–169. https://doi.org/10.1016/j.nbt.2017.07.005.

(69) Hansen, C. L.; Cheong, D. Y. Agricultural Waste Management in Food Processing. In *Handbook of Farm, Dairy and Food Machinery Engineering*; Elsevier Inc., 2019; pp 673–716. https://doi.org/10.1016/B978-0-12-814803-7.00026-9.

(70) Hazell, P.; Pachauri, R. K. *Bioenergy and Agriculture: Promises and Challenges.*; Ed. International Food Policy Research Institute (IFPRI), Washington, D. C., Ed.; 2006; Vol. 14. https://doi.org/https://doi.org/10.2499/2020focus14.

(71) Food and Agriculture Organization of the United Nations (FAO) & Organization for Economic Co-operation and Development. FAO Agricultural Outlook 2019-2028. **2019**. https://doi.org/http://www.fao.org/3/ca5308en/ca5308en.pdf.

(72) Mohan, D.; Singh, K. P. Single- and Multi-Component Adsorption of Cadmium and Zinc Using Activated Carbon Derived from Bagasse - An Agricultural Waste. *Water Res* **2002**, *36* (9), 2304–2318. https://doi.org/10.1016/S0043-1354(01)00447-X.

(73) Ayub, S.; Ali, S. I.; Khan, N. A. Adsorption Studies on the Low Cost Adsorbent for the Removal of Cr(VI) from Electroplating Wastewater. *Environmental Pollution Control Journal* **2002**, *5* (6), 10–20.

(74) Klass, D. L. Biomass for Renewable Energy and Fuels. In: Encyclopedia of Energy, Ed. Elsevier, San Diego,. **2004**, *1*, 193–212.

(75) Kainat, S.; Arshad, M. S.; Khalid, W.; Zubair Khalid, M.; Koraqi, H.; Afzal, M. F.; Noreen, S.; Aziz, Z.; Al-Farga, A. Sustainable Novel Extraction of Bioactive Compounds from Fruits and Vegetables Waste for Functional Foods: A Review. *Int J Food Prop* **2022**, *25* (1), 2457–2476. https://doi.org/10.1080/10942912.2022.2144884.

(76) More, P. R.; Jambrak, A. R.; Arya, S. S. Green, Environment-Friendly and Sustainable Techniques for Extraction of Food Bioactive Compounds and Waste Valorization. *Trends in Food Science and Technology*. Elsevier Ltd October 1, 2022, pp 296–315. https://doi.org/10.1016/j.tifs.2022.08.016.

(77) Zaidul, I. S. M.; Nik Nourlaini, N. A.; Mohd Omar, A. K.; Smith, R. L. Supercritical Carbon Dioxide (SC-CO 2) Extraction of Palm Kernel Oil from Palm Kernel. *J Food Eng* **2007**, *79*, 1007–1014. https://doi.org/10.1016/j.jfoodeng.2006.03.021.

(78) FAO. The State of Food and Agriculture. Climate Change, Agriculture and Food Security. **2016**. https://doi.org/http://www.fao.org/3/a-i6030e.pdf.

(79) Vaz, E.; Joanaz de Melo, C.; Pinto, C. Environmental History in the Making, In: Environmental History. Ed. Springer International Publishing, Switzerland. **2017**, *6*. https://doi.org/https://doi.org/10.1007/978-3-319-41139-2.

(80) Halisçelik, E.; Soytas, M. A. Sustainable Development from Millennium 2015 to Sustainable Development Goals 2030. *Sustainable Development* **2019**, *27* (4), 545–572. https://doi.org/10.1002/sd.1921.

(81) United Nations. Review of Implementation of the Rio Principles. Detailed Review of Implementation of the Rio Principles. Study Prepared by the Stakeholder Forum for a Sustainable Future. **2011**, 1–202. https://doi.org/https://sustainabledevelopment.un.org/content/documents/1127rioprinciples.pdf.

(82) FAO. Food and Agriculture. Driving Actions across the 2030 Agenda for Sustainable Development. **2017**. https://doi.org/http://www.fao.org/3/a-i7454e.pdf.

(83) United Nations, The Millennium Development Goals Report 2015. **2015**. https://doi.org/https://www.un.org/millenniumgoals/2015_MDG_Report/pdf/MDG 2015.

2. Aim and Structure of the Thesis

The common thread of this thesis is the valorisation of waste biomass, both from fishery as well as from agriculture, for the production of carbon dots, biopolymers and active molecules. The results have been collected and discussed in three chapters (*Chapter 3: Carbon Dots, Chapter 4: Biopolymers and Chapter 5: Supercritical* CO_2 *extractions).*

Chapter 3 describes the synthesis, characterization and applications of CDs. The first part contains a study on the correlation between the morphological and photo-optical behaviour of CDs synthesized starting from biobased molecules (citric acid, glucose and fructose) (**Chapter 3.2**). **Chapter 3.3** applies the obtained knowledge and describes how nitrogen-doped CDs made from citric acid photocatalyse the atom transfer radical polymerization of methacrylates. After understanding how to produce CDs from simple biobased molecules, complex organic fishery waste was investigated as the carbon source for the production of CDs with a view to Circular Economy. CDs prepared from sea bass scales were synthesized, characterized and tested for their single-electron transfer ability towards methyl viologen (**Chapter 3.4**). The fish-derived CDs were then used as photocatalyst for the continuous flow degradation of azo dyes, a typical wastewater source of pollution (**Chapter 3.5**). These studies gave us an insight on the possibility to valorise fishery waste for added-value products and processes.

Fish wastes are composed mainly by two biopolymers, collagen and chitin. The research described in **Chapter** 4 continued with the valorisation of these materials, through a combination of selective extraction and application of these two biopolymers. After a review study on the production of UV-shields from biopolymers (**Chapter 4.2**) an investigation on the possibility to extract collagen from mullet scales and use it to produce UV-blocking films with sea bass-derived CDs as additive (**Chapter 4.2.1**) was performed. A study on the possibility to extract chitin from crab shells using alternative methods based on ionic liquids was also performed (**Chapter 4.3**).

To have a complete overview on the possibility to exploit waste biomass for the production of added-value products, in **Chapter 5** an investigation on the valorisation of agro-waste is described. In this frame, supercritical CO_2 extraction methods were developed to obtain natural preservatives from hops and jimsonweed (**Chapter 5.2**) and fatty acids for cosmetic formulations from fruit pomaces (**Chapter 5.3**).

In **Figure 2.1** a graphical representation of the structure of this thesis is reported.

This thesis was developed in the Green Organic Synthesis Team (GOST) of the Università Ca' Foscari di Venezia, led by Prof. Alvise Perosa, Prof. Maurizio Selva and Prof. Giulia Fiorani. In addition, part of the research activities of this PhD program was carried at the Univeristé de Liège in Belgium in the laboratories of the Center of Integrated Technology and Organic Synthesis (CiTOS) led by Prof. Jean-Christophe Monbaliu. In particular, during the period at CiTOS group, the utilization of fish derived carbon dots for continuous flow photochemistry was investigated.

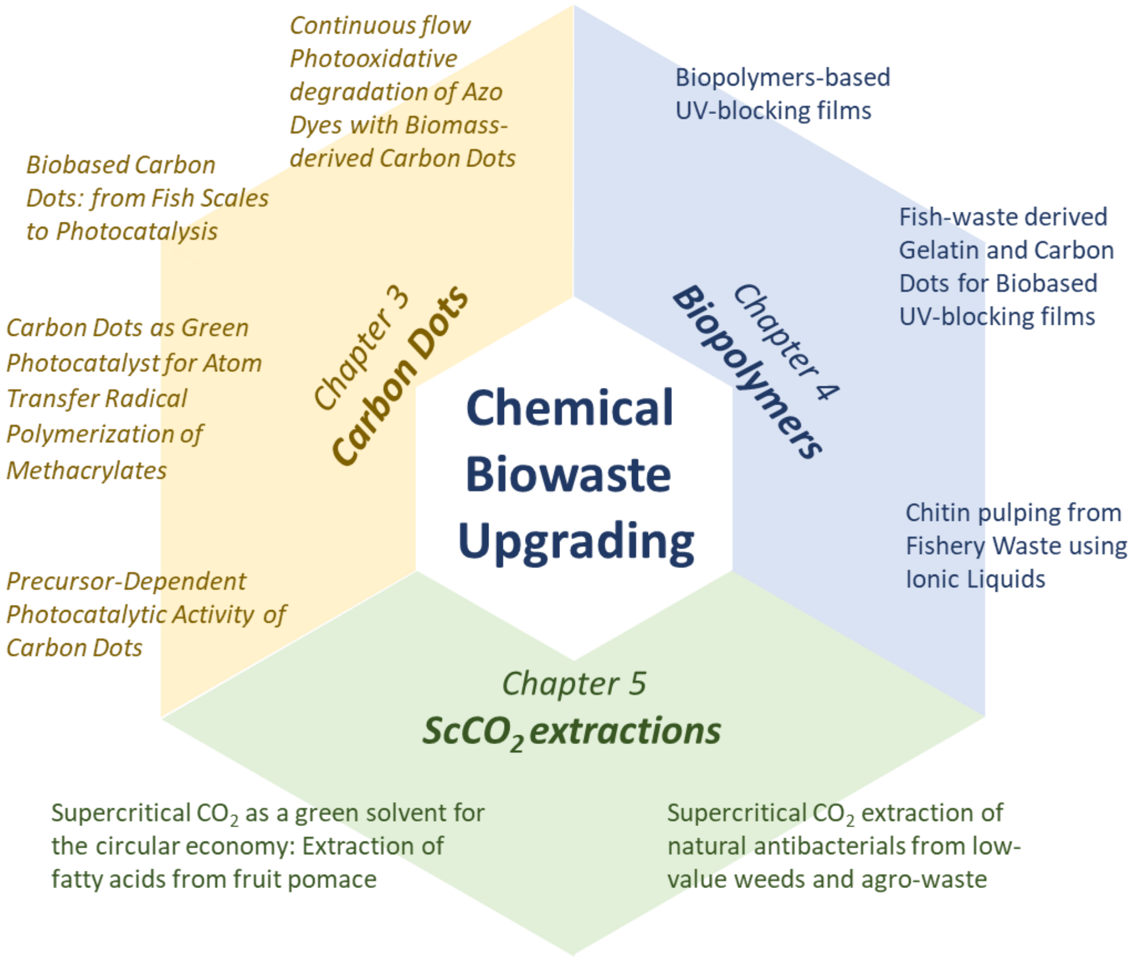

Figure 2.1. Schematic representation of the structure of this work of thesis.

3. Carbon Dots

Carbon Dots (CDs) are carbon nanoparticles discovered in the early 2000s by chance from the purification of single walled nanotubes. These nanoparticles have, nowadays, gained more and more interest in many different fields thanks to their unique properties: they are biodegradable and biocompatible, water soluble, non-toxic, easy to functionalise and possess a tunable fluorescence. Among the fields of utilization of CDs, photocatalysis appear as a promising area for the exploitation of their luminescence. This chapter revolves around the synthesis of CDs, from biobased molecules and from waste biomass, their characterization and their application as photocatalyst for the photoreduction of methyl viologen, the photopolymerization of methacrylates and the photodegradation of azo dyes.

3.1 Introduction: nanomaterials

The field of nanotechnology is considered to be one of the most promising of modern chemistry and materials research. Anyway, nanomaterials have been used and exploited for their unique properties since ancient times: more than a thousand years ago, for example, gold nanoparticles were used as inorganic red dye in Chinese porcelains.[1] The first time that the term "nanomaterial" was used, dates to 1959 during the famous lecture of Richard P. Feynman "There's Plenty of Room at the Bottom",[2] considered, for this reason, one of the fathers of nanotechnology. In his lecture, the Nobel prize hypothesized that the nanoscale can be small enough for extreme minimization but, at the same time, large enough to arrange structural complexity and raise interesting properties. Since then, numerous researchers put their effort to synthesize, characterize and apply a plethora of different classes of nanomaterials. To date nanomaterials are defined as materials that possess at least one dimension that is lower than 100 nm.[3] This dimension, called as a consequence nanoscale, was chosen as threshold after the observation that, under this value, new properties are observed in the material, such as new optical (e.g. fluorescence[4]) or physical properties (e.g. change in melting point or in conductive properties[5]). Different classes of nanomaterials are defined based on the number of dimensions that are in the nanoscales: nanoplates (only one dimension < 100 nm), nanofibers (two dimensions < 100 nm) and nanoparticles (NPs, all dimensions < 100 nm). Another distinction is made by looking at the composition and choice of the starting materials, dividing them in two families: metals or carbon-based. The first studied and applied family has been the one of metal nanomaterials. An example is given by gold NPs widely known for their versatility and applied in a variety of fields from sensors[6] to drug delivery.[7] Another representative case is titanium dioxide NPs that are nowadays one of the most diffused and used nanomaterial, finding applications that space from the food and personal care industry[8] to photocatalysis[9] and utilization in electronic devices.[10] However, the use of metal-based nanomaterials gave raise to questions related to their toxicity and possible accumulation in living organism or in the environment. For this reason, carbon-based nanomaterials emerged as a possible substitute thanks also to their high versatility. Besides the richness and diversity of carbon, indeed, carbon nanomaterials present outstanding thermal, chemical, mechanical and electrical properties. The discovery of these materials (see **Figure 3.1.1**) started in 1985 with the finding of fullerenes by Kroto, Curl and Smalley that proposed the formation of highly symmetrical molecules with 60 carbons at the vertices of a regular truncated icosahedron.[11] In the following years, a variety of other fullerenes were synthesized by changing the number of carbons or derivatizing their surface. Up to date, fullerenes are used in a great number of applications thanks, principally, to their high superconducibility.[12,13] In 1991, the discovery of carbon nanotubes gave again more interest to the field of carbon nanomaterials due to their incredible properties such as a thermal conductivity higher than diamond[14] and a high thermal stability.[15] Carbon nanotubes have the length > 100 nm and can have walls formed by a single or multi-layer of one-atom-thick sheets of carbon (single-walled nanotubes SWNTs or multi-walled nanotubes MWNTs). These discoveries, followed by the isolation of graphene in 2004 by Novoselov and co-workers[16] (for which he was awarded the Nobel prize in 2010 together with Geim), provided new possibilities in the physic and chemistry of carbon nanomaterials raising still more the interest in this field. In addition, always in 2004, carbon dots (CDs) were discovered as a new class of carbon nanomaterials from the purification of nanotubes.[17] In particular, one of the purification fractions resulted to be fluorescent and small nanoparticles were detected in it. The origin of the fluorescence was ascribed to the presence of these spherical NPs, afterward called carbon dots. After that, CDs gained an impressive attention in the scientific community, a great number of synthetic methods has been developed and their composition and characteristics are still a topic of interest.

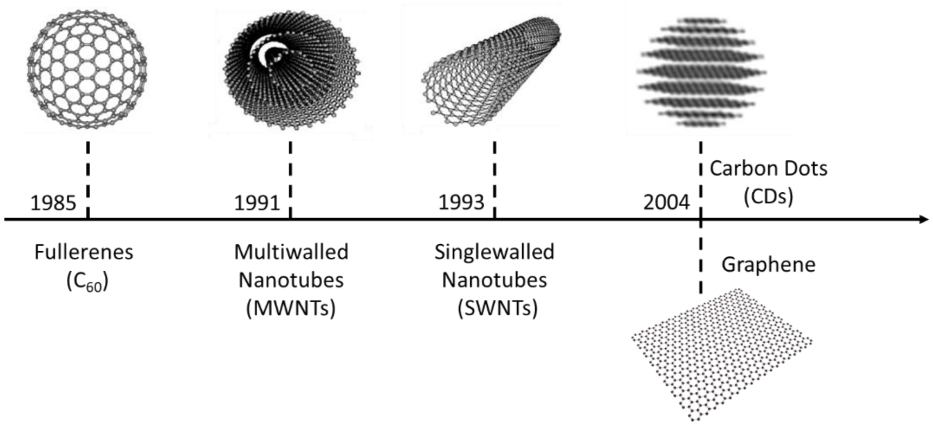

Figure 3.1.1 Short timeline of the discoveries concerning carbon-based nanomaterials.

In general, CDs are defined as carbon NPs with a diameter lower than 10 nm, a spherical shape and a highly functionalised surface. CDs have some unique properties such as high water solubility, non-toxicity, biodegradability, tunable fluorescence, ease of modification and chemical stability. Due to these characteristics, their applications vary in different fields: from the biomedical (e.g. bioimaging[18] and drug delivery[19]), to the production of sensors,[20] optoelectronic devices[21] and photocatalysis.[22] Along with these properties, CDs could be synthesized from a wide range of precursors, including cheap and abundant materials, such as biowaste, and with low-cost techniques, making them very appealing to replace other more expensive materials.

3.1.1 Synthesis

Lately a large number of different techniques have been developed in order to synthesize CDs starting from a wide range of different carbon precursors. These synthetic pathways can be divided in two main families, namely the Top Down approaches and the Bottom Up ones, depending on the choice of the starting material. The Top Down methods involve the breakage of large carbogenic structures (graphite, graphite layers, carbon nanotubes and so on), while in the Bottom Up the carbon NPs are obtained by carbonization of small organic molecules (see **Figure 3.1.2**).

Among the Top Down methods arc-discharge, laser ablation and electrochemical oxidation can be named. Arc-discharge was the first technique developed for the preparation of CDs but it is nowadays dismissed due to the high concomitant formation of impurities.[17] Laser ablation, instead, is widely used due to the ease in the control of size and morphology of the NPs by varying the pulsed laser width. However, the most spread Top Down approach for the preparation of CDs is the electrochemical oxidation. This technique, indeed, allows to obtain carbon NPs with high purity and yields, low costs, a good reproducibility and an extreme ease of manipulation regarding the size.

Despite the up-cited advantages of the Top Down methods, Bottom Up synthetic pathways are still the most spread and used. This is mainly due to the simplicity of the procedures and apparatus and to the possibility to use a wide range of precursors to tune the final properties of the nanomaterials. With these methods, the initial carbon precursor is treated for prolonged time at high temperatures and, undergoing dehydration or decarboxylation, it generates the aromatic network characteristic of CDs. Furthermore, the variation of the reaction parameters, can lead to amorphous or graphitic materials, allowing to achieve different properties in terms of fluorescence and reactivity (see **Chapter 3.2**). Among the Bottom Up synthesis, acid oxidation, microwave treatment and thermal-hydro/solvothermal method can be found. The microwave treatment is one of the most common methods to prepare CDs because of short reaction times, uniform size of the NPs and high yields. Anyway, the thermal-hydro/solvothermal approaches are the most widely used to date, due to their low cost, easy feasibility, environmental friendliness and possibility to use various carbon sources also from renewable origins. For these reasons these methods have been employed in this work of thesis. In particular, the thermal approach, or pyrolysis, involves the direct carbonization of the precursors in absence of any solvent. Relatively high temperatures between 200 and 400 ° C and long reaction times (24-100h) are normally required. The solvothermal and hydrothermal approaches, on the other hand, involve the carbonization of the organic molecules dissolved in an organic solvent or in water in an autoclave. In this case temperatures cannot exceed a certain threshold (usually around 140-200 ° C) due to the pressure restrictions of the apparatus. These synthetic pathways are very simple, and the choice of the suitable precursors is wide. In addition, this procedure allows to easily dope the CDs employing a multicomponent approach or using directly a carbogenic precursor that contains the desired heteroatom.

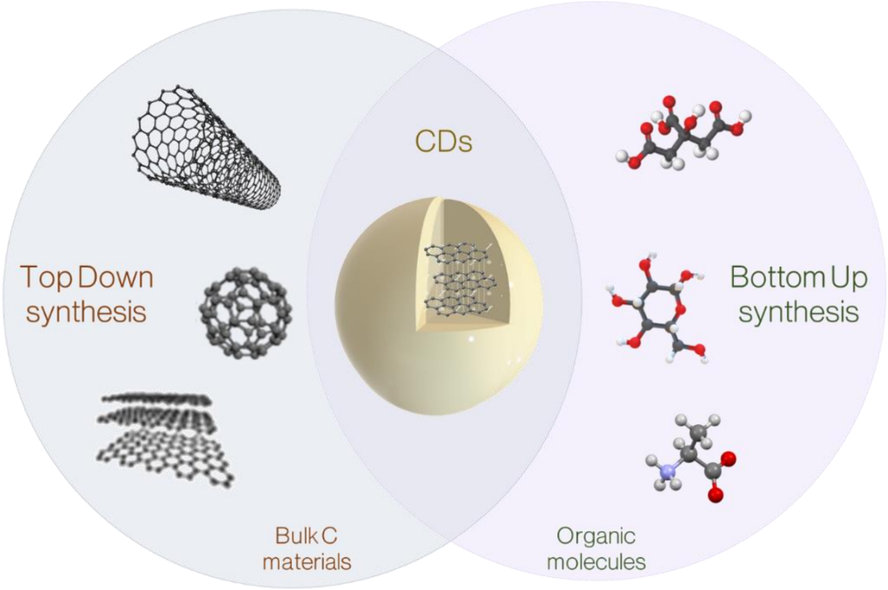

Figure 3.1.2 Schematic illustration of the two families of synthetic methods for the preparation of CDs.

3.1.2 Structure

As stated above, CDs are spherical nanoparticles with a carbogenic core and a surface that can present organic functional groups (hydroxyls, carbonyls, carboxyls…), molecular fluorophores and defects (see **Figure 3.1.3**). These NPs are mainly composed by carbon, hydrogen and oxygen and their ratio depends both on the carbon precursor and on the adopted synthetic method. In order to obtain CDs with different properties, other elements can be introduced during the synthesis. The most used doping atom is nitrogen that is known to increase the quantum yield (QY = number of emitted photons on number of absorbed photons %).[23,24] Other examples can be given by sulfur that helps widening the band-gap[25] and phosphorous that can yield green-emitting NPs important for bioimaging applications.[26] Concerning the morphology of the carbogenic core, it has been demonstrated that CDs can have a graphitic or amorphous nucleus depending on the synthetic method and reaction conditions. In general, the carbon NPs obtained from Top Down methods possess a highly crystalline core with well defined layers while, the morphology of CDs produced with Bottom Down approaches is still an open issue. For this reason, several studies have been conducted in the last years, to have a better comprehension on the structure of CDs and on how the synthetic procedure can affect this aspect. From a general point of view, however, CDs are composed by a graphitic-like carbogenic core, amorphous compounds and small molecular-like fluorophores. To better understand the differences between these three main components the term “degree of carbonization” has been introduced to quantify the efficiency of the conversion of the molecular precursors in the graphitic-like core. Summing up, it can be stated that using the hydro/solvothermal method is possible to produce more amorphous materials together with organic fluorophores, that guarantee high QY and tunable fluorescence, while using harsher conditions, like in the pyrolytic treatment, CDs with a more graphitic structure and surface defects can be obtained. The Top Down approaches, instead, usually yield graphitic nanoparticles.

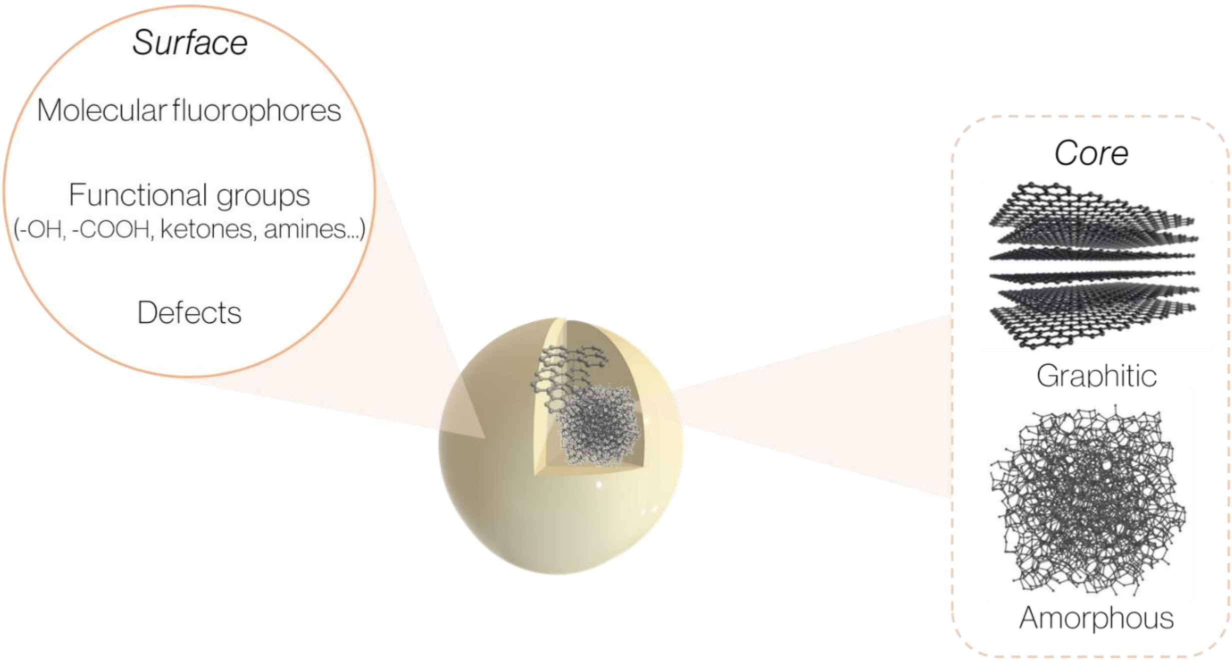

Figure 3.1.3 Pictorial representation of the structure of CDs.

3.1.3 Properties: photoluminescence

Among the numerous properties of CDs, one of the most fascinating and exploited behaviour is their luminescence. Concerning absorption and fluorescence, CDs have some optical similarities despite the variety of possible structures. Typically, CDs present a strong absorption in the ultraviolet (UV) region of the light spectrum, with a tail that extend to the visible range. Generally, a peak around 230 nm is ascribed to the π-π^* transition of the aromatic C-C bonds of the carbon core, while a less intense shoulder around 300 nm can be attributed to the n-π^* transition of C=O bonds or other related groups.[27] Furthermore, the functional groups on the surface can contribute too to the absorption of the nanomaterials and, some deviations in absorption spectra can indicate differences in the composition or structure of different hybridization derivatives. Concerning the photoluminescence (PL) properties, it can be generally stated that the emission spectra of CDs are approximately symmetrical on the wavelength scale, with wide peaks and large Stokes shifts if compared to organic dyes. Carbon nanoparticles normally have an excitation wavelength-dependent behaviour that can be the result of a wide distributions of differently sized dots and surface chemistry, different emissive traps or other mechanisms that are still unclear.[28] The majority of CDs demonstrate a good photostability thanks to a carbon core-based PL[29] but, when molecular state emission is prevalent, the PL intensity can decrease dramatically after UV exposure.[30]

The origins and the mechanisms of CDs PL are, however, still unclear and remain an open debate. To date, three respectable PL mechanisms have been confirmed: the quantum confinement effect, determined by the carbon core; the surface state due to the hybridization of the carbon backbone and functional groups; the molecule state, determined solely by molecular fluorophores.[31]

The quantum confinement effect can be defined by the dependence of the HOMO-LUMO gaps (highest occupied molecular orbital - lowest unoccupied molecular orbital) on the size of the graphitic fragments: as the size of the fragment increases, the bandgap gradually decreases. In other words, this effect is determined by the degree of π conjugation and by the presence and size of the graphitic core. The emission band that derives from this contribution results, in summary, to be size dependent, excitation independent and very narrow. Anyway, the absorption in CDs is different from the typical semiconductor quantum dots where a strong quantum confinement is observed (changing the size of the NPs, the bandgap changes and as a consequence also the absorption/emission wavelength). Indeed, clear evidence of real quantum confinement in CDs is yet to be univocally demonstrated and this subject is still largely controversial. Some studies concluded that the expansion of the carbon core has a major effect on the absorption characteristic of CDs rather than the actual expansion of their physical dimensions.[32,33]

Concerning the emission related to surface states (namely surface defects and functional groups), it is important to underline that functional groups have various energy levels that may results in a series of emissive traps that can dominate the emission. In addition, it must be highlighted that the surface state does not consist of isolated chemical groups but rather the hybridization of the carbon backbone and connected chemical groups. The emission that derives from this mechanism does not have a well-defined behaviour and is strongly dependent on the synthetic procedure. Even though it has been stated that the origin of the fluorescence of CDs is not completely clear, there are some evidences that the emission derives both from an intrinsic band gap (deriving from confined sp^2 conjugation in in the core) and an extrinsic one that results from a surface state and that can be directly excited or excited by energy transfer from the intrinsic band. For this reason, the luminescence of CDs can be tuned by either control of the sp^2 domain size or by modifying the chemical groups on the surface of the NPs.

The third possible PL mechanism in CDs is due to molecule state that is formed solely by an organic fluorophore that can be connected on the surface or interior of the carbon backbone and can directly exhibit PL emission. The molecule state results to be the emerging PL center especially in CDs prepared via Bottom Up routes. With these methods, indeed, small molecular fluorophores can be formed thanks to the lower temperatures while, as the carbonization temperature increases, the carbogenic core is formed by dehydration of the precursor or consumption of the formed fluorophores. This luminescence resulted to be strong and with high QY, excitation-independent and with a very broad emission band.

Summing up, so, the PL of CDs is the result of cooperative synergistic effects between the graphitic carbon core, the surface defects/functional groups and the molecular fluorophores as theorized by Fang et al. (see **Figure 3.1.4**).[34] In particular, under UV light irradiation, the fluorophores can generate excited electrons (process a). As a consequence, the electron in the π^* orbital may recombine with the holes in the π orbitals directly (process b) or they can be trapped by the lower energies defect states (process c). At the same time, some electron can be directly excited and trapped by the defect states (process d). The electrons that are in the defect state can relax through a radiative (process e) or non-radiative way (process f). The carbon core can act then as a quencher of the radiative relaxation pathways through a fluorescence resonance energy transfer (FRET, process g) thus lowering the QY. Concluding, if the PL spectra depends more on defect states and fluorophores, the magnitude of the QY is principally affected by the graphitic core of the nanoparticles.

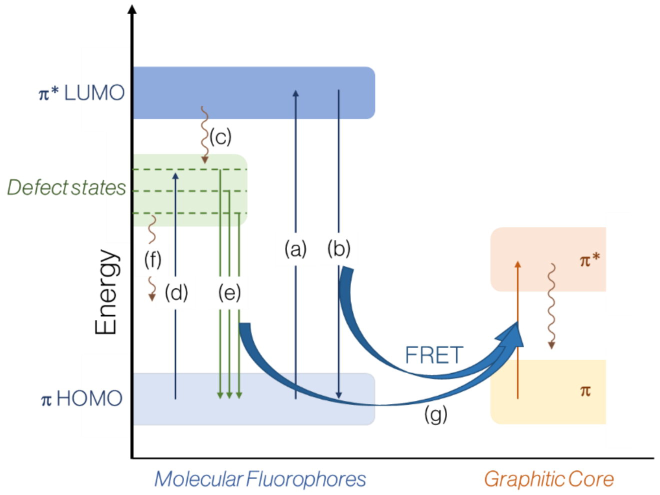

Figure 3.1.4 Proposed photoluminescence mechanism in CDs.

However, also if this PL mechanism can be satisfactory from an intuitive level, many other issues are still not effectively addressed and a real understanding on the fluorescence of these materials remain unresolved to date.

3.1.4 Applications: photocatalysis

The unique properties of CDs allowed their employment in many different applications such as chemical, medical and optoelectronic ones [35] or for the preparation of CDs-incorporated nanodevices.[36] In this work of thesis, CDs have been exploited as photocatalysts due to their great potential as light harvesters and their ability to act both as electron donors and acceptors. In particular, when involved in photochemical reactions, CDs can act in three different ways: as a photocatalyst, as a photosensitizer and as electron mediator.

Photocatalysis is commonly defined as the "change in the rate of a chemical reaction or its initiation under the action of ultraviolet, visible or infrared radiation in the presence of a substance (called photocatalyst) that absorbs light and is involved in the chemical transformation of the reaction partners".[37] Carbon nanoparticles are able to absorb light by direct absorption: the photons generate electron/hole pairs exciting electrons from the HOMO to the LUMO. The as formed e^-/h^+ pair results then in the chemical transformation of the reagents rendering CDs effectively photocatalyst (**Figure 3.1.5**).[38] In general, the photocatalytic process based on CDs follows three stages: firstly, the absorption of light generates e^-/h^+ pairs; secondly; the separation and transfer of the e^-/h^+ pairs contribute to the formation of reactive species; lastly, the reactive species lead to the photocatalytic reactions.[39] It must be noted that the rapid recombination rate of e^-/h^+ pairs can limit severely the photocatalytic activity of CDs.

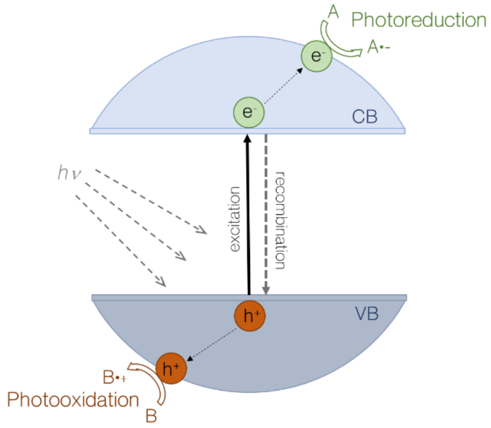

Figure 3.1.5 Schematic representation of the generation of the electron/hole pair in CDs.

The π-π^* transition of the sp^2 C=C double bonds render the CDs able to absorb light in the UV range, while the plethora of surface functional groups usually contribute to the absorption in ranges more shifted towards the visible due to the n-π^* transitions.[40,41,42] It is worth mentioning that, thanks to the similar C=C structure, also other carbon-based materials (e.g. graphene oxide, carbon nanotubes, multilayer graphene etc.) possess the ability to absorb in the UV-Vis range.[43] However, CDs demonstrate to have some more advantages such as their aqueous solubility, ultrasmall size and ease and cheapness of their synthesis. The light absorption in the UV range, anyway, is not always beneficial for photocatalysis and a great number of recent studies have been concentrated on the red shift to near infra-red region of the absorption of CDs.[44,45]

Photosensitization, on the other hand, is identified as the "process by which a photochemical alteration occurs in one molecular entity as a result of initial absorption of radiation by another molecular entity (photosensitizer)".[37] Common photosensitizers are organometallic complexes (with electron-rich metals such as iridium, ruthenium and rhodium) or aromatic hydrocarbons, both containing easy excitable electron and a large continuum of orbitals within both HOMO and LUMO that allows the excited electrons to switch multiplicities via intersystem crossing prolonging the lifetime of the excited state, necessary for the photosensitization process.[46] During this process, the photosensitizer absorbs light to move to an excited energy state. In the case of CDs, for example, this excited energy can transfer some excitation energy to an external entity, such as absorbed molecular oxygen. With this energy, the molecular oxygen (normally present in triplet ground state ($^3O_2$) can be transformed into the highly reactive singlet oxygen ($^1O_2$). Another possible process implies the transfer of excited electrons to oxygen with its conversion into reactive superoxide specie ($O_2^{\bullet-}$) but, in this case, the process of photosensitization is closely related to photocatalysis (see **Chapter 3.5**) while the production of singlet oxygen is exclusive of the photosensitization pathway. The photosensitizer action of CDs has been demonstrated in numerous researches and it is due to the presence of highly delocalized electrons and of additional energy levels between HOMO and LUMO.[47]

As last, CDs can act as electron mediators thanks to their bivalent redox character. Upon excitation, indeed, these NPs can act as electron acceptors or donors depending on their surface functionalities. Electron accepting properties in CDs are due to extensive π-networks in their core and they come in hand where efficient charge separation is needed.[48,49] In addition, CDs are able to accept photogenerated electrons from a semiconductor preventing the electron-hole recombination and leading to improved photocatalytic efficiency.[50] A manipulation of these properties can be achieved through the addition of electron-donor and electron-acceptor groups on CDs that lead to changes in the HOMO and LUMO energy levels.[51]

Surprisingly, to date, the use of sole CDs in photochemical reaction is still not well spread but, they are usually employed in combination with other materials and semiconductors. A clear and complete understanding on the properties, behaviour and characteristics of these carbon NPs is, indeed, fundamental to achieve efficient processes.

3.2 Precursor-Dependent Photocatalytic Activity of Carbon Dots

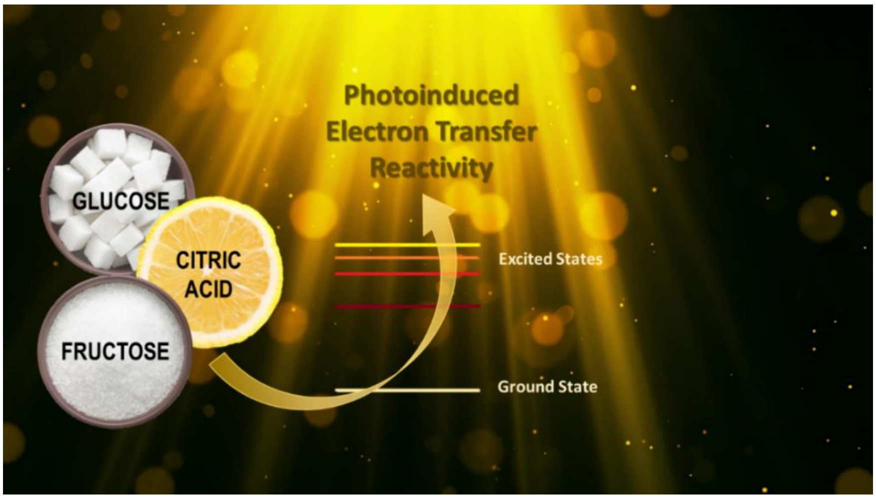

The investigation on Carbon Dots performed during this work of thesis, started with a preliminary study on the influence of precursor and synthetic method on the properties of the nanoparticles. This allowed us to widen our knowledge on the topic and then, to further explore the possibilities on the preparation of the carbon nanomaterials from biobased molecules/waste biomass and their application in photocatalysis. The results reported in this chapter have been published in E. Amadio, S. Cailotto, C. Campalani, L. Branzi, C. Raviola, D. Ravelli, E. Cattaruzza, e. Trave, A. Benedetti, M. Selva and A. Perosa, *Molecules*, **2020**, 25, 101. doi:10.3390/molecules25010101. [52]

In this study the morphological and optical features and the photocatalytic ability of a series of CDs, graphitic and amorphous prepared via bottom up techniques from fructose, glucose and citric acid, were compared. It has been demonstrated that the carbon precursor and the synthetic pathways influence diversely the structural and optical properties of the nanoparticles that, as a consequence, affect unpredictably their photo electron transfer (PET) ability. The photoreduction of methyl viologen (MV) has been used as a standard reaction to evaluate the PET capability of the synthesized CDs. Generally, citric acid-CDs provided the best photocatalytic performance followed by fructose- and glucose-CDs. Anyway, while for glucose and citric acid-derived NPs the graphitization favoured the reaction, a reverse dependence was observed for fructose-CDs. In this case the formation of large graphitic-like supramolecular assembly seemed to diminish the PET ability towards MV reduction. This chapter highlights the complexity of a design of CDs in advance to produce effective photocatalytic systems.

3.2.1 Introduction

As stated in the general introduction, CDs has drawn great attention in a wide range of applications comprising photocatalysis, thanks to their luminescence properties. Despite their remarkable light harvesting capacity and their ability to act both as electron and donor of electron, CDs are still under-explored for their use as sole photocatalysts. Indeed, the most reported photosystems exploit the co-presence of CDs with metal complexes or enzymes as redox mediators.[39,53,54,55] In order to achieve a real breakthrough in the utilization of CDs, an accurate design of these carbon NPs is needed since their luminescence properties are known to be structure dependent.[56,57,58,59] In particular, high photoluminescence has been observed in amorphous CDs synthesized under mild hydrothermal conditions, while the graphitic CDs usually show lower fluorescence. These evidences have been explained with the presence of molecular-like fluorophores and doping heteroatoms in the amorphous CDs that are able to enhance the luminescence.[25,60] On the other hand, the graphitic core of the CDs obtained with harsher conditions (e.g. with pyrolysis), can act as a quencher via the FRET mechanism.[34] Indeed, the degree of carbonization and the structure of CDs can influence their photocatalytic performances. An example has been given by Shi et al. that demonstrated how the photoreduction of methyl viologen was affected by the quinonic precursor employed from the authors in the multicomponent synthesis of amorphous nitrogen doped CDs.[61] However, a general and non-ubiquitous correlation between the structure of the nanomaterial and its photoactivity could not be highlighted because of the great variability in synthetic methods, carbon precursors and choice of doping agents. In this study we propose to evaluate the influence of the carbon source (citric acid, fructose and glucose) on both the structural features and photocatalytic activity of six different types of CDs with the aim to explore new synthetic procedures for the preparation of carbon nanomaterials suitable for photocatalytic applications.

3.2.2 Synthesis and Characterization

Six different types of CDs were prepared using two different synthetic pathways (hydrothermal synthesis and pyrolysis) and three sets of precursors (glucose Glu-, fructose Fru- and citric acid Cit-). In particular, amorphous CDs (a-CDs) were obtained with the hydrothermal procedure while graphitic ones (g-CDs) from the pyrolysis. The synthetic procedures are reported in detail in the Experimental section; in brief a-Cit, a-Glu and a-Fru were synthesized with a hydrothermal treatment from citric acid, glucose and fructose (autoclave, 24h, 180-200 °C)[62,63] and have been obtained as amorphous nanomaterials composed of poorly defined carbonaceous structures and light molecular-like carbonaceous compounds. On the other hand, graphitic g-Glu and g-Fru were synthesized for the first time using a harsh thermolysis (24h, 200 ° C) of neat glucose or fructose, following the already published procedures used for the preparation of the graphitic one based on citric acid (g-Cit).[62] From the ^{1}H NMR and ^{13}C{^{1}H} NMR analysis, that gave silent spectra, it was possible to underline the absence of any molecular species suggesting the presence of NMR inactive nano-carbonaceous materials.

The morphological and optical properties of the prepared nanomaterials were then characterized via high resolution transmission electron microscopy (HR-TEM), scanning electron microscopy (SEM), Fourier transform infrared spectroscopy (FT-IR), X-ray photoelectron spectroscopy (XPS), photoluminescence (PL) and ultraviolet-visible spectroscopy (UV-Vis) and time-resolved PL measurements.

As can be noticed from **Figure 3.2.1**, from the HR-TEM micrographs it was possible to understand that the synthetic pathway affected the morphology of the NPs. In particular, from the hydrothermal treatment, low density and amorphous CDs with a poorly defined structure were obtained: a-Glu, a-Fru and a-Cit, resulted to have an irregular shape and dimensions that range from 9 to 12 nm (see **Figure 3.2.1** a, b and c). Concerning the graphitic NPs, two different behaviours were observed. g-Glu and g-Cit were well-dispersed nanoparticles with a quasi-spherical shape and diameters around 7-9 and 2-5 nm respectively (see **Figure 3.2.1** d and f). The carbon nanomaterials obtained from fructose, instead, resulted to have a different structure: both HR-TEM (see **Figure 3.2.1** e, and **Figure 3.2.2** d, e and f) and SEM (**Figure 3.2.2** a, b and c) revealed the formation of supramolecular aggregates of graphene-like multi-layered crystalline sheets with a wide range of dimensions ranging from 0.5 and 1.5 μm. Additionally, from the selected area electron diffraction (SAED) pattern it was highlighted the single crystalline nature of the multilayer system with the expected six-fold symmetry (**Figure 3.2.2** i).[64,65] The HR-TEM micrographs acquired in the areas where more layers were superimposed revealed the presence of extended crystalline areas (**Figure 3.2.2** g and h).

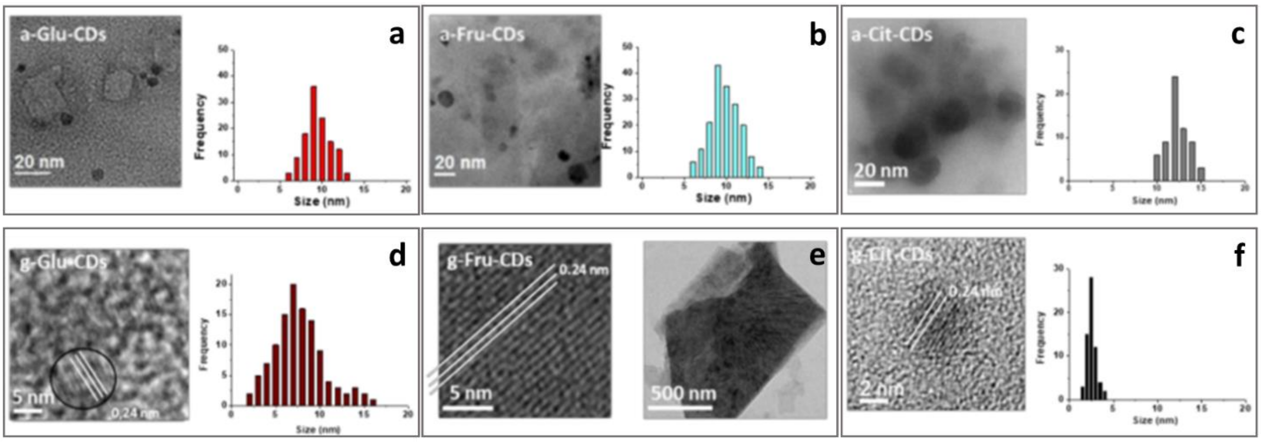

Figure 3.2.1 HR-TEM micrographs of the synthesized CDs and average size distribution.

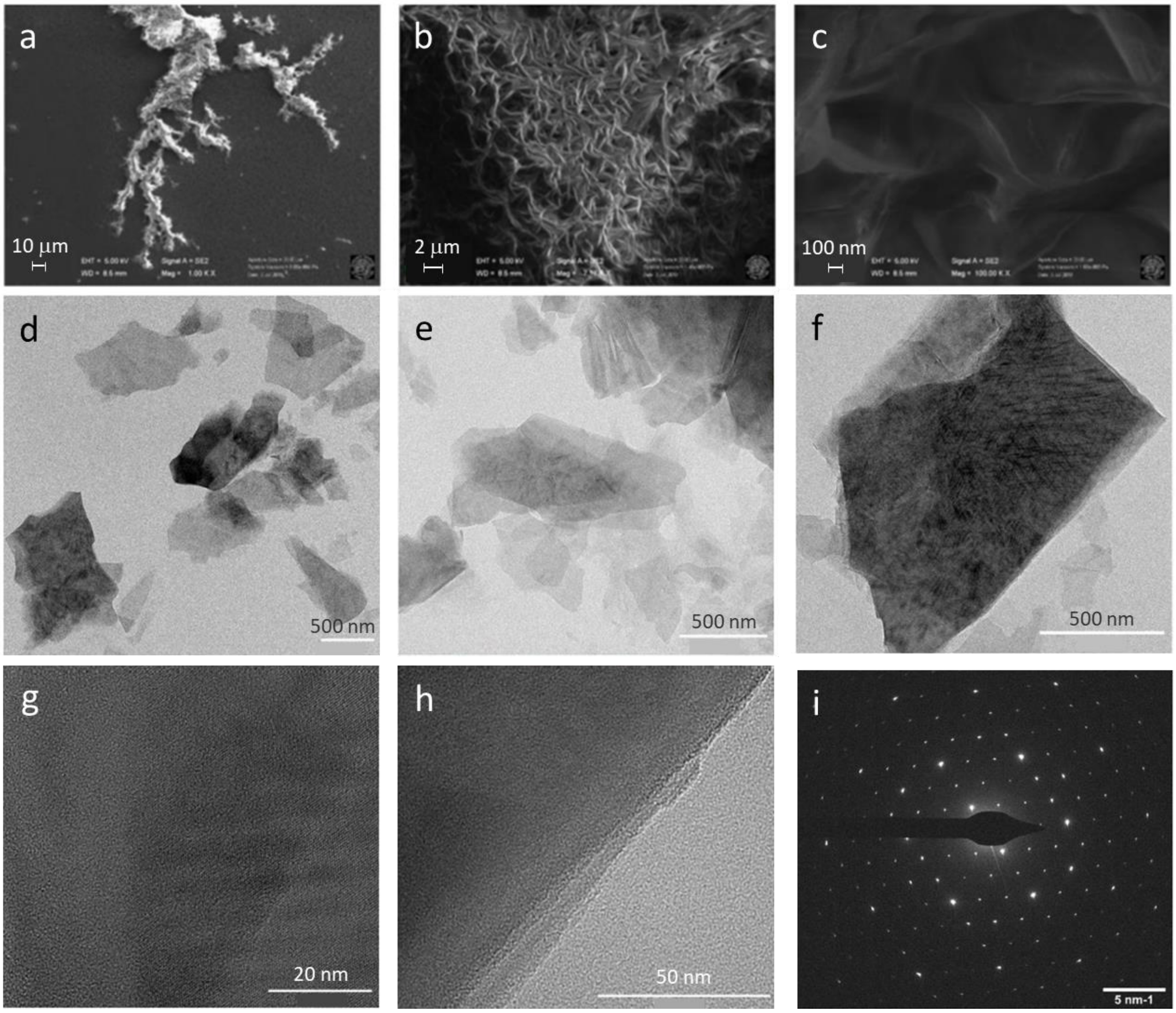

Figure 3.2.2 Morphological characterization of the graphitic CDs based on fructose at increasing magnifications. a, b and c = SEM images at increasing magnifications; d, e and f = HR-TEM micrographs; g and h = extended HR-TEM micrographs; i = SAED pattern.

The thermal decomposition of the carbon precursors caused structural differences in the graphitic CDs. As shown in **Figure 3.2.3**, it is worth mentioning that citric acid decomposition follows a known scheme that consists of the breakdown of the substrate into citraconic and itaconic anhydrides that act then as the effective precursors for Cit-CDs.[62] The two monosaccharide sugars, instead, follow a different pathway: formic acid was mainly detected during the thermal decomposition of fructose while acetic acid was revealed during the glucose breakdown pathway.[66] However, the carbonaceous core of the dots it is probably formed by the presence of other carbonaceous intermediates such as hydroxymethylfurfural, a well-known intermediate in the hydrothermal carbonization of saccharides.[67,68] Hence, the different decomposition mechanisms can affect on a certain extent the final morphology of the carbon nanoparticles. Reasonably, the higher is the reactivity of the precursors, the easier and larger is the formation of carbonaceous nanomaterials.

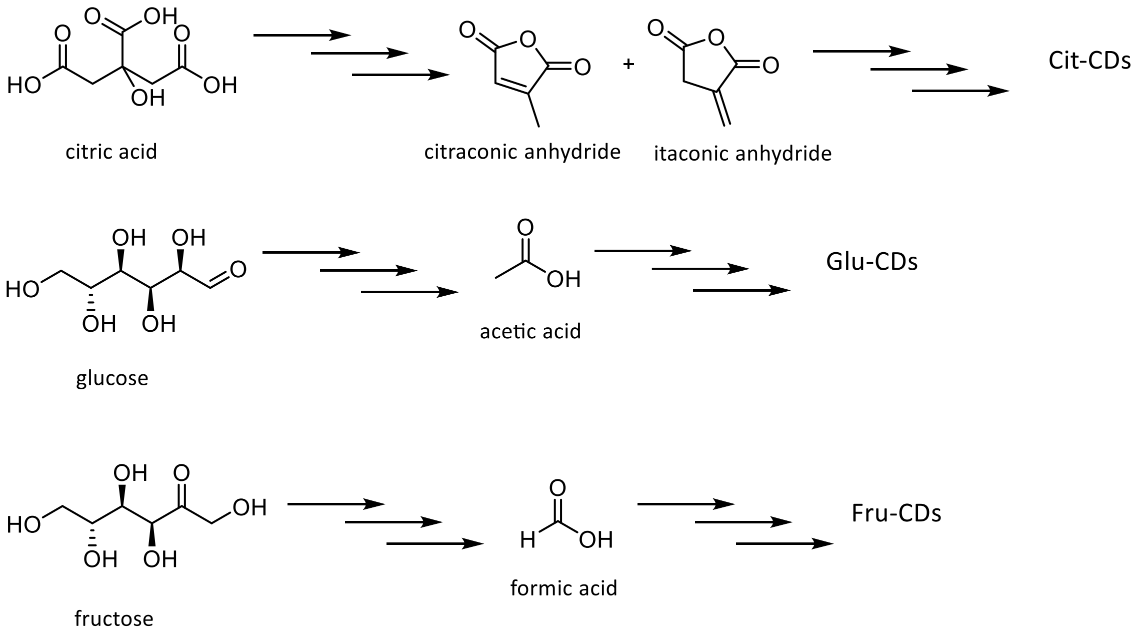

Figure 3.2.3 Intermediates of the thermal decomposition of citric acid, glucose and fructose during the preparation of CDs.

The pyrolytic synthetic pathway has been followed by ^{1}H NMR (see **Figure 3.2.4**) to understand the velocity of the carbonization of citric acid, glucose and fructose and different decomposition kinetics were observed. Concerning Cit-CDs, it was noticed that the signals relative to the precursors (citric acid but also citraconic and itaconic anhydrides) disappeared completely only after 4h of pyrolysis. On the other hand, glucose was not fully degraded after 4h and, in opposition, when fructose was used as the carbon source, the signals of the reagents disappeared within the first 60min, giving evidence of the formation of NMR inactive nanostructures. The high reactivity of fructose towards the thermal decomposition, reasonably led to the formation of the extended graphitic domains observed with the microscopy analyses. The pyrolytic decomposition of the reagents, therefore, followed the following order: fructose >> citric acid > glucose.

To better understand the composition and the nature of the functional groups on the surface of the CDs, FT-IR and XPS analyses have been performed. From the FT-IR spectra (see Appendix **Figure A.3.2.1**) no substantial differences between the six NPs were revealed. Indeed, the presence of carboxylates as most present surface functionality, and of sp^{2} carbons were highlighted in all the spectra. In addition, all the CDs showed a strong and broad absorption band around 3500-300 cm^{-1}, due to hydroxyl groups, a weak peak around 2900-2800 cm^{-1} characteristic of -C-H bonds, a band at 1800-1600 cm $^{-1}$ for carbonyls and carboxyls, another one around 1600-1400 cm^{-1} due to C=C and a signal around 1200 cm^{-1} due to C-O-C functional groups.

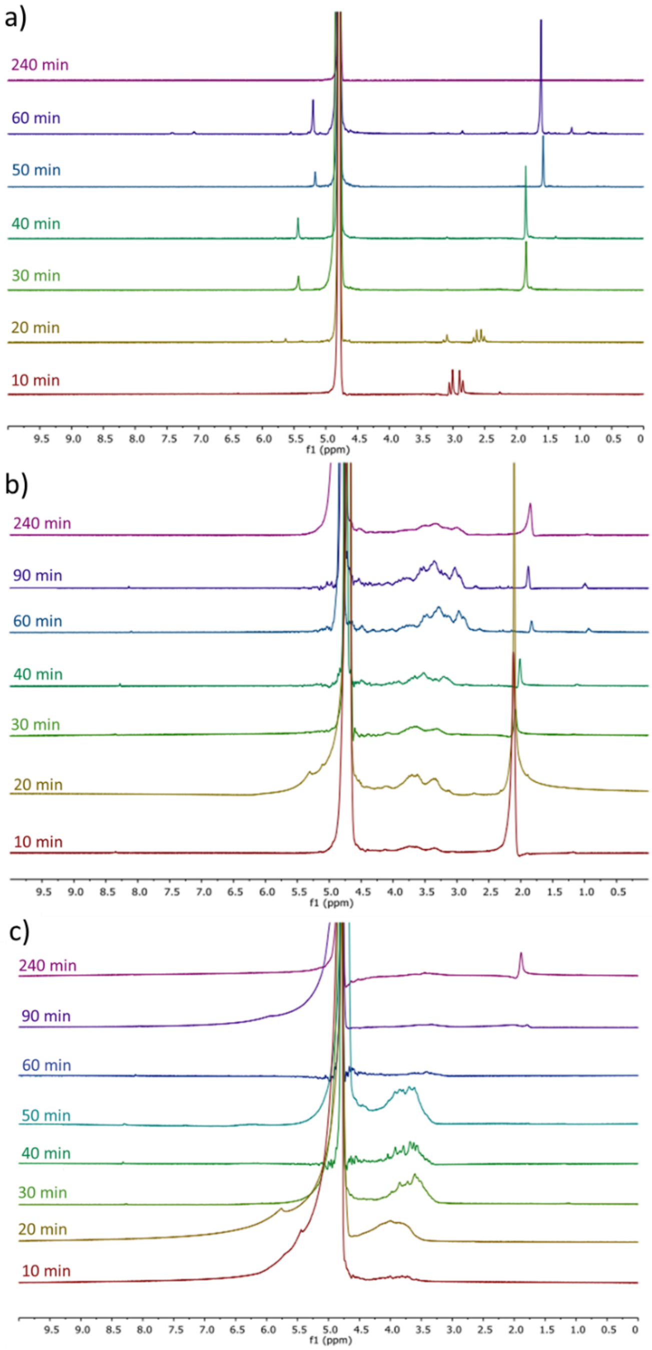

Figure 3.2.4 ^{1}H NMR in D_2O of the pyrolysis reaction mixture at different times. a = citric acid; b = glucose; c = fructose.

Anyway, from the XPS analysis (**Figure 3.2.5**), it was possible to observe some structural and compositional differences on the synthesized CDs. Indeed, although all samples showed the presence of three strong peaks in the C1 bands (284.6, 286.2 and 288.6 eV) relative to C=C, C-O and C=O, some variations were highlighted. In particular, the C=C signal was predominant in citric acid- and fructose-derived CDs while the peak relative to C-O was the most present in glucose-CDs. Additionally, the C-O band, that can be representative of the oxygen content in the nanoparticles, markedly decreased after the pyrolytic treatment of citric acid and fructose underlining the formation of crystalline structures with predominant graphitic carbon sp^2 and a lower content of carboxyl groups in respect to glucose-CDs.

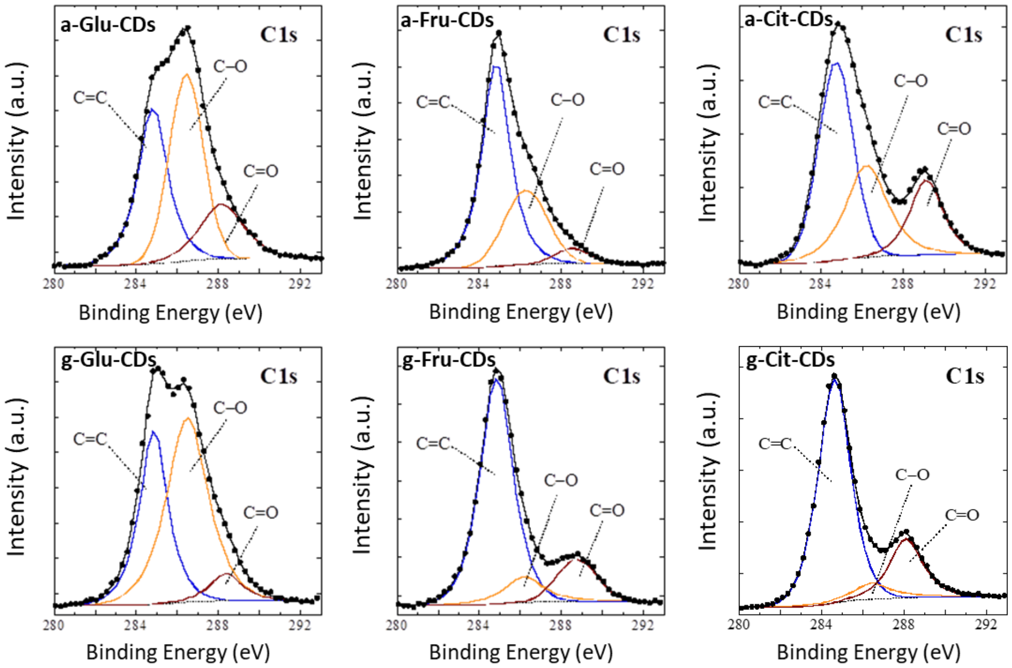

Figure 3.2.5 C1 XPS spectra of all CDs samples; the binding energy (BE) was corrected for surface charging.

From the optical point of view the nanomaterials have been characterized with PL-PLE and UV-Vis spectroscopy, time resolved PL and with the calculations of the quantum yield (QY). From the photoluminescence (PL) spectra (**Figure 3.2.6**) an emission quasi-independent from the excitation centered at 450 nm was observed for glucose- and fructose-based CDs (both amorphous and graphitic ones). On the other hand, analysing the Cit-CDs, a complex mixture of excitation-dependent emission bands was highlighted with a maximum ranging from 420 and 500 nm. Additionally, for the graphitic CDs derived from citric acid (g-Cit-CDs), another sharp band was noticed at 385 nm with only a slight influence by the excitation wavelength. The presence of this band is reasonably due to the crystalline nano-core. The respective photoluminescence excitation (PLE) spectra registered at different emission wavelength are reported in the Appendix (**Figure A.3.2.2**).

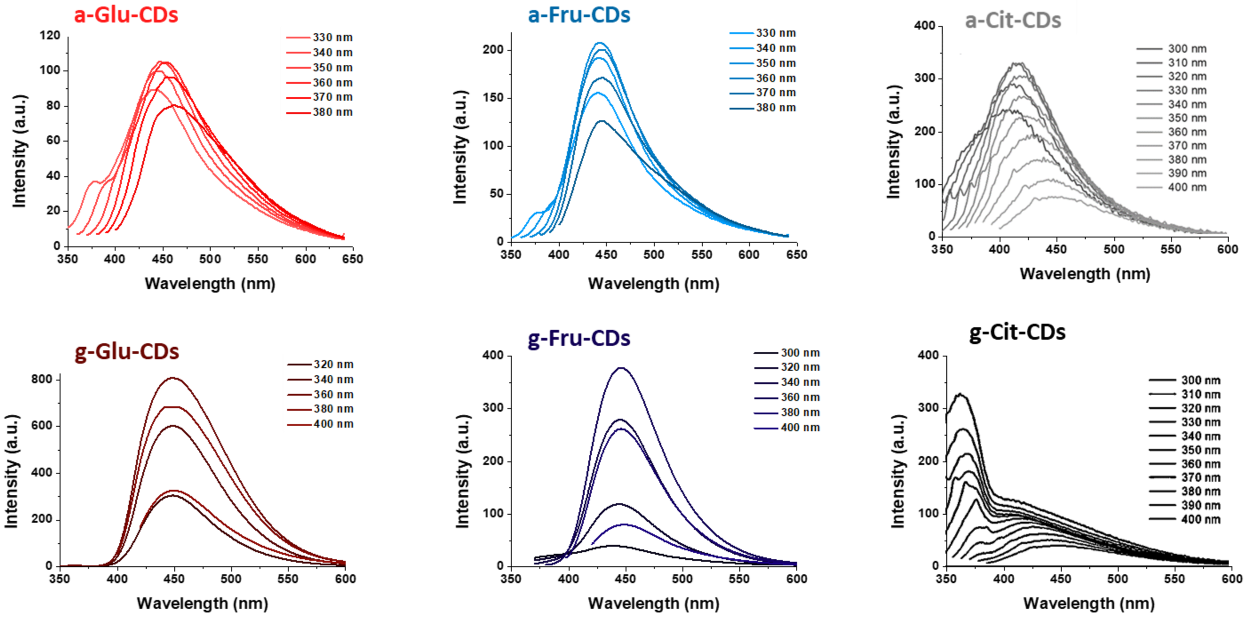

Figure 3.2.6 PL spectra of the six types of CDs.

The UV-Vis spectra (**Figure 3.2.7**) showed the characteristic absorption bands in the near-UV with a tailing in the visible region. In detail, g-Cit-CDs exhibited a weak absorption band at 365 nm, due to the n-π* transitions in defect states, and a stronger one around 220 nm ascribed to the π-π* transitions in the aromatic domains. The other five materials (a-Glu-CDs, g-Glu-CDs, a-Fru-CDs, g-Fru-CDs and a-Cit-CDs) showed, instead, three defined absorption regions. The first one, around 220-225 nm, related to the π-π* transition of the sp^2 C=C conjugated systems, a second one at 260-280 nm due to the n-π* and the third one around 365-370 nm ascribed to surface state transitions.

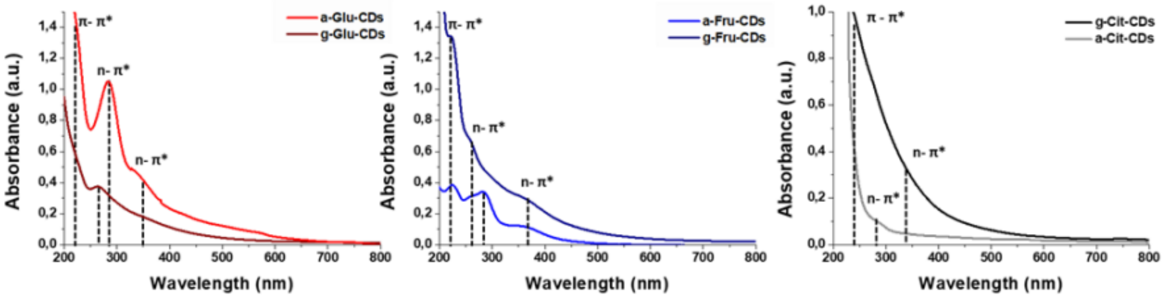

Figure 3.2.7. UV-Vis spectra of the six types of CDs.

Quantum yields (%), mass extinction coefficients ($L\cdot g^{-1}\cdot cm^{-1}$) and lifetime of the excited state (ns) are reported in **Table 3.2.1**.

The quantum yields were calculated based on quinine sulphate. In particular, for citric acid-based CDs 1.0% was found for the amorphous one and 1.2% for the graphitic material, the CDs prepared from glucose gave slightly higher values (1.8% for a-Glu-CDs and 2.3% for g-Glu-CDs) while the fructose-CDs had lower QY (0.3% and 0.7% for a-Fru and g-Fru respectively). Mass extinction coefficients (ε) were calculated at 365 nm and, for citric acid- and fructose-based CDs a significant increased value was observed for the graphitic materials when compared with the amorphous ones (4.0 and 1.4 times higher for g-Cit and g-Fru respectively). In opposition, concerning the glucose-derived nanomaterials, it was observed an enhancement on the ε value for the amorphous one about 2.7 times higher than the g-Glu-CDs. A similar trend was observed also for the lifetime of the excited states: the graphitic domain seemed to enhance the lifetimes of g-Cit-CDs and g-Fru-CDs when compared to their amorphous homologues, while when using glucose, the amorphous material resulted in a longer lifetime when compared to the graphitic one. All the six samples exhibited a multiexponential PL decay indicating a synergistic effect due to a plethora of mechanisms. The parameters for the time resolved PL and calculations of the lifetime of the excited state are reported in **Figure 3.2.8** and in the Appendix (**Table A.3.2.1**).

Table 3.2.1 Quantum yields, mass extinction coefficient (ε, calculated at 365 nm) and lifetime of the excited state (τ) for the six synthesized CDs.

Entry	CDs	QY (%)	ε ($L\cdot g^{-1}\cdot cm^{-1}$)	τ (ns)
1	a-Glu-CDs	1.8	1.71	4.6
2	g-Glu-CDs	2.3	0.63	2.4
3	a-Fru-CDs	0.3	1.63	4.4
4	g-Fru-CDs	0.7	2.01	5.9
5	a-Cit-CDs	1.0	1.16	3.3
6	g-Cit-CDs	1.2	4.68	5.4

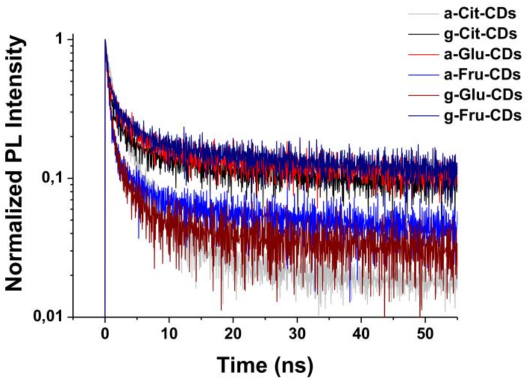

Figure 3.2.8. Time-resolved photoluminescence measurements for the six types of CDs.

3.2.3 Photocatalytic experiments

The six nanomaterials were then tested as photocatalysts in the single electron photoreduction of methyl viologen (MV^{2+}, -0.45 V vs NHE[69]) to its mono-reduced specie ($MV^{\bullet+}$) in order to investigate the relations between the morphological and structural features and their photoactivity. All the tests were carried out in aqueous media, under UV irradiation (LED at 365 nm), with a concentration of CDs normalized for absorption (0.5 a.u.) and using ethylenediaminetetraacetate (EDTA) as a sacrificial electron donor. All the blank tests were performed (see Appendix, **Figure A.3.2.3**): in particular, a test in the absence of light, one without CDs and then one without EDTA for each type of CDs. When performing the reaction in absence of light, no activity was detected, highlighting the primary role of the excited CD-states in the photoinduced electron transfer (PET) reactivity. As can be clearly see from **Figure 3.2.9** and **Table 3.2.2**, the PET ability was strongly dependent on the choice of the carbon precursor but also on the synthetic pathway. Generally, the citric acid-based ones were found to be more photo-active, followed by the fructose-derived and lastly by the glucose-CDs. The morphology of the nanomaterials, in particular their amorphous or graphitic nature, influenced the reactivity too in an unpredicted way. The graphitization of citric acid- and glucose-derived CDs, indeed, enhanced their PET performance of about 1.5 and 1.6 times respectively. However, a-Glu-CDs showed an induction time of 10 min. Concerning Fru-CDs an opposite behaviour was observed: the amorphous material resulted to be 6.7 times more reactive than the graphitic counterpart. This inversion in the trend is probably due to the formation of the large graphitic supramolecular aggregates that evidently affect the PET efficiency. These results highlight the complexity in assessing PET and in designing CDs-based photocatalytic organic applications.

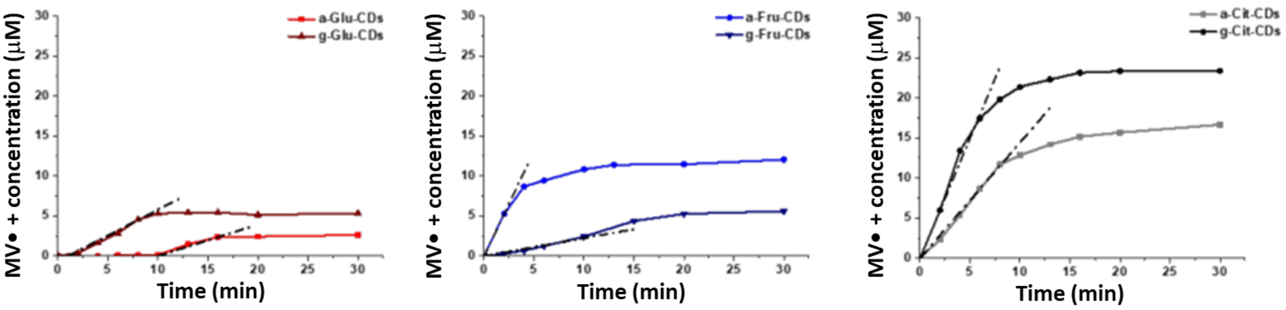

Figure 3.2.9. Reaction kinetics of formation of $MV^{\bullet+}$ using CDs as photo-redox catalysts. Reaction conditions: MV^{2+} 60 μM, EDTA 0.1 M, λ_{ex}: 365 nm with an absorbance-normalized amount of CDs and water as solvent (see Experimental section for more details).

Table 3.2.2 Photocatalytic performances for the six synthesized CDs, initial rate v_0 has been calculated without considering the induction time.

Entry	CDs	$v_0 \cdot 10^{-8}$ (M·s^{-1})	Relative rate
1	a-Glu-CDs	0.65	1
2	g-Glu-CDs	1.07	1.6
3	a-Fru-CDs	4.37	6.7
4	g-Fru-CDs	0.67	1
5	a-Cit-CDs	3.45	5.3
6	g-Cit-CDs	5.06	7.8

3.2.4 Conclusions

In conclusion, in this work the synthesis, characterization and photocatalytic properties of six different CDs were investigated. The nanomaterials were prepared through hydrothermal and pyrolytic treatment, leading to amorphous and graphitic CDs, using three carbon precursors (citric acid, glucose and fructose). It has been demonstrated how the choice of the carbonaceous substrate and, consequently, the morphology of the nanomaterials, can influence the photo-redox behaviour of CDs. Firstly, it was highlighted how the hydrothermal treatment of citric acid, glucose and fructose, produced amorphous nanoaggregates containing molecular-like compounds, while using pyrolysis, nanomaterials composed by extended graphene-like carbonaceous core were observed. Moreover, it has been underlined that the higher is the reactivity of the carbon precursors towards the decomposition/thermal treatment, the easier and larger the formation of the nanoparticles. In particular, the graphitic CDs obtained from fructose resulted as a supramolecular aggregate of graphene-like crystalline sheets with multi-layered structure. It was also demonstrated that both the synthetic technique and the molecular precursor were related to the photo and optical properties of the dots. Among the six nanomaterials prepared, the two deriving from citric acid yielded the best photocatalytic performances towards the single electron transfer on MV^{2+}, followed by glucose and lastly by fructose. Also the graphitization of the carbon core was found to affect the PET activity of the CDs. The morphology of the carbon-dots induced either a positive or negative photo-reactivity trend, which in turn was influenced by the carbon-precursor employed. For fructose-CDs, the amorphous structure provided optimal results in terms of initial rates; likewise, the graphitic nanoparticles were more active when formed by citric acid and glucose. Overall, these results provide important insights into carbon source/structure/activity relationships and may pave the way for a more rational development of carbon-derived nano-photocatalysts for organic synthesis.

3.2.5 Experimental

General. Citric acid, glucose, fructose, sodium hydroxide (NaOH) and methyl viologen (MV^{2+}) were purchased from Sigma-Aldrich and used as received without further purification. MilliQ water was employed in all the experiments.

^{1}H, ^{13}C{^{1}H} and DOSY NMR spectra were recorded on a Bruker AV 300 (^{1}H: 300 MHz; ^{13}C: 75.5 MHz) spectrometer. For ^{1}H and ^{13}C{^{1}H} NMR the chemical shifts (δ) have been reported in parts per million (ppm) relative to the solvent signal as an internal reference.

UV-Vis absorption spectra were recorded by using an Agilent 8456 spectrophotometer.

Photoluminescence (PL) experiments were performed with a Perkin Elmer LS 55 fluorescence spectrophotometer.

The Fourier transform infrared spectroscopy (FT-IR) was measured at wavenumbers ranging from 400 to 4000 cm^{-1} using a Perkin-Elmer spectrum one FT-IR spectrometer.

The morphologies of the resulting CDs were analysed by a JEM-2200FS transmission electron microscope (TEM) operating at 200 kV. For g-Fru-CDs high resolution electron microscopy images were recorder using FEI TALOS F2005 (voltage 200 kV). The sample was prepared by dispersion of the powder in bi-distilled water (concentration around 1 mg/ml), the as prepared solution was sonicated for 20 min to increase the dispersion of the material. One drop of solution was deposited onto a copper grid and dried at ambient temperature before the analysis.

X-ray photoelectron spectroscopy (XPS) was performed using a Perkin Elmer Φ 5600ci spectrometer using nonmonochromatic Al Kα radiation (1486.6 eV) in the 10−7 Pa pressure range. The binding energy (BE) values are referred to the Fermi level. The calibration of the BE scale was verified by checking the position of both Au4f7/2 and Cu2p3/2 bands (from pure metal targets), falling at 84.0 and 932.6 eV, respectively. After a Shirley-type background subtraction, the raw spectra were fitted using a nonlinear least-squares fitting program adopting Gaussian−Lorentzian peak shapes for all the peaks. Samples presented different shifts of all bands toward higher BEs as a consequence of surface charging: it was carefully determined and corrected in two steps: i) by using an internal reference (the C1s position of the band related to C=C bonds); ii) by checking, after the charging correction, the consistency of the BE positions of all the components evidenced in all the different XPS peaks. The final uncertainty of the determined BEs was not larger than 0.2 eV. The atomic composition was evaluated using sensitivity factors as provided by Φ V5.4A software. The relative uncertainty of the atomic fraction of the different elements is lower than 0.1.

CDs Synthesis. The nanomaterials were obtained as follow:

1. amorphous citric acid CDs (a-Cit-CDs) were hydrothermally synthesized, as already reported,[62] by heating an aqueous solution of citric acid (2 mg in 20 mL milliQ water) in a sealed autoclave (volume = 100 mL) for 24 h at 180 °C. The mixture was then neutralized to pH 7 with aqueous NaOH and evaporated to dryness leading to a dark yellow luminescent oil (25% wt yield) which was used without any further purifications.
2. graphitic citric acid CDs (g-Cit-CDs) were synthetized, as already reported,[62] by pyrolysis heating neat citric acid (100 g) under air at 220 °C for 48 h. The resulting solid was then neutralized to pH 7 with aqueous NaOH, and the crude mixture dialyzed (cut-off Mn: 1.0 kDa) for 24 h against fresh water. The inner solution was evaporated to dryness leading to a dark-black solid (20% wt yield).
3. amorphous glucose and fructose CDs (a-Glu-CDs and a-Fru-CDs) were hydrothermally synthesized, as already reported,[63] by heating an aqueous solution of glucose or fructose (2 mg in 20 mL milliQ water) in a sealed autoclave (volume = 100 mL) for 24 h at 200 °C. The mixtures were centrifugated to remove the black precipitate, the supernatant was then filtered and evaporated to dryness leading to a dark solid (34% wt yield and 29% wt for glucose and fructose respectively) which were used without any further purifications.
4. graphitic glucose and fructose CDs (g-Glu-CDs and g-Fru-CDs) were synthetized by a pyrolysis treatment of 100 g of glucose or fructose, respectively, in a conical flask at 220 °C for 48 h under air. As the reaction proceeds, the solution turns from colourless to orange and, in the end, to dark brown. The as formed suspension was cooled at r.t., neutralized to pH 7 by the addition of NaOH 5M and the resulting solution was then dried leading to a dark brown solid. The crude was dissolved in milliQ water and dialyzed (cutoff Mn: 1.0 kDa) for 24 h against fresh water, that was refreshed after 12 hours, to isolate the pure carbogenic core from the residual volatile NMR-active molecules, yielding 65% wt and 48% wt of g-Glu-CDs and g-Fru-CDs after freeze-drying.

Thermal decomposition of citric acid, glucose and fructose. 1 g of citric acid, glucose or fructose were heated in a conical flask at 220 °C and the decomposition kinetics were monitored via ^{1}H-NMR spectroscopy at different reaction time within 4 hours. As the reaction proceeds the samples were dissolved in D_2O neutralized to pH 7 by the addition of NaOD.

Photocatalytic experiments. A solution composed by 0.1M of EDTA, 60 μM of MV^{2+} with an absorbance-normalized amount of CDs (absorbance = 0.5 a.u.; 1.2 mg a-Cit-CDs, 0.21 mg g-Cit-CDs, 0.75 mg a-Glu-CDs, 1.5 mg g-Glu-CDs, 0.75 mg a,g-Fru-CDs) were placed under inert atmosphere in a quartz cuvette. The solutions were then irradiated at 365 nm (Hangar s.r.l.; ATON LED-UV 365; 80 W/m^2 of irradiance in the UV-A spectral range 315-400 nm). The progress of the reaction was monitored using an UV spectrophotometer following the formation of the typical absorption band of the reduced $MV^{\bullet+}$ radical cation species centered at 605 nm and its concentration was estimated using ε = 13700 M^{-1} cm^{-1}.[69]

3.3 Carbon Dots as Green Photocatalyst for Atom Transfer Radical Polymerization of Methacrylates

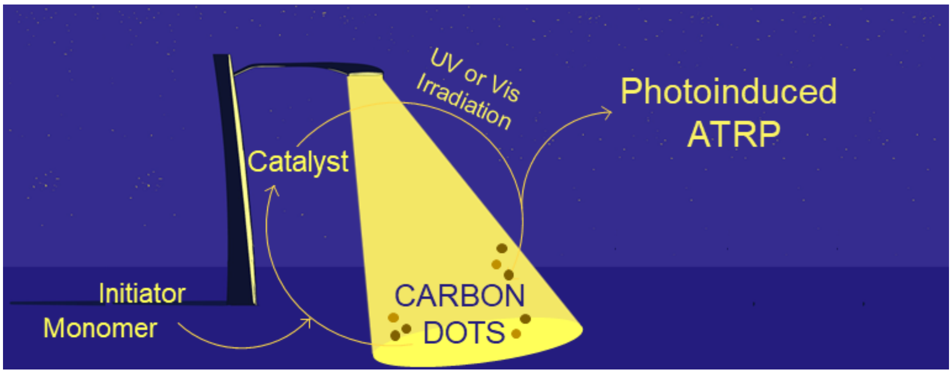

*With the information acquired from the previous study (see **Chapter 3.2**) and from other investigations performed in our research group,*[62,63] *we decided to apply the high photoreactivity of nitrogen-doped CDs synthesized from citric acid and diethylenetriamine for the atom transfer radical polymerization of methacrylates. In this section a practical use of CDs for the preparation of polymethacrylates is reported. The results reported in this chapter are currently submitted for publication.*

In this chapter the use of carbon dots (CDs) in photoinduced atom transfer radical polymerizations (ATRP) as green metal-free sensitizers is reported. In particular, the production of a polymethacrylate by using cheap and easily affordable CDs made from citric acid and diethylenetriamine, under both ultraviolet (UV, λ = 365 nm) and visible light was studied. Different solvent systems have been tested and a Cu^{II} complex was used as catalyst. Under the best conditions a polymer in 89% conversion and with a narrow dispersity (1.4) was obtained. The first order kinetics and the "on-off" experiments gave further evidence of the constant concentration of radicals and of the controlled mechanism of the polymerization.

3.3.1 Introduction

Since 1995, where for the first time atom transfer radical polymerizations (ATRP) were reported,[70,71,72] immense progresses have been developed in the field of synthetic polymers. Indeed, differently from ionic or radical polymerizations, ATRP processes can have active and versatile metal catalytic systems that can lead to well-defined polymers and controlled architectures, can be applied to a wide variety of different monomers and are not too sensitive to the reaction conditions.[73] Indeed, radical processes are more tolerant of functional groups and impurities and are the leading methodologies in industry to produce polymers.[74]
ATRP are redox processes mediated by the reversible reaction between a low oxidation state complex (the catalyst, Mt^n/L) and an alkyl halide (the initiator, P_n-X). This activation process, that occurs with a rate constant of activation k_{act}, implies the oxidation of the metal catalyst ($Mt^n \rightarrow Mt^{n+1}$) with formation of an active species $P_n\bullet$ that initiates the polymerization (**Figure 3.3.1**). The subsequent deactivation pathway comprises the addition of the monomer with formation of the initial dormant species (P_n-X) and reduction of the catalyst to its former low oxidation state (rate constant of deactivation k_{deact}). Polymer chains grow by the addition of the intermediate radicals to monomers in a manner similar to a conventional radical polymerization, with a rate constant of propagation k_p. The generation of the oxidized metal complex (Mt^{n+1}) is able to reduce the stationary concentration of growing radicals and thereby minimize the contribution of termination reactions.[75] Termination reactions (k_t) also occur in ATRP, mainly through radical coupling and disproportionation; however, in a well-controlled ATRP, no more than a few percent of the polymer chains

undergo termination. In order to have a successful ATRP together with a small contribution of terminated chains, a uniform growth of all the chains is required. This last is accomplished through fast initiation and rapid reversible deactivation.

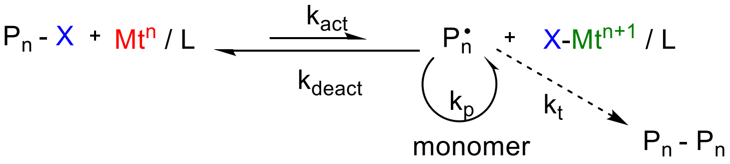

Figure 3.3.1. General mechanism of the equilibrium in ATRP processes.

The rate of ATRP depends on the rate constant of propagation (k_p) and on the concentrations of monomer and growing radicals.[76] The latter is defined by the ATRP equilibrium constant ($K_{ATRP} = k_{act}/k_{deact}$), the concentration of dormant species (P_n-X) and the ratio of the concentrations of activator (Mt^n/L) and deactivator (XMt^{n+1}/L), as can be seen in **Equation 3.3.1**.

$$R_p = \ln\frac{[M]_0}{[M]_t} = k_p K_{ATRP}\left(\frac{[P_nX][Mt^n/L]}{[XMt^{n+1}/L]}\right)$$

Equation 3.3.1. ATR Polymerization rate.

Reaction conditions, temperature, solvent and pressure as well as the nature of the monomer, the dormant species and the ligand can considerably affect the values of k_{act}[77] and k_{deact},[78] and therefore their ratio K_{ATRP}. The quantification of the K_{ATRP} constant can provide a measure of the activity of the catalyst in a polymerization reaction.[79] The catalyst complexes, however, are formed dynamically and their formation is governed by certain stability constants that is responsible, indeed, of the concentration of the catalytic species itself together with the reaction medium. In conclusion, the rate of ATRP increase with the K_{ATRP} (catalyst activity) but, under some conditions it can diminish due to radical termination and significant reduction of $(Mt^n/L)/(Mt^{n+1}/L)$ ratio, because of the persistent radical effect.[75] Considering an ideal ATRP (in absence of chain termination and transfer reactions), it can be stated that the uniformity of polymer's chain (namely the dispersity of molecular weights $Đ = M_w/M_n$ where M_w is the weight-average molar mass and M_n is the number-average molar mass) relates to the concentration of dormant species (P_n-X) and deactivator (Mt^{n+1}/L), to the rate constant of propagation (k_p) and deactivation (k_{deact}) and to the conversion of monomer (x) (**Equation 3.3.2**).[76]

$$Đ = \frac{M_w}{M_n} = 1 + \left(\frac{k_p\,[P_nX]}{k_{deact}[XMt^{n+1}/L]}\right)\left(\frac{2}{x} - 1\right)$$

Equation 3.3.2. Dispersity for polymers prepared via ATRP.

Hence, using the same monomers, a catalyst that deactivate the growing chains faster will result in smaller ratio k_p/k_{deact} and produce polymers with a narrower dispersity. The dispersity can be decreased also by increasing the concentration of deactivator and reducing the concentration of the dormant species.

As already stated, ATRP are multicomponent systems composed of the monomer, an initiator and a catalyst. A plethora of different monomers (styrenes, methacrylates, methacrylamides and acrylonitrile just to name a few) can be successfully polymerized via ATRP.[80] Even using the same conditions, each monomer has its proper equilibrium constant for its active and dormant species, as well as its own radical propagation rate. Indeed, for a specific monomer, the concentration of propagating radicals and the rate of radical deactivation need to be adjusted to maintain polymerization control.

The initiator has the role to determine the number of growing chains. It must be kept in mind that, if the initiation is fast, and termination and transfer negligible, the number of growing chains is constant and correspond to the initial concentration of initiator. Typical initiators are alkyl halides (RX) were the halide group (X) must quickly and selectively migrate between the growing chain and the catalyst in order to obtain well-defined polymers with narrow molecular weight distributions. For this, when X is chlorine or bromine, the control over molecular weight is the best. Generally, any RX species with activating substituents on the α carbon can be used as ATRP initiator.

The catalyst, usually a transition metal complex, is the most important component of ATRPs because it is responsible of the position of the atom transfer equilibrium and of the exchange dynamics between dormant and active species. In order to be efficient, the catalysts must undergo several prerequisites. The metal center must have at least two easily accessible oxidation states separated by only one electron, and it should have affinity toward halogens. In addition, the coordination sphere should be expandable to accommodate selectively a halogen and the ligand should complex the metal relatively strongly.

Other key parameters for ATRPs are the choice of the solvent, the temperature and the reaction time. Concerning the solvent, ATRP can be performed in bulk, in solution or in heterogeneous systems and many different solvent have been used (e.g. benzene, toluene, acetone, ethyl acetate, water).[74] A solvent can be necessary especially when the product polymer is not soluble in its monomer, but it must be considered that the chain transfer to the solvent should be minimal and that an interaction of the solvent with the catalyst can take place. In ATRP processes, the polymerization rate increases with the temperature due to the increase of radical propagation rate constant and the atom transfer equilibrium constant. On the other hand, chain transfer, other side reactions[81] and catalyst decomposition[82, 83] can take place easier at elevated temperatures. Lastly, prolonged reaction times can lead to almost complete monomer conversion while may not increase the dispersity of the final polymer but will induce loss of end groups.[74]

One of the major drawbacks of ATRP is the necessity to use large amounts of catalyst in order to have better control over the whole polymerization process. Lately, to overcome environmental and practical issues, different initiation techniques to generate *in situ* the metal catalyst have been reported. These methods focus on different reduction pathways for the formation of the activator Mt^n species, and, to date, they have been conducted using different reducing agents,[84] electrochemical processes,[85] copper-containing nanoparticles[86] and photochemical redox processes.[87,88,89,90,91,92] Referring to this last protocol, it must be noticed how light is an environmental friendly, widely available and non-invasive reagent that can lead to spatial and temporal control of different ATRP processes.[93] Different photoactive molecules (e.g. dyes or commercial photoinitiators) are, indeed, effective as reducing agents and can, so, facilitate the photoinitiated ATRP process. The *in situ* photolytic generation of the reduced complex (usually a Cu^I complex from Cu^{II}) under irradiation enables polymerization also with small concentrations of catalyst (**Figure 3.3.2**).[94] In addition, the polymerization reaction can be stopped and restarted easily by switching light. The photoinduced ATRP has been successfully performed using different sources of light, from UV,[88,90] to visible[95] or near infrared.[96]

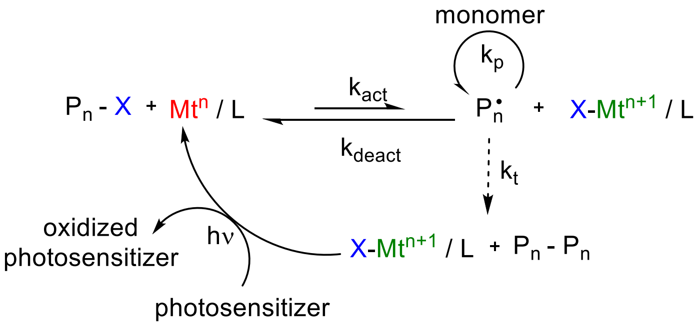

Figure 3.3.2. General mechanism of the equilibrium in ATRP processes with regeneration of the activator via electron transfer induced by light.

Anyway, some drawbacks and challenges must be overcome. In particular, the majority of the photosensitizers tested for photo-ATRP relies on synthetic pathways that are not sustainable and can be harmful for the environment and the user. In this frame, CDs based on natural feedstocks can be a valid alternative. Lately, CDs received attention for photoinduced reversible addition-fragmentation chain-transfer polymerization,[97] which was the first report regarding the use of these nanoparticles in a photo-controlled radical polymerization. In addition, in 2020, CDs produced from sodium alginate and ethylenediamine has been successfully employed for the first time in the photo-ATRP of methylmethacrylate in dimethylsulfoxide, yielding polymers with a narrow dispersity but low (30%) conversion.[94] Under irradiation, indeed, CDs can be excited to their excited state, which act as reducing agents to obtain Cu^{I} from Cu^{II} in the polymerization system: the Cu^{I} complex reacts with a bromine initiator and forms active free radicals that initiate the polymerization.

As already stated in the introductory part, CDs have been demonstrated to be promising photocatalysts for photooxidations, photodegradations and photoreductions[98,99,100] and can be easily synthesized from cheap and abundant carbon precursors. Moreover, their synthesis is easily tailored by, for example, the addition of doping agents that can enhance their photoactivity. Doping, in fact, has been demonstrated to be an effective method to customize the optical, electrical and chemical properties of CDs, resulting in a plethora of different nanoparticles for specific requirements.[49,101]

In this chapter the possibility to use CDs derived from citric acid and diethylenetriamine as photosensitizer for the photoinduced ATRP of a methacrylate is reported. The polymerization has been conducted in different media using always non harmful solvent systems and irradiating with both UV (λ = 365 nm) and visible light.

3.3.2 Results and Discussion

Carbon Dots synthesis and characterization

As novel type of photosensitizer to activate the ATRP, two different types of CDs has been tested. Using always citric acid as the carbon source, doped (N-cit-CDs) and non-doped (cit-CDs) nanoparticles were obtained through a bottom up technique (see Experimental section). These two families of CDs have already been synthesized and tested for their photocatalytic performances elsewhere.[52,102] In our previous studies, extensive HR-TEM, FT-IR, UV-Vis, XPS, PL/PLE, ESI-MS, ^{1}H/ ^{13}C{^{1}H} NMR and DOSY analyses indicated the amorphous nature of both nanoparticles. Concerning cit-CDs, from HR-TEM it was possible to observe nanoparticles with a poorly defined shape and diameters ranging from 9 to 12 nm,[52] while for N-cit-CDs diameters in the range of 13 nm were confirmed via atomic force microscopy.[99] As can be seen in **Figure 3.3.3**, both CDs are able to absorb in the UV region, but only the N-cit-CDs presented some absorption also in the visible range: this evidence prompted us to test this class of nanoparticles also for visible light photoinduced ATRP. In addition, the ability of nitrogen doping for the enhancement of the activation of this type of polymerizations has been demonstrated: in the N-doped electron-rich carbon nanostructure, the π electrons were activated by its conjugation with the lone pair electron of nitrogen, resulting in excellent electrochemical and catalytic performances.[101,103] The amount of nitrogen doping in N-Cit-CDs was evaluated via elemental analysis showing a carbon/nitrogen ratio equal to 3.2.

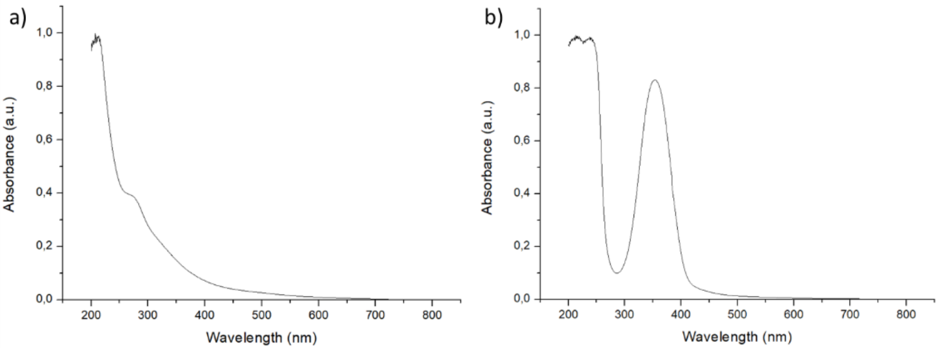

Figure 3.3.3. UV-Vis spectra of the synthesized CDs. a) non doped cit-CDs; b) doped N-Cit-CDs.

ATRP experiments

The ability of CDs to mediate photoinduced ATRP was tested irradiating (UV light λ = 365 nm LEDs and visible light 5600 K LEDs) solutions of CDs in different solvent systems (water, water/methanol and water/acetonitrile) with 2-hydroxyethyl-2-brom-2-methylpropanoate (HEBIB, see synthetic procedure in Experimental section) as the initiator together with the $CuBr_2$/ *N,N,N′,N″,N″*-pentamethyldiethylenetriamine (PMDTA) complex as the catalyst for the polymerization of [2-(methacryloyloxy)ethyl]trimethylammonium chloride (METAC)] under inert atmosphere. A proposed mechanism on the role of CDs is reported in **Scheme 3.3.1**.

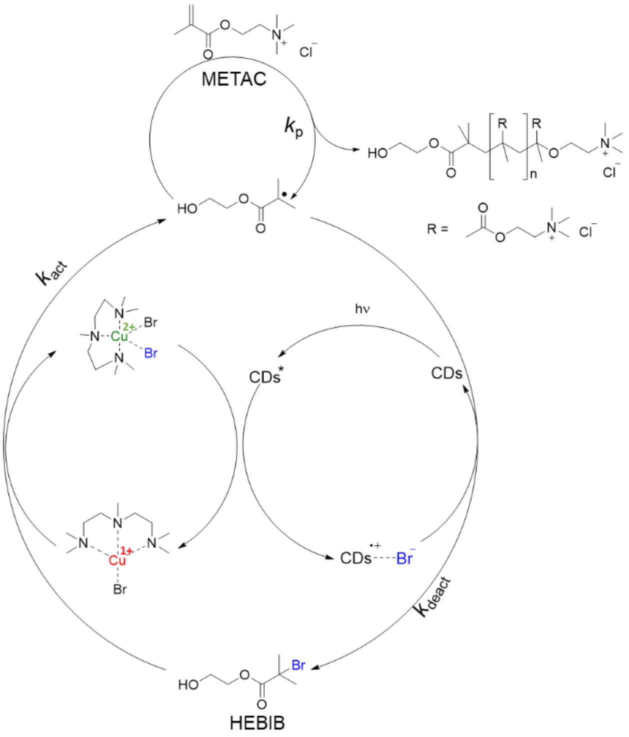

Scheme 3.3.1. Proposed mechanism for photoinduced ATRP of METAC using CDs.

After irradiation, the photoexcitation of CDs results in the population of the excited state (CDs*) that can perform an electron transfer to [Cu^{II} PMDTA]Br_2. This results in the reduction of the Cu^{II} complex to the respective Cu^{I} form that can initiate the radical polymerization of the alkyl bromide (HEBIB). The regeneration of CDs takes place in the photocatalytic cycle, when the oxidized CDs ($CDs^{\bullet +}$) react with bromide.[94]

All the experiments were conducted at room temperature, under different light sources and in different solvents, with constant ratio between the reagents [METAC]/[HEBIB]/[CDs]/[$CuBr_2$]/[PMDTA] = 100/1/1/1/3 and constant exposure time (1 h). Lower ratios of catalyst ([METAC]/[$CuBr_2$]/[PMDTA] = 100/0.1/0.3, 100/0.25/0.75 and 100/0.5/1.5) have also been tested but no production of polymer was observed.

The investigation started by testing the CDs under UV irradiation at 365 nm. Three different solvent system were tested, namely water, water/methanol and water/acetonitrile. As can be seen in **Table 3.3.1**, using the doped CDs (entries 1, 2 and 3) high conversions of the monomer (from 85 to 89%) were obtained in all the three solvents after only 1 hour of light exposure. The obtained polymers showed dispersity (Đ) always < 2 demonstrating a good control over the polymerization reaction. Anyway, changing the solvents, some differences concerning the weight-average molar mass, number-average molar mass and dispersity were observed. The 1:1 mixture of water and methanol was selected as the best performing environment resulting in slightly higher conversions (89%, entry 2, **Table 3.3.1**) and narrower dispersity (1.4). The addition of methanol, probably, allows a longer lifetime of the Cu^{I} catalytic species in the solution modifying the kinetic constants leading to a more favourable pathway.

Table 3.3.1. UV light (λ = 365 nm) induced ATRP of METAC using different CDs and in different solvents. [a]

Entry	CDs	Solvent	Conversion (%) [b]	M_n ($g\cdot mol^{-1}$) [c]	M_w ($g\cdot mol^{-1}$) [c]	Đ [c]
1	N-cit-CDs	Water	88	1600	2500	1.5
2	N-cit-CDs	Water:methanol (1:1)	89	1896	2655	1.4
3	N-cit-CDs	Water:acetonitrile (1:1)	85	1430	2610	1.8
4	Cit-CDs	Water:methanol (1:1)	-	-	-	-
5	-	Water:methanol (1:1)	-	-	-	-

[a]Experiments were conducted at ambient temperature for 1 h using a ratio [METAC]/[HEBIB]/[CDs]/[$CuBr_2$]/[PMDTA] = 100/1/1/1/3; [b] determined gravimetrically; [c] determined by gel permeation chromatography using PEG standards.

To have more insight into the mechanism of polymerization, an experiment using the same conditions but in absence of CDs was performed (**Table 3.3.1**, entry 5). In this case no polymer was obtained demonstrating the necessity to photoactivate the copper catalyst. The absence of polymer was confirmed via GPC analysis where only molecular weights lower than 200 $g\cdot mol^{-1}$ were observed. Other blank tests, namely in absence of light, catalyst and without CDs/irradiation, were performed to confirm the importance of all the components for photoinduced ATRP of METAC. All the blank tests were accomplished using the 1:1 mixture of water and methanol as the designed solvent and in all tested condition no formation of polymer was observed (see **Table A.3.3.1** in the Appendix).

Chosen the best reaction conditions, a kinetic study was performed to confirm the linear increase of the conversion during the irradiation time. As shown in **Figure 3.3.4**, a linear correlation between the logarithm of monomer concentration (ln [M_0]/[M_t]) and time (t, starting at t = 0), highlighted a first order kinetic. This evidence indicates that the concentration of active free radicals can be seen as constant during the reaction.[94,104]

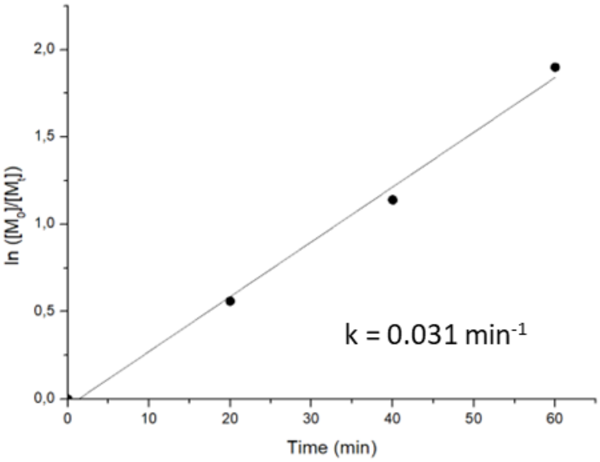

Figure 3.3.4. Kinetic plot of the polymerization system using N-cit-CDs under UV irradiation and relative rate constant. Conditions reported in **Table 3.3.1**, entry 2.

To better understand the influence of the nitrogen doping in the photosensitizer, non-doped CDs (Cit-CDs) were tested in the best conditions found for N-cit-CDs (**Table 3.3.1**, entry 4). However, the non-doped nanoparticles did not show a consistent activity in activating the copper catalyst and no polymer was detected after 1 h of irradiation. This result was a further evidence of the importance of nitrogen doping in CDs in order to obtain valuable photosensitizers. Nitrogen doping on CDs, indeed, allows the presence of more defect states on the surface of the dots together with molecular like fluorophores that are able to effectively promote a more effective excitation of the electron.[62]

Concerning visible light, the non-doped CDs were not used since they have negligible absorbance in the visible region (see UV spectrum in **Figure 3.3.3**). As for UV exposed experiments, three different solvents were examined but, in this case only using water/methanol (1:1) it was possible to observe the presence of the polymer (**Table 3.3.2**, entry 2). After 1 h of irradiation, poly-METAC was obtained with 70% conversion and a narrow dispersity (1.5) highlighting the possibility to activate this reaction using visible light as a green, cheap and safe reagent.

Table 3.3.2. Visible light (5600 K) induced ATRP of METAC using N-cit-CDs in different solvents.[a]

Entry	CDs	Solvent	Conversion (%) [b]	M_n (g·mol^{-1}) [c]	M_w (g·mol^{-1}) [c]	Đ [c]
1	N-cit-CDs	Water	-	-	-	-
2	N-cit-CDs	Water:methanol (1:1)	70	1460	2170	1.5
3	N-cit-CDs	Water:acetonitrile (1:1)	-	-	-	-
4	-	Water:methanol (1:1)	-	-	-	-

[a]Experiments were conducted at ambient temperature for 1 h using a ratio [METAC]/[HEBIB]/[CDs]/[$CuBr_2$]/[PMDTA] = 100/1/1/1/3; [b] determined gravimetrically; [c] determined by gel permeation chromatography using PEG standards.

An experiment under the same conditions but without the addition of CDs has been performed (**Table 3.3.2**, entry 4) but no polymer was detected, underlying once again the fundamentality of the presence of the carbon nanoparticles in order to activate the reaction. Another blank test in absence of the copper catalyst was performed and, also in this case, no poly-METAC was observed (see **Table A.3.3.1** in the Appendix). The absence of polymer was confirmed via GPC analysis where only molecular weights lower than 200 g·mol^{-1} were detected.

To further confirm the linearity of the relationship between the monomer concentration and the irradiation time, a kinetic study was conducted also under Vis light. As can be seen in **Figure 3.3.5**, a first order kinetic was observed indicating once again an almost constant concentration of free radicals during the polymerization. The difference in the rate constant of the ATRP under UV irradiation (k = 0.031 min^{-1}) and visible one (k = 0.023 min^{-1}) underlined the higher speed of the polymerization at 365 nm, confirming a major activity of the carbon nanoparticles at that wavelength.

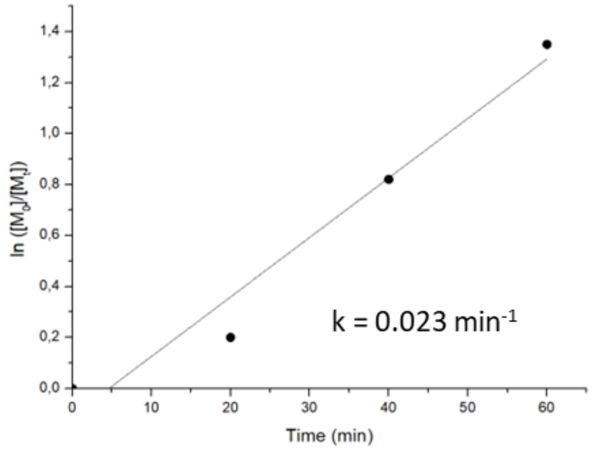

Figure 3.3.5. Kinetic plot of the polymerization system using N-cit-CDs Under Vis irradiation and relative rate constant. Conditions reported in **Table 2**, entry 2.

Polymer characterization

The characterization of the obtained polymer has been conducted using gel permeation chromatography (**Table 3.3.1** and **3.3.2**), thermogravimetric analysis, differential scanning calorimetry and NMR (see Appendix, **Figure A.3.3.1-2**). The product resulted as a thermoplastic, amorphous and transparent polymer with a glass transition temperature (T_g) of 100 °C (see **Figure A.3.3.3** in the Appendix), similar to polymethylmethacrylate (T_g = 110 °C). The thermogravimetric analysis of the polymer (**Figure A.3.3.4**, Appendix) showed a first small weight loss (circa 2.5%) at 100 °C due to the dehydration of water in the polymer and elimination of residual humidity.[105] The second stage, at circa 280-300 °C, corresponds to the thermal decomposition of the groups that protruded from the polymer chain,[106] while, the third weight loss at 390-400 °C, corresponds to exothermic reactions due to the decomposition of the ammonium salts.[107]

"On-off" experiments

Light "on-off" experiments were performed both under UV (conditions in **Table 3.3.1**, entry 2) and Vis light (conditions in **Table 3.3.2**, entry 2). The polymerization mixtures were subjected to repeated light exposure by irradiating the sample for 20 min and then kept in dark for 10 min. The obtained results (**Figure 3.3.6**) highlighted the dependence of the polymerization on the irradiation: no polymerization occurred when the solutions were kept in a dark environment. During the light exposure time, light induced ATRP were carried out showing also the different polymerization rates under UV and visible light.

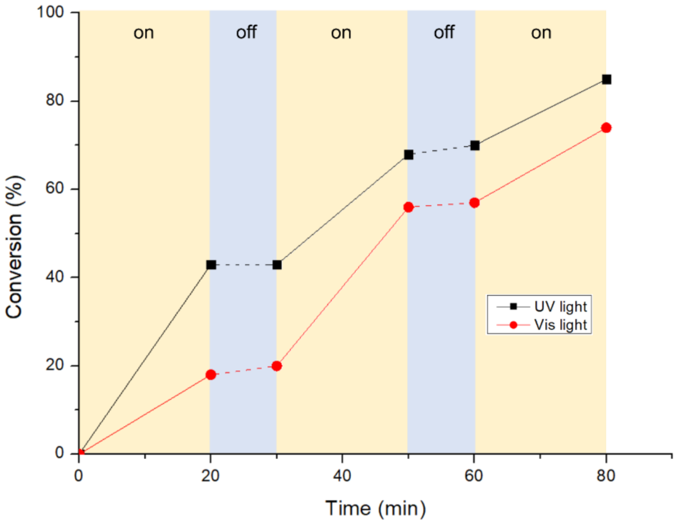

Figure 3.3.6. Monomer conversion (%) versus time using CDs to determine the dependency on irradiation (UV = black line, Vis = red line). Yellow regions refer to light on, blue regions to light off. The UV irradiated experiment was performed following the conditions reported in **Table 3.3.1**, entry 2; the Vis irradiated following the conditions in **Table 3.3.2**, entry 2.

3.3.3 Conclusions

We herein report an efficient photoinduced atom transfer radical polymerization (ATRP) protocol activated by citric acid-derived CDs. In particular, nitrogen doped carbon nanoparticles were synthesized and used as photosensitizer for the preparation of poly-METAC (2-(methacryloyloxy)ethyl]trimethylammonium chloride) with a greener and sustainable synthetic procedure. The reaction, indeed, was found to be efficient in water-based solvent, in particular in water/methanol (1:1) solution, and the presence of a photosensitizer allowed to use small amounts of metal catalyst (1:100 in respect to the monomer). It was highlighted that N-cit-CDs are able to activate the polymerization under both UV and visible light paving the way towards an eco-friendly, cheap and affordable synthetic procedure for the obtainment of polymethacrylates. After only 1 h of irradiation it was possible to retrieve the polymer with 89% conversion and 1.4 dispersity under UV light and with 70% conversion and 1.5 dispersity under visible one. A first order kinetic was observed in both cases, confirming an almost constant concentration of radicals, typical of ATRP mechanisms. "On-off" experiments and blank tests confirmed the necessity of all the reagents (light, CDs, initiator and catalyst) in order to obtain the polymer. In comparison with the only other example in the literature,[94] the present procedure was more effective in terms of polymer conversion (70-89% in 1 h versus 30% in 2.5 h) and it allowed to perform ATRP avoiding hazardous solvents (dimethyl sulfoxide was previously used). In conclusion, a new, cheap and effective photosensitizer for ATR polymerization has been herein studied demonstrating the possibility to achieve greener and efficient processes in polymer preparation.

3.3.4 Experimental

Materials and Methods. All the reagents were purchased from Merck Life Science S.r.l. (Milano, Italy), were of analytical grade and used without further purification. MilliQ water, used as a solvent throughout the experiment, was obtained with a Merck Millipore C79625 system. CHNS analysis was performed on an Elemental Unicube (Elementar Italia Srl, Lomazzo, Italy). For the optical characterization of CDs, an UV–Vis spectrophotometer Agilent 8456 (Agilent Technologies Italia, Milano, Italy) has been used. ^{1}H and ^{13}C{^{1}H} NMR spectra were recorded on a Bruker AV 400 (^{1}H: 400 MHz; ^{13}C: 100 MHz; 51V: 78.28 MHz) spectrometer (Bruker GmbH, Mannheim, Germany). The chemical shifts (δ) were reported in parts per million (ppm) relative to the residual undeuterated solvent as an internal reference. Gel permeation chromatography (GPC) was performed on an Agilent Infinity 1260 system equipped with refractive index detector and using an injection volume of 20 µL and a flow rate of 1 mL/min. A Phenomenex PolySep linear was used as column maintaining a constant temperature of 40 °C during the analysis. An aqueous solution of LiCl 0.1 M was used as eluent and polyethylene glycol was used as standard. DSC analyses were performed on a DSC 3 analyser (Mettler Toledo, USA). The temperature of the instrument was calibrated using indium as standard. Poly-METAC (about 10.0 mg) was weighed into aluminium oxidized melting pots, sealed, and heated from room temperature to 300 °C at 10 °C/min. An empty sealed melting pot was used as reference. Thermogravimetric analyses were performed using a Perkin Elmer TGA 4000 instrument. The analyses were carried out weighting 10 mg of poly-METAC in a ceramic crucible, in a temperature range from 30 °C to 600 °C with a heating rate of 10 °C/min and under a nitrogen flow of 20 mL/min.

Synthesis of Cit-CDs. The non-doped nanoparticles were hydrothermally synthesized, as already reported.[52] In detail, 2 g of citric acid were dissolved in 20 mL of MilliQ; the solution was heated in a sealed autoclave for 24 h at 180 °C. The mixture was then neutralized to neutral pH with an aqueous NaOH solution, filtered on paper and evaporated to dryness leading to a dark yellow luminescent oil (25% wt yield) which was used without any further purifications. The obtained nanoparticles have been characterized via NMR, UV-Vis and CHNS elemental analysis.

Synthesis of N-cit-CDs. The nitrogen doped CDs were hydrothermally synthesized by heating an aqueous solution of citric acid (2 g in 20 mL of MilliQ water) and diethylenetriamine (0.67 g) in a sealed autoclave for 6 h at 180 °C.[102] The mixture was then filtered and evaporated to dryness leading to a brown solid (72% wt yield) which was used without any further purifications. The obtained nanoparticles have been characterized via NMR, UV-Vis and CHNS elemental analysis.

Synthesis of 2-hydroxyethyl-2-brom-2-methylpropanoate (HEBIB). For the synthesis of the initiator, 1.5 mol of ethylene glycol and 60 mmol of triethylamine were dissolved in 30 mL of anhydrous tetrahydrofuran and placed in a round bottom flask. The reaction flask was put under inert atmosphere and kept under stirring in an ice bath while adding dropwise (in 30 min) 30 mmol of α-bromoisobutyryl bromide. After stirring at room temperature for 16 h, 200 mL of deionized water were added to the flask and the product has been extracted with dichloromethane (3 x 30 mL). The organic fraction has been washed with 30 mL of an aqueous solution of HCl (1M). The solvent has been removed by rotary evaporation leading to HEBIB as a yellow oil in 94.5% yield. ^{1}H NMR (400 MHz, CDCl3): 1.96(s, 6H), 3.87 (t, 2H), 4.31 (t, 2H). ^{13}C NMR (100 MHz, CDCl3): 30.7, 55.8, 60.7, 63.3, 67.4, 171.8

ATRP experiments. In a Schlenk reactor, 10 mmol of [2-(methacryloyloxy)ethyl]trimethylammoniumchloride (METAC), 0.1 mmol of 2-hydroxyethyl-2-brom-2-methylpropanoate (HEBIB), 6.3 mg of CDs (N-cit-CDs or Cit-CDs) and 1 mL of an aqueous solution of $CuBr_2$ and e N,N′,N″,N″ pentamethyldiethylenetriamine ($CuBr_2$ 0.1 mmol : PMDTA 0.3 mmol) were added. The chosen solvent was added in quantity equal to the volume of monomer and $CuBr_2$/PMDTA solution. After 5 vacuum/nitrogen cycles the reactor was kept under continuous stirring and irradiation (UV = 365 nm or Vis = 5400 K LEDs) for 1h. The polymer was precipitated using acetone as counter solvent. After remotion of the solvent, the product was dissolved in methanol subsequently removed by rotary evaporation. The polymer was kept in vacuum oven at 70 °C (80 mbar) overnight. The product was obtained as a glassy, transparent solid and characterized via NMR, DSC and TGA.

3.4 Biobased Carbon Dots: from Fish scales to Photocatalysis

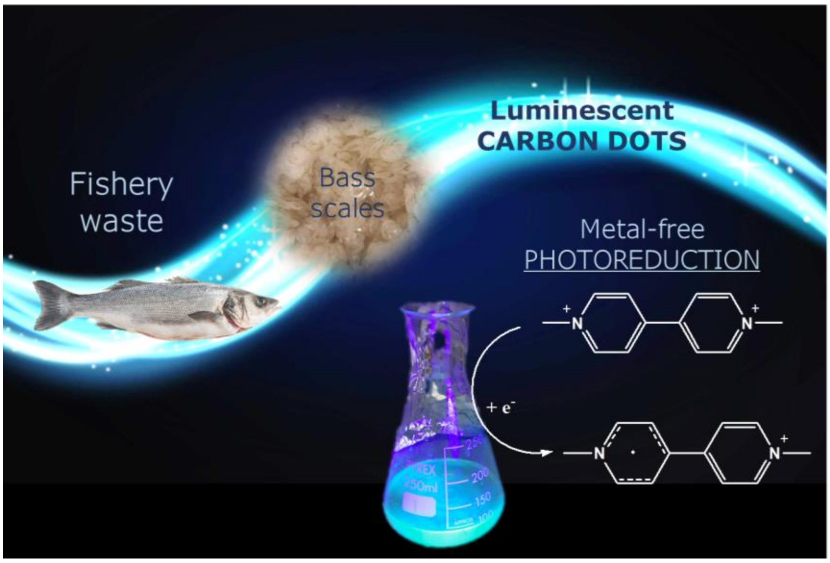

*The knowledge obtained from the investigations conducted on the synthesis, properties and photocatalytic activity of CDs prepared from biobased molecules, in particular citric acid (see **Chapters 3.2** and **3.3**), prompted us to explore the possibility to use waste biomass as carbon precursor to synthesize CDs. This study paved the way to a more sustainable approach to obtain CDs in the view of circular economy and their application in photocatalysis. The results reported in this chapter are published in* C. Campalani, E. Cattaruzza, S. Zorzi, A. Vomiero, S. You, L. Matthews, M. Capron, C. Mondelli, M. Selva and A. Perosa, *Nanomaterials*, **2021**, 11, 524. doi:10.3390/nano11020524.[99]

In this chapter the synthesis, characterization and photoelectron transfer ability of a new type of CDs prepared from fish scales is reported. Fish scales are an abundant biowaste that contain valuable materials among which chitin and collagen are the most present. The chemical composition of these two biopolymers make the scales rich, not only in carbon, oxygen and hydrogen, but also in nitrogen, making this biomass suitable for the preparation of CDs naturally nitrogen-doped. The self-nitrogen-doped nanomaterials were then synthesized from sea bass scales with a hydrothermal method in absence of any external doping agent: the morphology, structure and optical properties of bass-CDs were investigated. Their photocatalytic activity was compared with the one of conventional nitrogen doped-CDs prepared from citric acid and diethylenetriamine for the photoreduction of methyl viologen (MV^{2+}*).*

3.4.1 Introduction

The recovery and the conversion of waste into useable materials, chemicals and products is nowadays one of the goals for research in chemistry and it is one of the pillars of circular economy. As stated in **Chapter 1.2**, fish industry is a big source of valuable biowaste: in 2016 the global production of fish amounted to 171 million tons with China as the major productor.[108] The increase in fish production led also to an increase in the average fish consumption that grew from 12.6 to 19.8 kg per person in the past forty years.[109] As a consequence, also the quantity of fish biowaste is increasing more and more: the exact amount of this waste is still a matter of debate but it is estimated to be in the order of dozens of million tons every year.[110] Common fish residues are composed by fish heads, skin, viscera, bones and scale but their composition is widely variable depending on the specie, age, sex, geographic area and time of the year. Despite the possible differences, all fishery waste contains a plethora of valuable and interesting molecules such as collagen, chitin, oils and pigments representing a resource of sustainable chemical richness (**Figure 3.4.1**).[111,112]

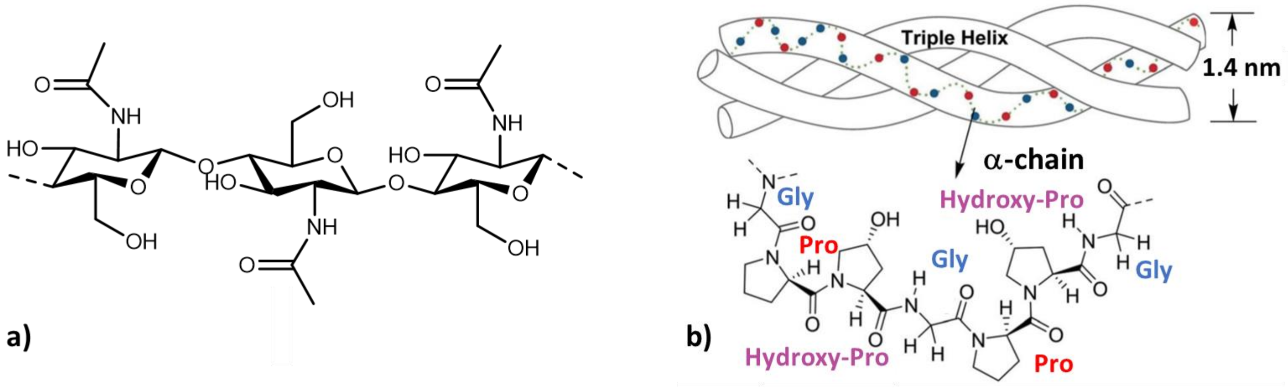

Figure 3.4.1. a) Chemical structure of chitin and b) pictorial representation of collagen.[110] Two of the major components of fishery biowaste.

To date, the most common options for the treatment of such waste are low-tech solutions for the obtainment of fertilizers and fishmeal (a product used for animal feed)[113] but various processes have also been reported for the preparation of high added-value products.[114] In this chapter, an investigation about the exploitation of sea bass scales for the production of carbon dots (CDs): luminescent carbon nanomaterials (see **Section 3.1**). Bass (*Dicentrarchus labrax*) is a fish that is easily found in sea and brackish water of Northern Adriatic Sea and in the Mediterranean Sea but is widely spread worldwide (**Figure 3.4.2**). Its fishing and aquaculture are very common, especially in the Mediterranean area where sea bass is one of the most important species.

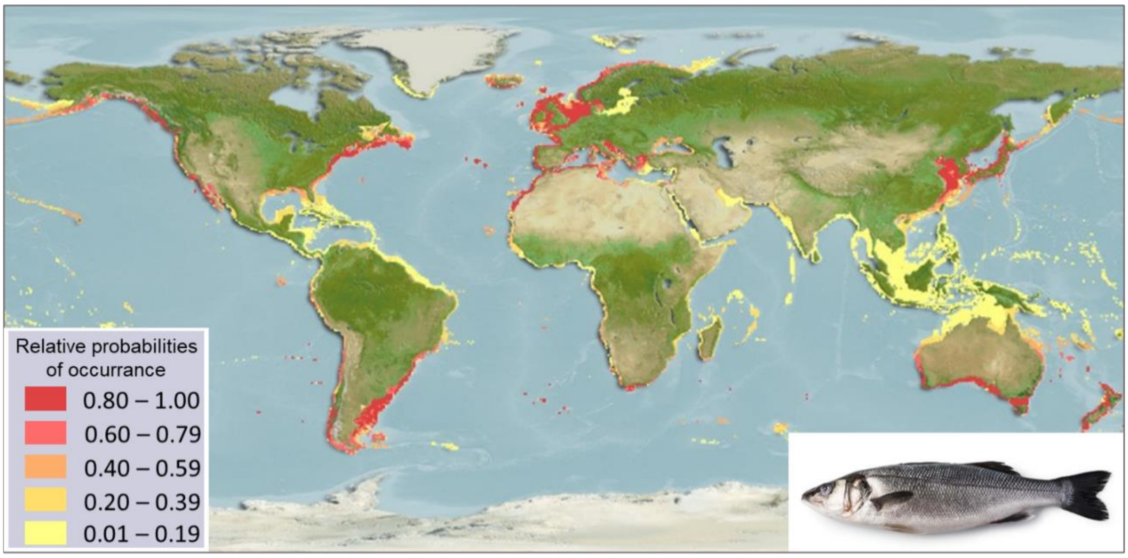

Figure 3.4.2. Relative probability of occurrence of sea bass worldwide. In bottom right insert, a picture of sea bass.

Along with the growing global awareness for the creation of sustainability via waste minimization, the choice of recycling and reusing waste for the generation of efficient materials for nanotechnology is preferred. The choice of using fish scales as the carbon source for the preparation of CDs was made also based on their chemical composition. In fact, they represent an inexpensive, accessible source of nitrogen-containing biomass that does not directly impact the food chain. The principal components of fish scales are collagen, chitin, minerals, lipids and pigments. Chitin is the main organic component and is a natural nitrogen containing polysaccharide (poly-β(1/4)-N-acetyl-D-glucosamine, see **Chapter 4.3**) that provides an efficient precursor for the N-doped CDs.[115] To date, CDs are inspiring intensive research efforts thanks to their superiority in water solubility, low toxicity, resistance to photobleaching, chemical inertness and ease of functionalization.[116,117] As stated in **Section 3.1**, these carbon nanoparticles are showing high adaptability in a wide range of applications, ranging from energy-related[25,118] to biomedical fields.[18,63] Among them, CDs appeared to be promising also as photocatalysts thanks to their remarkable light harvesting properties and excellent electron donor/acceptor capabilities but, to date, their photocatalytic activity is still under-explored. In addition, the majority of the reported photosystems are limited by the co-presence of enzymes or metal complexes as redox mediators.[53,54,119] A precise design of CDs together with the possibility of tuning their photoelectric properties is one of the major concerns faced to achieve a real breakthrough in this field. Many efforts have been, so, focused on the nitrogen doping of CDs demonstrating that it can significantly enhance the properties of the nanoparticles and thus expand their applicability.[120,121] As reported in **Chapter 3.2**, one of our previous works demonstrated how the choice of the carbon source and synthetic pathway can affect optical and structural properties of CDs, influencing in turn their photoelectron transfer ability.[52] Among the six types of CDs tested in that study (amorphous or graphitic made from glucose, fructose and citric acid), citric acid-CDs were found to provide the best photocatalytic performances toward the photoreduction of methyl viologen. For this reason, citric acid-based CDs were further investigated in our group: four different CDs were synthesized by using two different methods (hydrothermal and pyrolytic) and two sets of reagents (neat citric acid and a mixture of citric acid and diethylenetriamine). The most active CDs, for the photoreduction of MV^{2+} was shown the amorphous N-doped one (a-N-CDs, obtained with a hydrothermal treatment from citric acid and diethylenetriamine).[62]

This evidence led us to compare the new CDs synthesized from fish scales (bass-CDs) with a-N-CDs for the photoreduction of MV^{2+}.

Thanks to the wide availability, inexpensiveness, greenness and safety of biomass, in recent years a lot of studies about the possibility to use it as starting material for the preparation of CDs have been reported. Compared with classical molecular carbon sources, biomass, and specifically waste biomass, can therefore have many advantages.[122] For example, biomass naturally contains heteroatoms in contrast with man-made carbon sources that require external addition.[123] Recently, a large number of different biomasses have thus been used to synthesize CDs, such as goose feather,[124] bee pollen,[125] papaya juice[126] or walnut peel,[127] and they have been applied in different fields: bioimaging, drug delivery, sensors and others. Fish scales have also been employed recently for the synthesis of fluorescent NPs. An example is reported from Zhang et al. who reported a synthetic route for the obtainment of CDs from grass carp scales, used then for the detection of hypochlorite.[115] Other researches demonstrated the suitability of fish scales-derived CDs for the determination of the presence of ferric ions in real water samples and human serum,[128] but also for the detection of pharmaceuticals molecules as lidocaine hydrochloride.[129] Another spread application of fish-CDs is in the biomedical field. Alshatwi et al., for example, used *Lethrinus lentjan* scales to produce simultaneously CDs and hydroxyapatite and employed the NPs for bio-imaging and bone-tissue engineering applications.[130] In this frame, however, the photocatalytic activity and application of this type of CDs is still underexplored.

3.4.2 Synthesis and Characterization

All the carbonaceous NPs were prepared with a hydrothermal method as previously reported.[52,62] The unit operations for the synthesis of CDs from fish scales are summarized in **Figure 3.4.3**. Briefly, fresh sea bass scales were washed and dried in a vacuum oven. The dry scales were put in a Teflon lined autoclave together with water and heated at 200 °C for 24 h under continuous stirring. After filtration and water removal crude bass-CDs were obtained in 30-50% yields. Bass-CDs were then purified via dialysis using dialysis membrane with a cut-off of 1 KDa yielding 2-6% of pure fish-derived CDs (further details are provided in experimental section 3.4.5).

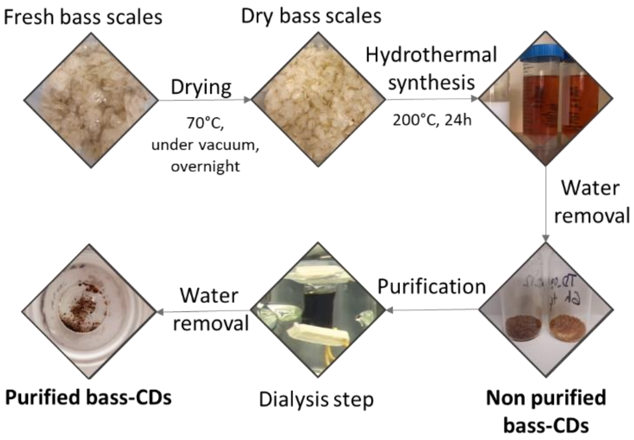

Figure 3.4.3. Diagram with unit operations for the synthesis of bass-CDs.

The variability in bass-CDs' yields was probably due to the differences in the composition of the scales depending on fish age and sex, season of fishing, habitat etc. On the other hand, for a-N-CDs higher yields were obtained (72%). The lower yields for bass-CDs clearly indicate that a high fraction of the selected biomass is not convertible into CDs. Indeed, sea bass scales contain also a large fraction of minerals, like $CaCO_3$, that can vary from 27 to 47%.[131,132,133] In **Table 3.4.1** the proximate composition of seabass scales reported in three literature works is shown.

Table 3.4.1. Proximate composition of seabass scales in different studies.

Composition (g/100 g wet weight)	**Razumovskaya et al.**[131]	**Bayram et al.**[132]	**Kishimura et al.**[133]
Moisture	38.61	40.95	26.72
Protein	29.44	28.47	24.32
Fat	0.20	0.10	0.68
Ash	30.92	27.86	47.31
Carbohydrate	0.83	0.80	-

An average elemental composition of the scales used for the synthesis of CDs is reported, instead, in **Table 3.4.2**. An exploratory test for the removal of minerals from scales was also performed: bass scales were pre-treated by stirring in 0.25 M HCl for 30 min at room temperature followed by rinsing to neutral pH and drying. The demineralized scales were then used as the starting material for the synthesis of CDs by hydrothermal treatment (200 °C, 24 h). The nanoparticles obtained from the demineralized scales were analysed by CHNS analysis and showed a C:N ratio of 3.2, the same as for bass-CDs prepared from non-treated scales (see **Table 3.4.2**). This evidence implies that the minerals present in the scales are not involved in the formation of the nanoparticles. For this reason, all the following CDs syntheses were performed without demineralizing the scales. As stated above, bass-CDs were then dialyzed for 24 h in milliQ water (cut-off 1KDa) and the purified dots obtained in 2-6% yields. The resulting materials were predominantly carbonaceous solids as confirmed by silent ^1H, $^{13}C\{^1H\}$ and two dimensional (2D) DOSY NMR spectra (see Appendix, **Figure A.3.4.1-A.3.4.3**). With NMR experiments it was possible to exclude the presence of soluble molecular and/or oligomeric species in the final products. However, the photocatalytic ability of the CDs obtained after dialysis and of the demineralized ones has been compared with that of the CDs made by simple treatment of the scales and no significant differences were observed. This evidence highlighted that both the molecular/oligomeric impurities present in the reaction mixture before purification and the minerals in the starting material are not involved in the photoactivity of CDs. On the other hand, a-N-CDs resulted to be sufficiently small to totally permeate the dialysis membrane. This is probably indicative of a significant formation of molecular-like fluorophores. As reported in **Chapter 3.2**, hydrothermal treatment - used in the present case - yields predominantly amorphous CDs. To better understand the morphology, composition and surface properties of the fish derived-nanoparticles, they were analysed by Small Angle X-ray Scattering (SAXS), Static Light Scattering (SLS), Fourier Transform InfraRed spectroscopy (FT-IR), X-ray Photoelectron Spectroscopy (XPS), Atomic Force Microscopy (SFM) and elemental analysis. The elemental composition of the nanoparticles indicated a C:N ratio of 3.2 for both bass-CDs and the CDs derived from citric acid and diethylenetriamine (a-N-CDs) used for comparison (**Table 3.4.2**). This result allowed to conclude that the carbon NPs obtained from bass scales have the same amount of nitrogen as the classic a-N-CDs, without the need of any doping agent.

Table 3.4.2. Elemental percentage composition of bass scales, bass-CDs and amorphous nitrogen doped CDs from citric acid (a-N-CDs).

	%N	**%C**	**%H**	**%S**	**C/N**
Bass scales	9.00	25.00	4.50	0.20	2.78
Bass-CDs	13.78	44.24	7.05	0.77	3.21
a-N-CDs	16.50	53.30	5.84	0.17	3.23

To evaluate the surface morphology of the nanoparticles FT-IR and XPS analyses have been performed (summary in **Table 3.4.3** and XPS in **Figure 3.4.4**). FT-IR spectra (see Appendix, **Figure A.3.4.4**) showed a broad absorption band around 3400 cm^{-1} corresponding to the O−H vibrations and a peak around 3300 cm^{-1} due to the N–H stretching. The strong absorption bands around 1700−1600 cm^{-1} reflected the presence of carboxylic acid, ketone and amide groups. Multiple signals in the region between 1600–1400 cm^{-1} were assigned to both C–C stretching of aromatic or conjugated double bonds and to the N–H bending of the N-containing groups. The XPS wide range spectrum of bass-CDs evidenced bands related to the presence of carbon, oxygen, and nitrogen. The quantitative analysis obtained by the intensity of C1s, O1s and N1s single spectra gave a relative composition of 66% carbon, 26% oxygen and 8% nitrogen (for a-N-CDs, the ratio was 70:20:10 of C:O:N). XPS analysis gave a different C/N ratio in respect to CHNS, because this technique refers only to the surface of the nanoparticles, whereas elemental analysis is related to the whole composition of the material. With this in mind, it can be highlighted that for both bass-CDs and a-N-CDs the nitrogen concentration is lower at the surface than in the bulk. In **Figure 3.4.4 a**, the C1s band, recorded in high-resolution mode, evidences three different contributions centered at 284.6 eV (related to C=C bonds, 60% of total area), at 285.8 eV (related to C=O and/or C=N bonds, 25% of total area) and at 288.0 eV (related to C–O and/or C–N bonds, 15% of total area) [62]. The O1s band is centered around 531.6 eV, in agreement with the presence of carbon-oxygen bonds. As far as nitrogen is concerned, the N1s band (**Figure 3.4.4 b**) can be well-fitted only by assuming the overlap of two different components, having approximately the same intensity, centered at 399.8 and at 401.1 eV of binding energy. The first component is in agreement with the presence of nitrogen involved in amine functional groups, the second one in amide compounds.[134]

Table 3.4.3. Comparison of morphology, composition and surface properties of bass-CDs and a-N-CDs.

	Elemental Analysis	**FT-IR**	**XPS**
Bass-CDs	C/N = 3.21	-OH -CH -NH (amines/amides) -Carbonyls -Aromatic C=C	-C-C -C-O or C-N -C=O or C=N -NH$_2$ -Amides C/O/N = 66/26/8
a-N-CDs	C/N = 3.23	-OH -CH -NH (amines/amides) -Ammonium -Carbonyls -Aromatic C=C	-C-C -C-O or C-N -C=O or C=N -NH$_2$ -C-N-C C/O/N = 70/20/10

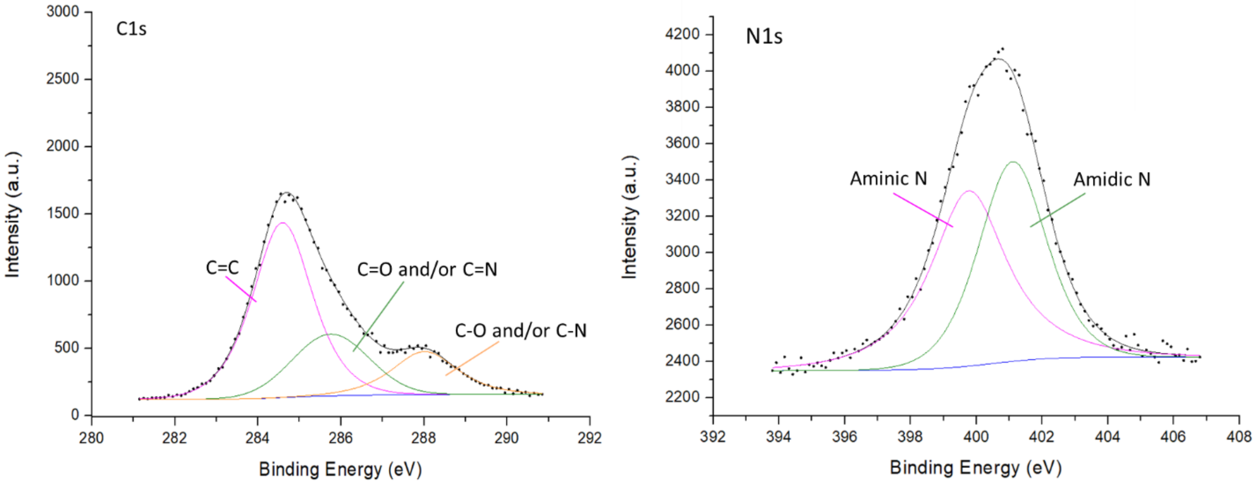

Figure 3.4.4. a) C1s and b) N1s XPS spectra of bass-CDs.

Concerning the shape and dimension of the carbon nanoparticles, SAXS measurements showed the presence of clusters of hundreds of nanometers, from the upturn in intensity in the low Q region of the scattering curves of both samples (see Appendix, **Figure A.3.4.5**). The surface fractal dimensions (D_s), extracted from the fitting procedures (described in the Appendix), informs about the roughness of the clusters surface. The D_s values are 2.29 for the a-N-CDs sample and 2.14 for the bass-CDs, describing quite smooth surfaces. The low roughness of the clusters' surface indicates that they consist of small primary particles, with low porosity and a smooth surface. Furthermore, SAXS measurements showed that the bass-CDs sample is characterized by the presence of smaller aggregates with a mass fractal behaviour, evidenced by the characteristic power law behaviour in the middle Q region (from approx. 0.0045 to 0.045 $Å^{-1}$) (more details in Appendix). The best fit, with a specific fractal model, confirmed their mass fractal behaviour, indicating the presence of aggregates with size of (127 ± 8) nm. The presence of these agglomerates was confirmed also by SLS measurement, which revealed the presence of clusters with an average diameter of (120 ± 30) nm (see Appendix, **Figure A.3.4.6**). The used model for SAXS measurements gives also the radius of the primary particles composing the aggregates, that is (4 ± 1) nm. For a-N-CDs, SLS turned out to be an unsuitable technique. In fact, they absorb the majority of the incident radiation and no intensity is able to reach the detector. AFM measurements highlight the spherical shape of both bass-CDs and a-N-CDs. The bass-CDs sample showed nanoparticles and clusters of different sizes. In **Figure 3.4.5 a**, visible clusters of hundreds of nanometers (center and bottom of the image) and agglomerates with a diameter around 120 nm (top left of the image) can be seen. In **Figure 3.4.5 b, c** single smaller spherical nanoparticles with a diameter around 10 nm are shown. The nanoparticle diameters estimated by AFM are in accordance with the ones measured by SAXS and SLS. It appears that the a-N-CDs have a more homogeneous size distribution compared to the bass-CDs, with nanoparticles having a diameter of 13 nm (**Figure 3.4.5 d, e**).

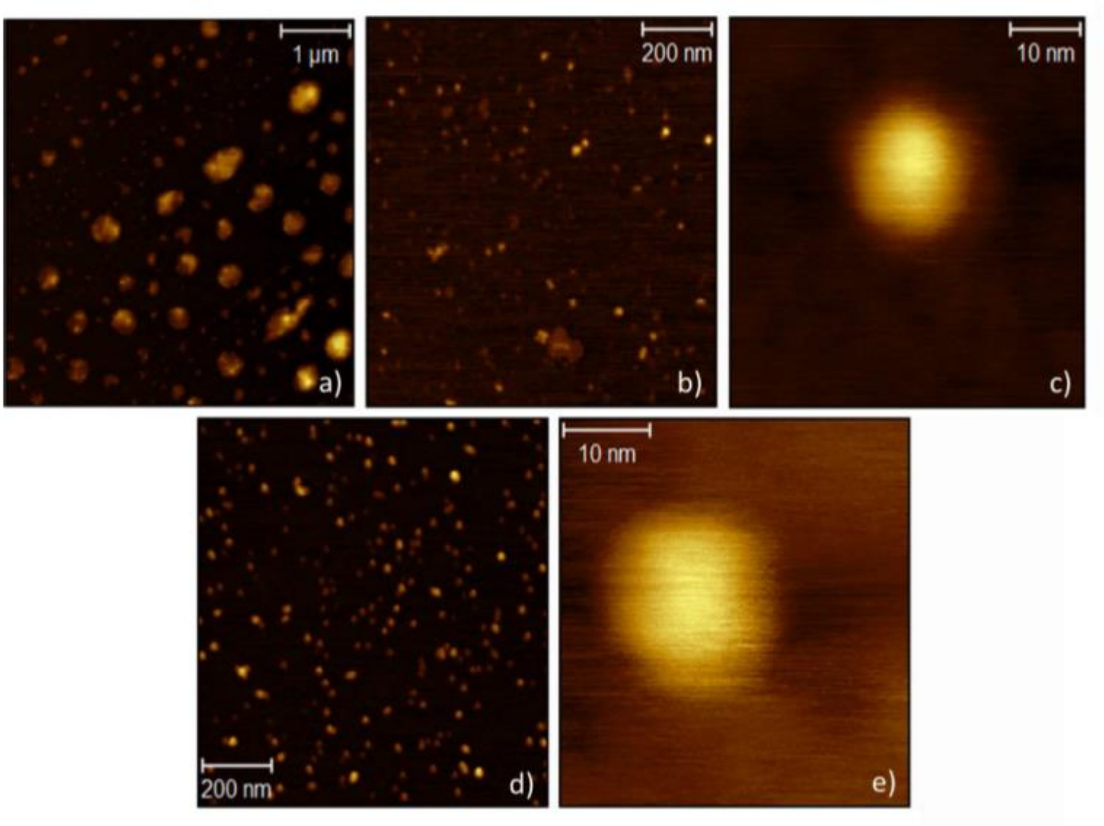

Figure 3.4.5. AFM images of bass-CDs (a-c) and a-N-CDS (d-e).

Ultraviolet-Visible (UV-Vis) spectroscopy, photoluminescence (PL) and time-resolved PL measurements were performed to investigate the optical properties of CDs. UV–Vis absorption spectroscopy of aqueous solution (0.25 mg/mL) of bass-CDs exhibits a characteristic absorption peak around 250 nm, which is mainly derived from the π-π * transition of aromatic carbons. The other peak around 350 nm could be ascribable to the n-π * transition of double bonds containing groups such as C=O and C=N.[135] As seen in **Figure 3.4.6**, both bass-CDs and a-N-CDs have the same absorption peaks but the absorbances are far more intense in citric acid-derived nanoparticles.

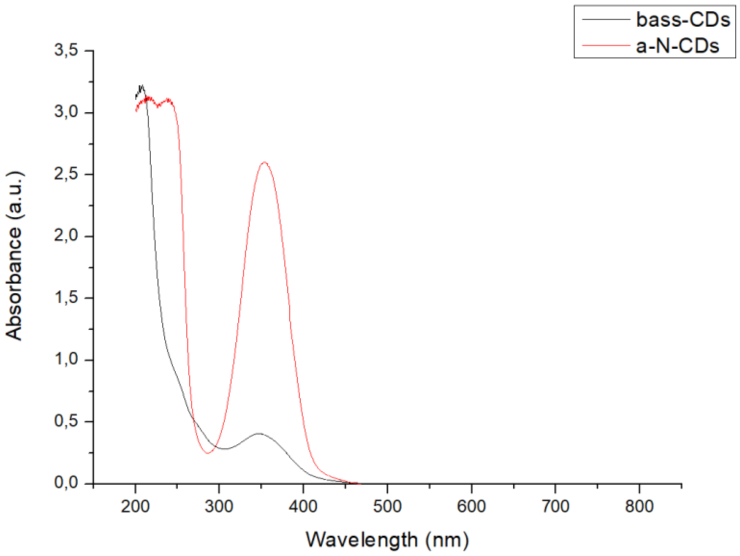

Figure 3.4.6. UV-Vis spectra of bass-CDs (black line) and a-N-CDs (red line).

The PL-PLE analysis of the bass-CDs revealed an excitation-dependent emission around 450 nm (see Appendix, **Figure A.3.4.7**), with a decrease in the emission wavelength decreasing the excitation wavelength, highlighting that the emission is probably due to surface defects and not from well-defined electronic levels. On the other hand, for a-N-CDs, the strong presence of one fluorophore gave a very stable and excitation-independent emission peak at 450 nm. In addition, time-resolved photoluminescence (PL) was applied to evaluate the PL lifetime of the excited states of the carbon nanoparticles (**Figure 3.4.7 a**). The average lifetime (τ) for bass-CDs was 7.0 ns, while for a-N-CDs a τ = 13.5 ns was observed. The τ of the dialyzed sample of bass-CDs was 6.5 ns, similar to the one of non-dialyzed bass-CDs, confirming the close similarity between the purified and non-purified samples. To fit the emission of bass-CDs, three constants were needed, while for a-N-CDs, only two were needed bot showing a multiexponential decay that underline the coexistence of different emission pathways; the behaviours of the PL decays and the parameters are reported in **Table A.3.4.2** in the Appendix chapter. The more linear character of a-N-CDs was consonant with a molecular-like emission, explained by the presence in its structure of molecular fluorophores.[62] Quantum yields (QYs, based on quinine sulphate) were also measured for the three types of CDs (a-N-CDs, bass-CDs and dialyzed bass-CDs). In **Figure 3.4.7 b**, the spectra collected in the integration sphere are reported (λ_{ex} = 372 nm). The curves refer to: the scattering from a blank reference (Sr, blue line), the scattering from the sample (Ss, red line), the emission from the reference (Er, green line) and the emission from the sample (Es, yellow line). The respective QY were then calculated using the following equation:

$$QY(\eta) = \frac{(Es - Er)}{(Sr - Ss)}$$

Equation 3.4.1. Calculation of the quantum yield.

The QYs for a-N-CDs, bass-CDs and dialyzed bass-CDs resulted to be, respectively, 17.3%, 6.0% and 3.1%. The larger QY observed for the a-N-CDs was attributed to the presence of molecular fluorophores, while the purified bass-CDs have a ≈ 48% lower QY, probably due to the loss of fluorophores occurred during the dialysis step. Another parameter that was taken into account was the mass absorption coefficient ε. From a previous work it was demonstrated that ε is dependent on the presence of nitrogen;[62] however, in this study ε = 10.93 $L \cdot g^{-1} \cdot cm^{-1}$ for a-N-CDs and ε = 0.37 $L \cdot g^{-1} \cdot cm^{-1}$ for bass-CDs were observed. These experimental data highlighted that ε was independent from the N-doping of the CDs: even if the C/N ratio is almost the same (3.23 for a-N-CDs and 3.21 bass-CD), the mass absorption coefficient is very different. For easier comparison, in **Table 3.4.4** the average lifetime (τ) of the excited state, the QY, and ε for the CDs, together with the photocatalytic activities (initial rate and conversion), are summarized. The observed trend indicates that higher QY of a-N-CDs (17.3%) with respect to the bass-CDs (6.0%) does not strictly correlate with the kinetics (4.9 $M \cdot s^{-1}$ for a-N-CDs and 7.5 $M \cdot s^{-1}$ for a-N-CDs). This apparent inconsistency was explained because QY, ε and τ are helpful in understanding PET but not strictly correlated with the catalytic activity that depends on multiple variables.

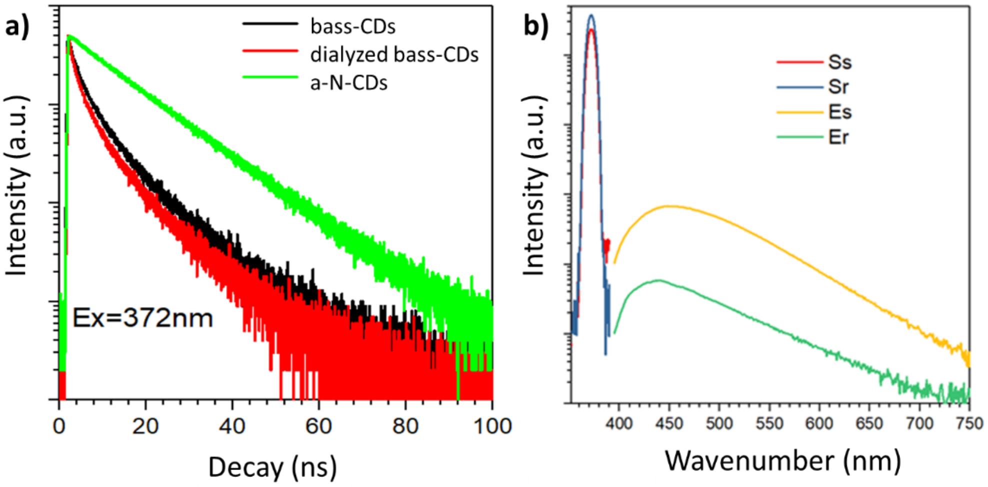

Figure 3.4.7. a) Time-resolved PL measurements of a-N-CDs (green), bass-CDs (black) and dialyzed bass-CDs (red); b) PL spectra collected in the integration sphere.

3.4.3 Photocatalytic experiments

Based on the assumption that the photocatalytic activity of CDs (e.g. their photoelectron transfer (PET) ability) is affected by their structure, morphology and optical properties, we decided to investigate it by studying the photoreduction of methyl viologen MV^{2+} to its radical cation $MV^{+\cdot}$. In this reaction, an electron is transferred from the photo-excited state of the CDs to the MV^{2+} that acts as acceptor molecule and is an established reactivity-test to prove the PET efficiency of CDs (**Figure 3.4.8 a**).[54,119,136] To understand the photoredox activity and correlate it with the structure of the bass-CDs, we measured the photoreduction rates of MV^{2+} (−0.45 V vs NHE) in aqueous solution in the presence of ethylenediaminetetraacetate (EDTA) as a sacrificial electron donor under light-emitting diode (LED) irradiation at 365 nm (time resolved UV-Vis spectra are shown in **Figure 3.4.8 b**) and compared with the one obtained with the already known a-N-CDs.[62]

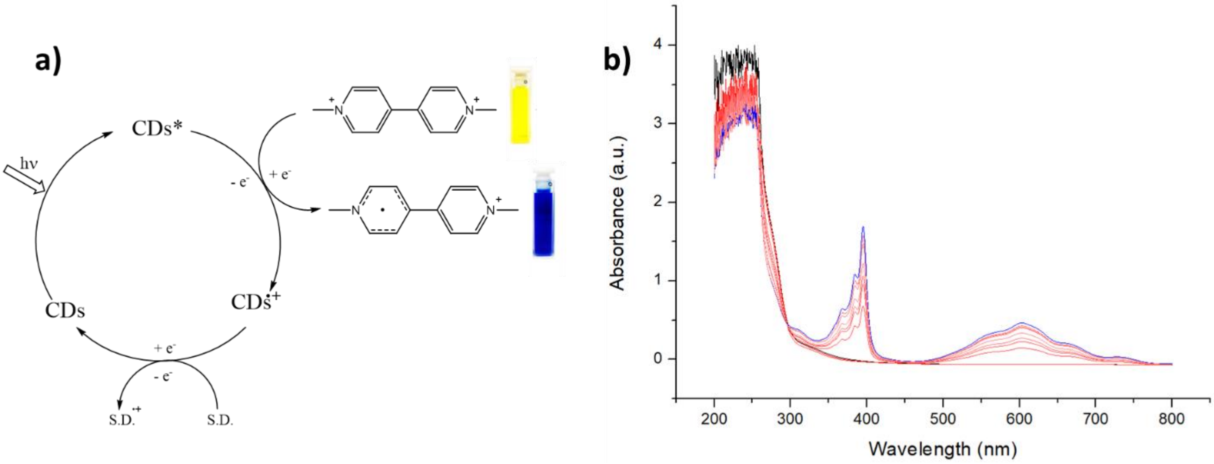

Figure 3.4.8. a) Catalytic scheme for the single electron photoreduction of methyl viologen with carbon dots (CDs); b) Time resolved UV-Vis spectra of bass-CDs (0.2 mg/mL) with methyl viologen (MV^{2+}, 60μM) in aqueous EDTA (0.1 M) under inert atmosphere (blue line after 30 minutes of reaction).

In order to compare the photocatalytic activity of the two prepared set of CDs, two different experiments were carried on: one using a concentration of NPs normalized for absorption at 365 nm, and another one using the same concentration of photocatalyst (mg of CDs/mL). Concerning the experiment with the normalized absorption concentration of CDs, bass-CDs resulted to be far less luminescent, and a higher concentration was needed to reach the same absorption as a-N-CDs (0.2 mg/mL of bass-CDs vs 0.005 mg/mL a-N-CDs to have an absorbance of 0.13 a.u.). However, as can be seen in **Figure 3.4.9** and **Table 3.4.4**, bass-

CDs showed a higher initial photoreduction rate ($7.5 \cdot 10^{-8}$ vs $4.9 \cdot 10^{-8}$ $M \cdot s^{-1}$) and a higher MV^{2+} conversion (34.0 vs 21.8 µM). On the other hand, using the same concentration of photocatalyst, a-N-CDs resulted to be far more luminescent (2.90 vs 0.13 a.u. at 365 nm) but only slightly more reactive toward PET to MV^{2+}. Indeed, after 30 min, a-N-CDs gave a substrate conversion of 62.5% (37.5 µM) compared to the 56.6% of bass-CDs (**Figure 3.4.9** and **Table 3.4.4**). These results highlighted the strong PET ability of bass-CDs, without the need of additional external nitrogen doping agent and despite their lower absorbance when compared to a-N-CDs. A series of control reactions with a-N-CDs (tested in the absence of light, without CDs and without EDTA) were already reported in a previous work[62] and demonstrated that, in the absence of irradiation, EDTA or CDs, no MV^{2+} reduction was observed, implying that all three were indispensable. Two additional control experiments, with the bass-CDs and in the absence of light (pink data in **Figure 3.4.9**) and with bass-CDS and without EDTA (green datapoints in **Figure 3.4.9**), further confirmed these requirements for the photochemical reduction of MV^{2+}. Cyclic Voltammetry (CV) experiments were carried out on a-N-CDs in a previous work of our group[102] to measure their redox activity and correlate the energy levels of the nanomaterials with the relative band gap. a-N-CDs showed a negative potential (E onset red = −1.94 vs Ag|AgCl), suggesting a good reducing capability. The energy gap of the nanomaterials resulted to be of 3 eV, thanks to the presence of molecular-like fluorophores that ensure a high PET efficiency, implying a great energy of the excited electron generated upon irradiation.

Table 3.4.4. Initial photoreduction rate (v_0), quantum Yields (QY), mass absorption coefficient (ε), average lifetime (τ), and MV^{2+} conversion of the synthesized CDs.

	CDs concentration (mg/mL)	**Absorbance at 365 nm**	**$v_0 \cdot 10^{-8}$ ($M \cdot s^{-1}$)**	**QY (%)**	**ε ($L \cdot g^{-1} \cdot cm^{-1}$)**	**τ (ns)**	**MV^{2+} conversion (%)**
Bass-CDs	0.2	0.13	7.5	6.0	0.37	7.0	56.6
a-N-CDs	0.005	0.13	4.9	17.3	10.93	13.0	36.3
a-N-CDs	0.2	2.9	9.6	17.3	10.93	13.0	62.5

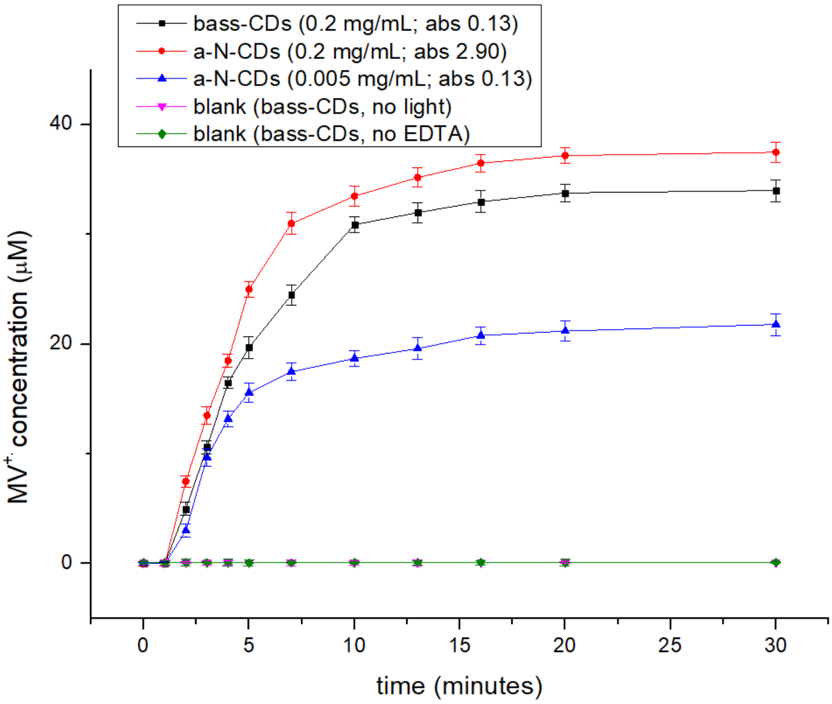

Figure 3.4.9. Reaction kinetics of the formation of methyl viologen radical ($MV^{+\cdot}$) using bass-CDs (black datapoints) and a-N-CDs (red and blue datapoints). Blank tests in absence of light (pink datapoints) and of EDTA (green datapoints).

3.4.4 Conclusions

The valorisation of fishery biowaste, in particular bass scales, for the production of luminescent carbon NPs with high photoelectron transfer ability, has been demonstrated in this study. The new class of prepared CDs (bass-CDs) was characterized in-depth regarding their composition, morphology and surface properties: the fish-derived dots showed a considerable nitrogen content (C/N = 3.2 from elemental analysis) without the need of any external doping agent. Since nitrogen doping in CDs is known to enhance the photocatalytic activity of the nanoparticles, bass-CDs were then compared with CDs obtained from citric acid and diethylenetriamine (a-N-CDs) toward the single electron reduction of MV^{2+}. Bass-CDs resulted to have lower lifetime of the excited state (7.0 ns vs 13.0 ns of a-N-CDs), mass absorption coefficient (0.37 $L\cdot g^{-1}$ cm^{-1} vs 10.93) and QY (6.0% vs 17.3%), but higher initial photoreduction rate ($7.5\cdot10^{-8}$ $M\cdot s^{-1}$ vs $4.9\cdot10^{-8}$ $M\cdot s^{-1}$ for absorption normalized experiment). This experimental evidence contributes to highlight the fact that τ, ε and QY are important parameters to understand the photoelectron transfer activity of CDs, but they are not strictly correlated with the photocatalytic ability of the nanoparticles. However, a lower value of QY seems to favour the photocatalytic activity of CDs, presumably because the absorbed photons are not immediately re-emitted but can instead transfer their energy to perform the photoreduction. The fish scale-derived CDs have similar morphology to that of the a-N-CDs, but less intense absorbance, lower QY, τ and ε. Despite this, bass-CDs resulted to function as a valuable photocatalyst and to have a higher photoelectron transfer ability toward methyl viologen.

3.4.5 Experimental

Materials. All the reagents were purchased from Merck Life Science S.r.l. (Milano, Italy), were of analytical grade and used without further purification. MilliQ water, obtained with a Merck Millipore C79625 system, was used as a solvent throughout the experiment. The scales were of sea bass (*Dicentrarchus labrax*) and were purchased from a local market. Before use, the scales were washed thoroughly with water and dried in a vacuum oven at 70 °C overnight.

Synthesis of CDs from Fish Scales. In a typical experiment 2 g of dried and grounded fish scales were put in a Teflon-lined autoclave with 20 mL of MilliQ water. The system was heated at 200 °C for 24 h. The obtained brownish suspension was filtered, and the water was removed by rotary evaporation to obtain a brown solid with 30–50% yield. For some studies the CDs were further purified via dialysis: A total of 200 mg was dispersed in 3 mL of milliQ water and dialyzed for 24 h using a 1KDa dialysis membrane in 2 L milliQ water. The resulted purified CDs were obtained with 2–6% yield.

Characterization of CDs. The physical characterization of the nanoparticles was determined by CHNS elemental analysis, Fourier-Transform Infrared (FT-IR) spectroscopy, X-Ray Photoelectron Spectroscopy (XPS), Small Angle X-Ray Scattering (SAXS) and Static Light Scattering (SLS). CHNS analysis was performed on an Elemental Unicube (Elementar Italia Srl, Lomazzo, Italy) and FT-IR spectra have been recorded on a Perkin-Elmer Spectrum One FT-IR spectrometer (PerkinElmer Italia, Milano, Italy) at wavenumbers ranging from 400 to 4000 cm^{-1}. XPS was performed with a Perkin Elmer Φ 5600ci spectrometer (PerkinElmer Italia, Milano, Italy) in the 10^{-7} Pa pressure range, by using nonmonochromatic Al Kα radiation (1486.6 eV). The binding energy (BE) values are referred to the Fermi level. BE scale calibration was confirmed by the position of both Au4f 7/2 and Cu2p 3/2 bands in pure metal samples, falling, respectively, at 84.0 and 932.6 eV. Wide range survey spectra were recorded for all the sample. Single spectra were recorded for C1s, O1s and N1s regions. The recorded XPS bands were fitted using a non-linear least-square fitting procedure adopting a Shirley-type background and Gaussian–Lorentzian peak shapes for all the peaks (XPSPEAK41 free software, 4.1, Raymund W.M. Kwok, Hong Kong, China). The BE correction from the surface charging evidenced during analysis (around 2–3 eV) was done by using as internal reference, with the position at 284.6 eV of the C1s band related to C=C bonds [62], checking, in addition, the consistency of the BE positions of all the other bands evidenced in the different XPS peaks. The BE values final uncertainty was not larger than 0.2 eV. The atomic composition of the analyzed region (about 5–10 nm of thickness from the surface) was estimated by using sensitivity factors provided by Φ V5.4A software (Perkin Elmer, Physical Electronics, Eden Prairie, MN, USA): the relative uncertainty of the atomic fraction of the different elements was lower than 0.1. SAXS measurements were performed at the European Synchrotron Radiation Facility (ESRF; Grenoble, France) on the ID02 beamline [137], using an X-ray wavelength of ~ 0.1 nm. Two sample-to-detector distances (SDD) were used (1 and 8 m) to obtain a Q-range of 0.0008–0.74 $Å^{-1}$ (Q = scattering angle). Scattering patterns were collected by taking 10 successive exposures of 0.05 s to reduce radiation damage. The measured two-dimensional scattering patterns were normalized to an absolute intensity scale and azimuthally averaged to obtain the one-dimensional scattering profiles. The corresponding background was then subtracted before the profiles, from different SDDs, were merged. The one-dimensional SAXS profiles were analyzed using the SasView software [138]. Static Light Scattering (SLS) measurements were performed using a Malvern Zetasizer (Malvern Products, Palaiseau, France) with a He-Ne laser light source (633 nm). The measurements were carried out at 25.0 °C for a duration of 30 s for each one, and the samples were dispersed in water, filtered at 0.22 mm and placed in 1 mL cuvettes. The high-resolution Atomic Force Microscopy (AFM, Oxford Instruments Cypher Asylum Research, available at the AFM platform of the PSCM at Grenoble) was used in tapping mode to investigate dimensions and morphology of the obtained nanoparticles or of their aggregates. The samples were prepared in accordance with the standard procedures using a spin coater. For the optical characterization of CDs, an UV–Vis spectrophotometer Agilent 8456 (Agilent Technologies Italia, Milano, Italy) and photoluminescence excitation (PLE) were used and emission (PL) spectra were recorded by a Perkin Elmer LS 55 fluorescence spectrophotometer (PerkinElmer Italia, Milano, Italy). ^{1}H, ^{13} C{^{1}H}, DOSY NMR spectra were recorded on a Bruker AV 300 (^{1}H: 300 MHz; ^{13}C: 75.5 MHz; 51V: 78.28 MHz) spectrometer (Bruker GmbH, Mannheim, Germany). For ^{1}H and ^{13}C\{^{1}H\} NMR, the chemical shifts (δ) were reported in parts per million (ppm) relative to the residual undeuterated solvent as an internal reference.

Photoreduction of Methyl Viologen (MV). A solution composed by 0.1 M of EDTA, 60 µM of MV with an absorbance normalized amount of CDs (a.b.s. = 0.13 a.u.; 0.005 mg/mL a-N-CDs, 0.2 mg/mL bass-CDs) were placed under inert atmosphere in a quartz cuvette. The solutions were then irradiated at 365 nm fixed wavelength emission (Hangar s.r.l.; ATON LED-UV 365; 80 W/m^2 of irradiance in the UVA spectral range 315–400 cm^{-1}). The progress of the reactions was monitored using an UV spectrophotometer following the formation of the typical absorption band of the reduced $MV^{+\cdot}$ radical cation form centered at 605 nm, and its concentration was estimated using ε = 13700 M^{-1} cm^{-1}. The same experiment was conducted also using the same concentration of bass-CDs and a-N-CDs (0.2 mg/mL). A series of blank reaction were also performed to assess the effectiveness of the CDs in catalyzing the reduction of MV (E = -0.45V vs NHE). All the blank tests performed reveal that CDs is essential to guarantee the effectiveness of the photochemical reduction of the MV.

3.5 Continuous flow Photooxidative degradation of Azo Dyes with Biomass-derived Carbon Dots

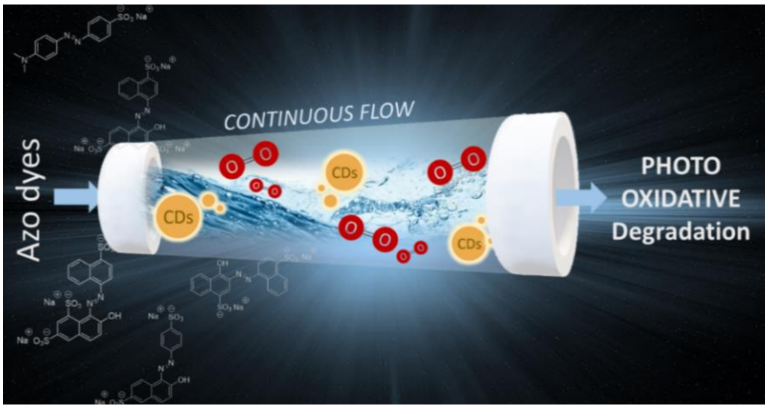

The investigation conducted on the preparation of fish based-CDs (see ***Chapter 3.4****) prompted us to explore other photocatalytic applications. In this chapter the advantages of CDs as photocatalysts have been merged with the one of flow-chemistry for the continuous flow degradation of azo-dyes. This study has been conducted in the laboratories of Prof. Jean-Christophe Monbaliu in the Université de Liège, Belgium and the results have been published in* C. Campalani, G. Petit, J.C.-M. Monbaliu, M. Selva and A. Perosa, *ChemPhotoChem*, **2022**, e202200234. doi: 10.1002/cptc.202200234.[139]

The presence of persistent organic pollutants in industrial wastewaters is becoming a problem of major concern. In the present study we explored the degradation of azo dyes, well-known common hazardous contaminants, by a green and efficient procedure using continuous flow photooxidative degradation. In particular, carbon dots synthesized from fishery waste (bass-CDs) were used as a cheap and readily available photocatalyst in combination with oxygen and UV light. Methyl orange, acid red 18, amaranth, sunset yellow and chromotrope were chosen as model substrates and their degradation was studied both in batch and in continuous flow conditions. All the azo dyes were fully degraded with both techniques highlighting the suitability of bass-CDs for the decontamination of wastewater. The main advantages are of using a "disposable" photocatalyst, in aqueous solvent and in continuous flow. In particular, continuous flow operation allowed faster decompositions: ca. 2 min versus 1-3 hours needed in batch.

3.5.1 Introduction

In recent years the release of toxic and persistent pollutants in the aquatic environment is becoming a topic of major concern. Synthetic dyes, in particular, form the largest group of chemicals that are produced worldwide and are among the most serious source of environmental contaminants. The global market relative to dyes and pigments is expected to rise to USD 37 billion by 2023 with an estimated annual growth rate of 5.46% (years 2018-2023).[140] Concerning the type, volume and complexity, the textile sector occupies a major role in the dyes market.[141] About 10,000 different dyes are used in the textile industry,[142] with 60-70% constituted by azo dyes[143,144] that can be toxic and nonbiodegradable. The release of these dyes into water bodies has been posing severe threats to humans and aquatic organisms due to their carcinogenic effects on liver, kidney and on the cardiovascular system.[142,145] Reactive azo dyes are characterized by one or more azo chromophores in the molecular structure.[146] Their structure and synthetic origin make them difficult to degrade even at low concentrations because of their resistance to light, heat, chemicals and microbial action, rendering their removal by conventional wastewater treatment very difficult.[147,148,149,150]

In order to minimize the impact of these dyes on the environment, different approaches are currently used. These common processes include adsorption by activated carbon,[151] precipitation,[152] coagulation,[153] membrane ultrafiltration[154] and reverse osmosis.[155] However classical methods are inefficient because they merely transfer the dye from one phase to another producing secondary waste. Photocatalysis, on the other hand, is an advanced oxidation process (AOP), considered as an effective technique to purify wastewater by chemical degradation of the dyes.[156,157] Upon excitation, the formation of electron-hole pairs on semiconductors leads to the production of chemically active free radicals in the reaction media, in particular in water. These radicals, in particular hydroxyl (•OH), superoxide (•OO$^-$) and hydroperoxyl (•OOH), are able to attack specific bonds of organic compounds and to decompose them, resulting in less harmful by products such as carbon dioxide, water and mineral acids.[158] The photocatalytic activity of various semiconductor materials has been investigated over the years to degrade aqueous organic pollutants[159] with a major attention towards titanium dioxide,[160,161,162,163,164,165,166,167,168] zinc oxide[169,170] or other metal oxides.[171]

As a new class of semiconductor nanomaterials, Carbon Dots (CDs) are gaining attention also in the field of wastewater treatment for the removal of dyes.[172] CDs are, in fact, luminescent, biodegradable and bio-based carbon material that are promising for photocatalytic applications[52] but even with the immense progress in their synthesis, there are still few reports where bare CDs were directly used as active photocatalytic material for the degradation of dyes,[38] and in particular azo dyes. For this application, in fact, CDs are used mainly as synthetic hybrid composites with other wide bandgap semiconductors.[173,174,175]

In one of our previous work we demonstrated the possibility to hydrothermally synthesize CDs with high ability in photoelectron transfer starting from fishery waste.[99] These carbon nanomaterials are fully biobased and biodegradable and, in the present work, the idea to exploit their photocatalytic behaviour in order to degrade azo dyes was developed. One of the main advantages is that such CD photocatalysts are cheap, easily available and biocompatible, all features that make these materials disposable along with the treated effluent. In particular, the decomposition of five azo dyes, namely methyl orange (MO), acid red 18 (AR), amaranth (AM), sunset yellow (SY) and chromotrope (CH) (**Figure 3.5.1**), was studied in batch and with a continuous flow (CF) microfluidic reactor.

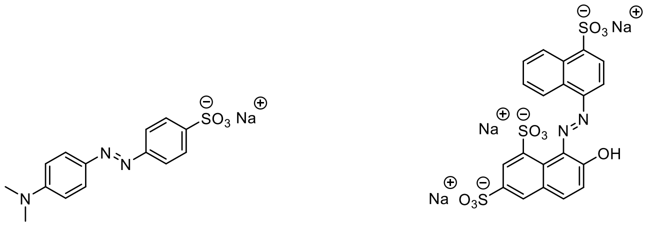
1 - Methyl orange (MO)

2 - Acid red 18 (AR)

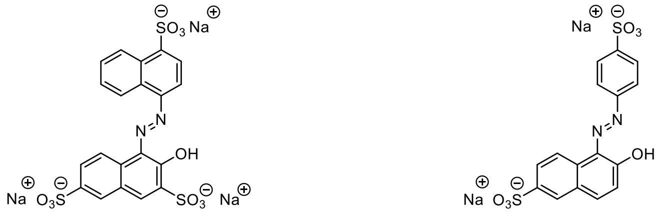
3 - Amaranth (AM)

4 - Sunset yellow (SY)

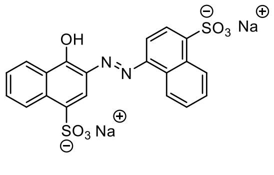
5 - Chromotrope (CH)

Figure 3.5.1. Azo dyes studied in the present work.

In 2019, indeed, the International Union of Pure and Applied Chemistry (IUPAC) has nominated flow chemistry as one of the top ten emerging technologies in chemistry with high potential for sustainable processes.[176,177,178,179] Batch reactors, despite being versatile, easy to operate and able to process most chemicals, are characterized by low surface/volume ratio while flow systems offer an alternative to improve the reaction efficiency by enhancing both mass and heat transfers and by allowing a precise control of the reaction parameters.[178] Thanks to their outstanding advantages, in the past decades, CF technologies started to have a crucial role for process intensification: they permit to decrease equipment size/production ratio, energy consumption and waste production leading to cheaper and more sustainable pathways.[180] Flow chemistry allows chemical reactions in a continuous manner within a well-defined micro- or mesometric environment. A continuous flow reactor is typically made of narrow channels through which streams of chemicals are pumped and set to react for a definite time at given temperature and pressure. Their dimensions can range from sub-millimetric (microfluidic reactors) to sub-centimetric (mesofluidic reactors),[177] allowing better reaction rates. This is achievable thanks to the possibility to easily pressurize and heat above their normal boiling point the reagents: from a general point of view, CF permits a quick variation of reaction conditions (T, p, flow rate, molar ratio, concentration, etc.) together with a rapid reaction optimization and scale-up. Another unique aspect of flow systems compared to batch ones is the option to carry out multistep syntheses by designing a set-up comprised of several flow reactors.[181] The small size of microreactors (<1 mm in at least one dimension) offers additional multiple advantages in minimizing the reagent consumption and energy waste, and in improving safety during handling of hazardous chemicals and/or the conduction of exothermic reactions.[182] In addition, an almost instantaneous mixing can be achieved in micro-structured devices.[183] Lately, as stated above, many conventional batch plants have been replaced by CF technologies as witnessed by the fact that the top 30 petrochemicals and most of the top 300 chemicals produced worldwide are obtained through flow reactions that have proved to be more efficient and sustainable than batchwise counterparts.[184] In a lab configuration, different kinds of pumps (HPLC, syringe, etc.) are used to deliver liquid reactants (or their solutions) at the desired flow rate, into the reactor. If gases are necessary, the relative amounts are set and checked by a mass-flow controller. Four main types of reactors can be employed: continuous flow stirred tank reactors; packed-bed reactors; coil reactors; and chip reactors. Continuous flow stirred tank reactors are the most conventional ones in which the reactants are continuously delivered and stirred at the desired conditions. A packed bed reactor is a tubular reactor filled with a catalytic bed where, very often, the active phase (metal, ionic liquid, etc.) is dispersed/grafted in/on a support (carbon, alumina, silica, etc.) or even a simple inert matrix (Raschig rings or sand).[185] Coiled reactors are also tubular reactors, but in the form of coils with outer diameters of 1/8" - 1/16" and inner diameters >1mm. Microfluidic reactors belong to this subclass, and they have been demonstrated to suit catalyst-free high T/p applications, photochemical reactions, and processes where the catalyst is deposed at a molecular level. Finally, despite the significant cost, chip reactors systems offer extremely high surface-to-volume ratios and high accuracy in heat transfer. For instance, glass chip reactors are a thin pane of glass with a micro-channel in between, allowing for reagents to travel through. A CF-apparatus is then completed by a back-pressure regulator (BPR) which allows to operate at a constant upstream system pressure, and one or more samplers to withdraw and analyse the products mixture without affecting the reactions conditions.
The photodegradation of azo dyes in continuous flow conditions is still an underexplored topic even if inherent advantages of the microreactor system, such as the high surface-to-volume ratio, short diffusion distances, and rapid mass transfer, can improve the photocatalytic performance degrading organic contaminants.[186,187,188,189] Only few works reported this kind of approach by using more conventional photocatalysts such as titanium dioxide, zinc oxide, metal nanoparticles or hydrogen peroxide.[140,190,191,192,193,194,195,196]

We herein report an efficient and sustainable process for the degradation of azo dyes using a continuous flow microfluidic photoreactor, exploiting oxygen and fish waste-derived CDs as photocatalyst.

3.5.2 Results and Discussion

CDs derived from fish waste were selected as photocatalyst for the degradation of five azo dyes (MO, AR, AM, SY and CH). These nanoparticles were obtained by hydrothermal synthesis using bass scales as carbon precursor resulting in nitrogen self-doped spherical dots with diameter around 10 nm. Bass-CDs exhibited two UV-Vis absorptions at 250 and 350 nm ascribable to the π-π^* transition of aromatic carbons and n-π^* transition of double bonds containing groups respectively. An excitation-dependent emission around 450 nm was observed, highlighting the role of defects in the emission mechanism.[99]

The photooxidative degradation of dyes induced by CDs can be described as follows (**Figure 3.5.2**). When CDs absorb light at the proper wavelength, electrons in the valence band are excited to the conduction band creating holes in the valence band (**Equation 3.5.1**). The electrons in the conduction band (e^-_{CB}) and the holes in the valence band (h^+_{VB}) can undergo recombination releasing heat (**Equation 3.5.2**) or can react with water or oxygen dissolved in the aqueous medium. In particular, the holes in the valence band can react with water to produce hydroxyl radicals (**Equation 3.5.3**) or can directly convert the organic dye to highly reactive intermediates leading to subsequent oxidation (**Equation 3.5.4**). On the other hand, the electrons in the conduction band can react with oxygen to form superoxide radicals (**Equation 3.5.5**) and, further, hydroperoxyl radicals (**Equation 3.5.6**). All these radicals play a crucial role in degrading the organic dye, finally leading to mineralization (**Equations 3.5.7** and **3.5.8**).[158]

(3.5.1) $\text{CDs} + h\nu \rightarrow \text{CDs}\,(e^-_{CB} + h^+_{VB})$
(3.5.2) $e^-_{CB} + h^+_{VB} \rightarrow$ heat
(3.5.3) $h^+_{VB} + H_2O \rightarrow \bullet OH + H^+$
(3.5.4) h^+_{VB} + organic pollutants → degraded products
(3.5.5) $e^-_{CB} + O_2 \rightarrow \bullet OO^-$
(3.5.6) $\bullet OO^- + H^+ \rightarrow \bullet OOH$
(3.5.7) $\bullet OH$ + organic pollutant → degraded products
(3.5.8) $\bullet OOH$ + organic pollutant → degraded products

Equations 3.5.1-8. Possible degradation mechanism of azo dyes in presence of CDs and oxygen.

By looking at the mechanism the crucial role of oxygen in the degradation of organic pollutants is evident. A hypothetical mineralization pathway for methyl orange is reported in the Appendix in **Scheme A.3.5.1**. The investigation started with batch experiments for the decomposition of the selected azo dyes to further continue with the implementation in continuous flow.

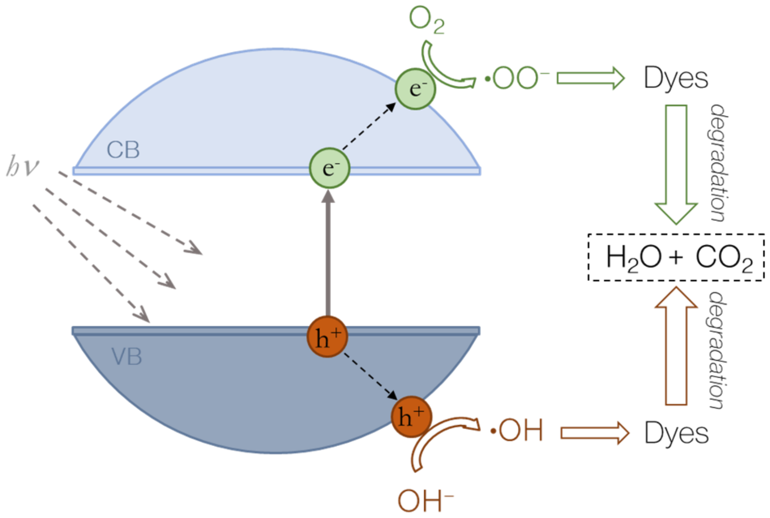

Figure 3.5.2. Schematic representation of the photooxidative degradation mechanism of azo dyes.

Batch experiments

The investigation started in batch, using UV light, bass-CDs as photocatalyst and by bubbling oxygen inside the reaction flask. Using these conditions all the five selected azo dyes were completely degraded in 1 to 3 hours (entries 1, 4, 7, 10 and 13 **Table 3.5.1**) demonstrating the ability of CDs to produce the oxygenated radicals necessary to initiate the reaction pathway that leads to the decomposition.

To further confirm the importance of all the components, control tests without CDs or oxygen were performed. Using only the carbon nanoparticles it was possible to degrade consistent portions of the dyes (86% for MO, 73% for AR, 75% for AM, 67% for SY and 100% for CH) but in longer reaction times (24h, entries 2, 5, 8, 11 and 14 **Table 3.5.1**). This is probably due to the ability of CDs either to produce radicals directly from water (**Equation 3.5.3**) to photoactivate the dissolved oxygen (**Equation 3.5.5**), or to degrade directly the dye (**Equation 3.5.4**). In any case, following these pathways, the degradation resulted to be slower confirming the need of external oxygen. On the other hand, using only oxygen it was possible to observe some degradation but again the degradation rate resulted to be slower than all the other cases (entries 3, 6, 9, 12 and 15 **Table 3.5.1**). In fact, degradation yields of 24% (for SY) up to a maximum of 62% (for CH) in 24 hours were reached using only oxygen in absence of bass-CDs. In these cases, probably the direct photolysis of the dyes under irradiation can result in partial mineralization. As reported from Wang et al.,[197] indeed, the dye can be excited to produce singlet and triplet states dyes (**Equation 3.5.9**) and it can be consequently involved in the generation of the hydrated electron (e_{aq}^-) rather than the injection of an electron in the conduction band of the semiconductor (**Equations 3.5.10-12**). The reaction pathways described then in **Equations 3.5.13-15** can then take place to produce hydrogen peroxide that is easily decomposed to hydroxyl radicals by irradiation (**Equation 3.5.16**). As already showed in **Equation 3.5.7**, the hydroxyl radicals have a major role in the degradation of pollutants (**Equation 3.5.17**). However, this degradation pathway resulted to be far way less efficient than the one with the addition of a semiconductor, CDs in our case.

(3.5.9) Azo dye + $h\nu \rightarrow$ Azo dye *
(3.5.10) Azo dye* $\rightarrow$ •Azo dye$^+$ + e^-
(3.5.11) •Azo dye$^+$ + e^- $\rightarrow$ •Azo dye$^+$ + e_{aq}^-
(3.5.12) Azo dye * + $h\nu \rightarrow$ •Azo dye$^+$ + e_{aq}^-
(3.5.13) $e_{aq}^- + O_2 \rightarrow \bullet OO^-$
(3.5.14) $\bullet OO^- + H^+ \rightarrow \bullet OOH$
(3.5.15) $\bullet OOH + \bullet OO^- + H^+ \rightarrow O_2 + H_2O_2$
(3.5.16) $H_2O_2 + h\nu \rightarrow 2\ \bullet OH$
(3.5.17) Azo dye + •OH $\rightarrow$ degraded products

Equations 3.5.9-17. Possible degradation mechanism of azo dyes in presence of oxygen and under irradiation (in absence of CDs).

Other control experiments in the absence of light were also performed for 24 hours: almost no degradation was observed for all the five dyes confirming the need of the combination of oxygen/CDs/irradiation (see Appendix **Figure A.3.5.2**).

The observed trend for MO is reported as an example in **Figure 3.5.3** (for the AR, AM, SY and CH, see Appendix **Figure A.3.5.1**). The UV-Vis spectra are reported in the Appendix in **Figures A.3.5.13-22**.

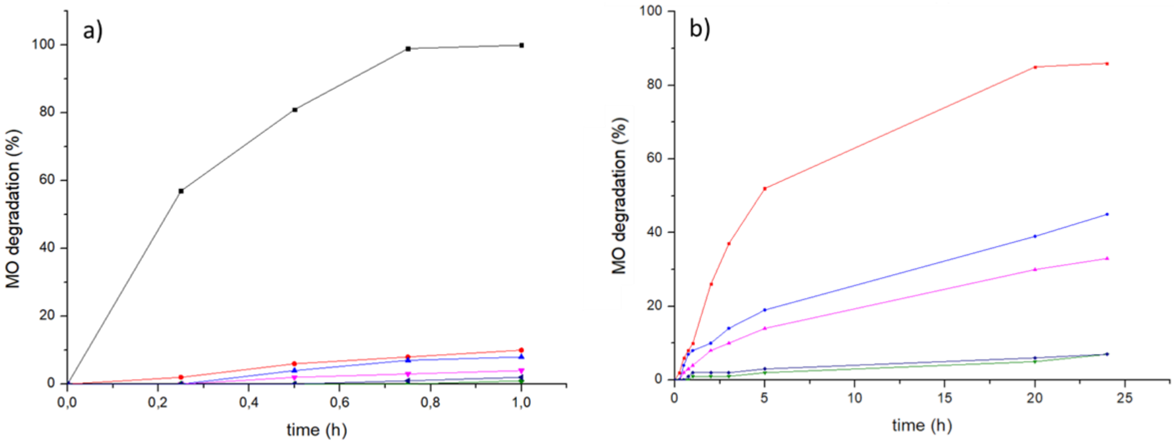

Figure 3.5.3. Observed trend for the photooxidative degradation of methyl orange in batch conditions. a) trends in 1 hour: b) trends in 24 hours. Black = using CDs and Oxygen, red = no oxygen, blue = no CDs, pink = no CDs no oxygen, green = no oxygen no light, dark blue = no CDs no light.

As can be seen in **Table 3.5.1** and in **Figure A.3.5.1** the trend is similar for all the azo dyes except for CH. In that case, in fact, also the test performed using CDs without oxygen was effective and managed to reach 100% of degradation in 24 h. The chemical structure is similar for all the dyes but, reasonably, in CH the hydroxyl group in *para* to the sulfonic group allows an easier oxidation leading to a quinone intermediate.

Table 3.5.1. Best degradation percentage reached for MO, AR, AM, SY and CH in batch conditions.

Entry	Azo dye	Conditions	Degradation (%), (time)	k ($M \cdot min^{-1}$)
1	MO	Oxygen + CDs	quant. (1 h)	$1.4 \cdot 10^{-4}$
2		Only CDs	86 (24 h)	$2.7 \cdot 10^{-5}$
3		Only Oxygen	45 (24 h)	$2.5 \cdot 10^{-5}$
4	AR	Oxygen + CDs	quant. (1 h)	$1.4 \cdot 10^{-4}$
5		Only CDs	73 (24 h)	$8.0 \cdot 10^{-6}$
6		Only Oxygen	59 (24 h)	$3.3 \cdot 10^{-6}$
7	AM	Oxygen + CDs	quant. (2.5 h)	$6.1 \cdot 10^{-5}$
8		Only CDs	75 (24 h)	$7.1 \cdot 10^{-6}$
9		Only Oxygen	30 (24 h)	$6.9 \cdot 10^{-6}$
10	SY	Oxygen + CDs	quant. (2 h)	$1.5 \cdot 10^{-4}$
11		Only CDs	67 (24 h)	$1.3 \cdot 10^{-5}$
12		Only Oxygen	24 (24 h)	$1.4 \cdot 10^{-5}$
13	CH	Oxygen + CDs	quant. (3 h)	$5.5 \cdot 10^{-5}$
14		Only CDs	quant. (24 h)	$3.4 \cdot 10^{-5}$
15		Only Oxygen	62 (24 h)	$6.7 \cdot 10^{-6}$

To further confirm the complete mineralization of the dyes ^{1}H NMR experiment were conducted on the reaction mixtures. As can be seen in the spectra reported in **Figures A.3.5.3-12** (Appendix), all the peaks related to the azo dye molecules disappeared and silent NMR spectra were recorded. This evidence highlights the absence of organic molecules: the starting material disappeared, and no other organic compound was detected. As already observed in the literature,[198,199,199] all the degradation plots can be approximated to a straight line suggesting a zero-order reaction kinetic (see Appendix, **Figures A.3.5.23-37)**. The rate constants (see **Table 3.5.1**) were obtained by the slope of the degradation plots and calculated using **Equation 3.5.18**, where [dye] is the molar concentration of the dye, t is the time (min), r is the degradation rate and k the rate constant ($M \cdot min^{-1}$).[200]

Equation 3.5.18. Zero-order kinetic model.

$$-\frac{d[dye]}{dt} = r = k$$

Analysis of the rate constants confirmed the higher degradation rate in the tests performed using CDs and oxygen together: for all the five dyes tested, k was one or two orders of magnitude higher respect to the experiments with only the CDs or only oxygen. It must be noted that for SY the calculations were performed disregarding the first three experimental points indicative of an induction period. In addition, for SY the rate constants with only CDs or with only oxygen were comparable in the first 2 h, while the final degradation percentage (after 24 h of irradiation) resulted to be higher when using the CDs.

Continuous-flow experiments

The encouraging results obtained investigating the degradation of azo dyes in batch mode prompted us to extend the protocol under continuous flow (CF) conditions to have faster and more efficient processes.

First, the CF experiments were conducted without the addition of oxygen; the setup was composed of an HPLC pump to convey the feed (5ppm azo dye and 2 mg/mL of bass-CDs in D.I. water) to a PFA reactor (internal volume 2.6 mL). The reactor was homogeneously irradiated using four LEDs at a wavelength of 365 nm and the pressure of the system was controlled downstream using a backpressure regulator at 7 bar (**Figure 3.5.4 a** and **c**).

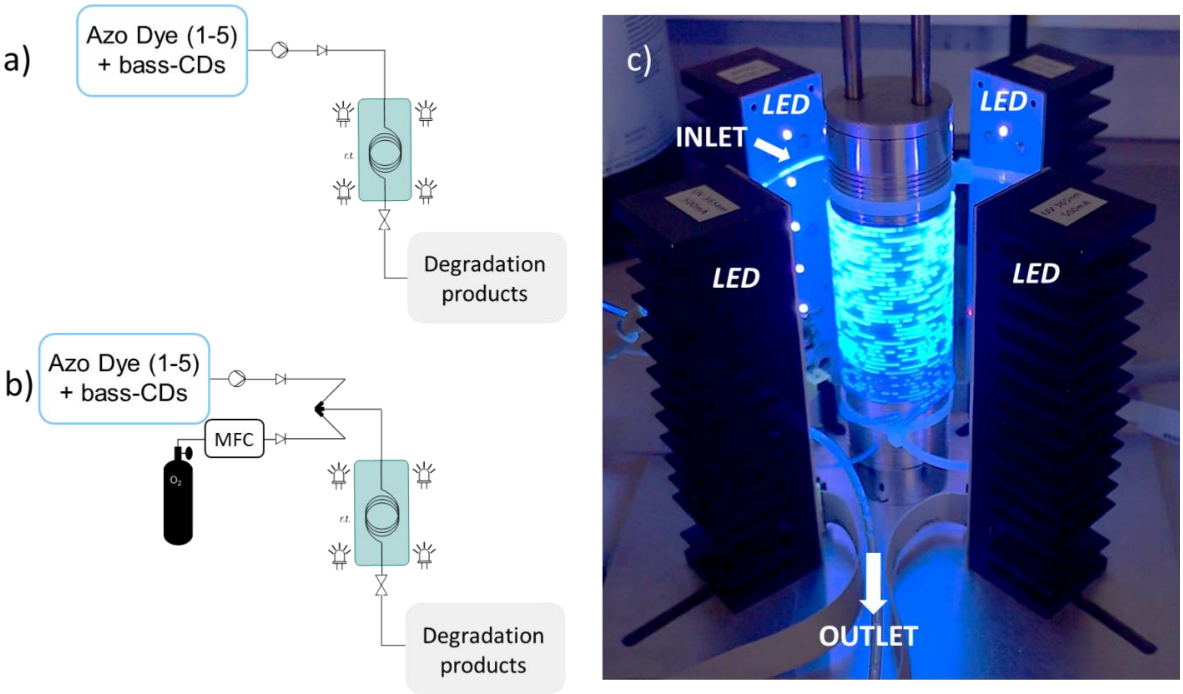

Figure 3.5.4. Simplified flowchart of a) continuous flow set up for the degradation of azo dyes without oxygen and b) continuous flow set up for the degradation of azo dyes with oxygen. c) photograph of the photoreactor.

To determine the best conditions in term of flow rate (Φ), and consequently of residence/irradiation time (R_t), MO was chosen as a model substrate and some preliminary tests were conducted (see **Table 3.5.2**). As expected, decreasing the flow from 1.5 to 0.5 mL/min (and therefore increasing the R_t) the degradation percentage increased. To avoid excessively long residence times, a flow equal to 0.5 mL/min was selected. With these conditions, the degradation percentage reached a satisfactory 49% of degradation in 5.2 min, while in batch conditions without oxygen almost 5 hours were necessary to reach the same result (see **Figure 3.5.3 b**).

Table 3.5.2. Flow conditions tests performed on MO and relative MO degradation percentages. Feed: [MO] = 5ppm, [bass-CDs] = 2 mg/mL; λ=365 nm.

Entry	Φ (mL/min)	R_t (min)	MO degradation (%)
1	1.5	1.7	34
2	1.0	2.6	39
3	0.5	5.2	49

The same conditions were then applied to the other four azo dyes. For AR, 37% degradation was reached in 5.2 min (entry 3, **Table 3.5.3**) compared to 7 h in batch; for AM 23% (entry 5, **Table 3.5.3**) compared to 2 hours in batch. For SY, 5.2 min allowed to reach 59% degradation percentage compared to 17 hours in batch (entry 7, **Table 3.5.3**); while for CH, 66% was obtained (entry 9, **Table 3.5.3**), same as in the batch experiment in 5 hours.

Control experiments without CDs were also performed demonstrating the need to use a photocatalyst for the decomposition of these type of pollutants. As can be seen in **Table 3.5.3** (entries 2, 4, 6, 8 and 10) without the addition of bass-CDs the degradation hardly proceeded reaching a maximum value of only 4% in the case of CH.

Table 3.5.3. Dye degradation percentages for continuous flow experiments performed without oxygen. Feed: [dye] = 5ppm, [bass-CDs] = 2 mg/mL; λ=365 nm; Φ = 0.5 mL/min; R_t = 5.2 min.

Entry	Azo dye	CDs	Dye degradation %
1	MO	Yes	49
2		No	0
3	AR	Yes	37
4		No	0
5	AM	Yes	23
6		No	0
7	SY	Yes	59
8		No	1
9	CH	Yes	66
10		No	4

The continuous-flow investigation continued then with the addition of oxygen. A new continuous flow setup was then assembled using an oxygen supply and a mass flow controller to regulate the oxygen flow rate. The feed and the oxygen were conveyed through an arrowhead mixer and successively to the same reactor used for the experiments without oxygen (**Figure 3.5.4 b** and **c**). The residence times calculations were done following **Equations A.3.5.1-2-3** in the Appendix.

As in the previous case, MO was chosen as a model dye to define the best conditions. As can be seen in **Table 3.5.4**, the flow rate of the feed was kept constant (0.5 mL/min) while the oxygen flow was changed to obtain the best degradation percentage. With MO, using an oxygen flow of 5.5 mL_N/min, and a residence time of *ca.* 2 min, complete degradation was observed. The complete decomposition of this azo dye was obtained in batch conditions bubbling oxygen for 1 hour, demonstrating the major effectiveness of continuous flow for this type of wastewater treatment.

Table 3.5.4. Oxygen flow conditions tests performed on MO and relative MO degradation percentages. Feed: [MO] = 5ppm, [bass-CDs] = 2 mg/mL; λ=365 nm; Φfeed = 0.5 mL/min.

Entry	$\Phi_{\text{oxygen on MFC}}$ (mL$_N$/min)	$\Phi_{\text{oxygen real}}$ (mL/min)	Φ_{TOT} (mL/min)	R$_t$ (min)	MO degradation (%)
1	5.5	0.78	1.28	2.03	quant.
2	7.5	1.07	1.57	1.65	51
3	10.0	1.43	1.93	1.35	46

For these tests the feed was always composed by an aqueous solution containing 5 ppm of the dye and 2 mg/mL of bass-CDs. Considering the high efficiency of the continuous flow degradation using oxygen, the amount of CDs in the feed was decreased to see if it was possible to obtain the same result with lower amounts of photocatalyst. However, using 1 mg/mL of CDs, lower degradation percentages were observed: with a total residence time of 2.03 min (Φ_{feed} = 0.5 min, $\Phi_{\text{oxygen on MFC}}$ = 5.5 mL$_N$/min) only 29% of MO was decomposed, and increasing the residence time to 2.71 min (Φ_{feed} = 0.5 min, $\Phi_{\text{oxygen on MFC}}$ = 3.5 mL$_N$/min) only 31% (see UV spectra in Appendix, **Figure A.3.5.14**).

The optimal conditions for the decomposition tests of the other four azo dyes were set as follows: 2 mg/mL of bass-CDs, Φ_{feed} = 0.5 mL/min, $\Phi_{\text{oxygen on MFC}}$ = 5.5 mL$_N$/min and R$_t$ = 2.03 min. AR, AM, SY and CH were fully degraded under these conditions (**Table 3.5.5**, entries 3, 5, 7 and 9) highlighting the high efficiency of this process. In control experiments preformed without the bass-CDs, none or very low degradation percentages were observed reaching a maximum of 9% with CH (entry 10, **Table 3.5.5**).

Table 3.5.5. Dye degradation percentages for continuous flow experiments performed with oxygen. Feed: [dye] = 5ppm, [bass-CDs] = 2 mg/mL; λ=365 nm; Φ_{feed} = 0.5 mL/min, Φ_{oxygen} = 5.5 mL$_N$/min, $\Phi_{\text{oxygen real}}$ = 0.78 mL/min, Φ_{tot} = 1.28 mL/min, Rt = 2.03 min.

Entry	Azo dye	CDs	Dye degradation %
1	MO	Yes	100
2		No	0
3	AR	Yes	100
4		No	5
5	AM	Yes	100
6		No	0
7	SY	Yes	100
8		No	1
9	CH	Yes	100
10		No	9

From these experiments the importance of both oxygen and carbon dots for the degradation process of azo dyes was highlighted. It was demonstrated that bass-CDs acted like an efficient photocatalyst for the formation of oxygenated radicals responsible for the decomposition of water pollutants, and that the addition of oxygen increased the degradation rate both in batch and in continuous flow. Using the batch setup bubbling oxygen with a frit it was possible to completely degrade the pollutant in times varying from 1 to 3 hours depending on the azo dye. In continuous flow, on the other hand, in only 2 minutes of residence time all the five selected azo dyes reached 100% degradation (**Table 3.5.6**).

Table 3.5.6. Comparison of the time necessary to have complete degradation of the five azo dyes in batch or in continuous flow. Batch conditions: Feed: [dye] = 5ppm, [bass-CDs] = 2 mg/mL; λ=365 nm; oxygen bubbled with a frit. Continuous flow conditions: Feed: [dye] = 5ppm, [bass-CDs] = 2 mg/mL; λ=365 nm; Φ_{feed} = 0.5 mL/min, Φ_{oxygen} = 5.5 mL_N/min, $\Phi_{oxygen\ real}$ = 0.78 mL/min, Φ_{tot} = 1.28 mL/min, Rt = 2.03 min.

Entry	Azo dye	Conditions	Time to have 100% degradation
1 2	MO	Batch Continuous flow	1 h 2 min
3 4	AR	Batch Continuous flow	1 h 2 min
5 6	AM	Batch Continuous flow	2.5 h 2 min
7 8	SY	Batch Continuous flow	2 h 2 min
9 10	CH	Batch Continuous flow	3 h 2 min

3.5.3 Conclusions

In the present work, a method for the complete degradation of azo dyes pollutants in a fast and eco-sustainable way is reported. A continuous flow photoreactor was used taking advantage of the photocatalytic behaviour of carbon dots to perform the photooxidations of azo contaminants. The employed CDs derived, in addition, from fish waste sources fitting in the idea of Circular Economy. These nanoparticles are readily available, biodegradable and biocompatible, as opposed to the majority of common semiconductor photocatalyst, leading to a green, sustainable and non-harmful photocatalytic process. Thanks to the advantages of flow chemistry, such as high surface-to-volume ratio, short diffusion distances, and rapid mass transfer, it was possible to fully degrade five different azo dyes (methyl orange, acid red 18, amaranth, sunset yellow and chromotrope) in only 2 minutes. Using the combination of bass-CDs, oxygen and UV irradiation (λ = 365 nm), it was possible to totally decompose the dyes also in batch conditions, but longer reaction times were needed (from 1 to 3 hours depending on the azo dye). The tested flow methodology should be easy to apply to the purification of industrial wastewaters in a continuous, cheap and affordable way. The bass-derived CDs did not require dialysis because they were free from other soluble molecular species, making the photoactivity of the dialyzed bass-CDs identical to the non-dialyzed CDs. We wish to stress that one of the advantages of our system is that it uses CDs without the need for purification. A second advantage is that the simple synthesis, wide availability, full biodegradability and biocompatibility of these CDs eliminates the need to recover them after the reaction and allows to use them as “disposable” catalysts that can be discarded together with the dye decomposition products without creating new harmful contaminants. In conclusion, the photocatalytic application of fish waste derived CDs, in combination with the benefits of flow chemistry, for the degradation of pollutant and resistant azo dyes is reported.

3.5.4 Experimental

General. All the reagents were purchased from Merck Life Science S.r.l. (Milano, Italy). Oxygen was industrial grade (99.99%, ALPHAGAZ 1, Air Liquide).

UV-Vis absorbance spectra were recorded with an AvaSpec-ULS2048XL EV spectrometer using a deuterium–halogen light source. The absorbances were measured at the characteristic absorption wavelength for every azo dye: 464 nm for MO, 506 nm for AR, 520 nm for AM, 482 nm for SY and 516 nm for CH.

The degradation percentage was calculated using **Equation 3.5.19**, where C_0 is the initial concentration of the dye and C_i is the dye concentration at the selected time. The concentrations were calculated by calibration curve at UV-Vis.

$$degradation\% = \frac{C_0 - C_i}{C_0} \times 100$$

Equation 3.5.19. Calculation for the azo dyes degradation percentage.

^{1}H NMR spectra were collected at 25 °C on a Bruker Ascend 400 operating at 400 MHz using D_2O as solvent; The chemical shifts (δ) have been reported in parts per million (ppm) relative to the residual non-deuterated solvent as an internal reference and are given in δ values downfield from TMS.

Synthesis of fish derived carbon dots (bass-CDs). Bass-CDs were synthesized and characterized according to our previously reported work.[99] Briefly 2 g of dried and grounded sea bass (*Dicentrarchus labrax*) scales were put in a Teflon-lined autoclave with 20 mL of MilliQ water. The system was heated at 200 °C for 24 h. The obtained brownish suspension was filtered, and the water was removed by rotary evaporation to obtain a brown solid with 30–50% yield.

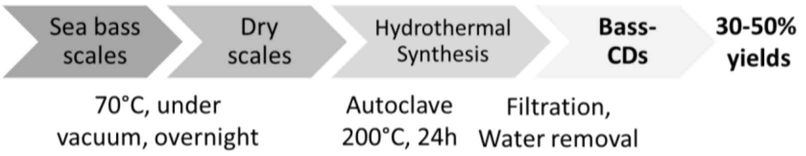

Figure 3.5.5. Simplified flowchart of the synthetic procedure for the preparation of carbon dots from bass scales.

*Feed Preparation.*The feed solutions were composed of azo-dyes 1-5 (**Figure 3.5.1**) 5 ppm and 2 mg/mL of bass-CDs in D.I. water.

*Batch Experiments***.** The solution of the selected dye (5 ppm) and bass-CDs was irradiated with four LEDs pillars containing each 6 high power LEDs (λ = 365 nm, 1100 mW) while oxygen was bubbled inside using a frit. For the experiments without oxygen the solution was continuously stirred. Samplings were performed at different time intervals and analysed via UV-Vis spectroscopy.

Control experiments in absence of light and of photocatalyst were also performed.

Continuous Flow Experiments

Continuous-Flow Setup for experiments without oxygen. The continuous-flow setup for the experiments without oxygen involved an HPLC pump (Knauer Azura P41S equipped with a 10 mL stainless steel head) conveying the feed to the reactor that consisted in a perfluoroalkoxyalkane (PFA) tubing (1/16”, internal volume = 2.6 mL) coiled on a stainless-steel cylinder and irradiated with four LEDs pillars containing each 6 high power LEDs (λ = 365 nm, 1100 mW). The pressure of the system was controlled with a Zaiput dome-type back pressure regulator (BPR) inserted downstream (set point: 7 bar). Further details on the continuous flow setup are reported in the Appendix and in **Figure 3.5.4 a**.

Typical Run. The HPLC pump used to deliver the aqueous solution of the selected azo dye (5 ppm) and CDs (2 mg/mL) was set to 0.5 mL/min. The feed was conveyed to the photoreactor through PFA tubing (1/16’’).

Irradiation occurred along the entire reaction channel (2.6 mL internal volume, 5.2 min residence time) under 7 bar of pressure.

Control experiments in absence of light and of photocatalyst were also performed.

Continuous Flow setup for experiments with oxygen. The continuous-flow setup for the experiments with oxygen involved an HPLC pump (Knauer Azura P41S equipped with a 10 mL stainless steel head) connected to an arrowhead mixer with PFA tubing (1/16”). The oxygen flow rate was controlled through a Bronkhorst mass flow controller (MFC) and conveyed to the arrow head mixer using a 1/16” PFA tubing too. The reactor consisted in a PFA tubing (1/16”, internal volume = 2.6 mL) coiled on a metal cylinder and irradiated with four LEDs pillars containing each 6 high power LEDs (λ = 365 nm, 1100 mW). The pressure of the system was controlled with a Zaiput dome-type back pressure regulator (BPR) inserted downstream (set point: 7 bar). Further details on the continuous flow setup are reported in the Appendix and in **Figure 3.5.4 b**.

Typical run. The HPLC pump used to deliver the aqueous solution of the selected azo dye (5 ppm) and CDs (2 mg/mL) was set to 0.5 mL/min and the oxygen flow was set to 5.5 mL_N/min with MFC. Both fluids were conveyed to the photoreactor through PFA tubing (1/16’’). Irradiation occurred along the entire reaction channel (2.6 mL internal volume, 5.2 min residence time) under 7 bar of counterpressure.

Control experiments in absence of light and of photocatalyst were also performed.

3.6 Bibliography

(1) Huaizhi, Z.; Yuantao, N. Techniques Used for the Preparation and Application of Gold Powder in Ancient China. *Gold Bull* **2000**, *33* (3), 103–105. https://doi.org/10.1007/BF03215486.

(2) Feynman, R. P. There's Plenty of Room at the Bottom, an Invitation to Enter a New Field of Physics. *Engineering and Science magazine* **1960**, *23* (5), 22–36.

(3) Christian, P.; Von Der Kammer, F.; Baalousha, M.; Hofmann, T. Nanoparticles: Structure, Properties, Preparation and Behaviour in Environmental Media. *Ecotoxicology* **2008**, *17* (5), 326–343. https://doi.org/10.1007/s10646-008-0213-1.

(4) Gleiter, H. Nanostructured Materials: Basic Concepts and Microstructure. *Acta Mater* **2000**, *48* (1), 1–29. https://doi.org/10.1016/S1359-6454(99)00285-2.

(5) Iqbal, M. J.; Ahmad, Z. Electrical and Dielectric Properties of Lithium Manganate Nanomaterials Doped with Rare-Earth Elements. *J Power Sources* **2008**, *179* (2), 763–769. https://doi.org/10.1016/j.jpowsour.2007.12.115.

(6) Zeng, S.; Yong, K. T.; Roy, I.; Dinh, X. Q.; Yu, X.; Luan, F. A Review on Functionalized Gold Nanoparticles for Biosensing Applications. *Plasmonics* **2011**, *6* (3), 491–506. https://doi.org/10.1007/s11468-011-9228-1.

(7) Ghosh, P.; Han, G.; De, M.; Kim, C. K.; Rotello, V. M. Gold Nanoparticles in Delivery Applications. *Adv Drug Deliv Rev* **2008**, *60* (11), 1307–1315. https://doi.org/10.1016/j.addr.2008.03.016.

(8) Weir, A.; Westerhoff, P.; Fabricius, L.; Hristovski, K.; Von Goetz, N. Titanium Dioxide Nanoparticles in Food and Personal Care Products. *Environ Sci Technol* **2012**, *46* (4), 2242–2250. https://doi.org/10.1021/es204168d.

(9) Chen, X.; Mao, S. S. Titanium Dioxide Nanomaterials: Synthesis, Properties, Modifications and Applications. *Chem Rev* **2007**, *107* (7), 2891–2959. https://doi.org/10.1021/cr0500535.

(10) Bai, J.; Zhou, B. Titanium Dioxide Nanomaterials for Sensor Applications. *Chem Rev* **2014**, *114* (19), 10131–10176. https://doi.org/10.1021/cr400625j.

(11) Kroto, H. W.; Heath, J. R.; O'Brien, S. C. O.; Curl, R. F.; Smalley, R. E. C60: Buckminsterfullerene. *Nature* **1985**, *318*, 162–163. https://doi.org/https://doi.org/10.1038/318162a0.

(12) Kausar, A. Advances in Polymer/Fullerene Nanocomposite: A Review on Essential Features and Applications. *Polymer - Plastics Technology and Engineering* **2017**, *56* (6), 594–605. https://doi.org/10.1080/03602559.2016.1233278.

(13) Coro, J.; Suárez, M.; Silva, L. S. R.; Eguiluz, K. I. B.; Salazar-Banda, G. R. Fullerene Applications in Fuel Cells: A Review. *Int J Hydrogen Energy* **2016**, *41* (40), 17944–17959. https://doi.org/10.1016/j.ijhydene.2016.08.043.

(14) Kwon, Y. K.; Kim, P. Unusually High Thermal Conductivity in Carbon Nanotubes. *High Thermal Conductivity Materials* **2006**, 227–265. https://doi.org/10.1007/0-387-25100-6_8.

(15) Shenogin, S.; Xue, L.; Ozisik, R.; Keblinski, P.; Cahill, D. G. Role of Thermal Boundary Resistance on the Heat Flow in Carbon-Nanotube Composites. *J Appl Phys* **2004**, *95* (12), 8136–8144. https://doi.org/10.1063/1.1736328.

(16) K. S. Novoselov et al. Electric Field Effect in Atomically Thin Carbon Films. *Science (1979)* **2004**, *306*, 666–669. https://doi.org/10.1126/science.1102896.

(17) Xu, X.; Ray, R.; Gu, Y.; Ploehn, H. J.; Gearheart, L.; Raker, K.; Scrivens, W. A. Electrophoretic Analysis and Purification of Fluorescent Single-Walled Carbon Nanotube Fragments. *J Am Chem Soc* **2004**, *126* (40), 12736–12737. https://doi.org/10.1021/ja040082h.

(18) Chen, B.; Li, F.; Li, S.; Weng, W.; Guo, H.; Guo, T.; Zhang, X.; Chen, Y.; Huang, T.; Hong, X.; You, S.; Lin, Y.; Zeng, K.; Chen, S. Large Scale Synthesis of Photoluminescent Carbon Nanodots and Their Application for Bioimaging. *Nanoscale* **2013**, *5* (5), 1967–1971. https://doi.org/10.1039/c2nr32675b.

(19) Lee, H. U.; Park, S. Y.; Park, E. S.; Son, B.; Lee, S. C.; Lee, J. W.; Lee, Y. C.; Kang, K. S.; Kim, M. Il; Park, H. G.; Choi, S.; Huh, Y. S.; Lee, S. Y.; Lee, K. B.; Oh, Y. K.; Lee, J. Photoluminescent Carbon Nanotags from Harmful Cyanobacteria for Drug Delivery and Imaging in Cancer Cells. *Sci Rep* **2014**, *4*, 1–7. https://doi.org/10.1038/srep04665.

(20) Zhang, Z.; Shi, Y.; Pan, Y.; Cheng, X.; Zhang, L.; Chen, J.; Li, M. J.; Yi, C. Quinoline Derivative-Functionalized Carbon Dots as a Fluorescent Nanosensor for Sensing and Intracellular Imaging of Zn2+. *J Mater Chem B* **2014**, *2* (31), 5020–5027. https://doi.org/10.1039/c4tb00677a.

(21) Tang, L.; Ji, R.; Cao, X.; Lin, J.; Jiang, H.; Li, X.; Teng, K. S.; Luk, C. M.; Zeng, S.; Hao, J.; Lau, S. P. Deep Ultraviolet Photoluminescence of Water-Soluble Self-Passivated Graphene Quantum Dots. *ACS Nano* **2012**, *6* (6), 5102–5110. https://doi.org/10.1021/nn300760g.

(22) Cao, L.; Sahu, S.; Anilkumar, P.; Bunker, C. E.; Xu, J.; Fernando, K. A. S.; Wang, P.; Guliants, E. A.; Tackett, K. N.; Sun, Y. P. Carbon Nanoparticles as Visible-Light Photocatalysts for Efficient CO 2 Conversion and Beyond. *J Am Chem Soc* **2011**, *133* (13), 4754–4757. https://doi.org/10.1021/ja200804h.

(23) Li, Y.; Zhao, Y.; Cheng, H.; Hu, Y.; Shi, G.; Dai, L.; Qu, L. Nitrogen-Doped Graphene Quantum Dots with Oxygen-Rich Functional Groups. *J Am Chem Soc* **2012**, *134* (1), 15–18. https://doi.org/10.1021/ja206030c.

(24) Dong, Y.; Pang, H.; Yang, H. bin; Guo, C.; Shao, J.; Chi, Y.; Li, C. M.; Yu, T. Carbon-Based Dots Co-Doped with Nitrogen and Sulfur for High Quantum Yield and Excitation-Independent Emission. *Angewandte Chemie - International Edition* **2013**, *52* (30), 7800–7804. https://doi.org/10.1002/anie.201301114.

(25) Chandra, S.; Patra, P.; Pathan, S. H.; Roy, S.; Mitra, S.; Layek, A.; Bhar, R.; Pramanik, P.; Goswami, A. Luminescent S-Doped Carbon Dots: An Emergent Architecture for Multimodal Applications. *J Mater Chem B* **2013**, *1* (18), 2375–2382. https://doi.org/10.1039/c3tb00583f.

(26) Wang, W.; Li, Y.; Cheng, L.; Cao, Z.; Liu, W. Water-Soluble and Phosphorus-Containing Carbon Dots with Strong Green Fluorescence for Cell Labeling. *J Mater Chem B* **2014**, *2* (1), 46–48. https://doi.org/10.1039/c3tb21370f.

(27) Wang, Y.; Kalytchuk, S.; Zhang, Y.; Shi, H.; Kershaw, S. V.; Rogach, A. L. Thickness-Dependent Full-Color Emission Tunability in a Flexible Carbon Dot Ionogel. *Journal of Physical Chemistry Letters* **2014**, *5* (8), 1412–1420. https://doi.org/10.1021/jz5005335.

(28) Wang, Y.; Li, Y.; Yan, Y.; Xu, J.; Guan, B.; Wang, Q.; Li, J.; Yu, J. Luminescent Carbon Dots in a New Magnesium Aluminophosphate Zeolite. *Chemical Communications* **2013**, *49* (79), 9006–9008. https://doi.org/10.1039/c3cc43375g.

(29) Sun, Y. P.; Zhou, B.; Lin, Y.; Wang, W.; Fernando, K. A. S.; Pathak, P.; Meziani, M. J.; Harruff, B. A.; Wang, X.; Wang, H.; Luo, P. G.; Yang, H.; Kose, M. E.; Chen, B.; Veca, L. M.; Xie, S. Y. Quantum-Sized Carbon Dots for Bright and Colorful Photoluminescence. *J Am Chem Soc* **2006**, *128* (24), 7756–7757. https://doi.org/10.1021/ja062677d.

(30) Zhu, S.; Meng, Q.; Wang, L.; Zhang, J.; Song, Y.; Jin, H.; Zhang, K.; Sun, H.; Wang, H.; Yang, B. Highly Photoluminescent Carbon Dots for Multicolor Patterning, Sensors, and Bioimaging. *Angewandte Chemie* **2013**, *125* (14), 4045–4049. https://doi.org/10.1002/ange.201300519.

(31) Zhu, S.; Song, Y.; Zhao, X.; Shao, J.; Zhang, J.; Yang, B. The Photoluminescence Mechanism in Carbon Dots (Graphene Quantum Dots, Carbon Nanodots, and Polymer Dots): Current State and Future Perspective. *Nano Res* **2015**, *8* (2), 355–381. https://doi.org/10.1007/s12274-014-0644-3.

(32) Yuan, F.; Wang, Z.; Li, X.; Li, Y.; Tan, Z.; Fan, L.; Yang, S. Bright Multicolor Bandgap Fluorescent Carbon Quantum Dots for Electroluminescent Light-Emitting Diodes. *Advanced Materials* **2017**, *29* (3). https://doi.org/10.1002/adma.201604436.

(33) Tian, Z.; Zhang, X.; Li, D.; Zhou, D.; Jing, P.; Shen, D.; Qu, S.; Zboril, R.; Rogach, A. L. Full-Color Inorganic Carbon Dot Phosphors for White-Light-Emitting Diodes. *Adv Opt Mater* **2017**, *5* (19), 1–9. https://doi.org/10.1002/adom.201700416.

(34) Fang, Q.; Dong, Y.; Chen, Y.; Lu, C. H.; Chi, Y.; Yang, H. H.; Yu, T. Luminescence Origin of Carbon Based Dots Obtained from Citric Acid and Amino Group-Containing Molecules. *Carbon N Y* **2017**, *118*, 319–326. https://doi.org/10.1016/j.carbon.2017.03.061.

(35) Lim, S. Y.; Shen, W.; Gao, Z. Carbon Quantum Dots and Their Applications. *Chem Soc Rev* **2015**, *44* (1), 362–381. https://doi.org/10.1039/c4cs00269e.

(36) Essner, J. B.; Baker, G. A. The Emerging Roles of Carbon Dots in Solar Photovoltaics: A Critical Review. *Environ Sci Nano* **2017**, *4* (6), 1216–1263. https://doi.org/10.1039/c7en00179g.

(37) Michelin, C.; Hoffmann, N. Photosensitization and Photocatalysis - Perspectives in Organic Synthesis. *ACS Catal* **2018**, *8* (12), 12046–12055. https://doi.org/10.1021/acscatal.8b03050.

(38) Akbar, K.; Moretti, E.; Vomiero, A. Carbon Dots for Photocatalytic Degradation of Aqueous Pollutants: Recent Advancements. *Adv Opt Mater* **2021**, *9* (17), 2100532. https://doi.org/10.1002/adom.202100532.

(39) Han, M.; Zhu, S.; Lu, S.; Song, Y.; Feng, T.; Tao, S.; Liu, J.; Yang, B. Recent Progress on the Photocatalysis of Carbon Dots: Classification, Mechanism and Applications. *Nano Today* **2018**, *19*, 201–218. https://doi.org/10.1016/j.nantod.2018.02.008.

(40) Mondal, S.; Yucknovsky, A.; Akulov, K.; Ghorai, N.; Schwartz, T.; Ghosh, H. N.; Amdursky, N. Efficient Photosensitizing Capabilities and Ultrafast Carrier Dynamics of Doped Carbon Dots. *J Am Chem Soc* **2019**, *141* (38), 15413–15422. https://doi.org/10.1021/jacs.9b08071.

(41) Ehrat, F.; Bhattacharyya, S.; Schneider, J.; Löf, A.; Wyrwich, R.; Rogach, A. L.; Stolarczyk, J. K.; Urban, A. S.; Feldmann, J. Tracking the Source of Carbon Dot Photoluminescence: Aromatic Domains versus Molecular Fluorophores. *Nano Lett* **2017**, *17* (12), 7710–7716. https://doi.org/10.1021/acs.nanolett.7b03863.

(42) Reckmeier, C. J.; Schneider, J.; Xiong, Y.; Häusler, J.; Kasák, P.; Schnick, W.; Rogach, A. L. Aggregated Molecular Fluorophores in the Ammonothermal Synthesis of Carbon Dots. *Chemistry of Materials* **2017**, *29* (24), 10352–10361. https://doi.org/10.1021/acs.chemmater.7b03344.

(43) Shahriary, L.; Athawale, A. a. Graphene Oxide Synthesized by Using Modified Hummers Approach. *International Journal of Renewable Energy and Environmental Engineering* **2014**, *2* (1), 58–63.

(44) Permatasari, F. A.; Fukazawa, H.; Ogi, T.; Iskandar, F.; Okuyama, K. Design of Pyrrolic-N-Rich Carbon Dots with Absorption in the First Near-Infrared Window for Photothermal Therapy. *ACS Appl Nano Mater* **2018**, *1* (5), 2368–2375. https://doi.org/10.1021/acsanm.8b00497.

(45) Geng, B.; Shen, W.; Fang, F.; Qin, H.; Li, P.; Wang, X.; Li, X.; Pan, D.; Shen, L. Enriched Graphitic N Dopants of Carbon Dots as F Cores Mediate Photothermal Conversion in the NIR-II Window with High Efficiency. *Carbon N Y* **2020**, *162*, 220–233. https://doi.org/10.1016/j.carbon.2020.02.053.

(46) Zhang, Y.; Lee, T. S.; Petersen, J. L.; Milsmann, C. A Zirconium Photosensitizer with a Long-Lived Excited State: Mechanistic Insight into Photoinduced Single-Electron Transfer. *J Am Chem Soc* **2018**, *140* (18), 5934–5947. https://doi.org/10.1021/jacs.8b00742.

(47) Wu, S.; Zhou, R.; Chen, H.; Zhang, J.; Wu, P. Highly Efficient Oxygen Photosensitization of Carbon Dots: The Role of Nitrogen Doping. *Nanoscale* **2020**, *12* (9), 5543–5553. https://doi.org/10.1039/c9nr10986b.

(48) Chen, J.; Shu, J.; Anqi, Z.; Juyuan, H.; Yan, Z.; Chen, J. Synthesis of Carbon Quantum Dots/TiO2 Nanocomposite for Photo-Degradation of Rhodamine B and Cefradine. *Diam Relat Mater* **2016**, *70*, 137–144. https://doi.org/10.1016/j.diamond.2016.10.023.

(49) Zhang, Z.; Yi, G.; Li, P.; Zhang, X.; Fan, H.; Zhang, Y.; Wang, X.; Zhang, C. A Minireview on Doped Carbon Dots for Photocatalytic and Electrocatalytic Applications. *Nanoscale* **2020**, *12* (26), 13899–13906. https://doi.org/10.1039/d0nr03163a.

(50) Sodeifian, G.; Behnood, R. Hydrothermal Synthesis of N-Doped GQD/CuO and N-Doped GQD/ZnO Nanophotocatalysts for MB Dye Removal Under Visible Light Irradiation: Evaluation of a New Procedure to Produce N-Doped GQD/ZnO. *J Inorg Organomet Polym Mater* **2020**, *30* (4), 1266–1280. https://doi.org/10.1007/s10904-019-01232-x.

(51) Srivastava, I.; Khamo, J. S.; Pandit, S.; Fathi, P.; Huang, X.; Cao, A.; Haasch, R. T.; Nie, S.; Zhang, K.; Pan, D. Influence of Electron Acceptor and Electron Donor on the Photophysical Properties of Carbon Dots: A Comparative Investigation at the Bulk-State and Single-Particle Level. *Adv Funct Mater* **2019**, *29* (37). https://doi.org/10.1002/adfm.201902466.

(52) Emanuele, A.; Cailotto, S.; Campalani, C.; Branzi, L.; Raviola, C.; Ravelli, D.; Cattaruzza, E.; Trave, E.; Benedetti, A.; Selva, M.; Perosa, A. Precursor-Dependent Photocatalytic Activity of Carbon Dots. *Molecules* **2019**, *25* (101), 1–9. https://doi.org/10.3390/molecules25010101.

(53) Hutton, G. A. M.; Martindale, B. C. M.; Reisner, E. Carbon Dots as Photosensitisers for Solar-Driven Catalysis. *Chem Soc Rev* **2017**, *46*, 6111–6123. https://doi.org/10.1039/C7CS00235A.

(54) Martindale, B. C. M.; Hutton, G. A. M.; Caputo, C. A.; Prantl, S.; Godin, R.; Durrant, J. R.; Reisner, E. Enhancing Light Absorption and Charge Transfer Efficiency in Carbon Dots through Graphitization and Core Nitrogen Doping. *Angewandte Chemie - International Edition* **2017**, *56* (23), 6459–6463. https://doi.org/10.1002/anie.201700949.

(55) Wang, R.; Lu, K. Q.; Tang, Z. R.; Xu, Y. J. Recent Progress in Carbon Quantum Dots: Synthesis, Properties and Applications in Photocatalysis. *J Mater Chem A Mater* **2017**, *5* (8), 3717–3734. https://doi.org/10.1039/c6ta08660h.

(56) Shi, L.; Yang, J. H.; Zeng, H. B.; Chen, Y. M.; Yang, S. C.; Wu, C.; Zeng, H.; Yoshihito, O.; Zhang, Q. Carbon Dots with High Fluorescence Quantum Yield: The Fluorescence Originates from Organic Fluorophores. *Nanoscale* **2016**, *8* (30), 14374–14378. https://doi.org/10.1039/c6nr00451b.

(57) Wang, S.; Chen, Z. G.; Cole, I.; Li, Q. Structural Evolution of Graphene Quantum Dots during Thermal Decomposition of Citric Acid and the Corresponding Photoluminescence. *Carbon N Y* **2015**, *82* (C), 304–313. https://doi.org/10.1016/j.carbon.2014.10.075.

(58) Krysmann, M. J.; Kelarakis, A.; Dallas, P.; Giannelis, E. P. Formation Mechanism of Carbogenic Nanoparticles with Dual Photoluminescence Emission. *J Am Chem Soc* **2012**, *134* (2), 747–750. https://doi.org/10.1021/ja204661r.

(59) Song, Y.; Zhu, S.; Zhang, S.; Fu, Y.; Wang, L.; Zhao, X.; Yang, B. Investigation from Chemical Structure to Photoluminescent Mechanism: A Type of Carbon Dots from the Pyrolysis of Citric Acid and an Amine. *J Mater Chem C Mater* **2015**, *3* (23), 5976–5984. https://doi.org/10.1039/c5tc00813a.

(60) Rodríguez-Padrón, D.; Algarra, M.; Tarelho, L. A. C.; Frade, J.; Franco, A.; De Miguel, G.; Jiménez, J.; Rodríguez-Castellón, E.; Luque, R. Catalyzed Microwave-Assisted Preparation of Carbon Quantum Dots from Lignocellulosic Residues. *ACS Sustain Chem Eng* **2018**, *6* (6), 7200–7205. https://doi.org/10.1021/acssuschemeng.7b03848.

(61) Ren, W. jie; Bai, J. jing; Zhao, Y. liang; Wang, Y. long; Liu, F.; Li, Z. zhong. One-Pot Synthesis of Carbon Dots Co-Doped with N and S: High Quantum Yield Governed by Molecular State and Fluorescence Detection of Ag+. *Mol Phys* **2019**, *117* (18), 2500–2510. https://doi.org/10.1080/00268976.2019.1569734.

(62) Cailotto, S.; Mazzaro, R.; Enrichi, F.; Vomiero, A.; Cattaruzza, E.; Cristofori, D.; Amadio, E.; Perosa, A. Design of Carbon Dots for Metal-Free Photoredox Catalysis. *ACS Appl Mater Interfaces* **2018**, *10*, 40560–40567. https://doi.org/10.1021/acsami.8b14188.

(63) Cailotto, S.; Amadio, E.; Facchin, M.; Selva, M.; Pontoglio, E.; Rizzolio, F.; Riello, P.; Toffoli, G.; Benedetti, A.; Perosa, A. Carbon-Dots from Sugars and Ascorbic Acid : Role of the Precursors on Morphology , Properties , Toxicity and Drug Uptake. *ACS Med Chem Lett* **2018**, *9* (8), 832–837. https://doi.org/10.1021/acsmedchemlett.8b00240.

(64) Huang, S. W.; Lin, Y. F.; Li, Y. X.; Hu, C. C.; Chiu, T. C. Synthesis of Fluorescent Carbon Dots as Selective and Sensitive Probes for Cupric Ions and Cell Imaging. *Molecules* **2019**, *24* (9), 1–12. https://doi.org/10.3390/molecules24091785.

(65) Pardo, J.; Peng, Z.; Leblanc, R. M. Cancer Targeting and Drug Delivery Using Carbon-Based Quantum Dots and Nanotubes. *Molecules* **2018**, *23* (2). https://doi.org/10.3390/molecules23020378.

(66) Huang, X.; Duan, H.; Barringer, S. A. Effects of Buffer and Temperature on Formation of Furan, Acetic Acid and Formic Acid from Carbohydrate Model Systems. *LWT - Food Science and Technology* **2011**, *44* (8), 1761–1765. https://doi.org/10.1016/j.lwt.2011.03.016.

(67) Srokol, Z.; Bouche, A. G.; van Estrik, A.; Strik, R. C. J.; Maschmeyer, T.; Peters, J. A. Hydrothermal Upgrading of Biomass to Biofuel; Studies on Some Monosaccharide Model Compounds. *Carbohydr Res* **2004**, *339* (10), 1717–1726. https://doi.org/10.1016/j.carres.2004.04.018.

(68) Ischia, G.; Cutillo, M.; Guella, G.; Bazzanella, N.; Cazzanelli, M.; Orlandi, M.; Miotello, A.; Fiori, L. Hydrothermal Carbonization of Glucose: Secondary Char Properties, Reaction Pathways, and Kinetics. *Chemical Engineering Journal* **2022**, *449*. https://doi.org/10.1016/j.cej.2022.137827.

(69) Striepe, L.; Baumgartner, T. Viologens and Their Application as Functional Materials. *Chemistry - A European Journal* **2017**, *23* (67), 16924–16940. https://doi.org/10.1002/chem.201703348.

(70) Wang, J.-S.; Matyjaszewski, K. Controlled /" Living " Radical Polymerization . Atom Transfer Radical Polymerization in the Presence of Transition-Metal Complexes. *J. Am. Chem. Soc.* **1995**, *117* (6), 5614–5615. https://doi.org/10.1021/ja00125a035.

(71) Kato, M.; Kamigaito, M.; Sawamoto, M.; Higashimura, T. Polymerization of Methyl Methacrylate with the Carbon Tetrachloride/Dichlorotris(Triphenylphosphine)Ruthenium(II)/ Methylaluminum Bis(2,6-Di-Tert-Butylphenoxide) Initiating System: Possibility of Living Radical Polymerization. *Macromolecules* **1995**, *28*, 1721–1723. https://doi.org/10.1021/ma00109a056.

(72) Percec, V.; Barboiu, B. "Living" Radical Polymerization of Styrene Initiated by Arenesulfonyl Chlorides and CuI(Bpy)NCl. *Macromolecules* **1995**, *28*, 7970–7972. https://doi.org/10.1021/ma00127a057.

(73) Dadashi-Silab, S.; Tasdelen, M. A.; Yagci, Y. Photoinitiated Atom Transfer Radical Polymerization: Current Status and Future Perspectives. *Polym Chem* **2014**, *52*, 2878–2888. https://doi.org/10.1002/pola.27327.

(74) Matyjaszewski, K.; Xia, J. Atom Transfer Radical Polymerization. *Chem. Rev.* **2001**, *101*, 2921–2990. https://doi.org/10.1021/cr940534g.

(75) Fischer, H. The Persistent Radical Effect in Controlled Radical Polymerizations. *J Polym Sci A Polym Chem* **1999**, *37* (13), 1885–1901. https://doi.org/10.1002/(SICI)1099-0518(19990701)37:13<1885::AID-POLA1>3.0.CO;2-1.

(76) Matyjaszewski, K. Atom Transfer Radical Polymerization: From Mechanisms to Applications. *Isr J Chem* **2012**, *52* (3–4), 206–220. https://doi.org/10.1002/ijch.201100101.

(77) Tang, W.; Matyjaszewski, K. Effects of Ligand Structure on Activation Rate Constants in ATRP. *Macromolecules* **2006**, *39*, 4953–4959. https://doi.org/10.1021/ma0609634.

(78) Tang, W.; Kwak, Y.; Braunecker, W.; Tsarevsky, N. V.; Coote, M. L.; Matyjaszewski, K. Understanding Atom Transfer Radical Polymerization: Effect of Ligand and Initiator Structures on the Equilibrium Constants. *J Am Chem Soc* **2008**, *130* (32), 10702–10713. https://doi.org/10.1021/ja802290a.

(79) Tang, W.; Tsarevsky, N. V.; Matyjaszewski, K. Determination of Equilibrium Constants for Atom Transfer Radical Polymerization. *J Am Chem Soc* **2006**, *128* (5), 1598–1604. https://doi.org/10.1021/ja0558591.

(80) Matyjaszewski, K. Transition Metal Catalysis in Controlled Radical Polymerization: Atom Transfer Radical Polymerization. *Chemistry - A European Journal* **1999**, *5* (11), 3095–3102. https://doi.org/10.1002/(sici)1521-3765(19991105)5:11<3095::aid-chem3095>3.0.co;2-%23.

(81) Matyjaszewski, K. Inner Sphere and Outer Sphere Electron Transfer Reactions in Atom Transfer Radical Polymerization. *Macromol Symp* **1998**, *134*, 105–118. https://doi.org/10.1002/masy.19981340112.

(82) Percec, V.; Barboiu, B.; Neumann, A.; Ronda, J. C.; Zhao, M. Metal-Catalyzed "Living" Radical Polymerization of Styrene Initiated with Arenesulfonyl Chlorides. From Heterogeneous to Homogeneous Catalysis. *Macromolecules* **1996**, *29*, 3665–3668.

(83) Uegaki, H.; Kotani, Y.; Kamigaito, M.; Sawamoto, M. Nickel-Mediated Living Radical Polymerization of Methyl Methacrylate. *Macromolecules* **1997**, *30* (8), 2249–2253. https://doi.org/10.1021/ma961367k.

(84) Matyjaszewski, K.; Jakubowski, W.; Min, K.; Tang, W.; Huang, J.; Braunecker, W. A.; Tsarevsky, N. V. Diminishing Catalyst Concentration in Atom Transfer Radical Polymerization with Reducing Agents. *Proc Natl Acad Sci U S A* **2006**, *103* (42), 15309–15314. https://doi.org/10.1073/pnas.0602675103.

(85) Magenau, A. J. D.; Strandwitz, N. C.; Gennaro, A.; Matyjaszewski, K. Electrochemically Mediated Atom Transfer Radical Polymerization. *Science (1979)* **2011**, *332*, 81–84. https://doi.org/10.1017/cbo9781139167291.033.

(86) Matyjaszewski, K.; Tsarevsky, N. V.; Braunecker, W. A.; Dong, H.; Huang, J.; Jakubowski, W.; Kwak, Y.; Nicolay, R.; Tang, W.; Yoon, J. A. Role of Cu 0 in Controlled/"living" Radical Polymerization. *Macromolecules* **2007**, *40*, 7795–7806. https://doi.org/10.1021/ma0717800.

(87) Konkolewicz, D.; Schröder, K.; Buback, J.; Bernhard, S.; Matyjaszewski, K. Visible Light and Sunlight Photoinduced ATRP with Ppm of Cu Catalyst. *ACS Macro Lett* **2012**, *1* (10), 1219–1223. https://doi.org/10.1021/mz300457e.

(88) Tasdelen, M. A.; Uygun, M.; Yagci, Y. Photoinduced Controlled Radical Polymerization. *Macromol Rapid Commun* **2011**, *32* (1), 58–62. https://doi.org/10.1002/marc.201000351.

(89) Tasdelen, M. A.; Uygun, M.; Yagci, Y. Photoinduced Controlled Radical Polymerization in Methanol. *Macromol Chem Phys* **2010**, *211* (21), 2271–2275. https://doi.org/10.1002/macp.201000445.

(90) Tasdelen, M. A.; Uygun, M.; Yagci, Y. Studies on Photoinduced ATRP in the Presence of Photoinitiator. *Macromol Chem Phys* **2011**, *212* (18), 2036–2042. https://doi.org/10.1002/macp.201100267.

(91) Ribelli, T. G.; Konkolewicz, D.; Bernhard, S.; Matyjaszewski, K. How Are Radicals (Re)Generated in Photochemical ATRP? *J Am Chem Soc* **2014**, *136* (38), 13303–13312. https://doi.org/10.1021/ja506379s.

(92) Discekici, E. H.; Anastasaki, A.; Read De Alaniz, J.; Hawker, C. J. Evolution and Future Directions of Metal-Free Atom Transfer Radical Polymerization. *Macromolecules* **2018**, *51* (19), 7421–7434. https://doi.org/10.1021/acs.macromol.8b01401.

(93) Yagci, Y.; Jockusch, S.; Turro, N. J. Photoinitiated Polymerization: Advances, Challenges, and Opportunities. *Macromolecules* **2010**, *43* (15), 6245–6260. https://doi.org/10.1021/ma1007545.

(94) Kütahya, C.; Wang, P.; Li, S.; Liu, S.; Li, J.; Chen, Z.; Strehmel, B. Carbon Dots as a Promising Green Photocatalyst for Free Radical and ATRP-Based Radical. *Angewandte Chemie - International Edition* **2020**, *59*, 3166–3171. https://doi.org/10.1002/anie.201912343.

(95) Pan, X.; Malhotra, N.; Simakova, A.; Wang, Z.; Konkolewicz, D.; Matyjaszewski, K. Photoinduced Atom Transfer Radical Polymerization with Ppm-Level Cu Catalyst by Visible Light in Aqueous Media. *J Am Chem Soc* **2015**, *137* (49), 15430–15433. https://doi.org/10.1021/jacs.5b11599.

(96) Kütahya, C.; Schmitz, C.; Strehmel, V.; Yagci, Y.; Strehmel, B. Near-Infrared Sensitized Photoinduced Atom-Transfer Radical Polymerization (ATRP) with a Copper(II) Catalyst Concentration in the Ppm Range. *Angewandte Chemie - International Edition* **2018**, *57* (26), 7898–7902. https://doi.org/10.1002/anie.201802964.

(97) Jiang, J.; Ye, G.; Wang, Z.; Lu, Y.; Chen, J.; Matyjaszenski, K. Heteroatom-Doped Carbon Dots CDs as a Class of Metal-Free Photocatalysts for PET-RAFT. *Angewandte Chemie* **2018**, *130*, 12213–12218. https://doi.org/10.1002/anie.201807385.

(98) Xie, Y.; Yu, S.; Zhong, Y.; Zhang, Q.; Zhou, Y. SnO 2 /Graphene Quantum Dots Composited Photocatalyst for Efficient Nitric Oxide Oxidation under Visible Light. *Appl Surf Sci* **2018**, *448*, 655–661. https://doi.org/10.1016/j.apsusc.2018.04.145.

(99) Campalani, C.; Cattaruzza, E.; Zorzi, S.; Vomiero, A.; You, S.; Matthews, L.; Capron, M.; Mondelli, C.; Selva, M.; Perosa, A. Biobased Carbon Dots: From Fish Scales to Photocatalysis. *Nanomaterials* **2021**, *11* (2), 524. https://doi.org/10.3390/nano11020524.

(100) Yan, M.; Zhu, F.; Gu, W.; Sun, L.; Shi, W.; Hua, Y. Construction of Nitrogen-Doped Graphene Quantum Dots-BiVO4/g-C3N4 Z -Scheme Photocatalyst and Enhanced Photocatalytic Degradation of Antibiotics under Visible Light. *RSC Adv* **2016**, *6* (66), 61162–61174. https://doi.org/10.1039/c6ra07589d.

(101) Hao, Q.; Qiao, L.; Shi, G.; He, Y.; Cui, Z.; Fu, P.; Liu, M.; Qiao, X.; Pang, X. Effect of Nitrogen Type on Carbon Dot Photocatalysts for Visible-Light-Induced Atom Transfer Radical Polymerization. *Polym Chem* **2021**, *12* (20), 3060–3066. https://doi.org/10.1039/d1py00148e.

(102) Cailotto, S.; Negrato, M.; Daniele, S.; Luque, R.; Selva, M.; Amadio, E.; Perosa, A. Carbon Dots as Photocatalysts for Organic Synthesis: Metal-Free Methylene-Oxygen-Bond Photocleavage. *Green Chemistry* **2020**, *22* (4), 1145–1149. https://doi.org/10.1039/c9gc03811f.

(103) Soin, N.; Sinha Roy, S.; Roy, S.; Hazra, K. S.; Misra, D. S.; Lim, T. H.; Hetherington, C. J.; McLaughlin, J. A. Enhanced and Stable Field Emission from in Situ Nitrogen-Doped Few-Layered Graphene Nanoflakes. *Journal of Physical Chemistry C* **2011**, *115* (13), 5366–5372. https://doi.org/10.1021/jp110476m.

(104) Stenzel, M. H.; Barner-Kowollik, C. The Living Dead – Common Misconceptions about Reversible Deactivation Radical Polymerization. *Mater Horiz* **2016**, *3* (6), 471–477. https://doi.org/10.1039/c6mh00265j.

(105) Tanan, W.; Panichpakdee, J.; Saengsuwan, S. Novel Biodegradable Hydrogel Based on Natural Polymers: Synthesis, Characterization, Swelling/Reswelling and Biodegradability. *Eur Polym J* **2019**, *112* (October 2018), 678–687. https://doi.org/10.1016/j.eurpolymj.2018.10.033.

(106) Roa, K.; Tapiero, Y.; Thotiyl, M. O.; Sánchez, J. Hydrogels Based on Poly([2-(Acryloxy)Ethyl] Trimethylammonium Chloride) and Nanocellulose Applied to Remove Methyl Orange Dye from Water. *Polymers*. 2021. https://doi.org/10.3390/polym13142265.

(107) Sánchez, J.; Mendoza, N.; Rivas, B. L.; Basáez, L.; Santiago-García, J. L. Preparation and Characterization of Water-Soluble Polymers and Their Utilization in Chromium Sorption. *J Appl Polym Sci* **2017**, *134* (39), 1–10. https://doi.org/10.1002/app.45355.

(108) Khawli, F. Al; Pateiro, M.; Domínguez, R.; Lorenzo, J. M.; Gullón, P.; Kousoulaki, K.; Ferrer, E.; Berrada, H.; Barba, F. J. Innovative Green Technologies of Intensification for Valorization of Seafood and Their By-Products. *Mar Drugs* **2019**, *17* (12), 1–20. https://doi.org/10.3390/md17120689.

(109) FAO. FAO Aquaculture Newsletter. Rome. **2018**, *58* (April).

(110) Maschmeyer, T.; Luque, R.; Selva, M. Upgrading of Marine (Fish and Crustaceans) Biowaste for High Added-Value Molecules and Bio(Nano)-Materials. *Chem Soc Rev* **2020**, *49* (13), 4527–4563. https://doi.org/10.1039/c9cs00653b.

(111) Xu, C.; Nasrollahzadeh, M.; Selva, M.; Issaabadi, Z.; Luque, R. Waste-to-Wealth: Biowaste Valorization into Valuable Bio(Nano)Materials. *Chem Soc Rev* **2019**, *48* (18), 4791–4822. https://doi.org/10.1039/c8cs00543e.

(112) Kerton, F. M.; Liu, Y.; Omari, K. W.; Hawboldt, K. Green Chemistry and the Ocean-Based Biorefinery. *Green Chemistry* **2013**, *15* (4), 860–871. https://doi.org/10.1039/c3gc36994c.

(113) Santos, V. P.; Marques, N. S. S.; Maia, P. C. S. V.; de Lima, M. A. B.; Franco, L. de O.; de Campos-Takaki, G. M. Seafood Waste as Attractive Source of Chitin and Chitosan Production and Their Applications. *Int J Mol Sci* **2020**, *21* (12), 1–17. https://doi.org/10.3390/ijms21124290.

(114) Jayathilakan, K.; Sultana, K.; Radhakrishna, K.; Bawa, A. S. Utilization of Byproducts and Waste Materials from Meat, Poultry and Fish Processing Industries: A Review. *J Food Sci Technol* **2012**, *49* (3), 278–293. https://doi.org/10.1007/s13197-011-0290-7.

(115) Wu, G.; Feng, M.; Zhan, H. Generation of Nitrogen-Doped Photoluminescent Carbonaceous Nanodots via the Hydrothermal Treatment of Fish Scales for the Detection of Hypochlorite. *RSC Adv* **2015**, *5* (55), 44636–44641. https://doi.org/10.1039/c5ra04989j.

(116) Baker, S. N.; Baker, G. A. Luminescent Carbon Nanodots: Emergent Nanolights. *Angewandte Chemie - International Edition* **2010**, *49* (38), 6726–6744. https://doi.org/10.1002/anie.200906623.

(117) Li, H.; Kang, Z.; Liu, Y.; Lee, S. T. Carbon Nanodots: Synthesis, Properties and Applications. *J Mater Chem* **2012**, *22* (46), 24230–24253. https://doi.org/10.1039/c2jm34690g.

(118) Tuerhong, M.; XU, Y.; YIN, X. B. Review on Carbon Dots and Their Applications. *Chinese Journal of Analytical Chemistry* **2017**, *45* (1), 139–150. https://doi.org/10.1016/S1872-2040(16)60990-8.

(119) Martindale, B. C. M.; Hutton, G. A. M.; Caputo, C. A.; Reisner, E. Solar Hydrogen Production Using Carbon Quantum Dots and a Molecular Nickel Catalyst. *J Am Chem Soc* **2015**, *137* (18), 6018–6025. https://doi.org/10.1021/jacs.5b01650.

(120) Zhang, H.; Li, Y.; Liu, X.; Liu, P.; Wang, Y.; An, T.; Yang, H.; Jing, D.; Zhao, H. Determination of Iodide via Direct Fluorescence Quenching at Nitrogen-Doped Carbon Quantum Dot Fluorophores. *Environ Sci Technol Lett* **2013**, *1* (1), 87–91. https://doi.org/10.1021/ez400137j.

(121) Wang, C.; Wu, X.; Li, X.; Wang, W.; Wang, L.; Gu, M.; Li, Q. Upconversion Fluorescent Carbon Nanodots Enriched with Nitrogen for Light Harvesting. *J Mater Chem* **2012**, *22* (31), 15522–15525. https://doi.org/10.1039/c2jm30935a.

(122) Meng, W.; Bai, X.; Wang, B.; Liu, Z.; Lu, S.; Yang, B. Biomass-Derived Carbon Dots and Their Applications. *Energy and Environmental Materials* **2019**, *2* (3), 172–192. https://doi.org/10.1002/eem2.12038.

(123) Zhao, S.; Lan, M.; Zhu, X.; Xue, H.; Ng, T. W.; Meng, X.; Lee, C. S.; Wang, P.; Zhang, W. Green Synthesis of Bifunctional Fluorescent Carbon Dots from Garlic for Cellular Imaging and Free Radical Scavenging. *ACS Appl Mater Interfaces* **2015**, *7* (31), 17054–17060. https://doi.org/10.1021/acsami.5b03228.

(124) Liu, R.; Zhang, J.; Gao, M.; Li, Z.; Chen, J.; Wu, D.; Liu, P. A Facile Microwave-Hydrothermal Approach towards Highly Photoluminescent Carbon Dots from Goose Feathers. *RSC Adv* **2015**, *5* (6), 4428–4433. https://doi.org/10.1039/c4ra12077a.

(125) Zhang, J.; Yuan, Y.; Liang, G.; Yu, S. H. Scale-Up Synthesis of Fragrant Nitrogen-Doped Carbon Dots from Bee Pollens for Bioimaging and Catalysis. *Advanced Science* **2015**, *2* (4), 1–6. https://doi.org/10.1002/advs.201500002.

(126) Kasibabu, B. S. B.; D'Souza, S. L.; Jha, S.; Kailasa, S. K. Imaging of Bacterial and Fungal Cells Using Fluorescent Carbon Dots Prepared from Carica Papaya Juice. *J Fluoresc* **2015**, *25* (4), 803–810. https://doi.org/10.1007/s10895-015-1595-0.

(127) Yang, W.; Shimanouchi, T.; Kimura, Y. Characterization of the Residue and Liquid Products Produced from Husks of Nuts from Carya Cathayensis Sarg by Hydrothermal Carbonization. *ACS Sustain Chem Eng* **2015**, *3* (4), 591–598. https://doi.org/10.1021/acssuschemeng.5b00103.

(128) Zhang, Y.; Gao, Z.; Yang, X.; Chang, J.; Liu, Z.; Jiang, K. Fish-Scale-Derived Carbon Dots as Efficient Fluorescent Nanoprobes for Detection of Ferric Ions. *RSC Adv* **2019**, *9* (2), 940–949. https://doi.org/10.1039/C8RA09471C.

(129) Zhang, Y.; Gao, Z.; Zhang, W.; Wang, W.; Chang, J.; Kai, J. Sensors and Actuators B : Chemical Fluorescent Carbon Dots as Nanoprobe for Determination of Lidocaine Hydrochloride. *Sens Actuators B Chem* **2018**, *262*, 928–937. https://doi.org/10.1016/j.snb.2018.02.079.

(130) Athinarayanan, J.; Periasamy, V. S.; Alshatwi, A. A. Simultaneous Fabrication of Carbon Nanodots and Hydroxyapatite Nanoparticles from Fish Scale for Biomedical Applications. *Materials Science and Engineering C* **2020**, *117* (August), 111313. https://doi.org/10.1016/j.msec.2020.111313.

(131) Cao, T. H.; Nguyen, T. T. O.; Nguyen, T. M. H.; Le, N. T.; Razumovskaya, R. G. Characteristics and Physicochemical Properties of Gelatin Extracted from Scales of Seabass (Lates Calcarifer) and Grey Mullet (Mugil Cephalus) in Vietnam. *Journal of Aquatic Food Product Technology* **2017**, *26* (10), 1293–1302. https://doi.org/10.1080/10498850.2017.1390026.

(132) Dinçer, M. T.; Ağçay, Ö. Y.; Sargin, H.; Bayram, H. Functional Properties of Gelatin Recovered from Scales of Farmed Sea Bass (Dicentrarchus Labrax). *Turk J Vet Anim Sci* **2015**, *39* (1), 102–109. https://doi.org/10.3906/vet-1406-68.

(133) Chuaychan, S.; Benjakul, S.; Kishimura, H. Characteristics of Acid- and Pepsin-Soluble Collagens from Scale of Seabass (Lates Calcarifer). *Lwt* **2015**, *63* (1), 71–76. https://doi.org/10.1016/j.lwt.2015.03.002.

(134) Kehrer, M.; Duchoslav, J.; Hinterreiter, A.; Cobet, M.; Mehic, A.; Stehrer, T.; Stifter, D. XPS Investigation on the Reactivity of Surface Imine Groups with TFAA. *Plasma Processes and Polymers* **2019**, *16* (4), 1–8. https://doi.org/10.1002/ppap.201800160.

(135) Yang, Y.; Cui, J.; Zheng, M.; Hu, C.; Tan, S.; Xiao, Y.; Yang, Q.; Liu, Y. One-Step Synthesis of Amino-Functionalized Fluorescent Carbon Nanoparticles by Hydrothermal Carbonization of Chitosan. *Chemical Communications* **2012**, *48* (3), 380–382. https://doi.org/10.1039/c1cc15678k.

(136) Rigodanza, F.; Đorđević, L.; Arcudi, F.; Prato, M. Customizing the Electrochemical Properties of Carbon Nanodots by Using Quinones in Bottom-Up Synthesis. *Angewandte Chemie* **2018**, *130* (18), 5156–5161. https://doi.org/10.1002/ange.201801707.

(137) Narayanan, T. Small-Angle Scattering, in Structure from Diffraction Methods. E d. D. W. Bruce, D. O'Hare and R. I. Walton, Wiley Online Library. **2014**, 259–324.

(138) Doucet, M.; Cho, J. H.; Alina, G.; Attala, Z.; Bakker, J.; Bouwman, W.; Butler, P.; Campbell, K.; Cooper- Benun, T.; Durniak, C. et al. SasView Version 5.0.3 Zenodo (2020, July 4), (Accessed on February 2021). **2021**, *3930098* (1996), 6. https://doi.org/http://doi.org/10.5281/zenodo.http://doi.org/10.5281/zenodo.

(139) Campalani, C.; Petit, G.; Monbaliu, J. C. M.; Selva, M.; Perosa, A. Continuous Flow Photooxidative Degradation of Azo Dyes with Biomass-Derived Carbon Dots. *ChemPhotoChem* **2022**. https://doi.org/10.1002/cptc.202200234.

(140) Vaiano, V.; Sacco, O.; Libralato, G.; Lofrano, G.; Siciliano, A.; Carraturo, F.; Guida, M.; Carotenuto, M. Degradation of Anionic Azo Dyes in Aqueous Solution Using a Continuous Flow Photocatalytic Packed-Bed Reactor: Influence of Water Matrix and Toxicity Evaluation. *J Environ Chem Eng* **2020**, *8* (6), 104549. https://doi.org/10.1016/j.jece.2020.104549.

(141) Lofrano, G.; Libralato, G.; Carotenuto, M.; Guida, M.; Inglese, M.; Siciliano, A.; Meriç, S. Emerging Concern from Short-Term Textile Leaching: A Preliminary Ecotoxicological Survey. *Bull Environ Contam Toxicol* **2016**, *97* (5), 646–652. https://doi.org/10.1007/s00128-016-1937-x.

(142) Golka, K.; Kopps, S.; Myslak, Z. W. Carcinogenicity of Azo Colorants: Influence of Solubility and Bioavailability. *Toxicol Lett* **2004**, *151* (1), 203–210. https://doi.org/10.1016/j.toxlet.2003.11.016.

(143) Neamtu, M.; Siminiceanu, I.; Yediler, A.; Kettrup, A. Kinetics of Decolorization and Mineralization of Reactive Azo Dyes in Aqueous Solution by the UV/H2O2 Oxidation. *Dyes and Pigments* **2002**, *53* (2), 93–99. https://doi.org/10.1016/S0143-7208(02)00012-8.

(144) Ravadelli, M.; Da Costa, R. E.; Lobo-Recio, M. A.; Akaboci, T. R. V.; Bassin, J. P.; Lapolli, F. R.; Belli, T. J. Anoxic/Oxic Membrane Bioreactor Assisted by Electrocoagulation for the Treatment of Azo-Dye Containing Wastewater. *J Environ Chem Eng* **2021**, *9* (4), 105286. https://doi.org/10.1016/j.jece.2021.105286.

(145) Shanker, U.; Rani, M.; Jassal, V. Degradation of Hazardous Organic Dyes in Water by Nanomaterials. *Environ Chem Lett* **2017**, *15* (4), 623–642. https://doi.org/10.1007/s10311-017-0650-2.

(146) Ahmad, R.; Kumar, R. Adsorptive Removal of Congo Red Dye from Aqueous Solution Using Bael Shell Carbon. *Appl Surf Sci* **2010**, *257* (5), 1628–1633. https://doi.org/10.1016/j.apsusc.2010.08.111.

(147) Khan, A.; Wang, X.; Gul, K.; Khuda, F.; Aly, Z.; Elseman, A. M. Microwave-Assisted Spent Black Tea Leaves as Cost-Effective and Powerful Green Adsorbent for the Efficient Removal of Eriochrome Black T from Aqueous Solutions. *Egyptian Journal of Basic and Applied Sciences* **2018**, *5* (2), 171–182. https://doi.org/10.1016/j.ejbas.2018.04.002.

(148) Jung, K. W.; Choi, B. H.; Lee, S. Y.; Ahn, K. H.; Lee, Y. J. Green Synthesis of Aluminum-Based Metal Organic Framework for the Removal of Azo Dye Acid Black 1 from Aqueous Media. *Journal of Industrial and Engineering Chemistry* **2018**, *67*, 316–325. https://doi.org/10.1016/j.jiec.2018.07.003.

(149) Pirkarami, A.; Olya, M. E.; Najafi, F. Removal of Azo Dye from Aqueous Solution Using an Anionic Polymeric Urethane Absorbent (APUA). *Journal of Industrial and Engineering Chemistry* **2015**, *21*, 387–393. https://doi.org/10.1016/j.jiec.2014.02.050.

(150) Parsa, J. B.; Golmirzaei, M.; Abbasi, M. Degradation of Azo Dye C.I. Acid Red 18 in Aqueous Solution by Ozone-Electrolysis Process. *Journal of Industrial and Engineering Chemistry* **2014**, *20* (2), 689–694. https://doi.org/10.1016/j.jiec.2013.05.034.

(151) Spahis, N.; Addoun, A.; Mahmoudi, H.; Ghaffour, N. Purification of Water by Activated Carbon Prepared from Olive Stones. *Desalination* **2008**, *222* (1–3), 519–527. https://doi.org/10.1016/j.desal.2007.02.065.

(152) Zhao, H. Z.; Wang, H. Y.; Dockko, S.; Zhang, Y. The Formation Mechanism of Al13 and Its Purification with an Ethanol-Acetone Fractional Precipitation Method. *Sep Purif Technol* **2011**, *81* (3), 466–471. https://doi.org/10.1016/j.seppur.2011.08.025.

(153) Mo., L.; Huang, X. Fouling Characteristics and Cleaning Strategies in a Coagulation-Microfiltration Combination Process for Water Purification. *Desalination* **2003**, *159* (1), 1–9. https://doi.org/10.1016/S0011-9164(03)90040-3.

(154) Shen, J. nan; Li, D. dan; Jiang, F. yan; Qiu, J. hong; Gao, C. jie. Purification and Concentration of Collagen by Charged Ultrafiltration Membrane of Hydrophilic Polyacrylonitrile Blend. *Sep Purif Technol* **2009**, *66* (2), 257–262. https://doi.org/10.1016/j.seppur.2009.01.002.

(155) Baudequin, C.; Couallier, E.; Rakib, M.; Deguerry, I.; Severac, R.; Pabon, M. Purification of Firefighting Water Containing a Fluorinated Surfactant by Reverse Osmosis Coupled to Electrocoagulation-Filtration. *Sep Purif Technol* **2011**, *76* (3), 275–282. https://doi.org/10.1016/j.seppur.2010.10.016.

(156) Qu, X.; Alvarez, P. J. J.; Li, Q. Applications of Nanotechnology in Water and Wastewater Treatment. *Water Res* **2013**, *47* (12), 3931–3946. https://doi.org/10.1016/j.watres.2012.09.058.

(157) Jangid, N. K.; Jadoun, S.; Yadav, A.; Srivastava, M.; Kaur, N. Polyaniline-TiO2-Based Photocatalysts for Dyes Degradation. *Polymer Bulletin* **2021**, *78* (8), 4743–4777. https://doi.org/10.1007/s00289-020-03318-w.

(158) Gao, Z.; Pan, C.; Choi, C.; Chang, C. Continuous-Flow Photocatalytic Microfluidic-Reactor for the Treatment of Aqueous Contaminants, Simplicity, and Complexity: A Mini-Review. *Symmetry (Basel)* **2021**, *13* (1325). https://doi.org/10.3390/sym13081325.

(159) Chatterjee, D.; Dasgupta, S. Visible Light Induced Photocatalytic Degradation of Organic Pollutants. *Journal of Photochemistry and Photobiology C: Photochemistry Reviews* **2005**, *6* (2–3), 186–205. https://doi.org/10.1016/j.jphotochemrev.2005.09.001.

(160) Ge, M.; Guo, C.; Zhu, X.; Ma, L.; Han, Z.; Hu, W.; Wang, Y. Photocatalytic Degradation of Methyl Orange Using ZnO/TiO2 Composites. *Frontiers of Environmental Science and Engineering in China* **2009**, *3* (3), 271–280. https://doi.org/10.1007/s11783-009-0035-2.

(161) Konstantinou, I. K.; Albanis, T. A. TiO2-Assisted Photocatalytic Degradation of Azo Dyes in Aqueous Solution: Kinetic and Mechanistic Investigations: A Review. *Appl Catal B* **2004**, *49* (1), 1–14. https://doi.org/10.1016/j.apcatb.2003.11.010.

(162) Mozia, S.; Tomaszewska, M.; Morawski, A. W. Photocatalytic Degradation of Azo-Dye Acid Red 18. *Desalination* **2005**, *185* (1–3), 449–456. https://doi.org/10.1016/j.desal.2005.04.050.

(163) Naik, A. P.; Salkar, A. V.; Majik, M. S.; Morajkar, P. P. Enhanced Photocatalytic Degradation of Amaranth Dye on Mesoporous Anatase TiO2: Evidence of C-N, NN Bond Cleavage and Identification of New Intermediates. *Photochemical and Photobiological Sciences* **2017**, *16* (7), 1126–1138. https://doi.org/10.1039/c7pp00090a.

(164) Qamar, M.; Saquib, M.; Muneer, M. Photocatalytic Degradation of Two Selected Dye Derivatives, Chromotrope 2B and Amido Black 10B, in Aqueous Suspensions of Titanium Dioxide. *Dyes and Pigments* **2005**, *65* (1), 1–9. https://doi.org/10.1016/j.dyepig.2004.06.006.

(165) Roşu, M. C.; Socaci, C.; Floare-Avram, V.; Borodi, G.; PogĂcean, F.; Coroş, M.; MĂgeruşan, L.; Pruneanu, S. Photocatalytic Performance of Graphene/TiO2-Ag Composites on Amaranth Dye Degradation. *Mater Chem Phys* **2016**, *179*, 232–241. https://doi.org/10.1016/j.matchemphys.2016.05.035.

(166) Shahmoradi, B.; Maleki, A.; Byrappa, K. Photocatalytic Degradation of Amaranth and Brilliant Blue FCF Dyes Using in Situ Modified Tungsten Doped TiO2 Hybrid Nanoparticles. *Catal Sci Technol* **2011**, *1* (7), 1216–1223. https://doi.org/10.1039/c1cy00023c.

(167) Sobana, N.; Muruganadham, M.; Swaminathan, M. Nano-Ag Particles Doped TiO2 for Efficient Photodegradation of Direct Azo Dyes. *J Mol Catal A Chem* **2006**, *258* (1–2), 124–132. https://doi.org/10.1016/j.molcata.2006.05.013.

(168) Zhu, C.; Wang, L.; Kong, L.; Yang, X.; Wang, L.; Zheng, S.; Chen, F.; Maizhi, F.; Zong, H. Photocatalytic Degradation of AZO Dyes by Supported TiO22 + UV in Aqueous Solution. *Chemosphere* **2000**, *41* (3), 303–309. https://doi.org/10.1016/S0045-6535(99)00487-7.

(169) Chen, T.; Zheng, Y.; Lin, J. M.; Chen, G. Study on the Photocatalytic Degradation of Methyl Orange in Water Using Ag/ZnO as Catalyst by Liquid Chromatography Electrospray Ionization Ion-Trap Mass Spectrometry. *J Am Soc Mass Spectrom* **2008**, *19* (7), 997–1003. https://doi.org/10.1016/j.jasms.2008.03.008.

(170) Sobana, N.; Swaminathan, M. The Effect of Operational Parameters on the Photocatalytic Degradation of Acid Red 18 by ZnO. *Sep Purif Technol* **2007**, *56* (1), 101–107. https://doi.org/10.1016/j.seppur.2007.01.032.

(171) Morajkar, P. P.; Naik, A. P.; Bugde, S. T.; Naik, B. R. *Photocatalytic and Microbial Degradation of Amaranth Dye*; Elsevier Inc., 2019. https://doi.org/10.1016/B978-0-12-817497-5.00020-3.

(172) Cailotto, S.; Massari, D.; Gigli, M.; Campalani, C.; Bonini, M.; You, S.; Vomiero, A.; Selva, M.; Perosa, A.; Crestini, C. N-Doped Carbon Dot Hydrogels from Brewing Waste for Photocatalytic Wastewater Treatment. *ACS Omega* **2022**, *7* (5), 4052–4061. https://doi.org/10.1021/acsomega.1c05403.

(173) Zhang, H.; Huang, H.; Ming, H.; Li, H.; Zhang, L.; Liu, Y.; Kang, Z. Carbon Quantum Dots/Ag 3PO 4 Complex Photocatalysts with Enhanced Photocatalytic Activity and Stability under Visible Light. *J Mater Chem* **2012**, *22* (21), 10501–10506. https://doi.org/10.1039/c2jm30703k.

(174) Shen, K.; Xue, X.; Wang, X.; Hu, X.; Tian, H.; Zheng, W. One-Step Synthesis of Band-Tunable N, S Co-Doped Commercial TiO2/Graphene Quantum Dots Composites with Enhanced Photocatalytic Activity. *RSC Adv* **2017**, *7* (38), 23319–23327. https://doi.org/10.1039/c7ra01856h.

(175) Ham, S.; Kim, Y.; Park, M. J.; Hong, B. H.; Jang, D. J. Graphene Quantum Dots-Decorated ZnS Nanobelts with Highly Efficient Photocatalytic Performances. *RSC Adv* **2016**, *6* (29), 24115–24120. https://doi.org/10.1039/c5ra28026e.

(176) Gomollón-Bel, F. Ten Chemical Innovations That Will Change Our World. *Chemistry International* **2020**, *42* (4), 3–9. https://doi.org/10.1515/ci-2020-0402.

(177) Gérardy, R.; Emmanuel, N.; Toupy, T.; Kassin, V. E.; Tshibalonza, N. N.; Schmitz, M.; Monbaliu, J. C. M. Continuous Flow Organic Chemistry: Successes and Pitfalls at the Interface with Current Societal Challenges. *European J Org Chem* **2018**, No. 20, 2301–2351. https://doi.org/10.1002/ejoc.201800149.

(178) Plutschack, M. B.; Pieber, B.; Gilmore, K.; Seeberger, P. H. The Hitchhiker's Guide to Flow Chemistry. *Chem Rev* **2017**, *117* (18), 11796–11893. https://doi.org/10.1021/acs.chemrev.7b00183.

(179) Emmanuel, N.; Mendoza, C.; Winter, M.; Horn, C. R.; Vizza, A.; Dreesen, L.; Heinrichs, B.; Monbaliu, J. C. M. Scalable Photocatalytic Oxidation of Methionine under Continuous-Flow Conditions. *Org Process Res Dev* **2017**, *21* (9), 1435–1438. https://doi.org/10.1021/acs.oprd.7b00212.

(180) Stankiewicz, A. I.; Moulijn, J. A. Process Intensification: Transforming Chemical Engineering. *Chemical Egineering Progress* **2000**, *96*, 22–34.

(181) Wegner, J.; Ceylan, S.; Kirschning, A. Flow Chemistry - A Key Enabling Technology for (Multistep) Organic Synthesis. *Adv Synth Catal* **2012**, *354* (1), 17–57. https://doi.org/10.1002/adsc.201100584.

(182) Tanimu, A.; Jaenicke, S.; Alhooshani, K. Heterogeneous Catalysis in Continuous Flow Microreactors: A Review of Methods and Applications. *Chemical Engineering Journal* **2017**, *327*, 792–821. https://doi.org/10.1016/j.cej.2017.06.161.

(183) Gutmann, B.; Cantillo, D.; Kappe, C. O. Continuous-Flow Technology - A Tool for the Safe Manufacturing of Active Pharmaceutical Ingredients. *Angewandte Chemie - International Edition* **2015**, *54* (23), 6688–6728. https://doi.org/10.1002/anie.201409318.

(184) Poechlauer, P.; Colberg, J.; Fisher, E.; Jansen, M.; Johnson, M. D.; Koenig, S. G.; Lawler, M.; Laporte, T.; Manley, J.; Martin, B.; O'Kearney-Mcmullan, A. Pharmaceutical Roundtable Study Demonstrates the Value of Continuous Manufacturing in the Design of Greener Processes. *Org Process Res Dev* **2013**, *17* (12), 1472–1478. https://doi.org/10.1021/op400245s.

(185) Cantillo, D.; Kappe, C. O. Immobilized Transition Metals as Catalysts for Cross-Couplings in Continuous Flow - A Critical Assessment of the Reaction Mechanism and Metal Leaching. *ChemCatChem* **2015**, *6* (12), 3286–3305. https://doi.org/10.1002/cctc.201402483.

(186) He, Z.; Li, Y.; Zhang, Q.; Wang, H. Capillary Microchannel-Based Microreactors with Highly Durable ZnO/TiO2 Nanorod Arrays for Rapid, High Efficiency and Continuous-Flow Photocatalysis. *Appl Catal B* **2010**, *93* (3–4), 376–382. https://doi.org/10.1016/j.apcatb.2009.10.011.

(187) Emmanuel, N.; Bianchi, P.; Legros, J.; Monbaliu, J. C. M. A Safe and Compact Flow Platform for the Neutralization of a Mustard Gas Simulant with Air and Light. *Green Chemistry* **2020**, *22* (13), 4105–4115. https://doi.org/10.1039/d0gc01142h.

(188) Kassin, V.-E. H.; Silva-Brenes, D. V.; Bernard, T.; Legros, J.; Monbaliu, J.-C. M. A Continuous Flow Generator of Organic Hypochlorites for the Neutralization of Chemical Warfare Agent Simulants. *Green Chemistry* **2022**, *24* (8), 3167–3179. https://doi.org/10.1039/d2gc00458e.

(189) Zhang, Q.; Zhang, Q.; Wang, H.; Li, Y. A High Efficiency Microreactor with Pt/ZnO Nanorod Arrays on the Inner Wall for Photodegradation of Phenol. *J Hazard Mater* **2013**, *254–255* (1), 318–324. https://doi.org/10.1016/j.jhazmat.2013.04.012.

(190) Hoang, N. T.-T.; Tran, A. T.-K.; Le, T.-A.; Nguyen, D. D. Enhancing Efficiency and Photocatalytic Activity of TiO2-SiO2 by Combination of Glycerol for MO Degradation in Continuous Reactor under Solar Irradiation. *J Environ Chem Eng* **2021**, *9* (5), 105789. https://doi.org/10.1016/j.jece.2021.105789.

(191) Jain, P.; Kumar, A.; Verma, N.; Gupta, R. K. In-Situ Synthesis of TiO2 Nanoparticles in ACF: Photocatalytic Degradation under Continuous Flow. *Solar Energy* **2019**, *189* (July), 35–44. https://doi.org/10.1016/j.solener.2019.07.042.

(192) Behnajady, M. A.; Modirshahla, N.; Daneshvar, N.; Rabbani, M. Photocatalytic Degradation of an Azo Dye in a Tubular Continuous-Flow Photoreactor with Immobilized TiO2 on Glass Plates. *Chemical Engineering Journal* **2007**, *127* (1–3), 167–176. https://doi.org/10.1016/j.cej.2006.09.013.

(193) Chan, Y. L.; Pung, S. Y.; Sreekantan, S. Degradation of Organic Dye Using ZnO Nanorods Based Continuous Flow Water Purifier. *J Solgel Sci Technol* **2013**, *66* (3), 399–405. https://doi.org/10.1007/s10971-013-3022-9.

(194) Miri, A.; Ghorbani, F. Syntheses of Ag[Cu@Ag]\APTMS\boehmite as a Photocatalyst for Methylene Blue Degradation in Batch and Continuous Flow Systems under Visible Light. *Environ Nanotechnol Monit Manag* **2021**, *16* (April), 100493. https://doi.org/10.1016/j.enmm.2021.100493.

(195) Fard, N. E.; Fazaeli, R. A Novel Kinetic Approach for Photocatalytic Degradation of Azo Dye with CdS and Ag/CdS Nanoparticles Fixed on a Cement Bed in a Continuous-Flow Photoreactor. *Int J Chem Kinet* **2016**, *48* (11), 691–701. https://doi.org/10.1002/kin.21025.

(196) Daneshvar, N.; Rabbani, M.; Modirshahla, N.; Behnajady, M. A. Photooxidative Degradation of Acid Red 27 in a Tubular Continuous-Flow Photoreactor: Influence of Operational Parameters and Mineralization Products. *J Hazard Mater* **2005**, *118* (1–3), 155–160. https://doi.org/10.1016/j.jhazmat.2004.10.007.

(197) Zhang, X.; Sun, D. D.; Li, G.; Wang, Y. Investigation of the Roles of Active Oxygen Species in Photodegradation of Azo Dye AO7 in TiO2 Photocatalysis Illuminated by Microwave Electrodeless Lamp. *J Photochem Photobiol A Chem* **2008**, *199* (2–3), 311–315. https://doi.org/10.1016/j.jphotochem.2008.06.009.

(198) Machado, L. C. R.; Torchia, C. B.; Lago, R. M. Floating Photocatalysts Based on TiO2 Supported on High Surface Area Exfoliated Vermiculite for Water Decontamination. *Catal Commun* **2006**, *7* (8), 538–541. https://doi.org/10.1016/j.catcom.2005.10.020.

(199) Chuan, X. Y.; Hirano, M.; Inagaki, M. Preparation and Photocatalytic Performance of Anatase-Mounted Natural Porous Silica, Pumice, by Hydrolysis under Hydrothermal Conditions. *Appl Catal B* **2004**, *51* (4), 255–260. https://doi.org/10.1016/j.apcatb.2004.03.004.

(200) Hou, M.; Li, F.; Liu, X.; Wang, X.; Wan, H. The Effect of Substituent Groups on the Reductive Degradation of Azo Dyes by Zerovalent Iron. *J Hazard Mater* **2007**, *145* (1–2), 305–314. https://doi.org/10.1016/j.jhazmat.2006.11.019.

4. Biopolymers

In this chapter, an investigation on the extraction of biopolymers from fishery waste is described. Biopolymers are natural polymers produced by living organisms and they have great importance and interest in a wide range of applications from biomedical (e.g. tissue engineering) to pharmaceutical and materials production. In particular, focus was placed on the extraction of collagen from fish scales for the production of UV-shielding materials and on the possibility to obtain chitin from crab shells using a more sustainable pathway with ionic liquids.

4.1 Introduction: biopolymers from fishery waste

Biopolymers are polymers produced by living organisms and they are the most widespread organic compounds in the ecosphere.[1] Depending on the type of monomer and on the structure of the biopolymer itself, they can be divided in three main classes: polynucleotides (made by nucleotide units, like DNA and RNA), polysaccharides (or polycarbohydrates, made by repetitive monosaccharide or sugar units) and polypeptides (composed by amino acids sequences). Other classes can also be considered as biopolymers, such as lipids, polyphenols and also synthetic polymers deriving from biobased monomers (**Figure 4.1.1**).[2]

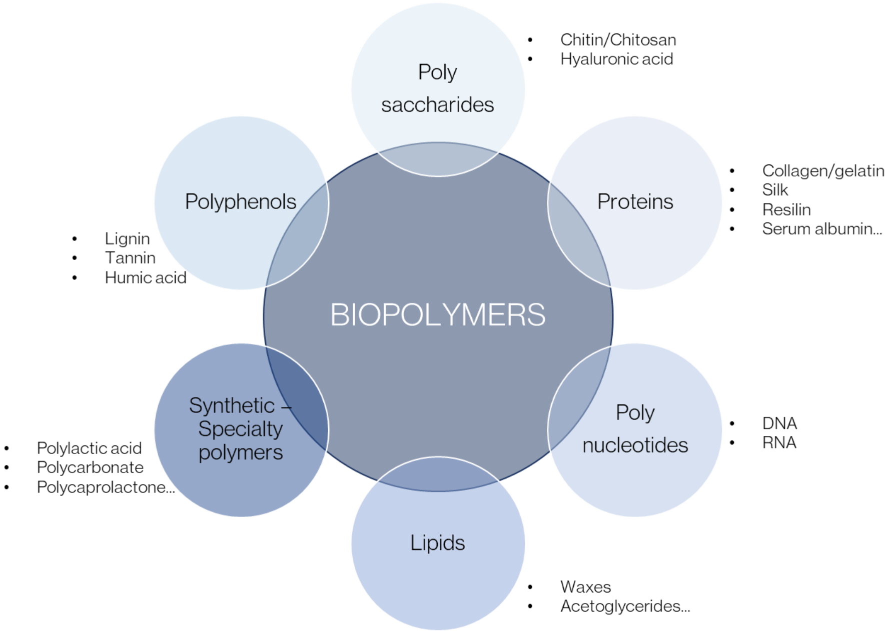

Figure 4.1.1. General classification of biopolymers.

The terms “biopolymers” or “bioplastics” have been generally applied to a large number of plastics with different properties and applications with a variety of different meanings.[3] Bio-based plastics, indeed, can be produced from a plethora of different renewable sources, such as cellulose and starch, but some of them can also be non-biodegradable, such as bio-based polyethylene.[4] The potential great contribution of biodegradable plastic to the reduction of pollution in the environment, especially in the marine one, is evident. Plastic litter is, indeed, one of the most impacting environmental problems, causing a great number of ecologically negative consequences, like the presence of micro and nanoplastics in the aquatic habitat.[5] Around 320 MT·y^{-1} of plastic for different applications are currently produced from petroleum resources and production rates are expected to increase in the near future, exceeding 500 MT·y^{-1} by 2050.[6] Over 150 MT of plastic solid waste are produced globally every year.[7] Most plastic wastes take hundreds of years to degrade naturally under ambient conditions, and thus they accumulate in nature. Wildlife habitat and its biodiversity are endangered due to the contamination of plastic wastes, especially in the marine ecosystem.[8] Burning municipal solid waste containing plastic in the open field also releases toxic gases, including dioxins, furans, mercury, and polychlorinated biphenyls.[9] For this and other reasons, the production of bioplastics has largely increased during the last decade, with the aim of decreasing the negative impact of synthetic polymers on the environment. In fact, biopolymers are fully or partially bio-based and can be biodegradable and/or biocompatible.[10] However, they still represent a small portion of the market being roughly 1% of the yearly plastic supply. In 2020 the bioplastic production worldwide was estimated to be around 2.11 million tons, and it is expected to rise to about 2.87 million tons in 2025.[11] Nevertheless, since the demand is continually growing, the market for biopolymers is incessantly expanding and differentiating, including more advanced materials, applications and innovations. Packaging is the major sector for bioplastic use with 47% of the total bioplastic market in 2020 (0.99 million tons) with a particular increasing interest in the production of green edible/biodegradable films for food packaging. In addition, biopolymers have the potential to be used in medical applications, water treatment, cosmetics, food additives, absorbent and biosensors among others. Due to their considerable biocompatibility and biodegradability, they have, in particular, an important role in biomedical applications for drug delivery systems, tissue engineering and wound treatment, dialysis membrane and biosensors.[12] A biopolymer, indeed, should be non-toxic, non-antigenic, non-irritant, non-carcinogenic, sterilisable and available for widespread applications.[13]

As stated in the introduction, fish waste represents a growing issue that can be solved with innovative approaches. The need for an implementation of more sustainable practices in fishery sectors, indeed, involves the valorisation of by-products and discards:[14] this could contribute to reduce the costs of a safe waste disposal and to generate additional value arising from the recovery of several potentially interesting molecules (e.g. oils, proteins, pigments, bio-active peptides, chitin, gelatin…).[15,16] Of particular interest nowadays is the production of biopolymers starting from discarded fish materials. In particular, as illustrated in **Figure 4.1.2**, different types of fishery waste can be advantageously converted into natural polymers: muscles, skin, fins, scales and shells.

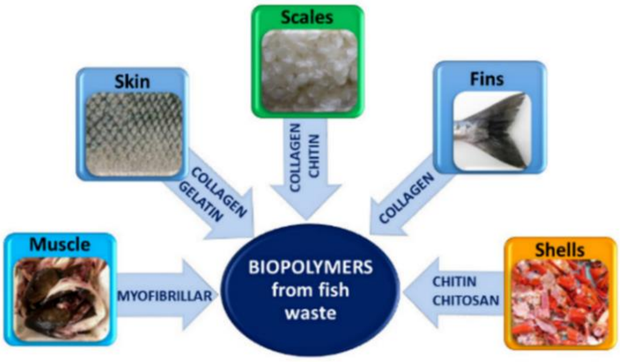

Figure 4.1.2. Types of fishery waste possibly used for biopolymers production.[11]

Polymers derived from fishery waste, indeed, are a particularly promising substitute for synthetic plastics thanks to their greener characteristics.[17] The main biopolymers that can be obtained from this type of waste are collagen and chitin/chitosan. Proteins, like collagen, are among the most used biomaterials in the food industry, thanks to their nutritional values, biodegradability, ability to form gels and non-toxicity. In addition, the materials produced from proteins have several advantages, such as good barrier properties, transparency and potential to produce active packaging. [18,19] A more detailed description of collagen and its properties is reported in **Section 4.2.1**. On the other hand, chitin is a widespread biopolymer: it is a polysaccharide with a crystalline structure that led to an intrinsic high resistance and insolubility of the polymer.[20] Chitosan is easily prepared from chitin, being its deacetylated form, and present a higher solubility that allows its conversion into hydrogels, membrane and films that are known to possess antimicrobial activity. A detailed description of chitin and chitosan is reported in **Section 4.3**.

4.2 Biopolymers-based UV-blocking Films

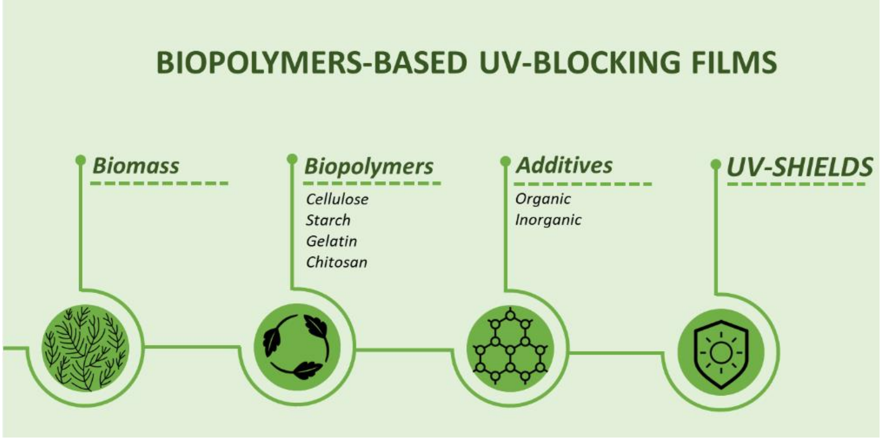

Among the different portions of the electromagnetic spectrum, UV emissions (100-400 nm) are known to be harmful for human health and damaging for organic matter, including commercially and industrially relevant molecules and polymers, such as foodstuff, pharmaceuticals, cosmetics and coatings. To avoid undesired/uncontrolled organic matter degradation upon UV light exposure, the development of UV-blocking materials has gained increasing interest in the past few years. Commercially available UV-blocking polymers are currently derived from petrochemicals, which are associated to well-known end-of-life issues including non-biodegradability and environmental pollution problems. It is therefore necessary to produce new bioderived and biocompatible polymers with UV barrier properties. This chapter summarizes the recent progress made in the field of biopolymer-based UV-blocking films, focusing mainly on chitosan and gelatin as matrices combined with UV absorbing organic and/or inorganic fillers. This chapter is part of an extensive review that is currently under preparation and its submission for publication is expected by the end of this year.

Introduction

Earth's stratospheric ozone layer depletion over the southern hemisphere has become an alarming problem in the last 40 years, due to the accumulation of volatile halogenated ozone depleting substances (ODS). A significant reduction in ODS consumption has been achieved globally since 1986, thanks to government driven global actions such as the 1987 United Nations Environment Programme (UNEP) Montreal Protocol. Although the ozone hole is currently under control and slowly reducing its size, its UV shielding effect is somewhat reduced, and the amount of UV radiation levels at Earth's surface has increased. UV radiation is commonly divided into three main types: UV-A (400 nm – 315 nm), UV-B (315 nm – 280 nm) and UV-C (280 nm – 100 nm). The Earth's ozone layer blocks the UV-C portion and part of the UV-B, but the remaining fraction of UV-B and all UV-A are transmitted through the atmosphere and reach the Earth's surface. Therefore, recent applied research on materials' development is focused on creating UV-shielding materials.[21] Direct and prolonged exposure to UV light can lead to harmful effects on human health, ranging from skin aging and eye damage to melanoma[22] and other diseases of the immune system.[23] UV light irradiation promotes the generation of free radicals with detrimental effects on the short- and long-term stability of organic materials. Indeed, by UV irradiation singlet oxygen is produced, a short lived radical species which is the main cause of lipid oxidation, antioxidants decomposition and irreversible damage of vitamins and proteins.[24] Limiting and/or preventing UV light exposure is a major concern within the food industry sector, as oxidation reactions can alter the flavour and appearance of food and decrease its nutritional quality, eventually producing toxic compounds.[25] UV radiation has a photodegradation effect also on polymers: [26] for this reason industries producing paints, plastics and cosmetics are constantly facing the challenge of developing and producing materials capable of retaining their physical and optical properties even after prolonged exposure to solar radiation. These issues have led to the addition of UV blocking agents to various commercial formulations, in particular for food and pharmaceutical packaging,[27] biomedical,[28] construction and cosmetics applications.[29] So far, fossil-derived materials, such as polystyrene, polyurethanes or polymethylmethacrilates, have been used as matrixes for UV-shields. However, due to increasing environmental and health concerns, it is crucial to shift towards the development of materials derived from renewable resources with a clear and controllable end-of-life cycle. Recently, biopolymer-based nanocomposites reinforced with a low fraction of functional fillers have been considered owing to their distinctive and characteristic properties. In this context, several environmentally friendly and biodegradable biopolymers, like chitin, starch, gelatin and cellulose, have come to be extensively used.

Nowadays, a wide number of different additives have been used to impart UV-shielding properties to biopolymers-based materials. The purpose of this chapter is to review the state-of-the-art on bio-based UV blocking materials, derived mainly from gelatin and chitosan, doped with different UV absorbers.

Additives

Most renewable-based polymers are UV transparent, therefore one of the most commonly employed strategies to include UV-shielding abilities in such bio-based materials relies on the incorporation of organic and/or inorganic UV absorbers.

Organic UV blockers (benzophenone and its derivatives) have been widely applied in industrial products, e.g., textiles, personal care and packaging products, thanks to their significant UV shielding power. Aromatic compounds, indeed, exerts a protective effect via $n \rightarrow \pi^*$ and $\pi \rightarrow \pi^*$ electronic transitions involving the benzene ring structure and other intramolecular charge-transfer transitions of carbonyl and hydroxyl groups respectively.[30] However, it is reported that such benzophenone-type UV absorber are unstable and prone to photodegrade to generate toxic adducts that can easily permeate and be released into the environment, inhibiting the practical application of those additives.[31] On the other hand, inorganic nanomaterials, in particular metal oxides NPs, are regarded as more effective UV blockers and have been widely introduced into coating systems to absorb wavelengths in the range of 200-400 nm. This type of nanomaterials can rapidly convert the photon energy into heat and, in addition they lead to light scattering. However, absorbing UV light, free radical formation takes place causing possible attack on the polymer structure with consequent photo-oxidative degradation.[32,33] In fact, the majority of inorganic metal oxides shows photocatalytic actions resulting in the depletion of some of the intrinsic properties of nanocomposite materials, such as their physical, mechanical and chemical properties. In addition, most of them can be used only for opaque and coloured products limiting the field of application. The characteristics of the more currently used inorganic and organic additives for the preparation of UV-blocking materials will be here discussed.

Organic UV-blockers

Organic UV absorbers based on benzophenone, but also triazine and benzotriazole (**Figure 4.2.1**) are widely used [34] but, due to the risks related to human health and the environment,[35,36] current challenges to replace them are developing.

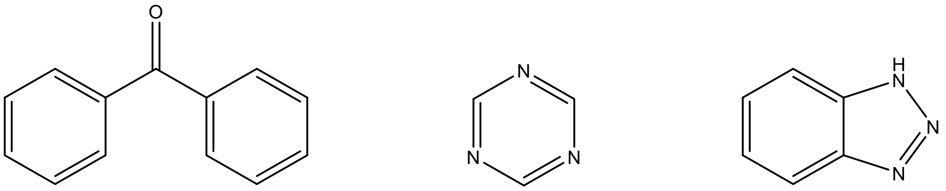

Figure 4.2.1. Chemical structure of (from left to right) benzophenone, triazine and benzotriazole.

Natural extracts, polyphenols, tannins and lignin can be valuable alternatives thanks to the π-conjugated system that can absorb efficiently UV light.[37] Among the most promising candidates to replace conventional organic UV absorbers, lignin and carbon dots are gaining more and more interest.

Lignin is the most abundant natural aromatic polymer worldwide with an estimated annual production of 50 million tons.[38] It is an amorphous polyphenolic branched structure formed from enzyme-assisted dehydrogenative polymerization of the phenyl propanoid units. Only 2% of all industrial lignin and 100 000 tons of kraft lignin available are valorised per year.[39] Lignin can be used as a natural broad-spectrum UV blocker thanks to its functional groups, namely phenolic units, ketones and other chromophores.[40] In addition, the aromatic structure of lignin can increase the stability of polymers in blend towards oxidation and heat, thanks also to the free radical scavenging ability of its phenolic groups.[41] On account of these extraordinary properties, this natural polymer has been extensively blended as an active material with other biopolymers to achieve films with UV protection capabilities.[42] However, the poor water solubility and highly branched structure of lignin present challenges in regard to the compatibility with other biopolymers. In addition, products with the presence of lignin can turn brown over time due to the oxidative degradation of aromatic rings induced by the light.[43]

As stated in the previous chapter, CDs are a new class of carbon nanomaterials with spherical shape, diameter lower than 10 nm and broad and strong UV absorbance [44] that have drawn considerable attention in a wide range of applications. CDs have distinct electronic and optical properties that can be controlled through size, structure and surface chemistry: all these parameters can be easily tailored with different synthetic approaches and a wide variety of possible carbon precursors.[45,46,47] In addition, different studies have demonstrated the low cytotoxicity and high biocompatibility of these carbon nanostructures.[48] Bio-nanocomposites based on CDs with superior properties on UV-shielding, together with low permeability, thermal and mechanical properties and so on, have been prepared with different polymers such as chitosan [49], cellulose [50] and others.[51,52] However, a precise control over the structural aspects of CDs is needed since the wide variety of functional groups on their surface can heavily influence their chemical and photophysical properties. In addition, the optoelectronic properties of these carbon nanomaterials are not yet fully understood.

Inorganic UV-blockers

Inorganic materials are good UV-light screens and have high ability to absorb/scatter the light. Particular attention is given to nanomaterials; nanotechnology has become, indeed, the leading technology for the improvement of advanced materials in the last decade.[53] In fact, extensive research has been carried out in the sector of nanocomposite films containing nanofillers to improve barrier, mechanical, thermal and physico-chemical properties,[54,55,56] with particular attention to titanium dioxide (TiO_2), zinc oxide (ZnO) and graphene. Nonetheless, some drawbacks, like aggregation after a certain concentration and nonbiodegradability, must be taken into account.

Titanium dioxide, especially in its nano size, is one of the most used materials nowadays: it is generally recognized as stable, biocompatible and cheap. In addition TiO_2 has intrinsic chemical-inertness, non-toxicity, antimicrobial ability, high photocatalytic activity and UV-blocking properties.[57,58,59] TiO_2 NPs have been extensively used in a plethora of different fields, such as pollution treatment, wound repairing and biosensors but also for food preservation and for the development of active packaging films.[53,60] Titanium dioxide exists in three crystalline forms (anatase, rutile and brookite) and can be obtained in different sizes, shapes and surface feature allowing a tailorable and customizable preparation of the NPs. Thanks to its small size and high surface area, TiO_2 NPs possess unique physical and chemical properties and are able to interact with polymer matrixes enhancing their mechanical and physical properties.[61,62]

Zinc oxide NPs are used in many applications from food to cosmetics[63,64] thanks to its wide band-gap, low-toxicity and optical transparency. In particular, its UV absorbing behaviour made it an interesting functional filler in pharmaceutical materials, pigments, cosmetics and coating materials.[65] Indeed, ZnO is a well-known nanofiller that can improve the properties of the material with its outstanding antimicrobial action, non-cytotoxicity and high stability.[66] The size, morphology, composition, crystallinity and shape of ZnO particles are some important parameters; for example, it has been demonstrated that ZnO nanorods exhibit an optimal UV absorption activity and that can be a suitable candidate as nanofiller for UV-shields.[67] Indeed, the incorporation of ZnO in biopolymers enhance their mechanical and barrier properties providing materials with improved behaviours. Both ZnO and TiO_2, however, undergoes the classical inconvenient of inorganic fillers, such as aggregation, production of coloured/opaque and non-degradable materials and the possibility to start radical photocatalytic reactions detrimental for the polymer matrix.

Graphene is two-dimensional sheet of sp^2 carbon one atom thick, that has a great potential in a huge range of applications including UV-protection.[68,69] Thanks to the extent of the π domain, graphene has a large variety of promising physical properties: ultrahigh specific area, mobility of charge carrier, quantum hall effects at room temperature, high flexibility, mechanical, thermal, electrical properties, and excellent optical transmittance.[70,71] All these exceptional features contribute to the enhancement of the intrinsic characteristics of polymers after incorporation of graphene. In addition, the optical band gap of graphene oxide (1.5 eV) indicates its strong UV absorption and weak visible light absorption, making it a promising candidate as a UV absorber with noncatalytic activity, overcoming the deficiencies of conventional organic and inorganic additives.[72]

Biopolymers

In this section an excursus on the production of UV-shields starting from gelatin and chitin, two well-known biopolymers that can be obtained from fishery waste, is presented. It is important to remark that, besides the UV-blocking capability, the visible light transmittance is an important parameter for films applications because it affects the appearance and the acceptability of the material. Transparency is, indeed, the physical property of allowing light to pass through the film.[73,74] Finding a good balance between UV barrier properties and Vis light transparency is one of the main challenges in the field of biopolymers-based materials.

Gelatin

Collagen is the main protein present in the extracellular matrix of human tissues and it constitutes up to the 30% of the dry weight of the body.[75] The structure of collagen is in form of triple helix constituted of three α-chains formed by an aminoacidic sequence of glycine-X-Y where X and Y are mostly occupied by proline and hydroxyproline.[76] A more detailed description of collagen is reported in **Chapter 4.2.1**. The common procedure to obtain collagen is its extraction from animal connective tissues using acidic, basic, or neutral solubilization or enzymatic treatments. The as obtained material shows non-immunogenicity, low antigenicity, and biocompatibility.[77] From the denaturation of collagen it is possible to obtain gelatin, a protein-based biopolymer that is gaining attention for the preparation of active materials thanks to its film-forming ability and worldwide abundance.[78] Gelatin is renewable and classified as a "generally recognized as safe" substance by the U.S. Food and Drug Administration becoming a candidate to substitute fossil-based plastics in food packaging. Beyond their biocompatible and biodegradable nature, gelatin-based films showed to have adequate gas permeability, thermo-reversible sol-gel transition, high elasticity in a dry state and satisfactory mechanical properties[79,80] and, due to its high content of aromatic amino acids, UV-shielding properties.[81,82] However, gelatin is highly sensitive to moisture and might undergo post-processing changes when stored at high relative humidity.[83] In order to enhance their physicochemical properties, in particular UV-blocking ability, gelatin-based biofilms are usually reinforced with an enormous number of functional fillers varying from organic compounds to nanostructured materials. In this regard gelatin contains many suspended functional groups that can facilitate the chemical cross-linking and derivatization. In **Table 4.2.1** some of the UV-blockers used for the production of UV-shields from gelatin are reported: for brevity only the most significant examples are herein discussed. It is not here examined, but it is worth to mention, that in the majority of cases the high UV blocking percentage implies also a scarce transparency towards visible light.

Table 4.2.1. Gelatin-based UV shields, type of additive and UV-blocking percentage reported in recent literature.

Entry	*Gelatin*	Additives	UV-blocking %	Ref
1	Gelatin/chitosan	Capsaicine encapsulated in MOFs	90	84
2	Commercial gelatin	Copper sulfide NPs	89-99%	85
3	Commercial gelatin	Ag NPs	91.9%	86
4	Commercial gelatin	Ag NPs	100	87
5	Collagen hydrolysate	TiO_2 NPs	55.5-100	88
6	Fish scale gelatin/chitosan	$CaCO_3$ NPs	70	89
7	Commercial gelatin	Melanin NPs	100	90
8	Commercial (bloom fish)	ZnO nanorods	100	91
9	Commercial bovine gelatin	ZnO nanorods	100	67
10	Gelatin from yellow stripe trevally fish	ZnO nanoparticles	50-100	92
11	Commercial gelatin	Choline salicylate	100	93
12	Gelatin/chitosan	Tannic acid	100	94
13	Commercial gelatin	Tannic acid	88-100	95
14	Commercial gelatin	Tannic acid-modified microfibrilalted cellulose	85-98	96
15	Fish gelatin	Gallic acid	97-99	97
16	Commercial gelatin	Choline citrate/lignin	95	82
17	Fish gelatin/pectin	Resveratrol	100	98
18	Bovine gelatin	Epoxidized soybean oil/glyoxal	99.9	99
19	Commercial gelatin	Dialdehyde starch crystals	100	100

Roy et al. [85], for example used different amounts of copper sulfide NPs (CuSNPs) to reinforce gelatin-based films (entry 2, **Table 4.2.1**). Improved UV blocking properties of gelatin/CuSNPs nanocomposite was observed increasing the percentage of additive and it was primarily due to the UV absorption capacity of the used NPs. In particular the transmittance at 280 (T280) nm was demonstrated to be equal to 1.0% after the addition of 2.0% of CuSNPs. On the other hand, also the transmittance in the visible region decreased increasing the amount of nanofiller (transmittance at 660 nm T660 = 39.5% with 2.0% of CuSNPs). However, the reduction in the transmittance for visible and ultraviolet light was different: T660 decreased linearly with increasing CuSNPs concentration, while T280 decreased exponentially. These results imply that the UV-blocking property of the film improved significantly whilst transparency could be partially maintained. Numerous other types of inorganic nanomaterials were used as UV absorbers in gelatin matrices: Ag NPs, TiO_2 NPs, $CaCO_3$ NPs or ZnO nanorods to cite a few. Among the organic additives both nanomaterials, like melanin NPs, and a plethora of aromatic compounds have been employed. For example, the high content of aromatic moieties present in polyphenols was exploited to impart UV shielding ability to gelatin biofilms. Zhang and co-workers[94] developed a composite film using gelatin, chitosan and tannic acid for the preservation of fresh-cut apples (entry 12, **Table 4.2.1**). With the addition of 0.5 wt% of tannic acid the materials showed the ability to block almost all of UV-B and UV-C portions and most of UV-A maintaining a high transparency to visible light. In their work, Kriechbaum et al.[95] reported the preparation of multifunctional materials based on the tannin-induced precipitation of gelatin grafted onto cellulose nanofibrils (entry 13, **Table 4.2.1**). The tannin-containing films displayed excellent UV-blocking properties: almost 100% of UV-B and UV-C and 88% of UV-A were absorbed. Interestingly, the transmittance of visible light was not significantly affected by the introduction of tannin and was around 30% for all films.

Chitosan

Chitosan is an important resource to produce eco-friendly alternatives to common petroleum-based plastics. This biopolymer is predominantly obtained from crustacean waste in the form of raw chitin and it has attracted the attention of many researchers due to its "waste to wealth" prospects.[75] Chitosan is, indeed, obtained from the partial deacetylation of chitin that is widely spread in nature being a constituent of the exoskeletons of marine arthropods, molluscs and fungal cell walls. A more detailed description of chitin and chitosan is reported in **Chapter 4.3**. The cationic nature of chitosan imparts to this natural polymer the ability to form complex structures with other negatively charged polymers (natural or synthetic) and gives chitosan an excellent film-forming capacity.[101,102] Together with this behaviour it is able to inhibit the growth of a wide variety of fungi, bacteria and yeast, it is biocompatible, biodegradable and non-toxic.[103] For these reasons it is widely used for biological and biomedical applications[104,105] but also for the production of packaging and coating materials.[106] However, several disadvantages of pristine chitosan film, which include low UV blocking properties and poor mechanical barrier, have limited its use.[107,108] Therefore, researchers have been focused on the development of methodologies to improve the properties of these biopolymer-based materials [109] by combining it with appropriate reinforcement fillers.[110]

A wide number of chitosan-based biofilm with UV-blocking properties have been produced thanks to the addition of different compounds varying from organic substances to inorganic NPs to natural extracts (**Table 4.2.2**).

Concerning organic molecules, a variety of aromatics (like alizarin, curcumin, anthocyanins, ellagic acid among others) has been used. Gasti et al. [112], for example, exploited the light-absorption properties of ripe *Phyllanthus reticulatus* fruit anthocyanins to obtain smart chitosan/methyl cellulose films (entry 3, **Table 4.2.2**). Thanks to the $n \rightarrow \pi^*$ electronic transition that occurs in anthocyanins, the materials were able to block almost all the UV radiation between 250-300 nm while maintaining a transparency towards visible light of 66.6%. Anthocyanins derived from red cabbage were also used with this purpose by Chen et al. (entry 4, **Table 4.2.2**).[113] Anthocyanins were added to chitosan and oxidized chitin nanocrystals to obtain halochromic smart films that managed to block almost 100% of the UV radiation (250-300 nm) but with quite high values of opacity (from 6.02 to 11.04 a.u./mm depending on the amount of anthocyanins loaded). Nano-additives, both inorganic and organic, are also widespread in the production of chitosan-based light shields. In the work reported from Krishnan et al.[121] , for example, ZnO nanostructures have been synthesized starting from orange peel oil and then used as UV absorber into chitosan matrix (entry 12, **Table 4.2.2**). The chitosan-ZnO nanocomposite was able to block 60% of UV-A region, 75% of UV-B and up to 90% of the UV-C range while maintaining a transparency in the visible of 80%.

Table 4.2.2. Chitosan-based UV shields, type of additive and UV-blocking percentage reported in recent literature.

Entry	**Polymer**	**Additives**	**UV-blocking %**	**Ref**
1	Chitosan	Alizarin	97	[111]
2	Chitosan	Cellulose nanofibers/curcumin	77	[108]
3	Chitosan/methyl cellulose	Anthocyanins	100	[112]
4	Chitosan	Anthocyanins/oxidized chitin nanocrystals	100	[113]
5	Chitosan	Ellagic acid	20-100	[114]
6	Chitosan	Quercetin	100	[115]
7	Chitosan/gelatin	Rutin/cinnamon essential oil	90	[116]
8	Chitosan	Teatree essential oil	56-96	[117]
9	Chitosan	Black soybean extract	42	[118]
10	Chitosan	Poplar extract/bentonite	100	[119]
11	Chitosan	Black plum peel extract/ nano TiO_2	100	[120]
12	Chitosan	Nano ZnO from orange oil	60-90	[121]
13	Chitosan	Melanin NPs	90	[122]
14	Chitosan	Cellulose nanocrystals	50-60	[123]
15	Chitosan/gelatin	Hollow metal organic frameworks/capsaicin	57	[84]

4.2.1 Fish-Waste-Derived Gelatin and Carbon Dots for Biobased UV-Blocking Films

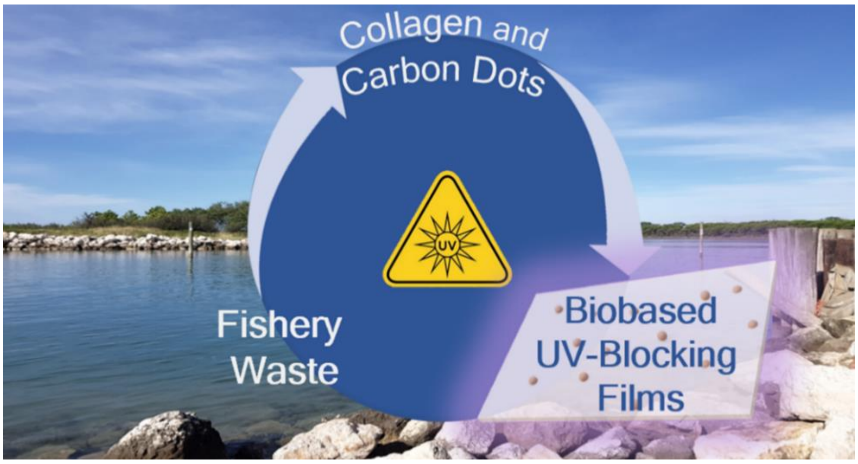

After the production of luminescent nanoparticles for photocatalysis (see ***Chapter 3.4****), we decided to exploit the fishery biowaste for the obtainment of biopolymers to produce materials with a high added value. The experimental investigation on fishery waste-derived biopolymers started with a study on the production of UV-blocking materials. These UV-shields were prepared using collagen extracted from mullet scales and using bass scales-derived CDs as additive to impart the blocking properties. The results of this chapter were published in* C. Campalani, V. Causin, M. Selva and A. Perosa, *ACS Appl. Mater. Interfaces,* **2022**, 14, 35148-35146. https://doi.org/10.1021/acsami.2c11749.[124]

The huge amount of waste produced by the fish industry represents an underexploited source of chemical richness. In this chapter, type I collagen has been extracted from Mugil cephalus scales and CDs were synthesized from Dicentrarchus labrax scales. By casting a mixture of gelatin, glycerol (15%), and CDs (0, 1, 3 and 5%) hybrid films with UV-blocking ability were produced. The films were fully characterized from the morphological, mechanical, and optical point of view. 40 μm thick materials with a high water-solubility (70%) were obtained; in addition, the presence of the carbon nanoparticles enhanced the mechanical properties increasing the elongation at break (EAB) up to 40% and tensile strength (TS) up to 17 MPa. The addition of CDs also modified the thermal stability and water vapour permeability of the films. From the optical point of view, by adding just 5% of CDs the materials blocked almost 70% of the UV radiation with negligible change in opacity (1.32 for non-loaded vs 1.61 for 5% CDs) and in transparency (88.6% for the non-loaded vs 84.4% for 5% CDs). These types of hybrid biobased films hold promise for the production of sustainable UV-shields both for human health and for prolonging the shelf life of food.

4.2.1.1 Introduction

Our ongoing studies on the valorisation of fish waste with a view towards the circular economy, along with the need to develop transparent UV-shielding materials with high environmental- and bio-compatibility inspired us to develop functional films from fish-waste derived photoactive CDs embedded in a fish gelatin matrix. In literature, there are some instances of UV-blocking CD-based films, including a few made from biobased materials, but never in an integrated bio-waste-to-product approach such as in the present case.[50, 125, 126, 127, 128, 129, 130, 131, 132]

Using discarded fish scales to produce high added-value materials addresses the need to recover waste and convert it into new materials, chemicals and products towards a more circular economy. In this context the fishery industry can provide dozens of million tons per year[75] of biowaste that represents a virtually inexhaustible source of sustainable chemical richness.[16] In particular, fish waste can be used as a natural source for oils, collagen, chitin, pigments and gelatin.[75]

Gelatin is a biodegradable protein derived from the partial hydrolysis of collagen that is gaining increasing interest in a large variety of fields such as photography, pharma and cosmetic. This is due to its favourable properties like high water-solubility, non-toxicity, thermo-reversible sol–gel transition, high mechanical strength and elasticity in the dry state.[80] Collagen exists in a great number of different forms classified as fibril forming and non-fibril forming collagen; among the fibrous collagen the most studied and present worldwide are type I, II and III and, in particular, type I collagen is the most abundant accounting for 80-85% of the total.[133,134] Indeed, type I collagen plays a crucial role in the cellular architecture, shape and mechanical properties of animal tissues. Collagen has a triple helix structure formed by amino acids chains bounded by hydrogen bonds. Concerning type I collagen (**Figure 4.2.1.1**) the fibers have a diameters around 1.4-1.5 nm, length about 280-300 nm with circa 1000 amino acids per chain.[135]

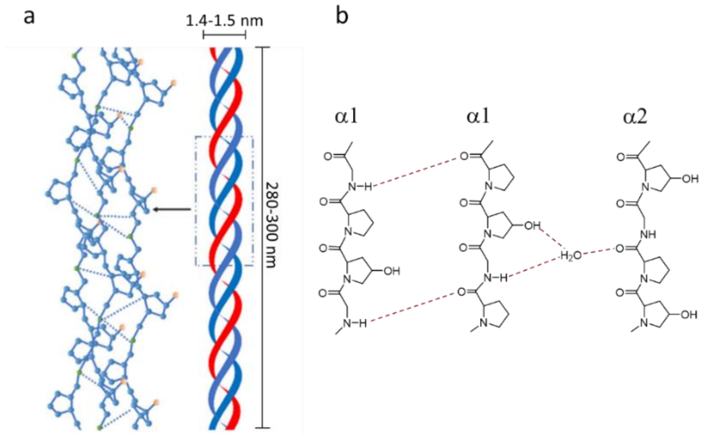

Figure 4.2.1.1. a) the triple helix of type I collagen and b) hydrogen bonds network.

These fibers show a quaternary structure involving three polypeptides (α chains) left-handed α helixes, organized in a coiled-coil right-handed helix. This structure is stabilized by the presence of a hydrogen bonds network both perpendicularly between the chains and with water molecules that can bridge two chains (**Figure 4.2.1.1 b**). The primary sequence of type I collagen is constituted by a repetition of a tripeptide Gly-X-Y, where Gly is Glycine and X and Y can be Proline (Pro) or Hydroxyproline (Hyp), two amino acids with a rigid pyrrolidine ring and high steric hindrance (**Figure 4.2.1.2**).

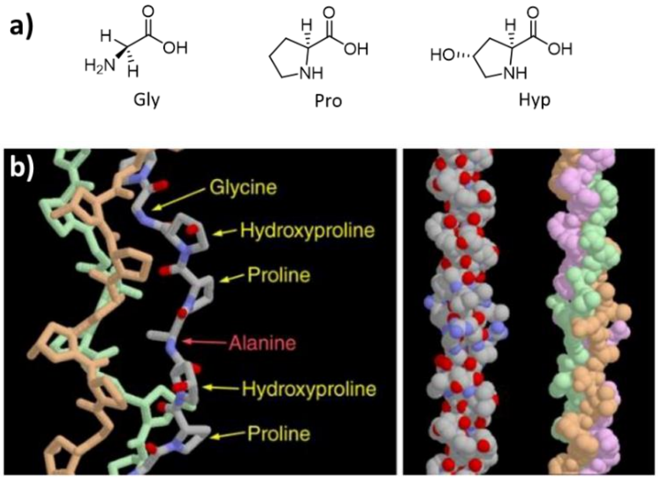

Figure 4.2.1.2. a) Common amino acids of type I collagen. Gly = glycine, Pro = proline and Hyp = hydroxyproline. b) Collagen primary structure.

The presence of Gly allows the three polypeptide chains to pack closer while Pro and Hyp have a structural role enhancing the stiffness of the chains.[136] Moreover, Hyp reinforces the structure and improve the thermal stability of the protein thanks to its ability to form hydrogen bonds. Type I collagen is a heterotrimer of two different α chains ($\alpha1$ and $\alpha2$) in the structure $(\alpha1)_2\alpha2$. Conventionally the dimer is called β chain while the trimer γ chain. The triple helical structure comprises the 96% of the length of the fiber and at the two extremities two non-helical domains are present (N and C-telopeptides) (**Figure 4.2.1.3**).[133]

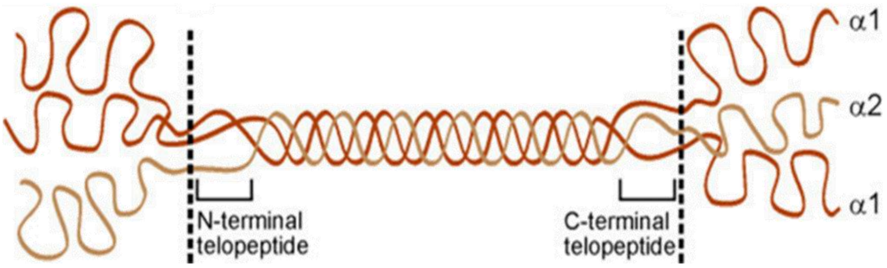

Figure 4.2.1.3. Collagen I trimeric structure and two telopeptides regions.

Traditionally gelatin is produced from collagen derived from bovines and swine and the annual world output is around 326000 tons. However, mammalian and swine gelatin has some problems mainly due to the transmission of bovine spongiform encephalopathy disease, commonly known as mad cow disease, as well as to religious and social issues. For these reasons, fish gelatin is gaining prominence in recent years, especially when derived from the by-products of the fish processing industries (**Figure 4.2.1.4**).[137] The majority of the studies performed gelatin extraction from skin and bones of different fish species,[137,138,139] while the production from scales was reported using black tilapia,[140] bass and mullet,[141] *Labeo rohita*,[80] sea bream,[142] deep-sea redfish [143] and some others.

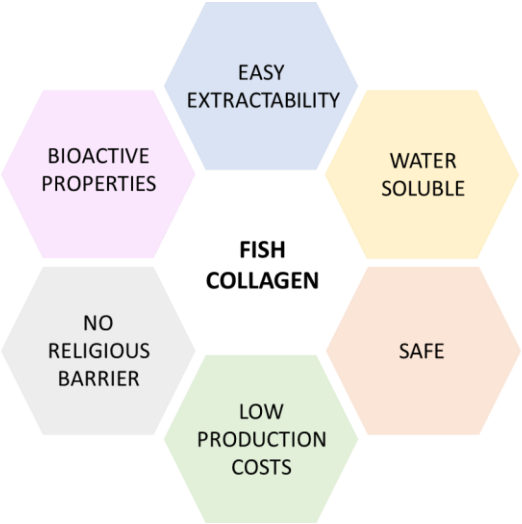

Figure 4.2.1.4. Advantages in the use of fish derived collagen instead of mammalian gelatin.

Gelatin has been extensively studied for its film-forming ability and applicability for protecting foods,[144] but also as carrier of bioactive compounds[145] suggesting the possibility to use it as an alternative to synthetic plastics. Protein-based biopolymers generally show a good film-forming ability, oxygen permeability and mechanical properties better than those of polysaccharides and lipids films but lower than those of synthetic biopolymers (e.g low or high density polyethylene).[146] In particular, to overcome the brittleness of collagen-based materials plasticizers must be added. One of the most used plasticizers is glycerol that is able to create hydrogen bonds increasing the free volume between the polymer's chain and, as a consequence, improving flexibility, elasticity, workability and distensibility of the films.[147]

Table 4.2.1.1. Different additives and applications for gelatin-based biofilms.

Entry	Gelatin Source	Additives	Applications	Ref.
		Natural Additives		
1	Sole skin	Borage extract	Antioxidant	139
2	Tilapia skin	Basil and citronella essential oil, surfactants	Active packaging	144
3	Tuna fish skin	Murta leaves extracts	Edible films	145
4	Commercial	Curcumin	Food packaging	148
5	Rohu swim bladder	Brown seaweed fucoidan	Biodegradable edible films	149
6	Commercial	Pomegranate peel powder	Packaging	150
7	Commercial (warm-water fish)	Lignin	Antioxidant	151
8	Cod	Sunflower oil	-	152
9	Squid	Gelatin hydrolysates	Antioxidant packaging	153
10	Catfish skin	Triacetin	Edible film	154
11	Cuttlefish skin	Cinnamon, clove and star anise extracts	-	155
12	Commercial	Sugars	Food applications	156
13	Commercial (cold water fish skin)	Chitosan	Packaging	157
14	Commercial (cold water fish skin)	Beeswax and carnauba wax	Food packaging	158
		Nanomaterials		
15	Commercial (bloom fish)	ZnO nanorods	Packaging, food packaging, UV-shielding systems.	91
16	Shark skin	TiO_2 nanoparticles	Food packaging	159
17	Blackchin guitarfish skin	TiO_2-Ag nanoparticles	Food packaging	160
18	Commercial	TiO_2-Ag	Food packaging	161
19	Commercial	ZnO nanoparticles	Medicine applications	162
20	Commercial (bovine skin)	Nano hydroxyapatite	Food packaging	163
21	Commercial (cold water fish skin)	Chitosan nanoparticles, origan essential oil	Antimicrobial	164
22	Fish scales	Ag nanowires	Flexible electroluminescent devices	165
23	Commercial (bovine)	ZnO nanorods	Pharmaceutical, food packaging	67
24	Yellow stripe trevally fish	ZnO nanoparticles	Active food packaging	92
25	Commercial (bovine skin)	CDs from citric acid	Drug delivery	166

Nowadays gelatin films are made mostly to be antibacterial and protective against oxidation. For example, Rhim et. al[148] made fish gelatin films with added curcumin that provided excellent antioxidant activity. Other researchers added natural extracts, such as borage,[139] basil and citronella,[144] that showed antioxidant and antibacterial behaviour. Other types of additives, such as fucoidan from seaweeds,[149] pomegranate peel powder[150] and lignin,[151] were used to enhance the antioxidant and antimicrobial properties of fish gelatin films. Also a variety of nanomaterials, such as TiO_2,[159] TiO_2-Ag,[161] ZnO,[162] nano hydroxyapatite,[163] chitosan nanoparticles[164] and others, were added to gelatin film for a plethora of different purposes. Few works exploited nanoparticles to obtain gelatin films with electroluminescent and UV-shielding properties using inorganic nanofillers such as Ag nanowires[165] or ZnO nanorods[67,91] or ZnO nanoparticles.[92] Only Banerjee et al.[166] used CDs as an additive for gelatin films. In their work CDs were synthesized from citric acid with a pyrolytic treatment and then used as nano-additives in a bovine gelatin matrix to obtain hydrogels for intestinal drug delivery and near-neutral pH sensing. In **Table 4.2.1.1** different applications and additives used for gelatin films are summarized.

Among the wide variety of applications of CDs, they seem to be a promising candidate for UV-shields preparation. These carbon nanomaterials, indeed, were exploited for the preparation of UV-blocking films using them as additives in polyvinyl alcohol,[125,127,128,129] nanocellulose,[130,167] starch[168] or carboxymethylcellulose.[132] In summary, UV-shielding materials made with gelatin do not contain CDs, and vice versa if they contain CDs the films are not made from gelatin. Instead, gelatin is commonly used to obtain films with a large variety of different additives and applications, but only few works reported the addition of carbon nanoparticle inside this type of matrix (**Table 4.2.1.1**). In this framework the absence of completely renewable UV barriers made using fish-derived gelatin and carbon dots clearly emerges, especially from waste sources (**Figure 4.2.1.5**).

As stated in **Chapter 3.4**, we demonstrated the possibility to obtain luminescent CDs from bass scales (bass-CDs) with high photoelectron transfer properties.[46] This new class of CDs was characterized in-depth regarding their morphology, composition, optical and surface properties, showing a considerable nitrogen content without the need of any external doping agent.

Therefore, the purpose of this work was to demonstrate that the abundance and chemical richness of fishery waste (namely mullet and bass scales) can be exploited to produce high-tech and high added-value materials and go a step towards the concept of Circular Economy. In particular, gelatin was obtained from mullet scales with a three steps chemical extraction, and it was used to produce bioderived films with UV-shielding properties thanks to the addition of bass-CDs as UV absorbers.

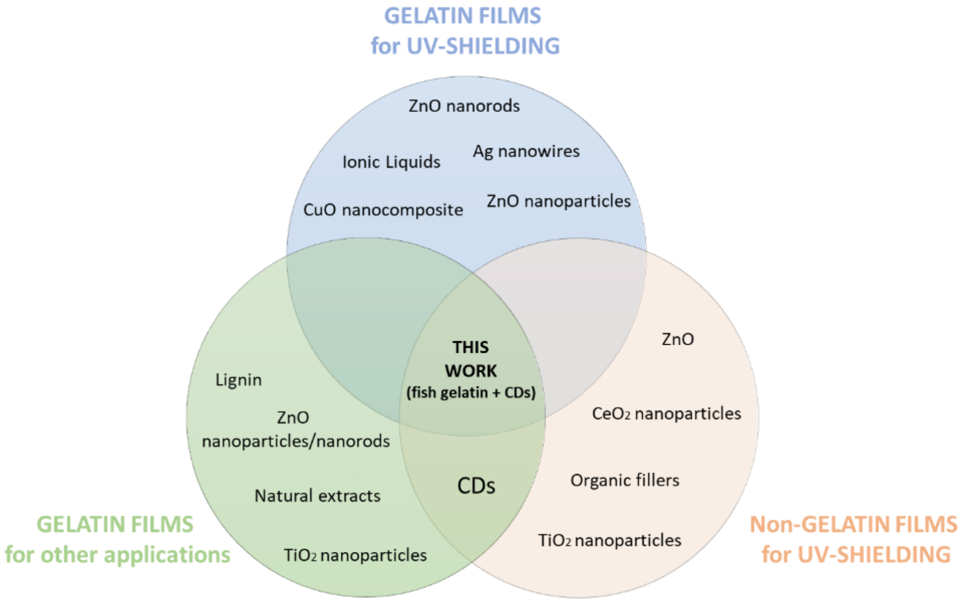

Figure 4.2.1.5. Contextualization of this work in the literature framework.

4.2.1.2 Gelatin Extraction and Characterization

Gelatin was obtained from mullet scales in a 14% yield using a three-step chemical protocol (deproteinization, demineralization and hydrothermal extraction).

Bradford Protein Assay and Molecular Weight Distribution by Gel Electrophoresis

The effective protein content in the gelatin obtained from mullet scales were equal to 52% (measured by the Bradford protein assay), indicative of the presence of residual water bound to the protein network and/or of impurities like minerals or chitin. However, as will be shown later, thermogravimetric analysis showed that both the pristine gelatin and the CDs-containing films had similar contents of inorganic impurities and water; therefore, no composition effect was expected to jeopardize the reproducibility. Gel electrophoresis was consistent with a typical pattern of type I collagen: four bands related to $\alpha1$, $\alpha2$, β and γ chains were identified in each sample (**Figure 4.2.1.6**). In detail, at 135 kDa is visible the $\alpha1$ chain, at 118 kDa the $\alpha2$, the β at 245 kDa and the γ bands at higher molecular weights. The less intense bands at lower molecular weights (around 70 kDa) were attributed to the hydrolysis of collagen in smaller fragments. The average contribution of $\alpha1$, $\alpha2$, β, and γ (total γ 1 + γ 2) chains further confirmed the type I nature of the extracted collagen. In fact, as in type I collagen, the content of the $\alpha1$ chains is usually twice the $\alpha2$.

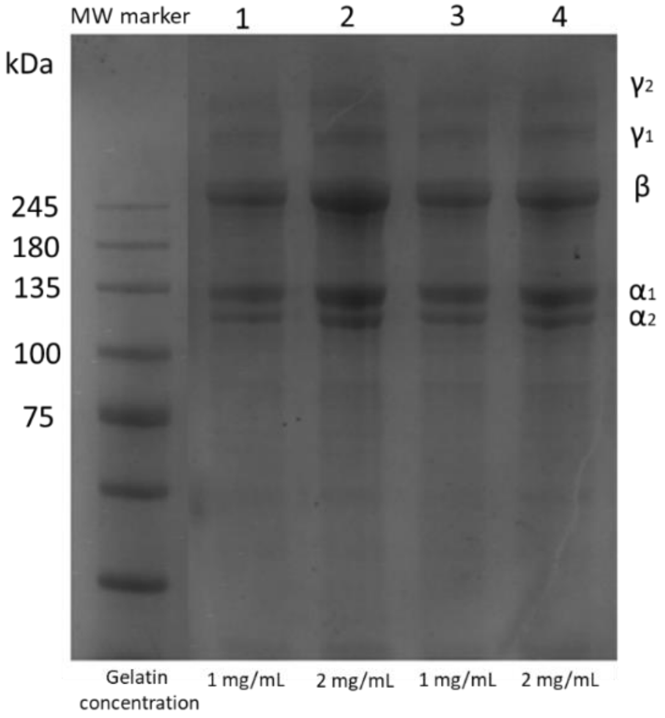

Figure 4.2.1.6. Gel electrophoresis of the gelatin extracted from mullet scales.

Gel Permeation Chromatography

The molecular weight distribution of the extracted collagen was further confirmed by GPC. From this analysis only a broad peak was observed, comprehensive of all the molecular weight observed from the electrophoretic evaluation. This evidence was an additional proof that the latter is a more suitable technique for the determination of the MW of collagen. In any case, the results obtained with GPC were consistent and complementary to electrophoresis: the peak observed via GPC was centered at 124 kDa, a MW value close to the ones found for the α chains (135 and 118 kDa) confirming that the most abundant form of collagen in the sample was the α chain.

Viscoelastic Properties

The elastic modulus (G’) and the viscous modulus (G”) were determined during heating of an aqueous gelatin solution in order to determine its viscoelastic properties. The measurement was performed at 2 different frequencies, viz. 0.3 and 1 Hz, obtaining similar results. An initial profile with values of G’ > G” indicated an elastic and solid-like behaviour that was maintained up to circa 26° C; at this temperature was then identified the crossover point that corresponds to the gel-point of the solution, after which the gelatin showed a liquid-like behaviour (G’ = G” and δ = 45°) as can be seen in **Figure 4.2.1.7**. The observed temperature can be ascribable to the denaturation temperature (Td) of collagen; this result, indeed, is similar to those reported for collagen obtained from carp scales.[169] Td of collagen deriving from marine fish scales is usually about 26-29° C [134], resulting to be generally less thermally stable than the common mammalian one (Td ≈ 41° C).[170] This difference is probably due to the low imino acid content (Hyp and Pro) in marine fish collagen[171]: these two amino acids, indeed, are known to increase the heat resistance of the protein. In the works reported by Cao et al.[141] and Thuy et al.,[134] the imino acid content for grey mullet scales gelatin is around 171-197/1000 residues. However, the low Td of mullet scales collagen highlights the possibility to extract it at lower temperatures compared to the mammalian one, leading to economic advantages for the use of the scales as a raw material.

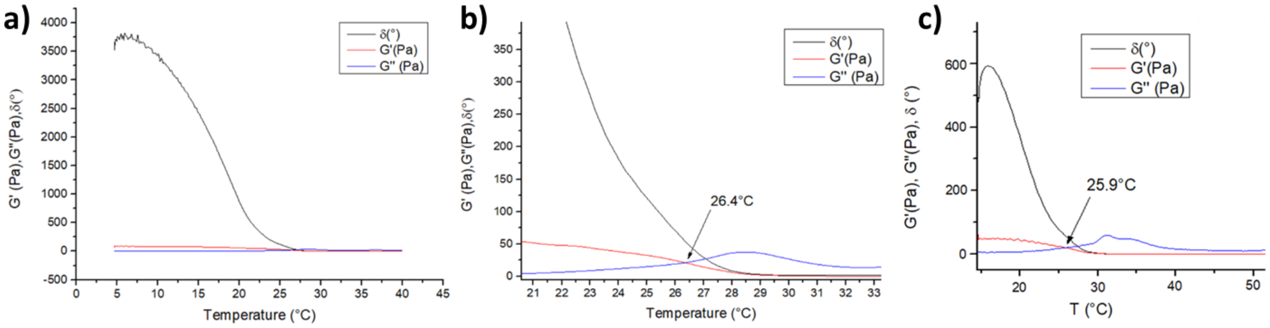

Figure 4.2.1.7. Rheological profile a) from -5 to 40° C, at 1 Hz (heating ramp: 5° C/min); b) zoom on the crossover point; c) from 12 to 90°C, at 0.3 Hz (heating ramp: 5° C/min).

4.2.1.3 Film Formation and Characterization

CDs, used as additives for the preparation of the films, were obtained as described in **Chapter 3.4**. Briefly, 10 nm NPs were produced via hydrothermal synthesis in autoclave (200°C, 24h) using sea bass scales as the carbon source.[46] The film forming solution was then prepared by mixing fish gelatin, glycerol (15%) as plasticizer and CDs in different loading percentages (0, 1, 3 and 5%); casting of this mixture yielded the films.

Film Thickness and Mechanical Properties

Table 4.2.1.3 shows the mechanical properties and the thickness of the gelatin films with different percentages of CDs. The control film (fish gelatin + 15% glycerol) was rather ductile (elongation at break, EAB = 27.5%) and exhibited a tensile strength, TS = 12.5 MPa in accordance with fish gelatin films produced by Hanani et al.[150] The addition of small amounts of CDs (1− 3%) produced a slight increase in the tensile strength (t test *p* value = 0.039) of the material, with rather constant elongation at break and Young modulus. However, the addition of 5% of CDs produced an evident plasticizing effect, as can be seen from the significant decreases in both tensile strength (*p* < 0.003 in a t test comparing 1 or 3%CD-containing films with 5%CD-containing sample) and Young’s modulus (*p* value < 0.00001), together with a noticeable increase in elongation at break (*p* value = 0.0262 in a comparison with the 1% CD-containing sample).

Therefore, CDs seem to have a double role. When particles are small, they have a reinforcing effect, analogous to that of other nanofillers. When agglomeration of the nanoparticles in the matrix becomes significant, such as in the case of 5% CD-containing materials (see Appendix **Section A-4.2**, for TEM and SEM micrographs) they no longer stiffen the structure, but they rather act as plasticizers.

Table 4.2.1.3. Thickness, tensile strength (TS), elongation at break (EAB) and Young modulus (YM) of gelatin films at different CDs %. Values are given as mean ± standard deviation.

%CDs	Thickness (mm)	TS(MPa)	EAB%	YM (MPa)
0	40 ± 3	12 ± 2	27 ± 4	160 ± 13
1	41 ± 4	17 ± 3	32 ± 4	171 ± 14
3	41 ± 4	17 ± 3	28 ± 4	185 ± 15
5	42 ± 2	10 ± 2	40 ± 6	80 ± 6

Water Solubility and Water Vapor Permeability

Water solubility (WS) and water vapor permeability (WVP) are important measures of water resistance and integrity of a film. The control film without CDs exhibited a normally high WS of 70.06% but still lower than the one reported for gelatin films made from rohu (91.49%),[149] cod (88%),[152] squid (>90%),[153] catfish (83.3%),[154] and cuttlefish (96.02%).[155] The formation of low molecular weight monomers and small peptides during film formation is probably the main reason for the high water-solubility. These low molecular weight components immobilized in the film, account for the water-soluble protein component of the film.[172] Despite the water-soluble nature of CDs due to the abundance of polar groups on their surface, the solubility of gelatin films was reduced by adding small amounts (1% and 3%) of carbonaceous nanoparticles. This trend was ascribed to the cross-linking effect of the hydroxyl groups present on the surface of the CDs [46] that initiate the formation of a network which incorporates low molecular fractions leading to the decreased water solubility of gelatin.[150,156] On the other hand, adding higher concentrations of nanoparticles (5%, entry 4 in **Table 4.2.1.4**) the WS returned to the value of the control film (ca. 70%), probably because the hydrophilic nature of CDs prevailed making the films more water-soluble. Another argument is that the crystal structure of fish gelatin protein can be disrupted by the nanoparticles, resulting in increased water solubility of the film [150]. As shown in **Table 4.2.1.4**, WVP decreased when CDs were added to the gelatin meaning that the films behaved as a stronger barrier against water vapor. Also this behaviour can be explained by considering that CDs can cause a decrease in the diffusion rate of water molecules through the films, resulting in lower WVP values [173] by their ability to enhance the cross-linking of gelatin, and as a consequence, to decrease the free volume of the polymeric matrix. Nanoparticles, in fact, can lead to a long and tortuous transport path of water vapor in thin films, which is one of the main reasons for the reduction of WVP.[161]

Table 4.2.1.4. Water Solubility (WS%) and Water Vapour permeability (WVP) of the composite gelatin/CDs films at different CDs%. Values are given as mean ± standard deviation.

Entry	CDs%$_{w/w}$	WS%	WVP 10^{-7} g h $^{-1}$ m $^{-1}$ Pa $^{-1}$
1	0	70.1 ± 0.2	1.05 ± 0.05
2	1	54.9 ± 0.4	0.776 ± 0.006
3	3	60.0 ± 0.3	0.75 ± 0.01
4	5	69.9 ± 0.3	0.75 ± 0.01

Optical Properties

A crucial insight into both structure and optical properties of the films was obtained by UV–vis spectroscopy. In **Figure 4.2.1.8**, the spectra in transmittance of the films with different percentage of CDs are shown (absorbance spectra are reported in the Appendix, **Figure A.4.2.1**). The thickness of the analysed samples was ~40 µm. The dependence of the film's optical transparency in the visible region (light transmittance at 550 nm[127]) against different CDs content is reported in **Table 4.2.1.5**. The loading of CDs affects the visible transparency of the film limitedly (*p* value = 0.004): it decreases from 89% (non-loaded film) to 84% (5% of CDs). The decrease in the transparency of the material is probably related to the agglomeration of the nanoparticles inside the gelatin matrix (see Appendix **Section 4.2** for Sem and TEM micrographs). The addition of the carbon nanoparticles marginally increases (*p* value = 0.0005) the opacity of the films, causing a maximum increase from 1.3 (0% CDs) to 1.6 (5% CDs). Concerning the UV-blocking ability of the gelatin–CDs films it can be easily seen from the transmittance UV–vis spectra that the addition of the carbon nanoparticles caused an increase in their shielding properties. Three different wavelengths were chosen to represent the three portions of the UV spectrum: 365 nm for UV-A, 300 nm for UV-B, and 275 nm for UV-C. The transmittance percentage values at these wavelengths are reported in **Table 4.2.1.5** versus the CDs content. These data highlight how higher percentages of CDs lead to a higher UV-shielding behaviour, reaching the ability to block almost 70% of the UV light. Colorimetric parameters were assessed to obtain essential information regarding the optical properties of the films. In **Table 4.2.1.5**, the colorimetric data are reported. L* values (lightness), that vary from 0 (black) to 100 (white), were >88% for all the measured samples. Increasing the percentage of CDs, indeed, the b* values increased, indicating a predominance of more yellow. This is clearly highlighted also from the growing yellow index values and the consequent decrease of the whiteness index (ΔE, YI, and WI calculated with **Equations 4.2.1.4**, **5**, and **6** in experimental section).

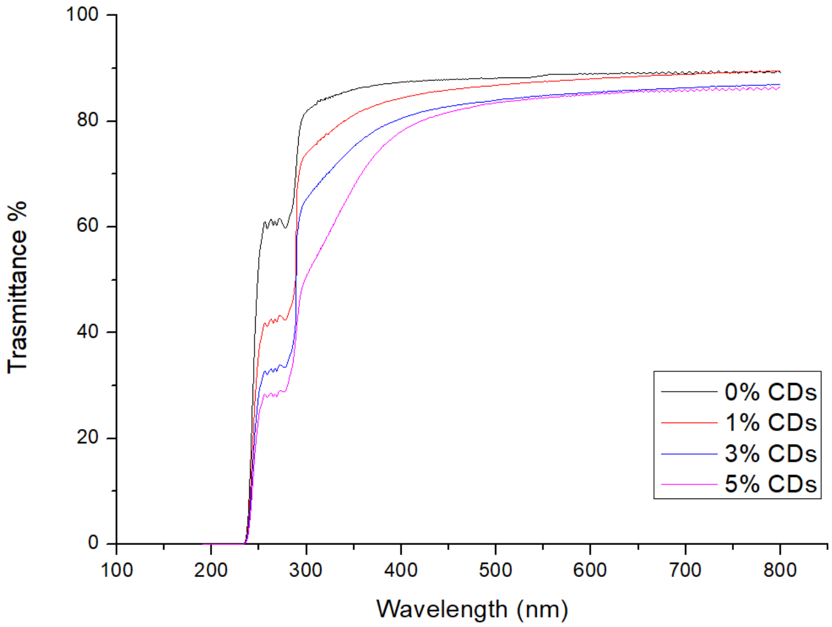

Figure 4.2.1.8. UV-Visible transmittance spectrum of gelatin films with different concentrations of CDs (0% black line, 1% red line, 3% blue line and 5% pink line).

Table 4.2.1.5. Colorimetric data and shielding behaviour (transmittance % at 275, 300, 365 and 550 nm) of fish gelatin-CDs films at different %w/w of CDs.

CDs %	L*	a*	b*	ΔE	YI	WI	Opacity	Transmittance (%)			
								275 nm	300 nm	365 nm	550 nm
0	98.56	-0.12	0.49	0.89	0.74	98.47	1.3	60.6	81.9	86.4	88.6
1	96.77	-0.58	6.47	7.01	9.95	92.74	1.4	42.8	73.9	82.1	87.5
3	88.75	0.04	25.40	27.55	42.60	72.22	1.5	33.6	65.3	76.7	84.8
5	88.86	-0.07	30.34	32.12	50.80	67.68	1.6	28.9	50.7	70.6	84.4

The results were expressed as L* (lightness), a* (redness/greeness) and b*(yellowness/blueness). The total colour difference (ΔE), yellow index (YI) and white index (WI) where calculated using **Equation 4.2.1.4**, **5** and **6** (in Experimental section).

Differential Scanning Calorimetry (DSC) and Thermogravimetric Analysis (TGA)

Differential scanning calorimetry (DSC) was used to determine the thermal properties of the gelatin−CDs films and the corresponding glass transition temperature (Tg). The Tg is defined as the temperature at which the polymer relaxes and changes from the glassy state to the elastic one, for a given heating rate due to the onset of long-range coordinated molecular motion of the amorphous structure. The measurement of Tg was complicated by the onset of the wide endothermal peak due to water evaporation. However, an estimation could still be made. The fish gelatin film without the addition of CDs resulted to have a Tg of about 25 °C, in accord with the transition from solid-like to liquid-like behaviour observed by rheology. Upon addition of the CDs, an increase in the Tg value was observed. In fact, the glass transition temperature increased to about 50 °C, independent of CDs content (see Appendix, **Figure A.4.2.2**). This trend evinced the ability of CDs to form additional intermolecular forces inside the gelatin matrix, as reflected also by the changes in the mechanical properties of the materials. Thermogravimetric analysis was used to evaluate the thermal stability of the materials and the results are shown in **Figure 4.2.1.9**. A three-step weight loss was observed for all the samples. The first weight change occurred at 45−110 °C due to loss of water. The onset of the second step was at 125 °C and ended around 325 °C, and it was attributed to the breakdown of glycerol and of the gelatin chains. The last thermal degradation step started around 350 °C and it is consistent with the decomposition of gelatin. The addition of CDs caused no significant variation in the thermal stability of the materials.[158]

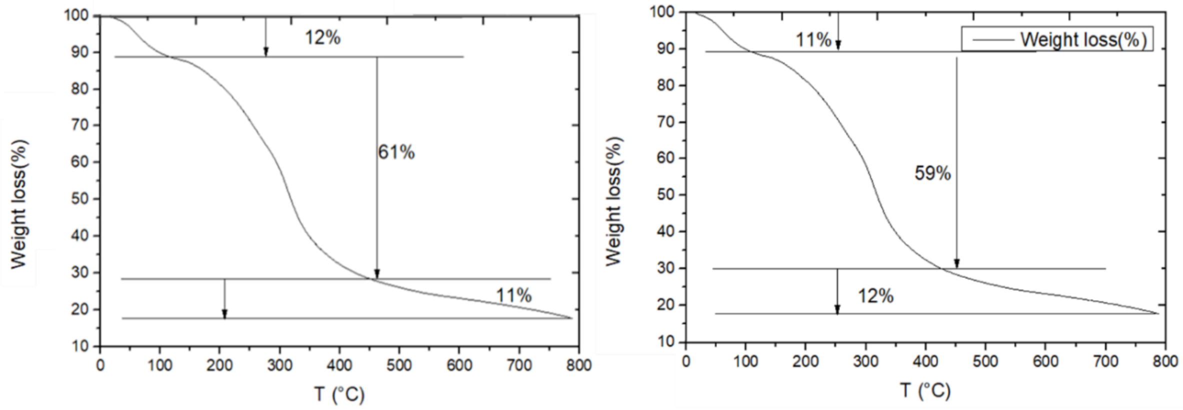

Figure 4.2.1.9. Thermogravimetric analysis of fish gelatin film with 0% of CDs (left) and 5% of CDs (right).

Transmission Electron Microscopy (TEM) and Scanning Electron Microscopy (SEM)

The size of the CDs and their dispersion inside the gelatin matrix were investigated by transmission electron microscopy (TEM). The carbon nanoparticles obtained from fish scales have near-spherical shape and a diameter of 10 nm, as already shown in our previous work (see Appendix, **Figure A.4.2.3-5**).[46] The micrographs of the films indicate that the CDs tend to aggregate resulting in relatively large clusters. With just 1% loading of nanoparticles, it is already possible to observe agglomerates with diameters in the order of 40 nm (see Appendix, **Figure A.4.2.9-11**). Increasing the loading of CDs, the clusters became bigger (see Appendix, **Figure A.4.2.12-17**) leading to a change in mechanical properties and in the decrease in optical transparency of the material (see Film Thickness and Mechanical Properties and Optical Properties). The pristine film, however, showed darker spots as well (see Appendix, **Figure A.4.2.6-8**) attributed to air bubbles due to the casting technique. In addition, scanning electron microscopy (SEM) on the pristine film (15% glycerol, 0% CDs) was performed to observe the structure of the gelatin in the matrix. A dense and filamentous like structure was highlighted due to the organization of the renaturated gelatin (see Appendix, **Figure A.4.2.18-23**).

4.2.1.4 Conclusions

In this section, new hybrid completely biobased gelatin−CDs films with UV-shielding ability starting from fishery waste were described. Gelatin was extracted from mullet scales using a chemical protocol yielding type I collagen. The denaturation temperature was found to be lower than that of common mammalian gelatin making extraction possible under milder conditions. The carbon dots used to dope the films were obtained as 10 nm nanoparticles using a hydrothermal treatment starting from bass scales as a natural carbon and nitrogen source.[46] The films were prepared by mixing fish gelatin, glycerol (15%), and CDs in different percentages (0, 1, 3, and 5%) by the casting technique. Here, 40 µm thick materials were obtained and improved mechanical properties were observed upon addition of the CDs: the EAB% increased from 27% (non-loaded film) to 40% (5% CDs) showing a clear plasticizing effect while, on the other hand, the stiffness decreased, probably due to the aggregation of the nanoparticles in the gelatin matrix. The films exhibited high water-solubility and decreasing WVP upon addition of the nano-additive, indicating that the hybrid materials are less permeable to water. From the optical point of view, the addition of CDs has only a limited effect on transparency (88.6% for the non-loaded vs 84.4% for 5% CDs) and on opacity (1.32 for non-loaded vs 1.61 for 5% CDs); while the material loaded with 5% CDs blocked almost the 70% of the UV radiation. These results can pave the way toward the production of innovative films from waste with a view on the circular economy.

4.2.1.5 Experimental

Materials. All the reagents, of analytical grade and used without further purification, were purchased from Merck Life Science S.r.l. (Milano, Italy). Milli-Q water (obtained with a Merck Millipore C79625 system) was used as a solvent throughout the experiment. The fish scales were from sea bass and mullet and were sourced from a local market. Prior to use, the scales were thoroughly washed with water and dried overnight in a vacuum oven at 70 °C before storage at −18 °C.

CDs Synthesis. Bass-scale CDs were synthesized according to our previously reported work.[46] In summary, a Teflon-lined autoclave was charged with 2 g of dried and ground sea bass scales and 20 mL of Milli-Q water. After heating at 200 °C for 24 h, the obtained suspension was filtered. Residual water was removed by rotary evaporation and CDs were obtained as a brown solid (30−50% yield).

Fish Gelatin Extraction. Gelatin was extracted from mullet scales by adapting the method described by Niu et al.[174] The scales were first rinsed and dried, then immersed in aqueous NaOH 0.3 M (1:6 w/v) for 1.5 h at room temperature for the removal of non-collagenous proteins. The scales were then filtered and rinsed until neutral pH. Next, the biomass was soaked in aqueous HCl 0.2 M (1:6 w/v) for 1.5 h at room temperature for the removal of minerals and then filtered and rinsed to neutral pH. The scales were then immersed in acidic Milli-Q water (pH = 5 with HCl, 1:4 w/v) at 78 °C for 1 h to extract collagen, the solid was filtered off, and the resulting liquid was centrifuged at 6000 rpm for 30 min to remove impurities. The solution was then cast in plexiglass molds and water was allowed to evaporate at room temperature for 20 h. Gelatin gave a transparent solid film in 14% yield.

Fish Gelatin Characterization

Bradford Protein Assay. The Bradford method[175] was used to determine the protein content in the extracted gelatin. The protein standard used to obtain the calibration curve was bovine serum albumin. The mixture of gelatin solution (2.5, 4, 5.5, 7, and 9 µg/mL) and Coomassie Blue dye (200 µL) was incubated for 30 min before the absorbance at 595 nm was recorded with a UV−vis spectrophotometer (Shimadzu UV-1800). Two different batches of mullet scales were used for gelatin extraction, and the assay was run in duplicate.

Molecular Weight Distributions by Gel Electrophoresis. Gelatin solutions were prepared at two different concentrations (1 and 2 mg/mL) by dissolving gelatin into Milli-Q water (60 °C for 10 min) and adding dithiothreitol (350 mM final concentration). SDS-PAGE (sodium dodecyl sulfate-polyacrylamide gel electrophoresis) was conducted using as the standard a molecular weight marker with 5−245 kDa (Sharpmass VI-protein MW marker). The samples were denaturated at 90 °C for 10 min and the loading volume was 10 µL. Stacking gel and running gel used were 4% and 6% respectively and the instrument was set at 20 mA current. Following the separation, the separating gel was stained with Coomassie Blue dye (2.5 µL) to identify the bands. After the process, the electrophoresis gel was stained in a methanol solution to remove residual buffer and dye. The percentage proportion of each band was estimated using Imagej software. All samples were analysed in duplicate.

Gel Permeation Chromatography. Gel permeation chromatography (GPC) was performed on an Agilent Infinity 1260 system equipped with refractive index detector and using an injection volume of 20 µL and a flow rate of 1 mL/min. A Phenomenex PolySep linear was used as column maintaining a constant temperature of 40 °C during the analysis. An aqueous solution of LiCl 0.1 M was used as eluent and polyethylene glycol was used as standard. The sample was prepared dissolving 2 mg/mL of mullet scales collagen directly in the eluent solution at 50 °C.

Viscoelastic Properties. Gelatin was dissolved in Milli-Q water (60 °C for 10 min) to yield a 6.67% (w/v) gelatin solution. Viscoelastic studies were carried out on a Rheometer Kinexus lab+ (Malvern Instruments) by using a parallel plate with a diameter of 2 cm, a gap of 0.2 mm and a constant strain of 5 Pa. Analyses were performed by heating the solution in two ways: from 5 to 40 °C at a scan rate of 5 °C/min and a frequency sweep of 1 Hz and from 12 to 90 °C at a scan rate of 5 °C/min and a frequency sweep of 0.3 Hz. The elastic modulus (G′, Pa), viscosity modulus (G″, Pa), and angle phase (δ = G′/G″, deg) were calculated and plotted as a function of the temperature.

Gelatin−CDs Film Formation. The gelatin−CDs films were prepared by the casting technique. The film-forming solution was obtained dissolving in Milli-Q water 2% (w/v) of fish gelatin at 45 °C for 30 min under continuous stirring. Glycerol was added as plasticizer in 15% ($w/w_{gelatin}$) and CDs as additive at different percentages (1, 3 and 5% $w/w_{gelatin}$). Then, aliquots of 8 mL of film forming solution were poured in Plexiglas molds (7 × 5 cm) and dried at room temperature (25 °C) for 20 h.

Gelatin−CDs Film Characterization

Film Thickness and Mechanical Properties. Film thickness was measured using a handheld micrometer (TESA, sensitivity of ±0.01 mm) averaging nine different points. Tensile strength (TS, MPa), elongation at break (EAB, %), and Young modulus (YM) were determined using an INSTRON3345 instrument following ASTM standard method D882-97. Samples were cut into strips of 15 × 50 mm, which were fixed on the grips of the device with an initial grip distance of 30 mm and a crosshead speed of 1.0 mm/min until the films were broken. The samples were not conditioned before the measurements, which were, however, performed all in a single session, at the same temperature and relative humidity. Five replicates were acquired for each sample. Reproducibility of the measurements was checked preparing a new lot of 5% CD containing film and of neat gelatin. Results confirmed those obtained on the pristine lots. Relative errors were 20% for tensile strength, 8% for the Young modulus, and 14% for elongation at break.

Water Solubility. The method reported by Gomez-Estacá et al.[139] was applied with some modifications to determine the water solubility (WS%) of the films. 4 cm^2 portions of the films were dried in a vacuum oven (20 mbar) at 70 °C for 24 h (constant weight was achieved). The samples were then weighted, placed in beakers with 15 mL of Milli-Q water, which was sealed, and stirred at 25 °C for 15h. The solution was then filtered to recover the undissolved film that was then desiccated in a vacuum oven (20 mbar) at 70 °C for 24 h. Water solubility was then calculated using **Equation 4.2.1.1**, where W_0 referred to the initial weight of the film (as dry matter) and W_f was the undissolved desiccated film residue weight. All tests were carried out in triplicate.

$$WS\% = \frac{(W_o - W_f)}{W_0} * 100$$

Equation 4.2.1.1. Water solubility % of gelatin films.

Water Vapor Permeability (WVP). WVP values were determined according to ASTM method E96 [ASTM E96-95] using 5 mL cups. Every cup containing anhydrous $CaCl_2$ (RH% = 0%), was covered using a portion of film sealed using silicone vacuum grease and was placed inside a desiccator that contained a saturated solution of NaCl (RH = 75%) at 25 °C. Cups were weighted every hour for the first 7 h and finally after 24h. The slope of the weight increase per hour (g/h) divided by the exposed film area (m^2) yielded the water vapor transmission rate (WVTR) [176]. WVP was then calculated using **Equation 4.2.1.2** where WVTR is the water vapor transmission rate, t is the thickness of the films (m), P is the saturation vapor pressure at 25 °C (Pa), R_1 is the RH in the desiccator (0.75), and R_2 is the RH in the cup (0). The difference between desiccator RH and anhydrous calcium chloride corresponds to water vapor partial pressure (753 Pa[154]) and is the driving force of water vapor transition.[177] All tests were carried out in duplicate.

$$WVP = \frac{WVTR * t}{P(R_1 - R_2)}$$

Equation 4.2.1.2. Water Vapor Permeability of gelatin films.

Optical Properties (UV−Visible, Colour). UV−visible spectra of the films were recorded on a Shimadzu UV-1800 spectrophotometer both in absorption and transmittance mode at wavelength from 800 to 190 nm. All tests were carried out in triplicate. Opacity was then evaluated using **Equation 4.2.1.3**, where A_{600} is the absorbance value at 600 nm wavelength and t is the film thickness (mm).

$$Opacity = \frac{A_{600}}{t}$$

Equation 4.2.1.3. Opacity of gelatin films.

Colour measurements were performed using a spectrophotometer Konica-Minolta Co Ltd. (Osaka, Japan), model 2600d with an illuminant D65 and 10 degrees observer. All data were extracted using the instrument software. Parameters such as L* (lightness), a* (redness/greeness) and b* (yellowness/blueness) were used to express the results. A white plate was used as standard (L_{std}* = 99.27, a_{std}* = −0.07 and b_{std}* = −0.06). The total colour difference (ΔE), yellow index (YI), and white index (WI) were calculated using **Equations 4.2.1.4**, **5** and **6**.

$$4) \qquad \Delta E = \sqrt{(L^*_{std} - L^*)^2 + (a^*_{std} - a^*)^2 + (b^*_{std} - b^*)^2}$$

$$5) \qquad YI = \frac{148.86 * b^*}{L^*}$$

$$6) \qquad WI = 100 - \sqrt{\left(100 - L^*\right)^2 + a^{*2} + b^{*2}}$$

Equations 4.2.1.4, 5, 6. Calculations for total colour difference (ΔE), yellow index (YI) and white index (WI).

Differential Scanning Calorimetry (DSC) and Thermogravimetric Analysis (TGA). The thermal properties and stability of film samples were determined by differential scanning calorimetry and thermogravimetry. For DSC measurements, a TA Instruments 2920 apparatus was used. The film samples (4−5 mg) were weighted into aluminium pans and accurately sealed, then scanned over the range −20 to 200 °C at heating rate of 10 °C/min. An empty aluminium pan was used as reference. Tg was measured with the graphical construction shown in **Figure A.4.2.2** in the Appendix.[178] TGA measurements were carried with a TA Instruments 2960 apparatus in a temperature range from 20 to 800 °C with a heating rate of 5 °C/min under a nitrogen flow of 1 mL/min. In order to quantify the repeatability of the measurements, three replicates were recorded for two of the samples (1% and 5% CD). The standard deviation of Tg was ±4 °C. TGA curves for replicate measurements were superimposable, so an instrumental uncertainty of ±1% for weight loss and ±0.5 °C were used.

Transmission Electron Microscopy (TEM) and Scanning Electron Microscopy (SEM). Transmission electron microscopy (TEM) observations of the CDs and fish gelatin/CDs composites were conducted at 120 kV. For the TEM images of the films, small droplets of the film forming solutions were deposited on TEM grids and dried at room temperature for 24 h to form ultrathin films transparent to the electron beam. Dimensions of nanoparticles and aggregates were estimated using Imagej software. Morphology of the surface of film samples were visualized using a scanning electron microscope (SEM-FEG Zeiss instrument) operating at 10000 kV and at different magnifications. Samples were cut into small pieces and placed on stub with double-sided carbon tape.

Statistical Tests. Two sample t tests, with pooled variance, using a 2-tailed distribution were applied at a 95% confidence level and were used to evaluate the statistical significance of comparisons between the data regarding different samples.

4.3 Chitin Pulping from Fishery Waste using Ionic Liquids

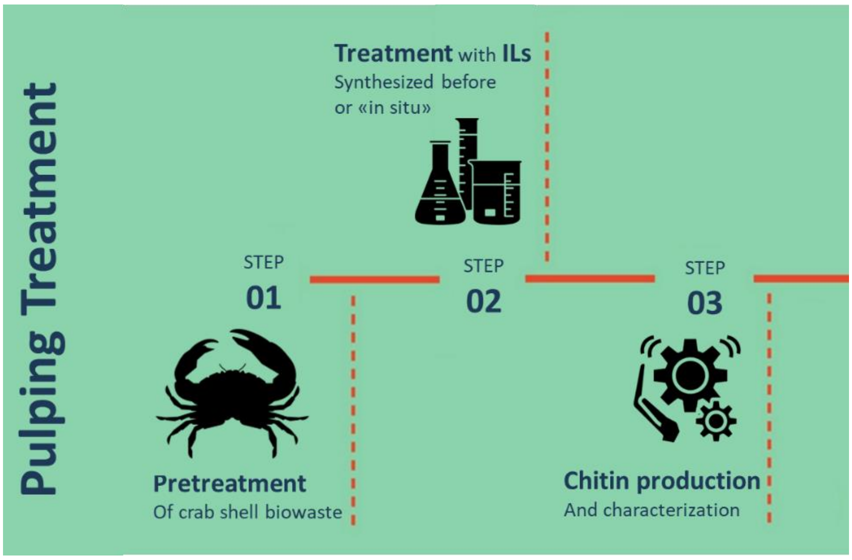

The investigation about the possibility to obtain valuable biopolymers from fishery waste continued then with a study on the valorisation of crab shell for the production of chitin. In particular, a sustainable pathway using ionic liquids was developed in contrast with the classical chemical extraction. The results of this study are the object of a manuscript that is currently under preparation and its submission for publication is expected by the end of this year.

We herein report a study on the valorisation of fishery waste biomass to obtain chitin with a sustainable and green approach using ionic liquids (ILs). In particular, attention was focused on the development of a pulping protocol of chitin from Spider Crab (Maja squinado) carapace, with a "waste to wealth" idea to obtain chitin as high added-value product. The key step of this work was the improvement of a one-step pulping procedure using ILs as opposed to the traditional chemical extraction which involves two steps using strong and hazardous acids and bases. The one-pot pulping method was investigated, using simple, readily available ILs such as ammonium acetate, ammonium formate and hydroxylammonium acetate. Each reaction was performed both using the neat IL as solid salt or by synthesizing it in situ as an aqueous solution. The as obtained chitin was fully characterized to define the acetylation degree, purity, molecular weight and dispersity. All characterization data confirm that in the conditions tested, ammonium formate prepared in situ seems to be the most promising IL for one-pot chitin pulping process, allowing quantitative isolation, high purity and a high degree of acetylation (DA > 90%).

4.3.1 Introduction

Chitin was first reported in 1811 by Henri Braconnot, who carried out some reactions on raw material isolated from different species of fungi, under the name of "fungine".[179] After cellulose, chitin (poly β-(1-4)-N-acetyl-D-glucosamine) is the second most abundant polysaccharide in nature.[180,181] In chitin, the degree of acetylation (DA), defined as the molar fraction of acetylated units in the polymer, varies typically between 0.80 and 0.95 depending on the source,[182] indicating the presence of a certain degree of free amino groups (**Figure 4.3.1**). [183]

Chitosan is known as the partially deacetylated derivative of chitin, and different definitions are available in literature. Most sources mention a deacetylation degree (DD), representing molar fraction of de-N-acetylated units in the polymer, of at least 50%[184] as a criterion for defining the molecule as chitosan (in other studies this threshold is at least 60-75%[185]).

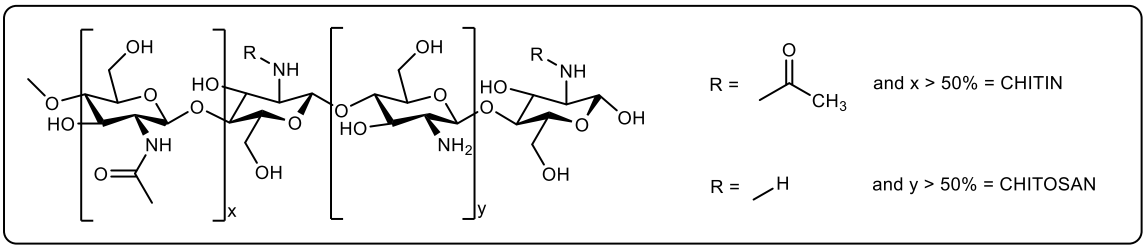

Figure 4.3.1. Repeating residues for chitin and chitosan. Chitin is composed predominantly of N-acetyl glucosamine (GlcNAc, x) units; Chitosan is mainly composed of glucosamine (GlcN, y) units.

Marine organisms are the principal source of chitin that constitutes the exoskeleton of arthropods (crab, lobsters and shrimps) and the endoskeleton of mollusks.[186] In addition, it is produced by several other living organisms in the lower plant and animal kingdoms, serving as a reinforcing and support constituent.[187] Arthropods are, in any case, the first source for chitin production (2.8 × 10^{12} kg/year for freshwater ecosystems and 1.3 × 10^{12} kg/year for marine ones[188]).

In living systems chitin chains aggregate to form microfibrils that are cross-linked with sugars, proteins, glycoproteins and proteoglycans. In insects and other invertebrates, chitin is always associated with specific proteins, with both covalent and noncovalent bonding, to produce ordered structures (**Figure 4.3.2**).

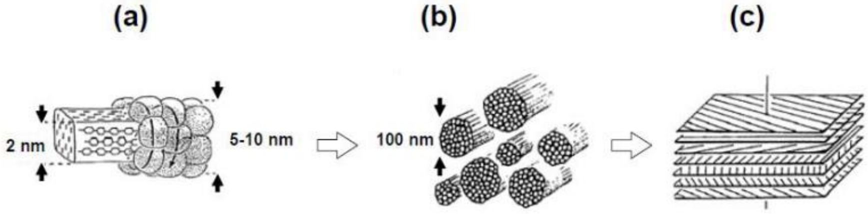

Figure 4.3.2. Hierarchical levels in the chitin-protein matrix in crustacean cuticles. (a) chitin crystals surrounded by proteins. (b) Chitin-protein fibrils. (c) Schematic representation of fibrils lying horizontal and parallel in successive planes.

Chitin exists in three polymorphic forms: α-, β-, and γ-chitin (**Figure 4.3.3**).[189] The most common form, α-chitin, derives from crustaceans and it is tightly compacted, characterized by a crystalline orthorhombic form where the chains are arranged in an antiparallel conformation, allowing maximum hydrogen bonding.[181] β-chitin is associated with proteins in squid pens[190] or in tubes of pogonophoran worms[191] and has a monoclinic form with a parallel disposition of the chains. Compared to the α- and β- chitins, γ-chitin is less common: it is considered a mixture (or an intermediate) of the two other forms,[192] where the chains are randomly arranged in parallel and antiparallel directions.

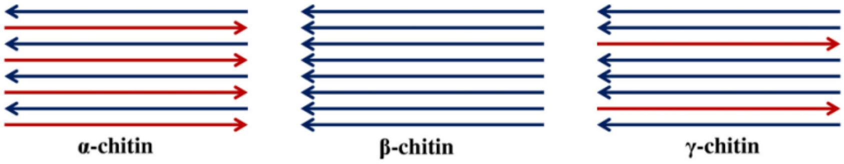

Figure 4.3.3. Polymorphic forms of chitin and relative disposition of chains.

In α- and β-chitin, the polymer chains are organized in sheets held together by a strong network of intermolecular hydrogen bonds[187] between the amide groups (C(2_1)NH···O=C(7_3)) approximately parallel to the a-axis (**Figure 4.3.4 d**). In α-chitin, each chain also has a C(3')OH···OC(5) intramolecular hydrogen bond along the c-axis (**Figure 4.3.4 a**), like the one present in cellulose. On different chains the CH_2OH group can then form hydrogen bonds in two different ways. On one hand these groups can bond with the oxygen of the amidic group of the adjacent monomer C(6_1')OH···O=C(7_1) (**Figure 4.3.4 b**). On the other hand, they can build a hydrogen bond with the CH_2OH group of the adjacent chain C(6_1')O···HOC(6_2)

approximately along b-c diagonal (**Figure 4.3.4 c**). The results indicate that a 50/50 statistical mixture of CH_2OH orientations is present, equivalent to half oxygens on each residue, forming inter-and intramolecular hydrogen bonds.[193] β-Chitin is more prone to intra-crystalline swelling compared to α-chitin due to the fewer hydrogen bonds.

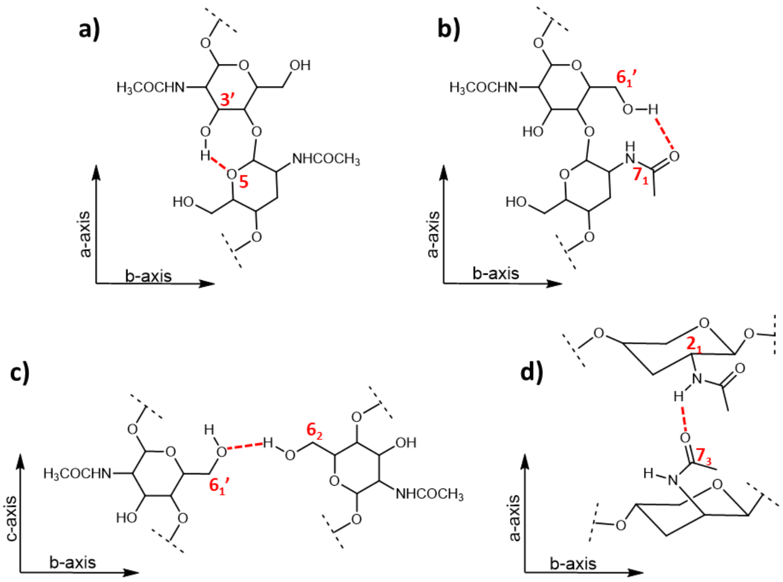

Figure 4.3.4. Modes of hydrogen bonding in α-chitin: (a) intrachain $C(3')\text{-}OH\cdots OC(5)$ bond; (b) intrachain $C(6'_1)OH\cdots O=C(7_1)$ bond; (c) interchain $C(6'_1)O\cdots HOC(6_2)$ bond; (d) interchain $C(2_1)NH\cdots O=C(7_3)$ bond.

The evolution of marine organisms that rely on chitin as a structural material determines the structural properties of this polymer, foremost water insolubility. Due to the high crystallinity and the strong intermolecular hydrogen bonding, chitin is in fact insoluble in water, dilute acidic and basic solutions and many common organic solvents. Indeed, despite its abundance, low cost and availability, its poor solubility still limits product development and market access in large volumes. In addition, batch-to-batch variability, non-precise characterization, and randomly distributed acetyl groups can result in bad reproducibility of chitin solubility. Even if some solvent systems have been proposed, these solvents are usually toxic, volatile, corrosive, or degradative (e.g. LiCl/dimethylacetamide, hexafluoroisopropyl alcohol, hexafluoroacetone sesquihydrate, trichloroacetic acid).[194] For this reason, the transformation of chitin into more soluble derivatives became an attractive topic. Various chemical modifications that can disrupt inter- and intra-molecular hydrogen bonds without glycosidic linkages cleavage are effective in making chitin soluble in water or other solvents. The most straightforward modification is the N-deacetylation to transforms chitin to chitosan[195] via alkaline treatment (**Scheme 4.3.1**). In any case, charge density, pH, DD, and the distribution of acetylated monomers in chitosan strongly influence its solubility and different reaction parameters (chitin source, time, temperature, alkali concentration) strongly affect the characteristic of the final product (MW and DD).

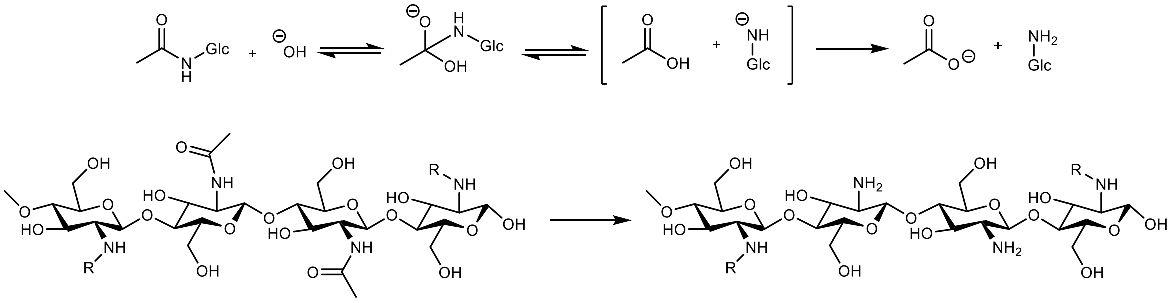

Scheme 4.3.1. Reaction mechanism of deacetylation promoted by strong alkali reagents (top) that convert chitin to chitosan (bottom). Glc-NH_2: glucosamine; R: amine or acetamide groups.

The laborious isolation process has led to a limited attention toward chitin and its derivatives in contrast to cellulose.[192] In addition, it has long been regarded just as a structural material without notable biological activities or functions while now its properties are becoming more and more studied and appreciated. Chitin and chitosan, indeed, are demonstrated to be cytocompatibile and biodegradable, to have analgesic and antimicrobial properties[196] but also to have antioxidant, anticholesterolemic and antitumoral activity. Due to these properties, these biopolymers, especially chitosan, have been exploited in many different applications such as in biomedicine, as food preservatives, as excipients in cosmetics, in antimicrobial packaging, and in biocatalysis.[185]

Conventional chemical chitin extraction. The process to isolate and purify chitin from biomass includes a series of consecutive steps: biomass pre-treatment, deproteinization (DP), demineralization (DM), decolouration and post-treatment processes. Depending on the biomass source and composition, the order of these steps may change, or some can even not be required. In addition, the DA, degree of crystallinity and MW of the final product may also vary with the source and be altered during the isolation process.[197] The pre-treatment process includes all the manipulation necessary to prepare the biomass sample for chitin extraction like the removal of soft tissues by scraping or boiling. The substrate is then dried and reduced in size. DM is generally performed by acid treatment using hydrochloric, nitric, sulphuric, acetic or formic acid. It is important to highlight that as the acidic conditions for DM become harsher, the molecular weight of the obtained product decreases.[198,199] Indeed, being chitin an acid-sensitive material, it can be degraded by several pathways: hydrolytic depolymerization, deacetylation, and heat degradation leading to a significant change of its physical properties(**Scheme 4.3.2**).[198]

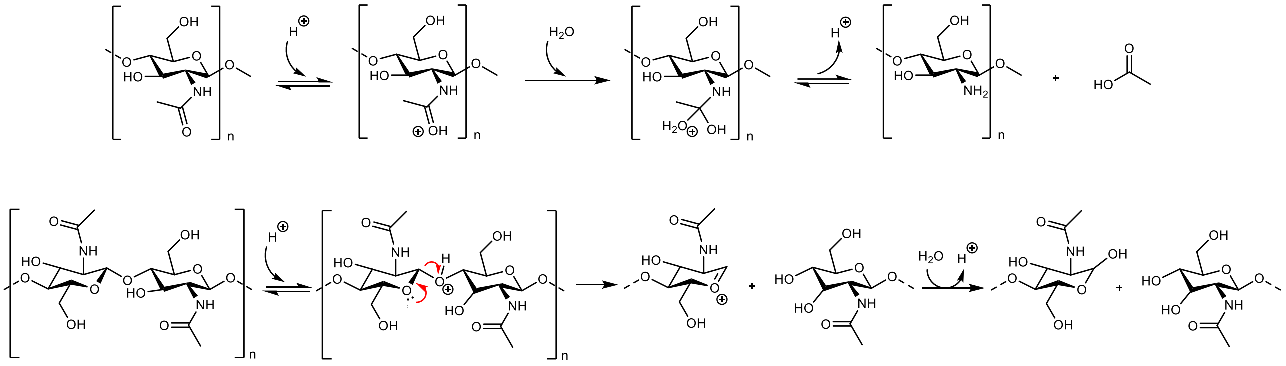

Scheme 4.3.2. Reaction mechanism of acid-catalysed deacetylation (top) and depolymerization (bottom).

The DP step, instead, is performed using alkali solutions, and the effectiveness depends on temperature, alkali concentration, and the solution/biomass ratio.[200] Typically, raw biomass is treated with approximately 1 M aqueous solutions of NaOH for 1-72 h at temperatures between 65 and 100 °C. When necessary, a decolouration step can be introduced to remove pigment traces using oxidizing agents.[201, 202] Some post-treatment steps, (neutralization, drying and milling) may be required at the end of the procedure. This extraction method is ecologically aggressive and energy-intensive[203] and it creates large amounts of wastewater[204]; anyway, it is still the most common procedure used on industrial and commercial scale.

Ionic Liquids chitin extraction. Given the peculiar properties of ILs, such as thermal stability, outstanding solvation potential and negligible vapour pressure, they constitute a potentially valid alternative to traditional volatile organic solvents and their use to isolate chitin from biomass has recently gained interest. In this context, chitin can be either "extracted" or "pulped" from a specific source. Extraction methods consist in complete or partial chitin dissolution in ILs, while in pulping methods minerals and proteins are removed from the biomass obtaining chitin in the solid state. Hydroxylammonium acetate and hydroxyethylammonium acetate have been reported for the isolation of chitin from shrimp shells with a > 80% purity, high DA and high degree of crystallinity.[205]

To overcome the disadvantages and problems associated with chemical extraction, in this work we studied a pulping method, where both the basic sites (responsible for DP) and the acidic ones (responsible for DM) are incorporated into a single IL, starting from spider crab shells as the starting material.

The Mediterranean spider crab (*Maja squinado)* (**Figure 4.3.5**) is one of the biggest crabs of European coasts spread from the north-eastern Atlantic to the Mediterranean Sea.[206] The total annual catches of spider crab ranged from a minimum of 5,168 tons registered in 2005 to a maximum of 6,982 in 2006[207] with France as main producer (more than 67% of the total catch in 2011). Spider crab is characterized by a reddish-brown to yellowish-brown carapace with an average length of 13 cm and a width of 18 cm, though it can reach a maximum length of 25 cm.[208]

Figure 4.3.5. Photograph of Maja squinado species.

The main components of crustacean shells are proteins (30-40%), minerals (30-50%), chitin (13-42%) and other minor components such as lipids, pigments and other metal salts (percentages refer to dry weight and depend on species and season). The chemical composition of spider crab's carapace has been scarcely investigated and, to our knowledge, only Pires and co-workers[209] in 2017 reported its chemical composition (16% of chitin, 19-20% of proteins, 62.9% of ashes and <3% of carotenoids). The remaining part is constituted by lipids, trace elements (rubidium, iron, copper, zinc and bromine) and contaminants (cadmium, arsenic and lead). Spider crab was chosen as it is widely available, possesses a high content of chitin, and because its tenacity and resistance to processing provides a benchmark for chitin extraction.

In this chapter, spider crab shells are exploited as starting material to extract chitin using an innovative pulping process with ILs (ammonium acetate, ammonium formate and hydroxylammonium acetate) (**Figure 4.3.6**).

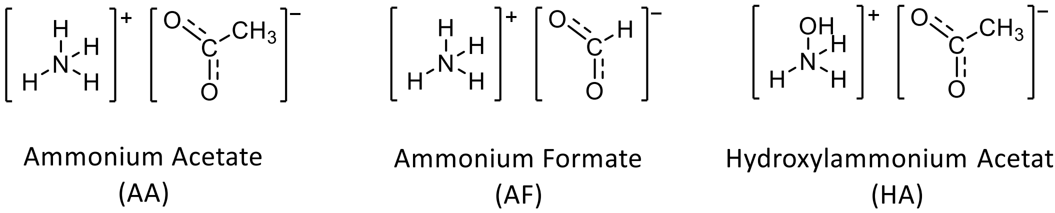

Figure 4.3.6. Structure of the ILs used for this study.

4.3.2 Results and discussion

Crab shells composition

To establish the chemical composition of our initial substrate, ash, chitin, and protein content have been evaluated (see Experimental section). The ash content, that is an approximate measure of the mineral content and other inorganic matter in the shells, was calculated with **Equation 4.3.1** where %ash is the mass percent of ashes, m_{ash} the final mass of ash and container (g), m_{cont} the mass of container (g), m_{ar} the initial mass of biomass sample and container (g).

$$\%\,ash = \frac{m_{ash} - m_{cont}}{m_{ar} - m_{cont}} \times 100$$

Equation 4.3.1. Equation for ash content determination.

Ash content value of 57.5 % was highlighted, confirming that inorganic matter is the major component of crab shells and underlining the importance of an effective DM to isolate chitin. Protein content was then evaluated by performing chemical deproteinization on crab shells.[200] Protein percentage was extrapolated using **Equation 4.3.2** where $m_{residue}$ is the total dry mass of residue free of proteins and $m_{biomass}$ refers to initial mass of dry shells. The amount of proteins resulted to be 21%.

$$\%\,proteins = 100 - \left(\frac{m_{residue}}{m_{biomass}} \times 100\right)$$

Equation 4.3.2. Equation for protein content determination.

Chitin percentage of 17 % was estimated by applying the conventional chemical extraction method to separate the totality of impurities from the starting material. To ensure the effectiveness of this method, the extract was further characterized by ^{1}H-NMR and FT-IR analysis (see Appendix). To perform a quantitative estimation of calcium salts content, with relation principally to calcium carbonate, Inductively Coupled Plasma Optical Emission Spectrometry (ICP-OES) analysis were performed. It has been highlighted that calcium salts are the major component of spider crab shells accounting for 51.50 wt% on dry basis. This result is also consistent with ash content analysis and shows that almost 90% of ash residue in the starting material is due to presence of calcium salts. Lipids, carotenoids and metal traces constitute only a minor fraction of the matrix. The results of our compositional study are summarized in the pie chart reported below (**Figure 4.3.7**). The results are in agreement with previous works, focused on spider crab shells of Maja Squinado species.[209]

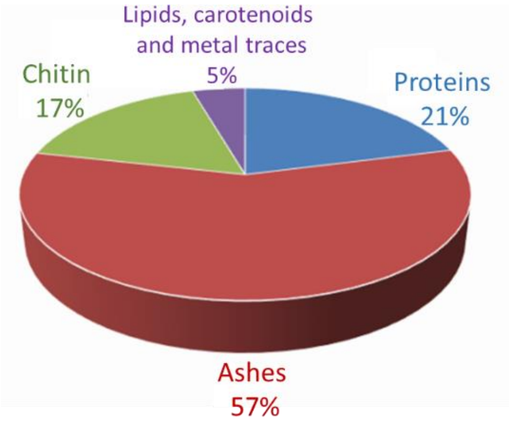

Figure 4.3.7. Pie chart representing all major components of spider crab.

Conventional chemical extraction

Chemical extraction was performed by adapting a procedure reported in literature (see Experimental section).[200] The biomass was subjected to subsequent acidic and basic treatments and after every step the product was washed until neutral pH and dried in a vacuum oven. Chitin was obtained as a white solid and its purity and DA were confirmed by ^{1}H-NMR and FT-IR analysis. A comparison with commercial chitin was performed. The two NMR spectra (see Appendix **Figure A.4.3.10** and **A.4.3.11**) presented all the characteristic signals, but the extracted sample resulted to be more prone to deacetylation under acidic treatment (necessary for complete dissolution of the sample). In fact, signals associated with acetic acid at 2.16 ppm and H-2 proton of de-N-acetylated units resulted to be more intense. DA values were calculated from the NMR spectra using **Equation 4.3.3** and **4.3.4** obtaining comparable results. DA% of 99% and 92% for commercial and extracted chitin respectively were obtained.

$$DA\% = \frac{\left(I_{\alpha H1A} + I_{\beta H1A+H1D} + I_{H1A}\right) - I_{H2D}}{I_{\alpha H1A} + I_{\beta H1A+H1D} + I_{H1A}} \, 100$$

Equation 4.3.3. Equation for DA% calculation based on the integrals of H-1 and H-2 signals.

$$DA\% = \frac{\frac{1}{3}A_{CH_3}}{\frac{1}{3}A_{CH_3} + A_{GlcN}} \, 100$$

Equation 4.3.4. Equation for DA% calculation based on the area of the H-2 of the GlcN units and of the acetyl protons of GlcNAc units.

The assignment of the resonances and their chemical shifts (ppm) are given in **Table 4.3.1**. **Figure 4.3.8** represent the model structures of dimeric N-acetyl glucosamine (GlcNAc) and glucosamine (GlcN).

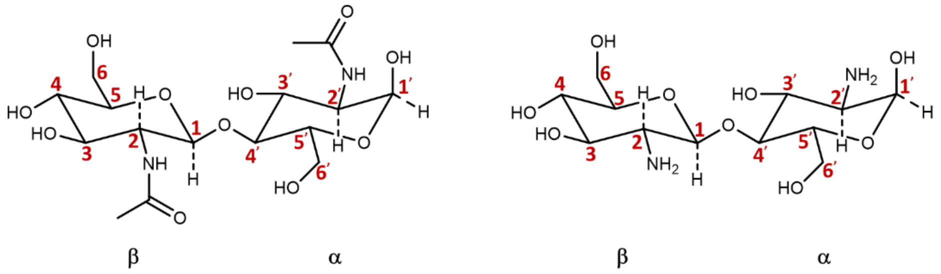

Figure 4.3.8. Chemical structure of N-acetyl glucosamine (GlcNAc, left) and glucosamine (GlcN, right).

Table 4.3.1. Assignments of resonances and relative chemical shifts of chitin signals.

	H-1	**H-1 of reducing ends**		**H-2**	**H-2/6**	**Acetyl-H**
GlcNAc	4.77	5.33 α	4.95 β	-	3.5-4.3	2.53
GlcN	4.98	5.55 α	5.11 β	3.33	3.5-4.3	2.53

Also from FT-IR analyses (see Appendix **Figure A.4.3.36** and **A.4.3.37**) it was possible to observe all the characteristic peaks both in the commercial and in the extracted chitin.

Pulping with ILs

Each pulping procedure was performed in two ways: using the neat IL as solid salt or synthesizing it *in situ*, by sequential addition of acid (acetic or formic) and base (ammonia or hydroxylamine) (A + B test) or vice versa (B + A test). In all cases, a 10 wt % loading of biomass was used with respect to total mass of solution (IL and biomass).[205] All the experiments were conducted at the same reaction time (2 h) but the temperatures varied with regard of the IL employed. Initial tests at 100°C were performed for all the experiments. However, Ammonium Acetate (AA) and Ammonium Formate (AF) have a melting point >

100°C and, for this reason, the experiments with the IL as solid salt were conducted at higher temperatures (145 and 130°C for AA and AF respectively). To have a better comparison, then also the A + B and B + A experiments were performed also at these temperatures, but no substantial differences were highlighted in terms of chitin yields (**Table 4.3.2**, entries 2-5 and 7-10). Experimental conditions and relative chitin yields are reported in **Table 4.3.2**. It must be noted that AA and AF were commercially available, while hydroxylammonium acetate (HA) has been synthesized[205] and fully characterized by NMR spectroscopy (see Appendix, **Figure A.4.3.29-32**).

Table 4.3.2. Experimental conditions tested. Reaction time always equal to 2h. A + B = sequential addition of acid and base, B + A = sequential addition of base and acid.

Entry	IL	IL form	Temperature (°C)	Chitin Yield (%)
1	AA	Solid salt	145	16.4
2		A + B	100	30.0
3			145	27.1
4		B + A	100	26.5
5			145	22.9
6	AF	Solid salt	130	20.3
7		A + B	100	17.2
8			130	17.2
9		B + A	100	17.6
10			130	18.8
11	HA	Solid salt	100	29.3
12		A + B	100	19.9
13		B + A	100	20.7

From the calculation of yields, it was noticed that, in some cases, the values resulted to be higher than the theoretical chitin content in crab shells (17%). This can be already a signal of the incomplete DM or DP of the starting biomass. To further confirm the purity of the pulped chitin, the samples have been characterized by TGA, NMR, ICP-OES and FT-IR spectroscopy.

Concerning the TGA analyses (Appendix, **Figures A.4.3.1-9**) it can be generally stated that two main weight losses were observed in all samples. The first one, between 40-100°C circa, account for the 8-9%, due to the evaporation of water molecules bound to chitin chains and the other one, between 345-415°C (42-69 wt%) probably caused by decomposition/depolymerization of the material through deacetylation and cleavage of glycosidic linkages. In addition, at higher temperature (415-670 °C) a progressive weight-loss can be observed probably due to the thermal destruction of pyranose ring and the decomposition of the residual carbon. In some cases, a third and clearly visible weight loss imputable to the release of CO_2 due to the presence of calcium carbonate residues was observed, indicative of an incomplete DM step. In particular, the occurrence of $CaCO_3$ was highlighted in the sample obtained using AA *in situ* (both A + B and B + A at 100 °C), using AF as solid salt and in all tests performed using HA. This evidence led us to the conclusion that acetic acid, responsible for the DM in AA and HA, is too week to have complete removal of minerals when working at 100°C. When using AF, instead, only the solid salt IL resulted to be inefficient for DM: this may be due to the minor viscosity of aqueous reagents that allows better penetration of chemicals in chitin chains domain.

The actual presence of calcium salts has been then confirmed by ICP-OES analyses (**Table 4.3.3**).

Table 4.3.3. ICP-OES results for chitin pulped with IL solid salt or formed in situ.

Entry	IL	IL form	Temperature (°C)	Ca (%)	$CaCO_3$ (%) [a]	$CaCO_3$ from TGA (%) [b]	Other Ca salts (%) [c]
1	AA	Solid salt	145	1.69	4.20	0	4.20
2		A + B	100	13.07	32.70	14.26	18.44
3		B + A	100	7.44	18.60	9.42	9.18
4	AF	Solid salt	130	4.34	10.85	5.78	5.07
5		A + B	100	0.42	1.05	0	1.05
6		B + A	100	0.48	1.20	0	1.20
7	HA	Solid salt	100	14.84	37.10	10.20	26.90
8		A + B	100	7.11	17.80	7.13	10.67
9		B + A	100	9.78	24.45	6.45	18.00

a) calculated with the hypothesis that all calcium is in form of carbonate salt; b) calcium carbonate content from TGA analysis; c) obtained from subtraction of the two previous values (a-b).

ICP-OES analyses highlighted the presence of calcium salts in high percentages in samples obtained with *in situ* preparation of AA at 100°C (32.7% for A + B sample **Table 4.3.3**, entry 2 and 18.60% for B + A sample **Table 4.3.3**, entry 2), probably underlining the major efficiency of higher temperatures (145°C) when using this IL. For AF, instead, when using the *in situ* preparation (**Table 4.3.3**, entries 5 and 6), lower amount of calcium salts were detected (also the experiments with the solid salt at 130°C revealed low percentages **Table 4.3.3** entry 4). All the experiments carried out using HA, on the other hand showed high amounts of residual minerals: IL prepared *in situ* resulted to be more efficient in DM, as for AF, but, in this case, also the order of addition of acid and base seems to play a crucial role. This is probably due to the fact that previous treatment with acetic acid accomplishes partial DM facilitating the DP step performed by aqueous hydroxylamine. However, if it was the case, it is not clear why this phenomenon was observed only with this IL.

From ^{1}H-NMR spectra (Appendix, **Figures A.4.3.10-35**), chitin structure and relative signals are clearly present in all samples. Furthermore, between 1.0 and 1.5 ppm the resonances of methyl-proton from proteins are always visible, although in small quantity. To verify that the resonances between 1.0 – 1.5 ppm were really ascribable to proteins, chemical deproteinization was performed on a representative pulped chitin sample, in which signals between 1.0-1.5 ppm were clearly evident. NMR spectra of pulped chitin before and after DP were registered, and the results are reported in **Figure 4.3.9**. NMR results confirm that the signals under discussion are unambiguously attributable to methyl protons of proteins, and that harsh DP conditions are efficient for their removal. We can conclude that all the studied procedure were not able to perform complete DP, probably because of the limited basicity of the IL in respect to the traditional bases used in the chemical extraction.

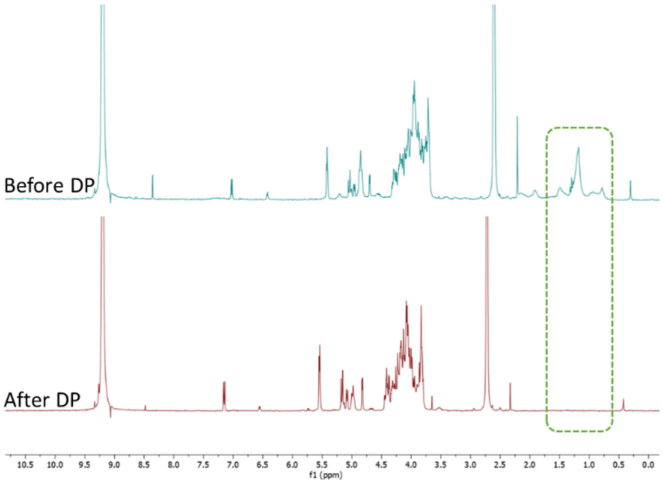

Figure 4.3.9. ^{1}H NMR spectra of a representative sample of pulped chitin before (top, blue) and after (bottom, red) chemical deproteinization.

From NMR spectra, and using both **Equation 4.3.3** and **4.3.4**, DA were calculated, and the two methods resulted to be in good agreement (**Table 4.3.4**). Partial deacetylation occurred during dissolution of all samples in the deuterated solvent causing an increase of the signals related to acetic acid and H-2 proton of de-N-acetylated chitin. This was taken into account in all calculation methods in order to avoid underestimation of DA. Concerning AA and AF, good DA values, higher than 88% and 86% for AA and AF respectively, were always found. With HA values always > 92% were calculated (**Table 4.3.4**, entry 11-13).

Table 4.3.4. DA of all pulped samples.

Entry	IL	IL form	Temperature (°C)	DA (%) from eq 4.3.3	DA (%) from eq 4.3.4
1	AA	Solid salt	145	99	99
2		A + B	100	88	93
3			145	96	92
4		B + A	100	97	97
5			145	98	99
6	AF	Solid salt	130	94	95
7		A + B	100	97	96
8			130	95	96
9		B + A	100	94	95
10			130	86	90
11	HA	Solid salt	100	98	98
12		A + B	100	96	97
13		B + A	100	93	94

FT-IR spectra of all samples (see Appendix, **Figure A.4.3.36-53**) showed the characteristic signals associated with chitin and are comparable to commercial sample. The presence of calcium carbonate (1420-30 cm^{-1} and 874 cm^{-1}) was further confirmed in the samples prepared with AA *in situ* at 100°C and with HA. Once again it was confirmed that the best IL, in term of minerals removal was AF.

A comparison of all the conditions, yields, calcium carbonate percentages and DA is reported in **Table 4.3.5**.

Table 4.3.5. Experimental results obtained with all pulping methods tested in this work.

Entry	IL	IL form	Temperature (°C)	Yield (%)	$CaCO_3$ (%)	DA (%)[a]
1	AA	Solid salt	145	16.4	0	99.0
2		A + B	100	30.0	14.26	91.0
3			145	27.1	-	94.0
4		B + A	100	26.5	9.42	97.0
5			145	22.9	-	98.5
6	AF	Solid salt	130	20.3	5.78	94.5
7		A + B	100	17.2	0	96.5
8			130	17.2	-	95.5
9		B + A	100	17.6	0	94.5
10			130	18.8	-	88.0
11	HA	Solid salt	100	29.3	10.20	98.0
12		A + B	100	19.9	7.13	96.5
13		B + A	100	20.7	6.45	93.5

a) DA are reported as average between the two values obtained with **Equations 4.3.3** and **4.3.4**.

In all samples pulped chitins contained a small amount of protein residues, indicating that further optimization is possible to obtain a purer biopolymer. Concerning the DM step, $CaCO_3$ was completely removed using AA as a solid salt and AF prepared *in situ* by sequential addition of acid and base or vice versa. Although AA was employed in the solid form, easy to handle and ready to use, higher reaction temperature of 145 °C was employed, which could cause more extensive depolymerization of the final product (resulting in lower MW). To minimize costs of pulping process and reduce energy demand, AF formed *in situ* seems to be a promising choice. Concerning DA values extrapolated from ^{1}H-NMR analysis, all methods proposed produced chitin with high DA in the range 88-99%.

Since AF was found to give best performances, further analysis on the chitin obtained using this IL have been performed. In **Figure 4.3.10**, a comparison between the XRD diffractograms is reported. To determine the actual degree of crystallinity, a quantitative X-ray phase analysis was performed. The background signal was subtracted and the diffractogram corrected. Crystalline and amorphous domain areas were properly deconvoluted and separated to provide CI with good accuracies. Results showed that commercial chitin sample possess the higher CI (56.5%) while chitin pulped with the solid salt or by sequential addition of formic acid followed by ammonia (A + B) had comparable CI (39.3 and 38.9 % respectively). When treating crab shells starting with ammonia followed by formic acid (B + A) the resulting material had slightly higher CI, equal to 46.0 %.

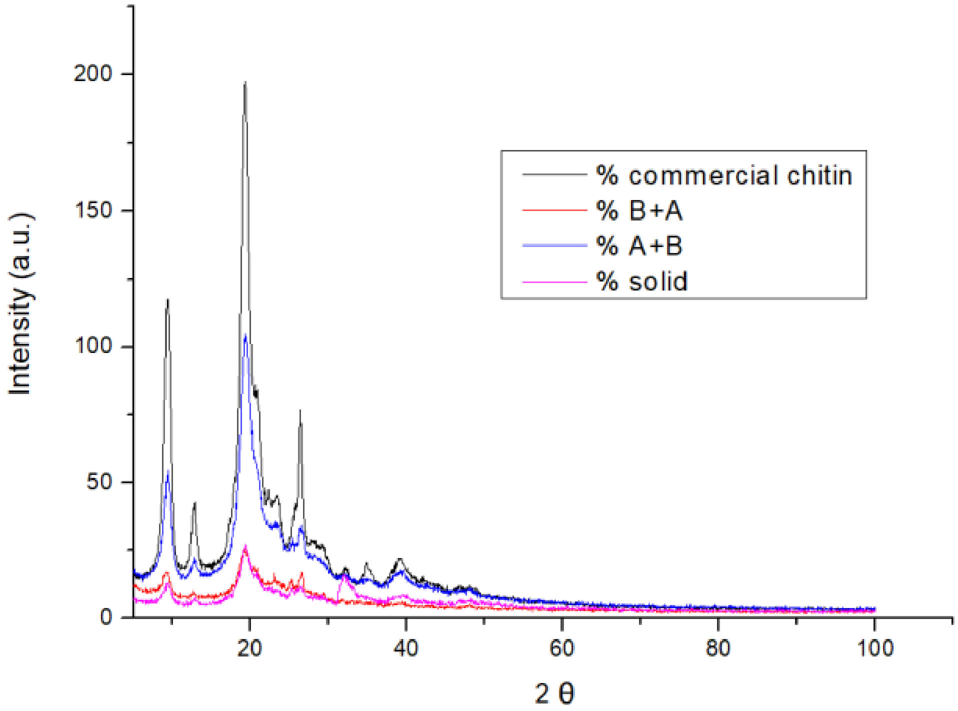

Figure 4.3.10. XRD diffractograms of commercial (black) and AF pulped chitin. AF was used in the form of solid salt (pink) or formed in situ by sequential addition of acid and base (blue) and base and acid (red) at 100 °C.

To evaluate the MW distribution of chitin by GPC avoiding the use of hazardous and toxic solvent systems required to dissolve it, we decided to carry out an indirect measurement on the more soluble chitin derivative, chitosan. Thus, chitin samples pulped with AF were further deacetylated to chitosan under heterogeneous conditions (see Experimental section). Samplings were performed at different reaction times. For each sample GPC measurements were executed: experimental results concerning MW distribution and dispersity are summarized in **Figure 4.3.11** and **Table 4.3.6**. At the beginning of the reaction shorter chains of chitin are deacetylated more efficiently and the resulting chitosan dissolves in the eluent phase, bringing to small MW and Đ. After 30 minutes, higher MW chitosan is formed, with lower Đ. It is clear that during the first hour of the reaction, deacetylation occurred rapidly, bringing to soluble chitosan samples. After the first hour, depolymerization occurred, competing with deacetylation mechanism. This fact could be deduced by the progressive decrease in MW distribution of samples and higher Đ. After two hours treatment, MW distribution levels off, and MW values between 2-3 hours are very similar.

Table 4.3.6. Values of M_p, M_n, M_w and Đ obtained from GPC analysis of chitosan samples.

Entry	Time (h)	Mp E+04 (Da)	Mn E+04 (Da)	Mw E+05 (Da)	Đ
1	0.1	3.78 E+01	3.78	1.77	4.7
2	0.5	1.05	5.73	2.47	4.3
3	1	8.16	2.81	2.45	8.7
4	2	8.88	2.61	1.89	7.2
5	3	8.16	2.41	1.89	7.8

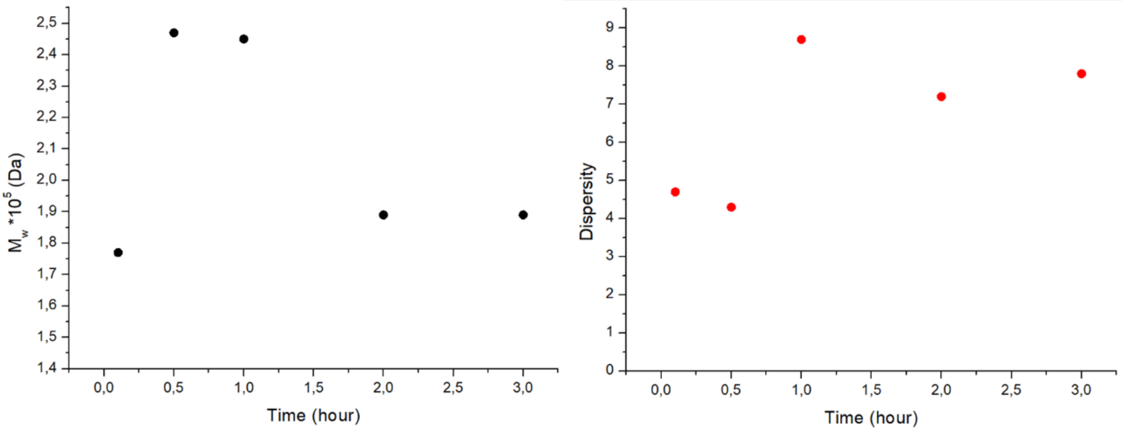

Figure 4.3.11. Molecular weight (left) and dispersity (right) trend of chitosan during deacetylation time.

4.3.3 Conclusions, challenges and perspectives

In this study, we evaluated the efficiency of three different ILs (ammonium acetate, ammonium formate and hydroxylammonium acetate) for chitin pulping from spider crab shells, as an alternative and green method to conventional chemical extraction procedures. Firstly, the chemical composition of spider crab shells was determined revealing 57% of ashes, 21% of proteins, 17% of chitin and a remaining 5% of lipids, metals and pigments. Pulping procedures with ILs were then performed in two ways: by using the neat IL as solid salt (with temperatures above its melting point) or by synthesizing it *in situ* as an aqueous solution. All characterization data confirm that in the conditions tested, ammonium formate prepared *in situ* seems to be the most promising IL for chitin one-pot pulping process, allowing the quantitative isolation (17-18% yields) of chitin with high purity and a high degree of acetylation (DA > 86%). TGA and ICP-OES analyses confirmed that all calcium minerals were efficiently removed. However, all ^{1}H-NMR spectra showed signals associated with methyl protons of proteins between 1.0 and 1.5 ppm, demonstrating that in these conditions, proteins were still present. In alternative, to assess pulping efficiency of all ILs, other parameter such reaction time and biomass/solution ratio should be tested. Furthermore, it must be highlighted the fact that in all procedure great amount of wastewaters were generated during washing step of the pulped material. Further studies could be aimed at eliminating residual proteins and to minimize water consumption in order to improve process intensification and ensure eco-sustainability. In any case these procedures eliminate one washing step, combining DM and DP steps. Due to the low solubility of chitin in almost all common organic solvents and water, the characterization of the product resulted to be very challenging. To evaluate purity and DA of chitin samples, ^{1}H-NMR has been extensively used in literature and was chosen in this work. However, the strong acidic conditions required for sample dissolution caused in all cases competitive deacetylation and depolymerization, making interpretation and signal identification elaborate. It was also noted that the same treatment used for dissolution, caused different polymer degradations depending on the sample treated. From XRD analysis it was possible to notice that the addition order of reactants played a crucial role in the crystallinity of the sample: higher

CI were obtained for samples treated with the *in situ* formed IL by sequential addition of base and then acid.

In conclusion we proposed a preliminary study on the use of innovative and simple ILs for one-pot chitin pulping. The IL can be used neat or made *in situ* by the sequential addition of acid and base. Though pulping with ammonium formate is the more promising procedure, the varying production costs, applicability on different fishing waste-derived substrates and safety issues are still unknown. This work presents a step toward narrowing the choices for chitin isolation technologies that can lead to an economically and environmentally sustainable process replacing the current hazardous, energy consuming, and environmentally unsafe process.

4.3.4 Experimental

Ash content. Ash content was determined using the Standard Test Method for Ash in Biomass E1755-01. For this purpose, 1.0 g of dried crab shells were placed in a porcelain crucible and put in a muffle furnace at 600°C for 3 h. The crucible was then removed, set in a desiccator, and allowed to cool to room temperature. The system was weighted to the nearest 0.1 mg. After weighting, the crucible was inserted again into the furnace for 1 h at 600°C, cooled in the desiccator, and reweighed. This last step was repeated until the mass of the crucible varied by less than 0.3 mg from the previous weighing. The procedure was performed in duplicate, and a mean-value calculation determined ash content.

Protein content. Protein content was determined by chemical deproteinization of crab shells. 0.5 g of ground spider crab shells were suspended in aqueous NaOH (1 M; 20 mL/g of solid), at 70 °C for 3 hours under continuous stirring. The solid product was centrifuged (6000 rpm for 10 minutes), washed with water (5 × 50 mL) until neutral pH, and dried in oven under reduced pressure (15 mbar) overnight. Protein percentage with respect to crude shell dry weight was then calculated.

Synthesis of hydroxylammonium acetate. Hydroxylammonium acetate was prepared according to a reported procedure.[205] Hydroxylamine solution 50 wt% (26.4 g, 0.4 mol) was stirred at 0 °C in a 250 mL round-bottomed flask while acetic acid (26.4 g, 0.44 mol) was added dropwise over three hours. The solution was then allowed to reach room temperature under continuous stirring. The mixture was then gently purged with air and heated at 40 °C to concentrate the solution. The precipitate was washed with methanol (100 mL) and diethyl ether (100 mL) to remove residual acetic acid and dried in oven under reduced pressure (15 mbar) for 2 h. The final product was obtained as a white solid (11.9 g, yield 32%) and was characterized by NMR spectroscopy (^{1}H and ^{13}C in DMSO-d_6 or D_2O). Characterization data are reported in the Appendix.

Chemical extraction protocol. In a typical procedure, a powdered sample (1 g) of spider crab shells was suspended in aqueous HCl (0.5 M; 40 mL/g of waste) and stirred at room temperature for 15 min. The residual solid was centrifuged (6000 rpm for 10 min), water was added (5 × 50 mL) to neutral pH, and the resulting solid was dried in oven under reduced pressure (15 mbar) overnight. The demineralized powder was then suspended in aqueous NaOH (1 M; 20 mL/g of solid), at 70 °C for 3 hours under continuous stirring. The solid product was centrifuged (6000 rpm for 10 minutes), washed with water (5 × 50 mL) until neutral pH, and dried in oven under reduced pressure (15 mbar) overnight. The final product was obtained as a white solid (0.169 g, yield 17%).

Pulping of crab shells using IL as solid salt. Ground crab shells (0.5 g) were mixed with solid IL (4.5 g) in a round-bottom flask equipped with a condenser. The solution was kept under magnetic stirring for 2 h at the chosen temperature (145°C for AA, 130°C for AF and 100 °C for HA). After complete melting of the IL, a vigorous bubbling/foaming could be observed. A yellowish solid precipitate after 2 h, while impurities were confined in the aqueous phase. The mixture was diluted with 50 mL of DI water and centrifuged. The solid was washed with water (5 × 50 mL) until neutral pH was reached and dried in oven under reduced pressure (15 mbar) overnight. The final product was obtained as a yellow-white solid.

Pulping of crab shells using IL prepared in situ at 100°C. 0.5 g of ground crab shells were put in a two-necked round-bottom flask equipped with a condenser. The acidic function (acetic or formic acid) was added, followed by dropwise addition of aqueous basic solution (ammonia or hydroxylamine). The solution was kept under stirring for 2 hours at 100 °C. Purification and isolation was performed as described in the pulping with solid salt. The same procedure was repeated by changing the addition order of reactants (first the base, then the acid). Used quantities are reported in **Table 4.3.7**.

Pulping of crab shells using IL prepared in situ at T>100°C. 0.5 g of ground crab shells were put in a two-necked round-bottom flask equipped with a condenser. The acidic function (acetic or formic acid) was added, followed by dropwise addition of aqueous ammonia solution over several minutes. The solution was kept under magnetic stirring for ca. 0.5 h at ambient temperature until foaming and bubbling occurred. The mixture was then placed in a stainless-steel autoclave equipped with a Teflon reactor and kept under magnetic stirring for 2 h at the desired temperature (145° C with AA and 130 °C for AF). The autoclave was then allowed to cool to room temperature. Purification and isolation were performed as described in the pulping with solid salt. The same procedure was repeated by changing the addition order of reactants (first the base, then the acid). Used quantities are reported in **Table 4.3.7**.

Table 4.3.7. Quantity of acidic and basic function used for chitin pulping with *in situ* formation of the IL.

	Acid		**Base**	
	g	**mol**	**g**	**mol**
AA	3.6	0.06	3.9	0.06
AF	3.4	0.07	3.9	0.06
HA	2.9	0.05	3.2	0.05

Deacetylation of chitin. Deacetylation under heterogeneous conditions was performed according to a reported procedure.[210] Crab shells were put in a two-neck bottom flask together with 70% (w/v) NaOH aqueous solution in a solid:alkali ratio of 1:10. The flask was put under nitrogen atmosphere and stirred at 110°C for 3h. The precipitate was washed with milliQ water (4 x 50 ml) until neutral pH and filtered.

^{1}H-NMR and ^{13}C-NMR. Chitin samples were dissolved in a deuterium chloride solution (DCl 35 wt % in D_2O) with vigorous stirring for 30 min at 50 °C. ^{1}H-NMR spectra were obtained using a Bruker UltraShield 300 operating at 300 MHz at ambient temperature. Chitin signals: ^{1}H NMR (300 MHz, DCl 35% in D_2O, 298 K) δ (ppm): 6.94 (d, H-1*, 5.33 (br, α-H1A), 4.95-4.98 (br, β-H1A + H1D), 4.87-4.88 (d, H-2*), 4.77 (br, H1A), 4.61 (d, H-3*), 3.5-4.3 (m, H2/H6), 2.53 (s, H-Acetyl), 2.13 (s, H-acetic acid). Signals denoted with an asterisk refers to glucofuranosyl oxazolinium ion existing in equilibrium with GlcNAc in concentrated DCl.

Fourier-transform infrared spectroscopy (FT-IR). The samples for FT-IR analysis were prepared by grinding the dry blended powders with powdered KBr (ratio of 1:100 Sample: KBr) and then compressed to form pellets of 5 mm-diameter using a hydraulic press at a pressure of 10 tons for one minute. Spectra were recorded on a Perkin-Elmer Spectrum One FT-IR spectrometer from 4000 to 450 cm^{-1}.

Thermogravimetric Analysis. TGA were carried out in a TA instruments SDT 2960. About 5 mg of all samples were placed in aluminium crucible and heated from ambient temperature to 800 °C with a heating rate of 10 °C/min under a nitrogen atmosphere (flow rate 1 mL/min).

Inductively Coupled Plasma Optical Emission Spectrometry. ICP-OES measurements were performed on a Perkin Elmer ICP-OES 5300 DV. All chitin samples were digested in nitric acid (3 mL) and hydrochloric acid (2 mL), dilute to 10 mL of final volume, and heated at 150 °C for 20 minutes to ensure complete dissolution.

X-Ray Diffraction. XRD measurements were performed employing a Philips diffractometer with a PW 1319 goniometer with Bragg-Brentano geometry, equipped with a focusing graphite monochromator and a proportional counter with a pulse-height discriminator. Nickel-filtered CuKα radiation and a step-by-step technique were employed (steps of 0.05° in 2θ), with a collection time of 30 s per step.

Gel Permeation Chromatography. GPC was performed using an Agilent Infinity 1260 GPC instrument equipped with a viscosimetric and a refractometric detectors using an injection volume of 100 μL and a flow rate of 0.5 mL/min. A Polysep-GFC-P linear column (1 kDa-10 MDa) was used maintaining a constant temperature of 5°C during the analysis. An aqueous solution of acetic acid (0.3M) and sodium acetate (0.2M) was used as eluent and PEO/PEG standards with sample weights of 601–1020000 Da were used for the calibration. Prior to analysis 2 mg of chitosan samples were dilute in 1 mL of eluent phase, and the solution was filtered.

4.4 Bibliography

(1) Vijayendra, S. V. N.; Shamala, T. R. Film Forming Microbial Biopolymers for Commercial Applications-A Review. *Crit. Rev. Biotechnol.* **2014**, *34* (4), 338–357. https://doi.org/10.3109/07388551.2013.798254.

(2) Onar, N. Usage of Biopolymers In Medical Applications In:3rd Indo-Czech Textile Conference, Istanbul, Turkey. **2004**.

(3) Jariyasakoolroj, P.; Leelaphiwat, P.; Harnkarnsujarit, N. Advances in Research and Development of Bioplastic for Food Packaging. *J. Sci. Food Agric.* **2020**, *100* (14), 5032–5045. https://doi.org/10.1002/jsfa.9497.

(4) Ferrari, F.; Striani, R.; Minosi, S.; De Fazio, R.; Visconti, P.; Patrono, L.; Catarinucci, L.; Esposito Corcione, C.; Greco, A. An Innovative IoT-Oriented Prototype Platform for the Management and Valorisation of the Organic Fraction of Municipal Solid Waste. *J. Clean. Prod.* **2020**, *247*, 119618. https://doi.org/10.1016/j.jclepro.2019.119618.

(5) Lionetto, F.; Esposito Corcione, C. An Overview of the Sorption Studies of Contaminants on Poly(Ethylene Terephthalate) Microplastics in the Marine Environment. *J. Mar. Sci. Eng.* **2021**, *9* (4). https://doi.org/10.3390/jmse9040445.

(6) Wang, W.; Themelis, N. J.; Sun, K.; Bourtsalas, A. C.; Huang, Q.; Zhang, Y.; Wu, Z. Current Influence of China's Ban on Plastic Waste Imports. *Waste Dispos. Sustain. Energy* **2019**, *1* (1), 67–78. https://doi.org/10.1007/s42768-019-00005-z.

(7) Singh, N.; Hui, D.; Singh, R.; Ahuja, I. P. S.; Feo, L.; Fraternali, F. Recycling of Plastic Solid Waste: A State of Art Review and Future Applications. *Compos. Part B Eng.* **2017**, *115*, 409–422. https://doi.org/10.1016/j.compositesb.2016.09.013.

(8) Sigler, M. The Effects of Plastic Pollution on Aquatic Wildlife: Current Situations and Future Solutions. *Water. Air. Soil Pollut.* **2014**, *225* (11). https://doi.org/10.1007/s11270-014-2184-6.

(9) Verma, R.; Vinoda, K. S.; Papireddy, M.; Gowda, A. N. S. Toxic Pollutants from Plastic Waste- A Review. *Procedia Environ. Sci.* **2016**, *35*, 701–708. https://doi.org/10.1016/j.proenv.2016.07.069.

(10) Mishra, P. K.; Gautam, R. K.; Kumar, V.; Kakatkar, A. S.; Chatterjee, S. Synthesis of Biodegradable Films Using Gamma Irradiation from Fish Waste. *Waste and Biomass Valorization* **2021**, *12* (5), 2247–2257. https://doi.org/10.1007/s12649-020-01143-w.

(11) Lionetto, F.; Esposito Corcione, C. Recent Applications of Biopolymers Derived from Fish Industry Waste in Food Packaging. *Polymers.* **2021**, *13* (14). https://doi.org/10.3390/polym13142337.

(12) Wankhade, V. Animal-Derived Biopolymers in Food and Biomedical Technology. In *Biopolymer-Based Formulations: Biomedical and Food Applications*; Elsevier Inc., 2020; pp 139–152. https://doi.org/10.1016/B978-0-12-816897-4.00006-0.

(13) Silva-Weiss, A.; Bifani, V.; Ihl, M.; Sobral, P. J. A.; Gómez-Guillén, M. C. Structural Properties of Films and Rheology of Film-Forming Solutions Based on Chitosan and Chitosan-Starch Blend Enriched with Murta

Leaf Extract. *Food Hydrocoll.* **2013**, *31* (2), 458–466. https://doi.org/10.1016/j.foodhyd.2012.11.028.

(14) Sotelo, C. G.; Blanco, M.; Ramos, P.; Vázquez, J. A.; Perez-Martin, R. I. Sustainable Sources from Aquatic Organisms for Cosmeceuticals Ingredients. *Cosmetics* **2021**, *8* (2), 1–16. https://doi.org/10.3390/cosmetics8020048.

(15) Gautam, R. K.; Kakatkar, A. S.; Karani, M. N. Development of Protein-Based Biodegradable Films from Fish Processing Waste. *Int. J. Curr. Microbiol. Appl. Sci.* **2016**, *5* (8), 878–888. https://doi.org/10.20546/ijcmas.2016.508.099.

(16) Xu, C.; Nasrollahzadeh, M.; Selva, M.; Issaabadi, Z.; Luque, R. Waste-to-Wealth: Biowaste Valorization into Valuable Bio(Nano)Materials. *Chem. Soc. Rev.* **2019**, *48* (18), 4791–4822. https://doi.org/10.1039/c8cs00543e.

(17) Claverie, M.; McReynolds, C.; Petitpas, A.; Thomas, M.; Fernandes, S. C. M. Marine-Derived Polymeric Materials and Biomimetics: An Overview. *Polymers.* **2020**, *12* (5), 1002. https://doi.org/10.3390/POLYM12051002.

(18) Rostamzad, H.; Paighambari, S. Y.; Shabanpour, B.; Ojagh, S. M.; Mousavi, S. M. Improvement of Fish Protein Film with Nanoclay and Transglutaminase for Food Packaging. *Food Packag. Shelf Life* **2016**, *7*, 1–7. https://doi.org/10.1016/j.fpsl.2015.10.001.

(19) Araújo, C. S.; Rodrigues, A. M. C.; Peixoto Joele, M. R. S.; Araújo, E. A. F.; Lourenço, L. F. H. Optmizing Process Parameters to Obtain a Bioplastic Using Proteins from Fish Byproducts through the Response Surface Methodology. *Food Packag. Shelf Life* **2018**, *16*, 23–30. https://doi.org/10.1016/j.fpsl.2018.01.009.

(20) Chen, C.; Li, D.; Yano, H.; Abe, K. Insect Cuticle-Mimetic Hydrogels with High Mechanical Properties Achieved via the Combination of Chitin Nanofiber and Gelatin. *J. Agric. Food Chem.* **2019**, *67* (19), 5571–5578. https://doi.org/10.1021/acs.jafc.9b00984.

(21) MacKie, R. M. Effects of Ultraviolet Radiation on Human Health. *Radiat. Prot. Dosimetry* **2000**, *91* (1–3), 15–18. https://doi.org/10.1007/978-3-540-71414-9_3.

(22) Wang, S. Q.; Setlow, R.; Berwick, M.; Polsky, D.; Marghoob, A. A.; Kopf, A. W.; Bart, R. S. Ultraviolet A and Melanoma: A Review. *J. Am. Acad. Dermatol.* **2001**, *44* (5), 837–846. https://doi.org/10.1067/mjd.2001.114594.

(23) Li, S.; Toprak, M. S.; Jo, Y. S.; Dobson, J.; Kim, D. K.; Muhammed, M. Bulk Synthesis of Transparent and Homogeneous Polymeric Hybrid Materials with ZnO Quantum Dots and PMMA. *Adv. Mater.* **2007**, *19* (24), 4347–4352. https://doi.org/10.1002/adma.200700736.

(24) Koutchma, T. Advances in Ultraviolet Light Technology for Non-Thermal Processing of Liquid Foods. *Food Bioprocess Technol.* **2009**, *2* (2), 138–155. https://doi.org/10.1007/s11947-008-0178-3.

(25) de Moraes Crizel, T.; de Oliveira Rios, A.; D. Alves, V.; Bandarra, N.; Moldão-Martins, M.; Hickmann Flôres, S. Active Food Packaging Prepared with Chitosan and Olive Pomace. *Food Hydrocoll.* **2018**, *74*, 139–150. https://doi.org/10.1016/j.foodhyd.2017.08.007.

(26) Diepens, M.; Gijsman, P. Photodegradation of Bisphenol A Polycarbonate. *Polym. Degrad. Stab.* **2007**, *92* (3), 397–406. https://doi.org/10.1016/j.polymdegradstab.2006.12.003.

(27) Pan, F.; Chen, L.; Jiang, Y.; Xiong, L.; Min, L.; Xie, J.; Qi, J.; Xiao, H.; Chen, Y.; De Hoop, C. F. Bio-Based UV Protective Films Prepared with Polylactic Acid (PLA) and Phoebe Zhennan Extractives. *Int. J. Biol. Macromol.* **2018**, *119*, 582–587. https://doi.org/10.1016/j.ijbiomac.2018.07.189.

(28) Campbell, J.; Vikulina, A. S. Layer-by-Layer Assemblies of Biopolymers: Build-up, Mechanical Stability and Molecular Dynamics. *Polymers.* **2020**, *12* (9), 1–30. https://doi.org/10.3390/polym12091949.

(29) Yang, D.; Wang, S.; Zhong, R.; Liu, W.; Qiu, X. Preparation of Lignin/TiO 2 Nanocomposites and Their Application in Aqueous Polyurethane Coatings. *Front. Chem. Sci. Eng.* **2019**, *13* (1), 59–69. https://doi.org/10.1007/s11705-018-1712-0.

(30) Corrêa, B. A. M.; Gonçalves, A. S.; De Souza, A. M. T.; Freitas, C. A.; Cabral, L. M.; Albuquerque, M. G.; Castro, H. C.; Dos Santos, E. P.; Rodrigues, C. R. Molecular Modeling Studies of the Structural, Electronic, and UV Absorption Properties of Benzophenone Derivatives. *J. Phys. Chem. A* **2012**, *116* (45), 10927–

10933. https://doi.org/10.1021/jp306130y.

(31) Anderson, W. A. C.; Castle, L. Benzophenone in Cartonboard Packaging Materials and the Factors That Influence Its Migration into Food. *Food Addit. Contam.* **2003**, *20* (6), 607–618. https://doi.org/10.1080/0265203031000109486.

(32) Nowicki, M.; Richter, A.; Wolf, B.; Kaczmarek, H. Nanoscale Mechanical Properties of Polymers Irradiated by UV. *Polymer.* **2003**, *44* (21), 6599–6606. https://doi.org/10.1016/S0032-3861(03)00729-8.

(33) Li, R. Z.; Hu, A.; Bridges, D.; Zhang, T.; Oakes, K. D.; Peng, R.; Tumuluri, U.; Wu, Z.; Feng, Z. Robust Ag Nanoplate Ink for Flexible Electronics Packaging. *Nanoscale* **2015**, *7* (16), 7368–7377. https://doi.org/10.1039/c5nr00312a.

(34) Rao, F.; Chen, Y.; Zhao, X.; Cai, H.; Li, N.; Bao, Y. Enhancement of Bamboo Surface Photostability by Application of Clear Coatings Containing a Combination of Organic/Inorganic UV Absorbers. *Prog. Org. Coatings* **2018**, *124*, 314–320. https://doi.org/10.1016/j.porgcoat.2018.05.023.

(35) Ao, J.; Yuan, T.; Gu, J.; Ma, Y.; Shen, Z.; Tian, Y.; Shi, R.; Zhou, W.; Zhang, J. Organic UV Filters in Indoor Dust and Human Urine: A Study of Characteristics, Sources, Associations and Human Exposure. *Sci. Total Environ.* **2018**, *640–641* (800), 1157–1164. https://doi.org/10.1016/j.scitotenv.2018.05.367.

(36) Krause, M.; Frederiksen, H.; Sundberg, K.; Jørgensen, F. S.; Jensen, L. N.; Nørgaard, P.; Jørgensen, C.; Ertberg, P.; Juul, A.; Drzewiecki, K. T.; Skakkebaek, N. E.; Andersson, A. M. Presence of Benzophenones Commonly Used as UV Filters and Absorbers in Paired Maternal and Fetal Samples. *Environ. Int.* **2018**, *110*, 51–60. https://doi.org/10.1016/j.envint.2017.10.005.

(37) Quideau, S.; Deffieux, D.; Douat-Casassus, C.; Pouységu, L. Plant Polyphenols: Chemical Properties, Biological Activities, and Synthesis. *Angew. Chemie - Int. Ed.* **2011**, *50* (3), 586–621. https://doi.org/10.1002/anie.201000044.

(38) Wei, Z.; Cai, C.; Huang, Y.; Wang, P.; Song, J.; Deng, L.; Fu, Y. Strong Biodegradable Cellulose Materials with Improved Crystallinity via Hydrogen Bonding Tailoring Strategy for UV Blocking and Antioxidant Activity. *Int. J. Biol. Macromol.* **2020**, *164*, 27–36. https://doi.org/10.1016/j.ijbiomac.2020.07.100.

(39) Gosselink, R. J. A.; De Jong, E.; Guran, B.; Abächerli, A. Co-Ordination Network for Lignin - Standardisation, Production and Applications Adapted to Market Requirements (EUROLIGNIN). *Ind. Crops Prod.* **2004**, *20* (2), 121–129. https://doi.org/10.1016/j.indcrop.2004.04.015.

(40) Qian, Y.; Qiu, X.; Zhu, S. Lignin: A Nature-Inspired Sun Blocker for Broadspectrum Sunscreens. *Green Chem.* **2015**, *17* (1), 320–324. https://doi.org/10.1039/c4gc01333f.

(41) Mondal, S. Preparation, Properties and Applications of Nanocellulosic Materials. *Carbohydr. Polym.* **2017**, *163*, 301–316. https://doi.org/10.1016/j.carbpol.2016.12.050.

(42) Sadeghifar, H.; Venditti, R.; Jur, J.; Gorga, R. E.; Pawlak, J. J. Cellulose-Lignin Biodegradable and Flexible UV Protection Film. *ACS Sustain. Chem. Eng.* **2017**, *5* (1), 625–631. https://doi.org/10.1021/acssuschemeng.6b02003.

(43) Rojo, E.; Peresin, M. S.; Sampson, W. W.; Hoeger, I. C.; Vartiainen, J.; Laine, J.; Rojas, O. J. Comprehensive Elucidation of the Effect of Residual Lignin on the Physical, Barrier, Mechanical and Surface Properties of Nanocellulose Films. *Green Chem.* **2015**, *17* (3), 1853–1866. https://doi.org/10.1039/c4gc02398f.

(44) Zhu, S.; Song, Y.; Zhao, X.; Shao, J.; Zhang, J.; Yang, B. The Photoluminescence Mechanism in Carbon Dots (Graphene Quantum Dots, Carbon Nanodots, and Polymer Dots): Current State and Future Perspective. *Nano Res.* **2015**, *8* (2), 355–381. https://doi.org/10.1007/s12274-014-0644-3.

(45) Lim, S. Y.; Shen, W.; Gao, Z. Carbon Quantum Dots and Their Applications. *Chem. Soc. Rev.* **2015**, *44* (1), 362–381. https://doi.org/10.1039/c4cs00269e.

(46) Campalani, C.; Cattaruzza, E.; Zorzi, S.; Vomiero, A.; You, S.; Matthews, L.; Capron, M.; Mondelli, C.; Selva, M.; Perosa, A. Biobased Carbon Dots: From Fish Scales to Photocatalysis. *Nanomaterials* **2021**, *11* (2), 1–14. https://doi.org/10.3390/nano11020524.

(47) Cailotto, S.; Massari, D.; Gigli, M.; Campalani, C.; Bonini, M.; You, S.; Vomiero, A.; Selva, M.; Perosa, A.; Crestini, C. N-Doped Carbon Dot Hydrogels from Brewing Waste for Photocatalytic Wastewater Treatment.

ACS Omega **2022**, *7* (5), 4052–4061. https://doi.org/10.1021/acsomega.1c05403.

(48) Luo, P. G.; Sahu, S.; Yang, S. T.; Sonkar, S. K.; Wang, J.; Wang, H.; Lecroy, G. E.; Cao, L.; Sun, Y. P. Carbon "Quantum" Dots for Optical Bioimaging. *J. Mater. Chem. B* **2013**, *1* (16), 2116–2127. https://doi.org/10.1039/c3tb00018d.

(49) Konwar, A.; Gogoi, N.; Majumdar, G.; Chowdhury, D. Green Chitosan-Carbon Dots Nanocomposite Hydrogel Film with Superior Properties. *Carbohydr. Polym.* **2015**, *115*, 238–245. https://doi.org/10.1016/j.carbpol.2014.08.021.

(50) Feng, X.; Zhao, Y.; Jiang, Y.; Miao, M.; Cao, S.; Fang, J. Use of Carbon Dots to Enhance UV-Blocking of Transparent Nanocellulose Films. *Carbohydr. Polym.* **2017**, *161*, 253–260. https://doi.org/10.1016/j.carbpol.2017.01.030.

(51) Wang, H.; Di, J.; Sun, Y.; Fu, J.; Wei, Z.; Matsui, H.; Alonso, A. C.; Zhou, S. Biocompatible PEG-Chitosan @ Carbon Dots Hybrid Nanogels for Two-Photon Fluorescence Imaging , Near-Infrared Light / PH Dual-Responsive Drug Carrier , and Synergistic Therapy. *Adv. Funct. Mater.* **2015**, *25*, 5537–5547. https://doi.org/10.1002/adfm.201501524.

(52) Jia, X.; Pei, M.; Zhao, X.; Tian, K.; Zhou, T.; Liu, P. PEGylated Oxidized Alginate-DOX Prodrug Conjugate Nanoparticles Cross-Linked with Fluorescent Carbon Dots for Tumor Theranostics. *ACS Biomater. Sci. Eng.* **2016**, *2* (9), 1641–1648. https://doi.org/10.1021/acsbiomaterials.6b00443.

(53) Youssef, A. M.; El-Sayed, S. M. Bionanocomposites Materials for Food Packaging Applications: Concepts and Future Outlook. *Carbohydr. Polym.* **2018**, *193*, 19–27. https://doi.org/10.1016/j.carbpol.2018.03.088.

(54) Gaidau, C.; Giurginca, M.; Dragomir, T.; Petica, A.; Chen, W. Study of Collagen and Leather Functionalization by Using Metallic Nanoparticles. *J. Optoelectron. Adv. Mater.* **2010**, *12* (10), 2157–2163.

(55) Teymourpour, S.; Abdorreza, M. N.; Nahidi, F. Functional, Thermal, and Antimicrobial Properties of Soluble Soybean Polysaccharide Biocomposites Reinforced by Nano TiO2. *Carbohydr. Polym.* **2015**, *134*, 726–731. https://doi.org/10.1016/j.carbpol.2015.08.073.

(56) Jang, J. W.; Min, B. G.; Yeum, J. H.; Jeong, Y. G. Structures and Physical Properties of Graphene/PVDF Nanocomposite Films Prepared by Solution-Mixing and Melt-Compression. *Fibers Polym.* **2013**, *14* (8), 1332–1338. https://doi.org/10.1007/s12221-013-1332-8.

(57) Fan, X.; Chen, K.; He, X.; Li, N.; Huang, J.; Tang, K.; Li, Y.; Wang, F. Nano-TiO2/Collagen-Chitosan Porous Scaffold for Wound Repairing. *Int. J. Biol. Macromol.* **2016**, *91*, 15–22. https://doi.org/10.1016/j.ijbiomac.2016.05.094.

(58) Ullattil, S. G.; Narendranath, S. B.; Pillai, S. C.; Periyat, P. Black TiO2 Nanomaterials: A Review of Recent Advances. *Chem. Eng. J.* **2018**, *343*, 708–736. https://doi.org/10.1016/j.cej.2018.01.069.

(59) Ali, A.; Ahmed, S. A Review on Chitosan and Its Nanocomposites in Drug Delivery. *Int. J. Biol. Macromol.* **2018**, *109*, 273–286. https://doi.org/10.1016/j.ijbiomac.2017.12.078.

(60) Jbeli, A.; Ferraria, A. M.; Botelho do Rego, A. M.; Boufi, S.; Bouattour, S. Hybrid Chitosan-TiO2/ZnS Prepared under Mild Conditions with Visible-Light Driven Photocatalytic Activity. *Int. J. Biol. Macromol.* **2018**, *116*, 1098–1104. https://doi.org/10.1016/j.ijbiomac.2018.05.141.

(61) Ningaraju, S.; Ravikumar, H. B. Effect of TiO2 Nano-Filler on the Electrical Conductivity and Free Volume Parameters of PSAN/TiO2 Nanocomposites. *Polym. Compos.* **2016**, *39* (5), 1403–1412. https://doi.org/10.1002/pc.24080.

(62) Praveena, S. D.; Ravindrachary, V.; Bhajantri, R. F.; Ismayil. Dopant-Induced Microstructural, Optical, and Electrical Properties of TiO2/PVA Composite. *Polym. Compos.* **2016**, *37*, 987. https://doi.org/10.1002/pc.

(63) Hu, D.; Zhang, Z.; Liu, M.; Lin, J.; Chen, X.; Ma, W. Multifunctional UV-Shielding Nanocellulose Films Modified with Halloysite Nanotubes-Zinc Oxide Nanohybrid. *Cellulose* **2020**, *27* (1), 401–413. https://doi.org/10.1007/s10570-019-02796-0.

(64) Amjadi, S.; Emaminia, S.; Heyat Davudian, S.; Pourmohammad, S.; Hamishehkar, H.; Roufegarinejad, L. Preparation and Characterization of Gelatin-Based Nanocomposite Containing Chitosan Nanofiber and ZnO Nanoparticles. *Carbohydr. Polym.* **2019**, *216*, 376–384. https://doi.org/10.1016/j.carbpol.2019.03.062.

(65) Li, J. H.; Hong, R. Y.; Li, M. Y.; Li, H. Z.; Zheng, Y.; Ding, J. Effects of ZnO Nanoparticles on the Mechanical and Antibacterial Properties of Polyurethane Coatings. *Prog. Org. Coatings* **2009**, *64* (4), 504–509. https://doi.org/10.1016/j.porgcoat.2008.08.013.

(66) Al-Naamani, L.; Dobretsov, S.; Dutta, J. Chitosan-Zinc Oxide Nanoparticle Composite Coating for Active Food Packaging Applications. *Innov. Food Sci. Emerg. Technol.* **2016**, *38*, 231–237. https://doi.org/10.1016/j.ifset.2016.10.010.

(67) Mohammadi Nafchi, A.; Moradpour, M.; Saeidi, M.; Alias, A. K. Effects of Nanorod-Rich ZnO on Rheological, Sorption Isotherm, and Physicochemical Properties of Bovine Gelatin Films. *LWT - Food Sci. Technol.* **2014**, *58* (1), 142–149. https://doi.org/10.1016/j.lwt.2014.03.007.

(68) Sarker, F.; Karim, N.; Afroj, S.; Koncherry, V.; Novoselov, K. S.; Potluri, P. High-Performance Graphene-Based Natural Fiber Composites. *ACS Appl. Mater. Interfaces* **2018**, *10* (40), 34502–34512. https://doi.org/10.1021/acsami.8b13018.

(69) Adak, B.; Joshi, M.; Butola, B. S. Polyurethane/Functionalized-Graphene Nanocomposite Films with Enhanced Weather Resistance and Gas Barrier Properties. *Compos. Part B Eng.* **2019**, *176*, 107303. https://doi.org/10.1016/j.compositesb.2019.107303.

(70) Bansala, T.; Joshi, M.; Mukhopadhyay, S. Electromagnetic Interference Shielding Behavior of Chemically and Thermally Reduced Graphene Based Multifunctional Polyurethane Nanocomposites: A Comparative Study. *J. Appl. Polym. Sci.* **2019**, *136* (25), 1–12. https://doi.org/10.1002/app.47666.

(71) De Moraes, A. C. M.; Andrade, P. F.; De Faria, A. F.; Simões, M. B.; Salomão, F. C. C. S.; Barros, E. B.; Gonçalves, M. D. C.; Alves, O. L. Fabrication of Transparent and Ultraviolet Shielding Composite Films Based on Graphene Oxide and Cellulose Acetate. *Carbohydr. Polym.* **2015**, *123*, 217–227. https://doi.org/10.1016/j.carbpol.2015.01.034.

(72) Xie, S.; Zhao, J.; Zhang, B.; Wang, Z.; Ma, H.; Yu, C.; Yu, M.; Li, L.; Li, J. Graphene Oxide Transparent Hybrid Film and Its Ultraviolet Shielding Property. *ACS Appl. Mater. Interfaces* **2015**, *7* (32), 17558–17564. https://doi.org/10.1021/acsami.5b04231.

(73) Jin, B.; Li, X.; Zhou, X.; Xu, X.; Jian, H.; Li, M.; Guo, K.; Guan, J.; Yan, S. Fabrication and Characterization of Nanocomposite Film Made from a Jackfruit Filum Polysaccharide Incorporating TiO2 Nanoparticles by Photocatalysis. *RSC Adv.* **2017**, *7* (28), 16931–16937. https://doi.org/10.1039/c6ra28648h.

(74) Vejdan, A.; Ojagh, S. M.; Adeli, A.; Abdollahi, M. Effect of TiO2 Nanoparticles on the Physico-Mechanical and Ultraviolet Light Barrier Properties of Fish Gelatin/Agar Bilayer Film. *LWT - Food Sci. Technol.* **2016**, *71*, 88–95. https://doi.org/10.1016/j.lwt.2016.03.011.

(75) Maschmeyer, T.; Luque, R.; Selva, M. Upgrading of Marine (Fish and Crustaceans) Biowaste for High Added-Value Molecules and Bio(Nano)-Materials. *Chem. Soc. Rev.* **2020**, *49* (13), 4527–4563. https://doi.org/10.1039/c9cs00653b.

(76) Chang, S.; Buehler, M. J. Molecular Biomechanics of Collagen Molecules. *Mater. Today* **2014**, *17* (2), 70–76. https://doi.org/10.1016/j.mattod.2014.01.019.

(77) Yamada, S.; Yamamoto, K.; Ikeda, T.; Yanagiguchi, K.; Hayashi, Y. Potency of Fish Collagen as a Scaffold for Regenerative Medicine. *Biomed Res. Int.* **2014**, *2014* (3), 302932. https://doi.org/http://dx.doi.org/10.1155/2014/302932.

(78) Hernandez-Izquierdo, V. M.; Krochta, J. M. Thermoplastic Processing of Proteins for Film Formation — A Review. *J. Food Sci.* **2008**, *73* (2), 30–39. https://doi.org/10.1111/j.1750-3841.2007.00636.x.

(79) Bhargava, N.; Singh, V.; Mor, R. S.; Kumar, K. Trends in Food Science & Technology Active and Intelligent Biodegradable Packaging Films Using Food and Food Waste-Derived Bioactive Compounds : A Review. *Trends Food Sci. Technol.* **2020**, *105*, 385–401. https://doi.org/10.1016/j.tifs.2020.09.015.

(80) Das, M. P.; R., S. P.; Prasad, K.; Jv, V.; M, R. Extraction and Characterization of Gelatin: A Functional Biopolymer. *Int. J. Pharm. Pharm. Sci.* **2017**, *9* (9), 239. https://doi.org/10.22159/ijpps.2017v9i9.17618.

(81) Ahmed, S.; Ikram, S. Chitosan and Gelatin Based Biodegradable Packaging Films with UV-Light Protection. *J. Photochem. Photobiol. B Biol.* **2016**, *163*, 115–124. https://doi.org/10.1016/j.jphotobiol.2016.08.023.

(82) Mehta, M. J.; Kumar, A. Ionic Liquid Stabilized Gelatin–Lignin Films: A Potential UV-Shielding Material with Excellent Mechanical and Antimicrobial Properties. *Chem. - Eur. J.* **2019**, *25* (5), 1269–1274. https://doi.org/10.1002/chem.201803763.

(83) Rivero, S.; García, M. A.; Pinotti, A. Correlations between Structural , Barrier , Thermal and Mechanical Properties of Plasticized Gelatin Fi Lms. *Innov. Food Sci. Emerg. Technol.* **2010**, *11* (2), 369–375. https://doi.org/10.1016/j.ifset.2009.07.005.

(84) Zhao, J.; Wei, F.; Xu, W.; Han, X. Enhanced Antibacterial Performance of Gelatin/Chitosan Film Containing Capsaicin Loaded MOFs for Food Packaging. *Appl. Surf. Sci.* **2020**, *510*, 145418. https://doi.org/10.1016/j.apsusc.2020.145418.

(85) Roy, S.; Rhim, J. W. Gelatin-Based Film Integrated with Copper Sulfide Nanoparticles for Active Packaging Applications. *Appl. Sci.* **2021**, *11* (14), 6307. https://doi.org/10.3390/app11146307.

(86) Kowsalya, E.; MosaChristas, K.; Balashanmugam, P.; Manivasagan, V.; Devasena, T.; Jaquline, C. R. I. Sustainable Use of Biowaste for Synthesis of Silver Nanoparticles and Its Incorporation into Gelatin-Based Nanocomposite Films for Antimicrobial Food Packaging Applications. *J. Food Process Eng.* **2021**, *44* (3), 1–13. https://doi.org/10.1111/jfpe.13641.

(87) Du, H.; Liu, W.; Zhang, M.; Si, C.; Zhang, X.; Li, B. Cellulose Nanocrystals and Cellulose Nano Fi Brils Based Hydrogels for Biomedical Applications. *Carbohydr. Polym.* **2019**, *209*, 130–144. https://doi.org/10.1016/j.carbpol.2019.01.020.

(88) Erciyes, A.; Ocak, B. Physico-Mechanical, Thermal, and Ultraviolet Light Barrier Properties of Collagen Hydrolysate Films from Leather Solid Wastes Incorporated with Nano TiO2. *Polym. Compos.* **2019**, *40* (12), 4716–4725. https://doi.org/10.1002/pc.25340.

(89) Fu, B.; Mei, S.; Su, X.; Chen, H.; Zhu, J.; Zheng, Z.; Lin, H.; Dai, C.; Luque, R.; Yang, D.-P. Integrating Waste Fish Scale-Derived Gelatin and Chitosan into Edible Nanocomposite Film for Perishable Fruits. *Int. J. Biol. Macromol.* **2021**, *191*, 1164–1174. https://doi.org/10.1016/j.ijbiomac.2021.09.171.

(90) Shankar, S.; Wang, L. F.; Rhim, J. W. Effect of Melanin Nanoparticles on the Mechanical, Water Vapor Barrier, and Antioxidant Properties of Gelatin-Based Films for Food Packaging Application. *Food Packag. Shelf Life* **2019**, *21*, 100363. https://doi.org/10.1016/j.fpsl.2019.100363.

(91) Rouhi, J.; Mahmud, S.; Naderi, N.; Raymond Ooi, C. H.; Mahmood, M. R. Physical Properties of Fish Gelatin-Based Bio-Nanocomposite Films Incorporated with ZnO Nanorods. *Nanoscale Res. Lett.* **2013**, *8* (1), 1–6. https://doi.org/10.1186/1556-276X-8-364.

(92) Arfat, Y. A.; Benjakul, S.; Prodpran, T.; Sumpavapol, P.; Songtipya, P. Physico-Mechanical Characterization and Antimicrobial Properties of Fish Protein Isolate/Fish Skin Gelatin-Zinc Oxide (ZnO) Nanocomposite Films. *Food Bioprocess Technol.* **2016**, *9* (1), 101–112. https://doi.org/10.1007/s11947-015-1602-0.

(93) Mehta, M. J.; Kumar, A. Ionic Liquid Assisted Gelatin Films: Green, UV Shielding, Antioxidant, and Antibacterial Food Packaging Materials. *ACS Sustain. Chem. Eng.* **2019**, *7* (9), 8631–8636. https://doi.org/10.1021/acssuschemeng.9b00423.

(94) Zhang, C.; Yang, Z.; Shi, J.; Zou, X.; Zhai, X.; Huang, X.; Li, Z.; Holmes, M.; Daglia, M.; Xiao, J. Physical Properties and Bioactivities of Chitosan/Gelatin-Based Films Loaded with Tannic Acid and Its Application on the Preservation of Fresh-Cut Apples. *LWT - Food Sci. Technol.* **2021**, *144*, 111223. https://doi.org/10.1016/j.lwt.2021.111223.

(95) Kriechbaum, K.; Bergström, L. Antioxidant and UV-Blocking Leather-Inspired Nanocellulose-Based Films with High Wet Strength. *Biomacromolecules* **2020**, *21* (5), 1720–1728. https://doi.org/10.1021/acs.biomac.9b01655.

(96) Wang, Z.; Tang, L.; Lin, F.; Shen, Y.; Chen, Y.; Chen, X.; Huang, B.; Lu, B. Multi-Functional Edible Film with Excellent UV Barrier Performance and Accurate Instant Ion Printing Capability. *Adv. Sustain. Syst.* **2020**, *4* (7), 1–10. https://doi.org/10.1002/adsu.202000043.

(97) Limpisophon, K.; Schleining, G. Addition of Gallic Acid to Enhance Antioxidative and Physical Properties of Fish Gelatin Film for Edible Oil Pouch. *Ital. J. Food Sci.* **2018**, *30* (5), 152–156.

(98) Huang, S.; Tu, Z.; Sha, X.; Hu, Y.; Chen, N.; Wang, H. Fabrication and Performance Evaluation of Pectin–Fish Gelatin–Resveratrol Preservative Films. *Food Chem.* **2021**, *361*, 129832. https://doi.org/10.1016/j.foodchem.2021.129832.

(99) Granados, M. L. G.; Martucci, J. F.; Ruseckaite, R. A. Enhancing Water Resistance , Tensile Properties and UV-Shielding Capacity of Bovine Gelatin Films Modified with Epoxidized Soy - Bean Oil and Glyoxal during Processing. *J. Clin. Nutr. Food Sci.* **2020**, *3* (1), 1–10.

(100) Wang, P.; Wang, Y.; Hong, P.; Zhou, C. Di-Aldehyde Starch Crystal: A Novel Bio-Crosslinker for Strengthening the Structure and Physio-Chemical Properties of Gelatin-Based Films. *Food Biosci.* **2021**, *43*, 101308. https://doi.org/10.1016/j.fbio.2021.101308.

(101) Zhang, X.; Liu, J.; Qian, C.; Kan, J.; Jin, C. Effect of Grafting Method on the Physical Property and Antioxidant Potential of Chitosan Film Functionalized with Gallic Acid. *Food Hydrocoll.* **2019**, *89*, 1–10. https://doi.org/10.1016/j.foodhyd.2018.10.023.

(102) Ogawa, Y.; Azuma, K.; Izawa, H.; Morimoto, M.; Ochi, K.; Osaki, T.; Ito, N.; Okamoto, Y.; Saimoto, H.; Ifuku, S. Preparation and Biocompatibility of a Chitin Nanofiber/Gelatin Composite Film. *Int. J. Biol. Macromol.* **2017**, *104*, 1882–1889. https://doi.org/10.1016/j.ijbiomac.2017.02.041.

(103) Wang, W.; Xue, C.; Mao, X. Chitosan : Structural Modification , Biological Activity and Application. *Int. J. Biol. Macromol.* **2020**, *164*, 4532–4546. https://doi.org/10.1016/j.ijbiomac.2020.09.042.

(104) Croisier, F.; Jérôme, C. Chitosan-Based Biomaterials for Tissue Engineering. *Eur. Polym. J.* **2013**, *49* (4), 780–792. https://doi.org/10.1016/j.eurpolymj.2012.12.009.

(105) Tran, C. D.; Duri, S.; Delneri, A.; Franko, M. Chitosan-Cellulose Composite Materials : Preparation , Characterization and Application for Removal of Microcystin. *J. Hazard. Mater.* **2013**, *252–253*, 355–366. https://doi.org/10.1016/j.jhazmat.2013.02.046.

(106) Broek, L. A. M. Van Den; Knoop, R. J. I.; Kappen, F. H. J.; Boeriu, C. G. Chitosan Films and Blends for Packaging Material. *Carbohydr. Polym.* **2015**, *116*, 237–242. https://doi.org/10.1016/j.carbpol.2014.07.039.

(107) Jung Liang, Rui Wang, R. C. The Impact of Cross-Linking Mode on the Physical and Antimicrobial Properties of a Chitosan / Bacterial Cellulose Composite. *Polymers.* **2019**, *11*, 491. https://doi.org/10.3390/polym11030491.

(108) Zhang, X.; Li, Y.; Guo, M.; Jin, T. Z.; Arabi, S. A.; He, Q.; Ismail, B. B.; Hu, Y.; Liu, D. Antimicrobial and UV Blocking Properties of Composite Chitosan Films with Curcumin Grafted Cellulose Nanofiber. *Food Hydrocoll.* **2021**, *112*, 106337. https://doi.org/10.1016/j.foodhyd.2020.106337.

(109) Nunes, C.; Coimbra, M. A.; Ferreira, P. Tailoring Functional Chitosan-Based Composites for Food Applications. *Chem. Rec.* **2018**, *18*, 1138–1149. https://doi.org/10.1002/tcr.201700112.

(110) Barra, A.; Ferreira, N. M.; Martins, M. A.; Lazar, O.; Pantazi, A.; Alexandru, A.; Neumayer, S. M.; Rodriguez, B. J.; En, M.; Ferreira, P.; Nunes, C. Eco-Friendly Preparation of Electrically Conductive Chitosan - Reduced Graphene Oxide Fl Exible Bionanocomposites for Food Packaging and Biological Applications. *Compos. Sci. Technol.* **2019**, *173*, 53–60. https://doi.org/10.1016/j.compscitech.2019.01.027.

(111) Ezati, P.; Rhim, J. W. PH-Responsive Chitosan-Based Film Incorporated with Alizarin for Intelligent Packaging Applications. *Food Hydrocoll.* **2020**, *102*, 105629. https://doi.org/10.1016/j.foodhyd.2019.105629.

(112) Gasti, T.; Dixit, S.; D’souza, O. J.; Hiremani, V. D.; Vootla, S. K.; Masti, S. P.; Chougale, R. B.; Malabadi, R. B. Smart Biodegradable Films Based on Chitosan/Methylcellulose Containing Phyllanthus Reticulatus Anthocyanin for Monitoring the Freshness of Fish Fillet. *Int. J. Biol. Macromol.* **2021**, *187*, 451–461. https://doi.org/10.1016/j.ijbiomac.2021.07.128.

(113) Chen, M.; Yan, T.; Huang, J.; Zhou, Y.; Hu, Y. Fabrication of Halochromic Smart Films by Immobilizing Red Cabbage Anthocyanins into Chitosan/Oxidized-Chitin Nanocrystals Composites for Real-Time Hairtail and Shrimp Freshness Monitoring. *Int. J. Biol. Macromol.* **2021**, *179*, 90–100. https://doi.org/10.1016/j.ijbiomac.2021.02.170.

(114) Vilela, C.; Pinto, R. J. B.; Coelho, J.; Domingues, M. R. M.; Daina, S.; Sadocco, P.; Santos, S. A. O.; Freire, C. S. R. Bioactive Chitosan/Ellagic Acid Films with UV-Light Protection for Active Food Packaging. *Food Hydrocoll.* **2017**, *73*, 120–128. https://doi.org/10.1016/j.foodhyd.2017.06.037.

(115) Roy, S.; Rhim, J. W. Fabrication of Chitosan-Based Functional Nanocomposite Films: Effect of Quercetin-Loaded Chitosan Nanoparticles. *Food Hydrocoll.* **2021**, *121*, 107065. https://doi.org/10.1016/j.foodhyd.2021.107065.

(116) Roy, S.; Rhim, J. W. Fabrication of Bioactive Binary Composite Film Based on Gelatin/Chitosan Incorporated with Cinnamon Essential Oil and Rutin. *Colloids Surfaces B Biointerfaces* **2021**, *204* (April), 111830. https://doi.org/10.1016/j.colsurfb.2021.111830.

(117) Cazón, P.; Antoniewska, A.; Rutkowska, J.; Vázquez, M. Evaluation of Easy-Removing Antioxidant Films of Chitosan with Melaleuca Alternifolia Essential Oil. *Int. J. Biol. Macromol.* **2021**, *186*, 365–376. https://doi.org/10.1016/j.ijbiomac.2021.07.035.

(118) Gao, Z.; Wang, C.; Li, Z. Effect of Ethanol Extract of Black Soybean Coat on Physicochemical Properties and Biological Activities of Chitosan Packaging Film. *Food Sci. Biotechnol.* **2021**, *30* (10), 1369–1381. https://doi.org/10.1007/s10068-021-00968-y.

(119) Sun, M.; Liu, N.; Ni, S.; Bian, H.; Fu, Y.; Chen, X. Poplar Hot Water Extract Enhances Barrier and Antioxidant Properties of Chitosan/Bentonite Composite Film for Packaging Applications. *Polymers.* **2019**, *11* (10). https://doi.org/10.3390/polym11101614.

(120) Zhang, X.; Liu, Y.; Yong, H.; Qin, Y.; Liu, J.; Liu, J. Development of Multifunctional Food Packaging Films Based on Chitosan, TiO 2 Nanoparticles and Anthocyanin-Rich Black Plum Peel Extract. *Food Hydrocoll.* **2019**, *94*, 80–92. https://doi.org/10.1016/j.foodhyd.2019.03.009.

(121) Krishnan, R. A.; Mhatre, O.; Sheth, J.; Prabhu, S.; Jain, R.; Dandekar, P. Synthesis of Zinc Oxide Nanostructures Using Orange Peel Oil for Fabricating Chitosan-Zinc Oxide Composite Films and Their Antibacterial Activity. *J. Polym. Res.* **2020**, *27*, 206. https://doi.org/10.1007/s10965-020-2033-9.

(122) Roy, S.; Van Hai, L.; Kim, H. C.; Zhai, L.; Kim, J. Preparation and Characterization of Synthetic Melanin-like Nanoparticles Reinforced Chitosan Nanocomposite Films. *Carbohydr. Polym.* **2020**, *231*, 115729. https://doi.org/10.1016/j.carbpol.2019.115729.

(123) Yadav, M.; Behera, K.; Chang, Y. H.; Chiu, F. C. Cellulose Nanocrystal Reinforced Chitosan Based UV Barrier Composite Films for Sustainable Packaging. *Polymers.* **2020**, *12*, 202. https://doi.org/10.3390/polym12010202.

(124) Campalani, C.; Causin, V.; Selva, M.; Perosa, A. Fish-Waste-Derived Gelatin and Carbon Dots for Biobased UV- Blocking Films. *ACS Appl. Mater. Interfaces* **2022**, *14*, 35148–35156. https://doi.org/10.1021/acsami.2c11749.

(125) Kumar Barman, B.; Nagao, T.; Nanda, K. K. Dual Roles of a Transparent Polymer Film Containing Dispersed N-Doped Carbon Dots: A High-Efficiency Blue Light Converter and UV Screen. *Appl. Surf. Sci.* **2020**, *510*, 145405. https://doi.org/10.1016/j.apsusc.2020.145405.

(126) Uthirakumar, P.; Devendiran, M.; Kim, T. H.; Lee, I. H. A Convenient Method for Isolating Carbon Quantum Dots in High Yield as an Alternative to the Dialysis Process and the Fabrication of a Full-Band UV Blocking Polymer Film. *New J. Chem.* **2018**, *42* (22), 18312–18317. https://doi.org/10.1039/c8nj04615h.

(127) Kovalchuk, A.; Huang, K.; Xiang, C.; Martí, A. A.; Tour, J. M. Luminescent Polymer Composite Films Containing Coal-Derived Graphene Quantum Dots. *ACS Appl. Mater. Interfaces* **2015**, *7* (47), 26063–26068. https://doi.org/10.1021/acsami.5b06057.

(128) Park, S. J.; Yang, H. K.; Moon, B. K. Ultraviolet to Blue Blocking and Wavelength Convertible Films Using Carbon Dots for Interrupting Eye Damage Caused by General Lighting. *Nano Energy* **2019**, *60* (February), 87–94. https://doi.org/10.1016/j.nanoen.2019.03.043.

(129) Hess, S. C.; Permatasari, F. A.; Fukazawa, H.; Schneider, E. M.; Balgis, R.; Ogi, T.; Okuyama, K.; Stark, W. J. Direct Synthesis of Carbon Quantum Dots in Aqueous Polymer Solution: One-Pot Reaction and Preparation of Transparent UV-Blocking Films. *J. Mater. Chem. A* **2017**, *5* (10), 5187–5194. https://doi.org/10.1039/c7ta00397h.

(130) Salimi, F.; Moradi, M.; Tajik, H.; Molaei, R. Optimization and Characterization of Eco-Friendly Antimicrobial Nanocellulose Sheet Prepared Using Carbon Dots of White Mulberry (Morus Alba L.). *J. Sci. Food Agric.* **2021**, *101* (8), 3439–3447. https://doi.org/10.1002/jsfa.10974.

(131) Javanbakht, S.; Namazi, H. Solid State Photoluminescence Thermoplastic Starch Film Containing Graphene Quantum Dots. *Carbohydr. Polym.* **2017**, *176*, 220–226. https://doi.org/10.1016/j.carbpol.2017.08.080.

(132) You, Y.; Zhang, H.; Liu, Y.; Lei, B. Transparent Sunlight Conversion Film Based on Carboxymethyl Cellulose and Carbon Dots. *Carbohydr. Polym.* **2016**, *151*, 245–250. https://doi.org/10.1016/j.carbpol.2016.05.063.

(133) Zhang, X.; Xu, S.; Shen, L.; Li, G. Factors Affecting Thermal Stability of Collagen from the Aspects of Extraction, Processing and Modification. *J. Leather Sci. Eng.* **2020**, *2* (1). https://doi.org/10.1186/s42825-020-00033-0.

(134) Minh Thuy, L. T.; Okazaki, E.; Osako, K. Isolation and Characterization of Acid-Soluble Collagen from the Scales of Marine Fishes from Japan and Vietnam. *Food Chem.* **2014**, *149*, 264–270. https://doi.org/10.1016/j.foodchem.2013.10.094.

(135) Felician, F. F.; Xia, C.; Qi, W.; Xu, H. Collagen from Marine Biological Sources and Medical Applications. *Chem. Biodivers.* **2018**, *15*, 1700557. https://doi.org/10.1002/cbdv.201700557.

(136) Djabourov, M.; Leblond, J.; Papon, P. Gelation of Aqueous Gelatin Solutions. I. Structural Investigation. *J. Phys. Fr.* **1988**, *49*, 319–332. https://doi.org/http://dx.doi.org/10.1051/jphys:01988004902031900.

(137) Jeya Shakila, R.; Jeevithan, E.; Varatharajakumar, A.; Jeyasekaran, G.; Sukumar, D. Comparison of the Properties of Multi-Composite Fish Gelatin Films with That of Mammalian Gelatin Films. *Food Chem.* **2012**, *135* (4), 2260–2267. https://doi.org/10.1016/j.foodchem.2012.07.069.

(138) Gòmez-Guìllen, M. C.; Turnay, J.; Fernàndez-Dìaz, M. D.; Ulmo, N.; Lizarbe, M. A.; Montero, P. Structure and Physical Properties of Gelatin Extracted from Different Marine Species: A Comparative Study. *Food Hydrocoll.* **2002**, *16*, 25–34. https://doi.org/https://doi.org/10.1016/S0268-005X(01)00035-2.

(139) Gómez-Estaca, J.; Giménez, B.; Montero, P.; Gómez-Guillén, M. C. Incorporation of Antioxidant Borage Extract into Edible Films Based on Sole Skin Gelatin or a Commercial Fish Gelatin. *J. Food Eng.* **2009**, *92* (1), 78–85. https://doi.org/10.1016/j.jfoodeng.2008.10.024.

(140) Zakaria, S.; Hidayah, N.; Bakar, A. Extraction and Characterization of Gelatin from Black Tilapia (Oreochromis Niloticus) Scales and Bones. In: Int'l Conf. on Advances in Science, Engg., Technology & Natural Resources (ICASETNR-15. **2015**, 77–80. https://doi.org/10.15242/iicbe.c0815040.

(141) Cao, T. H.; Nguyen, T. T. O.; Nguyen, T. M. H.; Le, N. T.; Razumovskaya, R. G. Characteristics and Physicochemical Properties of Gelatin Extracted from Scales of Seabass (Lates Calcarifer) and Grey Mullet (Mugil Cephalus) in Vietnam. *J. Aquat. Food Prod. Technol.* **2017**, *26* (10), 1293–1302. https://doi.org/10.1080/10498850.2017.1390026.

(142) Ikoma, T.; Kobayashi, H.; Tanaka, J.; Walsh, D.; Mann, S. Physical Properties of Type I Collagen Extracted from Fish Scales of Pagrus Major and Oreochromis Niloticas. *Int. J. Biol. Macromol.* **2003**, *32* (3–5), 199–204. https://doi.org/10.1016/S0141-8130(03)00054-0.

(143) Wang, L.; An, X.; Yang, F.; Xin, Z.; Zhao, L.; Hu, Q. Isolation and Characterisation of Collagens from the Skin, Scale and Bone of Deep-Sea Redfish (Sebastes Mentella). *Food Chem.* **2008**, *108* (2), 616–623. https://doi.org/10.1016/j.foodchem.2007.11.017.

(144) Tongnuanchan, P.; Benjakul, S.; Prodpran, T. Structural, Morphological and Thermal Behaviour Characterisations of Fish Gelatin Film Incorporated with Basil and Citronella Essential Oils as Affected by Surfactants. *Food Hydrocoll.* **2014**, *41*, 33–43. https://doi.org/10.1016/j.foodhyd.2014.03.015.

(145) Gómez-Guillén, M. C.; Ihl, M.; Bifani, V.; Silva, A.; Montero, P. Edible Films Made from Tuna-Fish Gelatin with Antioxidant Extracts of Two Different Murta Ecotypes Leaves (Ugni Molinae Turcz). *Food Hydrocoll.* **2007**, *21* (7), 1133–1143. https://doi.org/10.1016/j.foodhyd.2006.08.006.

(146) Weng, W.; Zheng, H.; Su, W. Characterization of Edible Films Based on Tilapia (Tilapia Zillii) Scale Gelatin with Different Extraction PH. *Food Hydrocoll.* **2014**, *41*, 19–26. https://doi.org/10.1016/j.foodhyd.2014.03.026.

(147) Chen, H.; Wang, J.; Cheng, Y.; Wang, C.; Liu, H.; Bian, H.; Pan, Y.; Sun, J.; Han, W. Application of Protein-Based Films and Coatings for Food Packaging: A Review. *Polymers.* **2019**, *11* (12), 1–32. https://doi.org/10.3390/polym11122039.

(148) Roy, S.; Rhim, J. W. Preparation of Antimicrobial and Antioxidant Gelatin/Curcumin Composite Films for Active Food Packaging Application. *Colloids Surfaces B Biointerfaces* **2020**, *188*, 110761. https://doi.org/10.1016/j.colsurfb.2019.110761.

(149) Govindaswamy, R.; Robinson, J. S.; Geevaretnam, J.; Pandurengan, P. Physico-Functional and Anti-Oxidative Properties of Carp Swim Bladder Gelatin and Brown Seaweed Fucoidan Based Edible Films. *J. Packag. Technol. Res.* **2018**, *2* (1), 77–89. https://doi.org/10.1007/s41783-017-0024-z.

(150) Hanani, Z. A. N.; Yee, F. C.; Nor-Khaizura, M. A. R. Effect of Pomegranate (Punica Granatum L.) Peel Powder on the Antioxidant and Antimicrobial Properties of Fish Gelatin Films as Active Packaging. *Food Hydrocoll.* **2019**, *89* (September 2018), 253–259. https://doi.org/10.1016/j.foodhyd.2018.10.007.

(151) Núñez-Flores, R.; Giménez, B.; Fernández-Martín, F.; López-Caballero, M. E.; Montero, M. P.; Gómez-Guillén, M. C. Physical and Functional Characterization of Active Fish Gelatin Films Incorporated with Lignin. *Food Hydrocoll.* **2013**, *30* (1), 163–172. https://doi.org/10.1016/j.foodhyd.2012.05.017.

(152) Pérez-Mateos, M.; Montero, P.; Gómez-Guillén, M. C. Formulation and Stability of Biodegradable Films Made from Cod Gelatin and Sunflower Oil Blends. *Food Hydrocoll.* **2009**, *23* (1), 53–61. https://doi.org/10.1016/j.foodhyd.2007.11.011.

(153) Giménez, B.; Gómez-Estaca, J.; Alemán, A.; Gómez-Guillén, M. C.; Montero, M. P. Improvement of the Antioxidant Properties of Squid Skin Gelatin Films by the Addition of Hydrolysates from Squid Gelatin. *Food Hydrocoll.* **2009**, *23* (5), 1322–1327. https://doi.org/10.1016/j.foodhyd.2008.09.010.

(154) Jiang, M.; Liu, S.; Du, X.; Wang, Y. Physical Properties and Internal Microstructures of Films Made from Catfish Skin Gelatin and Triacetin Mixtures. *Food Hydrocoll.* **2010**, *24* (1), 105–110. https://doi.org/10.1016/j.foodhyd.2009.08.011.

(155) Hoque, M. S.; Benjakul, S.; Prodpran, T. Properties of Film from Cuttlefish (Sepia Pharaonis) Skin Gelatin Incorporated with Cinnamon, Clove and Star Anise Extracts. *Food Hydrocoll.* **2011**, *25* (5), 1085–1097. https://doi.org/10.1016/j.foodhyd.2010.10.005.

(156) Bhat, R.; Karim, A. A. Towards Producing Novel Fish Gelatin Films by Combination Treatments of Ultraviolet Radiation and Sugars (Ribose and Lactose) as Cross-Linking Agents. *J. Food Sci. Technol.* **2014**, *51* (7), 1326–1333. https://doi.org/10.1007/s13197-012-0652-9.

(157) Fakhreddin Hosseini, S.; Rezaei, M.; Zandi, M.; Ghavi, F. F. Preparation and Functional Properties of Fish Gelatin-Chitosan Blend Edible Films. *Food Chem.* **2013**, *136* (3–4), 1490–1495. https://doi.org/10.1016/j.foodchem.2012.09.081.

(158) Zhang, Y.; Simpson, B. K.; Dumont, M. J. Effect of Beeswax and Carnauba Wax Addition on Properties of Gelatin Films: A Comparative Study. *Food Biosci.* **2018**, *26*, 88–95. https://doi.org/10.1016/j.fbio.2018.09.011.

(159) He, Q.; Zhang, Y.; Cai, X.; Wang, S. Fabrication of Gelatin-TiO2 Nanocomposite Film and Its Structural, Antibacterial and Physical Properties. *Int. J. Biol. Macromol.* **2016**, *84*, 153–160. https://doi.org/10.1016/j.ijbiomac.2015.12.012.

(160) Boughriba, S.; Souissi, N.; Jridi, M.; Li, S.; Nasri, M. Thermal, Mechanical and Microstructural Characterization and Antioxidant Potential of Rhinobatos Cemiculus Gelatin Films Supplemented by Titanium Dioxide Doped Silver Nanoparticles. *Food Hydrocoll.* **2020**, *103* (August 2019), 105695. https://doi.org/10.1016/j.foodhyd.2020.105695.

(161) Lin, D.; Yang, Y.; Wang, J.; Yan, W.; Wu, Z.; Chen, H.; Zhang, Q.; Wu, D.; Qin, W.; Tu, Z. Preparation and Characterization of TiO2-Ag Loaded Fish Gelatin-Chitosan Antibacterial Composite Film for Food Packaging. *Int. J. Biol. Macromol.* **2020**, *154*, 123–133. https://doi.org/10.1016/j.ijbiomac.2020.03.070.

(162) Nourbakhsh, S.; Talebian, A.; Faramarzi, S. Preparation and Characterization of Gelatin/ZnO Nano-Composite Film. *Mater. Today Proc.* **2017**, *4* (7), 7038–7043. https://doi.org/10.1016/j.matpr.2017.07.035.

(163) Wu, X.; Liu, Y.; Wang, W.; Han, Y.; Liu, A. Improved Mechanical and Thermal Properties of Gelatin Films Using a Nano Inorganic Filler. *J. Food Process Eng.* **2017**, *40* (3), 1–10. https://doi.org/10.1111/jfpe.12469.

(164) Hosseini, S. F.; Rezaei, M.; Zandi, M.; Farahmandghavi, F. Development of Bioactive Fish Gelatin/Chitosan Nanoparticles Composite Films with Antimicrobial Properties. *Food Chem.* **2016**, *194*, 1266–1274. https://doi.org/10.1016/j.foodchem.2015.09.004.

(165) Zhang, X.; Ye, T.; Meng, X.; Tian, Z.; Pang, L.; Han, Y.; Li, H.; Lu, G.; Xiu, F.; Yu, H. D.; Liu, J.; Huang, W. Sustainable and Transparent Fish Gelatin Films for Flexible Electroluminescent Devices. *ACS Nano* **2020**. https://doi.org/10.1021/acsnano.9b09880.

(166) Bhattacharyya, S. K.; Dule, M.; Paul, R.; Dash, J.; Anas, M.; Mandal, T. K.; Das, P.; Das, N. C.; Banerjee, S. Carbon Dot Cross-Linked Gelatin Nanocomposite Hydrogel for PH-Sensing and PH-Responsive Drug Delivery. *ACS Biomater. Sci. Eng.* **2020**, *6* (10), 5662–5674. https://doi.org/10.1021/acsbiomaterials.0c00982.

(167) Tuerhong, M.; XU, Y.; YIN, X. B. Review on Carbon Dots and Their Applications. *Chinese J. Anal. Chem.* **2017**, *45* (1), 139–150. https://doi.org/10.1016/S1872-2040(16)60990-8.

(168) Javanbakht, S.; Namazi, H. Solid State Photoluminescence Thermoplastic Starch Film Containing Graphene Quantum Dots. *Carbohydr. Polym.* **2017**, *176* (August), 220–226. https://doi.org/10.1016/j.carbpol.2017.08.080.

(169) Duan, R.; Zhang, J.; Du, X.; Yao, X.; Konno, K. Properties of Collagen from Skin, Scale and Bone of Carp (Cyprinus Carpio). *Food Chem.* **2009**, *112* (3), 702–706. https://doi.org/10.1016/j.foodchem.2008.06.020.

(170) Burjanadze, T. V. Thermodynamic Substantiation of Water-Bridged Collagen Structure. *Biopolymers* **1992**, *32*, 941–949. https://doi.org/https://doi.org/10.1002/bip.360320805.

(171) Bae, I.; Osatomi, K.; Yoshida, A.; Osako, K.; Yamaguchi, A.; Hara, K. Biochemical Properties of Acid-Soluble Collagens Extracted from the Skins of Underutilised Fishes. *Food Chem.* **2008**, *108* (1), 49–54. https://doi.org/10.1016/j.foodchem.2007.10.039.

(172) Cuq, B.; Aymard, C.; Cuq, J.-L.; Guilbert, S. Edible Packaging Films Based on Fish Myofibrillar Proteins: Formulation and Functional Properties. *J. Food Sci.* **1995**, *60* (6), 1369–1374. https://doi.org/10.1111/j.1365-2621.1995.tb04593.x.

(173) Fakhreddin Hosseini, S.; Rezaei, M.; Zandi, M.; Ghavi, F. F. Preparation and Functional Properties of Fish Gelatin-Chitosan Blend Edible Films. *Food Chem.* **2013**, *136* (3–4), 1490–1495. https://doi.org/10.1016/j.foodchem.2012.09.081.

(174) Niu, L.; Zhou, X.; Yuan, C.; Bai, Y.; Lai, K.; Yang, F.; Huang, Y. Characterization of Tilapia (Oreochromis Niloticus) Skin Gelatin Extracted with Alkaline and Different Acid Pretreatments. *Food Hydrocoll.* **2013**, *33* (2), 336–341. https://doi.org/10.1016/j.foodhyd.2013.04.014.

(175) Bradford, M. M. A Rapid and Sensitive Method for the Quantitation of Microgram Quantities of Protein Utilizing the Principle of Protein-Dye Binding. *Anal. Biochem.* **1976**, *72*, 248–254. https://doi.org/https://doi.org/10.1016/0003-2697(76)90527-3.

(176) Beghetto, V.; Gatto, V.; Conca, S.; Bardella, N.; Buranello, C.; Gasparetto, G.; Sole, R. Development of 4-(4,6-Dimethoxy-1,3,5-Triazin-2-Yl)-4-Methyl-Morpholinium Chloride Cross-Linked Carboxymethyl Cellulose Films. *Carbohydr. Polym.* **2020**, *249* (April), 116810. https://doi.org/10.1016/j.carbpol.2020.116810.

(177) Zolfi, M.; Khodaiyan, F.; Mousavi, M.; Hashemi, M. Development and Characterization of the Kefiran-Whey Protein Isolate-TiO2 Nanocomposite Films. *Int. J. Biol. Macromol.* **2014**, *65*, 340–345. https://doi.org/10.1016/j.ijbiomac.2014.01.010.

(178) Hatakeyama, T.; Quinn, F. X. *Thermal Analysis: Fundamentals and Applications to Polymer Science*; John Wiley & Sons Ltd., C., Ed.; 1999. https://doi.org/10.1016/0040-6031(95)91503-6.

(179) Muzzarelli, R. A. A.; Boudrant, J.; Meyer, D.; Manno, N.; Demarchis, M.; Paoletti, M. G. Current Views on Fungal Chitin/Chitosan, Human Chitinases, Food Preservation, Glucans, Pectins and Inulin: A Tribute to Henri Braconnot, Precursor of the Carbohydrate Polymers Science, on the Chitin Bicentennial. *Carbohydr. Polym.* **2012**, *87* (2), 995–1012. https://doi.org/10.1016/j.carbpol.2011.09.063.

(180) Yadav, M.; Goswami, P.; Paritosh, K.; Kumar, M.; Pareek, N.; Vivekanand, V. Seafood Waste: A Source for Preparation of Commercially Employable Chitin/Chitosan Materials. *Bioresour. Bioprocess.* **2019**, *6* (8). https://doi.org/10.1186/s40643-019-0243-y.

(181) Cho, Y. W.; Jang, J.; Park, C. R.; Ko, S. W. Preparation and Solubility in Acid and Water of Partially Deacetylated Chitins. *Biomacromolecules* **2000**, *1* (4), 609–614. https://doi.org/10.1021/bm000036j.

(182) Zhu, K. Y.; Merzendorfer, H.; Zhang, W.; Zhang, J.; Muthukrishnan, S. Biosynthesis, Turnover, and Functions of Chitin in Insects. *Annu. Rev. Entomol.* **2016**, *61*, 177–196. https://doi.org/10.1146/annurev-ento-010715-023933.

(183) Pillai, C. K. S.; Paul, W.; Sharma, C. P. Chitin and Chitosan Polymers: Chemistry, Solubility and Fiber Formation. *Prog. Polym. Sci.* **2009**, *34* (7), 641–678. https://doi.org/10.1016/j.progpolymsci.2009.04.001.

(184) Younes, I.; Rinaudo, M. Chitin and Chitosan Preparation from Marine Sources. Structure, Properties and Applications. *Mar. Drugs* **2015**, *13* (3), 1133–1174. https://doi.org/10.3390/md13031133.

(185) Aranaz, I.; Mengibar, M.; Harris, R.; Panos, I.; Miralles, B.; Acosta, N.; Galed, G.; Heras, A. Functional Characterization of Chitin and Chitosan. *Curr. Chem. Biol.* **2009**, *3*, 203–230. https://doi.org/10.2174/2212796810903020203.

(186) Vázquez, J. A.; Rodríguez-Amado, I.; Montemayor, M. I.; Fraguas, J.; Del González, M. P.; Murado, M. A. Chondroitin Sulfate, Hyaluronic Acid and Chitin/Chitosan Production Using Marine Waste Sources: Characteristics, Applications and Eco-Friendly Processes: A Review. *Mar. Drugs* **2013**, *11* (3), 747–774. https://doi.org/10.3390/md11030747.

(187) Rinaudo, M. Chitin and Chitosan: Properties and Applications. *Prog. Polym. Sci.* **2006**, *31* (7), 603–632. https://doi.org/10.1016/j.progpolymsci.2006.06.001.

(188) Cauchie, H. M. Chitin Production by Arthropods in the Hydrosphere. *Hydrobiologia* **2002**, *470*, 63–95. https://doi.org/10.1023/A:1015615819301.

(189) El Knidri, H.; Belaabed, R.; Addaou, A.; Laajeb, A.; Lahsini, A. Extraction, Chemical Modification and Characterization of Chitin and Chitosan. *Int. J. Biol. Macromol.* **2018**, *120*, 1181–1189. https://doi.org/10.1016/j.ijbiomac.2018.08.139.

(190) Rudall, K. M.; Kenchington, W. The Chitin System. *Biol. Rev. Camb. Philos. Soc.* **1973**, *48* (4), 597–633. https://doi.org/10.1111/j.1469-185x.1973.tb01570.x.

(191) Blackwell, J.; Parker, K. D.; Rudall, K. M. Chitin in Pogonophore Tubes. *J. Mar. Biol. Assoc. U.K.* **1965**, *45* (3), 659–661. https://doi.org/10.1017/S0025315400016489.

(192) Kurita, K. Controlled Functionalization of the Polysaccharide Chitin. *Prog. Polym. Sci.* **2001**, *26* (9), 1921–1971. https://doi.org/10.1016/S0079-6700(01)00007-7.

(193) Minke, R.; Blackwell, J. The Structure of α-Chitin. *J. Mol. Biol.* **1978**, *120* (2), 167–181. https://doi.org/10.1016/0022-2836(78)90063-3.

(194) Lusena, C. V.; Rose, R. C. Preparation and Viscosity of Chitosans. *J. Fish. Res. Board Canada* **1953**, *10* (8), 521–522. https://doi.org/10.1139/f53-029.

(195) Synowiecki, J.; Al-Khateeb, N. A. Production, Properties, and Some New Applications of Chitin and Its Derivatives. *Crit. Rev. Food Sci. Nutr.* **2003**, *43* (2), 145–171. https://doi.org/10.1080/10408690390826473.

(196) Chatelet, C.; Damour, O.; Domard, A. Influence of the Degree of Acetylation on Some Biological Properties of Chitosan Films. *Biomaterials* **2001**, *22* (3), 261–268. https://doi.org/10.1016/S0142-9612(00)00183-6.

(197) Li, J.; Revol, J. F.; Marchessault, R. H. Effect of Degree of Deacetylation of Chitin on the Properties of Chitin Crystallites. *J. Appl. Polym. Sci.* **1997**, *65* (2), 373–380. https://doi.org/10.1002/(sici)1097-4628(19970711)65:2<373::aid-app18>3.3.co;2-n.

(198) Percot, A.; Viton, C.; Domard, A. Optimization of Chitin Extraction from Shrimp Shells. *Biomacromolecules* **2003**, *4* (1), 12–18. https://doi.org/10.1021/bm025602k.

(199) Abdou, E. S.; Nagy, K. S. A.; Elsabee, M. Z. Extraction and Characterization of Chitin and Chitosan from Local

Sources. *Bioresour. Technol.* **2008**, *99* (5), 1359–1367. https://doi.org/10.1016/j.biortech.2007.01.051.

(200) Sagheer, F. A. A.; Al-Sughayer, M. A.; Muslim, S.; Elsabee, M. Z. Extraction and Characterization of Chitin and Chitosan from Marine Sources in Arabian Gulf. *Carbohydr. Polym.* **2009**, *77* (2), 410–419. https://doi.org/10.1016/j.carbpol.2009.01.032.

(201) Tolaimate, A.; Desbrieres, J.; Rhazi, M.; Alagui, A. Contribution to the Preparation of Chitins and Chitosans with Controlled Physico-Chemical Properties. *Polymer.* **2003**, *44* (26), 7939–7952. https://doi.org/10.1016/j.polymer.2003.10.025.

(202) Waśko, A.; Bulak, P.; Polak-Berecka, M.; Nowak, K.; Polakowski, C.; Bieganowski, A. The First Report of the Physicochemical Structure of Chitin Isolated from Hermetia Illucens. *Int. J. Biol. Macromol.* **2016**, *92*, 316–320. https://doi.org/10.1016/j.ijbiomac.2016.07.038.

(203) Kaur, S.; Dhillon, G. S. Recent Trends in Biological Extraction of Chitin from Marine Shell Wastes: A Review. *Crit. Rev. Biotechnol.* **2015**, *35* (1), 44–61. https://doi.org/10.3109/07388551.2013.798256.

(204) Khanafari, A.; Marandi, R.; Sanatei, S. Recovery of Chitin and Chitosan from Shrimp Waste by Chemical and Microbial Methods. *Iran. J. Environ. Heal. Sci. Eng.* **2008**, *5* (1), 19–24.

(205) Shamshina, J. L.; Barber, P. S.; Gurau, G.; Griggs, C. S.; Rogers, R. D. Pulping of Crustacean Waste Using Ionic Liquids: To Extract or Not to Extract. *ACS Sustain. Chem. Eng.* **2016**, *4* (11), 6072–6081. https://doi.org/10.1021/acssuschemeng.6b01434.

(206) Harlıoğlu, M. M.; Farhadi, A.; Ateş, A. S. A Review of the Marine Crab Fisheries in the Turkish Seas. *Ribar. Croat. J. Fish.* **2018**, *76* (3), 125–134. https://doi.org/10.2478/cjf-2018-0016.

(207) FAO. Fishbase Report. http://Www.Fishbase.Org/Report/FAO/FAOCatchList.Php?C_code=&areacode=&scientific=Maja+squi Nado&english=&yc=00. **2018**, (Accessed September 2022).

(208) Fischer, W.; Bauchot, M.-L.; Schneider, M. Fiches FAO d'identification Desespèces Pour Les Besoins de La Pêche (Révision 1). Méditerranée et Mer Noire. Zone de Pêche. Végétaux et Invertébrés. FAO, Rome. **1987**, *1*, 1–760.

(209) Pires, C.; Marques, A.; Carvalho, M. L.; Batista, I. Chemical Characterization of Cancer Pagurus, Maja Squinado, Necora Puber and Carcinus Maenas Shells. *Poultry, Fish. Wildl. Sci.* **2017**, *5* (1), 1000181. https://doi.org/10.4172/2375-446x.1000181.

(210) Galed, G.; Diaz, E.; Goycoolea, F. M.; Heras, A. Influence of N-Deacetylation Conditions on Chitosan Production from α-Chitin. *Nat. Prod. Commun.* **2008**, *3* (4), 543–550. https://doi.org/10.1177/1934578x0800300414.

5. Supercritical CO_2 Extractions

Supercritical Fluids Extractions (SFE) were developed in the mid-1980s for analytical applications with the aim to reduce the use of organic solvents and, nowadays, they offer an alternative method to conventional extraction techniques. Supercritical carbon dioxide (sc-CO_2) is the most widely used thanks to its outstanding properties. Indeed, sc-CO_2 is non-toxic, non-flammable, non-corrosive, recoverable and easy to handle. In addition, CO_2 is cheap, readily available with high purity degree and easily removable from the final products. This chapter presents the sc-CO_2 technique, its advantages and uses and reports two works developed by the author: extraction of antibacterials and of fatty acids from two different types of agro-waste.

5.1 Introduction: technique, advantages and uses

Carbon dioxide (CO_2) was firstly recognized as a distinct gas from Van Helmont only in the XVII century, despite its existence has been known for over thousands of years. Even though the high natural occurrence of CO_2 in the Earth's lithosphere, hydrosphere and atmosphere, it is nowadays seen prevalently as an issue due to its massive anthropogenic production for electricity, heat production, transport and industrial uses. This reason led to progressive research and increased interest in using carbon dioxide: different studies are now centred on its exploitation for the production of chemicals, fuels or construction materials. Another way to give value to CO_2 is to use it as a solvent to perform extractions in opposition to classical extractive techniques. The increase in the public awareness about health, environmental and safety hazards associated with the use of organic solvents is, in fact, giving more and more importance in finding extractive techniques that can replace the conventional ones. Indeed, the cost of organic solvents, new stringent environmental regulations and the requirement of the food and medical industries for pure compounds are increasing the need for the development of greener technologies.[1] Supercritical Fluids Extraction (SFE) is gaining considerable attention as a valuable substitute for conventional solvent extractions and its great number of potential applications is already part of the present scenery and continues to grow. For example, its use is spread from the pharmaceutical to the food, cosmetical and materials industry but also in the field of toxicology, chemistry, environment, textile and polymers among others.[2] The increase in the application of this technology is mainly due to the selectivity and separation capacity that it allows leading to the obtainment of a great number of organic compounds non-viable to extract with traditional processes. Summing up, the great interest of both scientific community and industries must be directly related to the restrictions to the use of organic solvents and a higher ecological consciousness but also to the high selectivity of the technique and its short extraction times.[3,4] SFE is based on the solvating properties of supercritical fluid, which can be obtained by employing pressure and temperature above the critical point. Every fluid is, in fact, characterized by a certain critical point defined in terms of critical temperature (T_c) and critical pressure (P_c). A substance above its T_c and P_c is to be considered as a supercritical fluid. A supercritical fluid exhibits physicochemical properties that lay in between those of a gas and a liquid, having density similar to that of a liquid and viscosity similar to that of gas.[5] Some of the solvents most commonly used as SFs, their T_c and P_c are reported in **Table 5.1.1**.

Table 5.1.1. Most common solvents used as SFs, critical temperature and critical pressure.

Substance	T_c (°C)	P_c (MPa)
Ethylene	9.4	5.04
Carbon dioxide	31.1	7.38
Ethane	32.3	4.87
Nitrous oxide	36.6	7.26
Propane	96.8	4.25
n-Hexane	234.5	3.01
Acetone	235.1	4.70
Methanol	239.6	8.09
Ethanol	240.9	6.14
Ethyl acetate	250.2	3.83
Water	374.1	22.06

By proper controlling of SFE parameters, the extractability of supercritical fluid can also be modified which enable this process to be applied in a plethora of different fields. Supercritical fluids have an outstanding ability to dissolve compounds that varies with the density of the fluid depending, so, on small changes in pressure and/or temperature. Also transport properties have a strict correlation with density, leading to the possibility to vary them easily, unlike liquid solvents.[6,7] Together with the dissolving power, another important parameter of supercritical fluids is their penetration ability. The low viscosity and high diffusivity of this fluids enhance, indeed, this property allowing an efficient extraction of the compounds from raw materials. The high-density values combined with the pressure dependent solvent power provides high solubility and selectivity to the supercritical fluid. In addition, low viscosity and intermediate values of diffusivity combined with the absence of surface tension allow the penetration of the SF into the cells and particles of the sample matrix extracting their interior material,[8,9] facilitating the extraction process of vegetal such as plants or algae.[10] Summarizing, the most important properties of SFs are density, viscosity, diffusivity, heat capacity and thermal conductivity. On one hand the low viscosity enables penetration of the fluid into solids and allow for flow with less friction, on the other hand the high densities of SFs contributes to greater solubilisation of compounds.[11] The manipulation of temperature and pressure above the critical point modifies the properties of SFs enhancing their ability to penetrate and extract targeted molecules from a plethora of different matrixes.[12] The SFE of targeted components from plant matrix undergoes, similarly to conventional techniques, to several parameters like pre-treatment of the biomass, particle size, temperature, pressure, time, solvent flow rate and solvent to feed ratio.[13]

Recently, SFE received particular attention specially in the fields of solid materials extractions and fractionation of liquid mixtures. Indeed, SFs are easily adaptable to separation processes: thanks to their characteristic they can be used to separate unstable materials (e.g. oils and polyunsaturated fatty acids, vitamins, antioxidants…) at low temperatures. In addition, it is possible to perform separations even with small variations of pressure, thanks to the exponential behaviour and high compressibility of the fluids.[14] Nowadays, the possibility to extract and fractionate oils is receiving widespread interest thanks to the direct application in industries, in particular food and pharmaceutical, for the generation of high added value products. Moreover, the possibility to work at lower temperatures, that can be responsible for the destruction of valuable substances, and the avoidance of product contamination with solvent residues[15] are contributing to candidate SFEs as a promising alternative to conventional extraction techniques. Nowadays, SFEs are used in different industrial applications including coffee decaffeination, fatty acid refining and essential oils and flavours extraction from natural sources.[16] One of the main disadvantages of SFE is the initial investment cost of its implantation. However, since the 1970s, this cost was offset by the establishment of several commercial plants for the decaffeination of coffee that is able to produce a valuable extract (caffeine) together with a high-value raffinate product (decaffeinated coffee beans).

Between the wide range of compounds that can be used as SFs, supercritical carbon dioxide ($scCO_2$) has gained considerable attention as a promising candidate to pave the way towards more sustainable extractions [17]. CO_2 is non-toxic, non-flammable, non-polluting, completely recoverable, inert and cheap[3,18,19] and it is readily available in bulk quantities with high purity degrees.[20] In addition, its critical conditions (T_c = 31.1 °C and P_c = 7.38 MPa, see **Figure 5.1.1**) are relatively safe and easy to reach, making it appropriate for the extraction of volatile or heat sensitive compounds.[21]

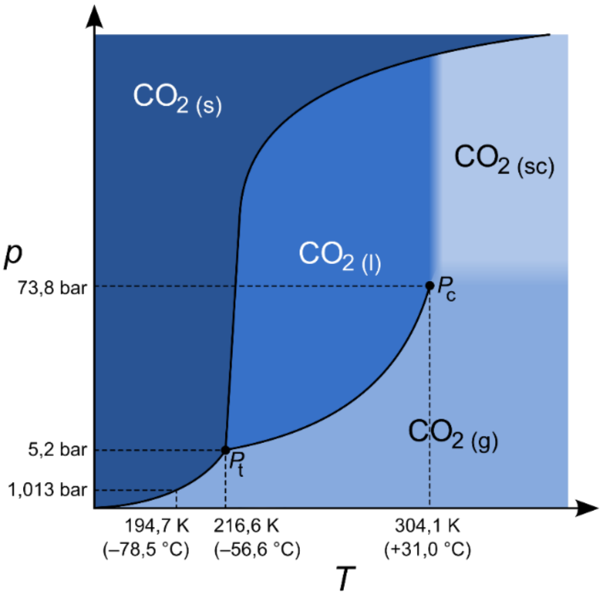

Figure 5.1.1. Phase diagram for carbon dioxide.

The solubility of a compound in $scCO_2$ is strictly dependent on temperature and pressure due to their influence on density and, as consequence, on solvent power. An increase in the pressure value leads to liquid-like density $scCO_2$ improving the probability of interactions between solute and solvent, thus leading to notable increases in solubility. On the other hand, increasing the temperature would cause a decrease in the SF density, while the vapor pressure of the solute would increase. The synergic effect of these two factors is the key to understand and manipulate the changes in solubility. At pressures close to the critical value, the decrease in density is so evident that an increase of the temperature would lead in a decrease in solubility, whereas working at higher pressures the vapor pressure effect takes over (since the density drop is relatively smaller) resulting in an enhanced solubility.[22] The properties of the solute, in particular its molecular weight, polarity and vapor pressure, strongly influence its solubility in $scCO_2$. The solubility is, indeed, influenced both by solute-solvent and solute-solute interactions. $ScCO_2$, due to its non-polar nature, solubilize preferentially apolar or weakly polar compounds such as lipids, cholesterol, aldehydes, esters and ketones. An increase in the molecular size, moreover, causes a decrease in the solubility of a molecule in $scCO_2$, so, high molecular weight polar substances such as polysaccharides, amino acids and proteins, are relatively insoluble (**Table 5.1.2**). Thus, high selectivity can be obtained simply modifying temperature and pressure of the system, which is one of the major advantages of $scCO_2$ extraction technology.

Table 5.1.2. Solubility of different compounds in sc-CO_2.

Highly soluble				**Moderately soluble**				**Poorly soluble**			
- High volatile substances (e.g. aromas and flavouring) - Organic compounds with low polarity and MW (< 250 g/mol)				- Substances with low volatility - Polar organic compounds with MW lower than 400 g/mol				- Non-volatile substances - Highly polar organic compounds with MW > 400 g/mol			
Name	**T (°C)**	**P (bar)**	**Solubility (mole fraction)**	**Name**	**T (°C)**	**P (bar)**	**Solubility (mole fraction)**	**Name**	**T (°C)**	**P (bar)**	**Solubility (mole fraction)**
β-carotene[23]	40	260	$5.5 \cdot 10^{6}$	Water[24]	50	200	$10.2 \cdot 10^{3}$	Paracetamol[25]	80	250	$1.5 \cdot 10^{-5}$
Squalene[26]	60	250	$46 \cdot 10^{3}$	Glycerol[26]	60	280	$0.08 \cdot 10^{3}$	Hydroquinone[27]	35	200	$9.1 \cdot 10^{-6}$

Anyway, it is possible to modify the solubility of these compounds in carbon dioxide also by the use of co-solvents that are able to increase the polarity of the SF.[28] A co-solvent is a solvent that has an intermediate volatility between the supercritical fluid and the target compound. Usually, co-solvents are liquids at ambient conditions, but gases can also be used, they must be miscible with the SF and compose only a small percentage of the total fluid composition. Co-solvents can enhance the solubility of the compound of interest by specific chemical interaction with the solute (by hydrogen bonds) as well as by interactions with the solvent (by increasing the density).[29] Between the most used co-solvents we can enumerate ethanol, methanol, isopropanol and acetonitrile.[30] One of the main problems in the use of co-solvents can be, however, the difficulty in separating it from the product after the extraction while sc-CO_2 become gaseous after depressurization and is easily removed from the system.[31]

5.2 Supercritical CO_2 extraction of natural antibacterials from low-value weeds and agro-waste

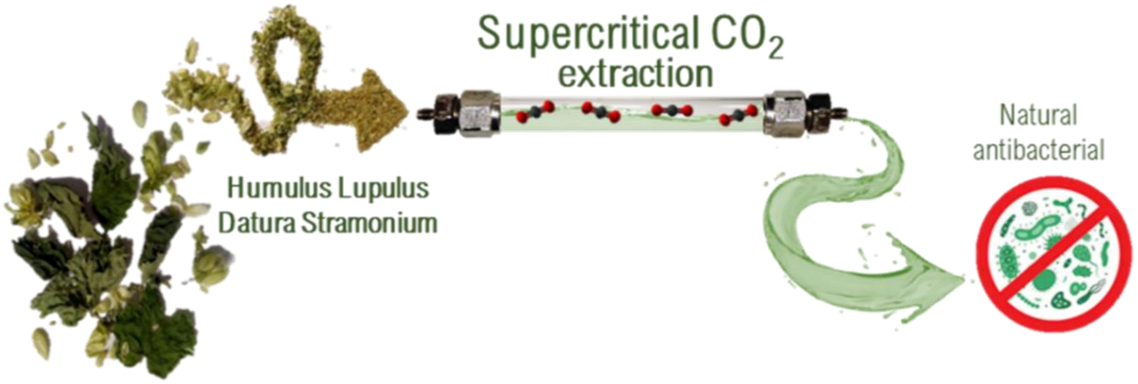

In this chapter, another way of valorising waste biomass was explored. The idea of circularity, indeed, prompted us to widen the possibilities of recycling different type of waste to give them an additional value. In particular agro-waste was used for the $scCO_2$ extraction of natural preservatives and the results herein reported are published in C. Campalani, F. Chioggia, E. Amadio, M. Gallo, F. Rizzolio, M. Selva and A. Perosa, *J. CO_2 Util.*, **2020**, 40, 101198. doi: 10.1016/j.jcou.2020.101198.[32]

The suitability of two different types of agro-waste, namely Datura stramonium and Humulus lupulus, were investigated for the extraction of preservatives using supercritical carbon dioxide ($scCO_2$). The antibacterial activity was evaluated against Escherichia coli with the perspective of using the extracts in cosmetic formulations. Both leaves and flowers were used as the starting materials and the essential oils obtained from $scCO_2$ extractions have been compared, in terms of composition and antibacterial activity, to the one obtained using a classical method: Soxhlet extraction using ethanol. The two techniques resulted to be very different in yields, selectivity, composition and antibacterial properties. In general, $scCO_2$ led to the selective extraction of volatile compounds, such as terpenes, terpenoids, bitter acids and fatty acids, resulting in a better recovery for preservatives.

5.2.1 Introduction

The majority of cosmetics and personal-care formulations are produced on organic- and water-base and, for this reason, are easily attacked and degraded by a plethora of microorganisms. In order to prevent microbial proliferation, prolong shelf-life and avoid health related issues, cosmetics must contain a certain amount of preservatives. Indeed, the microbial contamination can cause the spoilage of the product, ultimately leading to consumers being infected by the microorganism.[33] Anyway, the regulations about cosmetic products are becoming more and more stringent during the last years as can be seen in the last version (01-03-2022) of the "Regulation of the European Parliament on cosmetic products"[34] were a notable list of prohibited and restricted substances is present. In addition, environmental problems and a growing demand for improved biocompatibility are prompting replacement of the commonly used synthetic preservatives with natural antiseptic compounds. Another possible problem due to the presence of synthetic preservatives in formulations can be the development of allergic contact dermatitis,[35] sensory skin irritation, or other adverse effects in the users.[36] A huge number of cosmetic preservatives are nowadays available, both alone and in pre-prepared combinations, but the market is still dominated by a small number of compounds. Among the most frequently used preservatives there are: phenoxyalcohols (in particular phenoxyethanol), formaldehyde releasers (e.g. imidazolidinyl urea, diazolidinyl urea, tris(hydroxymethyl) nitromethane and others), *p*-hydroxybenzoic acid esters (parabens), isothiazolinones (in particular methylchloroisothiazolinone/methylisothiazolinone), quaternary ammonium compounds and organic acids (**Figure 5.2.1**). For example, phenoxyethanol is found approximately in almost 20% of registered products in the United States;[37] it is non-toxic to humas when administrated orally or percutaneously but, due to its relatively low antimicrobial activity, it is usually used in combination with other preservatives. Also parabens are widely spread both in cosmetics and in foods, they are rapidly absorbed and metabolized and have a very effective antimicrobial effect, but are considered to be cause of sensory skin irritation in cosmetics.[38] Methylchloroisothiazolinone/methylisothiazolinone (MCI/MI) and the formaldehyde releaser diazolidinyl urea are used approximately in 5% of cosmetic products, being the 9th and 10th most frequently used cosmetic preservative. By the way, MCI/MI, diazolidinyl urea and methylisothiazolinone alone are all frequent causes of allergic contact dermatitis.[39,40]

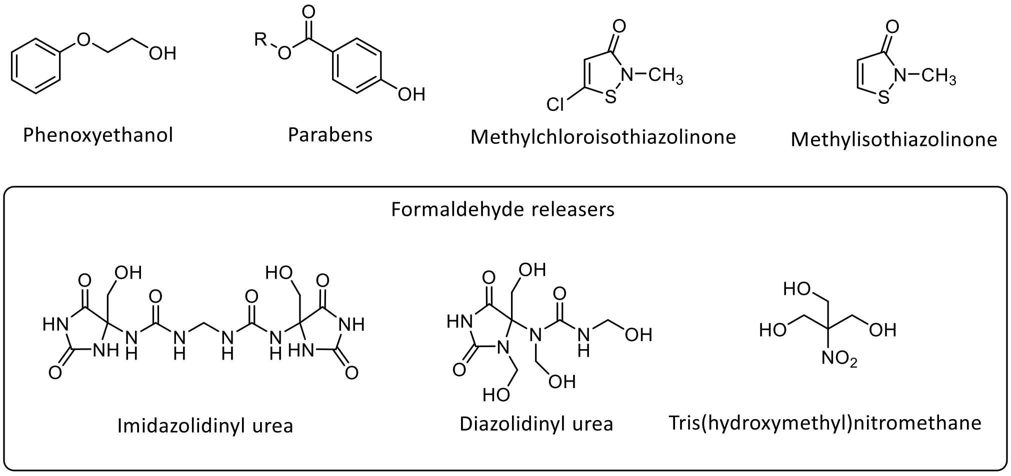

Figure 5.2.1. Structure of the most common synthetic cosmetic preservatives.

Plants, and more specifically their essential oils, are considered as one of the main sources of natural preservatives and several authors have proposed their use as natural conservation agent, alone or in combination with other compounds.[41,42] The use of essential oils in the production of cosmetics and related products may have several advantages, assuring protection against microorganisms and, in some instances, enhancing the dermato-cosmetic properties and preservation of the final product.[43] These substances are volatile liquids with variable viscosity, constituted typically by monoterpenes, terpenes, terpenoids, polyphenols and low molecular weight aromatic compounds.[44,45,46] Much of the antimicrobial activity of plant extracts and essential oils is attributed to their content of phenolic compounds, mainly flavonoids and derivatives, and of terpenes (**Figure 5.2.2**). In particular, flavonoids can interact with lipid bilayers and perturb plasma membrane functionality. The interaction of polyphenols with bacterial plasma membranes can trigger a plethora of effects that contribute to their antibacterial behaviour.[47] The disruption of the plasma membrane can, for example, cause the formation of pores, leakage, alter polarity, increase permeability, delocalize membrane proteins and other phenomena.[47] The antimicrobial mechanism of polyphenols that interact with membranes seems to revolve around the disruption of the latter by accumulation of hydroxyl groups that alters the hydrophobicity and surface charge of the membrane.[48,49] For example, polyphenols such as galloyl catechins are able to intercalate in membranes, reaching a deep position in the lipidic bilayer and causing remarkable biophysical changes to its structure.[50] Concerning the antimicrobial activity related to the presence of terpenes, this is, at the same way, attributed to their interaction with the membranes but the specific mechanism remains poorly understood.[51] The proposed specific molecular mechanism of action depends on the structure of the various terpenes. Certain terpenes, such as carvacrol, which have a phenolic hydroxyl group, can cross the bacterial plasma membrane, bind molecules (such as ATP) or monovalent cations (such as K^+) and transport them outside the bacterial cell, affecting the membrane potential and homeostasis.[52,53] Other terpenes, like thymol, can incorporate into the polar-head region of the lipid bilayer affecting its structural integrity and fluidity.[54] Another hypothesis is that terpenes have the ability to modify the lipid profile of the bacterial plasma membrane, inducing an increase in the presence of saturated fatty acids leading to an increased rigidity, probably triggered in response to the fluidifying action cited above.[55] All the cited phenomena cause membrane depolarization, reduced respiratory activity, loss of membrane integrity and coagulation of cytoplasmatic material.[56] In general, although a lower antimicrobial activity is usually observed for natural plant extracts than for synthetic compounds, some of them are very powerful probably for the synergistic effect among more components.[57,58,59,60]

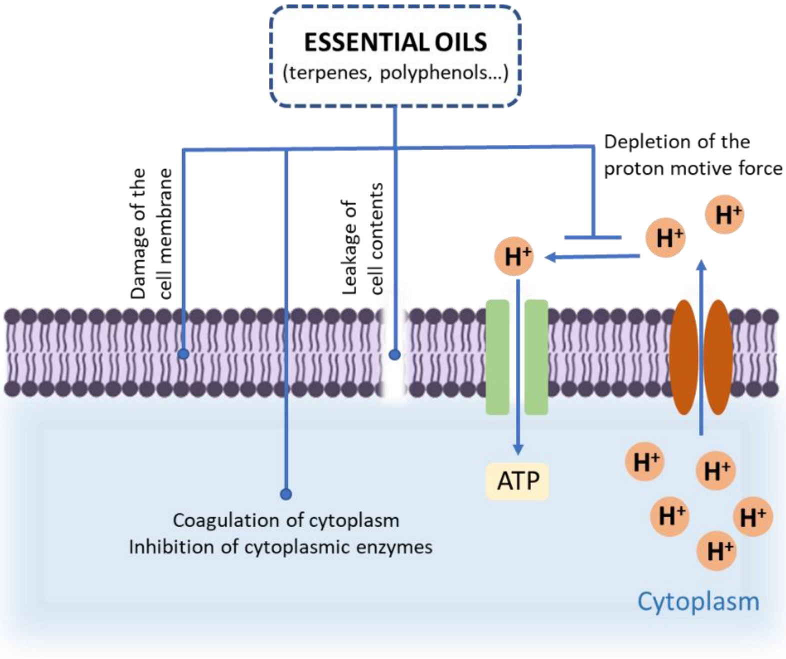

Figure 5.2.2 Antibacterial mechanisms of natural essential oils, specifically of terpenes and polyphenols.

With this in mind, we decided to investigate the extraction of natural preservatives from *Humulus lupulus* (hops) and *Datura stramonium* (jimsonweed). These two botanical species were chosen for their widespread availability and low value, belonging to the class of agricultural and agroindustrial waste. Both plants are known to be a natural reservoir of compounds with proven antiseptic properties[61,62,63,64,65,66,67] such as fatty acids, terpenes and terpenoids.[45,68,69] *Humulus lupulus* is a perennial herbaceous species of flowering plant belonging to the hemp family of *Cannabacee*, native to Europe, western Asia and North America, that can grow up to 10 meters and live up to 20 years (**Figure 5.2.3**). Over the last decades, hops flowers were intensively used for the extraction of its essential oil using different extractive techniques. Many works reported the extraction using conventional or microwave-assisted hydrodistillation,[61,70] $scCO_2$,[71,72,73,74,75] solid phase microextraction[76] or Soxhlet extraction with organic solvents.[75]

Figure 5.2.3. Picture of leaves and flowers of hops plant.

The flowers of this plants are used since ancient times to preserve and give flavour and bitterness to beer, so hops is widely cultivated from brewing industry. In addition, this common plant was used also as sedative, against sexual disorders, as appetisers and topically against neuralgic, rheumatic or arthritic pain. Through their wide range of biological and pharmacological effects, hops acids have proved interesting abilities for the treatment or the prevention of several human disorders, such as cancer, diabetes mellitus, osteoarthritis, cardio-vascular disease and osteoporosis.[77] Nowadays the crucial importance of hops in beer production, led to an extensive study on its intrinsic preservative properties. The antibacterial activity of hops extracts is mainly directed towards Gram-positive bacteria[62,63] and it is attributed to bitter acids, in particular humulone and lupulone (**Figure 5.2.4**).[78] The activity against Gram-positive bacteria (e.g. Micrococcus Staphylococcus, Mycobacterium and Streptomycetes) has been thought to involve primary membrane leakage, due to interaction of the hydrophobic parts of the molecules with the bacterial cell wall. To date, the most used and valorized part of *Humulus lupulus* is composed by the flowers; on the other hand, the leaves are usually discarded as a waste. However, it is known that also this part contains valuable volatile compounds and their use to obtain high-added value products seems to be an interesting topic to explore in the circular economy.[79,70,80,81]

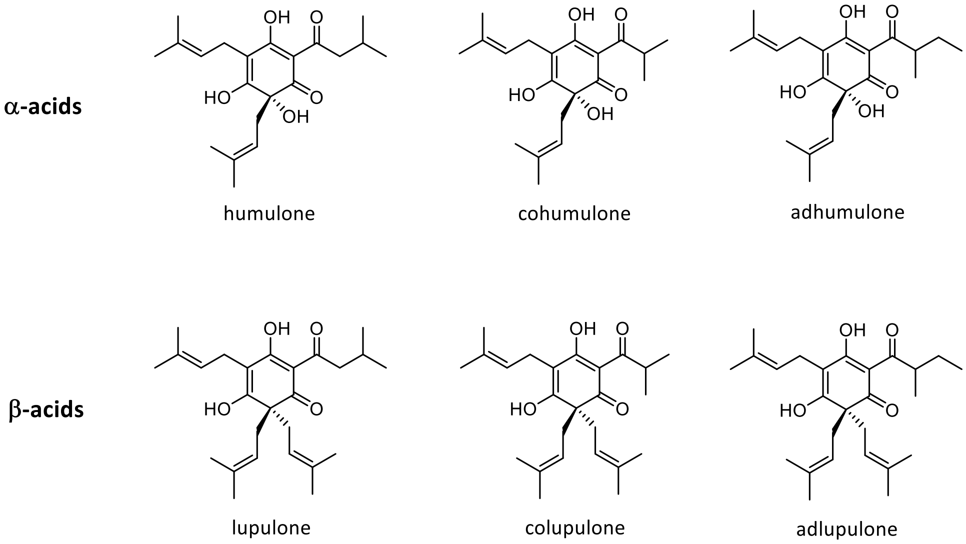

Figure 5.2.4. Chemical structure of hops bitter acids.

Datura stramonium, or jimsonweed, is an erect, annual, invasive, night-blooming plant of the *Solanacee* family (**Figure 5.2.5**). It is an aggressive invasive weed which grows forming bushes from 60 up to 150 cm, original from Central America but now it is widely spread worldwide. Having biologically active molecules in all its part, jimsonweed has frequently been employed in traditional medicine. In addition, it has been used as a hallucinogen since it is able to give a state of deep and long-lasting disorientation or delirium with potentially fatal outcome. Indeed, *Datura stramonium* contains a plethora of different compounds such as saponins, flavonoids, sterols, coumarins, quinines and a variety of alkaloids: molecules with a strong physiological and psychoactive effect that can lead to poisoning and death even in small doses.[82,83] However, jimsonweed is usually an undesired presence, especially in cultivated crops, and it is so discarded as agricultural waste. Many researches have been conducted on its toxicity and pharmacology[84,85,86] but, to our knowledge, only few reports are focused on the antibacterials activity of jimsonweed extracts obtained through maceration with organic solvents and/or water.[64,65,66,87,88]

Figure 5.2.5. Picture of leaves and flowers of jimsonweed plant.

In this work we aimed to valorise these two common agricultural wastes (*Humulus lupulus* leaves and *Datura stramonium* as a whole) by upgrading them to sources of antibacterial molecules exploiting a $scCO_2$ extraction protocol. To this end, the supercritical extraction methodology was firstly optimized using hops flowers (or cones) and then implemented to obtain the volatile fractions from hops leaves and from jimsonweed. The as obtained extracts were then characterized in order to investigate the chemical composition and antibacterial activity and to find out the bioactive compounds. A comparison in terms of composition and preservative efficacy was then performed between the $scCO_2$ extracts and ones obtained by conventional Soxhlet extraction using ethanol as the solvent. This last technique is known as a poorly selective albeit intensive extraction method, hardly sustainable in the industrial scale.[3,89]

5.2.2 Results and Discussion

Humulus lupulus

The investigation started with preliminary experiments to identify the optimal conditions for the $scCO_2$ extractions. Using hops flowers (3g in a typical run) the different parameters were changed in order to find the most suitable ones (See **Table 5.2.1**). In particular, several experiments were conducted changing the pressure of the system (that leads to a change in the density of the solvent), the CO_2 flow, and consequently the space velocity, and the extraction time. The space velocity can be described as the ratio between the volumetric flow of CO_2 (mL/min) and the volume of the used extractor (mL). As can be seen in **Table 5.2.1** and **Figure 5.2.6**, the results indicated that the extraction yields increased with increasing pressure, time and volumetric carbon dioxide flow. The highest extract final yield (8.6%) was achieved at 70°C, 300 bar, 5 mL/min of $scCO_2$ flow and after 5 h of extraction (entry 5, **Table 5.2.1**). It is interesting to notice that the curves obtained for the extraction at different pressures and flows showed a behaviour which correlates with the density of the fluid and the space velocity, used as a reactor design parameter (**Figure 5.2.6**).

Table 5.2.1 Experimental conditions and extraction yields (%) of the *Humulus lupulus* flowers with $scCO_2$ as solvent.

Entry	P (bar)	Density (g/mL)^a	Flow (mL/min)	Space velocity (min^{-1})^b	Time (h)	Yield$_{extract}$ (%)^c
1	100	0.248	5	0.5	5	2.3
2	150	0.506	5	0.5	5	5.6
3	200	0.659	5	0.5	5	7.2
4	250	0.737	5	0.5	5	8.1
5	300	0.788	5	0.5	5	8.6
6	300	0.788	5	0.5	4	8.2
7	300	0.788	5	0.5	3	7.8
8	300	0.788	5	0.5	2	7.4
9	300	0.788	5	0.5	1	6.7
10	300	0.788	5	0.5	5	5.9
11	300	0.788	4	0.4	5	5.2
12	300	0.788	3	0.3	5	6.1
13	300	0.788	2	0.2	5	6.9
14	300	0.788	1	0.1	5	7.8

Extraction conditions: 3 g of dry *Humulus lupulus* flowers, using a $scCO_2$ extractor with an internal volume of approximately 10 cm^3, bed diameter 3/8 and bed height of 15 cm. a) Density of pure CO_2 calculated using the Equation of State by Span and Wagner.[90] b) Space Velocity (min^{-1}) = Volumetric flow (mL/min)/Extractor Volume (mL). c) Amount of compounds extracted on weight of the sample used (% wt /wt $_{biomass}$).

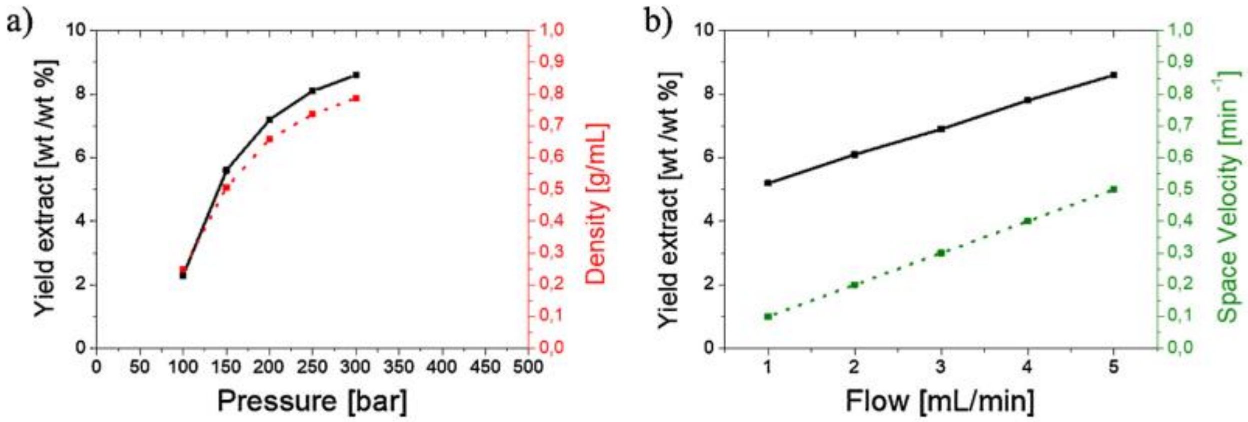

Figure 5.2.6. Effect of a) the pressure and b) the volumetric flow on the extraction yields of the *Humulus lupulus* flowers and their correlation with the CO_2 density and the space velocity.

Under the optimized conditions found with the preliminary tests, the $scCO_2$ extraction procedure was extended to hops leaves, usually discarded as a waste after the harvest. The yields of the $scCO_2$ extracts were then compared to the ones obtained by Soxhlet extraction using ethanol as the solvent for 24h. Although hexane is known to lead to yields and selectivity very similar to those obtained with $scCO_2$, we decided to use ethanol for the traditional extractions. The main reason for this choice is that the extracts are here proposed as antimicrobial additives for cosmetics and, while ethanol is allowed, hexane is banned due to its toxicological properties. 24 hours was selected as time for the Soxhlet procedure since it ensures complete extraction of all the components. Yields comparisons are reported in **Table 5.2.2**.

Table 5.2.2. Extraction yields of hops flowers and leaves with $scCO_2$ and ethanol as solvents.

Entry	Hops	Solvent	Yield$_{extract}$ (%)^c	Yield$_{volatile}$ (%)^d
1	Flowers	$scCO_2$^{a}	9	26
2	Flowers	Ethanol^b	27	4
3	Leaves	$scCO_2$^{a}	4	18
4	Leaves	Ethanol^b	14	2

Extraction conditions: a) 3 g of dry and ground *Humulus lupulus* flowers or leaves, $scCO_2$ at 70 °C, 300 bar, 5 mL/min, 5 h. b) 3 g of dry and ground *Humulus lupulus* flowers or leaves in Soxhlet, 150 mL of ethanol, reflux, 24 h. c) Amount of compounds extracted by weight of sample (% wt /wt biomass). d) Percentage of volatile compounds in the extract as determined by GC-FID using n-dodecane as internal standard (% wt/wt extract).

The obtained results matched the expectations based on the solvent properties: the $scCO_2$ extraction of the flowers (**Table 5.2.2**, entry 1) yielded a clear, pale-yellow extract with a lower extraction yield (9 $\%_{wt/wt\ biomass}$) compared to ethanol (**Table 5.2.2**, entry 2; 27 $\%_{wt/wt\ biomass}$). However, the selectivity towards the volatile fraction resulted to be notably higher using the supercritical fluid: 26 % versus 4 $\%_{wt/wt\ extract}$. Indeed, the high-yield and low-selectivity of the ethanolic extract were also reflected in the dark-brown colour and turbidity of the final solution. Similar behaviour was, then, observed for hops leaves: using $scCO_2$, 4 $\%_{wt/wt\ biomass}$ yield of a pale yellow-green coloured oil with a high selectivity towards volatiles (18 $\%_{wt/wt\ extract}$) was obtained (**Table 5.2.2**, entry 3). On the other hand, using ethanol a higher yield of brown coloured oil (14 $\%_{wt/wt\ biomass}$) with a low content of volatiles (2 $\%_{wt/wt\ extract}$) was obtained (**Table 5.2.2**, entry 4). A picture of the visual differences of the extracts obtained with $scCO_2$ and ethanol from the leaves is reported in **Figure 5.2.7**. The difference in yield and selectivity were not surprising. Anyway, considering the aim of this work of obtaining antimicrobial compounds, the higher selectivity reached with $scCO_2$ is preferable over the higher yield of a more heterogeneous mixture of substances obtained with ethanol.

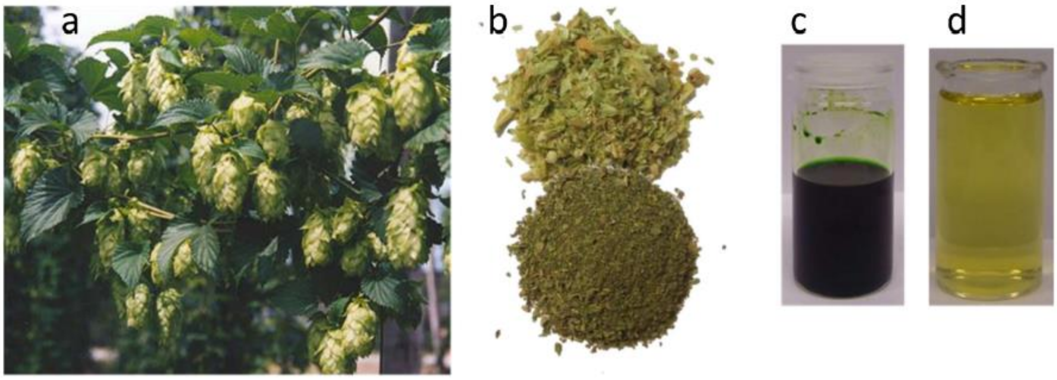

Figure 5.2.7. a) hops picture; b) dried and ground flowers and leaves; c) ethanolic extract and d) $scCO_2$ extract of the leaves.

In order to identify the main components of the volatile fractions, the solutions were then analysed by GC-MS by matching the spectra with those of the Mass Spectra Library (NIST 2.0) and with literature data. [91] [79] [73] [76] The classes of compounds highlighted by the structural analysis resulted to be of the family of terpenes (**Figure 5.2.8**, numbers 1-7), terpenoids (**Figure 5.2.8**, numbers 8-10), fatty acids (**Figure 5.2.8**, numbers 11-13) and bitter acids (**Figure 5.2.8**, numbers 14-18).

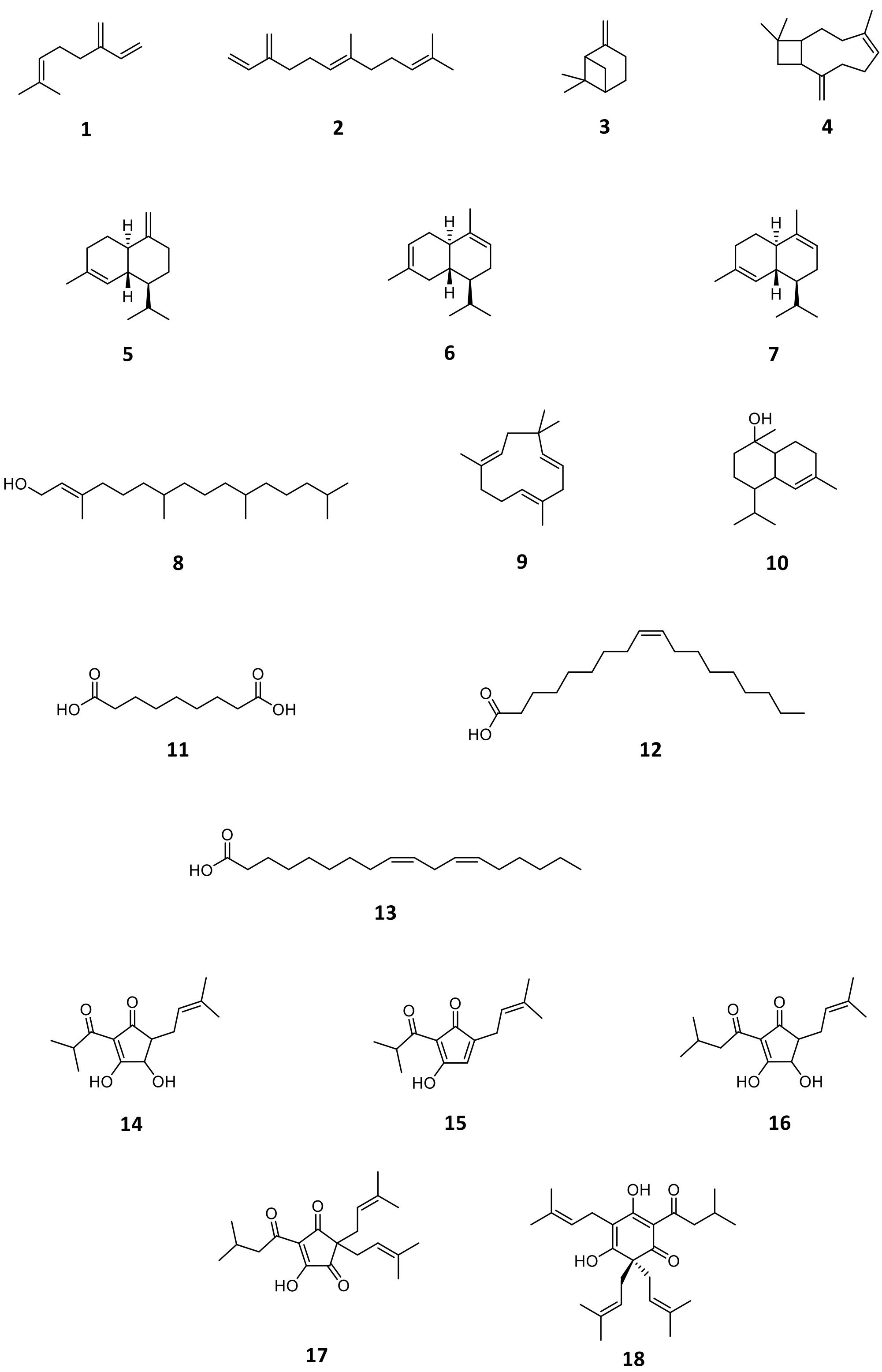

Figure 5.2.8. Proposed structures of the main volatile compounds detected by GC-MS analysis in the $scCO_2$ or Soxhlet extracts of *Humulus lupulus* flowers and leaves.

The distribution of these compounds was dependent on the extraction method. The bitter acids contained in hops flowers consisted of two related series of 6C-ring and 5C-ring compounds having isobutyroyl acyl (14-15) or isovaleroyl (16-18) side chains. **Table 5.2.3** reports the percentages of the predominant volatile components present in all the extracts ($scCO_2$ and ethanol) of hops flowers and leaves. Other component not detected by GC-FID are presumably heavier lipidic fractions.

Table 5.2.3. Identification of the main volatile components of the essential oils from hops flowers and leaves.

Compound	Flowers		Leaves		Retention time (min)
	scCO$_2$ (%$_{wt/wt\ extract}$)	Soxhlet (%$_{wt/wt\ extract}$)	scCO$_2$ (%$_{wt/wt\ extract}$)	Soxhlet (%$_{wt/wt\ extract}$)	
β-myrcene **(1)**	0.3	0.2	-	-	6.47
β-farnesene **(2)**	1.0	0.2	-	0.02	10.40
β-pinene **(3)**	0.5	-	-	-	6.46
β-caryophyllene **(4)**	0.5	0.1	0.2	0.01	10.26
γ-cadinene **(5)**	0.1	-	-	-	10.60
β-cadinene **(6)**	1.0	0.3	-	-	10.70
α-cadinene **(7)**	1.3	0.4	-	-	10.75
Phytol **(8)**	-	-	0.2	0.92	14.14
α-humulene **(9)**	0.3	-	-	-	11.72
Cadinol **(10)**	0.1	-	-	-	11.72
Azelaic acid **(11)**	-	-	0.5	-	11.43
Oleic acid **(12)**	-	-	0.1	-	13.10
Linoleic acid **(13)**	-	-	0.6	0.02	14.31
Cohumulinic acid **(14)**	-	-	2.3	-	12.07
Dehydrocohumulinic acid **(15)**	1.3	-	2.2	-	13.20
Humulinic acid **(16)**	1.3	-	2.9	-	13.75
Hulupone **(17)**	8.2	-	-	-	17.17
Lupulone **(18)**	8.7	1.1	-	-	18.43

As can be seen, the volatile oils obtained with the supercritical fluid extraction of the flowers comprised mainly β-myrcene (1), β-farnesene (2), β-pinene (3), β-caryophyllene (4), cadinene conformers (5-7) and bitter acids (15-18). In particular, hulupone (17) and lupulone (18) were extracted in higher percentages: 8.2 and 8.7 % respectively. These two compounds are already known for their antiseptic activity.[62,63,77] Concerning the scCO$_2$ extract of the leaves, it was noticed that it contained mainly β-caryophyllene (4), phytol (8), fatty acids (11-13) and 5C-ring bitter compounds (14-16). In this extract the main components resulted to be bitter acids, in particular cohumulinic (2.3%, 14), dehydrocohumulinic (2.2%, 15) and humulinic acid (2.9%, 16), that are known for having a certain antibacterial activity. Both for flowers and leaves, the ethanolic extracts resulted to have lower amount and lower variety of volatile compounds. It is worth mentioning that all the classes of compounds found in the obtained extracts have been reported to have a certain antiseptic behaviour.[46,67,69,92,93,94] Anyway, since most of them were preferentially found in the extracts obtained with scCO$_2$, this was considered as the most suitable method to recover preservatives compounds from *Humulus lupulus.* In addition, it is interesting to highlight that using the supercritical carbon dioxide extraction also the leaves can represent a sustainable source of antibacterial compounds. The scCO$_2$ extract of hops flowers resulted to be richer in terpenes and bitter acids while the leaves extracts were composed mainly by fatty acids and bitter acids. These differences affect the antibacterial activity of the extracts as discussed in the relative section (*Antibacterial Activity)*.

Datura stramonium

Dried and milled flowers and leaves of jimsonweed were then used as substrate to perform extractions using both $scCO_2$ and ethanol. The visual differences of the extracts obtained from jimsonweed using $scCO_2$ and ethanol are reported in **Figure 5.2.9** (c and d).

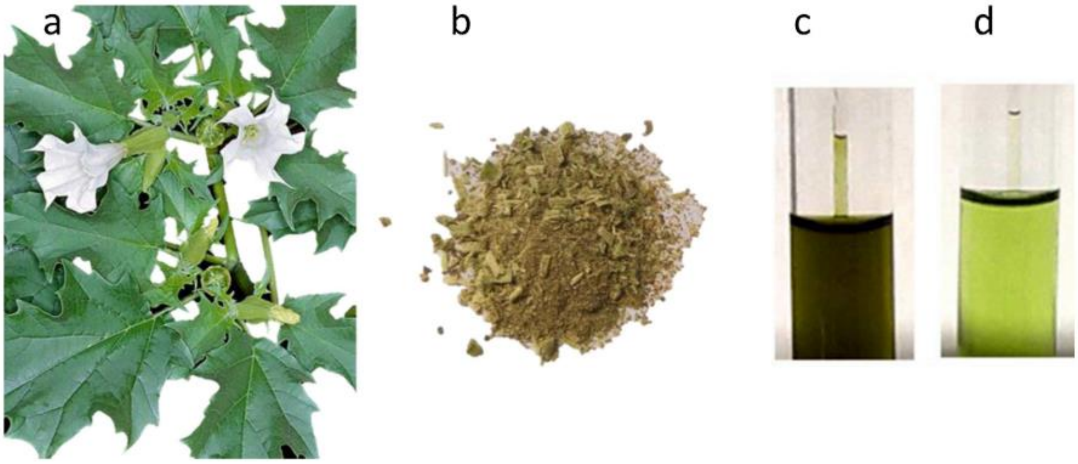

Figure 5.2.9. a) *Datura stramonium* plant; b) dried and ground biomass; c) ethanolic extract and d) $scCO_2$ extract (d) of jimsonweed.

As can be seen in **Table 5.2.4**, the extract obtained with carbon dioxide from flowers led to a light, clear extract with lower extraction yield compared to ethanol (1.2%$_{\text{wt/wt extract}}$ vs 22% $_{\text{wt/wt extract}}$) but with higher selectivity towards the volatile fraction (24.8% $_{\text{wt/wt extract}}$ vs 1.5% $_{\text{wt/wt extract}}$). When using *Datura stramonium* leaves, the same trend was observed but, in this case, the $scCO_2$ extract was characterized by a slightly lower selectivity for the volatile compounds. Indeed, using flowers as starting biomass 24.8% $_{\text{wt/wt extract}}$ of volatiles was observed, while using the leaves 16.4% $_{\text{wt/wt extract}}$ was obtained (entries 1 and 3, **Table 5.2.4**).

Table 5.2.4. Extraction of *Datura stramonium* flowers and leaves with $scCO_2$ as solvent and with ethanol using the Soxhlet apparatus.

Entry	Jimsonweed	Solvent	Yield$_{\text{extract}}$ (%)[c]	Yield$_{\text{volatile}}$ (%)[d]
1	Flowers	$scCO_2$[a]	1.2	24.8
2	Flowers	Ethanol[b]	22.0	1.5
3	Leaves	$scCO_2$[a]	2.3	16.4
4	Leaves	Ethanol[b]	21.9	3.3

Extraction conditions: a) 3 g of dry and ground *Datura stramonium* flowers or leaves, $scCO_2$ at 70 °C, 300 bar, 5 mL/min, 5 h. b) 3 g of dry and ground *Datura stramonium* flowers or leaves in Soxhlet, 150 mL of ethanol, reflux, 24 h. c) Amount of compounds extracted by weight of sample (% wt /wt biomass). d) Percentage of volatile compounds in the extract as determined by GC-FID using n-dodecane as internal standard (% wt/wt extract).

Concerning the chemical composition of the extracts (**Table 5..5.**), both ethanol and $scCO_2$ extracted preferentially phytol (**Figure 5.2.10**, number 8) and fatty acids (11-13, 21-25). All the detected compounds reasonably possess the desired preservative properties[65,66,85,87] that make them suitable for cosmetic formulations. However, some poisonous alkaloids (N-acetyltyramine (26), conhydrine (27), atropine (28) and scopolamine (29),[82,83,86,87,95] were also detected but they were extracted with very low selectivity.

Looking at the composition of the $scCO_2$ extracts it is easily noted the high percentage of fatty acids. Linoleic (**Figure 5.2.10**, number 13), γ-linolenic (21), stearic (22) and palmitic (25) acids were found, and they are known to have antibacterial activity.[68,69,93,96]

Table 5.2.5. Identification of the main volatile components of the essential oils from *Datura stramonium* flowers and leaves.

Compound	**Flowers**		**Leaves**		**Retention time (min)**
	scCO$_2$ (%$_{wt/wt\ extract}$)	**Soxhlet** (%$_{wt/wt\ extract}$)	**scCO$_2$** (%$_{wt/wt\ extract}$)	**Soxhlet** (%$_{wt/wt\ extract}$)	
Phytol **(8)**	2.5	-	5.3	0.4	14.15
Azelaic acid **(11)**	0.1	0.03	0.3	0.1	11.43
Oleic acid **(12)**	-	-	-	0.1	13.10
Linoleic acid **(13)**	3.1	-	-	-	14.31
1-tridecene **(19)**	1.3	-	0.8	0.2	9.95
16-heptadecenal **(20)**	0.1	-	-	-	12.59
γ-linolenic acid **(21)**	5.1	0.09	2.3	0.3	14.32
Stearic acid **(22)**	2.9	0.05	-	-	14.45
Diethyl adipate **(23)**	-	0.03	-	-	9.91
Capryl alcohol **(24)**	0.1	-	-	-	11.94
Palmitic acid **(25)**	5.5	0.15	3.1	0.4	13.19
N-acetyltyramine **(26)**	0.2	-	-	-	13.60
Conhydrine **(27)**	-	0.05	-	-	8.91
Atropine **(28)**	-	-	0.4	0.3	15.29
Scopolamine **(29)**	0.4	-	0.2	-	16.74

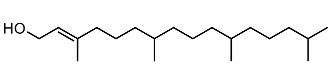

8

19

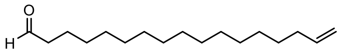

20

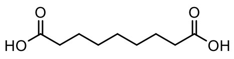

11

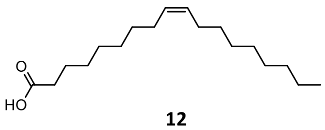

12

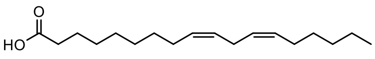

13

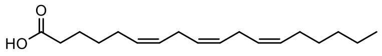

21

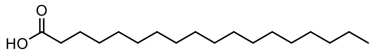

22

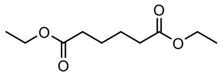

23

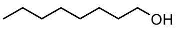

24

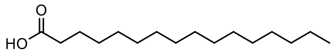

25

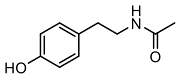

26

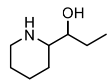

27

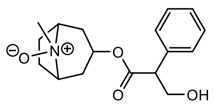

28

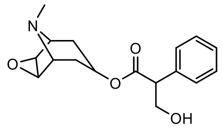

29

Figure 5.2.10. Proposed structures of the main volatile compounds detected by GC-MS analysis in the SC-CO$_2$ or Soxhlet extracts of *Datura stramonium* flowers and leaves.

Antibacterial Activity

The chemical composition of the extracts strictly influences the antibacterial activity that, indeed, is not related to a single mechanism but to a cascade of reactions. From a general point of view, it can be stated that essential oils are able to inhibit the growth of bacteria cells and the production of toxic bacterial metabolites, affecting both the external membrane of the cell and the cytoplasm. The hydrophobicity of the components of the natural oils, indeed, are responsible of bacterial disruption and, in particular, they are able to penetrate the microbial cell causing alteration both in its structure and functionalities.[45,92,97,98] Fatty acids, bitter acids, terpenes and terpenoids are among the most effective biocides that can be found in essential oils. Fatty acids act as antibacterials targeting the cell membrane: they modify the permeability of cell wall and disrupt both the electron transport chain and the oxidative phosphorylation. Another possible action of fatty acids is the inhibition of enzyme activity, the weakening of nutrient uptake, the generation of peroxidation and auto-oxidation products or the direct lysis of the bacterial cells.[96] In this frame, it has been demonstrated that unsaturated fatty acids are more active against bacteria than saturated ones.[69,93] As stated above, also bitter acids can act as preservatives. In particular, their action towards Gram-positive bacteria is similar to that of fatty acids: thanks to the interaction of the hydrophobic parts of the molecules with the phospholipid bilayer of the cell wall, they are able to leak the primary membrane.[62] At the same way, the antimicrobial action of terpenes and terpenoids has been explained with toxic effects on membrane structure and functions. Like the other classes of compounds already discussed, terpenes and terpenoids have a lipophilic character that promotes their partitioning into the membrane structure and leads to the expansion of cell walls and to the increase of the membrane fluidity and permeability. These effects inhibit the respiration and alter the ion transport processes due to structural modification of the proteins embedded in the membrane.[67,98,99] In this context, the antibacterial properties of the *Humulus lupulus* and *Datura stramonium* extracts were tested against *Escherichia coli*, a standard model for bacteria studies. These tests were performed on bacteria cells starting with an extract concentration of 40 mg/mL with a serial two-fold dilution. In **Figure 5.2.11** the results, reported as the percentage of cell viability at different extract concentrations (mg/mL), are shown. Overall, the extracts obtained with ethanol resulted to be less active than the one with $scCO_2$. In particular, jimsonweed $scCO_2$ extracts inhibit the bacteria cells growth more than 80% and hops leaves extracts more than 75%. In both cases, the equivalent ethanol derived extracts never exceed 60% of growth inhibition. Extracts from hops flowers are weakly active and their activity is independent from the extraction methods.

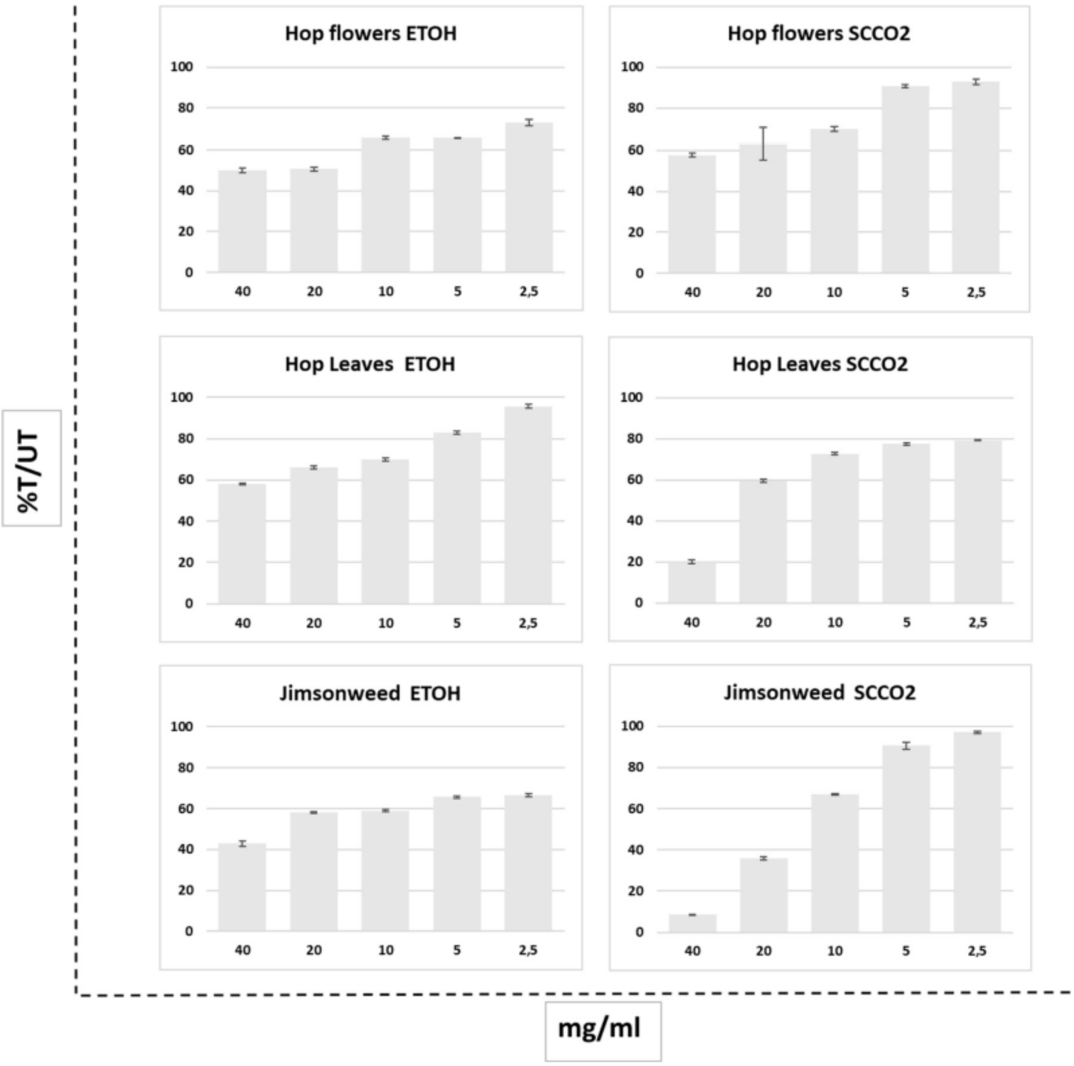

Figure 5.2.11. Antimicrobial activities on *Escherichia coli* of hops and jimsonweed extracts from ethanol and $scCO_2$ as solvents. On Y axis, the percentage of cell viability is reported of treated (T)/untreated (UT) samples. The values on X axis are extracts concentrations in mg/mL. Columns represent average values and error bars are standard deviations.

5.2.3 Conclusions

The results obtained in this study demonstrate that $scCO_2$ extraction of low-value agro-waste such as hops leaves, and jimsonweed represents a viable source of natural preservatives and may contribute an additional step in the circular economy context. Although the $scCO_2$ extraction gave lower extraction yields (8.6–4% $_{\text{wt/wt biomass}}$ for *Humulus lupulus* and 1.2–2.3% $_{\text{wt/wt biomass}}$ for *Datura stramonium* flowers or leaves respectively) compared to ethanol extraction performed with Soxhlet technique, $scCO_2$ always reached the highest selectivity (up to 26% $_{\text{wt/wt extract}}$) towards the light fraction that is rich in potentially antibacterial molecules (terpenes, terpenoids, bitter acids and fatty acids). Additionally, the potential loss of part of the volatile components extracted with $scCO_2$ during workup and the lower yield was considered acceptable in the present context, considering that our objective was to obtain antimicrobial compounds by a viable procedure. The extracts were tested towards *Escherichia coli*, showing that the $scCO_2$ extracts are more active as antibacterial compared to the ethanol ones. In conclusion, $scCO_2$ resulted to be an extractive method that is, not only safer from the operator and consumer point of view (non-flammable, non-toxic, no final product contamination), but also more efficient for the obtainment of the volatile fraction of essential oils, that resulted to be constituted mainly by compounds with proven antiseptic behaviour.

5.2.4 Experimental

Apparatus and chemicals. All chemicals and solvents were purchased from commercial sources and used without further purification. Ethanol (pharma-grade, purity ≥99.8%), *n*-dodecane (purity ≥99.0%) and the deuterated solvents (isotopic purity atom% D: acetone-d_6 ≥99.9, methanol-d_4 ≥99.8, chloroform-d ≥99.8) were all provided by Sigma-Aldrich. Supercritical CO_2 extractions were performed in a laboratory apparatus consisting of a Jasco PU-2080−CO2 Plus delivery Pump and a Jasco 2080 Plus Automatic Back Pressure Regulator used for the pressure control. A Chrompack CP-9003 oven was used to heat the connecting stainless steel tubing and the different reactors. The GC-FID was a HP 5890 equipped with an Elite-624 capillary column (30 m, internal diameter 0.32 mm, film 0.18 µm,) coupled with a FID detector. The GC–MS (EI, 70 eV) was a 6890 N Network GC System coupled with a 5973 inert Mass Selective Detector (both from Agilent) equipped with a HP5 column (30 m, internal diameter 0.25 mm, film 0.25 µm, 5% diphenyl 95% dimethyl siloxane). The following conditions were used. Carrier gas: He (1.2 mL/min, constant flow); inlet temperature 250 °C; split mode; ratio 30:1; detector temperature: 280 °C; ramp rate: 10 °C min^{-1}; final T: 230 °C (20 min). ^1H and $^{13}C\{^1H\}$ NMR spectra were collected at 25 °C on a Bruker Ascend 400 operating at 400 MHz for ^1H and 100 MHz for ^{13}C, or on a Bruker UltraShield 300 operating at 300 MHz for ^1H and 75MHz for ^{13}C. For ^1H and $^{13}C\{^1H\}$ NMR the chemical shifts (δ) have been reported in parts per million (ppm) relative to the residual non-deuterated solvent as an internal reference and are given in δ values downfield from TMS.

Sample preparation. The aerial parts of *Datura stramonium* and *Humulus lupulus* were hand-harvested from pesticide-free organically maintained fields (Veneto, Italy) and manually chopped into 1−2 cm pieces. The samples were store at 4° C after being dried at room temperature for 2 days under air and milled with a spice grinder to 0.5−1 mm pieces (**Figures 5.2.7** and **5.2.9**).

Soxhlet extraction procedures. The Soxhlet apparatus (containing a cellulose thimble) was filled with 3 g of dried and ground biomass and 150 mL of ethanol; the solvent was refluxed for 24 h. For the qualitative and quantitative characterisation of the volatile fraction, the solution was analysed by GC-FID/GC–MS, using *n*-dodecane (2 mg/mL) as internal standard. The solvent was then evaporated under reduced pressure to determine the extraction yield ($Y_{extract} = wt_{extract} / wt_{dry\ biomass}$ %).

Supercritical fluid extraction procedures. The $scCO_2$ extraction experiments were conducted on an analytical scale supercritical extraction unit (internal volume of approximately 10 cm^3, bed diameter 3/8" and bed height of 15 cm) using $scCO_2$ as solvent. Approximately 3 g of dry and ground biomass were loaded in the chamber and extracted with a constant flow rate of $scCO_2$ (5.0 cm^3 min^{-1}) at 300 bar and 70 °C for 5 h. The extracts were collected by venting in ethanol at ambient temperature and pressure. The extracts were gravimetrically quantified ($Y_{extract} = wt_{extract} / wt_{dry\ biomass}$ %) at the end of each run after the removal of ethanol at low temperature under a gentle flow of nitrogen. For the qualitative and quantitative analysis of the volatile fraction, an ethanol solution of a known quantity of extract was analysed by GC-FID/GC–MS, using *n*-dodecane (0.5 mg/mL) as internal standard.

Chromatographic analysis of the extracts. The extracts were analysed by GC–MS. The identification of the key components was performed by using the NIST database,[100] by comparison with the existing literature [79] [70] [71] [73] [82] [83] [87] [91] and, whenever informative, by integrating this MS information with the NMR spectra (see Appendix, figure A.5.2.1-A.5.2.11). For some compounds whose NIST reliability range did not allow to assign a structure with certainty, the proposed structures are tentative. Quantification was performed by GC–FID under the same analytical conditions used for the GC-MS system and with the same chromatographic column. For each chromatogram the peak area (A_x) was used to estimate the quantity of each compound (Q_x) with reference to the internal standard peak area (A_{std}) and its quantity added to the extract (Q_{std}), using the following formula:

$$Q_x = \frac{A_x}{A_{std}} Q_{std}$$

The estimated total amount of volatile compounds – defined as all the species with a GC retention time < 20 min at GC-FID (ΣQ_x) – was used to calculate the “yield of volatile compounds” ($Y_{volatile}$) referring to the total weight of the recovered extract (Q_{ext}), with the following formula:

$$Y_{volatile} = \frac{\sum_{x=1}^{n} Q_x}{Q_{ext}} * 100$$

Evaluation of the antibacterial activity. The antibacterial properties of the *Humulus lupulus* and *Datura stramonium* extracts were tested against *Escherichia coli*, as a standard model. The bacteria were grown overnight using LB medium on a 15 mL falcon shaken at 250 RPM at 37 °C. The bacteria were then diluted 1/10, transferred on a 96-well plate and finally treated with five different concentrations of the extracts in the range between 40 and 2.5 mg/mL using two-fold dilutions. The culture was grown for 6 h, then the antibacterial activity was evaluated by CellTiter-Glo® Luminescence Assay (Promega, Madison, WI, USA) with Synergy H1 instrument (Biotek, Milan, Italy).

5.3 Supercritical CO_2 as a green solvent for the circular economy: extraction of fatty acids from fruit pomace

The encouraging results obtained from the valorisation of hops and jimsonweed for the extraction of antibacterial compounds (see ***Chapter 5.2****) led us to explore the scCO$_2$ extraction of other waste matrixes. Indeed, in this chapter, the extraction of fatty acids for the cosmetic industry from different fruit pomaces has been investigated. This study was carried out in collaboration with Università degli studi di Padova for the analytical characterization of the extracts, and two industries, namely Rigoni di Asiago Srl (for the supplying of fruit pomace) and Unifarco SpA (for the possible cosmetic and nutraceutical application). The results are reported in* C. Campalani, E. Amadio, S. Zanini, S. Dall'Acqua, M. Panozzo, S. Ferrari, G. De Nadai, S. Francescato, M. Selva and A. Perosa, *J. CO_2 Util.*, **2020**, 41, 101259. doi:10.1016/j.jcou.2020.101259.[101]

The obtainment of value from waste is one of the empowering actions for the circular economy. In this frame, the recycle and reuse of waste from the agro-food sector to produce more sustainable products through greener technologies, can help to move away from the linear development model. In this investigation, the use of supercritical CO_2 (scCO$_2$) extraction to obtain fatty acids from waste pomace deriving from the preserves industry was performed and compared with classical Soxhlet technique using hexane as solvent. In particular seeds and peels of raspberry, blueberry, wild strawberry, pomegranate, blackberry and blackcurrant were used as starting materials. The fatty acids obtained using scCO$_2$ resulted to be purer and richer in essential fatty acids than the hexane ones. The wild strawberry pomace extraction with scCO$_2$ is a representative example: selectivity towards fatty acids was 26 wt% (vs. 1.4% with hexane) and the extracts contained, 145.8 mg mL^{-1} polyunsaturated, 64.0 mg mL^{-1} monounsaturated and 46.8 mg mL^{-1} saturated fatty acids (vs. 14.3 mg mL^{-1} total fatty acids with hexane).

5.3.1 Introduction

One of the crucial points in the value chain of industries of the agri-food sector is, evidently, the recovery and reuse of waste streams.[102] From the environmental point of view, indeed, these streams most often need to be disposed in particular and expensive ways or are converted to low-value compounds with low-tech technologies (e.g. production of animal feed, fertilizers or off-grade fuels). The implementation of new protocols to achieve high-value substances or materials from waste can imply lowering the environmental burden both directly (less waste) and indirectly (e.g. making new renewable products in place of petrochemical ones). From the economical standpoints, several advantages and drivers of the upgrading of residual biomass can be enumerated. The reduction of waste (i.e. lower costs for landfilling, composting, incinerating or converting it to low-value feed or fertilizers) as well as the production of high-value products for the market are only some examples. Also from the societal perspective, the extraction of value from waste can represent a positive asset for any business willing to commit to this vision. The resulting products are therefore more likely to be accepted by health- and environmentally conscious consumers as “green”, “sustainable”, “renewable”, “natural”, i.e. as contributors to circular economy,[103] and new employment opportunities.[104] One of the pillars of any strategy for waste upgrading is recycling which, as defined by the EU, encompasses any recovery operation for reprocessing waste into substances whether for the original or other purposes, excluding energy recovery.[105]

In this context, the aim of the work reported in this chapter has been to valorize seeds and peels (pomace) discarded from Rigoni di Asiago, one of the main Italian producers of fruit preserves, by recovering and reprocessing them into higher value products. During its fruit preserves production, Rigoni di Asiago generates about 80 tons of organic farming fruit waste every year – in the present case deriving from blackberry, raspberry, blackcurrant, wild strawberry, pomegranate and blueberry processing. The low-temperature processing generates a residual high-quality biowaste in which all the natural properties of the fruit are particularly well preserved. Currently Rigoni di Asiago pays to discard this waste as compost, although it is known to be a natural source of precious biomolecules such as anthocyanins (glycosides of anthocyanidines), flavonoids, phytosterols, tocopherols and fatty-acids (FAs) (**Figure 5.3.1**).[106,107]

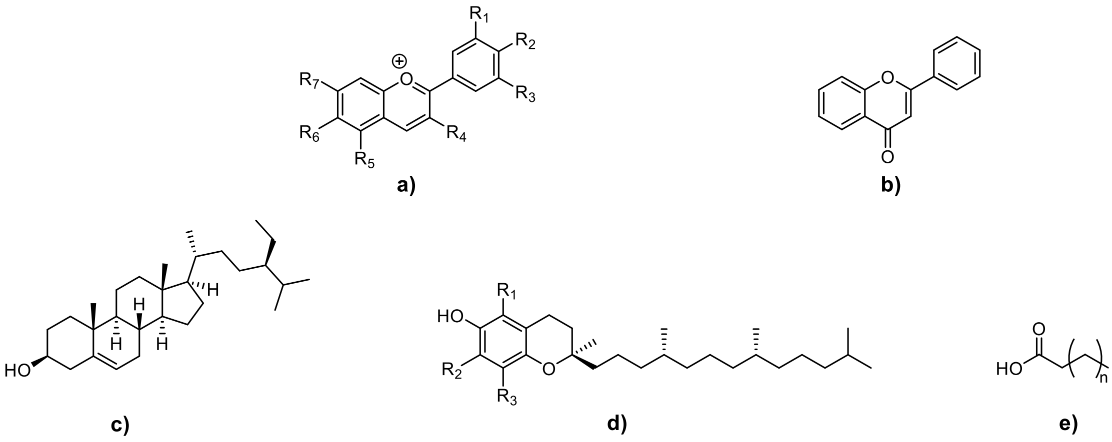

5.3.1. Structure of the main compounds that can be found in fruit pomace. a) anthocyanidines basic structure. R = -H, -OH or -OCH_3; b) flavone backbone (2-phenyl-1,4-benzopyrone); c) b-sitosterol, an example of phytosterol; d) tocopherols structure, R = -H or -CH_3; e) fatty acids structure, one or more double bonds can be present on the carbon chain.

More specifically, the berry pomace is a valuable raw material for cosmetic formulations, nutraceuticals and functional ingredients of foods thanks to it unique FAs composition, often in combination with high contents of lipid-soluble antioxidants.[108,109] For this, the recovery of these natural compounds would therefore add value to the whole productive chain. With a perspective towards the possible applications of the FAs obtained from fruit pomace, the importance of the cosmetic industry in this context has been highlighted and a collaboration with the company Unifarco SpA has been established to try to use the scCO_2 extracts in cosmetic formulations. During the last years, indeed, the cosmetic industry is becoming more and more interested in promising, sustainable, plant- and bio-based raw materials. Sustainability is, in fact, a major challenge that cosmetic manufacturers must take into account during the whole development process, starting from the selection of raw materials on to the manufacturing process and ending with a smart and easy to understand communication. In addition, sustainability is also becoming a big marketing trend. These new kinds of “greener” products must anyway meet specific quality standards, reproducibility, efficacy and, above all, a good or well- managed stability profile. Unifarco is an Italian-based company whose mission is to develop products with high scientific value. To reach this goal it develops cosmetics, food supplements and medical devices considering sustainability as an important aspect and in the same way one of the identifying characteristics of cosmetic products.

In recent years, fatty acids have gained increasing attention mainly because of their various biological functions related to health and disease.[110] FAs, indeed, play important roles in the prevention and treatment of autoimmune, cardiovascular and nervous diseases and in the improvement of learning ability.[111] Fatty acids are carboxylic acids with a carbon chain that can be saturated or non-saturated (**Figure 5.3.1**, e). In nature the carbon chain is usually made of a number from 4 to 28 of carbon atoms and is not branched. In some living organisms FAs are a major component of the lipids in their free form (free fatty acids, FFAs) but, in other, they exist only in three main classes of esters, namely triglycerides, phospholipids and cholesteryl esters. Any of these forms can be important as a dietary source and as structural component of cells. Among FAs, essential FAs are the ones that humans and other animals must ingest to overcome the inability of the body to synthesize them. Only two FAs are recognized as essential for humans: α-linolenic acid and linoleic acid. In the past two-decades, with respect to conventional technologies for the extraction of FAs (mainly cold pressing and extraction with organic solvents such as hexane), supercritical fluid extraction based on carbon dioxide (SFE-CO_2) has been identified as a privileged technique because, thanks to its low oxidative and thermal impact, it produces high quality oils that often do not require further refining, it preserves the original properties unaltered, and excludes contamination by residual liquid solvents.[21,112] For these reasons, SFE-CO_2 processing has become more and more relevant for the large-scale extraction of different types of matrices to produce lipids and other bioactive substances used in food, pharma, cosmetics and other high-value applications.[113,114] This chapter comparatively investigates the efficiency of SFE-CO_2 and traditional liquid extractions to obtain unsaturated fatty acid-rich fractions from waste of the fruit processing industry.

5.3.2 Results and Discussion

Six different fruit pomaces were considered for this study, namely deriving from blackberry, blackcurrant, pomegranate, wild strawberry, blueberry and raspberry. The investigation started with the pre-treatment and composition analysis of the biomasses. The composition of the berry pomace was provided by Rigoni di Asiago that was the supplier of the samples investigated in this study. The amounts of sugars, protein and lipids were determined within the process of nutritional analysis and labelling of food content. Sugar content was determined by the analytical lab of Rigoni di Asiago through HPLC analyses using a refractive index detector. The analyses of protein and lipids were carried out by an external lab commissioned by the industry itself. The results are summarized in **Table 5.3.1**.

Table 5.3.1. Composition of waste berry biomass used in this work in % values of sugars, proteins and lipids, before any treatment.

	Blackberry	Blackcurrant	Pomegranate	Wild strawberry	Blueberry	Raspberry
Sugars %	7.0	12.0	18.0	9.0	7.0	8.0
Proteins %	1.4	0.9	1.7	0.4	0.4	1.2
Lipids %	0.5	0.2	1.0	0.2	0.2	0.7

Different pre-treatment techniques were tested on the frozen pomace prior to extraction: cryogenic crushing, simple air drying, and air drying preceded by rinsing with water. The latter pre-treatment was chosen as it yielded similar results to cryogenic crushing and allowed to obtain purer extracts respect to simple drying. In particular, since the majority of the residues present on the agro wastes was composed by sugars, the frozen fruit pomace was rinsed with milliQ water for 15 min in order to remove them and then air dried for 24 h. The initial water content of the pomace was determined by difference between initial and dry samples and is shown in **Table 5.3.2**. Moreover, the residual water content was determined for each air-dried sample after heating in a vacuum-drying chamber (70 °C, 5 mbar, 24h).

Table 5.3.2. Initial and residual water content in the different pomace samples (wt/wt%).

	Blackberry	Blackcurrant	Pomegranate	Wild strawberry	Blueberry	Raspberry
Initial water (wt%)[a]	59.6	62.4	38.1	52.2	73.9	39.8
Pomace (wt%)	40.4	37.6	61.9	57.1	26.1	60.2
Residual water (wt%)[b]	8.2	2.6	7.2	2.4	5.2	8.7

a) Determined by difference of weight between initial and air-dried samples. b) Determined after heating of each air-dried sample in a vacuum-drying chamber. Most of the mass loss (≥98%) was water. The complement was plausibly due to a minor release of volatile organic compounds.

An initial water content varying from a minimum of 38.1% for pomegranate to a maximum value of 73.9% for blueberry was found. In every case after the mentioned pre-treatment the water content was drastically decreased, and it entered in a range between 2.4 and 8.7 % (for wild strawberry and raspberry relatively).

After defining the pre-treatment procedure for the biowastes we started the investigation about the experimental conditions for the $scCO_2$ extractions. Based on our previous recent experience,[32] we decided to operate at the maximum pressure allowed by the system (300 bar) and at 70° C in order to ensure a reasonably high carbon dioxide density (0.79 mg/mL) which was crucial for the extractions, with a constant flow of 5 mL/min of CO_2. In order to determine the minimum extraction time for the highest yield of lipidic fractions, control experiments using wild strawberry as an example and varying extraction time from 1 to 24 h were performed. After 5 h the obtained yields substantially levelled off at 13.5 wt/wt%, while prolonging the experiments at 10 and 24 h led to negligible effect (**Figure 5.3.2**). The other parameters, namely temperature and carbon dioxide flow, were then modified to ensure the best extractive conditions. Albeit the temperature conditions of **Figure 5.3.2** (70° C) are considered acceptable for the extraction of FAs, an investigation on the application of lower temperature for the potential benefit on preserving heat sensitive compounds was conducted. However, both experiments carried out at 50 and 40° C (300 bar, 5 mL/min) led to a decrease in the extract yield to 10.7 and 9.6% respectively (at 70° C it was 13.5%). These yields value corresponded to a substantial decrease in the extraction efficiency from 25 to 35%. This result appeared to be incoherent with the increase of the CO_2 density (0.87 and 0.91 g/mL at 50 and 40°C respectively), but it was probably due to the effect of the temperature on the vapour pressure of the extracted molecules (in particular unsaturated fatty acids, FA: see later). The yield was, so, improved at 70°C because the solute (FA) solubility was primarily affected by the increase of its vapour tension, rather than by the reduction of CO_2 density. Similar behaviours have been documented in the investigation of the solubility of apolar molecules in $scCO_2$.[115]

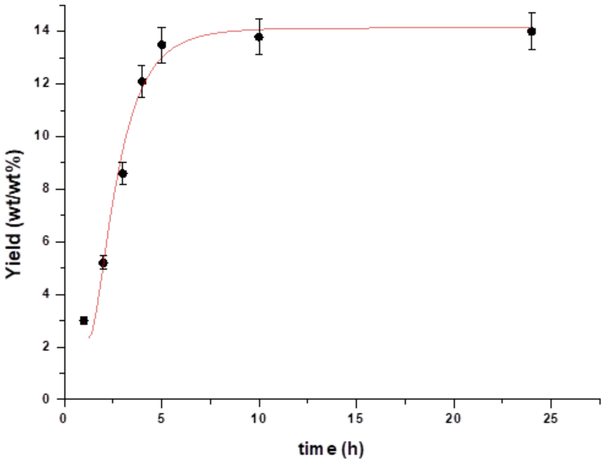

Figure 5.3.2. $scCO_2$ extraction yields (wt/wt%) of wild strawberry pomace as a function of time (300 bar, 70 °C, 5 mL/min).

The temperature of 70 °C was therefore selected to continue the study and to implement the extraction of a sample of wild strawberry pomace by halving the CO_2 flow to 2.5 mL/min maintaining the pressure at the constant value of 300 bar. In this case the extraction yield resulted to be 7.7 wt% which was almost one half the value (ca 14 wt%) achieved under the conditions of **Figure 5.3.2** (5 mL/min), suggesting a quasi-linear relationship between the yield and the CO_2 flow. Based on that, the further experiments were carried out using the highest flow to allow for the obtainment of the maximum amount of extracted oil. Although in this way the ratio of solvent to feed mass was apparently elevated (at 5 mL/min, it was approximatively 500 $mL_{CO2}/g_{dry\ pomace}$ in 5h) and potentially detrimental to the process economy, several other aspects should be assessed in this analysis. In particular it must be taken into account that, in case of commercial exploitation, the transfer from lab to commercial scale plants makes use of facilities for energy recovery operating under partial depressurization and recycle of carbon dioxide, with significant savings on compression cycles.[116] Additionally, if the extracts are comprised of high added value compounds with a specifical market interest, like the products herein investigated, the incidence of CO_2-derived costs is limited compared to the commercial value of the final compounds.

All the pomaces from different berries (blueberry, pomegranate, blackberry, raspberry and blackcurrant) were thereafter processed under the extraction conditions found for wild strawberry residues: 300 bar, 70°C, 5 mL/min of CO_2, 5h. All the obtained extracts were then compared in terms of yields and FA content to classical Soxhlet extractions performed using hexane as the solvent (68° C reflux, 24h). Hexane is, indeed, often chosen as a model non-polar solvent for conventional extractions albeit its toxicity, flammability and cost. Moreover, its boiling point matches the extraction temperature used in this study for the $scCO_2$ extractions, and its solvating properties are similar to carbon dioxide. The resulting yields and total FAs % are reported in **Table 5.3.3**. For each extract the percentage of FAs (defined also as the extraction selectivity towards FAs) was measured by GC (see Appendix, figures A.5.3.1-A.5.3.12) using methyl pentadecanoate as the internal standard. In addition the qualitative characterization of the extracts was based on MS (see Appendix, figures A.5.3.13-A.5.3.37) and on the Kovats retention index[117] (**Equation 5.3.1** and **Table 5.3.4**) and compared with literature data[118] (wild strawberry[119], blueberry[120], pomegranate[121], blackberry[122], raspberry[119], blackcurrant[123]). 25 different FAs were identified, and their structures are reported in **Figure 5.3.3**.

$$I_i = 100\left[n + \frac{\log(t_i) - \log(t_n)}{\log(t_{n+1}) - \log(t_n)}\right]$$

Equation 5.3.1. Temperature programmed chromatography Kovats index equation, where I_i is the Kovats retention index of peak *i*, *n* is the carbon number of *n*-alkane peak heading peak *i*, t_i retention time of compound *i* in minutes, t_n is the retention time of the heading *n*-alkane and t_{n+1} is the retention time of the trailing *n*-alkane.

Table 5.3.3. $scCO_2$ extraction yields (wt/wt%) of the different pomaces with supercritical CO_2 and hexane as solvents and total fatty acids percentages in the extracts.

Entry	Pomace	Solvent	Yield $_{\text{extract (\%)}}$ [c]	Total $_{\text{fatty-acids}}$ (%) [d]
1	Wild strawberry	$scCO_2$ [a]	13.5	26.0
2		hexane [b]	30.1	1.4
3	Blueberry	$scCO_2$ [a]	9.7	23.5
4		hexane [b]	29.5	0.7
5	Pomegranate	$scCO_2$ [a]	11.3	13.0
6		hexane [b]	20.3	0.3
7	Blackberry	$scCO_2$ [a]	6.6	29.5
8		hexane [b]	6.5	0.2
9	Raspberry	$scCO_2$ [a]	7.5	30.3
10		hexane [b]	5.8	0.02
11	Blackcurrant	$scCO_2$ [a]	4.6	16.5
12		hexane [b]	12.6	0.1

Extraction conditions: a) 3 g of pre-treated biomass, $scCO_2$ at 70 °C, 300 bar, 5 mL/min of CO_2, 5 h. b) 3g of pre-treated biomass in Soxhlet, 150 mL of hexane, reflux, 24 h. c) Amount of compounds extracted by weight of sample (% wt/wt $_{\text{biomass}}$). d) Percentage of FAs in the extract as determined by GC-MS using methyl pentadecanoate as internal standard (% wt/wt $_{\text{extract}}$).

Visually, the $scCO_2$ extracts were clear green oils, while the hexane-derived extracts resulted to be almost colourless liquids. The extraction yields of wild strawberry, blueberry, pomegranate and blackcurrant pomace obtained by using hexane as the solvent (**Table 5.3.3**, entries 2, 4, 6 and 12) were generally higher than with $scCO_2$ (**Table 5.3.3**, entries 1, 3, 5 and 11), while the selectivity towards FAs was always better when using carbon dioxide.

Concerning wild strawberry pomace, the extraction with hexane resulted in 30.1% extraction yield, with 1.4% of FAs (**Table 5.3.3**, entry 2) against 13.5% yield and 26.0% FAs with $scCO_2$ (**Table 5.3.3**, entry 1). The oil obtained from $scCO_2$ extraction was rich in essential FAs, linoleic (7.9%) and α-linolenic (6.7%), and other FAs such as palmitic (2.1%), stearic (1.7%) and oleic (6.4%), as shown in **Table 5.3.4.** Blueberry pomace yielded 29.5% of extract and 0.7% selectivity with hexane (**Table 5.3.3**, entry 4) and 9.7% yield and 23.5% FA with $scCO_2$ (**Table 5.3.3**, entry 3). Blueberry pomace $scCO_2$ extract was very rich in palmitic acid (1.8%), oleic acid (7.4%), linoleic acid (8.4%) and α-linolenic (5.4%), highlighting always the presence of the two essential FAs. The blackcurrant pomace yielded 12.6% of oil and 0.1% FAs using hexane (**Table 5.3.3**, entry 12) and 4.6% extract with 16.5% of FAs with $scCO_2$ (**Table 5.3.3**, entry 11). The $scCO_2$ extract of blackcurrant waste was rich in different FAs such as palmitic (2.2%), octadecanoic (2.2%), linoleic (5.1%) and octacosanoic (1.8%). Pomegranate seeds and peels extracted with hexane afforded a 20.3% yield with 0.3% FAs (**Table 5.3.3**, entry 6), while the oils obtained with $scCO_2$ were obtained in 11.3% yield, with 13.0% FAs (**Table 5.3.3**, entry 5). In this case also, the extracts contained interesting FAs such as palmitic (0.5%), oleic (0.7%), linolelaidic (0.8%) and tetracosanoic (10.3%). Concluding, the extraction yields for blackberry and raspberry waste was comparable for the two solvents, but the selectivity towards FAs was still higher with $scCO_2$: 29.5% FAs with $scCO_2$ versus 0.2% with hexane for blackberry (**Table 5.3.3**, entry 7, 8) and 30.3% versus 0.02% for raspberry (**Table 5.3.3**, entry 9, 10). Analytical data indicate that the blackberry waste $scCO_2$ extract is rich in linoleic acid (16.6%), oleic acid (6.6%), α-linolenic (3.0%) and palmitic acid (1.8%). The oil obtained from the extraction of raspberry seeds and peels has, instead, a FAs composition that contains linoleic acid (19.1%), oleic acid (6.1%), palmitic acid (1.4%), esacosanoic acid (0.7%), stearic acid (0.7%) and more. Although the conditions used for $scCO_2$ extractions were not strictly comparable to those of the conventional Soxhlet procedure, the higher yields of the extracts obtained using hexane as a solvent, were likely due to two factors.

Firstly, with hexane longer extraction times were used when compared with $scCO_2$ (24h vs 5h); this plausibly allowed progressive dissolution of les-soluble species. In addition, hexane resulted to have a slightly higher polarity compared to supercritical carbon dioxide as measured by the empirical Kamlet-Taft π^* solvent polarity parameter. Concerning $scCO_2$, π^* at 45° C and 200 bar is reported to be equal to -0.20[124] and extrapolation of the plot up to 300 bar indicates a value $-0.20 < \pi^* < -0.15$. The same parameter for hexane at 25 °C and atmospheric pressure is $\pi^*= -0.11$ indicative of a slightly higher polarity compared to $scCO_2$.[125] On the other hand, the observed higher selectivity of $scCO_2$ towards FAs compared to hexane, was attributed mainly to the combined effect of density and polarity of the supercritical fluid. As mentioned before, the density of carbon dioxide at 300 bar and 70° C is equal to 0.79 g cm^{-3}; this value is almost 20% higher than that of hexane (0.62 g cm^{-3}, at 60° C).[126] Higher density along with lower Kamlet-Taft polarity favours the selective extraction of the more lipophilic compounds such as the FAs.

Table 5.3.4. GC retention time and Kovats indices of the FAs.

	Fatty-acid [a]		**Retention time (min)**	**Kovats index**
1	Palmitic	C16:0	23.11	1908
2	Azelaic	C9 dicarboxylic	26.46	1629
3	Stearic	C18:0	27.55	2133
4	Oleic	C18:1 (9Z)	28.65	2082
5	Linoleic	C18:2 (9Z, 12Z)	30.38	2139
6	Eicosanoic	C20:0	31.75	2311
7	α-Linolenic	C18:3 (ω3) (9Z, 12Z, 15Z)	32.28	2077
8	Behenic	C22:0	35.58	2531
9	9.12-Octadecenoic	C18:1 (9E)	31.62	2069
10	γ-Linolenic	C18:3 (6Z, 9Z, 12Z)	32.38	2077
11	Linolelaidic	C18:2 (9E, 12E)	30.41	2080
12	Tetracosanoic	C24:0	38.29	2732
13	Decanoic	C10:0	26.53	1578
14	*trans*-Vaccenic	C18:1 (11E)	29.82	2089
15	Arachidonic	C24:4 (5Z, 8Z, 11Z, 14Z)	39.45	7462
16	Pentadecanoic	C15:0	24.38	1877
17	Undecanoic	C11:0	27.57	1506
18	10-Octadecenoic	C18:1 (10Z)	29.84	2100
19	Octadecanoic	C18:0	27.58	2133
20	Nonadecanoic	C19:0	26.54	2266
21	Cyclopropan octanoic	$C18\text{-}CH_2$	33.49	1627
22	Hexacosanoic	C26:0	42.35	2962
23	Octacosanoic	C28:0	45.45	3115
24	Pentacosanoic	C25:0	46.27	2829
25	Octanoic	C8:0	24.29	1154

[a] Fatty Acids Methyl Esters: a methylation step was conducted prior to GC-MS analysis.

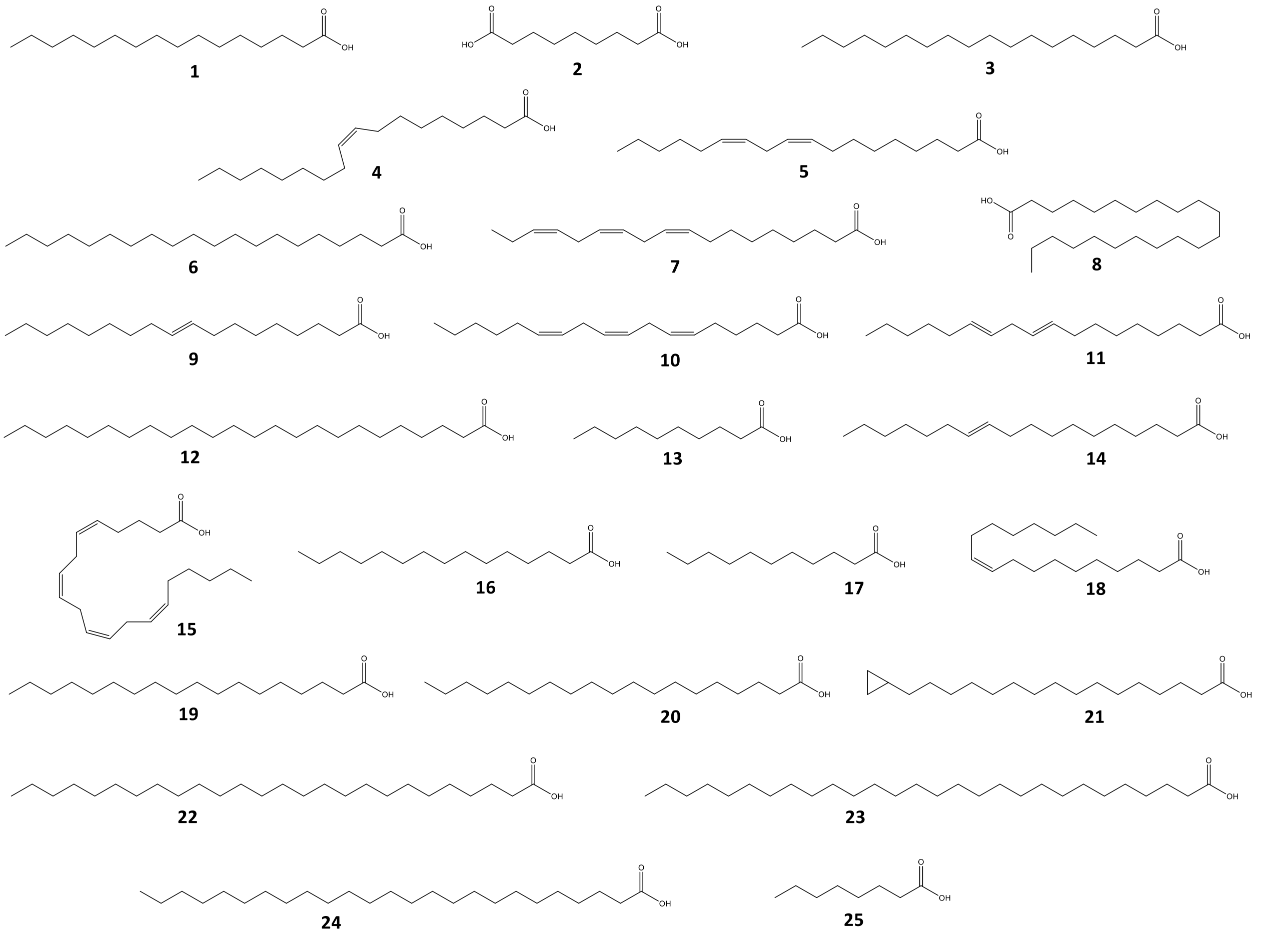

Figure 5.3.3. Chemical structures of the extracted fatty acids. Numbers refer to Table 5.3.4.

As highlighted, the scCO$_2$ extracts generally resulted in a higher content of FAs comprised a diversified range of saturated (SAFA), monounsaturated (MUFA) and polyunsaturated (PUFA) fatty acids. We identified 25 different acids (see **Figure 5.3.3** for structures), with each pomace yielding a different array. In **Table 5.3.5** the amount of FAs (in mg/g, reported as methyl esters, FAMEs) and the total amounts of SAFAs, MUFAs and PUFAs for each pomace and both studied extraction solvents, are reported. Together with the evidence that scCO$_2$ extracts were always richer in FAs than the hexanes ones, other aspects emerged. It was, indeed, evident that the distribution of SAFAs, MUFAs and PUFAs extracted by scCO$_2$ was different for each pomace: the mixtures obtained from wild strawberry, blueberry, blackberry and raspberry pomaces possessed high content of polyunsaturated fatty acids, such as linoleic (**Figure 5.3.3**, number **5**) and α-linolenic (**Figure 5.3.3**, number **7**) acid, and of the monounsaturated oleic acid (**Figure 5.15**, number **4**). On the other hand, pomegranate and blackcurrant scCO$_2$ extracts were richer in the SAFAs palmitic (**Figure 5.3.3**, number **1**), tetracosanoic (**Figure 5.3.3**, number **12**) and octadecanoic (**Figure 5.3.3**, number **19**) fatty acids. It should be however noted that the differences observed from the comparison of GC-chromatographic analyses of the extracts (both hexane and scCO$_2$ derived, appendix figures A.5.3.1-A.5.3.12), were not as such as to justify the greater yields obtained in hexane for wild strawberry, blueberry, pomegranate and blackcurrant (**Table 5.3.3**, entries 2, 4, and 12). NMR analyses were then carried out to explore in greater detail the composition of the hexane extracts (^{1}H NMR spectra for the case of wild strawberry are reported in **Figure 5.3.4**, ^{13}C NMR spectra are reported in the appendix figure A.5.3.38-A.5.3.39). Anyway, comparing the spectra of hexane-derived extract with the scCO$_2$ ones, results were not conclusive. Though, the greater intensity of chemical shifts in the regions of vinyl protons and C=C double bonds, was consistent with a more abundant presence of unsaturated compounds. Moreover, the presence of some peaks around 4.0 and 5.5 ppm in the hexane extract made us think about the possibility of the presence of terpenes and terpenoids while heavier compounds were not detected (**Figure 5.3.4**). This evidence suggested that with the traditional extraction with hexane, other light compounds were extracted, and they were probably lost before the analysis step. This could justify the higher yields obtained with hexane compared with the scCO_2 one and the higher selectivity of this last one for fatty acids. In any case this aspect will be further inspected in future investigations.

The extraction experiments however, demonstrated the efficacy of scCO_2 for the selective achievement of FAs from different pomaces, suggesting the opportunity to use these secondary products of the food industry as a source of high value oils for the cosmetic and food supplement areas. There is in fact widespread interest for the use of unsaturated vegetable oils in cosmetic formulations[127] especially due to their anti-inflammatory and protective effects on skin.[128] Particularly, among PUFAs of **Table 5.3.4**, linoleic and α-linolenic acids which are not synthesized by the human body, play a fundamental role to preserve the barrier-function of the skin and the integrity of the stratum corneum. Moreover, MUFAs and PUFAs such as oleic acid, α-linolenic acid, linoleic acid and γ-linolenic acid are frequent ingredients for the production of functional foods of food supplements due to their effects for the cardiovascular wellness, the regulatory activity of the cholesterol level in blood, the promotion of the cell's growth, and antioxidant properties.

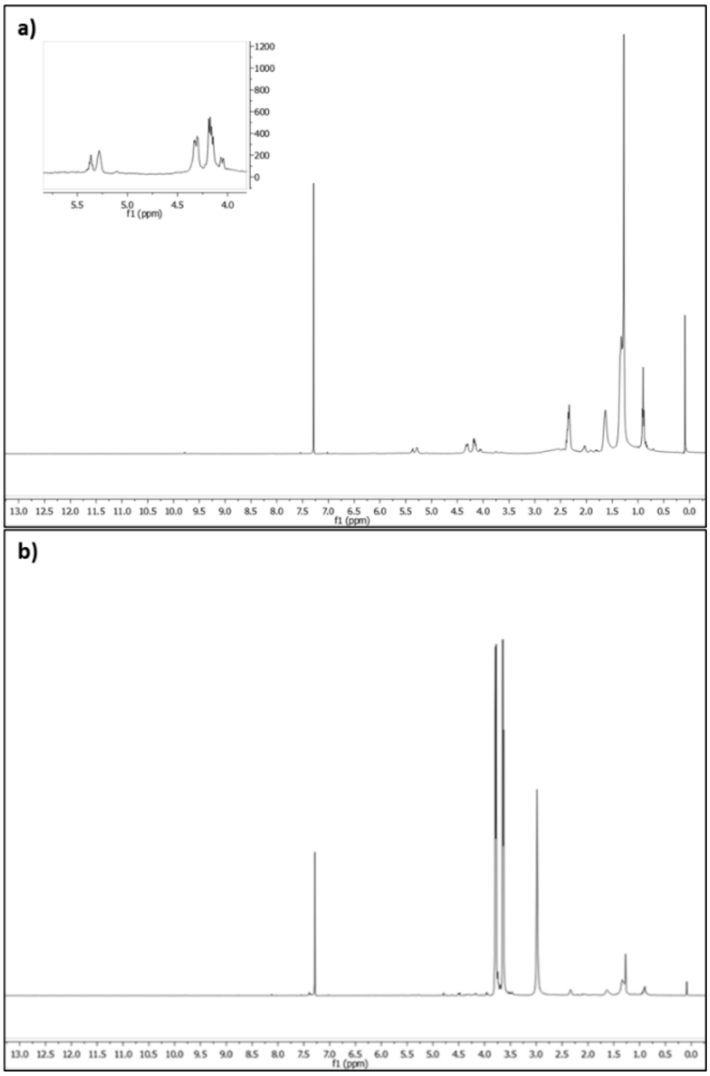

Figure 5.3.4. a) ^{1}H NMR spectra of the wild strawberry hexane extract in $CDCl_3$. Between 4.0 and 5.5 ppm are highlighted signals relative to the presence of terpenes or terpenoids. b) ^{1}H NMR spectra of the wild strawberry scCO_2 extract in $CDCl_3$.

Table 5.3.5. Yields of FAs in the extracts (mg/g, as FAMEs).

Pomace	Solvent	1	2	3	4	5	6	7	8	9	10	11	12	13	14	15	16	17	18	19	20	21	22	23	24	25	ΣSAFA	ΣMUFA	ΣPUFA	Total FAs
Wild strawberry	Hexane	0.9	-	0.5	1.8	-	0.2	-	-	4.6	6.3	-	-	-	-	-	-	-	-	-	-	-	-	-	-	-	1.6	6.4	6.3	14.3
	scCO$_2$	21.0	3.5	16.8	64.0	78.9	6.3	66.9	2.7	-	-	-	-	-	-	-	-	-	-	-	-	-	-	-	-	-	46.8	64.0	145.8	256.6
Blueberry	Hexane	0.5	-	-	-	2.6	-	2.5	-	-	-	-	-	-	-	-	-	-	1.1	-	-	-	-	-	-	-	0.5	1.1	5.1	6.7
	scCO$_2$	17.8	-	-	74.2	80.4	-	54.5	-	-	-	-	-	-	-	-	4.0	3.8	-	-	-	-	-	-	-	-	25.6	74.2	134.9	234.7
Pomegranate	Hexane	0.2	-	-	-	0.7	-	0.3	-	-	-	-	-	0.1	0.4	0.8	-	-	-	-	-	-	—	-	-	-	0.3	0.4	1.8	2.5
	scCO$_2$	4.8	-	3.1	6.9	-	-	-	-	-	-	7.7	103.0	-	-	-	-	-	-	-	-	-	-	-	-	-	110.9	6.9	7.7	125.5
Blackberry	Hexane	-	-	-	0.4	-	-	-	-	-	-	-	-	-	-	-	-	-	-	-	0.2	0.7	-	-	-	-	0.9	0.4	0.0	1.3
	scCO$_2$	18.2	-	-	66.3	166.7	-	30.3	-	-	-	-	-	-	-	-	-	-	-	13.2	-	-	-	-	-	-	31.4	66.3	197.0	294.7
Raspberry	Hexane	0.1	-	-	0.06	-	-	-	-	-	-	-	-	-	-	-	-	-	-	-	-	-	-	-	-	-	0.1	0.1	0.0	0.2
	scCO$_2$	14.3	-	6.9	61.2	191	-	-	5.5	-	-	-	4.1	-	-	-	-	-	-	-	-	-	7.2	6.9	-	5.8	50.7	61.2	191.0	302.9
Blackcurrant	Hexane	-	-	-	-	-	0.05	-	-	-	-	-	0.1	-	-	-	-	-	-	0.07	-	-	-	-	0.4	-	0.6	0.0	0.0	0.6
	scCO$_2$	22.0	-	-	-	51.2	7.1	-	6.2	-	9.1	-	11.7	-	-	-	-	-	-	21.7	-	-	17.4	18.2	-	-	104.3	0.0	60.3	164.6

SAFA: saturated fatty acids, MUFA: monounsaturated fatty acids, PUFA: polyunsaturated fatty acids.

5.3.3 Conclusions

With the aim to go toward a circular economy model, it results mandatory to recover, reprocess, reuse and recycle as much as possible of all materials. In this study we demonstrated that the agro-food waste pomaces obtained from juice and fruit preserves industries represent un under-explored and under-estimated source of valuable fatty acids that can have a potential wide interest for applications in the cosmetic and nutraceutical field. With a view on all-round sustainability, the processing of these wastes should also comply with the principles of green chemistry. Compared to conventional extractive method such as mechanical pressing or solvent extraction, supercritical carbon dioxide FAs extraction eliminates solvent residues, operates under mild conditions and in the absence of oxygen; thus, it can be considered valuable for the extraction of FAs from fruit pomaces with potential to improve the yields, to shorten the extraction times, and to obtain FAs that retain their unsaturated FAs content. Indeed, this paper proves that $scCO_2$ is not only successful for the upgrading of the investigated wastes but is also far more selective to obtain high-quality FAs compounds compared to conventional Soxhlet procedures based on toxic and dangerous hexane. The affinity of supercritical CO_2 for lipophilic compounds leads to purer extracts, with a higher percentage of FAs compared to hexane (e.g. for wild strawberry 26.0% of FAs was obtained with supercritical CO_2 and 1.4% using hexane), avoiding any solvent contamination of the products as well as additional process unit-operations.

5.3.4 Experimental

Equipment and chemicals. All chemicals and solvents were purchased from commercial sources and used without further purification. Ethanol (pharma-grade) and hexane were purchased from Sigma-Aldrich. The supercritical CO_2 extractions were performed in a laboratory apparatus consisting of a Jasco PU-2080-CO 2 Plus delivery Pump and a Jasco 2080 Plus Automatic Back Pressure Regulator used for the pressure control. A Chrompack CP-9003 oven was used to heat the connecting stainless tubes and the different reactors. GC–MS analysis were conducted using a GC system Agilent 7820A coupled with a single quadrupole mass detector Agilent 5977B MSD equipped with a HP88 column (60 m x0.25 mm, 0.2 µm).

Sample preparation. Frozen seeds and peels of six different types of fruits (raspberry, blueberry, wild strawberry, pomegranate, blackberry and blackcurrant) were provided by Rigoni di Asiago (Asiago, Italy). Pre-treatment involved weighing the frozen waste, followed by rinsing with milliQ water for 15 min and then air drying for 24 h. The initial water content of the pomace was determined by difference between initial and dry samples and is shown in **Table 5.3.2**. The residual water content was determined for each air-dried sample after heating in a vacuum-drying chamber (70 °C, 5 mbar, 24 h). Additional information on the composition in sugars, lipids and proteins of the biomass are reported in **Table 5.3.1**.

Soxhlet extraction. 3 g of dry pomace and 150 mL of solvent (hexane) were put in a Soxhlet apparatus (containing a cellulose thimble); the solvent was refluxed for 24h. The obtained solutions were then analysed by GC–MS, using methyl pentadecanoate (2 mg/mL) as internal standard for the qualitative and quantitative characterisation of the extracts. The solvent was evaporated under reduced pressure to determine the extraction yield ($Y_{extract} = wt_{extract} / wt_{dry\ biomass}$ %).

Supercritical fluid extraction. The extraction experiments were conducted on an analytical-scale supercritical fluid extraction unit (internal volume of approximately 10 cm^3, plug diameter 3/8'' and plug length 15 cm) using CO_2 as solvent. In a typical experiment, approximately 3 g of dry ground pomace were loaded in the vessel and a constant flow rate of supercritical CO_2 (5.0 $cm^3\ min^{-1}$) at 300 bar, 70 °C for 5 h. The extracts were collected by venting into hexane at ambient temperature and pressure and were gravimetrically quantified ($Y_{extract} = wt_{extract} / wt_{dry\ biomass}$ %) at the end of each run (after hexane removal). For the qualitative and quantitative analysis of the extract were used GC–MS, using methyl pentadecanoate (2 mg/mL) as internal standard.

Chromatographic analysis of the extracts. Prior to GC–MS analysis, the FAs containing extracts were converted to the corresponding methyl esters (FAMEs) by dissolving the extracts (50 mg exactly weighted) in chloroform (5 mL) followed by addition of methanol (25 mL), of the internal standard (methyl pentadecanoate 0.5 mL of solution in chloroform 500 μg/mL) and of a catalytic quantity of sulfuric acid. The resulting solution was refluxed overnight. The FAMEs were extracted with a mixture of water and diethyl ether (10:2). The organic fraction was analysed by GC–MS. Identification of fatty acid was obtained comparing the MS spectra and the retention index of compounds. Quantification was obtained using the methyl pentadecanoate as internal standard.

5.4 Bibliography

(1) Mohamed, R. S.; Mansoori, G. A. The Use of Supercritical Fluid Extraction Technology in Food Processing. *Food Technology Magazine* **2002**, *20*, 134–139.

(2) Erkucuk, A.; Akgun, I. H.; Yesil-Celiktas, O. Supercritical CO 2 Extraction of Glycosides from Stevia Rebaudiana Leaves : Identification and Optimization. *Journal of Supercritical Fluids* **2009**, *51*, 29–35. https://doi.org/10.1016/j.supflu.2009.07.002.

(3) Wang, L.; Weller, C. L. Recent Advances in Extraction of Nutraceuticals from Plants. *Trends Food Sci Technol* **2006**, *17*, 300–312. https://doi.org/10.1016/j.tifs.2005.12.004.

(4) Viganó, J.; Paula, A.; Martínez, J. Sub- and Supercritical Fluid Technology Applied to Food Waste Processing. *J Supercrit Fluids* **2015**, *96*, 272–286. https://doi.org/10.1016/j.supflu.2014.09.026.

(5) Wang, L.; Weller, C. L.; Schlegel, V. L.; Carr, T. P.; Cuppett, S. L. Supercritical CO 2 Extraction of Lipids from Grain Sorghum Dried Distillers Grains with Solubles. *Bioresour Technol* **2008**, *99*, 1373–1382. https://doi.org/10.1016/j.biortech.2007.01.055.

(6) Herrero, M.; Cifuentes, A.; Ibanez, E. Sub- and Supercritical Fluid Extraction of Functional Ingredients from Different Natural Sources : Plants , Food-by-Products , Algae and Microalgae A Review. *Food Chem* **2006**, *98*, 136–148. https://doi.org/10.1016/j.foodchem.2005.05.058.

(7) Sihvonen, M.; Jarvenpaa, E.; Hietaniemi, V.; Huopalahti, R. Advances in Supercritical Carbon Dioxide Technologies. *Trends Food Sci Technol* **1999**, *10*, 217–222. https://doi.org/https://doi.org/10.1016/S0924-2244(99)00049-7.

(8) da Silva, R. P. F. F.; Rocha-santos, T. A. P.; Duarte, A. C. Supercritical Fluid Extraction of Bioactive Compounds. *Trends in Analytical Chemistry* **2016**, *76*, 40–51. https://doi.org/10.1016/j.trac.2015.11.013.

(9) Babovic, N.; Djilas, S.; Jadranin, M.; Vajs, V.; Ivanovic, J.; Petrovic, S.; Zizovic, I. Supercritical Carbon Dioxide Extraction of Antioxidant Fractions from Selected Lamiaceae Herbs and Their Antioxidant Capacity. *Innovative Food Science and Emerging Technologies* **2010**, *11*, 98–107. https://doi.org/10.1016/j.ifset.2009.08.013.

(10) Herrero, M.; Cifuentes, A.; Ibanez, E. Sub- and Supercritical Fluid Extraction of Functional Ingredients from Different Natural Sources : Plants , Food-by-Products , Algae and Microalgae A Review. *Food Chem* **2006**, *98*, 136–148. https://doi.org/10.1016/j.foodchem.2005.05.058.

(11) Reverchon, E.; Kaziunas, A.; Marrone, C. Supercritical CO Extraction of Hiprose Seed Oil : Experiments and Mathematical Modelling. *Chem Eng Sci* **2000**, *55*, 2195–2201. https://doi.org/DOI: 10.1016/S0009-2509(99)00519-9.

(12) Dunford, N. T.; Teel, J. A.; King, J. W. A Continuous Countercurrent Supercritical Fluid Deacidification Process for Phytosterol Ester Fortification in Rice Bran Oil. *Food Research International* **2003**, *36*, 175–181. https://doi.org/https://doi.org/10.1016/S0963-9969(02)00134-5.

(13) Ceni, G.; Fernandes Silva, M.; Valério, C.; Cansian, R. L.; Oliveira, J. V.; Dalla Rosa, C.; Mazutti, M. A. Continuous Inactivation of Alkaline Phosphatase and Escherichia Coli in Milk Using Compressed Carbon Dioxide as Inactivating Agent. *Journal of CO2 Utilization* **2016**, *13*, 24–28. https://doi.org/10.1016/j.jcou.2015.11.003.

(14) Budich, M.; Brunner, G. Supercritical Fluid Extraction of Ethanol from Aqueous Solutions. *Journal of Supercritical Fluids* **2003**, *25*, 45–55. https://doi.org/https://doi.org/10.1016/S0896-8446(02)00091-8.

(15) Zaidul, I. S. M.; Nik Nourlaini, N. A.; Mohd Omar, A. K.; Smith, R. L. Supercritical Carbon Dioxide (SC-CO 2) Extraction of Palm Kernel Oil from Palm Kernel. *J Food Eng* **2007**, *79*, 1007–1014. https://doi.org/10.1016/j.jfoodeng.2006.03.021.

(16) Akinlua, A.; Torto, N.; Ajayi, T. R. Supercritical Fluid Extraction of Aliphatic Hydrocarbons from Niger Delta Sedimentary Rock. *Journal of Supercritical Fluids* **2008**, *45*, 57–63. https://doi.org/10.1016/j.supflu.2007.11.016.

(17) Zaidul, I. S. M.; Norulaini, N. A. N.; Omar, A. K. M.; Sato, Y.; Smith, R. L. Separation of Palm Kernel Oil from Palm Kernel with Supercritical Carbon Dioxide Using Pressure Swing Technique. *J Food Eng* **2007**, *81*, 419–428. https://doi.org/10.1016/j.jfoodeng.2006.11.019.

(18) Wang, L.; Weller, C. L.; Schlegel, V. L.; Carr, T. P.; Cuppett, S. L. Supercritical CO 2 Extraction of Lipids from Grain Sorghum Dried Distillers Grains with Solubles. *Bioresour Technol* **2008**, *99*, 1373–1382. https://doi.org/10.1016/j.biortech.2007.01.055.

(19) Cavero, S.; Garcia-Risco, M. R.; Marin, F. R.; Jaime, L.; Santoyo, S.; Senorans, F. J.; Reglero, G.; Ibanez, E. Supercritical Fluid Extraction of Antioxidant Compounds from Oregano Chemical and Functional Characterization via LC – MS and in Vitro Assays. *Journal of Supercritical Fluids* **2006**, *38*, 62–69. https://doi.org/10.1016/j.supflu.2005.01.003.

(20) Daintree, L. S.; Kordikowski, A.; York, P. Separation Processes for Organic Molecules Using SCF Technologies. *Advanced Drug Delivery Review* **2008**, *60*, 351–372. https://doi.org/10.1016/j.addr.2007.03.024.

(21) Sahena, F.; Zaidul, I. S. M.; Jinap, S.; Karim, A. A.; Abbas, K. A.; Norulaini, N. A. N.; Omar, A. K. M. Application of Supercritical CO2in Lipid Extraction - A Review. *J Food Eng* **2009**, *95* (2), 240–253. https://doi.org/10.1016/j.jfoodeng.2009.06.026.

(22) Ahmad, T.; Masoodi, F. A.; Rather, S. A.; Wani, S. M.; Gull, A. Supercritical Fluid Extraction: A Review. *J. Biol. Chem. Chron.* **2019**, *5* (1), 114–122. https://doi.org/10.33980/jbcc.2019.v05i01.019.

(23) Shi, J.; Mittal, G.; Kim, E.; Xue, S. J. Solubility of Carotenoids in Supercritical CO2. *Food Reviews International* **2007**, *23* (4), 341–371. https://doi.org/10.1080/87559120701593806.

(24) Sabirzyanov, A. N.; Il'in, A. P.; Akhunov, A. R.; Gumerov, F. M. Solubility of Water in Supercritical Carbon Dioxide. *High Temperature* **2002**, *40* (2), 203–206.

(25) York, P. Strategies for Particle Design Using Supercritical Fluid Technologies. *PSTT* **1999**, *2*, 430–440.

(26) Sovovà, H.; Jez, J.; Khachaturyan, M. Solubility of Squalane, Dinonyl Phthalate and Glycerol in Supercritical CO 2. *Fluid Phase Equilib* **1997**, *137*, 185–191.

(27) Yamini, Y.; Fat'hi, M. R.; Alizadeh, N.; Shamsipur, M. *Solubility of Dihydroxybenzene Isomers in Supercritical Carbon Dioxide*; 1998; Vol. 152.

(28) Taylor, S. L.; Eller, F. J.; King, J. W. A Comparison of Oil and Fat Content in Oilseeds and Ground Beef Using Supercritical Fluid Extraction and Related Analytical Techniques. *Food Research International* **1997**, *30* (5), 365–370. https://doi.org/https://doi.org/10.1016/S0963-9969(97)00060-4.

(29) Raventós, M.; Duarte, S.; Alarcón, R. Application and Possibilities of Supercritical CO2 Extraction in Food Processing Industry: An Overview. *Food Science and Technology International* **2002**, *8* (5), 269–284. https://doi.org/10.1106/108201302029451.

(30) Armenta, S.; de la Guardia, M. Green Chromatography for the Analysis of Foods of Animal Origin. *Trends in Analytical Chemistry* **2016**, *80*, 517–530. https://doi.org/10.1016/j.trac.2015.06.012.

(31) Pan, J.; Zhang, C.; Zhang, Z.; Li, G. Review of Online Coupling of Sample Preparation Techniques with Liquid Chromatography. *Anal Chim Acta* **2014**, *815*, 1–15. https://doi.org/10.1016/j.aca.2014.01.017.

(32) Campalani, C.; Chioggia, F.; Amadio, E.; Gallo, M.; Rizzolio, F.; Selva, M.; Perosa, A. Supercritical CO 2 Extraction of Natural Antibacterials from Low Value Weeds and Agro-Waste. *Journal of CO2 Utilization* **2020**, *40*, 101198. https://doi.org/10.1016/j.jcou.2020.101198.

(33) Álvarez-Lerma, F.; Maull, E.; Terradas, R.; Segura, C.; Planells, I.; Coll, P.; Knobel, H.; Vázquez, A. Moisturizing Body Milk as a Reservoir of Burkholderia Cepacia: Outbreak of Nosocomial Infection in a Multidisciplinary Intensive Care Unit. *Crit Care* **2008**, *12* (1), 1–6. https://doi.org/10.1186/cc6778.

(34) Regulation No 1223/2009 of the European Parliament and of the Council on Cosmetic Products. 02009R1223 — EN — 01.03.2022 — 030.002 — 1. *Official Journal of the European Union* **2009**.

(35) Lundov, M. D.; Johansen, J. D.; Zachariae, C.; Moesby, L. Low-Level Efficacy of Cosmetic Preservatives. *Int J Cosmet Sci* **2011**, *33* (2), 190–196. https://doi.org/10.1111/j.1468-2494.2010.00619.x.

(36) Lee, E.; An, S.; Choi, D.; Moon, S.; Chang, I. Comparison of Objective and Sensory Skin Irritations of Several Cosmetic Preservatives. *Contact Dermatitis* **2007**, *56* (3), 131–136. https://doi.org/10.1111/j.1600-0536.2007.01001.x.

(37) Lundov, M. D.; Johansen, J. D.; Zachariae, C.; Moesby, L. Low-Level Efficacy of Cosmetic Preservatives. *Int J Cosmet Sci* **2011**, *33* (2), 190–196. https://doi.org/10.1111/j.1468-2494.2010.00619.x.

(38) Lee, E.; An, S.; Choi, D.; Moon, S.; Chang, I. Comparison of Objective and Sensory Skin Irritations of Several Cosmetic Preservatives. *Contact Dermatitis* **2007**, *56* (3), 131–136. https://doi.org/10.1111/j.1600-0536.2007.01001.x.

(39) Lundov, M. D.; Thyssen, J. P.; Zachariae, C.; Johansen, J. D. Prevalence and Cause of Methylisothiazolinone Contact Allergy. *Contact Dermatitis* **2010**, *63* (3), 164–167. https://doi.org/10.1111/j.1600-0536.2010.01774.x.

(40) Thyssen, J. P.; Engkilde, K.; Lundov, M. D.; Carlsen, B. C.; Menné, T.; Johansen, J. D. Temporal Trends of Preservative Allergy in Denmark (1985-2008). *Contact Dermatitis* **2010**, *62* (2), 102–108. https://doi.org/10.1111/j.1600-0536.2009.01668.x.

(41) Pandey, A. K.; Kumar, P.; Singh, P.; Tripathi, N. N.; Bajpai, V. K. Essential Oils: Sources of Antimicrobials and Food Preservatives. *Front Microbiol* **2017**, *7*, 1–14. https://doi.org/10.3389/fmicb.2016.02161.

(42) Maccioni, A. M.; Anchisi, C.; Sanna, A.; Sardu, C.; Dessì, S. Preservative Systems Containing Essential Oils in Cosmetic Products. *Int J Cosmet Sci* **2002**, *24* (1), 53–59. https://doi.org/10.1046/j.0412-5463.2001.00113.x.

(43) Muyima, N. Y. O.; Zulu, G.; Bhengu, T.; Popplewell, D. The Potential Application of Some Novel Essential Oils as Natural Cosmetic Preservatives in a Aqueous Cream Formulation. *Flavour Fragr J* **2002**, *17* (4), 258–266. https://doi.org/10.1002/ffj.1093.

(44) A. Smith-Palmer; Stewart, J.; Fyfe, L. Antimicrobial Properties of Plant Essential Oils and Essences against Five Important Food-Borne Pathogens. *Lett Appl Microbiol* **1998**, *26* (1987), 118–122. https://doi.org/10.1046/j.1472-765x.1998.00303.x.

(45) F. Bakkali, S. Averbeck, D. Averbeck, M. I. Biological Effects of Essential Oils – A Review. *Food and Chemical Toxicology* **2008**, *46*, 446–475. https://doi.org/10.1016/j.fct.2007.09.106.

(46) Swamy, M. K.; Akhtar, M. S.; Sinniah, U. R. Antimicrobial Properties of Plant Essential Oils against Human Pathogens and Their Mode of Action: An Updated Review. *Evidence-based Complementary and Alternative Medicine* **2016**, *2016*, 21. https://doi.org/10.1155/2016/3012462.

(47) Álvarez-Martínez, F. J.; Barrajón-Catalán, E.; Herranz-López, M.; Micol, V. Antibacterial Plant Compounds, Extracts and Essential Oils: An Updated Review on Their Effects and Putative Mechanisms of Action. *Phytomedicine* **2021**, *90*, 153626. https://doi.org/10.1016/j.phymed.2021.153626.

(48) Chen, M.; Zhao, Z.; Meng, H.; Yu, S. The Antibiotic Activity and Mechanisms of Sugar Beet (Beta Vulgaris) Molasses Polyphenols against Selected Food-Borne Pathogens. *LWT - Food Science and Technology* **2017**, *82*, 354–360. https://doi.org/10.1016/j.lwt.2017.04.063.

(49) Taguri, T.; Tanaka, T.; Kouno, I. Antimicrobial Activity of 10 Different Plant Polyphenols against Bacteria Causing Food-Borne Disease. *Biol Pharm Bull* **2004**, *27* (12), 1965–1969. https://doi.org/10.1248/bpb.27.1965.

(50) Palacios, L.; Rosado, H.; Micol, V.; Rosato, A. E.; Bernal, P.; Arroyo, R.; Grounds, H.; Anderson, J. C.; Stabler, R. A.; Taylor, P. W. Staphylococcal Phenotypes Induced by Naturally Occurring and Synthetic Membrane-Interactive Polyphenolic β-Lactam Resistance Modifiers. *PLoS One* **2014**, *9* (4). https://doi.org/10.1371/journal.pone.0093830.

(51) Saad, N. Y.; Muller, C. D.; Lobstein, A. Major Bioactivities and Mechanism of Action of Essential Oils and Their Components. *Flavour Fragr J* **2013**, *28* (5), 269–279. https://doi.org/10.1002/ffj.3165.

(52) Hemaiswarya, S.; Doble, M. Synergistic Interaction of Eugenol with Antibiotics against Gram Negative Bacteria. *Phytomedicine* **2009**, *16* (11), 997–1005. https://doi.org/10.1016/j.phymed.2009.04.006.

(53) Yang, X. N.; Khan, I.; Kang, S. C. Chemical Composition, Mechanism of Antibacterial Action and Antioxidant Activity of Leaf Essential Oil of Forsythia Koreana Deciduous Shrub. *Asian Pac J Trop Med* **2015**, *8* (9), 694–700. https://doi.org/10.1016/j.apjtm.2015.07.031.

(54) Di Pasqua, R.; Betts, G.; Hoskins, N.; Edwards, M.; Ercolini, D.; Mauriello, G. Membrane Toxicity of Antimicrobial Compounds from Essential Oils. *J Agric Food Chem* **2007**, *55* (12), 4863–4870. https://doi.org/10.1021/jf0636465.

(55) Di Pasqua, R.; Hoskins, N.; Betts, G.; Mauriello, G. Changes in Membrane Fatty Acids Composition of Microbial Cells Induced by Addiction of Thymol, Carvacrol, Limonene, Cinnamaldehyde, and Eugenol in the Growing Media. *J Agric Food Chem* **2006**, *54* (7), 2745–2749. https://doi.org/10.1021/jf052722l.

(56) Bouhdid, S.; Abrini, J.; Amensour, M.; Zhiri, A.; Espuny, M. J.; Manresa, A. Functional and Ultrastructural Changes in Pseudomonas Aeruginosa and Staphylococcus Aureus Cells Induced by Cinnamomum Verum Essential Oil. *J Appl Microbiol* **2010**, *109* (4), 1139–1149. https://doi.org/10.1111/j.1365-2672.2010.04740.x.

(57) Álvarez-Martínez, F. J.; Barrajón-Catalán, E.; Micol, V. Tackling Antibiotic Resistance with Compounds of Natural Origin: A Comprehensive Review. *Biomedicines* **2020**, *8* (10), 1–30. https://doi.org/10.3390/biomedicines8100405.

(58) Herranz-López, M.; Losada-Echeberría, M.; Barrajón-Catalán, E. The Multitarget Activity of Natural Extracts on Cancer: Synergy and Xenohormesis. *Medicines* **2018**, *6* (1), 6. https://doi.org/10.3390/medicines6010006.

(59) Herranz-López, M.; Fernández-Arroyo, S.; Pérez-Sanchez, A.; Barrajón-Catalán, E.; Beltrán-Debón, R.; Menéndez, J. A.; Alonso-Villaverde, C.; Segura-Carretero, A.; Joven, J.; Micol, V. Synergism of Plant-Derived Polyphenols in Adipogenesis: Perspectives and Implications. *Phytomedicine* **2012**, *19* (3–4), 253–261. https://doi.org/10.1016/j.phymed.2011.12.001.

(60) Olivares-Vicente, M.; Sánchez-Marzo, N.; Encinar, J. A.; de La Luz Cádiz-Gurrea, M.; Lozano-Sánchez, J.; Segura-Carretero, A.; Arraez-Roman, D.; Riva, C.; Barrajón-Catalán, E.; Herranz-López, M.; Micol, V. The Potential Synergistic Modulation of AMPK by Lippia Citriodora Compounds as a Target in Metabolic Disorders. *Nutrients* **2019**, *11*, 2961. https://doi.org/10.3390/nu11122961.

(61) Boatwright, J. Antimicrobial Activity of Hop Oil Emulsion. *J. Inst. Brew.* **1976**, 334–335. https://doi.org/https://doi.org/10.1002/j.2050-0416.1975.tb06957.x.

(62) Zanoli, P.; Zavatti, M. Pharmacognostic and Pharmacological Profile of Humulus Lupulus L . *J Ethnopharmacol* **2008**, *116*, 383–396. https://doi.org/10.1016/j.jep.2008.01.011.

(63) Wendakoon, C.; Calderom, P.; Gagnon, D. Evaluation of Selected Medicinal Plants Extracted in Different Ethanol Concentrations for Antibacterial Activity against Human Pathogens. *Journal of Medicinally Active Plants* **2012**, *1* (2), 60–68. https://doi.org/10.7275/R5GH9FV2.

(64) Kumar, A.; Garg, B. R.; Rajput, G.; Chandel, D.; Muwalia, A.; Bala, I.; Singh, S. Antibacterial Activity and Quantitative Determination of Protein from Leaf of Datura Stramonium and Piper Betle Plants. *Pharmacophore* **2010**, *1* (3), 184–195.

(65) Eftekhar, F.; Yousefzadi, M.; Tafakori, V. Antimicrobial Activity of Datura Innoxia and Datura Stramonium. *Fitoterapia* **2005**, *76* (1), 118–120. https://doi.org/10.1016/j.fitote.2004.10.004.

(66) B.D. Gachande, E. M. K. In-Vitro Evaluation of Datura Species for Potential Antimicrobial Activity. *Bioscience discovery* **2013**, *4* (1), 78–81.

(67) Cowan, M. M. Plant Products as Antimicrobial Agents. *Clinical Microbiology Reviwes* **1999**, *12* (4), 564–582. https://doi.org/10.1128/CMR.12.4.564.

(68) Desbois, A. P.; Smith, V. J. Antibacterial Free Fatty Acids : Activities , Mechanisms of Action and Biotechnological Potential. *Appl. Microbiol. Biotechnol.* **2010**, *85*, 1629–1642. https://doi.org/10.1007/s00253-009-2355-3.

(69) Ouattara, B.; Simard, R. E.; Holley, R. A.; Piette, G. J. Antibacterial Activity of Selected Fatty Acids and Essential Oils against Six Meat Spoilage Organisms. *Int J Food Microbiol* **1997**, *37*, 155–162. https://doi.org/10.1016/s0168-1605(97)00070-6.

(70) Katsiotis, S. Composition of the Essential Oils from Leaves of Various Humulus Lupulus L. Cultivars. *Flavour Fragr J* **1990**, *5*, 178–193. https://doi.org/https://doi.org/10.1002/ffj.2730050208.

(71) K. Tyskiewicz, R. Gieysztor, M. Konkol, J. Szalas, E. R. Essential Oils from Humulus Lupulus ScCO2 Extract by Hydrodistillation and Microwave-Assisted Hydrodistillation. *Molecules* **2018**, *23*, 2866. https://doi.org/10.3390/molecules23112866.

(72) Valle, M.; Rivera, O.; Teuber, O.; Palma, M. T. Supercritical CO 2 Extraction of Chilean Hop (Humulus Lupulus) Ecotypes. *J Sci Food Agric* **2003**, *83*, 1349–1356. https://doi.org/10.1002/jsfa.1547.

(73) Z. Zekovic, I. Pfaf-Sovljanski, O. G. Supercritical Fluid Extraction of Hops. *J. Serb. Chem. Soc.* **2007**, *72* (1), 81–87. https://doi.org/10.2298/JSC0701081Z.

(74) Van Opstaele, F.; Goiris, K.; De Rouck, G.; Aerts, G.; De Cooman, L. Production of Novel Varietal Hop Aromas by Supercritical Fluid Extraction of Hop Pellets. Part 1: Preparation of Single Variety Total Hop Essential Oils and Polar Hop Essences. *Journal of Supercritical Fluids* **2012**, *71*, 147–161. https://doi.org/10.1016/j.cervis.2012.12.002.

(75) Rój, E.; Tadić, V. M.; Mišić, D.; Žižović, I.; Arsić, I.; Dobrzyńska-inger, A.; Kostrzewa, D. Supercritical Carbon Dioxide Hops Extracts with Antimicrobial Properties. *Open Chem.* **2015**, *13*, 1157–1171. https://doi.org/10.1515/chem-2015-0131.

(76) Van Opstaele, F.; De Causmaecker, B.; Aerts, G.; De Cooman, L. Characterization of Novel Varietal Floral Hop Aromas by Headspace Solid Phase Microextraction and Gas Chromatography-Mass Spectrometry/Olfactometry. *J Agric Food Chem* **2012**, *60*, 12270–12281. https://doi.org/10.1021/jf304421d.

(77) Van Cleemput, M.; Cattoor, K.; De Bosscher, K.; Haegeman, G.; De Keukeleire, D.; Heyerick, A. Hop (Humulus Lupulus)-Derived Bitter Acids as Multipotent Bioactive Compounds. *J Nat Prod* **2009**, *72* (6), 1220–1230. https://doi.org/10.1021/np800740m.

(78) Ohsugi, M.; Basnet, P.; Kadota, S.; Ishii, E.; Tamura, T.; Okumura, Y.; Namba, T. Antibacterial Activity of Traditional Medicines and an Active Constituent Lupulone from Humulus Lupulus against Helicobacter Pylori. *Journal of Traditional Medicines* **1997**, *14*, 186–191.

(79) Katsiotist, S. T.; Langezaal, C. R.; Scheffer, J. C.; Verpoorte, R.; Laboratories, G.; Instituut, V. T. Comparative Study of the Essential Oils from Hops of Various Humulus Lupulus L. Cultivars. *Flavour Fragr J* **1989**, *4*, 187–191. https://doi.org/10.1002/FFJ.2730040407.

(80) Langezaal, C. R.; Chandra, A.; Katsiotis, S. T.; Scheffer, J. J. C.; De Haan, A. B. Analysis of Supercritical Carbon Dioxide Extracts from Cones and Leaves of a Humulus Lupulus L Cultivar. *J Sci Food Agric* **1990**, *53*, 455–463. https://doi.org/10.1002/jsfa.2740530404.

(81) Grilc, V. Utilisation of Waste Hop Foliage by Solvent Extraction. *Bioresour Technol* **1994**, *49*, 7–12. https://doi.org/https://doi.org/10.1016/0960-8524(94)90166-X.

(82) A. El Bazaoui, M.A. Bellimam, A. S. Nine New Tropane Alkaloids from Datura Stramonium L . Identified by GC / MS. *Fitoterapia* **2011**, *82*, 193–197. https://doi.org/10.1016/j.fitote.2010.09.010.

(83) Ananth, A. Phytochemical Analysis of Datura Stramonium L. as a Potential Medicinal Tree: An Overview. *International Journal of Pharmaceutical Science and Healthcare* **2013**, *5* (3), 12–18.

(84) Cortinovis, C.; Caloni, F. Alkaloid-Containing Plants Poisonous to Cattle and Horses in Europe. *Toxins (Basel)* **2015**, *7*, 5301–5307. https://doi.org/10.3390/toxins7124884.

(85) Gaire, B. P.; Subedi, L. A Review on the Pharmacological and Toxicological Aspects of Datura Stramonium L. *J Integr Med* **2013**, *11* (2), 73–79. https://doi.org/10.3736/jintegrmed2013016.

(86) Bouzidi, A.; Mahdeb, N.; Kara, N. Toxicity Studies of Alkaloids of Seeds of Datura Stramonium and Synthesis Alkaloids in Male Rats. *Journal of Medicinal Plants Research* **2011**, *5* (15), 3421–3431. https://doi.org/10.5897/JMPR.9001253.

(87) Altameme, H. J.; Hameed, I. H.; Kareem, M. A. Analysis of Alkaloid Phytochemical Compounds in the Ethanolic Extract of Datura Stramonium and Evaluation of Antimicrobial Activity. *Afr J Biotechnol* **2015**, *14* (19), 1668–1674. https://doi.org/10.5897/AJB2015.14536.

(88) Baynesagne, S.; Berhane, N.; Sendeku, W.; Ai, L. Antibacterial Activity of Datura Stramonium against Standard and Clinical Isolate Pathogenic Microorganisms. *Journal of Medicinal Plants Research* **2017**, *11* (31), 501–506. https://doi.org/10.5897/JMPR2017.6381.

(89) M.D. Luque de Castro, L. E. G.-A. Soxhlet Extraction of Solid Materials: An Outdated Technique with a Promising Innovative Future. *Anal Chim Acta* **1998**, *369*, 1–10. https://doi.org/10.1097/00005053-190406000-00004.

(90) Youngil, K. Equation of State for Carbon Dioxide. *Journal of Mechanical Science and Technology* **2007**, *21* (5), 799–803. https://doi.org/10.1007/BF02916358.

(91) Stavri, M.; Schneider, R.; Donnell, G. O.; Lechner, D.; Bucar, F.; Gibbons, S. The Antimycobacterial Components of Hops (Humulus Lupulus) and Their Dereplication. *Phytotherapy Research* **2004**, *18*, 774–776. https://doi.org/10.1002/ptr.1527.

(92) Nazzaro, F.; Fratianni, F.; Martino, L. De. Effect of Essential Oils on Pathogenic Bacteria. *Pharmaceuticals* **2013**, *6*, 1451–1474. https://doi.org/10.3390/ph6121451.

(93) J.J. Kabara, D.M. Swieczkowski, A.J. Conley, J. P. T. Fatty Acids and Derivatives as Antimicrobial Agents. *Antimicrob Agents Chemother* **1972**, 23–28. https://doi.org/10.1128/aac.2.1.23.

(94) G.R. Siragusa, G.J. Haas, P.D. Matthews, R.J. Smith, R.J. Buhr, N.M. Dale, M. G. W. Antimicrobial Activity of Lupulone against Clostridium Perfringens in the Chicken Intestinal Tract Jejunum and Caecum. *Journal of Antimicrobial and Chemotherapy* **2008**, *61*, 853–858. https://doi.org/10.1093/jac/dkn024.

(95) Kumar, S.; Kumar, D.; Jusha, M.; Saroha, K.; Singh, N.; Vashishta, B. Antioxidant and Free Radical Scavenging Potential of Citrullus Colocynthis (L.) Schrad. Methanolic Fruit Extract. *Acta Pharmaceutica* **2008**, *58* (2), 215–221. https://doi.org/10.2478/v10007-008-0008-1.

(96) Nieman, C. Influence of Trace Amounts of Fatty Acids on the Growth of Microorganisms. *Bacteriol. Rev.* **1954**, *18*, 147–163. https://doi.org/10.1128/br.18.2.147-163.1954.

(97) Nascimento, G. G. F.; Locatelli, J.; Freitas, P. C.; Silva, G. L. Antibacterial Activity of Plant Extracts and Phytochemicals on Antibiotic-Resistant Bacteria. *Brazilian Journal of Microbiology* **2000**, *21*, 247–256. https://doi.org/https://doi.org/10.1590/S1517-83822000000400003.

(98) Knobloch, K.; Pauli, A.; Iberl, B.; Weigand, H.; Weis, N. Antibacterial and Antifungal Properties of Essential Oil Components. *Journal of Essential Oil Research* **1989**, *1*, 119–128. https://doi.org/http://dx.doi.org/10.1080/10412905.1989.9697767 PLEASE.

(99) Trombetta, D.; Castelli, F.; Sarpietro, M. G.; Venuti, V.; Cristani, M.; Daniele, C.; Saija, A.; Mazzanti, G.; Bisignano, G. Mechanisms of Antibacterial Action of Three Monoterpenes. **2005**, *49* (6), 2474–2478. https://doi.org/10.1128/AAC.49.6.2474.

(100) Wallace, W. E. "Mass Spectra" by NIST Mass Spectrometry Data Center. In *NIST Chemistry WebBook, NIST Standard Reference Database Number 69, National Institute of Standards and Technology, Gaithersburg MD*; Linstrom, P. J., Mallard, W. G., Eds.; 2009. https://doi.org/https://doi.org/10.18434/T4D303.

(101) Campalani, C.; Amadio, E.; Zanini, S.; Dall'Acqua, S.; Panozzo, M.; Ferrari, S.; De Nadai, G.; Francescato, S.; Selva, M.; Perosa, A. Supercritical CO2as a Green Solvent for the Circular Economy: Extraction of Fatty Acids from Fruit Pomace. *Journal of CO2 Utilization* **2020**, *41*, 101259. https://doi.org/10.1016/j.jcou.2020.101259.

(102) Park, J. Y.; Chertow, M. R. Establishing and Testing the "Reuse Potential" Indicator for Managing Wastes as Resources. *J Environ Manage* **2014**, *137*, 45–53. https://doi.org/10.1016/j.jenvman.2013.11.053.

(103) Geissdoerfer, M.; Savaget, P.; Bocken, N. M. P.; Hultink, E. J. The Circular Economy – A New Sustainability Paradigm? *J Clean Prod* **2017**, *143*, 757–768. https://doi.org/10.1016/j.jclepro.2016.12.048.

(104) Stahel, W. R. Circular Economy. *Nature* **2016**, *531*, 435–438. https://doi.org/10.4324/9781315270326-38.

(105) Sakai, S. ichi; Yoshida, H.; Hirai, Y.; Asari, M.; Takigami, H.; Takahashi, S.; Tomoda, K.; Peeler, M. V.; Wejchert, J.; Schmid-Unterseh, T.; Douvan, A. R.; Hathaway, R.; Hylander, L. D.; Fischer, C.; Oh, G. J.; Jinhui, L.; Chi, N. K. International Comparative Study of 3R and Waste Management Policy Developments. *J Mater Cycles Waste Manag* **2011**, *13* (2), 86–102. https://doi.org/10.1007/s10163-011-0009-x.

(106) Yang, B.; Ahotupa, M.; Määttä, P.; Kallio, H. Composition and Antioxidative Activities of Supercritical CO2-Extracted Oils from Seeds and Soft Parts of Northern Berries. *Food Research International* **2011**, *44* (7), 2009–2017. https://doi.org/10.1016/j.foodres.2011.02.025.

(107) Wajs-Bonikowska, A.; Stobiecka, A.; Bonikowski, R.; Krajewska, A.; Sikora, M.; Kula, J. A Comparative Study on Composition and Antioxidant Activities of Supercritical Carbon Dioxide, Hexane and Ethanol Extracts from Blackberry (Rubus Fruticosus) Growing in Poland. *J Sci Food Agric* **2017**, *97* (11), 3576–3583. https://doi.org/10.1002/jsfa.8216.

(108) Goffman, F. D.; Galletti, S. Gamma-Linolenic Acid and Tocopherol Contents in the Seed Oil of 47 Accessions from Several Ribes Species. *J Agric Food Chem* **2001**, *49* (1), 349–354. https://doi.org/10.1021/jf0006729.

(109) Parry, J.; Su, L.; Luther, M.; Zhou, K.; Peter Yurawecz, M.; Whittaker, P.; Yu, L. Fatty Acid Composition and Antioxidant Properties of Cold-Pressed Marionberry, Boysenberry, Red Raspberry, and Blueberry Seed Oils. *J Agric Food Chem* **2005**, *53* (3), 566–573. https://doi.org/10.1021/jf048615t.

(110) Mazza, M.; Pomponi, M.; Janiri, L.; Bria, P.; Mazza, S. Omega-3 Fatty Acids and Antioxidants in Neurological and Psychiatric Diseases: An Overview. *Prog Neuropsychopharmacol Biol Psychiatry* **2007**, *31* (1), 12–26. https://doi.org/10.1016/j.pnpbp.2006.07.010.

(111) Nielsen, N. S.; Göttsche, J. R.; Holm, J.; Xu, X.; Mu, H.; Jacobsen, C. Effect of Structured Lipids Based on Fish Oil on the Growth and Fatty Acid Composition in Rainbow Trout (Oncorhynchus Mykiss). *Aquaculture* **2005**, *250* (1–2), 411–423. https://doi.org/10.1016/j.aquaculture.2005.06.009.

(112) Castro-Vargas, H. I.; Rodríguez-Varela, L. I.; Ferreira, S. R. S.; Parada-Alfonso, F. Extraction of Phenolic Fraction from Guava Seeds (Psidium Guajava L.) Using Supercritical Carbon Dioxide and Co-Solvents. *Journal of Supercritical Fluids* **2010**, *51* (3), 319–324. https://doi.org/10.1016/j.supflu.2009.10.012.

(113) Laroze, L. E.; Díaz-Reinoso, B.; Moure, A.; Zúñiga, M. E.; Domínguez, H. Extraction of Antioxidants from Several Berries Pressing Wastes Using Conventional and Supercritical Solvents. *European Food Research and Technology* **2010**, *231* (5), 669–677. https://doi.org/10.1007/s00217-010-1320-9.

(114) Basegmez, H. I. O.; Povilaitis, D.; Kitrytė, V.; Kraujalienė, V.; Šulniūtė, V.; Alasalvar, C.; Venskutonis, P. R. Biorefining of Blackcurrant Pomace into High Value Functional Ingredients Using Supercritical CO2, Pressurized Liquid and Enzyme Assisted Extractions. *Journal of Supercritical Fluids* **2017**, *124*, 10–19. https://doi.org/10.1016/j.supflu.2017.01.003.

(115) Jessop, P. G.; Leitner, W. *Chemical Synthesis Using Supercritical Fluids. Ed. Wiley-VCH*; 1999.

(116) Martinez, J. L. *Supercritical Fluid Extraction of Nutraceuticals and Bioactive Compounds. Ed. CRC Press*; Martinez, J. L., Ed.; 2008.

(117) Kováts, E. Gas-chromatographische Charakterisierung Organischer Verbindungen. Teil 1: Retentionsindices Aliphatischer Halogenide, Alkohole, Aldehyde Und Ketone. *Helv Chim Acta* **1958**, *41* (7), 1915–1932. https://doi.org/10.1002/hlca.19580410703.

(118) Christie, W. W. Gas Chromatography-Mass Spectrometry Methods for Structural Analysis of Fatty Acids. *Lipids* **1998**, *33* (4), 343–353. https://doi.org/10.1007/s11745-998-0214-x.

(119) Blanch, M.; Álvarez, I.; Sanchez-Ballesta, M. T.; Escribano, M. I.; Merodio, C. Involvement of Fatty Acids in the Response to High CO2 and Low Temperature in Harvested Strawberries. *Postharvest Biol Technol* **2019**, *147* (April 2018), 196–205. https://doi.org/10.1016/j.postharvbio.2018.10.001.

(120) Li, Q.; Wang, J.; Shahidi, F. Chemical Characteristics of Cold-Pressed Blackberry, Black Raspberry, and Blueberry Seed Oils and the Role of the Minor Components in Their Oxidative Stability. *J Agric Food Chem* **2016**, *64* (26), 5410–5416. https://doi.org/10.1021/acs.jafc.6b01821.

(121) Paul, A.; Banerjee, K.; Goon, A.; Saha, S. Chemo-Profiling of Anthocyanins and Fatty Acids Present in Pomegranate Aril and Seed Grown in Indian Condition and Its Bioaccessibility Study. *J Food Sci Technol* **2018**, *55* (7), 2488–2496. https://doi.org/10.1007/s13197-018-3166-2.

(122) De Jesus Manriquez-Torres, J.; Sánchez-Franco, J. A.; Ramírez-Moreno, E.; Del Socorro Cruz-Cansino, N.; Ariza-Ortega, J. A.; Torres-Valencia, J. M. Effect of Thermoultrasound on the Antioxidant Compounds and Fatty Acid Profile of Blackberry (Rubus Fruticosus Spp.) Juice. *Molecules* **2016**, *21* (12). https://doi.org/10.3390/molecules21121624.

(123) Ruiz Del Castillo, M. L.; Dobson, G.; Brennan, R.; Gordon, S. Fatty Acid Content and Juice Characteristics in Black Currant (Ribes Nigrum L.) Genotypes. *J Agric Food Chem* **2004**, *52* (4), 948–952. https://doi.org/10.1021/jf034950q.

(124) Bulgarevich, D. S.; Sako, T.; Sugeta, T.; Otake, K.; Sato, M.; Uesugi, M.; Kato, M. Solvent Polarities of Supercritical CO2/Methanol Mixtures. *Review of High Pressure Science and Technology/Koatsuryoku No Kagaku To Gijutsu* **1998**, *7*, 1423–1425. https://doi.org/10.4131/jshpreview.7.1423.

(125) Laurence, C.; Nicolet, P.; Dalati, M. T.; Abboud, J. L. M.; Notario, R. The Empirical Treatment of Solvent-Solute Interactions: 15 Years of π. *Journal of Physical Chemistry* **1994**, *98* (23), 5807–5816. https://doi.org/10.1021/j100074a003.

(126) Dortmund Data Bank, (Accessed April 20, 2020), Http://Www.Ddbst.Com/En/EED/PCP/DEN_C89.Php.

(127) Vaughn, A. R.; Clark, A. K.; Sivamani, R. K.; Shi, V. Y. Natural Oils for Skin-Barrier Repair: Ancient Compounds Now Backed by Modern Science. *Am J Clin Dermatol* **2018**, *19* (1), 103–117. https://doi.org/10.1007/s40257-017-0301-1.

(128) Lin, T. K.; Zhong, L.; Santiago, J. L. Anti-Inflammatory and Skin Barrier Repair Effects of Topical Application of Some Plant Oils. *Int J Mol Sci* **2018**, *19* (1). https://doi.org/10.3390/ijms19010070.

6. Conclusions and future perspectives

In conclusion, this PhD work, aimed at the study of valuable alternative methods for the chemical upgrading of biowaste for their exploitation as added value products. The experimental part was divided into three main areas namely the production of carbon dots from biobased molecules or biowaste and their use as photocatalysts, the obtain of biopolymers from fishery waste and their exploitation for the preparation of films and the extraction of active molecules (preservatives and fatty acids) from different types of agro waste using supercritical CO_2 technique. These three main topics were all aimed at combining green technologies for the development of sustainable protocols for the upgrading of common wastes.

Carbon Dots

In **Chapter 3**, the synthesis, characterization and use as photocatalysts of CDs derived from biobased molecules or fishery waste was studied. In detail, the investigation started with a preliminary study aimed at the comprehension of the carbon precursor and synthetic method on the final features of the carbon nanoparticles (**Chapter 3.2**). Six different types of CDs were prepared using glucose, fructose and citric acid with two synthetic protocols (hydrothermal or pyrolytic treatment). Firstly, it was noticed how from hydrothermal treatment small amorphous nanoaggregates containing molecular-like compounds were obtained, while using pyrolysis, nanomaterials composed by extended graphene-like carbonaceous core were observed. Moreover, it has been underlined that the higher is the reactivity of the carbon precursors towards the decomposition/thermal treatment, the easier and larger the formation of the nanoparticles. In particular, the graphitic CDs obtained from fructose resulted as a supramolecular aggregate of graphene-like crystalline sheets with multi-layered structure. The photo-redox behaviour of the six materials have been then studied towards the single electron transfer on of methyl viologen and the citric acid-derived CDs yielded the best photocatalytic performances. The morphology of the carbon-dots induced either a positive or negative photo-reactivity trend, which in turn was influenced by the carbon-precursor employed.

The evidence that citric acid-based CDs possess a high photoreactivity prompted us to use them for more challenging applications. Nitrogen doped citric acid-derived CDs (N-cit-CDs) were then synthesized and used as photosensitizers for the atom transfer radical polymerization (ATRP) of methacrylates (**Chapter 3.3**). In particular, N-cit-CDs were obtained through the hydrothermal treatment of citric acid and diethylenetriamine and used to reduce the Cu^{II} catalysts to its Cu^{I} active form. The photo-ARTP has been tested using different solvent conditions and under both UV and visible irradiations. The reaction was found to be efficient in water-based solvent, in particular in water/methanol (1:1) solution, and the presence of a photosensitizer allowed to use small amounts of the metal catalyst (1:100 in respect to the monomer) describing a green and sustainable procedure. After only 1 h of irradiation it was possible to retrieve poly-METAC ([2-(methacryloyloxy)ethyl]trimethylammonium chloride) with 89% conversion and 1.4 dispersity under UV light and with 70% conversion and 1.5 dispersion under Vis one. A first order kinetic was observed in both cases, confirming an almost constant concentration of radicals, typical of ATRP mechanisms. “On-off” experiments and blank tests confirmed the necessity of all the reagents (light, CDs, initiator and catalyst) in order to obtain the polymer. In conclusion, a new, cheap and effective photosensitizer for ATR polymerization has been studied demonstrating the possibility to achieve greener and efficient processes in polymer preparation.

The knowledge obtained from the investigations conducted on the synthesis, properties and photocatalytic activity of CDs prepared from biobased molecules, in particular citric acid, prompted us to explore the possibility to use waste biomass as carbon precursor to synthesize CDs. In **Chapter 3.4**, the synthesis, characterization and photoelectron transfer ability of a new type of CDs prepared from fish scales is reported. The new class of CDs (bass-CDs) was characterized in-depth regarding their composition, morphology and surface properties: the fish-derived dots showed a considerable nitrogen content (C/N = 3.2) without the need of any external doping agent. Since nitrogen doping is known to enhance the photocatalytic activity of CDs, bass-CDs were compared with CDs obtained from citric acid and diethylenetriamine toward the single electron reduction of MV^{2+}. Bass-CDs resulted to have lower lifetime of the excited state (7.0 ns vs 13.0 ns of a-N-CDs), mass absorption coefficient (0.37 $L \cdot g^{-1}$ cm^{-1} vs 10.93) and QY (6.0% vs 17.3%), but higher initial photoreduction rate ($7.5 \cdot 10^{-8}$ $M \cdot s^{-1}$ vs $4.9 \cdot 10^{-8}$ $M \cdot s^{-1}$ for absorption normalized experiment). The fish scale-derived CDs have similar morphology to that of the a-N-CDs, but less intense absorbance, lower QY, τ and ε. Despite this, bass-CDs resulted to function as a valuable photocatalyst and to have a higher photoelectron transfer ability toward methyl viologen.

The photoactivity of bass-CDs were then explored for the continuous flow photooxidative degradation of azo dyes, well-known common hazardous contaminants (**Chapter 3.5**). This study has been conducted in the laboratories of Prof. Jean-Christophe Monbaliu in the Université de Liège, Belgium. Thanks to the advantages of flow chemistry, such as high surface-to-volume ratio, short diffusion distances, and rapid mass transfer, it was possible to fully degrade five different azo dyes (methyl orange, acid red 18, amaranth, sunset yellow and chromotrope) in only 2 minutes. Using the combination of bass-CDs, oxygen and UV irradiation (λ = 365 nm), it was possible to totally decompose the dyes also in batch conditions, but longer reaction times were needed (from 1 to 3 hours depending on the azo dye). The tested flow methodology could be easily applied to industrial wastewaters to perform water purifications in a continuous, cheap and affordable way. CDs are easily synthetized and being fully biodegradable and biocompatible, there's no need to recover them after the water treatment but they can be discarded together with the decomposition products without creating new harmful contaminants.

Biopolymers

In **Chapter 4**, an investigation on the extraction of biopolymers from fishery waste is described. Biopolymers are natural polymers produced by living organisms and they have great importance and interest in a wide range of applications from biomedical (e.g. tissue engineering) to pharmaceutical and materials production. In particular, focus was placed on the extraction of collagen from fish scales for the production of UV-shielding materials and on the possibility to obtain chitin from crab shells using a more sustainable pathway with ionic liquids.

The experimental investigation on fishery waste-derived biopolymers started with a study on the production of UV-blocking materials (**Chapter 4.2.1**). Hybrid biobased gelatin−CDs films with UV-shielding ability were produced starting from fishery waste. Type I fish collagen, extracted from mullet scales with a chemical protocol, resulted to have a denaturation temperature lower than that of common mammalian gelatin making extraction possible under milder conditions. On the other hand, CDs were obtained through the hydrothermal treatment of bass scales as previously described. The films were then prepared by casting a mixture of gelatin, glycerol (15%), and CDs (0, 1, 3 and 5%). 40 µm thick materials were obtained and improved mechanical properties were observed upon addition of the CDs: the EAB% increased from 27% (non-loaded film) to 40% (5% CDs) showing a clear plasticizing effect while, on the other hand, the stiffness decreased, probably due to the aggregation of the nanoparticles in the gelatin matrix. From the optical point of view, the addition of CDs has only a limited effect on transparency (88.6% for the non-loaded vs 84.4% for 5% CDs) and on opacity (1.32 for non-loaded vs 1.61 for 5% CDs); while the material loaded with 5% CDs blocked almost the 70% of the UV radiation. These types of hybrid biobased films hold promise for the production of sustainable UV-shields both for human health and for prolonging the shelf life of food.

The investigation about the possibility to obtain biopolymers from fishery waste continued then with a study on the valorisation of crab shell for the production of chitin (**Chapter 4.3**). The key step of this work was the improvement of a one-pot pulping procedure using ILs as opposed to the traditional chemical extraction which involves two steps using strong and hazardous acids and bases. Firstly, the chemical composition of spider crab shells was determined revealing 57% of ashes, 21% of proteins, 17% of chitin and a remaining 5% of lipids, metals and pigments. The one-pot pulping method was then investigated, using simple, readily available ILs such as ammonium acetate, ammonium formate and hydroxylammonium acetate; each reaction was performed both using the neat IL as solid salt or by synthesizing it in situ as an aqueous solution. All characterization data confirm that in the conditions tested, ammonium formate prepared *in situ* seems to be the most promising IL for chitin one-pot pulping process, allowing the quantitative isolation (17-18% yields) of chitin with high purity and a high degree of acetylation (DA > 86%).

scCO_2 Extractions

In **Chapter 5**, the feasibility of supercritical carbon dioxide (scCO_2) for the extraction of actives from agro waste was investigate. sc-CO_2 is the most widely used among supercritical fluids thanks to its outstanding properties. Indeed, sc-CO_2 is non-toxic, non-flammable, non-corrosive, recoverable and easy to handle. In addition, CO_2 is cheap, readily available with high purity degree and easily removable from the final products.

The investigation started studying the suitability of two different types of agro-waste, namely Datura Stramonium and Humulus lupulus, for the production of natural preservatives using scCO_2 (**Chapter 5.2**). Although the scCO_2 extraction gave lower extraction yields (8.6–4% $_{\text{wt/wt biomass}}$ for *Humulus lupulus* and 1.2–2.3% $_{\text{wt/wt biomass}}$ for *Datura stramonium* flowers or leaves respectively) compared to ethanol extraction performed with Soxhlet technique, scCO_2 always reached the highest selectivity (up to 26% $_{\text{wt/wt extract}}$) towards the light fraction that is rich in potentially antibacterial molecules (terpenes, terpenoids, bitter acids and fatty acids). The extracts were tested towards *Escherichia Coli*, showing that the scCO_2 extracts are more active as antibacterial compared to the ethanol ones. In conclusion, scCO_2 resulted to be an extractive method that is, not only safer from the operator and consumer point of view (non-flammable, non-toxic, no final product contamination), but also more efficient for the obtainment of the volatile fraction of essential oils, that resulted to be constituted mainly by compounds with proven antiseptic behaviour.

The encouraging results obtained from the valorisation of hops and jimsonweed for the extraction of antibacterial compounds led us to explore the scCO_2 extraction of other waste matrixes. Indeed, in **Chapter 5.3**, the extraction of fatty acids for the cosmetic industry from different fruit pomaces (seeds and peels of raspberry, blueberry, wild strawberry, pomegranate, blackberry and blackcurrant) has been investigated. This study was carried out in collaboration with Università degli studi di Padova for the analytical characterization of the extracts, and two industries, namely Rigoni di Asiago Srl (for the supplying of fruit pomace) and Unifarco SpA (for the possible cosmetic and nutraceutical application). It was demonstrated that scCO_2 is not only successful for the upgrading of the investigated wastes but is also far more selective to obtain high-quality FAs compounds compared to conventional Soxhlet procedures based on toxic and dangerous hexane. The extracts obtained using scCO_2 resulted to be purer and richer in essential fatty acids than the hexane ones. The wild strawberry pomace extraction with scCO_2 is a representative example: selectivity towards fatty acids was 26 wt% (vs. 1.4 % with hexane) and the extracts contained, 145.8 mg mL^{-1} polyunsaturated, 64.0 mg mL^{-1} monounsaturated and 46.8 mg mL^{-1} saturated fatty acids (vs. 14.3 mg mL^{-1} total fatty acids with hexane).

Final remarks and future perspectives

Overall, this PhD thesis tried to give additional hints and steps forward in valorising biowaste through diversified green and sustainable methodologies. Even though the upgrading protocols described in this work can be seen as promising procedures, the varying production costs, applicability on different waste-derived substrates and safety issues are still unknown. In particular, concerning the presented carbon dots, more insight on the relation between structure and photoreactivity and a study on the reproducibility are needed. This last issue must be faced in the future also for the preparation of biopolymers from fishery waste, together with an assessment on production costs. Last, the $scCO_2$ obtained actives must be tested for their stability and their application into cosmetical and nutraceutical formulations. In addition, for all the three reported applications, some investigations on the diversification of the starting materials together with a scale up study can be of great interest with the aim developing the reported protocols for industries.

This work presents, however, a step toward narrowing the choices for waste treatment that can lead to more sustainable processes, both form economical and environmental point of view, with the hope that green solutions and circular economy ideals will replace the current hazardous, energy consuming and environmental unsafe processes.

7. List of publications

- E. Amadio, S. Cailotto, C. Campalani, L. Branzi, C. Raviola, D. Ravelli, E. Cattaruzza, E. Trave, A. Benedetti, M. Selva and A. Perosa, Precursor-Dependent Photocatalytic Activity of Carbon Dots. *Molecules* **2019**, *25* (101), 101. doi:10.3390/molecules25010101
- C. Campalani, F. Chioggia, E. Amadio, M. Gallo, F. Rizzolio, M. Selva and A. Perosa, Supercritical CO 2 Extraction of Natural Antibacterials from Low Value Weeds and Agro-Waste. *J. CO_2 Util.*, **2020**, 40, 101198. doi:10.1016/j.jcou.2020.101198
- C. Campalani, E. Amadio, S. Zanini, S. Dall'Acqua, M. Panozzo, S. Ferrari, G. De Nadai, S. Francescato, M. Selva and A. Perosa, Supercritical CO2as a Green Solvent for the Circular Economy: Extraction of Fatty Acids from Fruit Pomace. *J. CO2 Util.* **2020**, *41*, 101259. doi:10.1016/j.jcou.2020.101259
- C. Campalani, E. Cattaruzza, S. Zorzi, A. Vomiero, S. You, L. Matthews, M. Capron, C. Mondelli, M. Selva and A. Perosa, Biobased Carbon Dots: From Fish Scales to Photocatalysis. *Nanomaterials* **2021**, *11* (2), 524. doi: 10.3390/nano11020524
- C. Campalani, V. Causin, M. Selva and A. Perosa, Fish-Waste-Derived gelatin and Carbon Dots for Biobased UV-blocking Films. *ACS Appl. Mater. Interfaces,* **2022**, 14, 35148-35146. doi:10.1021/acsami.2c11749
- C. Campalani, G. Petit, J.C. Monbaliu, M. Selva and A. Perosa, Continuous Flow Photooxidative Degradation of Azo Dyes with Biomass-derived Carbon Dots. *ChemPhotoChem*, **2022**, e202200234. doi:10.1002/cptc.202200234
- C. Campalani, N. Bragato, A. Morandini, M. Selva, G. Fiorani and A. Perosa, Carbon Dots as Green Photocatalysts for Atom Transfer Radical Polymerization of Methacrylates. Submitted.
- C. Campalani, I. Bertuol, M. Selva and A. Perosa, Fishery Waste Valorisation: a Novel Green Approach for Chitin Pulping using Water-soluble Ionic Liquids. Manuscript in preparation.
- C. Campalani, G. Fiorani, M. Selva and A. Perosa, Biopolymer-based UV-blocking Films. Manuscript in preparation.

Publications not related with this work of thesis

- S. Cailotto, D. Massari, M. Gigli, C. Campalani, M. Bonini, S. You, A. Vomiero, M. Selva, A. Perosa, C. Crestini. N-Doped Carbon Dot Hydrogels from Brewing Waste for Photocatalytic Wastewater Treatment. *ACS Omega,* **2022**, 7, 4052-4061. doi: 10.1021/acsomega.1c05403

Appendix

A-3.2 Precursor-Dependent Photocatalytic Activity of Carbon Dots

FT-IR spectra of CDs

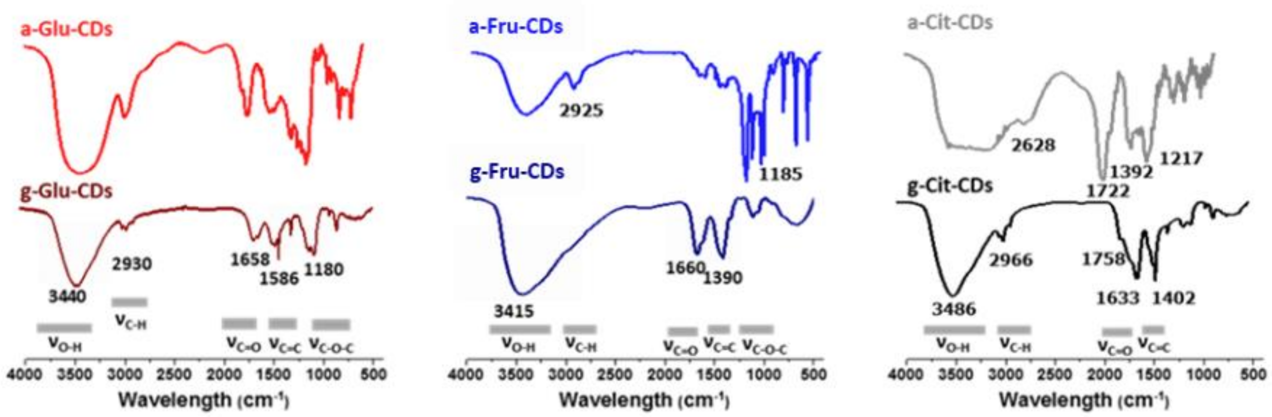

Figure A.3.2.1. FT-IR spectra for a,g-GLU-CDs, a,g-Fru-CDs and a,g-Cit-CDs, in KBr.

PLE spectra of CDs

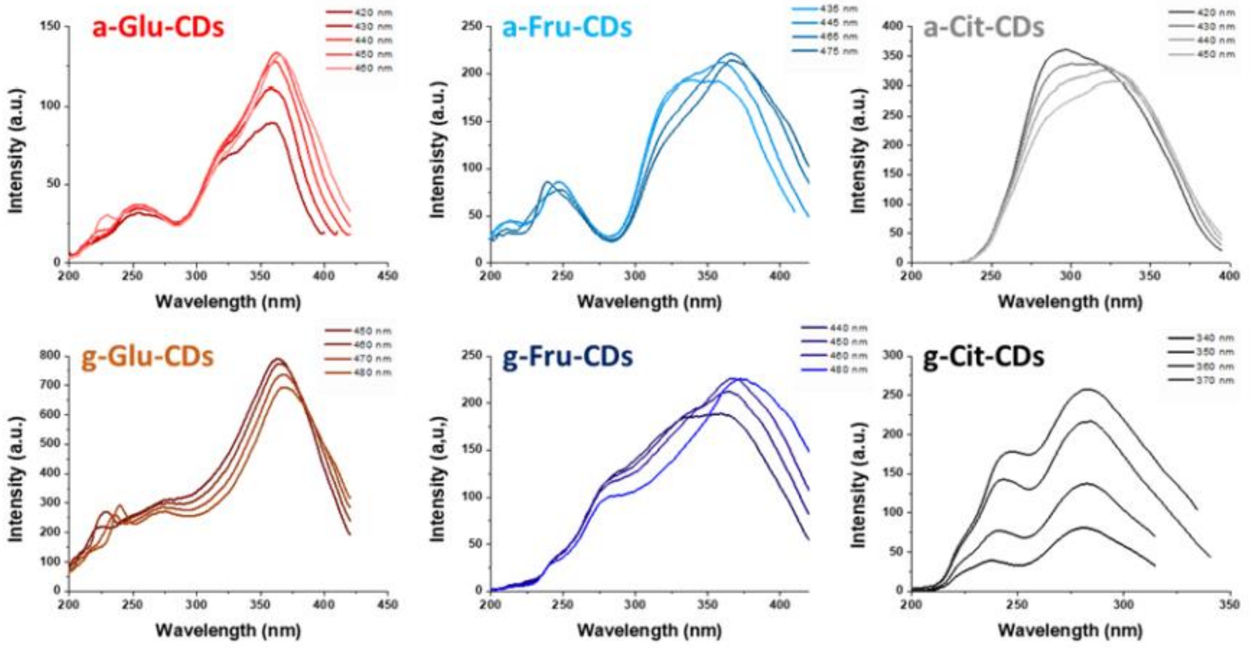

Figure A.3.2.2. PLE spectra of the six types of CDs.

Time-resolved photoluminescence measurements

The time-resolved photoluminescence measurements showed a decay which is multi exponential. Therefore, they were fitted by using a triple-exponential curve and the resulting parameters are reported in Table A.3.2.1.

Table A.3.2.1. The average lifetime has been calculated as follows: $\langle\tau\rangle = (A_1\tau_1^2 + A_2\tau_2^2 + A_3\tau_3^2)/(A_1\tau_1 + A_2\tau_2 + A_3\tau_3)$

Entry	CDs	A_1	τ_1	A_2	τ_2	A_3	τ_3	$\langle\tau\rangle$ (ns)
1	a-Cit-CDs	0.31	0.78	0.32	1.25	0.34	4.26	3.27
2	g-Cit-CDs	0.23	0.19	0.45	0.72	0.17	6.87	5.35
3	a-Glu-CDs	0.34	0.31	0.35	1.25	0.14	6.63	4.60
4	g-Glu-CDs	0.87	0.59	0.05	1.63	0.09	4.79	2.43
5	a-Fru-CDs	0.39	0.49	0.39	0.64	0.10	6.79	4.36
6	g-Fru-CDS	0.28	0.36	0.37	0.80	0.21	7.25	5.87

Photocatalytic experiments

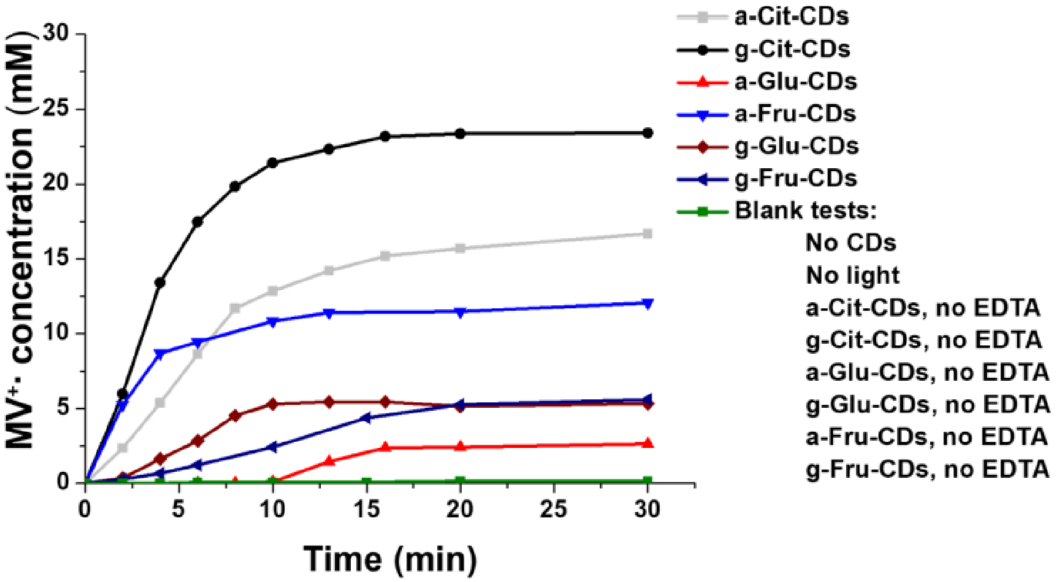

Figure A.3.2.3. Evolution of reaction with CDs, MV^{2+} (60 μM) and EDTA (0.1M) under inert atmosphere at different irradiation time (λ_{ex} = 365 nm).

A-3.3 Carbon Dots as Photocatalyst for Atom Transfer Radical Polymerization of Methacrylates

Blank photocatalytic tests

Table A.3.3.1. Blank tests for induced ATRP of METAC. [a]

Entry	CDs	Catalyst	Irradiation	Conversion (%) [b]
1	-	Yes	-	0
2	a-N-CDs	Yes	-	0
3	a-N-CDs	No	UV	0
4	a-N-CDs	No	Vis	0
5	-	Yes	UV	0
6	-	Yes	Vis	0

[a] Experiments were conducted at ambient temperature for 1h using a ratio [METAC]/[HEBIB]/[CDs]/[$CuBr_2$]/[PMDTA] = 100/1/1/1/3 and a 1:1 mixture of water and methanol as the solvent; [b] determined gravimetrically

Poly-METAC characterization

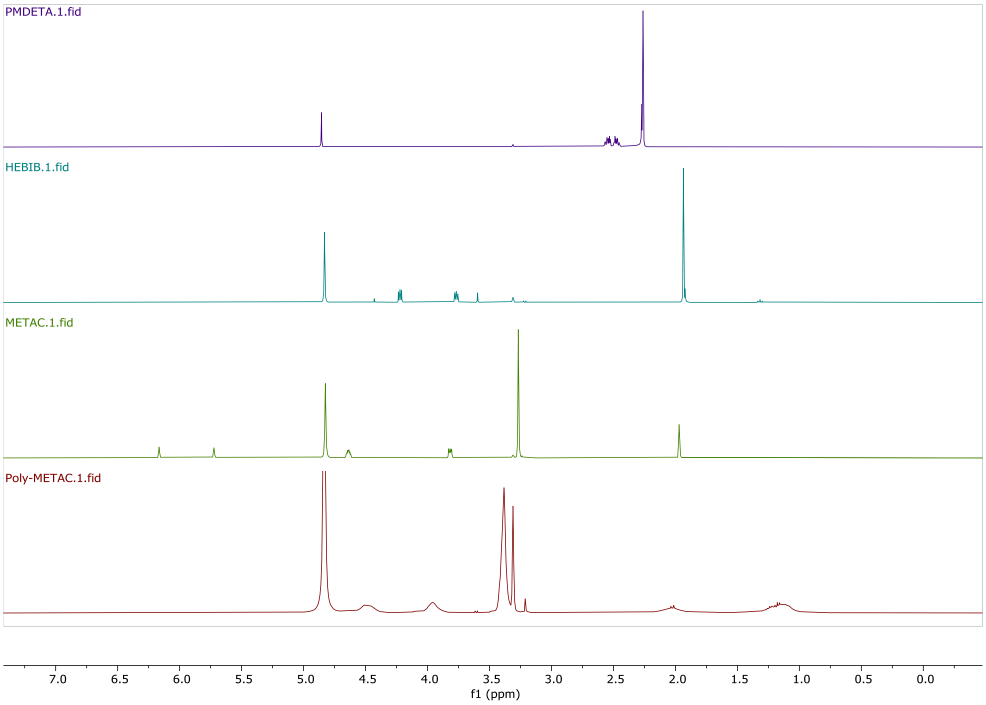

Figure A.3.3.1. ^1H NMR of the ligand (PMDETA, purple line), the initiator (HEBIB, blue line), the monomer (METAC, green line) and the product (poly-METAC, red line) in methanol-d_4.

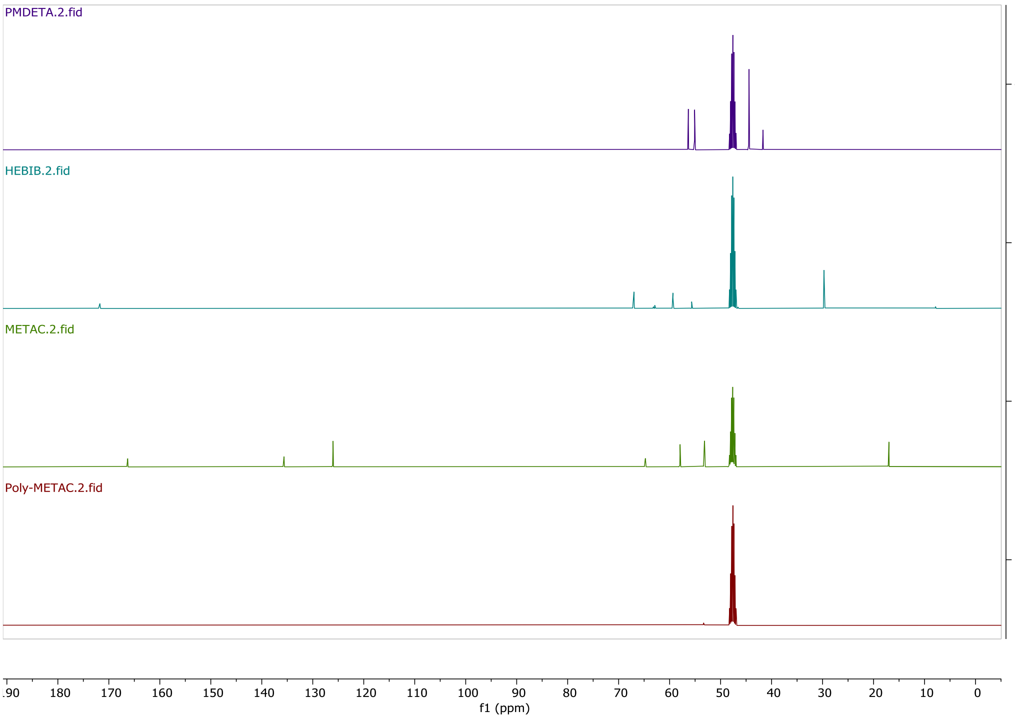

Figure A.3.3.2. ^{13}C NMR of the ligand (PMDETA, purple line), the initiator (HEBIB, blue line), the monomer (METAC, green line) and the product (poly-METAC, red line) in methanol-d$_4$.

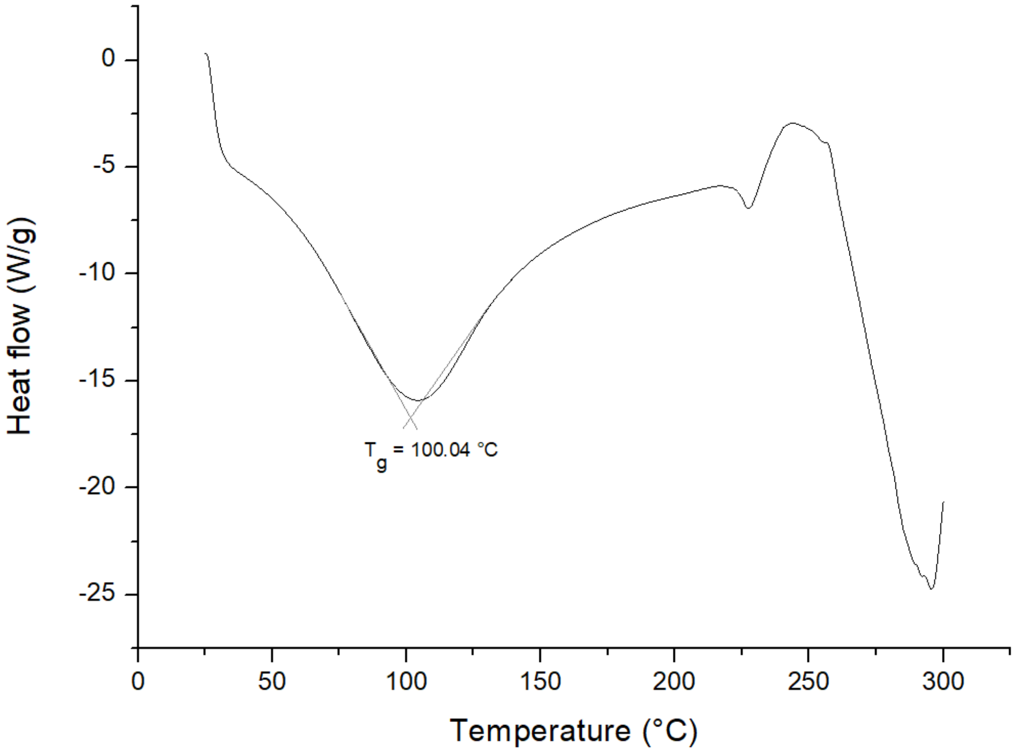

Figure A.3.3.3. DSC curve for the obtained poly-METAC.

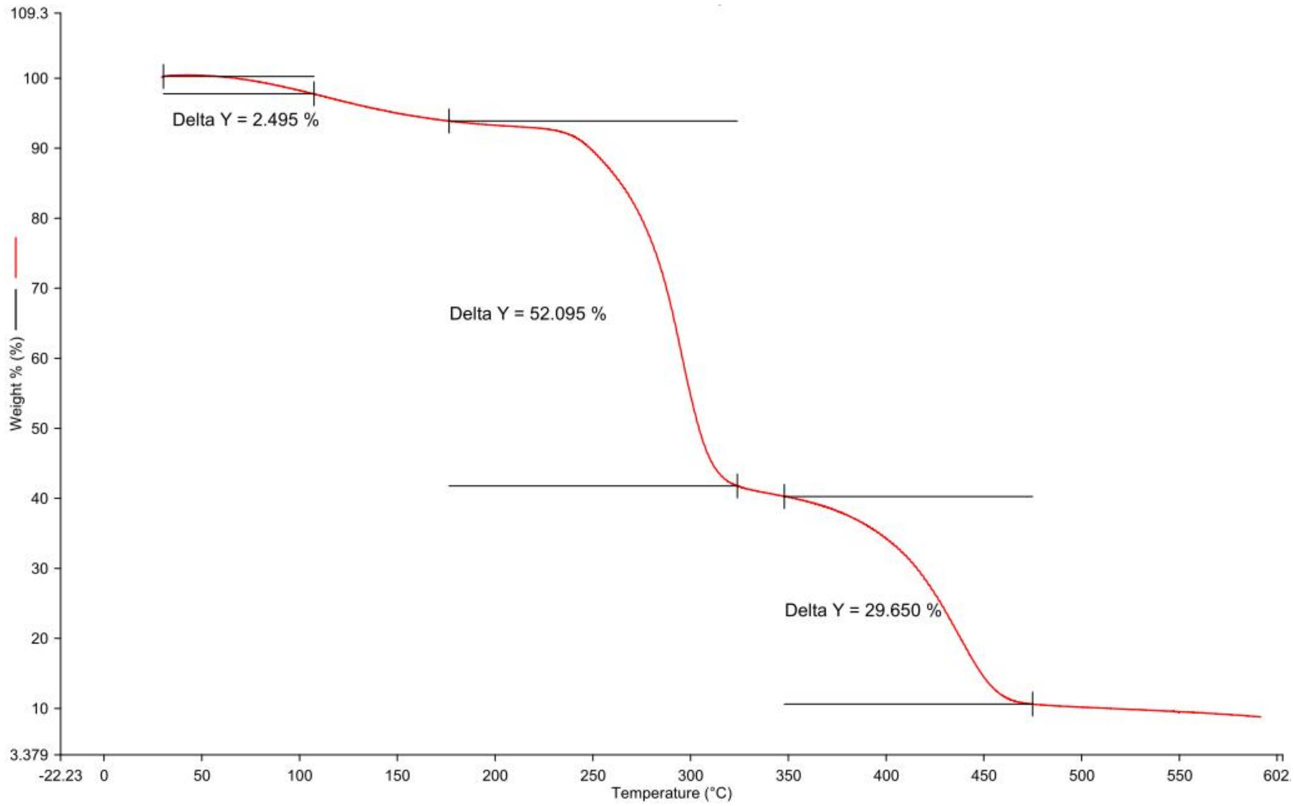

Figure A.3.3.4. Thermogravimetric analysis of the obtained poly-METAC.

A-3.4 Biobased Carbon Dots: from Fish Scales to Photocatalysis

NMR Spectra

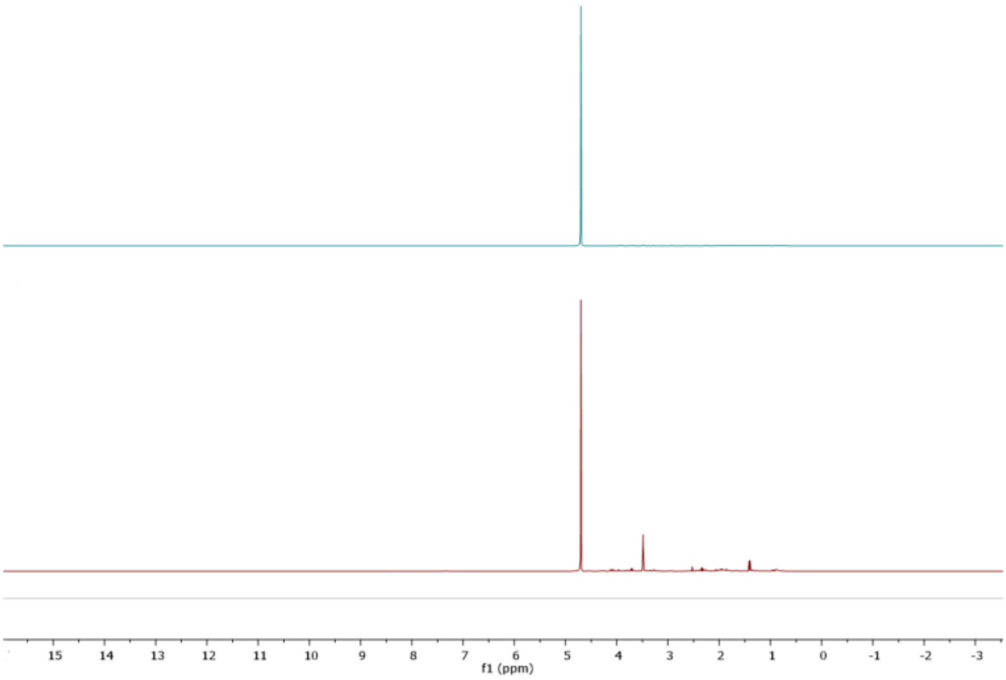

Figure A.3.4.1. ^1H NMR of crude (red line) and purified (blue line) bass-CDs in D_2O.

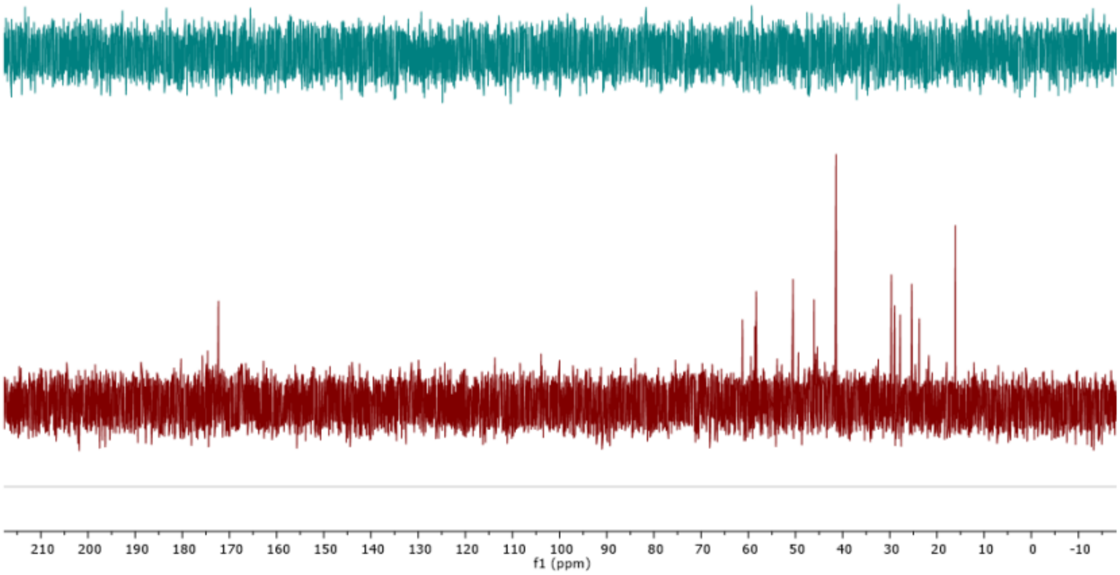

Figure A.3.4.2. $^{13}C\{^1H\}$ NMR of crude (red line) and purified (blue line) bass-CDs in D_2O.

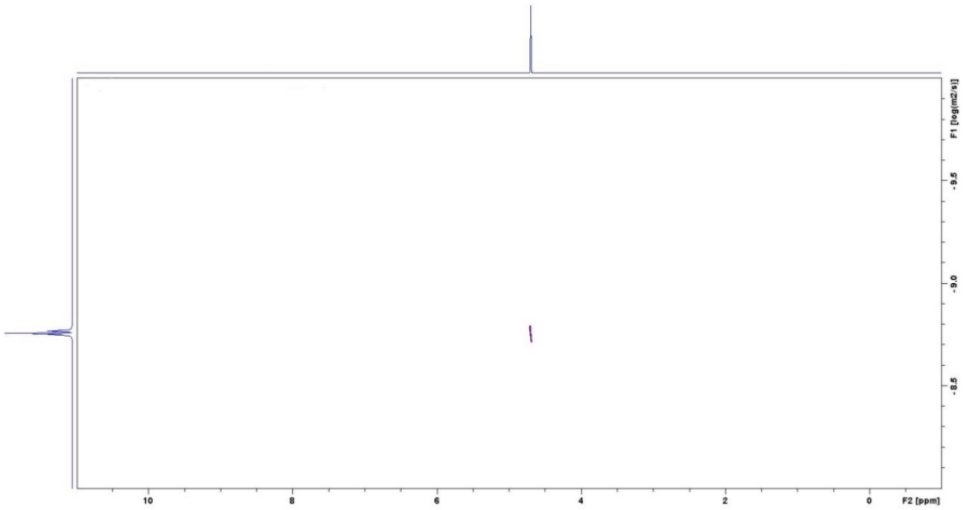

Figure A.3.4.3. 2D DOSY NMR of purified bass-CDs in D_2O.

FT-IR

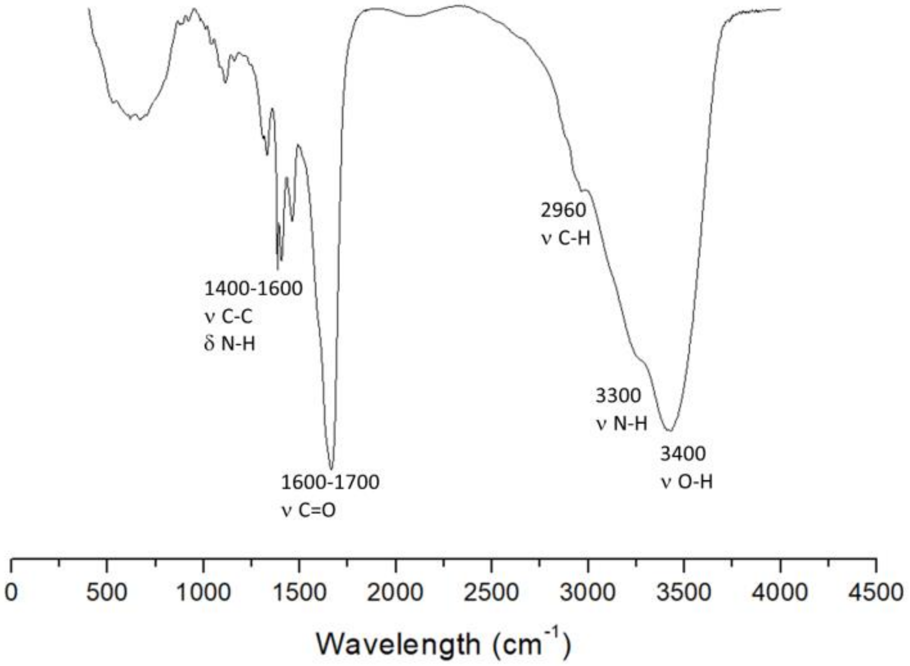

Figure A.3.4.4. FT-IR spectrum bass-CDs in KBr.

SAXS Data Analysis

The fitting procedures used in this paper to obtain information regarding the surface roughness of the clusters, have been performed using the SasView software [1].

For fractal structures, the scattering intensity I($\boldsymbol{Q}$) express a typical power law behaviour, which in the case of surface fractal structures can be expressed as

$$I(\boldsymbol{Q}) \propto \boldsymbol{Q}^{-(6-D_s)}, \qquad with \quad 2 < D_s < 3$$

where $\boldsymbol{Q}$ is the scattering vector and D_s is the surface fractal dimension. For a smooth surface the $D_s = 2$ and the exponent of the power law is equal to 4, while in the case of a rough surface the $D_s = 3$ and the exponent is equal to 3 [ref: https://iopscience.iop.org/article/10.1088/0022-3727/19/8/021/meta]. In the case of mass fractal structures the scattering intensity can be written as

$$I(\boldsymbol{Q}) \propto \boldsymbol{Q}^{-D_m}, \qquad with \quad 1 < D_m < 3$$

where D_m is the mass fractal dimension.

In the present work, the surface fractal dimension of the large clusters has been obtained by fitting the low $\boldsymbol{Q}$ region of the SAXS curves with a power law function, contained in the SasView model's library. The signal ascribed to the presence of carbon dot aggregates in the Bass-CDs sample, has been described using a power law model, which has highlighted its mass fractal behaviour and was promptly described with a mass fractal model. In this model the $\mathrm{I}(\boldsymbol{Q})$ is mostly described by a spherical form factor $\mathrm{P}(\boldsymbol{Q})$, that takes into account the scattering of the primary particles with radius R composing the clusters. The structure factor, $S(\boldsymbol{Q})$, is well described elsewhere [2], taking into account the mass fractal behaviour of the clusters, characterized by the cluster size ξ, and the mass fractal dimension D_m. For the fitting procedure, we used the cluster size obtained from SLS measurements (120 ± 30) nm. The scattered intensity $\mathrm{I}(\boldsymbol{Q})$ for the a-N-CDs has been described by a power law function, taking into account the scattering arising from the large aggregates. The precise cluster size cannot be obtained due to the fact that only the tail of their scattering contribution in the low Q region is seen in the SAXS curves. For the Bass-CDs sample, the $\mathrm{I}(\boldsymbol{Q})$ has been described by a sum of functions: the mass fractal model and the power law function, in order to compute the intensity originating from the smaller aggregates. In fig. S9 the best fits for the a-N-CDs and Bass-CDs are reported. There are some visible fluctuations in the curve between ~ 0.002 – 0.005 Å^{-1}, it is likely that, rather than real oscillations, this is a result of an uncertainty in the background subtraction. Where the data is similar in intensity to the water background and the oscillations are a result of noise in the sample scattering. The background in the high $\boldsymbol{Q}$ region of the scattering profile is not flat as expected, this is likely a result of the water background subtraction, which does not fully compensate the background of the sample. Despite this, the low signal in the high $\boldsymbol{Q}$ region indicates that no scattering other than the background was observed. The parameters of the best fit are reported in table A.3.4.1.

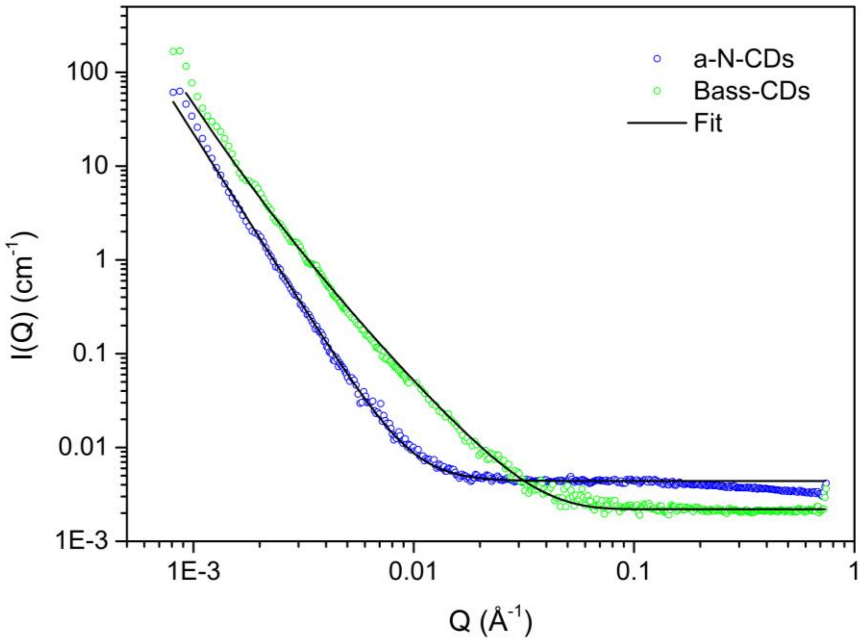

Figure A.3.4.5. Scattering intensity *I(Q)* vs *Q* for both CDs samples, together with the best curve fit obtained by using the model described in the text. Blue dots are related to the SAXS data of the a-N-CDs sample, green dots for the Bass-CDs and the solid black line is for the fit curves.

Table A.3.4.1. List of the parameters of the fit curves reported in Figure A.3.4.5. * The values between brackets are the surface fractal dimensions D_s.

sample	Power Law model	Mass Fractal model		
	Exponent*	Mass fract. dim D_m	Radius R (nm)	Cluster size ξ (nm)
Bass-CDs	3.86 ± 0.05 (2.14 ± 0.05)	2.3 ± 0.1	4 ± 1	127 ± 8
a-N-CDs	3.71 ± 0.05 (2.29 ± 0.05)			

SLS Measurements

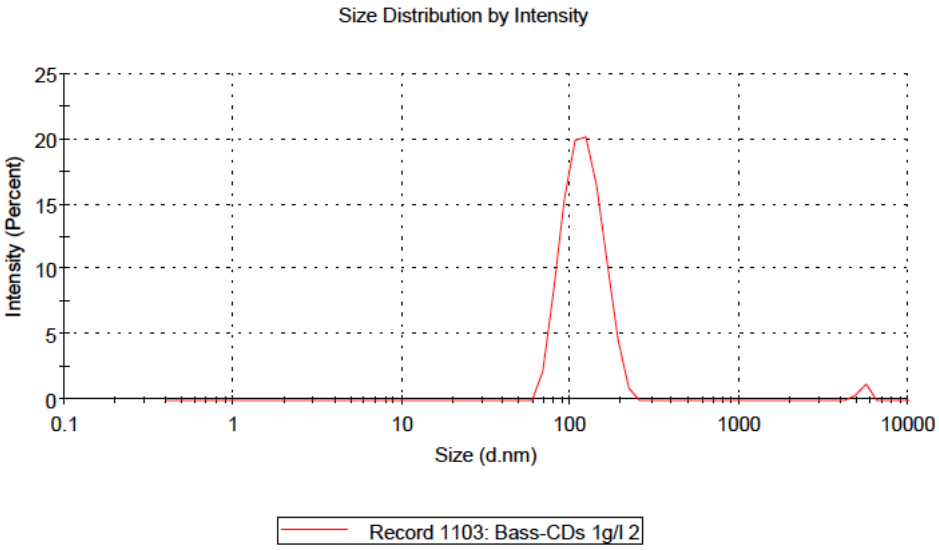

Figure A.3.4.6. SLS size distribution vs intensity in percent. The average size of the clusters is (120 ± 30) nm.

PL-PLE Spectrum

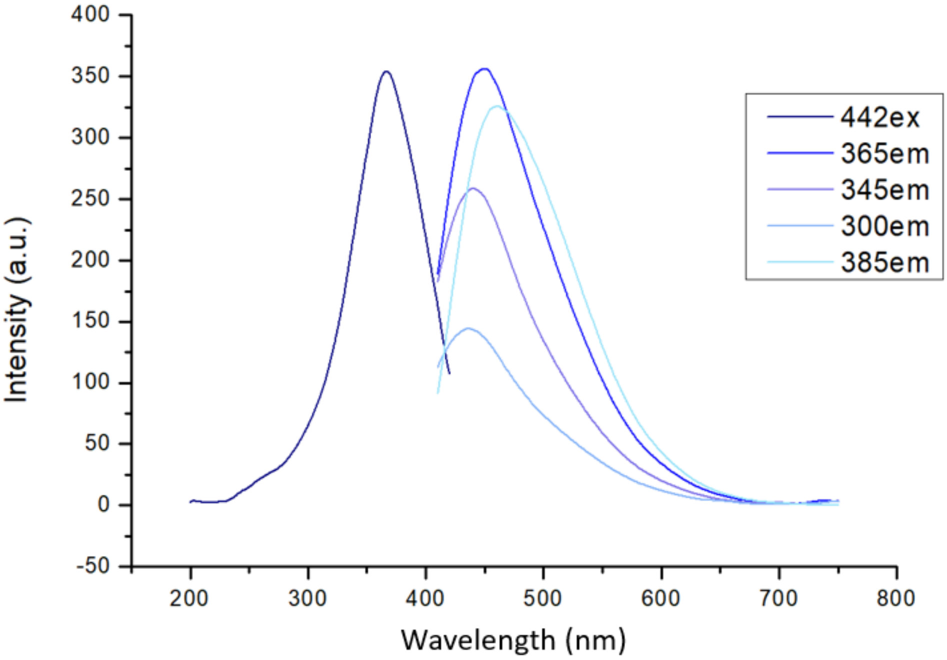

Figure A.3.4.7. PL-PLE spectrum of bass-CDs.

Time Resolved Photoluminescence (PL) Measurements

The time-resolved PL spectra (Figure 2) were analysed with exponential fitting. Three time-constants were used to fit the emission of synthesized CDs and two time-constants were employed for a-NCDs emission. Bass-CDs has much shorter decay compared to the a-N-CDs sample.

Table A.3.4.2. Biexponential fitting of lifetime data, excitation = 372 nm. Fitting parameters of photoluminescence decays displayed un figure 2. The average lifetime has been calculated as follows: $\tau_{av} = \frac{B_1\tau_1^2++B_2\tau_2^2+B_3\tau_3^2}{B_1\tau_1+B_2\tau_2+B_3\tau_3}$

	τ_1(ns)	τ_2(ns)	τ_3(ns)	B_1	B_2	B_3	τ_{av}(ns)
bass-CDs	1.151	4.343	12.07	1932	2257	633	6.98
dialyzed bass-CDs	0.873	3.572	11.87	2357	2123	542	6.55
a-N-CDs	6.654	13.89		541	4405		13.5

A-3.5 Continuous flow Photooxidative degradation of Azo Dyes with Biomass-derived Carbon Dots

Azo Dyes degradation trends in batch conditions

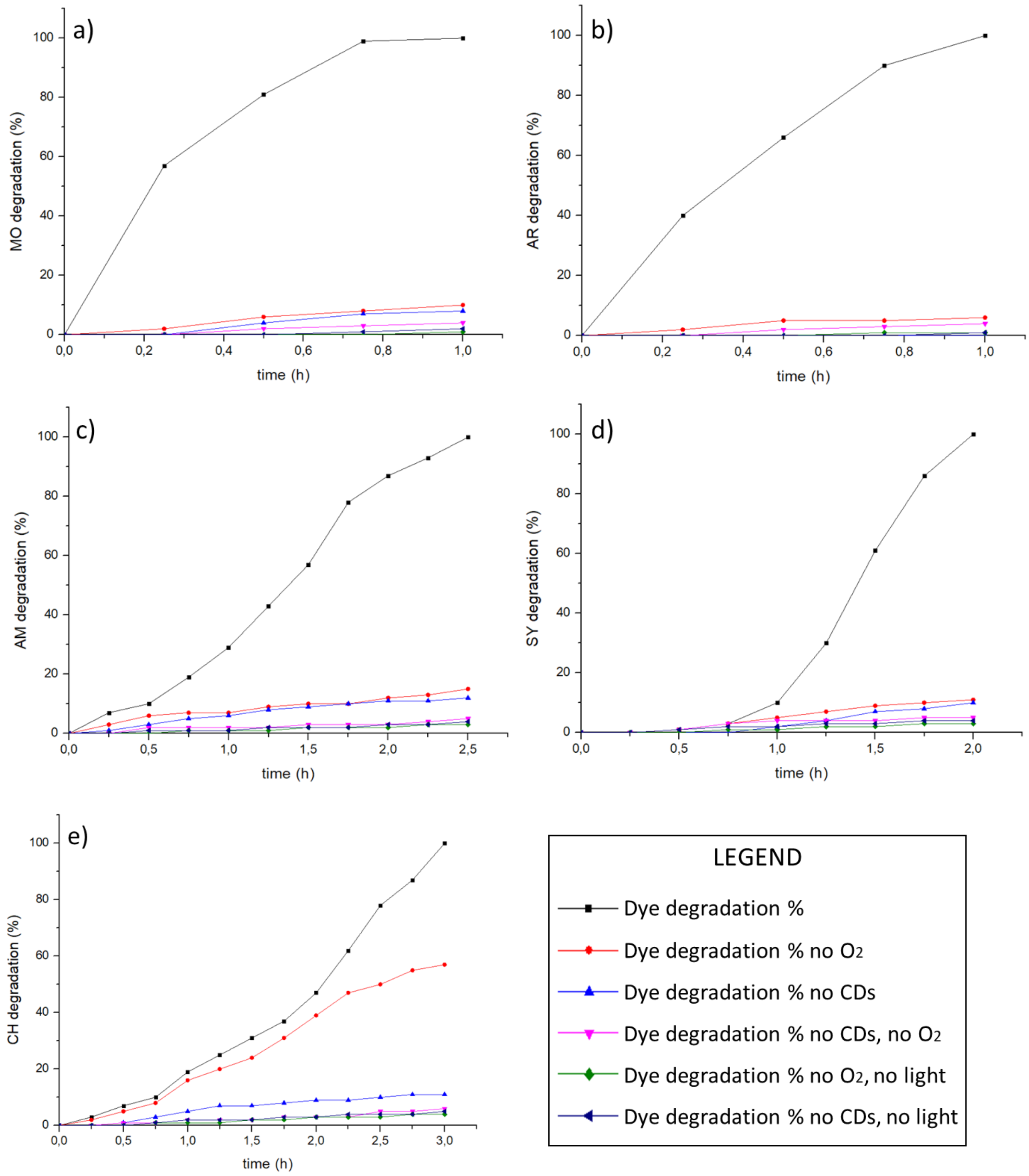

Figure A.3.5.1. Azo dye degradation percentage versus time for batch experiments. Black line = test using both bass-CDs and oxygen; red = without oxygen; blue = without bass-CDs; pink = without both bass-CDs and oxygen; green = without oxygen and irradiation; dark blue = without bass-CDs and irradiation.

Control experiments in batch conditions

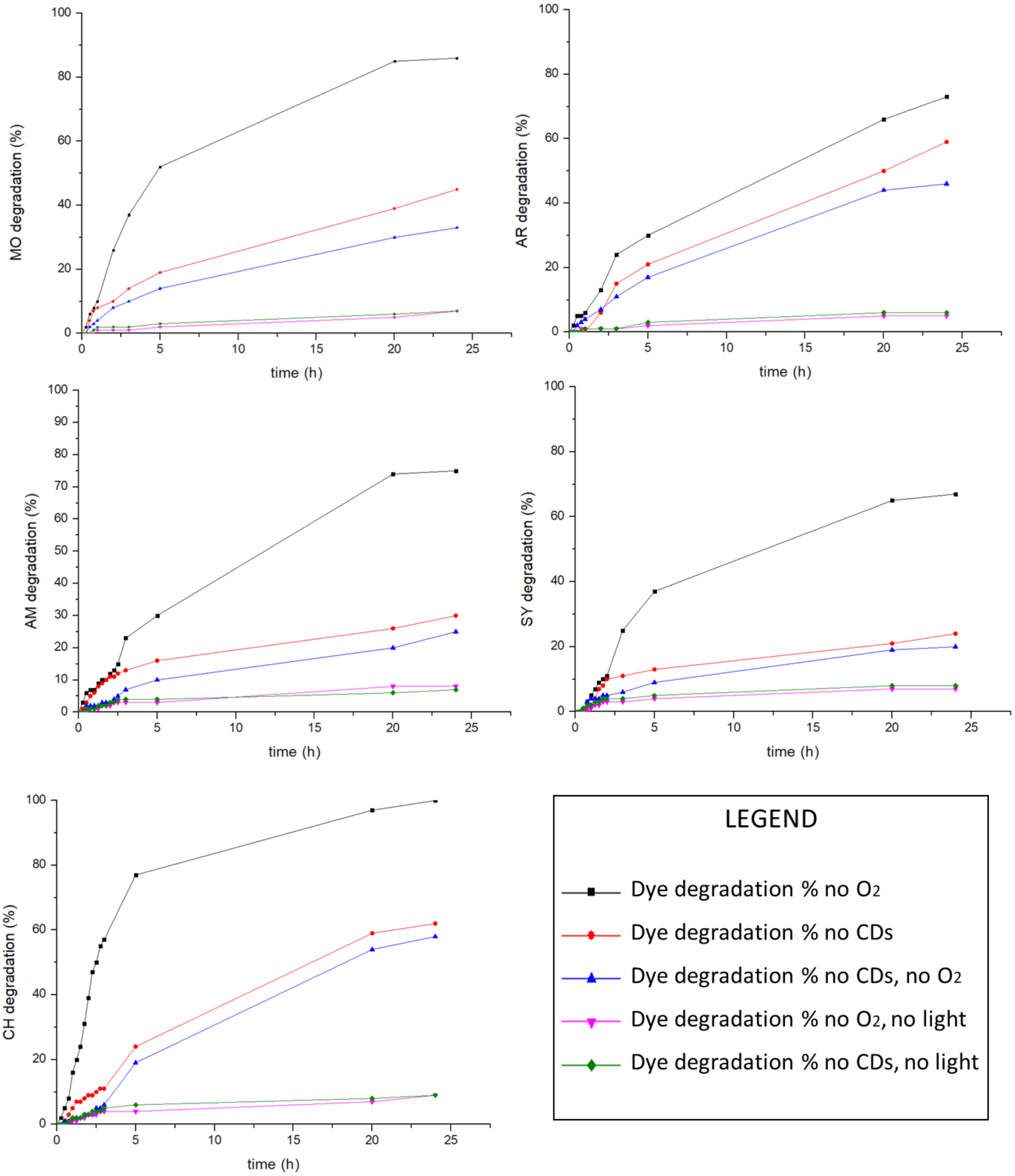

Figure A.3.5.2. Azo dye degradation percentage versus time for control batch experiments over 24 hours. Black line = without oxygen; red = without bass-CDs; blue = without both bass-CDs and oxygen; pink = without oxygen and irradiation; green = without bass-CDs and irradiation.

^{1}H NMR Spectra

METHYL ORANGE

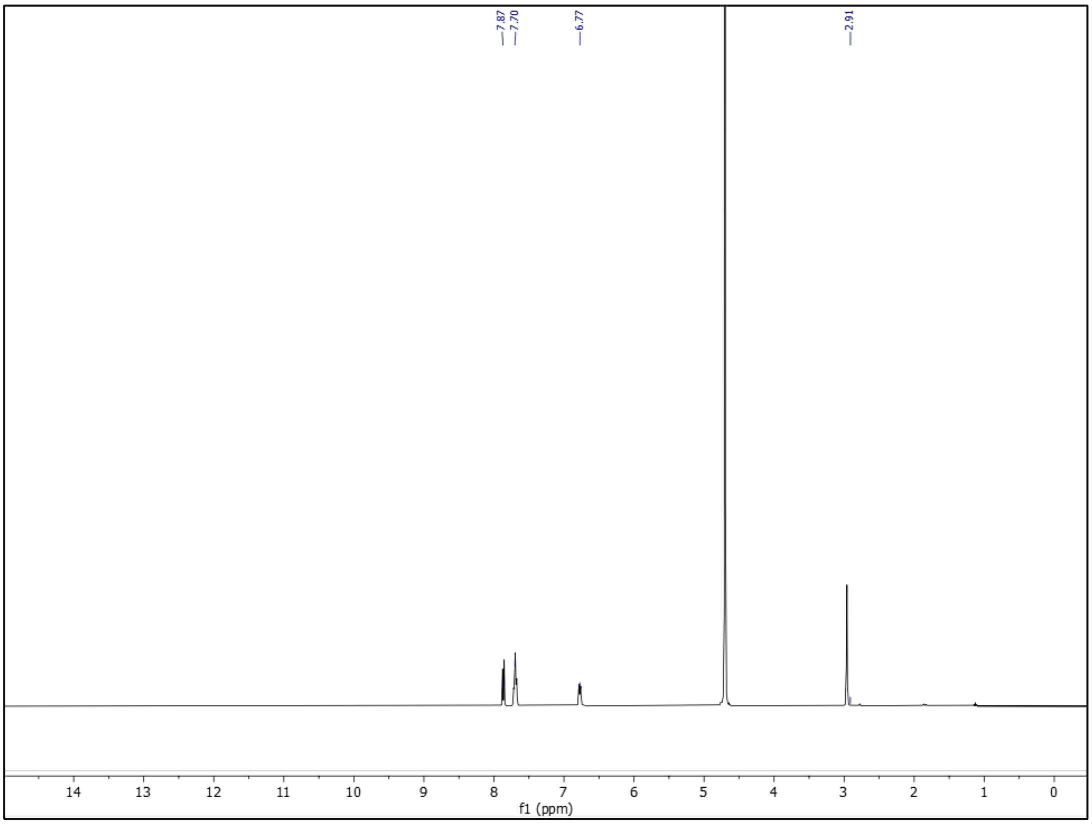

Figure A.3.5.3. ^{1}H NMR of methyl orange in D_2O.

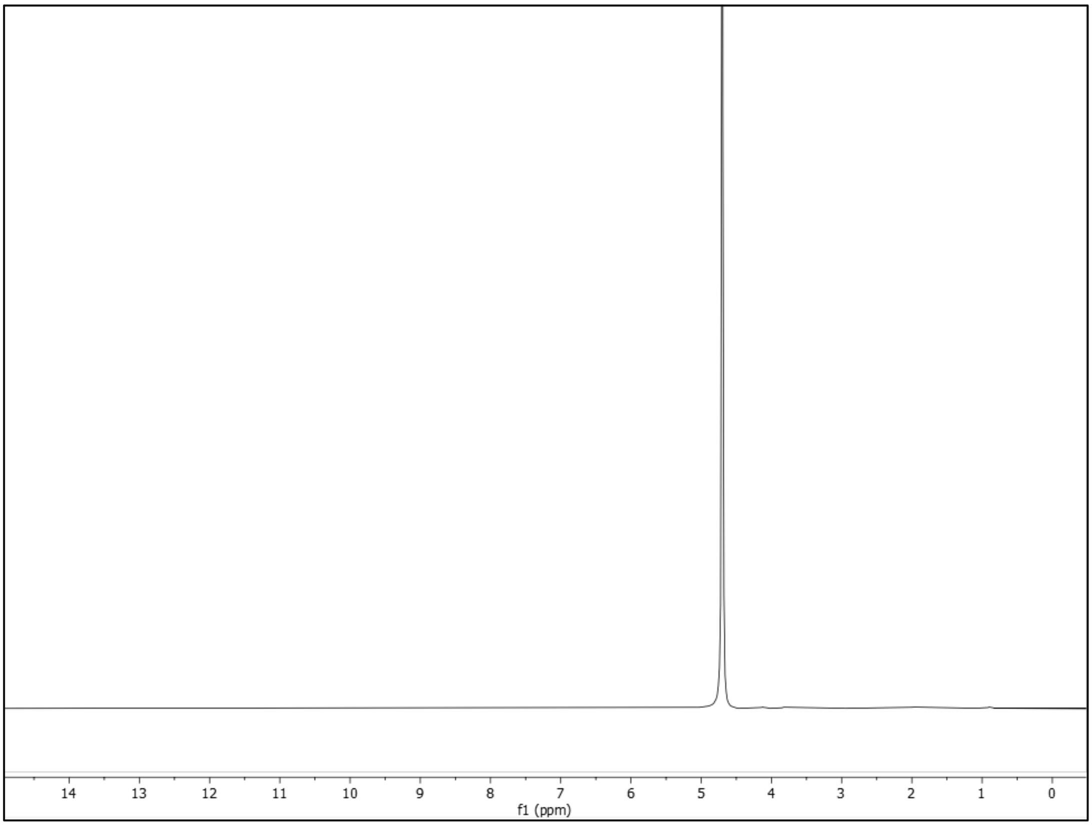

Figure A.3.5.4. ^{1}H NMR of methyl orange decomposition products in D_2O.

ACID RED 18

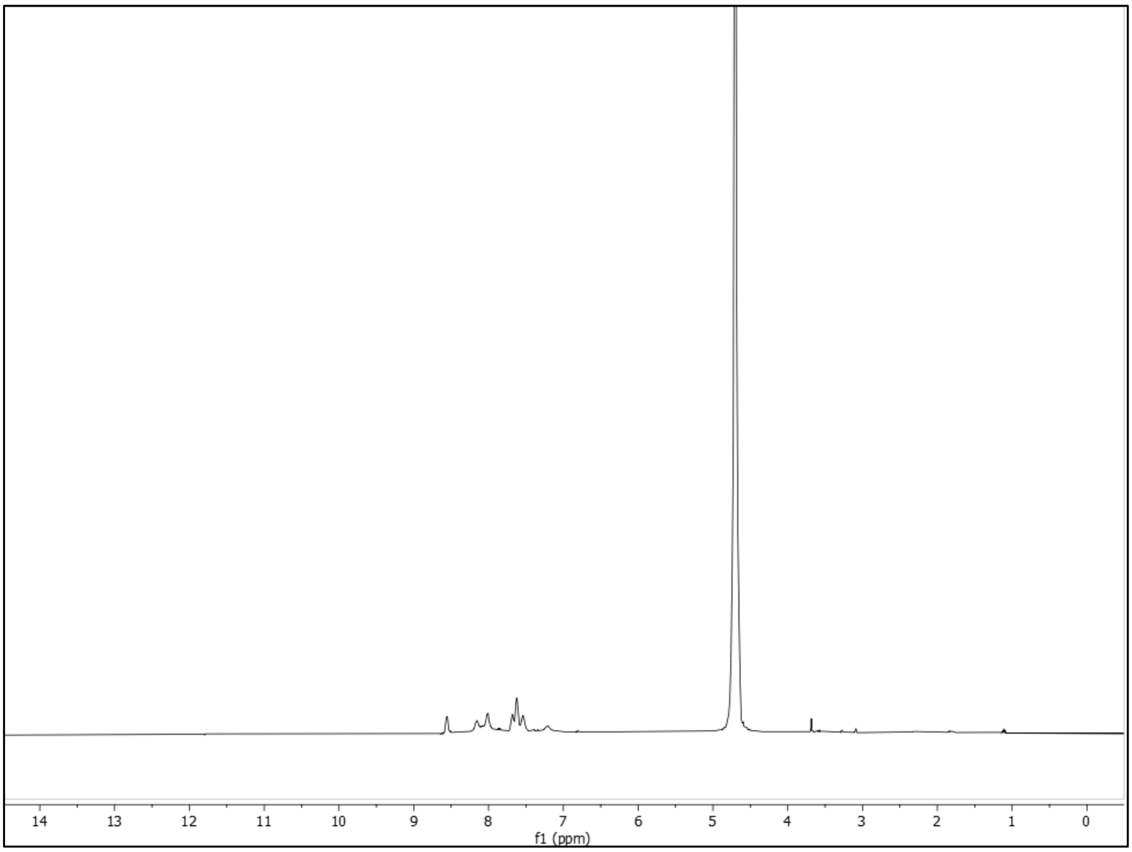

Figure A.3.5.5. ^{1}H NMR of acid red 18 in D_2O.

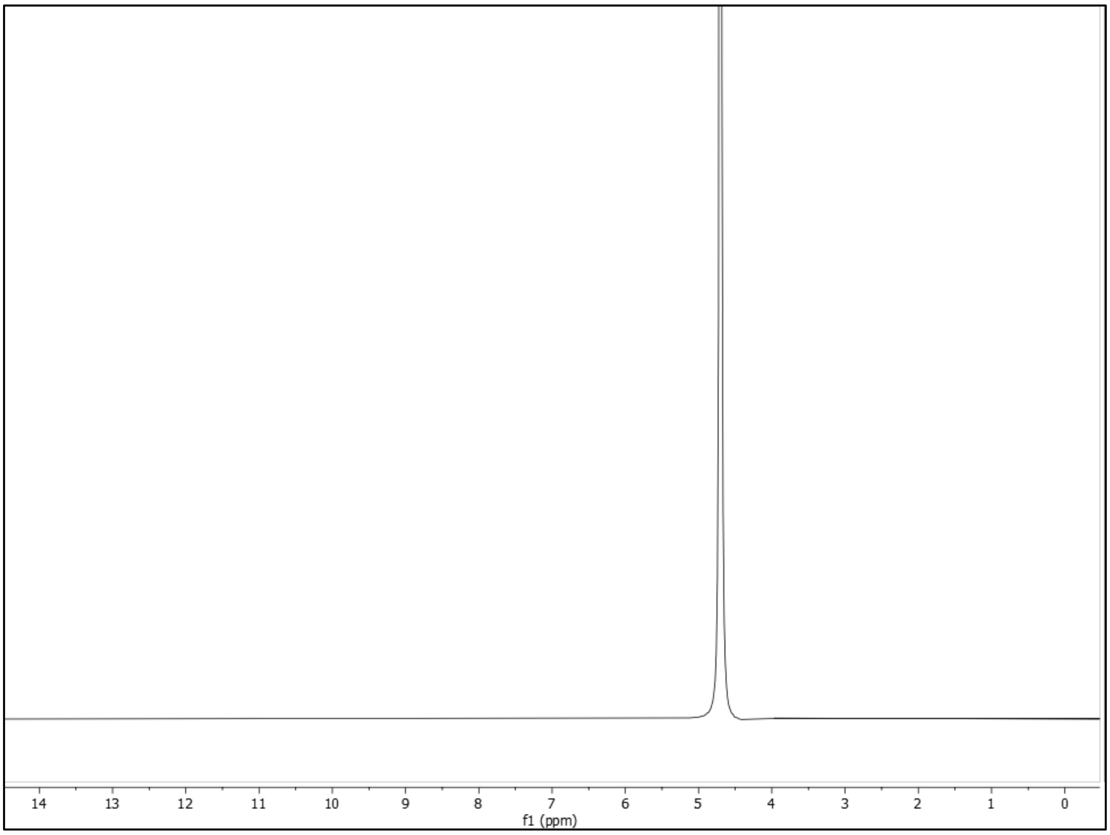

Figure A.3.5.6. ^{1}H NMR of acid red 18 decomposition products in D_2O.

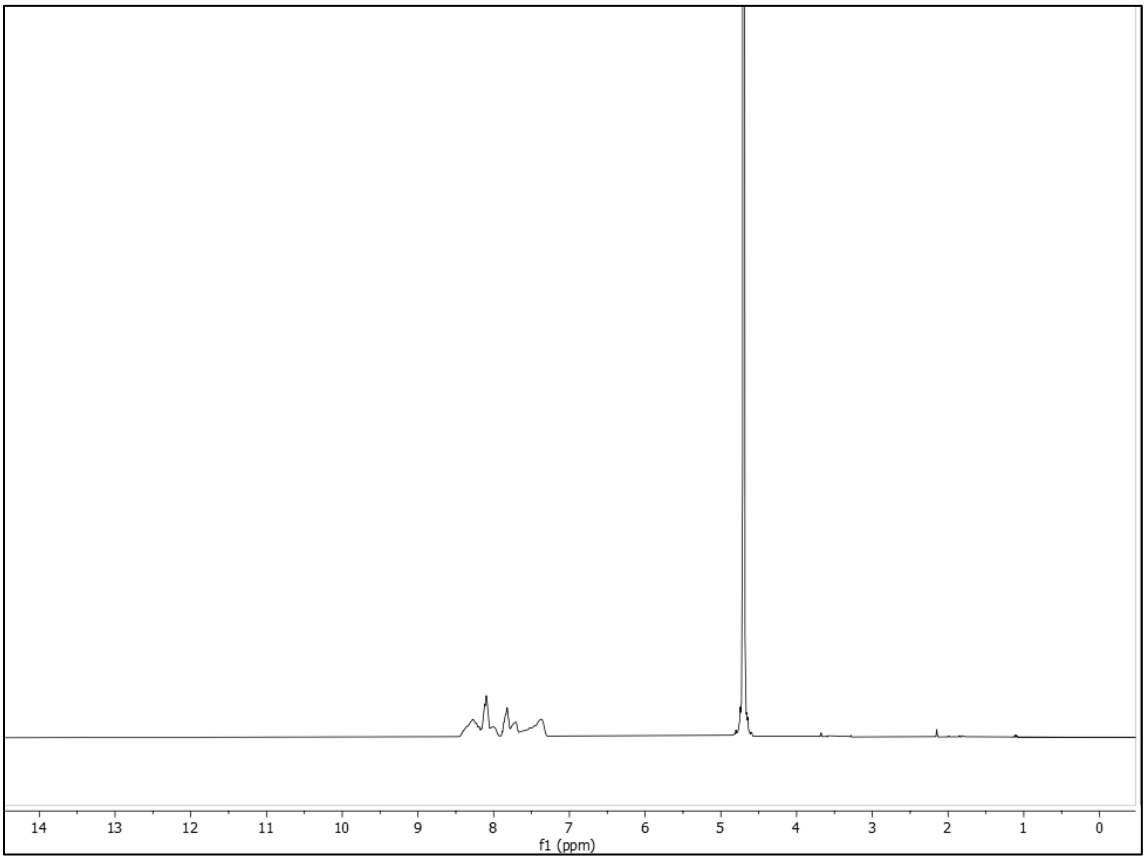

Figure A.3.5.7. ^{1}H NMR of amaranth in D_2O.

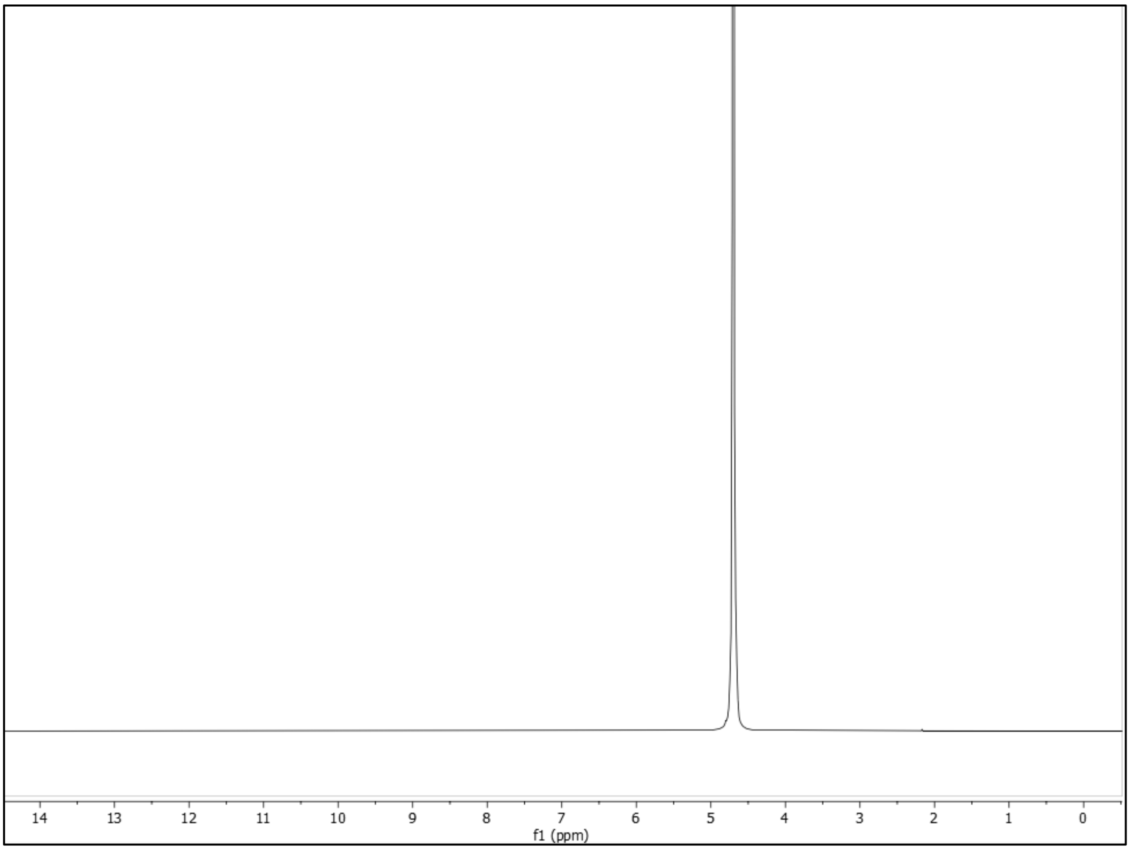

Figure A.3.5.8. ^{1}H NMR of amaranth decomposition products in D_2O.

SUNSET YELLOW

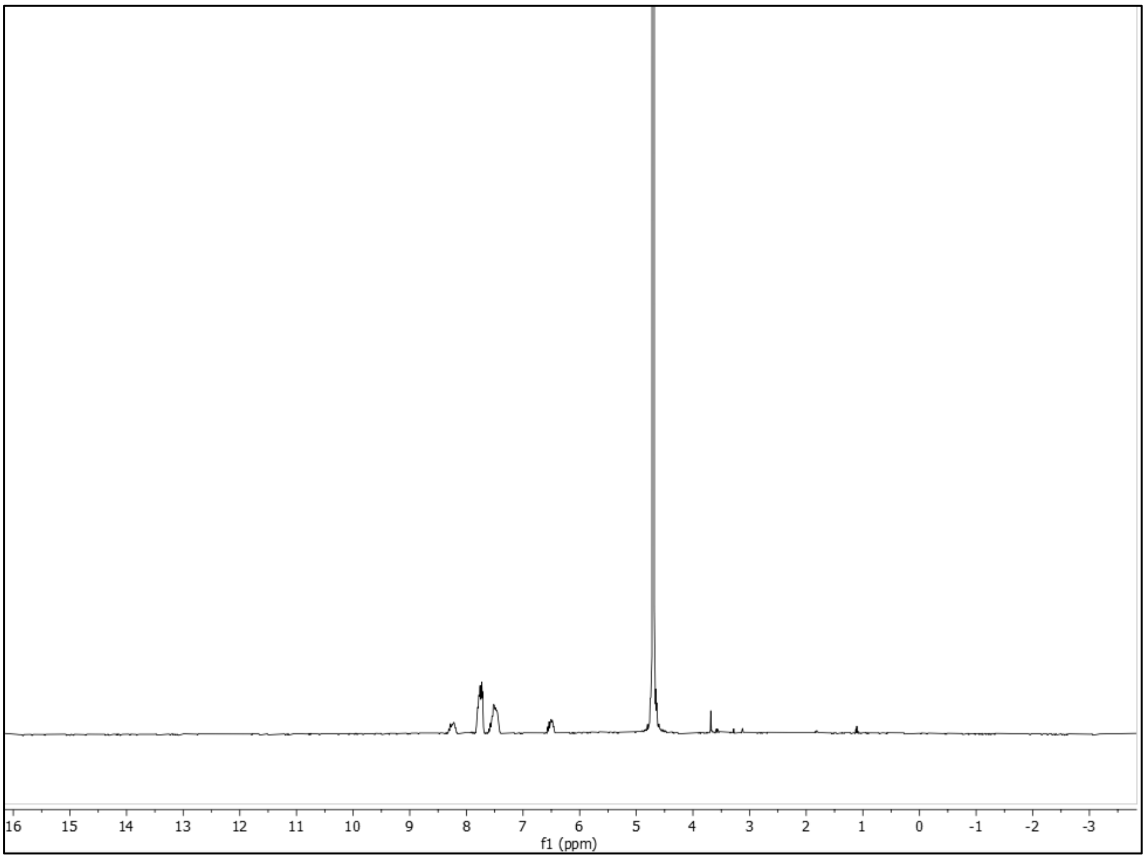

Figure A.3.5.9. ^1H NMR of sunset yellow in D_2O.

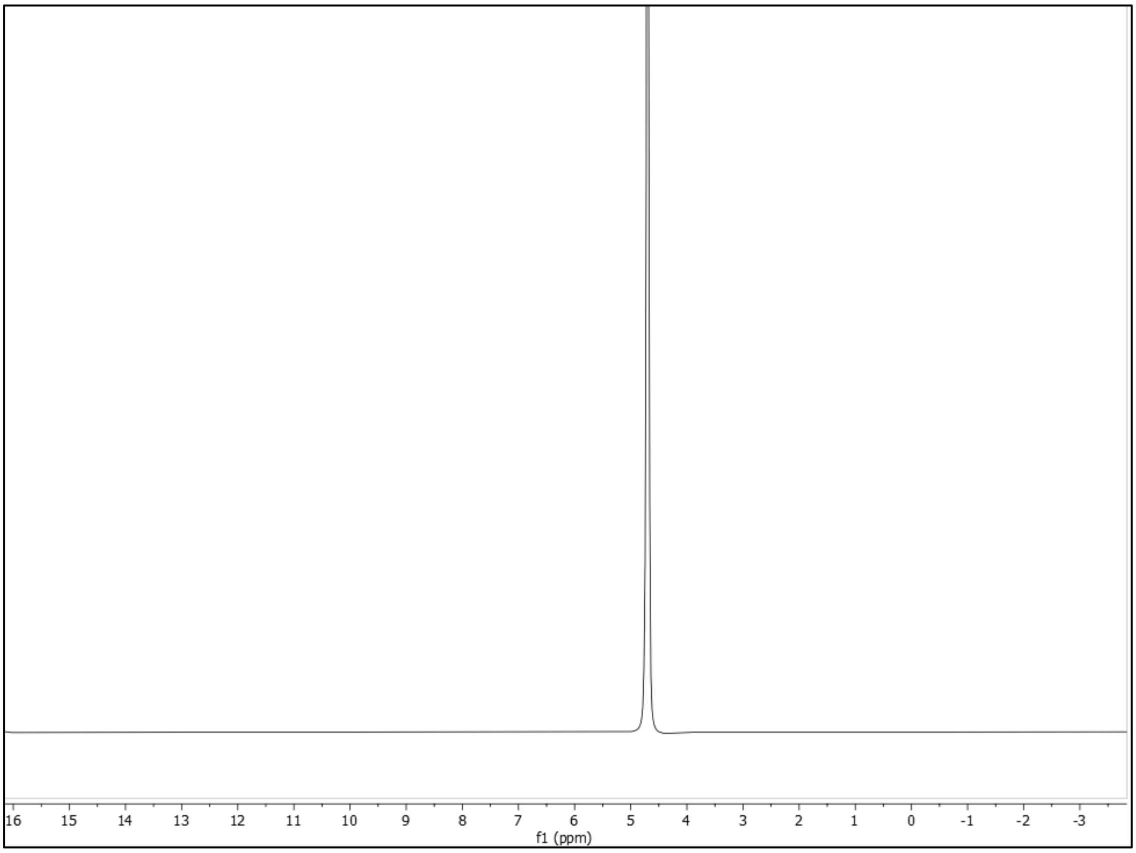

Figure A.3.5.10. ^1H NMR of sunset yellow decomposition products in D_2O.

CHROMOTROPE

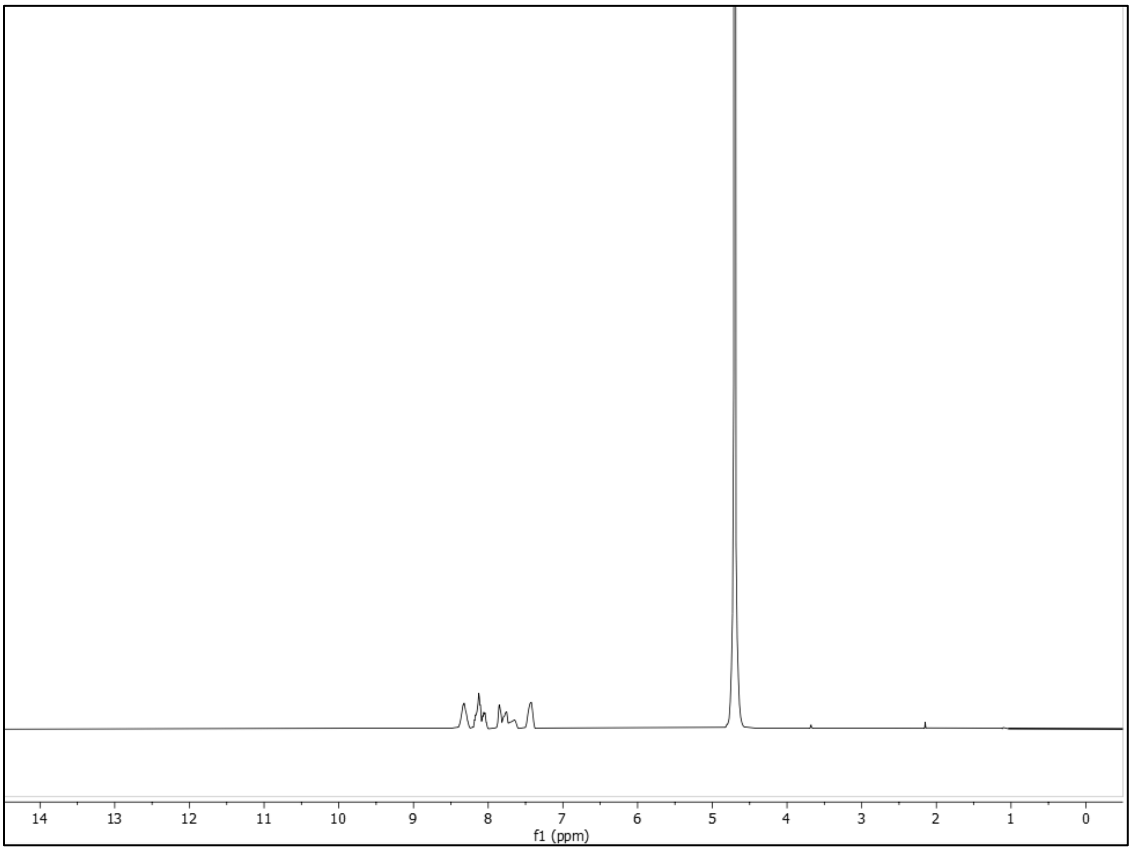

Figure A.3.5.11. ^{1}H NMR of chromotrope in D_2O.

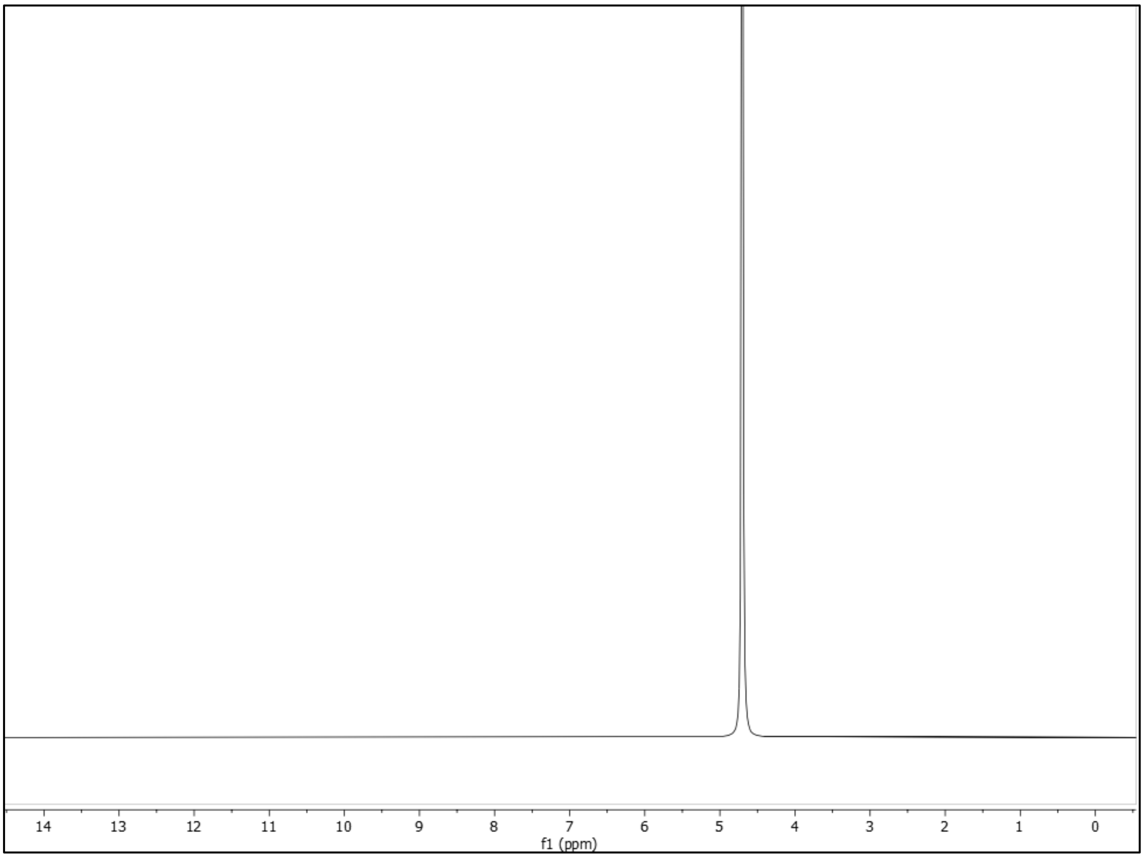

Figure A.3.5.12. ^{1}H NMR of chromotrope decomposition products in D_2O.

UV-Vis Spectra

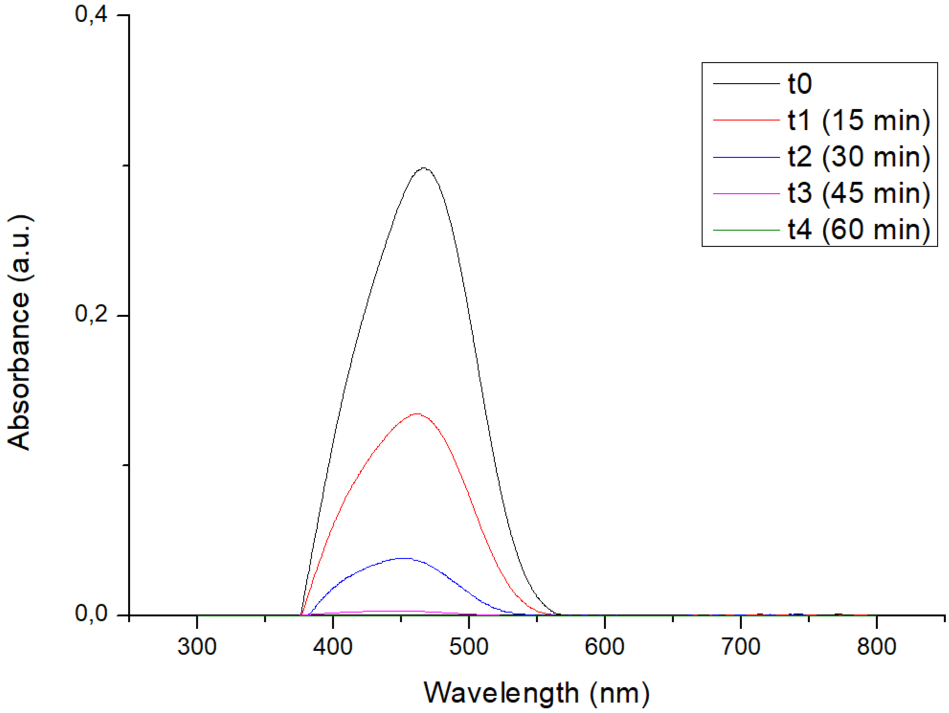

Figure A.3.5.13. UV-Vis spectra of methyl orange degradation in time in batch conditions with oxygen.

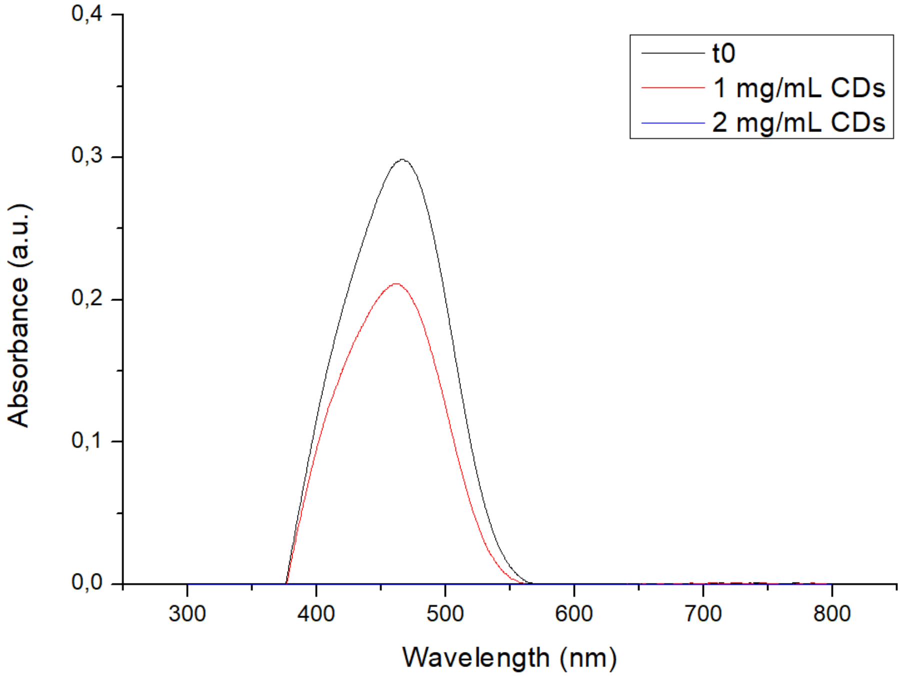

Figure A.3.5.14. UV-Vis spectra of methyl orange degradation in time in flow conditions with oxygen using different amount of CDs. Feed: [dye] = 5ppm, [bass-CDs] = 1 mg/ml (red line) or 2 mg/mL (blue line); λ=365 nm; Φ_{feed} = 0.5 mL/min, Φ_{oxygen} = 5.5 mL_N/min, $\Phi_{oxygen\ real}$ = 0.78 mL/min, Φ_{tot} = 1.28 mL/min, Rt = 2.03 min.

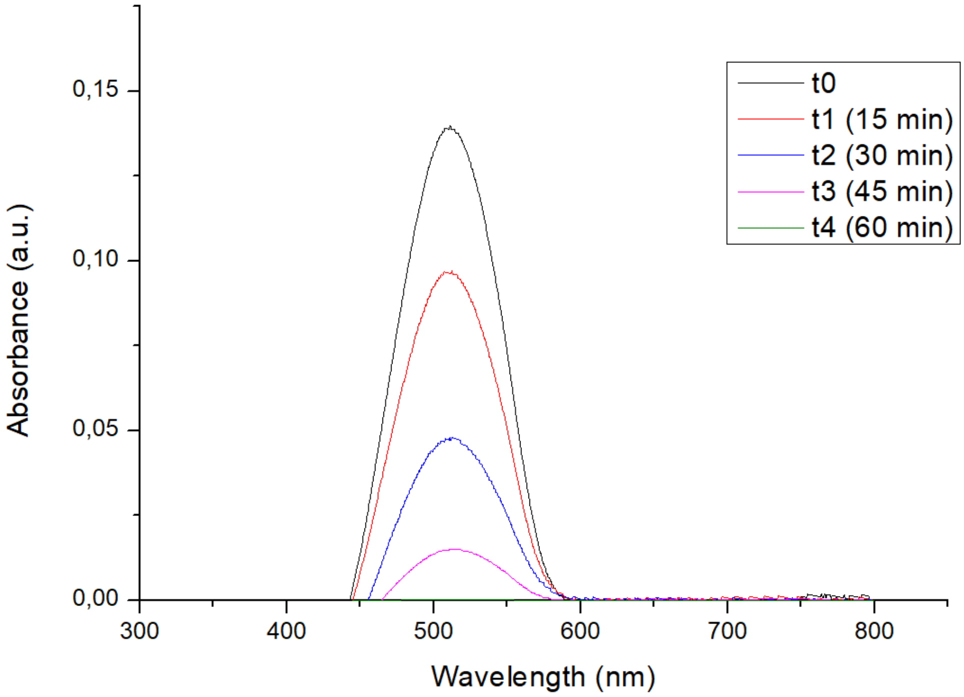

Figure A.3.5.15. UV-Vis spectra of acid red 18 degradation in time in batch conditions with oxygen.

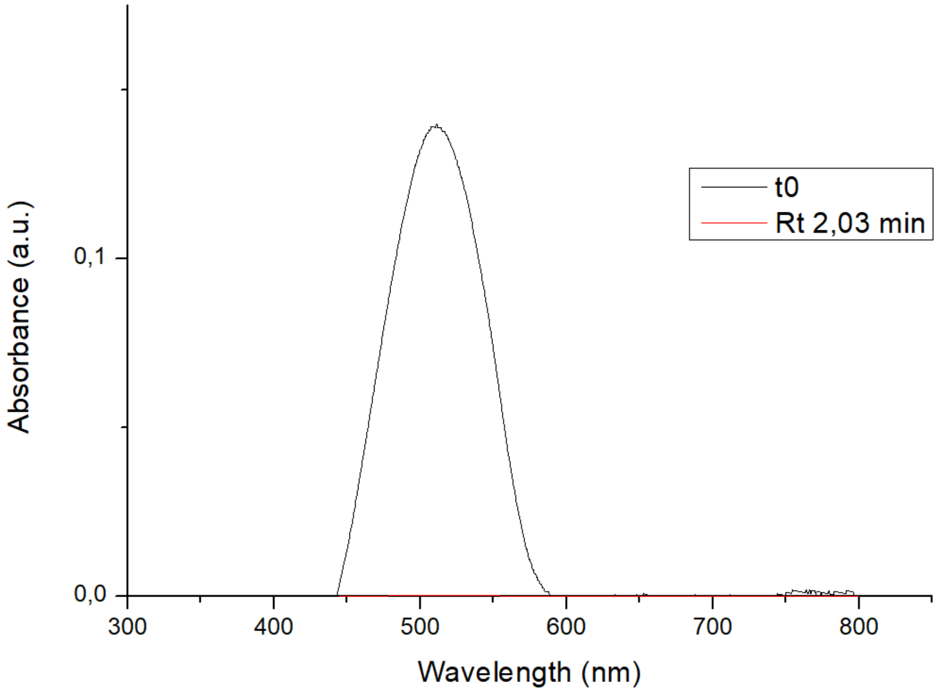

Figure A.3.5.16. UV-Vis spectra of acid red degradation in time in flow conditions with oxygen using different amount of CDs. Feed: [dye] = 5ppm, [bass-CDs] = 2 mg/mL; λ=365 nm; Φ_{feed} = 0.5 mL/min, Φ_{oxygen} = 5.5 mL$_N$/min, $\Phi_{oxygen\ real}$ = 0.78 mL/min, Φ_{tot} = 1.28 mL/min, Rt = 2.03 min.

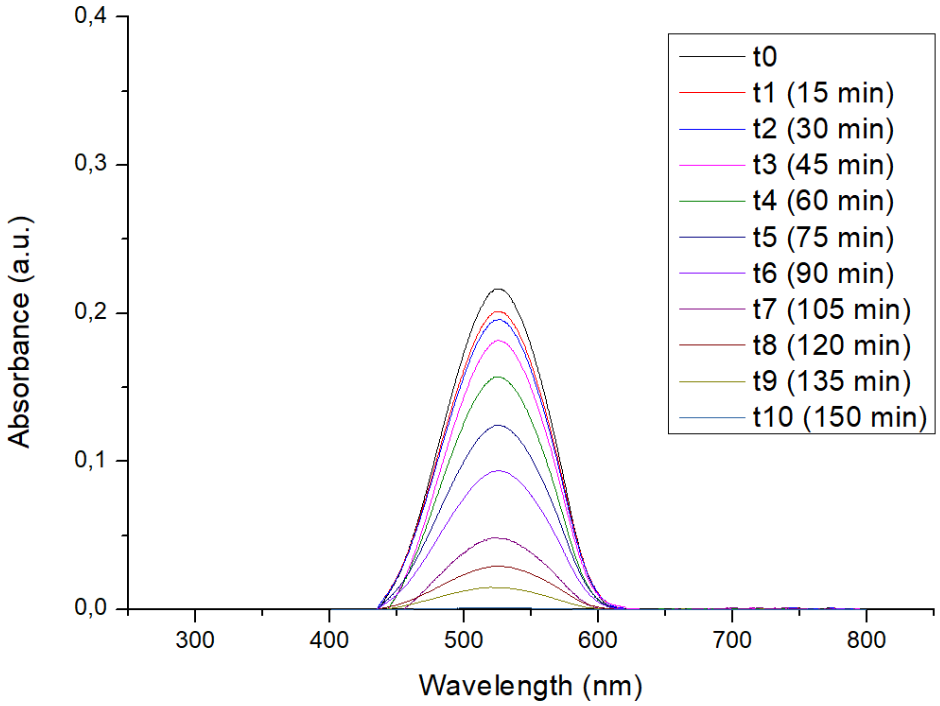

Figure A.3.5.17. UV-Vis spectra of amaranth degradation in time in batch conditions with oxygen.

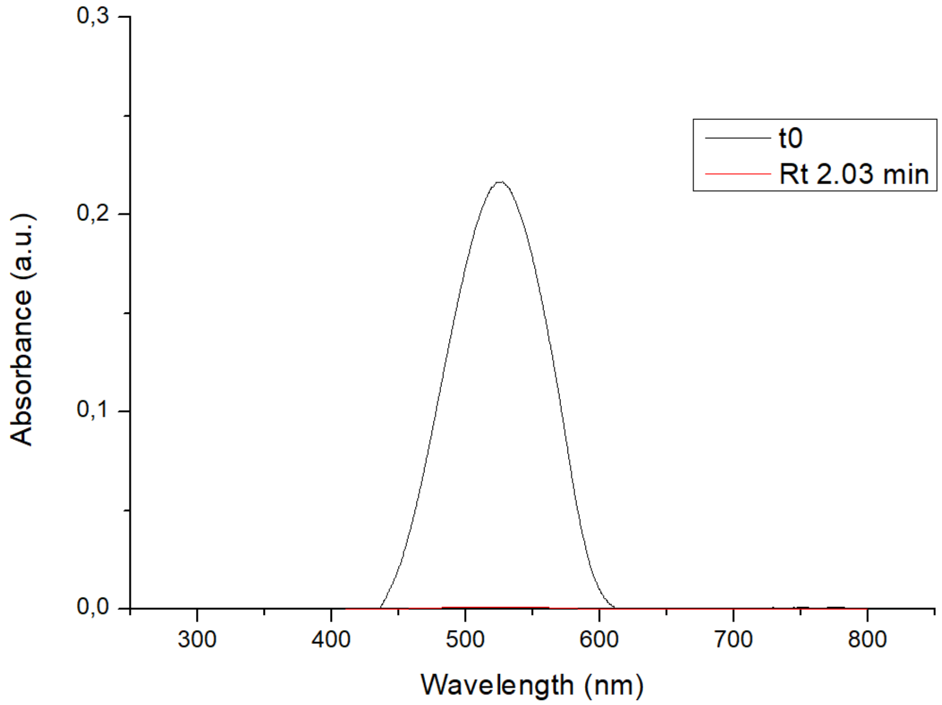

Figure A.3.5.18. UV-Vis spectra of amaranth degradation in time in flow conditions with oxygen using different amount of CDs. Feed: [dye] = 5ppm, [bass-CDs] = 2 mg/mL; λ=365 nm; Φ_{feed} = 0.5 mL/min, Φ_{oxygen} = 5.5 mL_N/min, $\Phi_{\text{oxygen real}}$ = 0.78 mL/min, Φ_{tot} = 1.28 mL/min, Rt = 2.03 min.

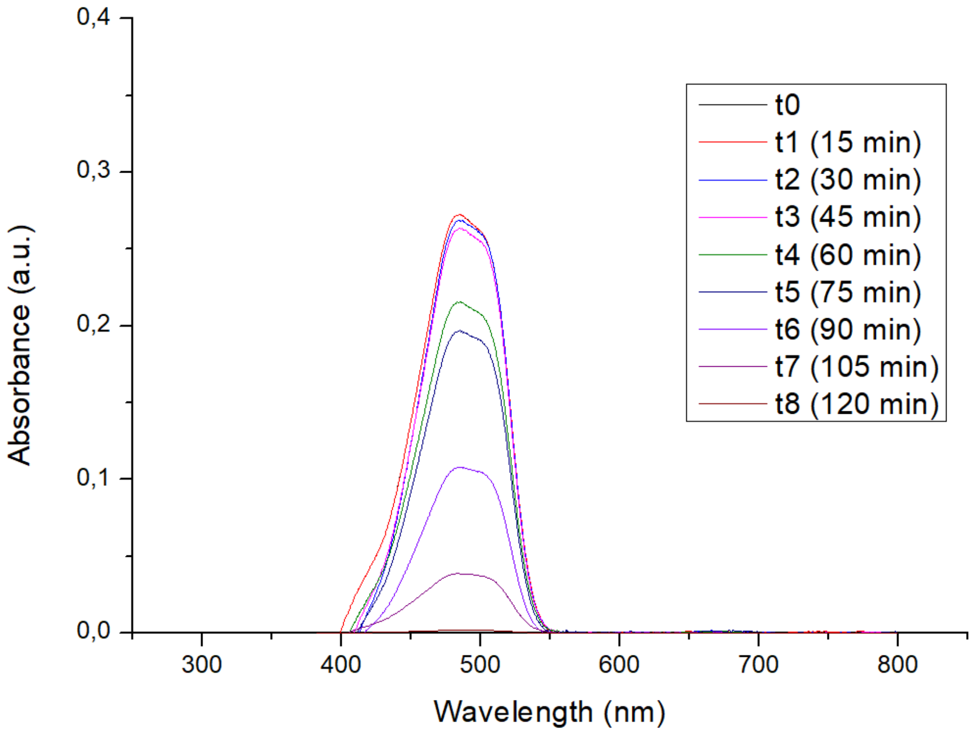

Figure A.3.5.19. UV-Vis spectra of sunset yellow degradation in time in batch conditions with oxygen.

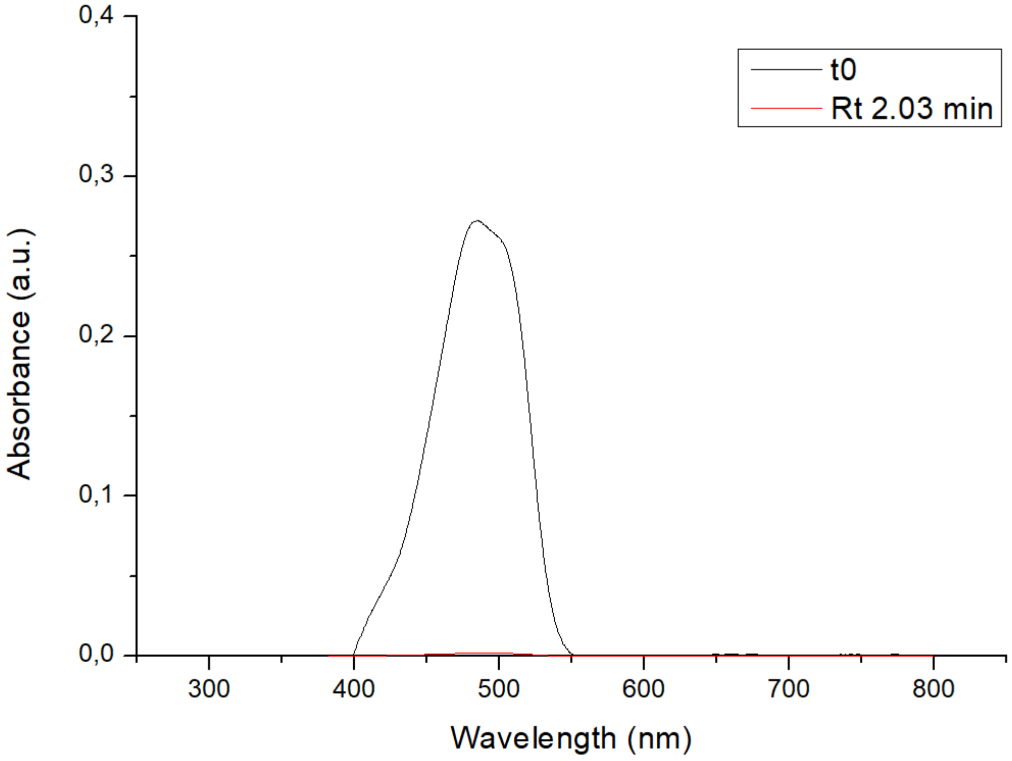

Figure A.3.5.20. UV-Vis spectra of sunset yellow degradation in time in flow conditions with oxygen using different amount of CDs. Feed: [dye] = 5ppm, [bass-CDs] = 2 mg/mL; λ=365 nm; Φ_{feed} = 0.5 mL/min, Φ_{oxygen} = 5.5 mL$_N$/min, $\Phi_{\text{oxygen real}}$ = 0.78 mL/min, Φ_{tot} = 1.28 mL/min, Rt = 2.03 min.

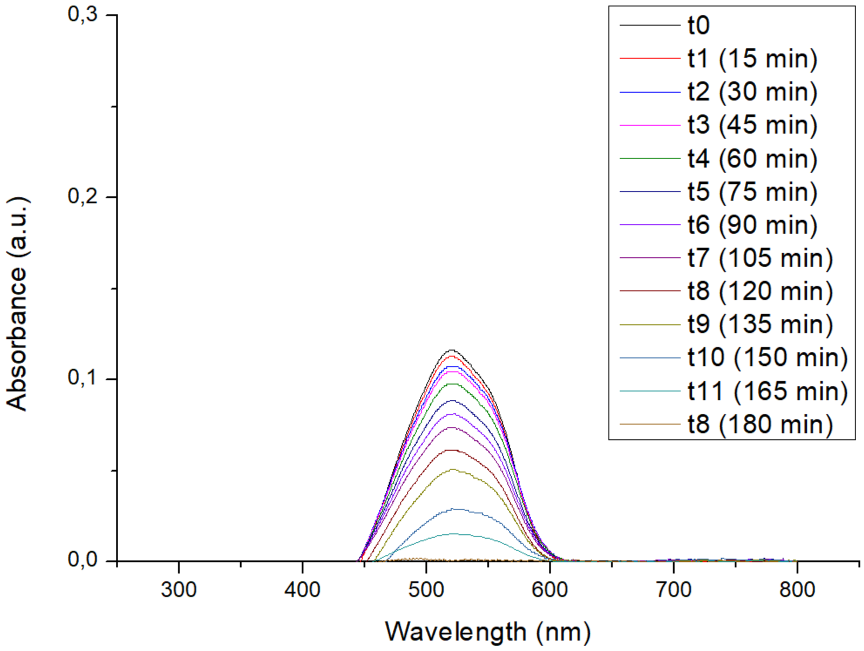

Figure A.3.5.21. UV-Vis spectra of chromotrope degradation in time in batch conditions with oxygen.

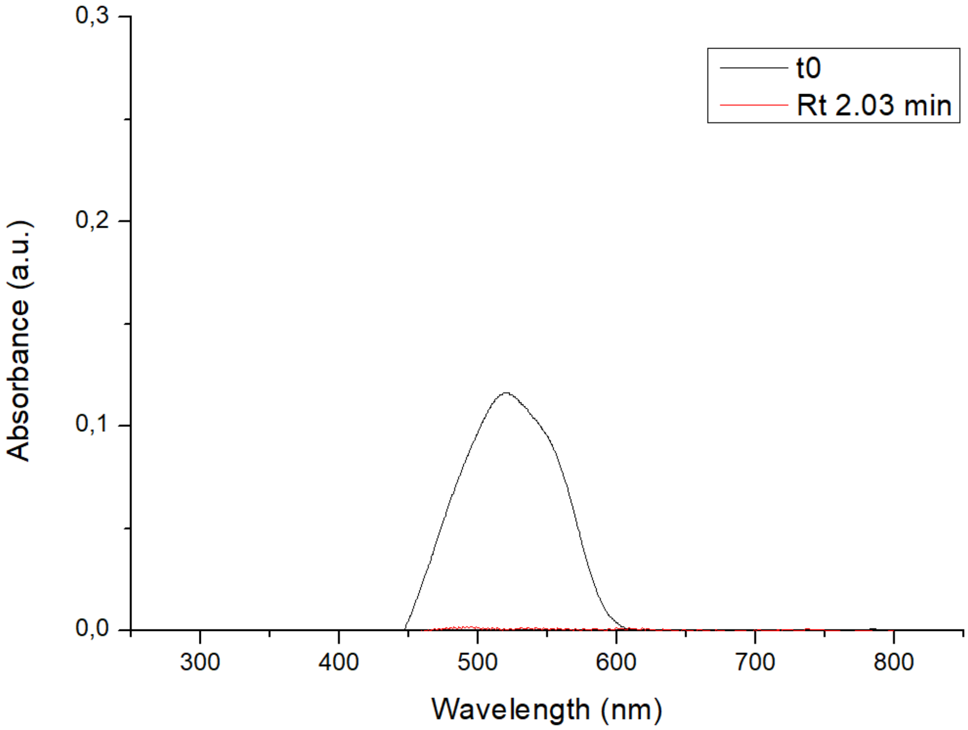

Figure A.3.5.22. UV-Vis spectra of chromotrope degradation in time in flow conditions with oxygen using different amount of CDs. Feed: [dye] = 5ppm, [bass-CDs] = 2 mg/mL; λ=365 nm; Φ_{feed} = 0.5 mL/min, Φ_{oxygen} = 5.5 mL$_N$/min, $\Phi_{\text{oxygen real}}$ = 0.78 mL/min, Φ_{tot} = 1.28 mL/min, Rt = 2.03 min.

Continuous flow Setup

All the parts used to assembly the CF setup are commercially available:

- HPLC pump Knauer P41S Azura equipped with a 10 mL SS head was used to handle the liquid feeds.
- PFA lines and coil reactors were constructed from PFA tubing 1/16” (high purity PFA. 1.58 mm outer diameter, 750 µm internal diameter).
- Arrowhead mixer, connectors and ferules were PEEK made and purchased from IDEX/Upchurch scientific.
- Check valves and Back-pressure regulators were purchased from IDEX/Upchurch scientific and used with a PEEK holder.
- The mass flow controller used to handle the oxygen feed was a Bronkhorst® EL-FLOW® Prestige mass flow controller.

Residence Time calculations

The residence time is calculated according to **Equation A.3.5.1**:

$$Residence\ time\ (\mathrm{min}) = \frac{Internal\ Volume\ (mL)}{Flow\ rate\ (mL\ min^{-1})}$$

The total flow rate combines the individual flow rates of all fluids fed into the reactor. The actual gas flow rate is calculated from the flow rate measured by the MFC according to **Equations A.3.5.2-3.**

$$n'_{O_2} = \frac{P_N(atm)V_N(L)}{R\ (L.atm.mol^{-1}.K^{-1})T_N(K)}$$

$$V'_{real} = \frac{n_{O_2}R\ T_{real}}{P_{real}} = \frac{m'_{O_2}.R.T_{real}}{MM_{O_2}.P_{real}}$$

Kinetics

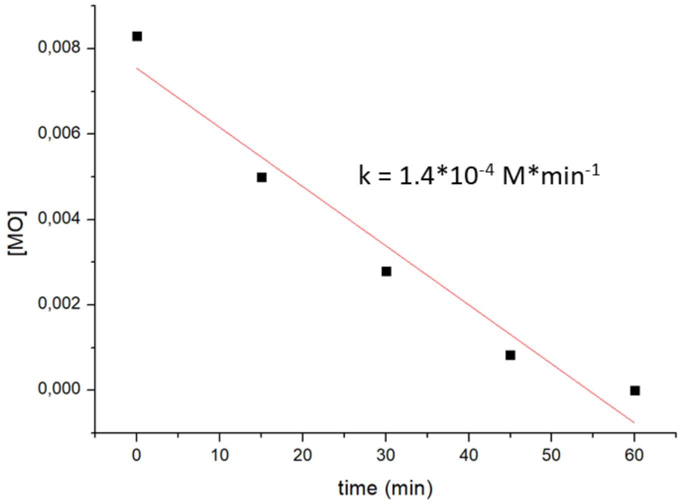

Figure A.3.5.23. Kinetic plot for the photodegradation of methyl orange using both CDs and oxygen and relative rate constant (k).

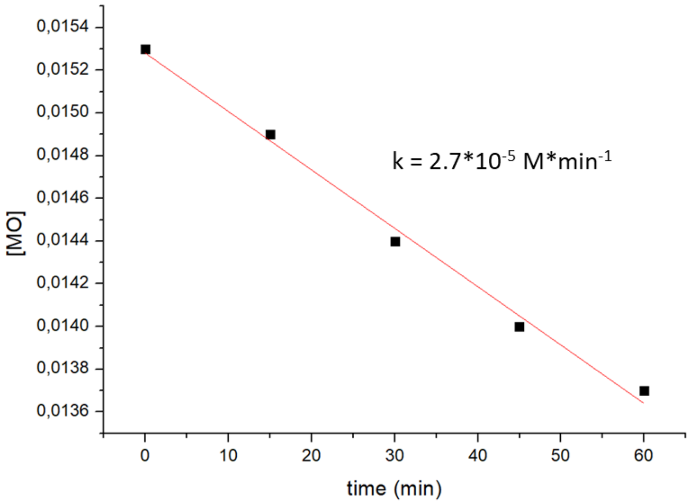

Figure A.3.5.24. Kinetic plot for the photodegradation of methyl orange using only CDs and relative rate constant (k).

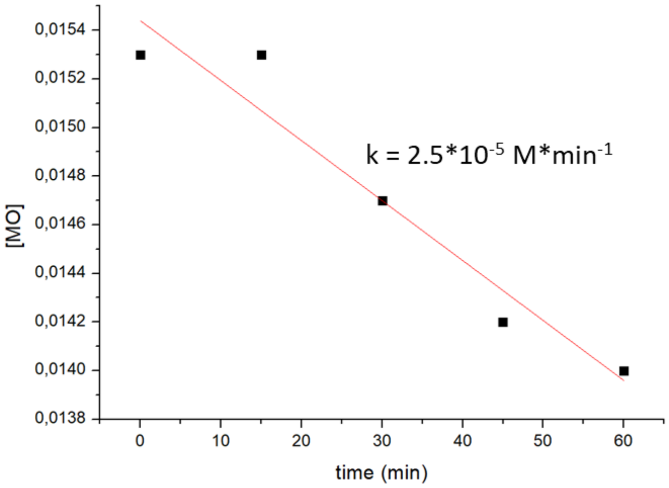

Figure A.3.5.25. Kinetic plot for the photodegradation of methyl orange using only oxygen and relative rate constant (k).

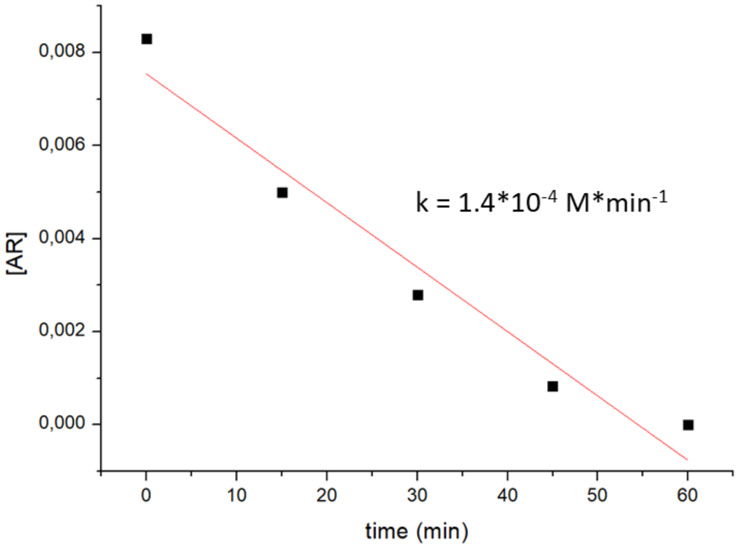

Figure A.3.5.26. Kinetic plot for the photodegradation of acid red 18 using both CDs and oxygen and relative rate constant (k).

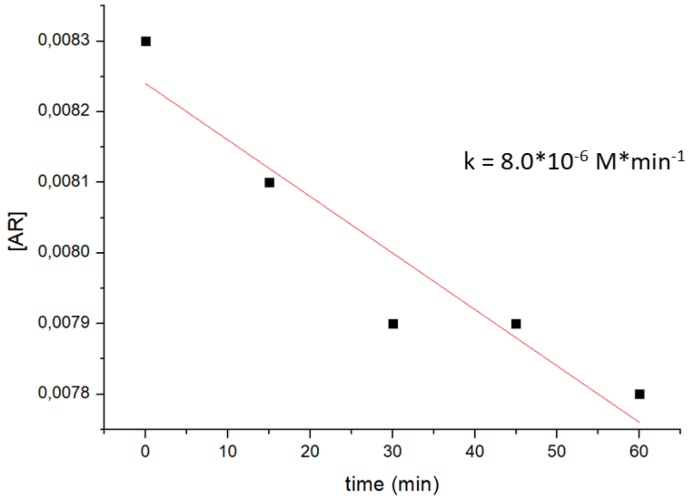

Figure A.3.5.27. Kinetic plot for the photodegradation of acid red 18 using only CDs and relative rate constant (k).

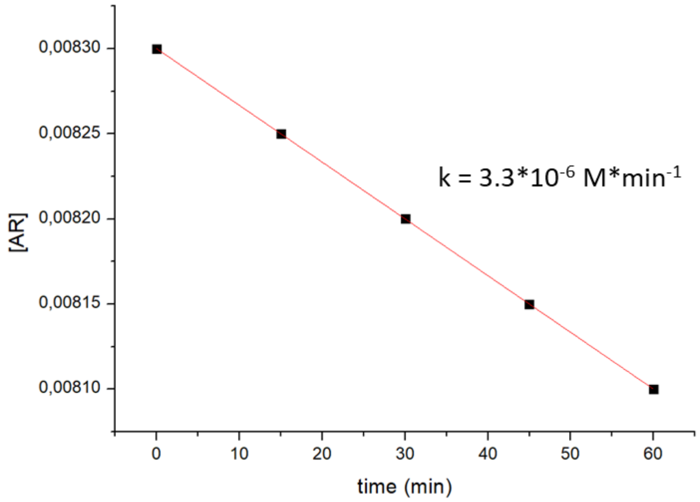

Figure A.3.5.28. Kinetic plot for the photodegradation of acid red 18 using only oxygen and relative rate constant (k).

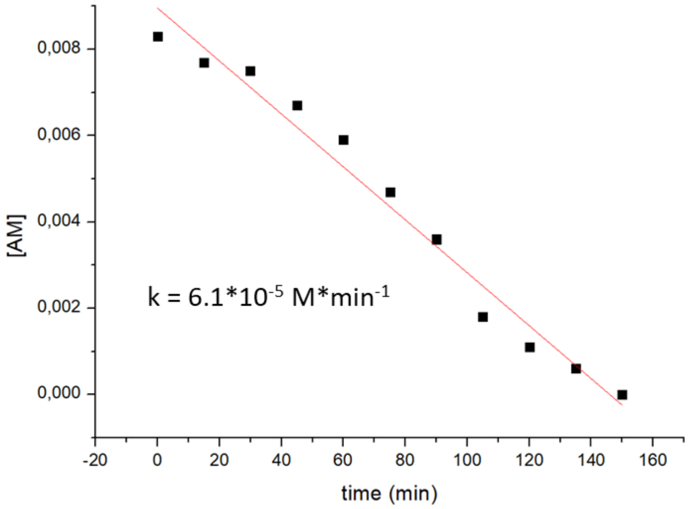

Figure A.3.5.29. Kinetic plot for the photodegradation of amaranth using both CDs and oxygen and relative rate constant (k).

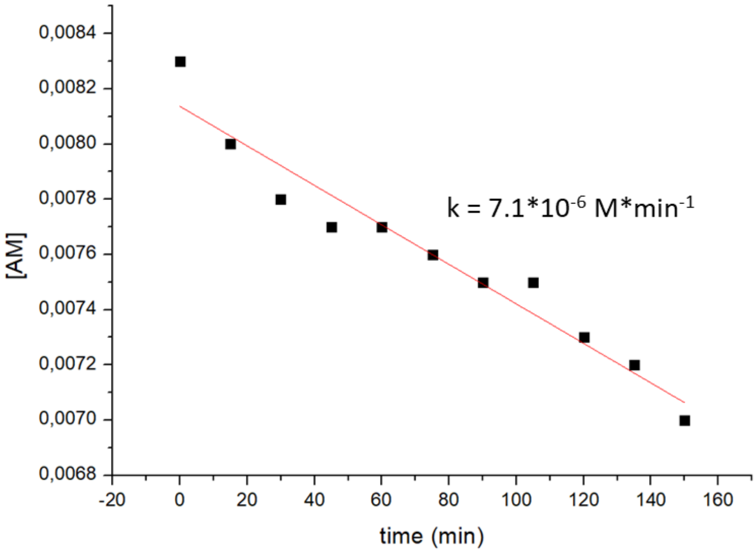

Figure A.3.5.30. Kinetic plot for the photodegradation of amaranth using only CDs and relative rate constant (k).

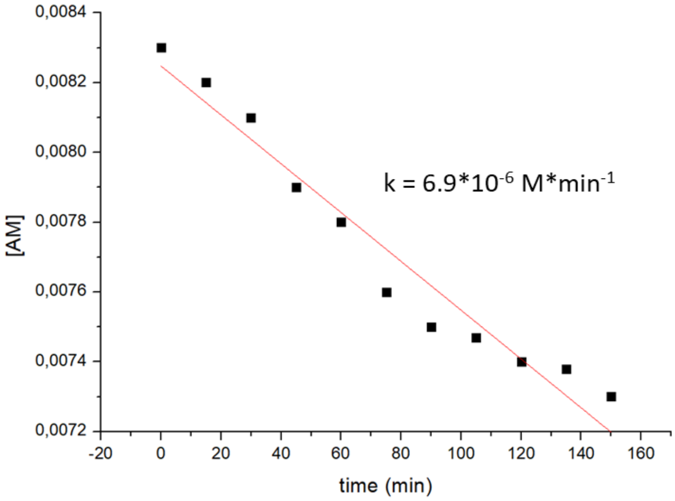

Figure A.3.5.31. Kinetic plot for the photodegradation of amaranth using only oxygen and relative rate constant (k).

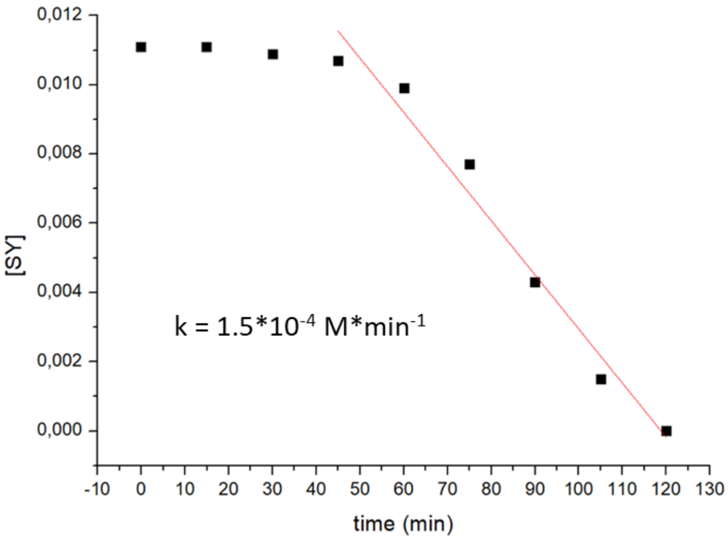

Figure A.3.5.32. Kinetic plot for the photodegradation of sunset yellow using both CDs and oxygen and relative rate constant (k).

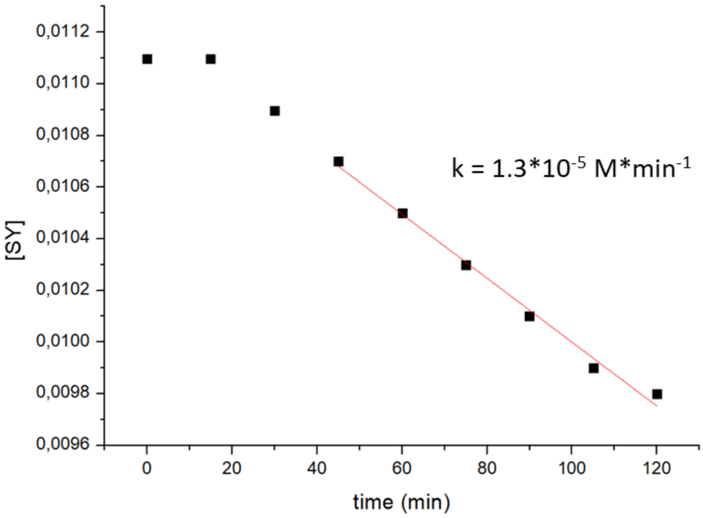

Figure A.3.5.33. Kinetic plot for the photodegradation of sunset yellow using only CDs and relative rate constant (k).

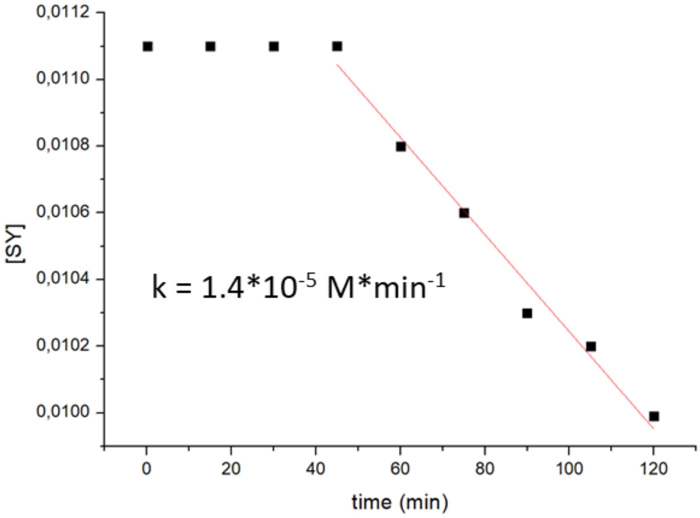

Figure A.3.5.34. Kinetic plot for the photodegradation of sunset yellow using only oxygen and relative rate constant (k).

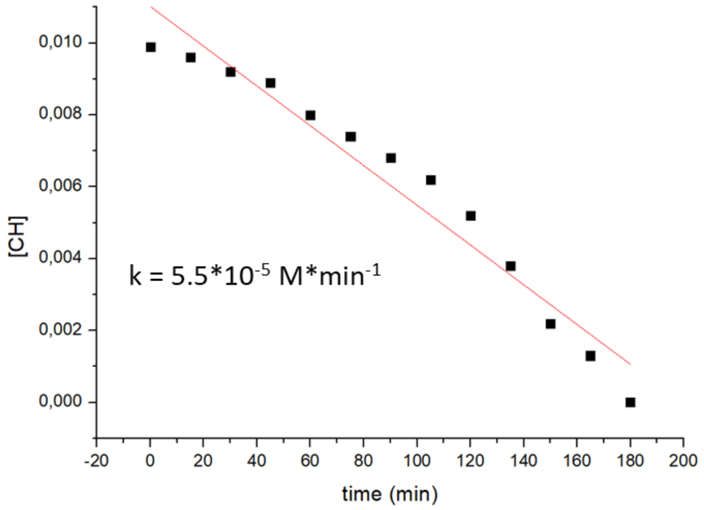

Figure A.3.5.35. Kinetic plot for the photodegradation of chromotrope using both CDs and oxygen and relative rate constant (k).

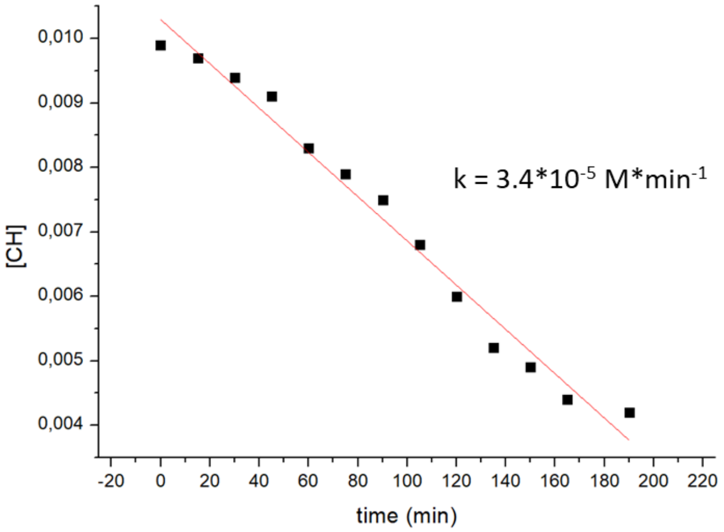

Figure A.3.5.36. Kinetic plot for the photodegradation of chromotrope using only CDs and relative rate constant (k).

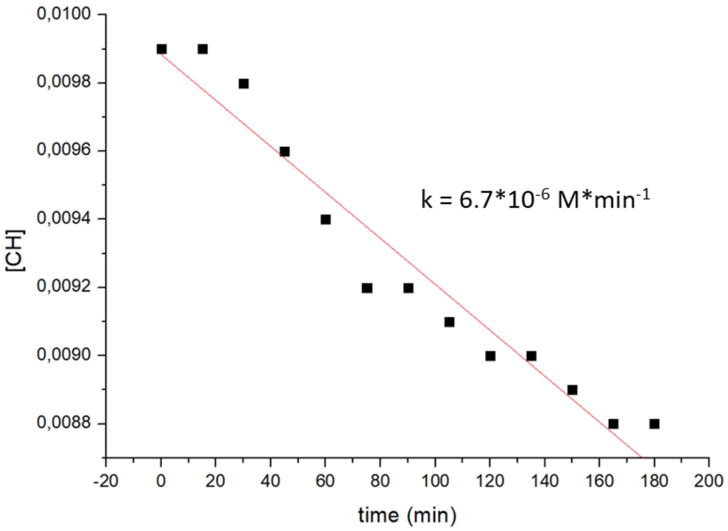

Figure A.3.5.37. Kinetic plot for the photodegradation of chromotrope using only oxygen and relative rate constant (k).

Mineralization pathway

Based on literature data,[3,4,5] a hypothetical mineralization pathway for methyl orange is herein reported. The same pathway can be applied to all the other azo dyes used in this study.

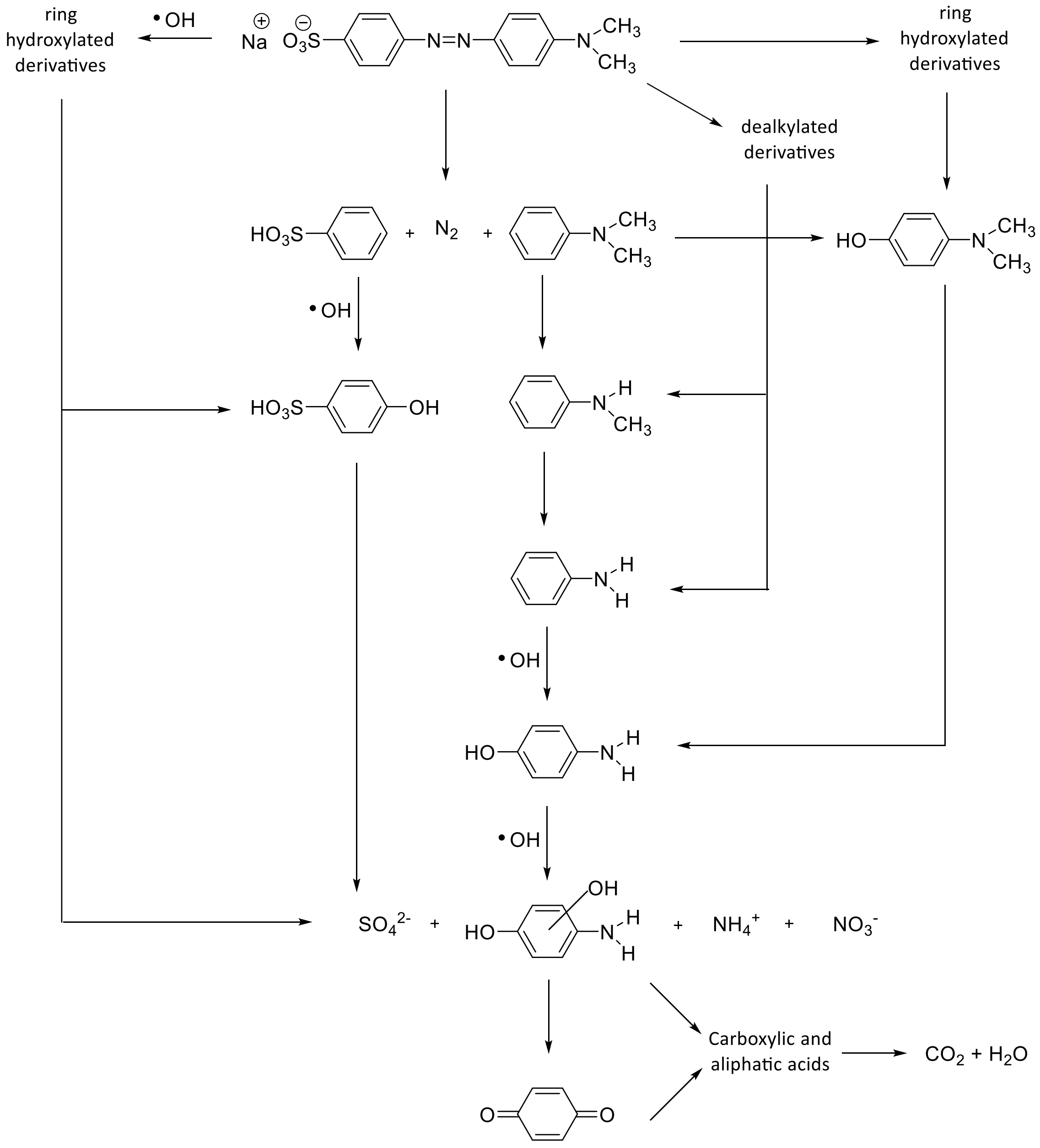

Scheme A.3.5.1. Mineralization pathway for MO.

A-4.2 Fish-waste derived Gelatin and Carbon Dots for Biobased UV-blocking Films

UV-Vis Absorbance Spectrum of Gelatin-CDs Films

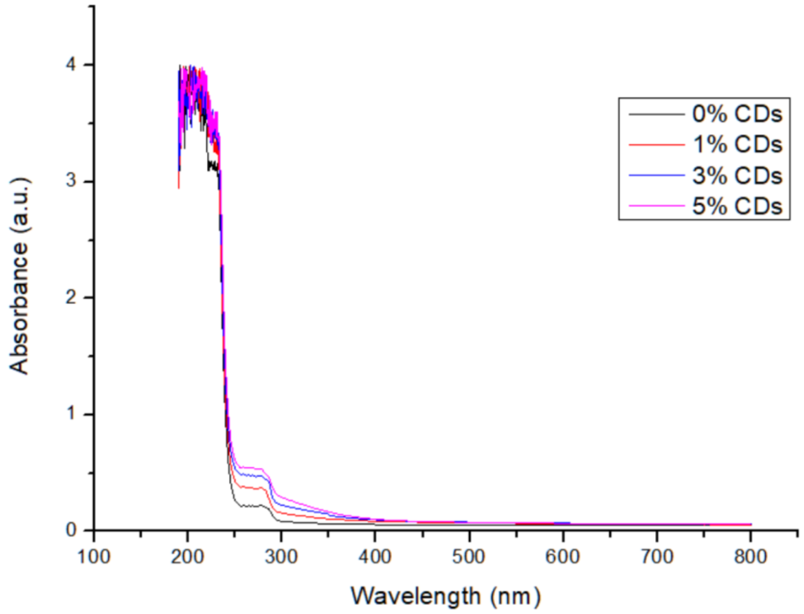

Figure A.4.2.1. Uv-Visible absorbance spectrum of gelatin films with different concentrations of CDs (0% black line, 1% red line, 3% blue line and 5% pink line).

Differential Scanning Calorimetry of Gelatin-CDs Films

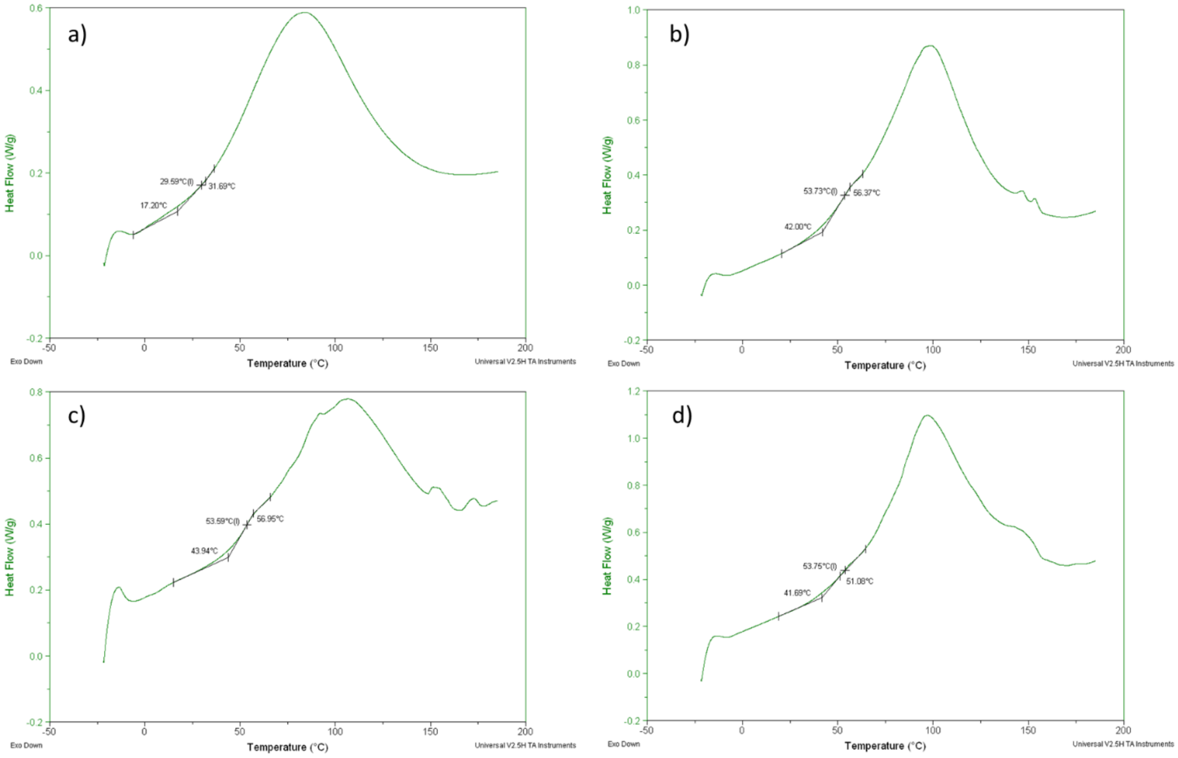

Figure A.4.2.2. DSC curves of fish gelatin films containing (a) 0% of CDs, (b) 1% of CDs, (c) 3% of CDs and (d) 5% of CDs.

Transmission Electron Microscopy of Gelatin-CDs Films

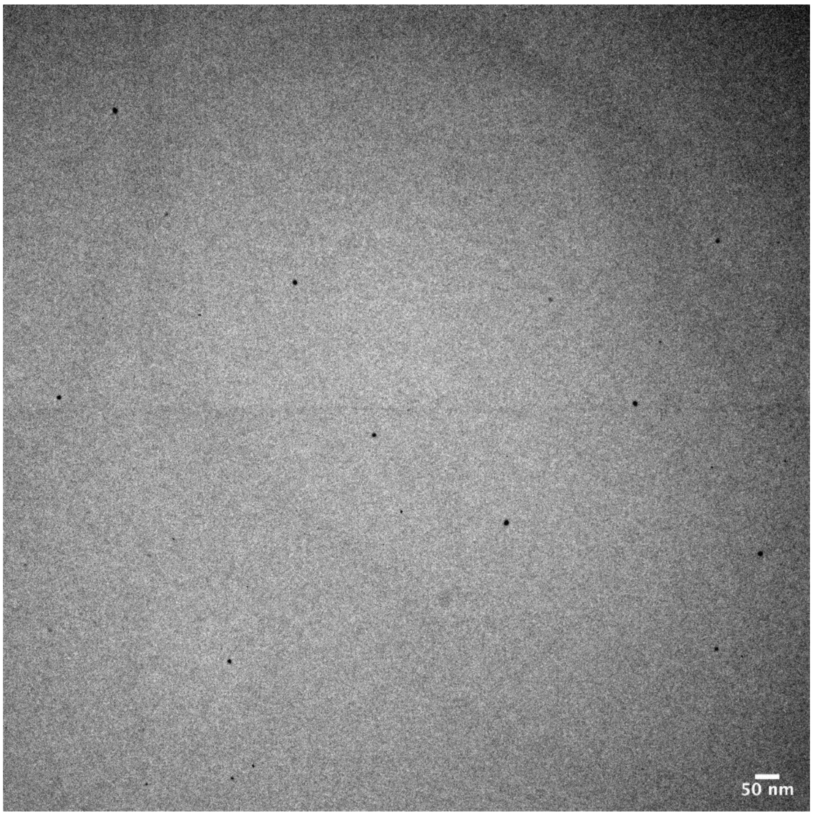

Figure A.4.2.3. TEM micrographs of fish derived CDs.

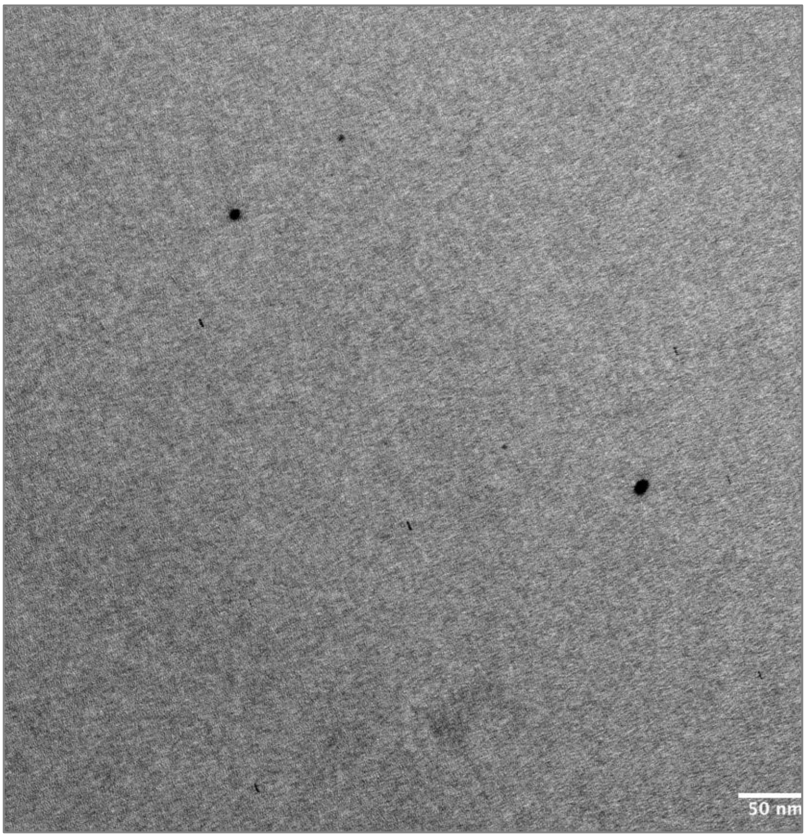

Figure A.4.2.4. TEM micrographs of fish derived CDs.

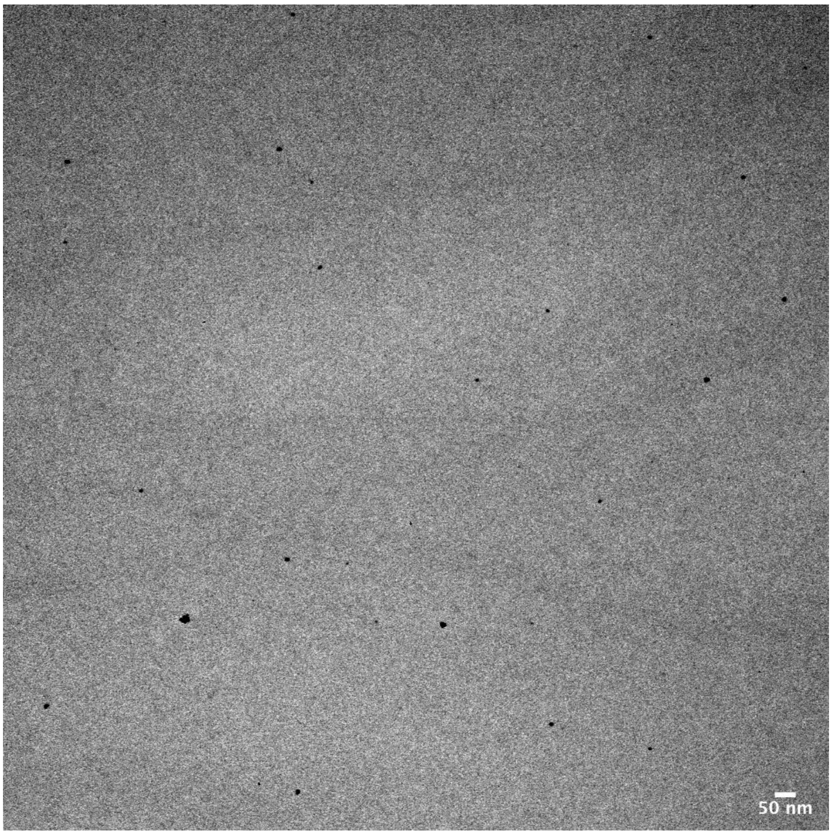

Figure A.4.2.5. TEM micrographs of fish derived CDs.

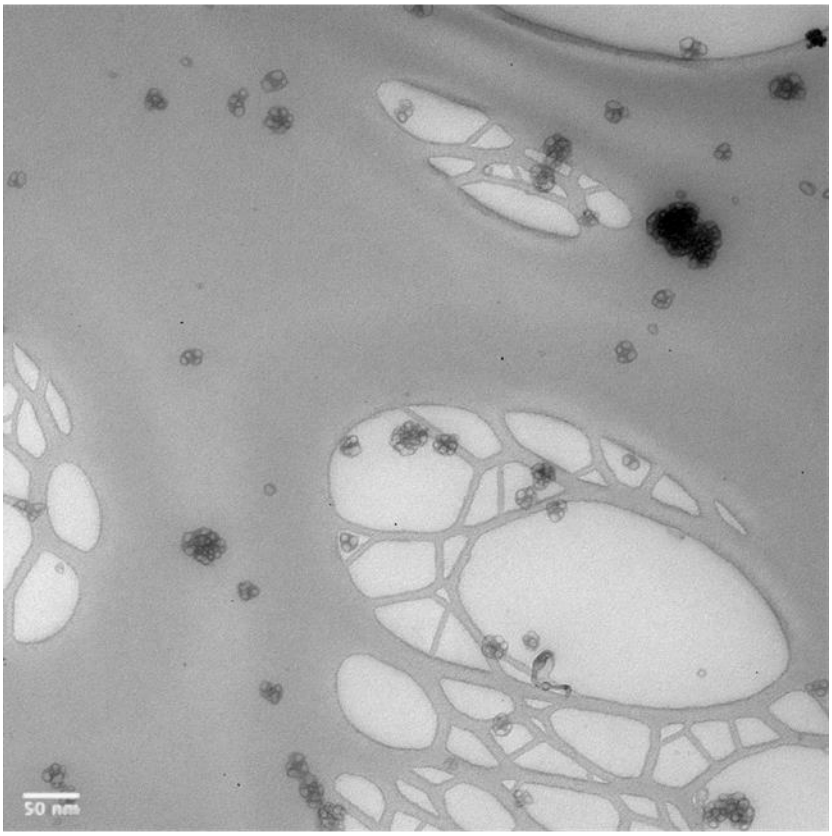

Figure A.4.2.6. TEM micrographs of gelatin-CDs films with 0% of CDs.

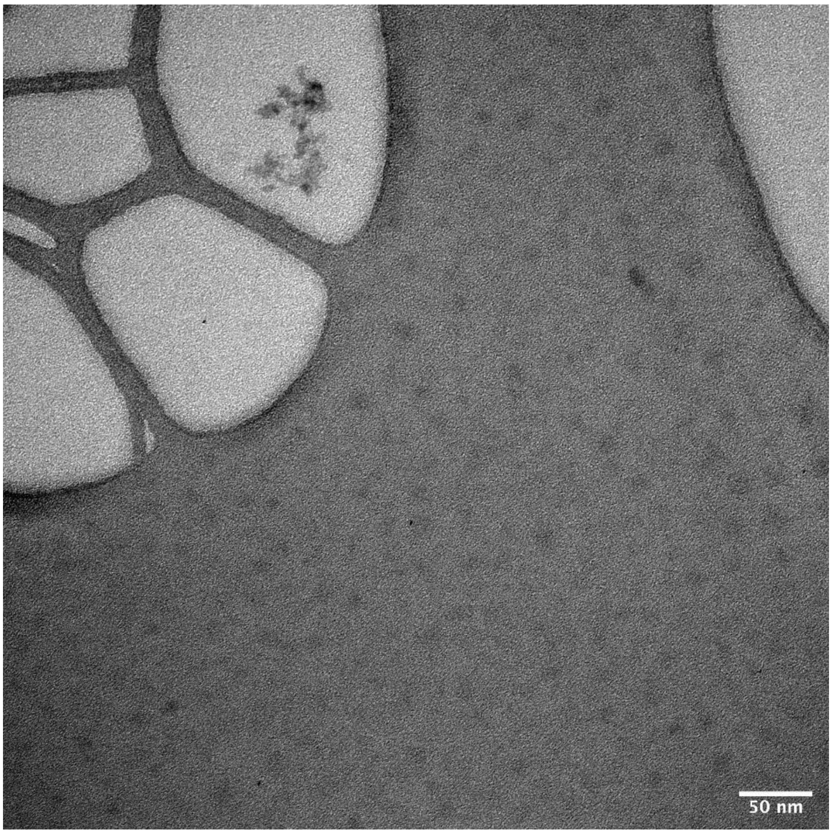

Figure A.4.2.7. TEM micrographs of gelatin-CDs films with 0% of CDs.

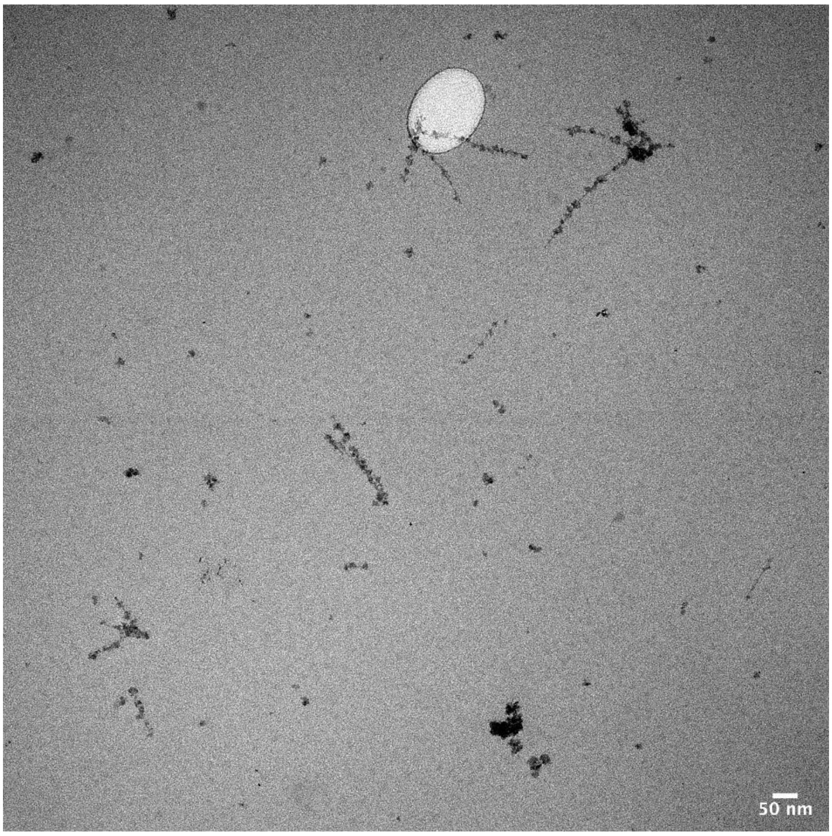

Figure A.4.2.8. TEM micrographs of gelatin-CDs films with 0% of CDs.

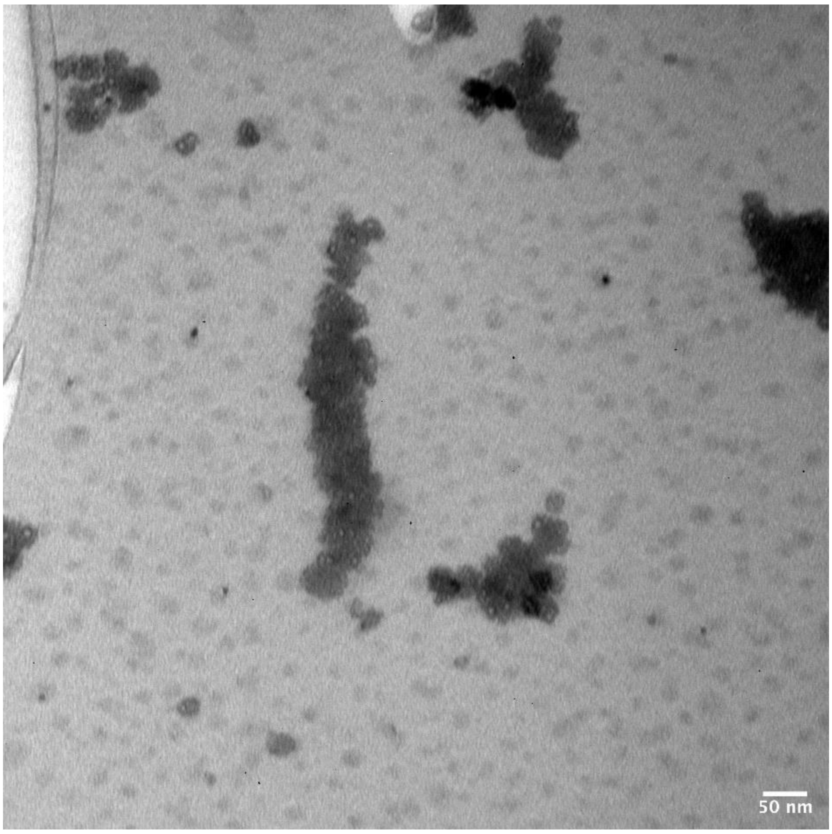

Figure A.4.2.9. TEM micrographs of gelatin-CDs films with 1% of CDs

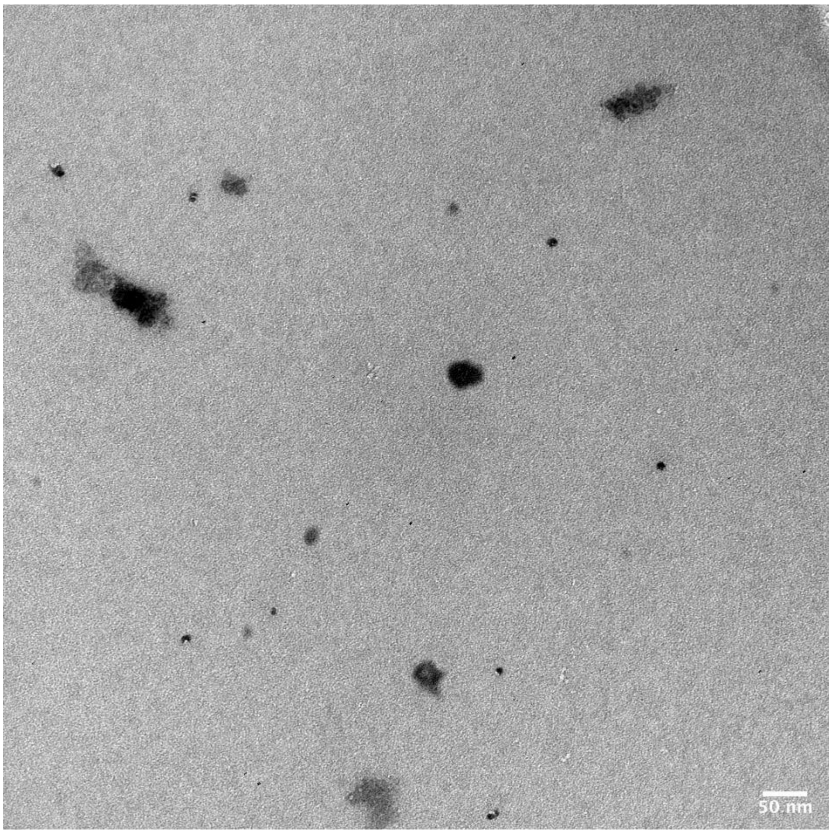

Figure A.4.2.10. TEM micrographs of gelatin-CDs films with 1% of CDs

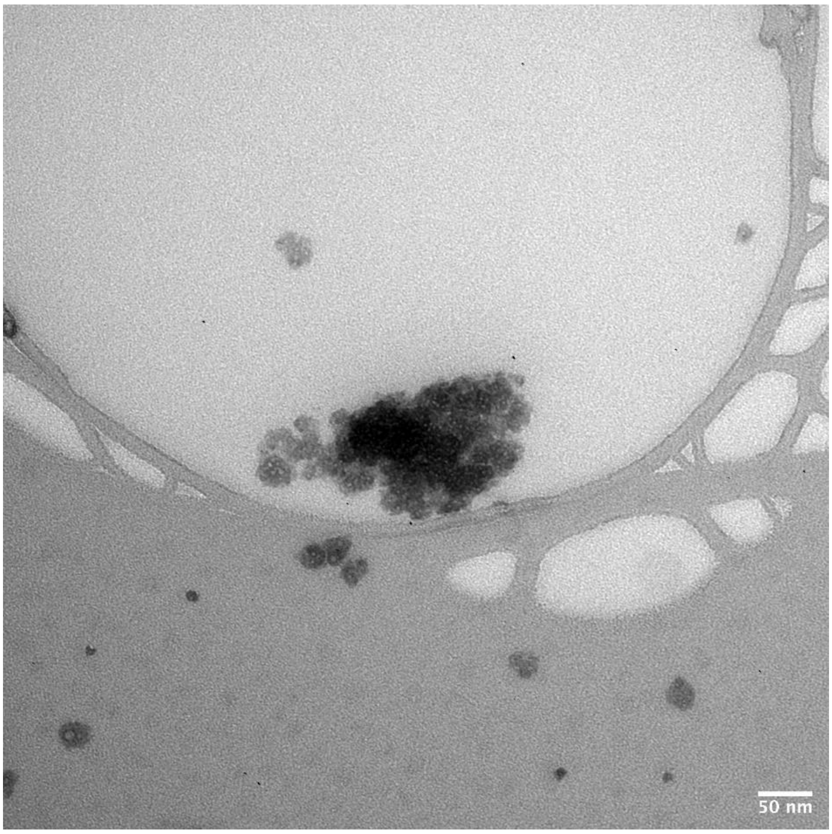

Figure A.4.2.11. TEM micrographs of gelatin-CDs films with 1% of CDs.

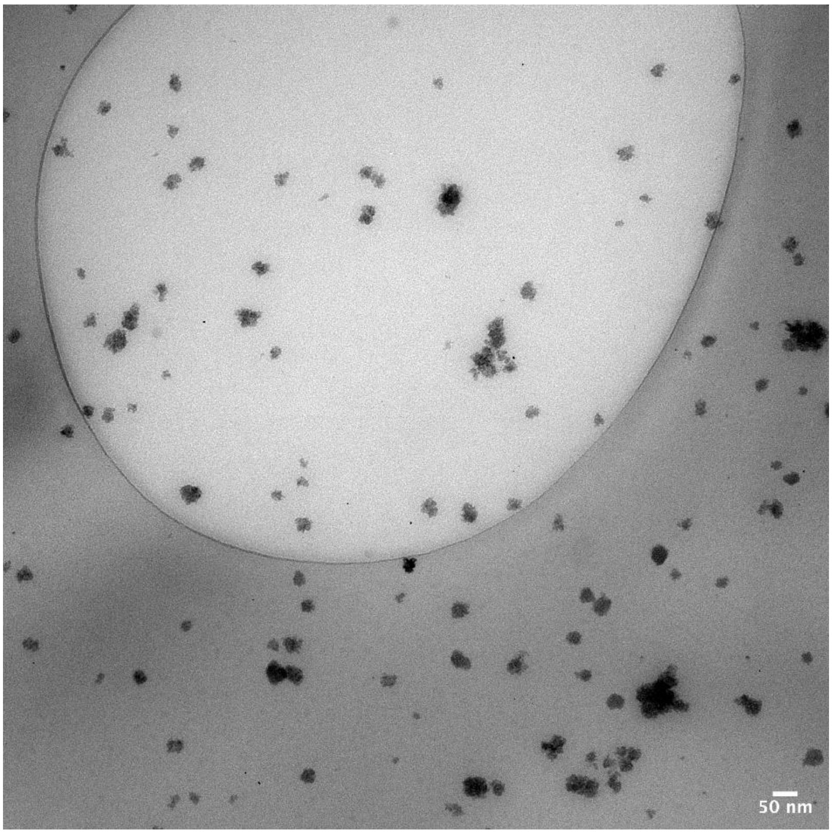

Figure A.4.2.12. TEM micrographs of gelatin-CDs films with 3% of CDs.

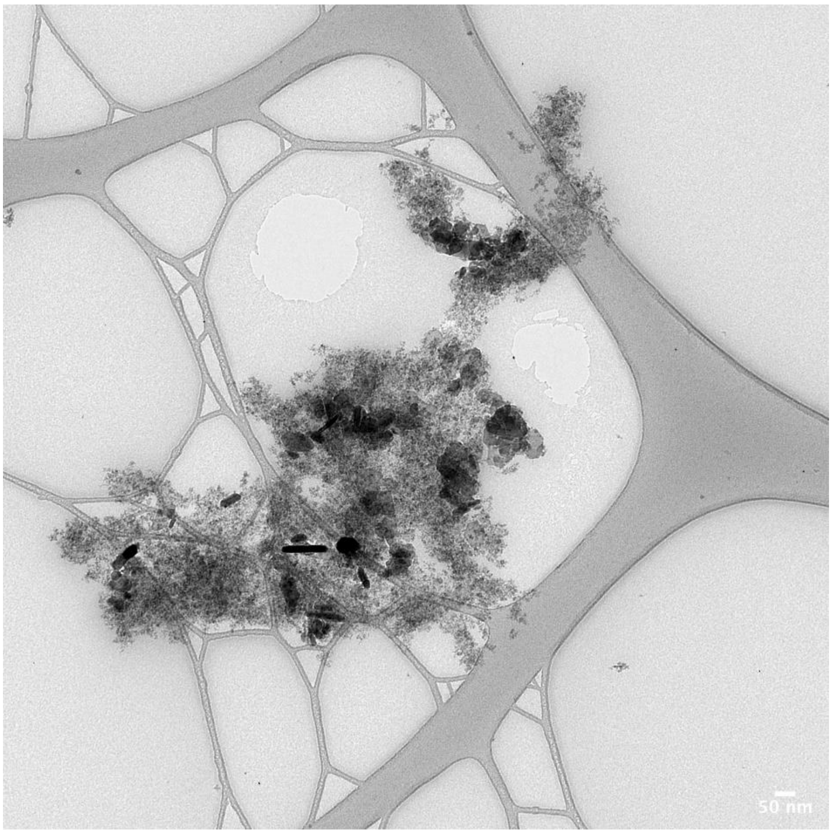

Figure A.4.2.13. TEM micrographs of gelatin-CDs films with 3% of CDs.

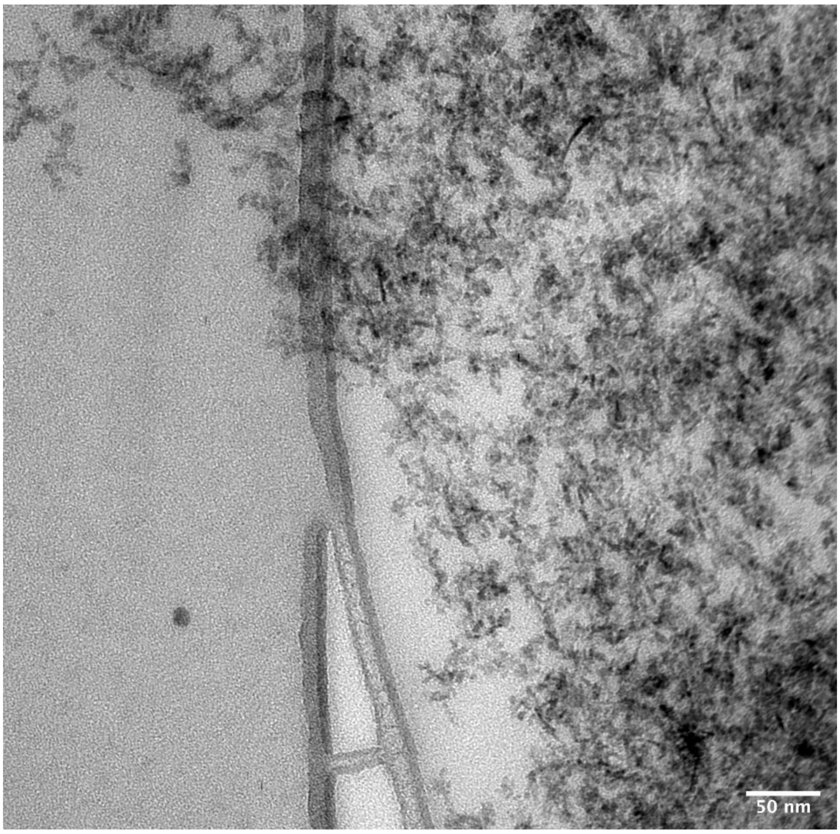

Figure A.4.2.14. TEM micrographs of gelatin-CDs films with 3% of CDs.

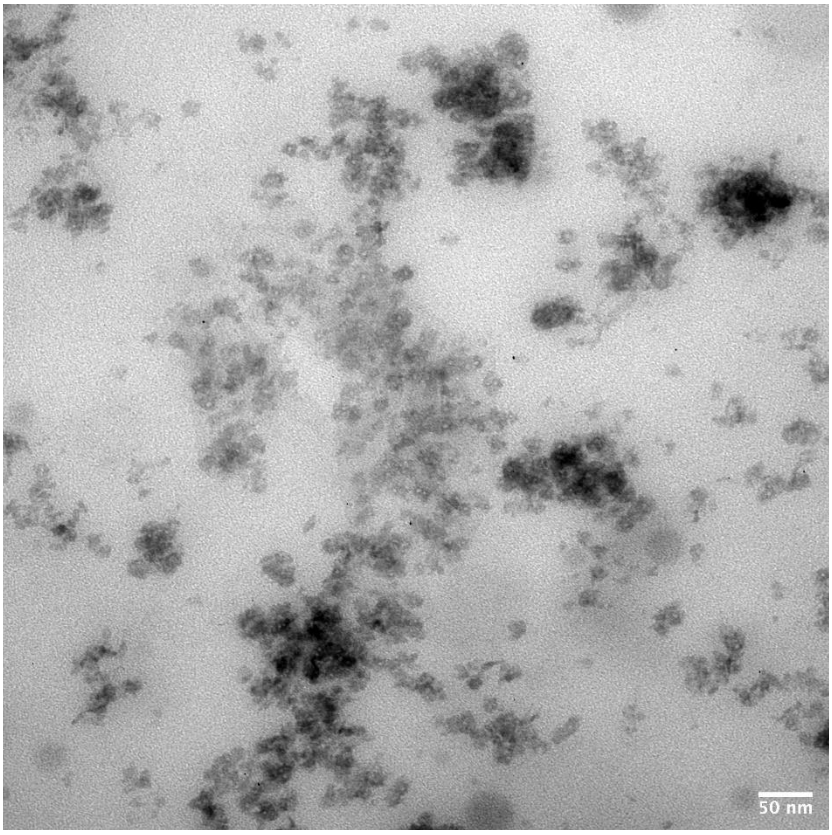

Figure A.4.2.15. TEM micrographs of gelatin-CDs films with 5% of CDs.

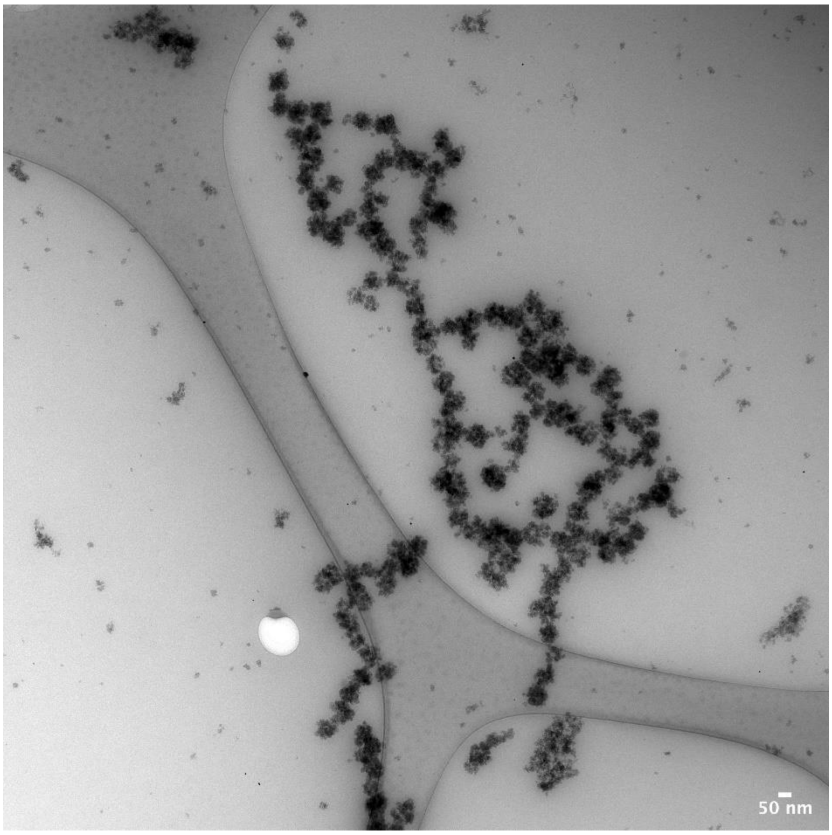

Figure A.4.2.16. TEM micrographs of gelatin-CDs films with 5% of CDs.

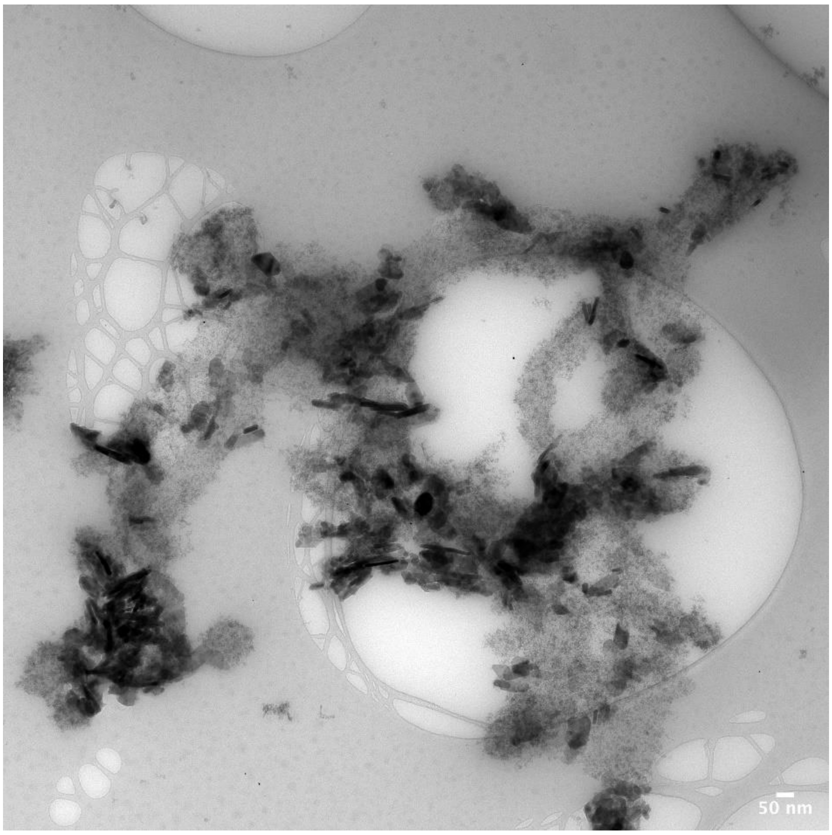

Figure A.4.2.17. TEM micrographs of gelatin-CDs films with 5% of CDs.

Scanning Electron Microscopy of Gelatin-CDs Films

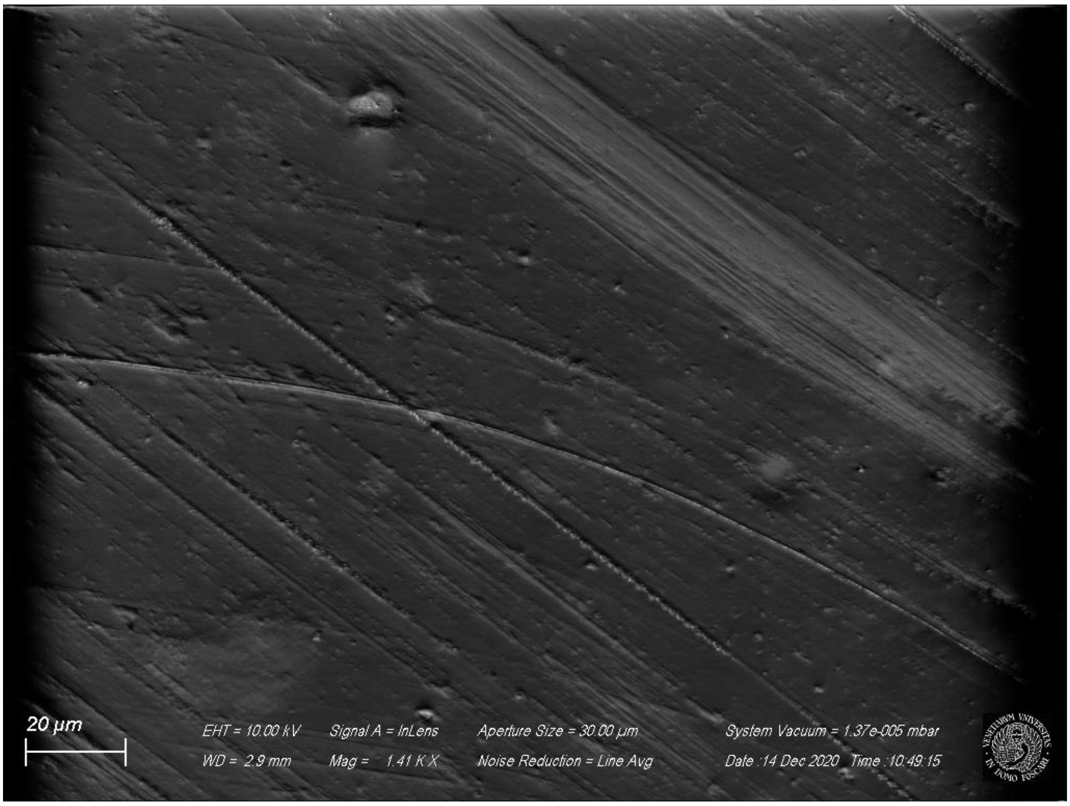

Figure A.4.2.18. SEM micrograph (X 1.41K) of the pristine fish gelatin films.

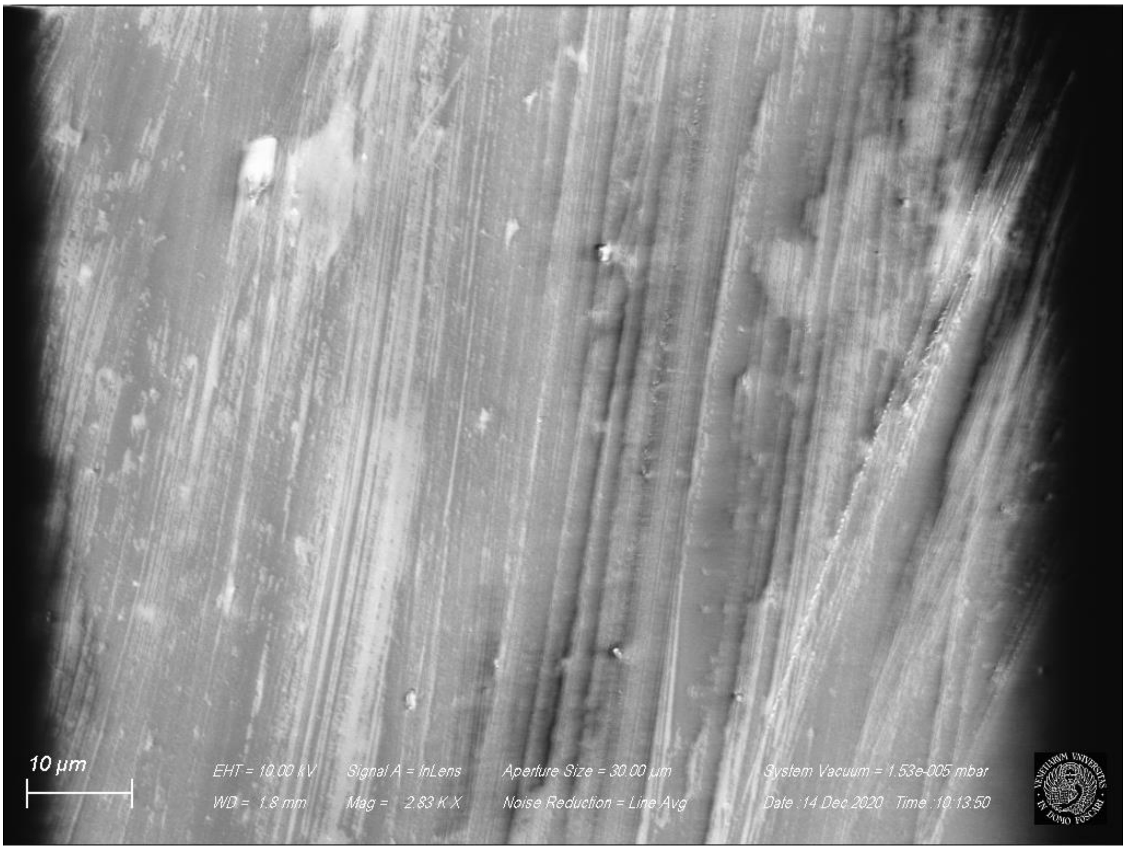

Figure A.4.2.19. SEM micrograph (X 2.83K) of the pristine fish gelatin films.

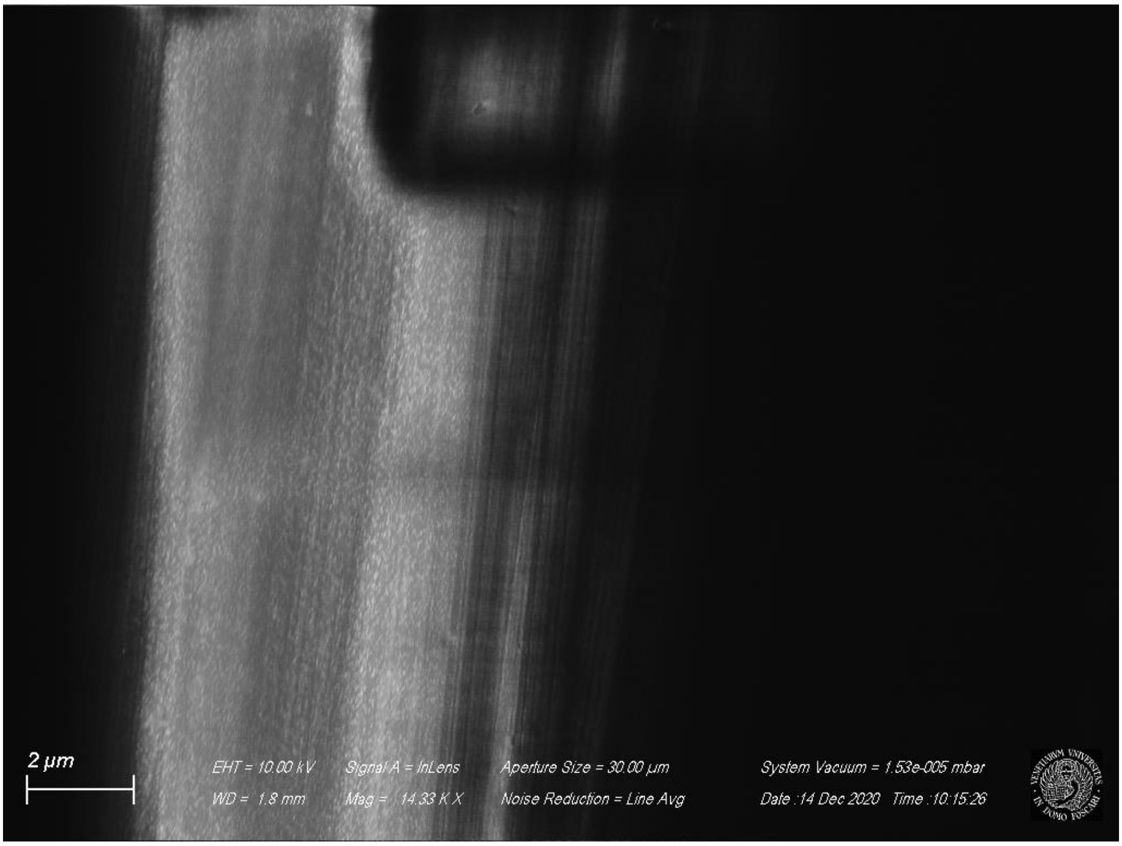

Figure A.4.2.20. SEM micrograph (X 14.33K) of the pristine fish gelatin films.

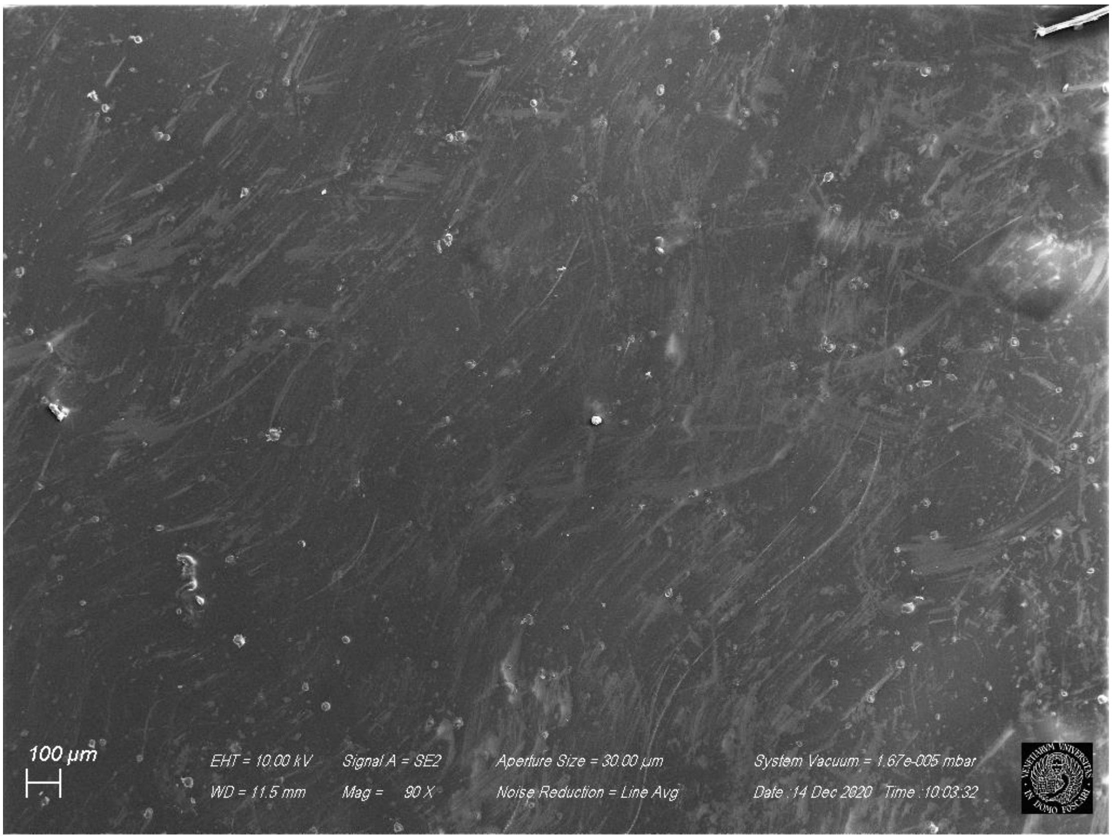

Figure A.4.2.21. SEM micrograph (X 90) of the pristine fish gelatin films.

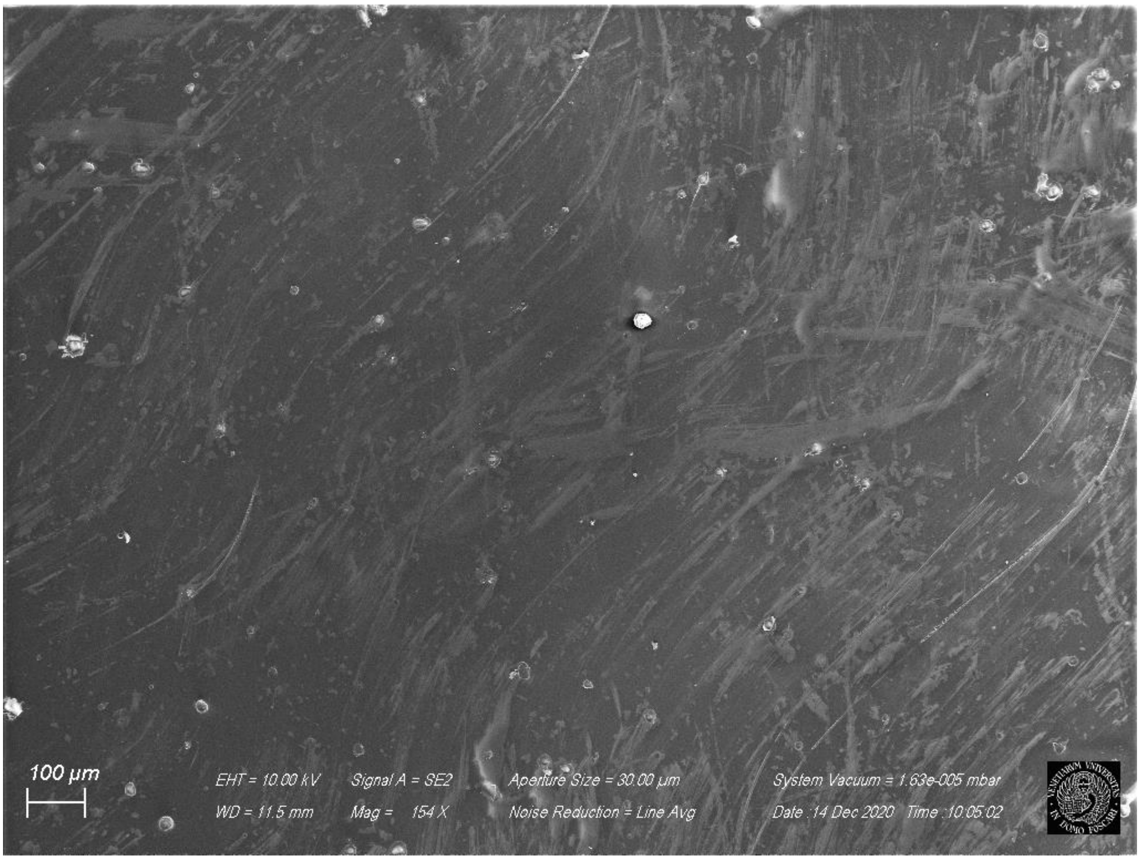

Figure A.4.2.22. SEM micrograph (X 154) of the pristine fish gelatin films.

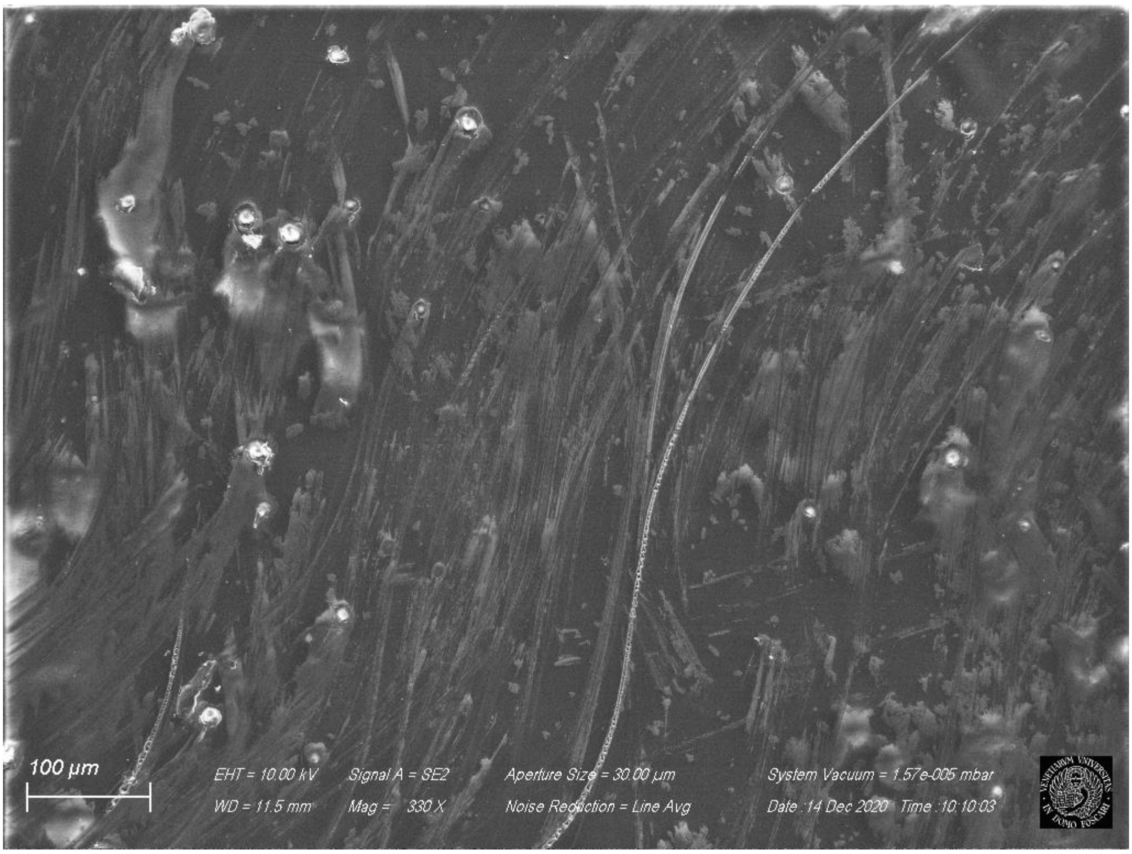

Figure A.4.2.23. SEM micrograph (X 330) of the pristine fish gelatin films.

A-4.3 Chitin Pulping using Ionic Liquids

TGA Analyses

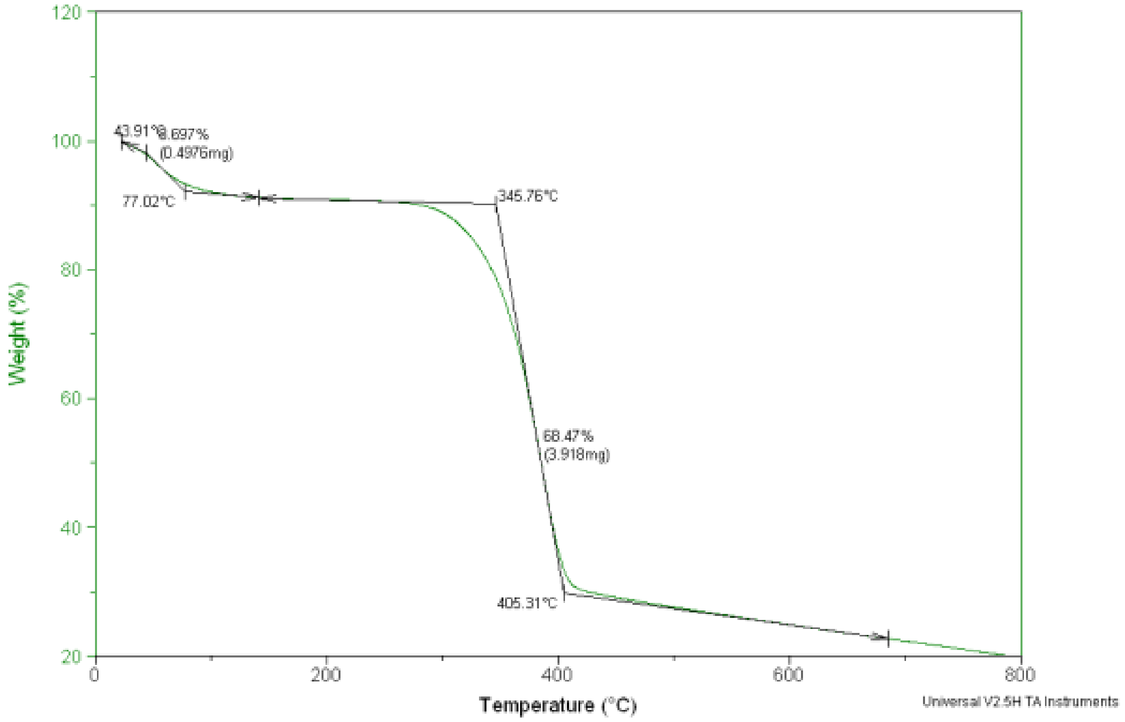

Figure A.4.3.1. TGA curve of chitin pulped with ammonium acetate solid salt (at 145 °C) in the range 25°C-800°C in nitrogen atmosphere.

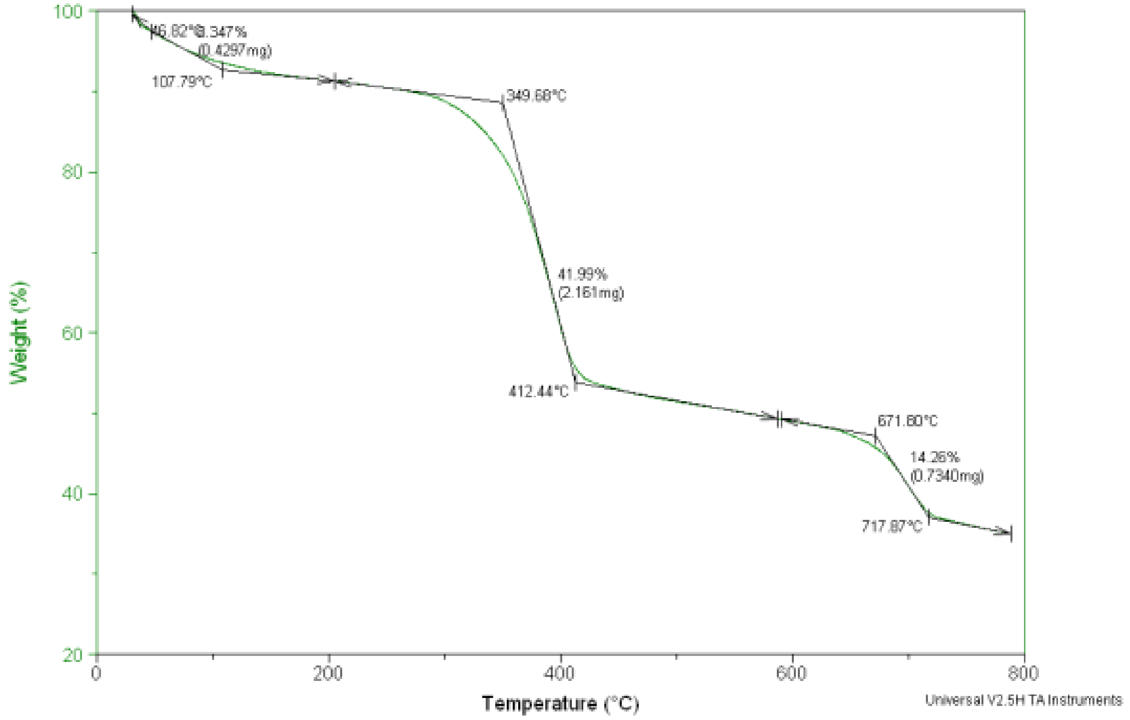

Figure A.4.3.2. TGA curve of chitin pulped with ammonium acetate prepared in situ in batch condition (at 100 °C) by sequential addition of acid prior to base in the range 25°C-800°C in nitrogen atmosphere.

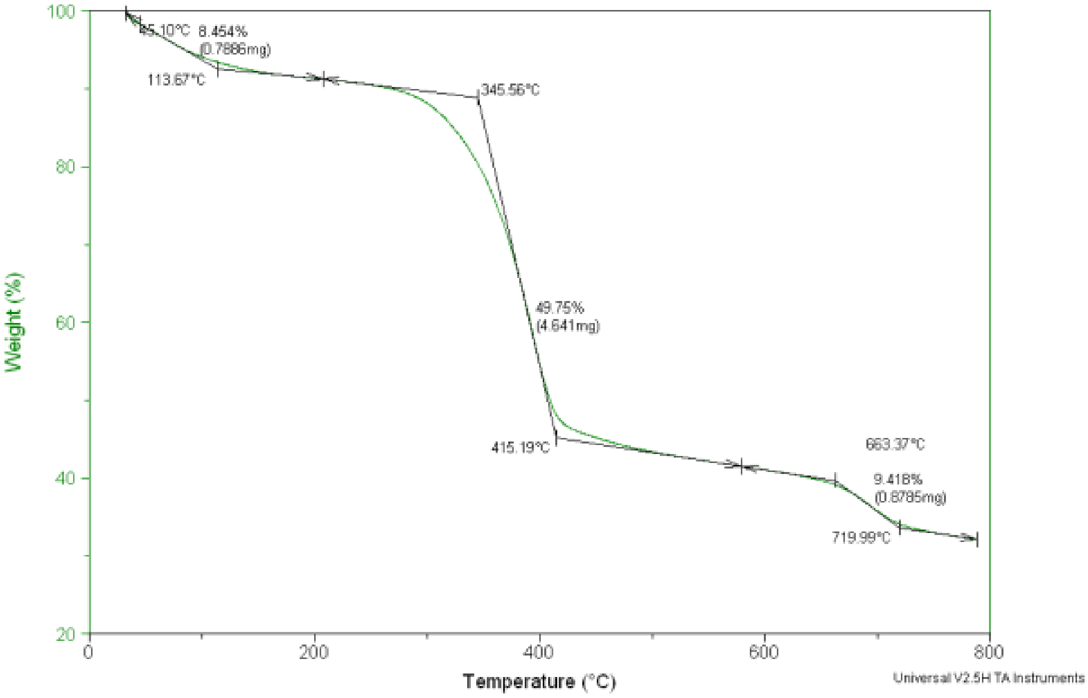

Figure A.4.3.3. TGA curve of chitin pulped with ammonium acetate prepared in situ in batch condition (at 100 °C) by sequential addition of base prior to acid in the range 25°C-800°C in nitrogen atmosphere.

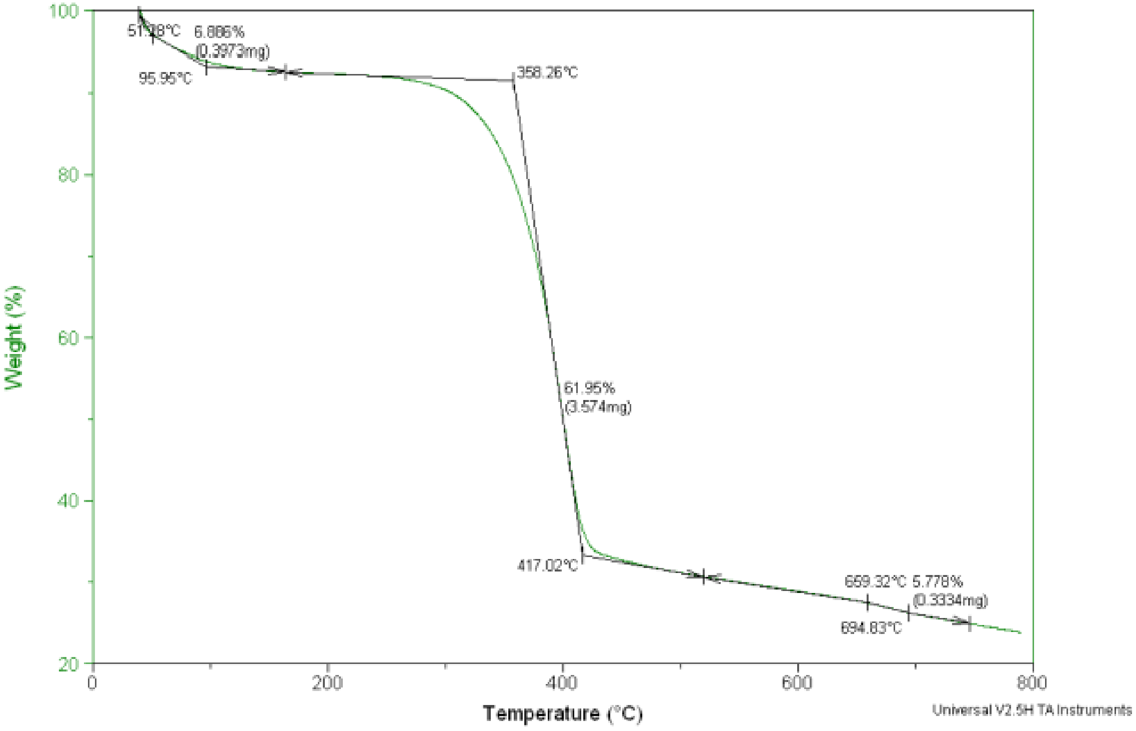

Figure A.4.3.4. TGA curve of chitin pulped with ammonium formate solid salt (at 130 °C) in the range 25°C-800°C in nitrogen atmosphere.

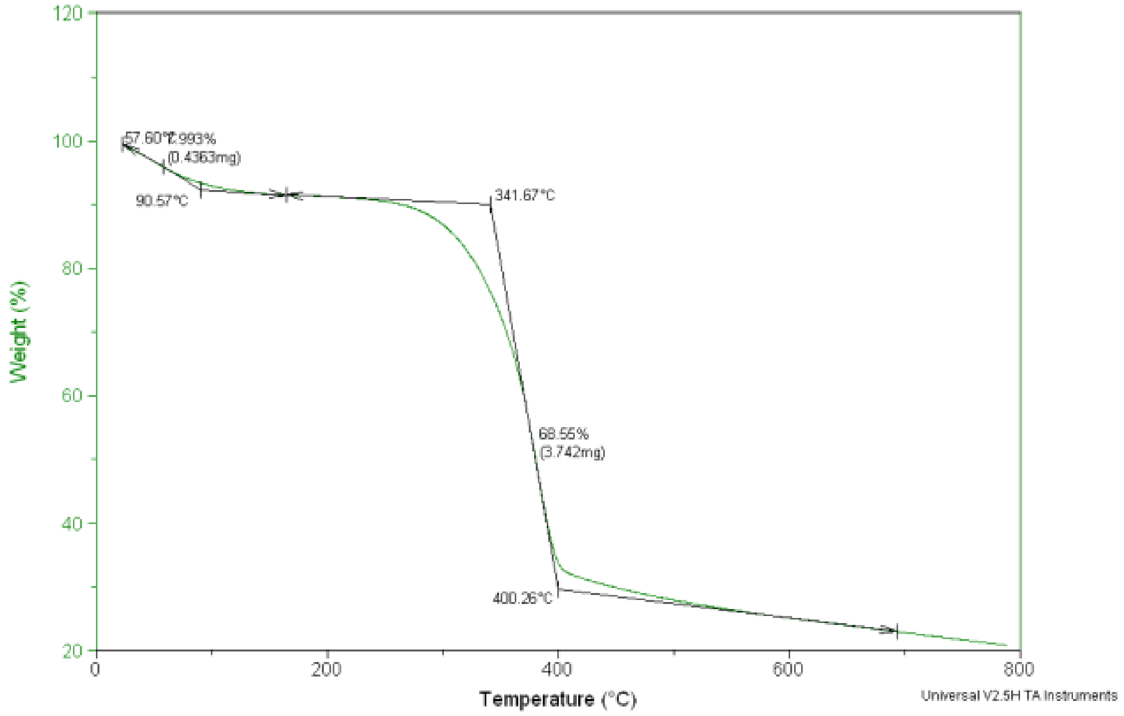

Figure A.4.3.5. TGA curve of chitin pulped with ammonium formate prepared in situ in batch condition (at 100 °C) by sequential addition of acid prior to base in the range 25°C-800°C in nitrogen atmosphere.

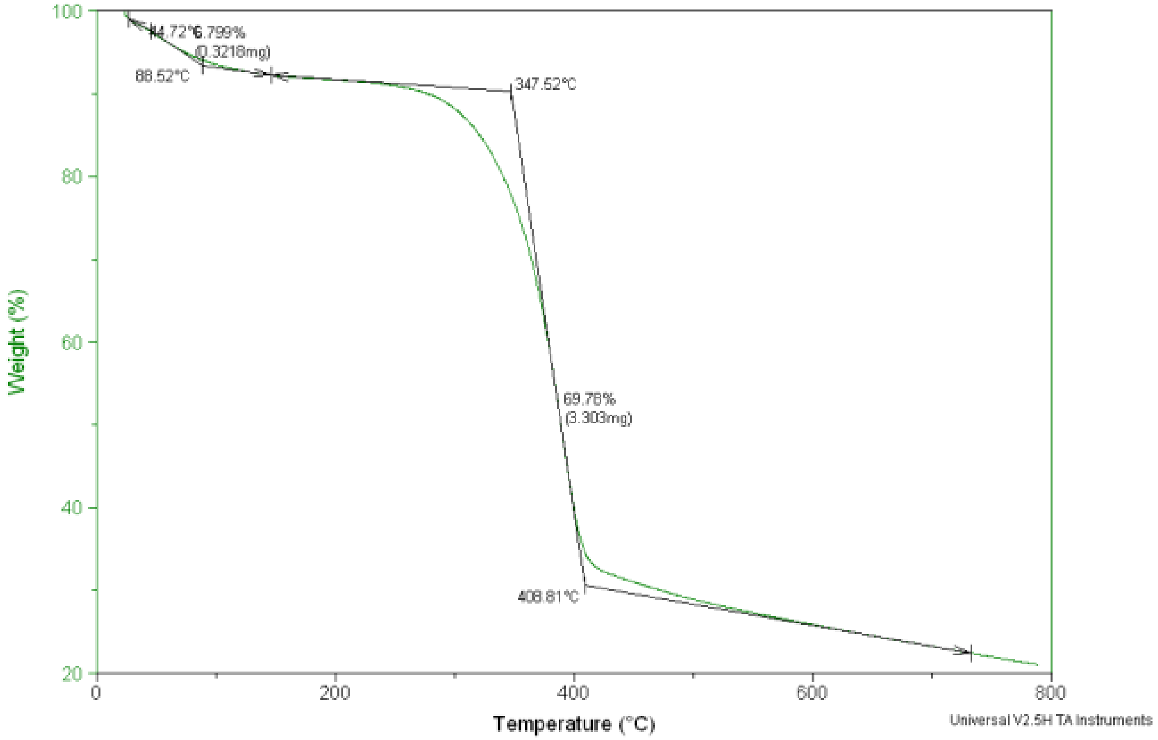

Figure A.4.3.6. TGA curve of chitin pulped with ammonium formate prepared in situ in batch condition (at 100 °C) by sequential addition of base prior to acid in the range 25°C-800°C in nitrogen atmosphere.

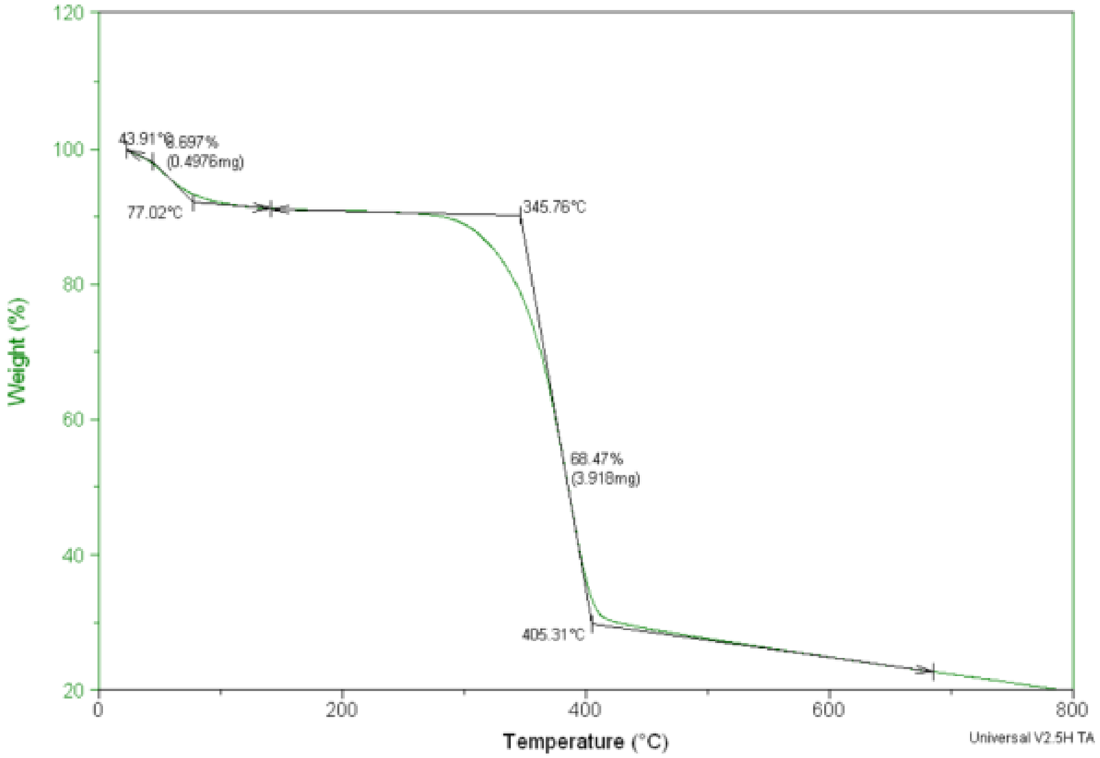

Figure A.4.3.7. TGA curve of chitin pulped with hydroxylammonium acetate solid salt (at 100 °C) in the range 25°C-800°C in nitrogen atmosphere.

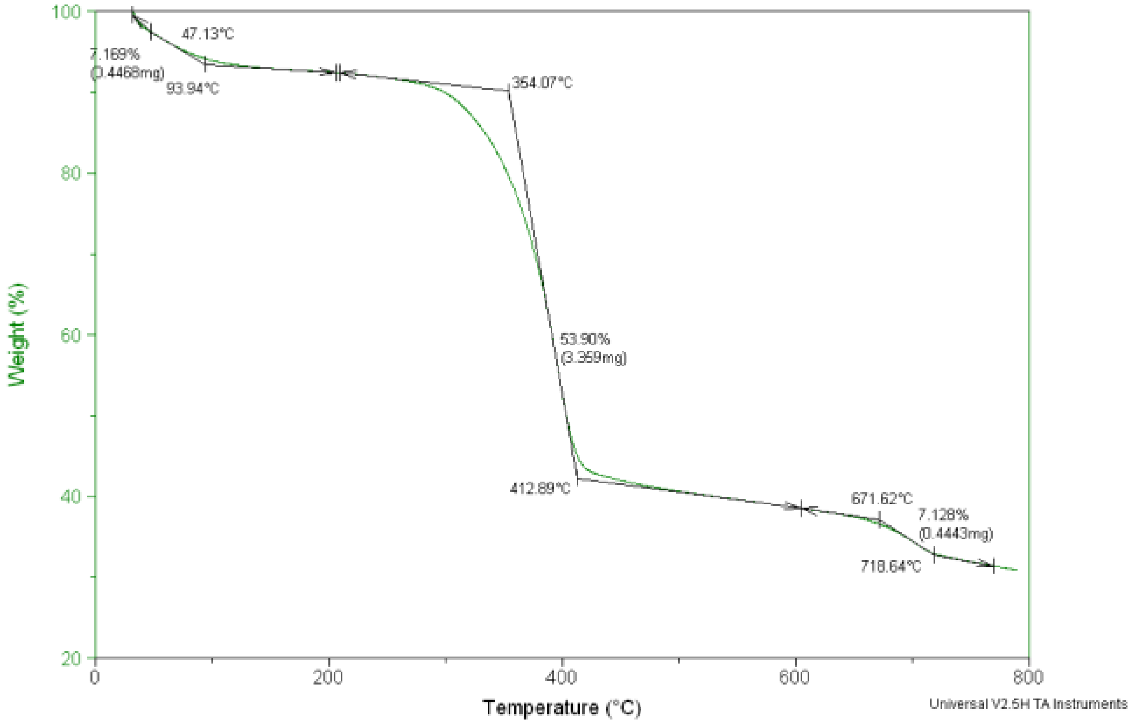

Figure A.4.3.8. TGA curve of chitin pulped with hydroxylammonium acetate prepared in situ (at 100 °C) by sequential addition of acid prior to base in the range 25°C-800°C in nitrogen atmosphere.

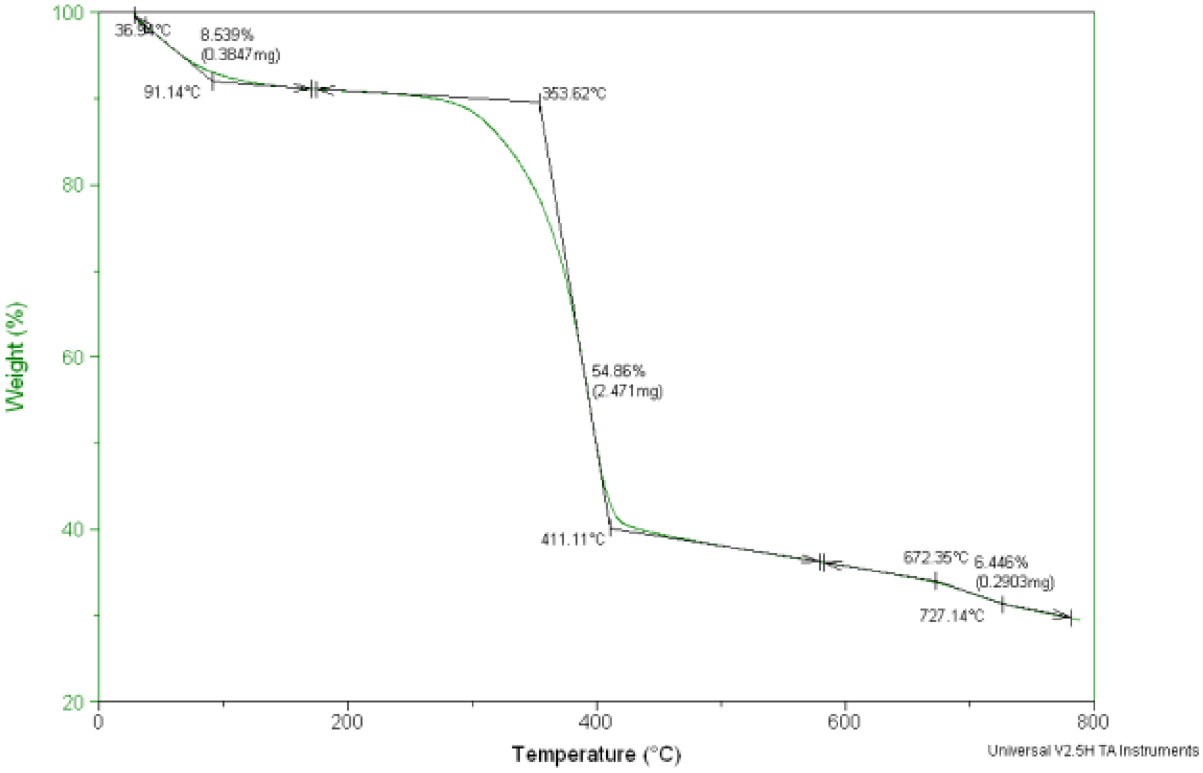

Figure A.4.3.9 TGA curve of chitin pulped with hydroxylammonium acetate prepared in situ (at 100 °C) by sequential addition of base prior to acid in the range 25°C-800°C in nitrogen atmosphere.

NMR Spectra

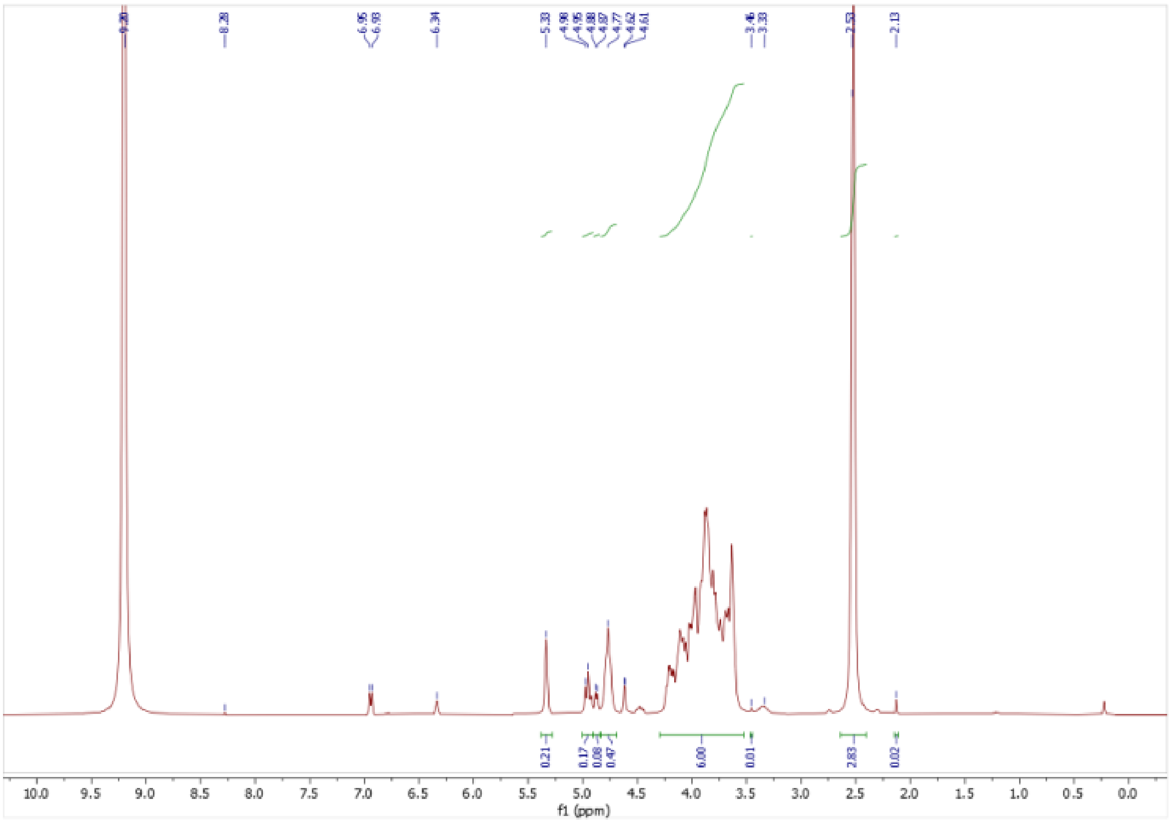

Figure A.4.3.10. ^{1}H-NMR spectrum of commercial chitin in DCl 35% in D_2O.

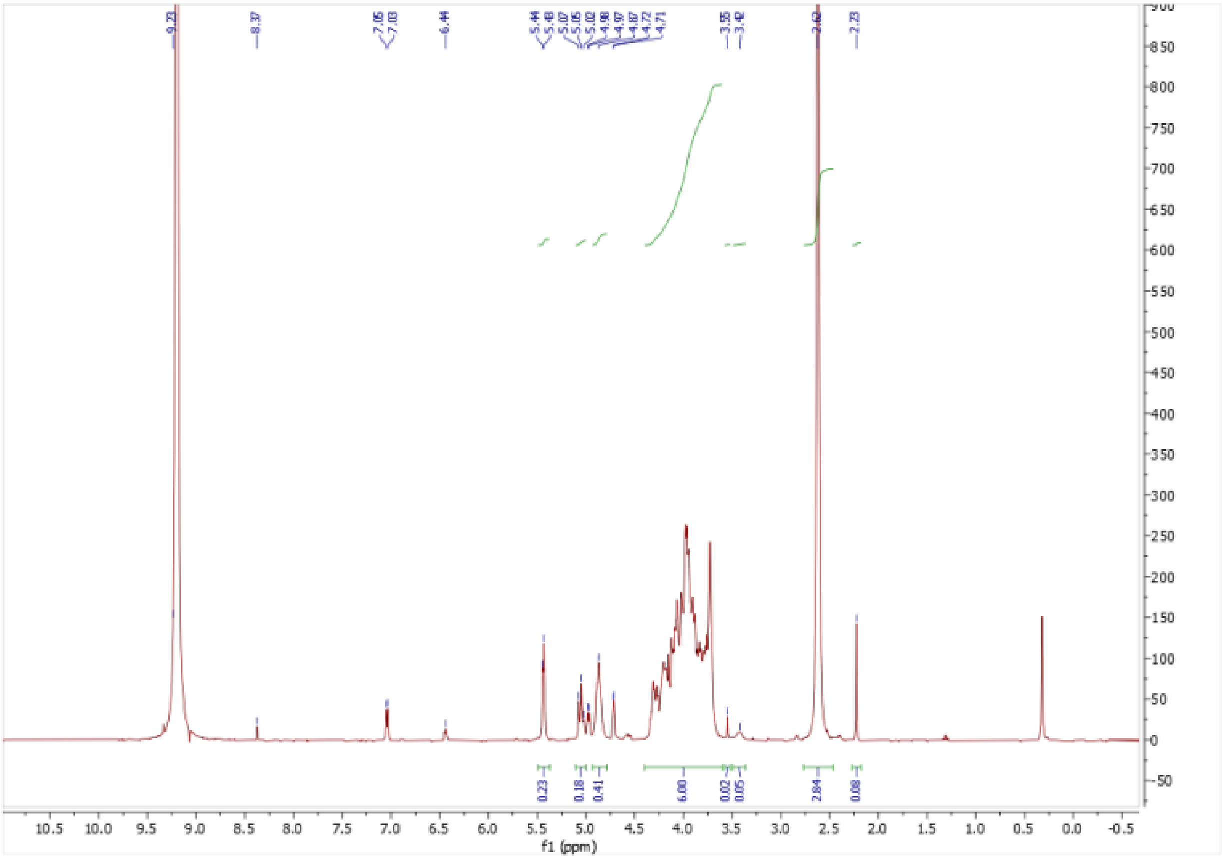

Figure A.4.3.11. ^{1}H-NMR spectrum of chitin extracted with chemical method in DCl 35% in D_2O.

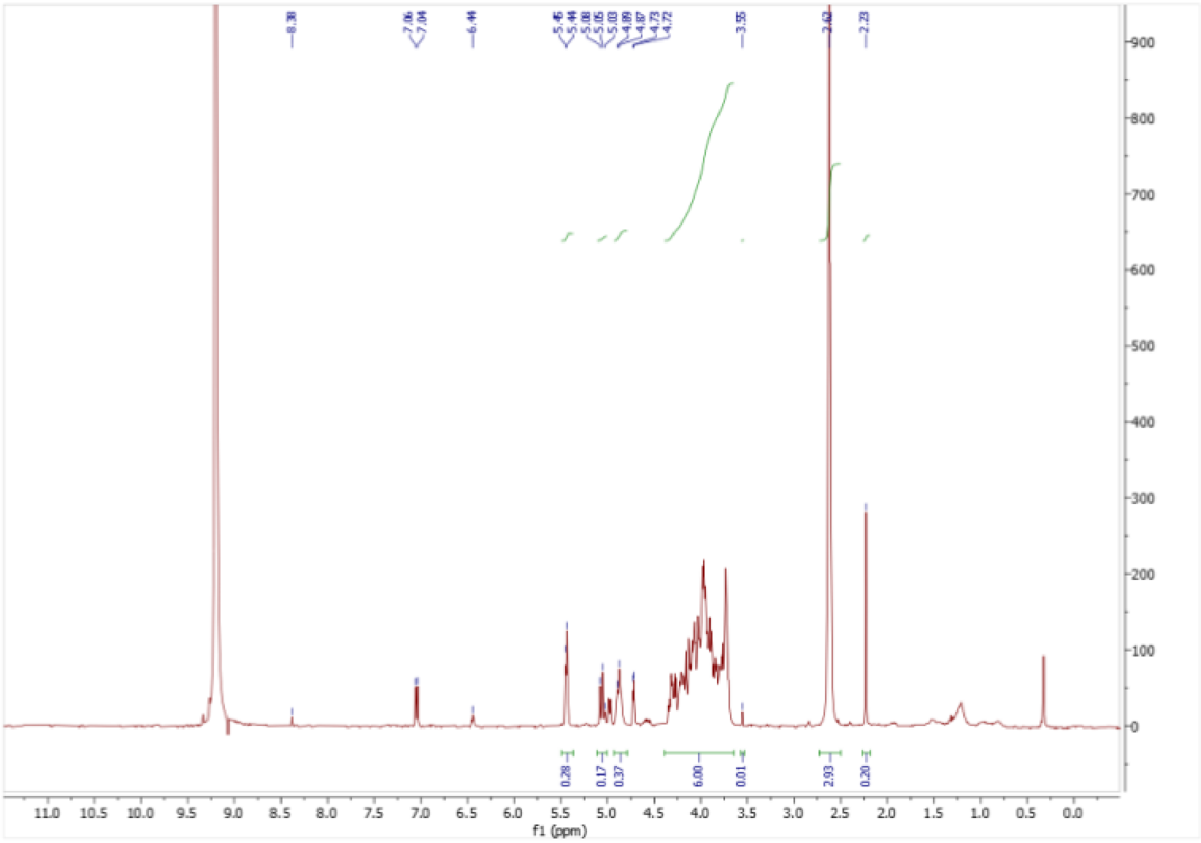

Figure A.4.3.12. ^{1}H-NMR spectrum of chitin pulped with ammonium acetate solid salt in DCl 35% in D_2O.

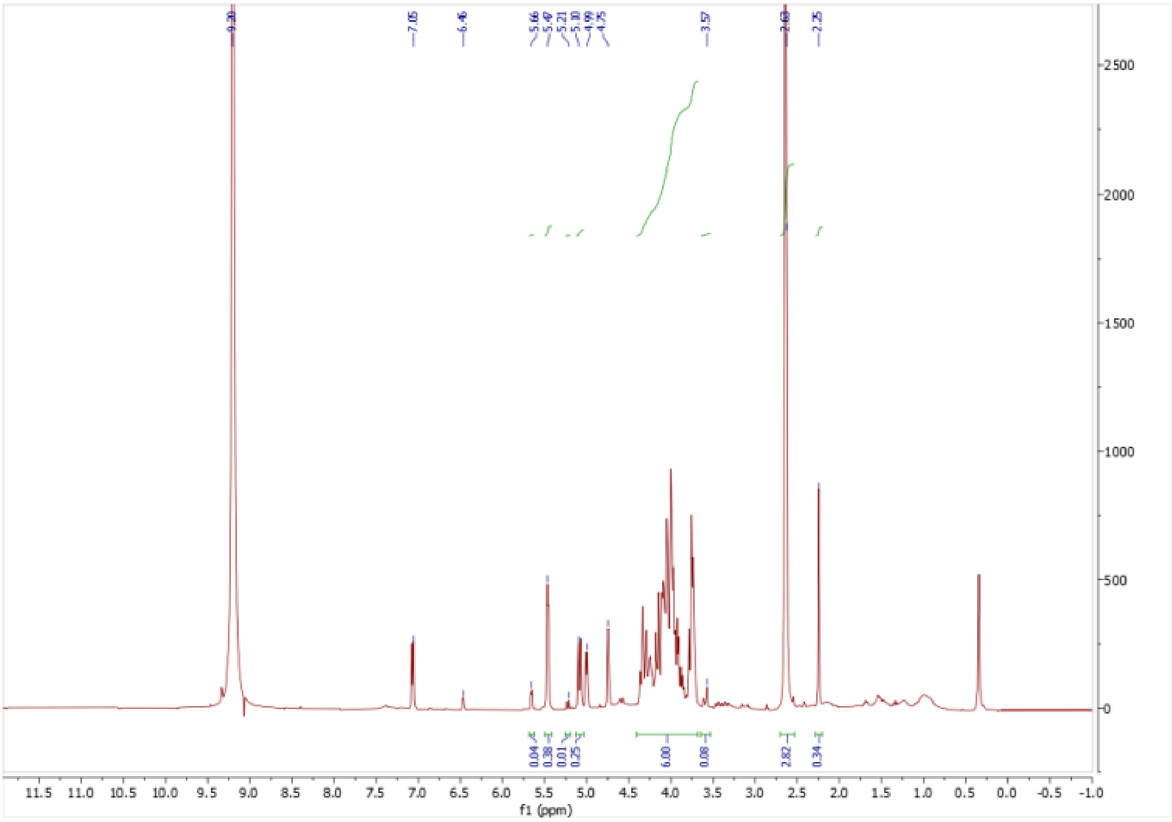

Figure A.4.3.13. ^{1}H-NMR spectrum of chitin pulped with ammonium acetate prepared in situ in batch conditions (100°C) by sequential addition of acid prior to base in DCl 35% in D_2O.

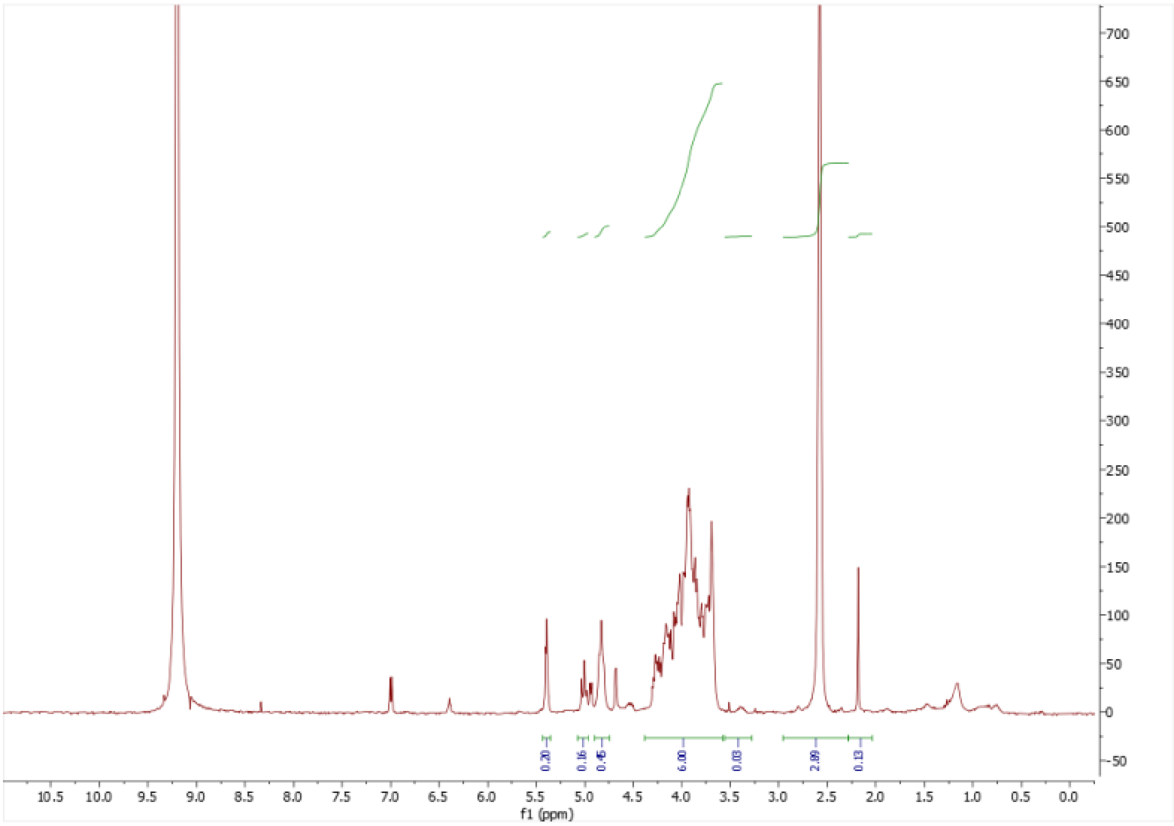

Figure A.4.3.14. ^{1}H-NMR spectrum of chitin pulped with ammonium acetate prepared in situ in autoclave (145 °C) by sequential addition of acid prior to base in DCl 35% in D_2O.

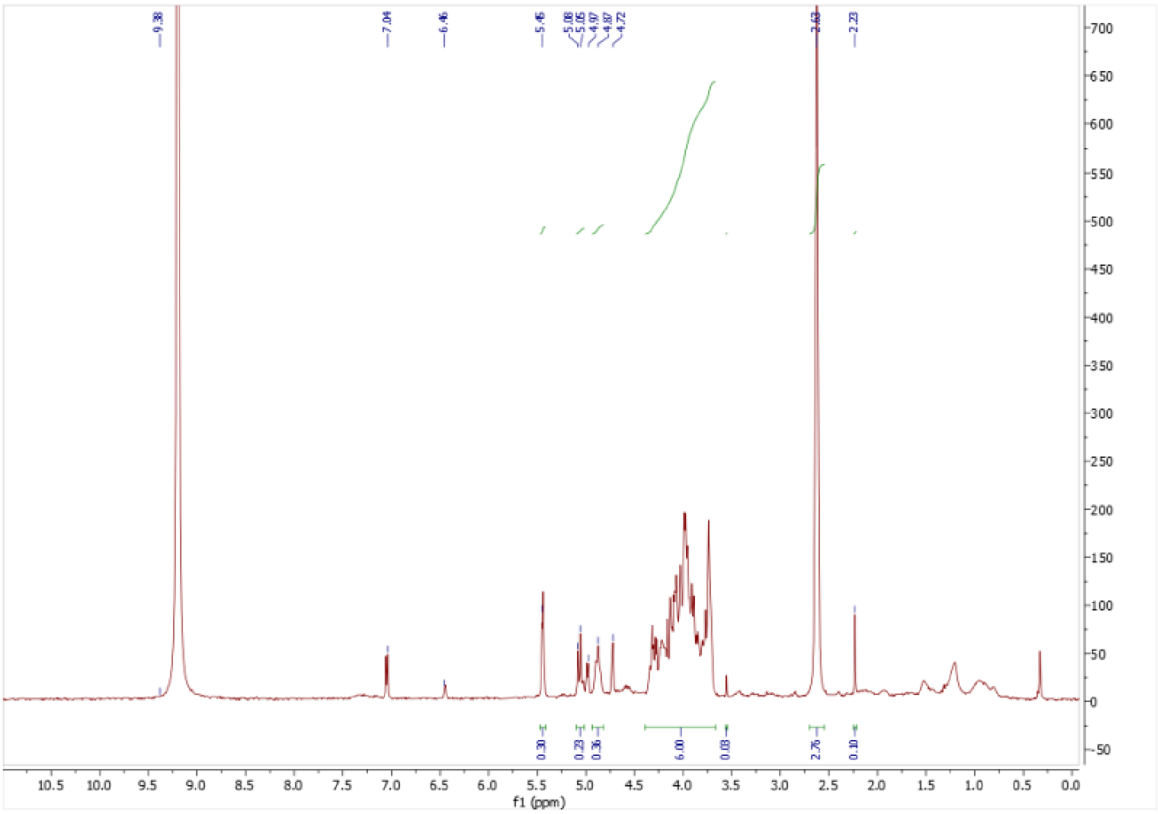

Figure A.4.3.15. ^{1}H-NMR spectrum of chitin pulped with ammonium acetate prepared in situ in batch conditions (100°C) by sequential addition of base prior to acid in DCl 35% in D_2O.

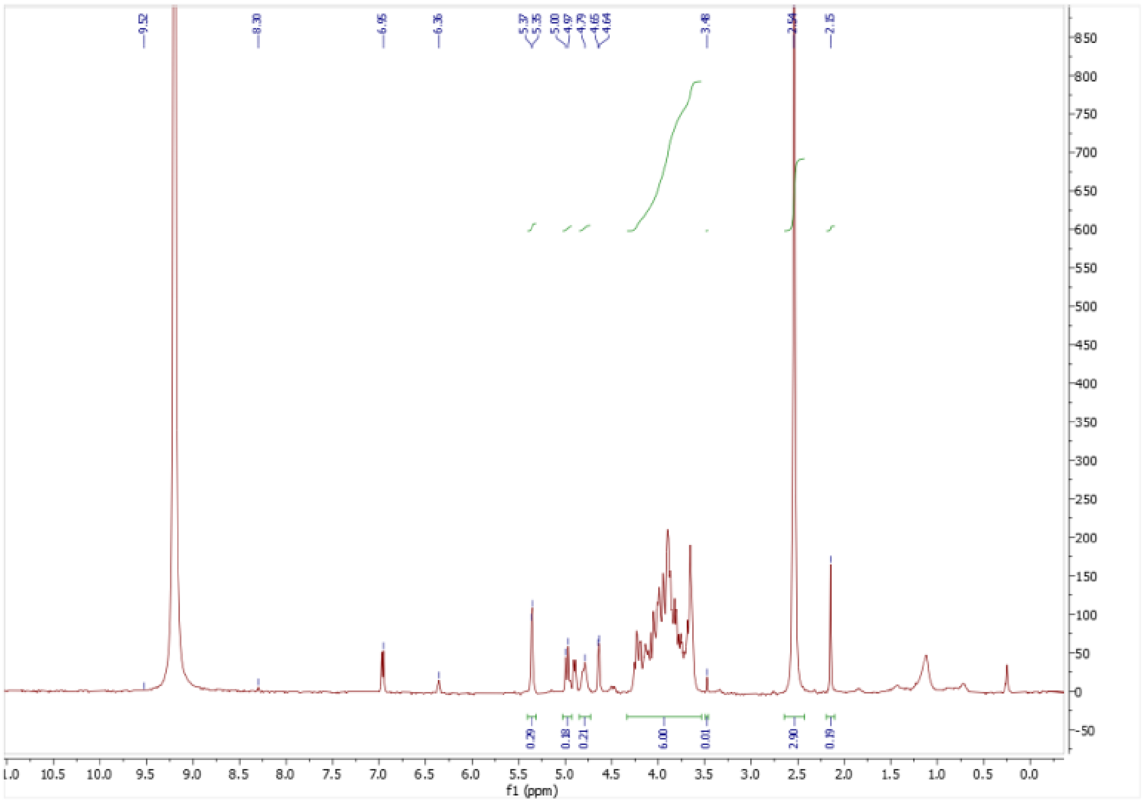

Figure A.4.3.16. ^{1}H-NMR spectrum of chitin pulped with ammonium acetate prepared in situ in autoclave (145 °C) by sequential addition of base prior to acid in DCl 35% in D_2O.

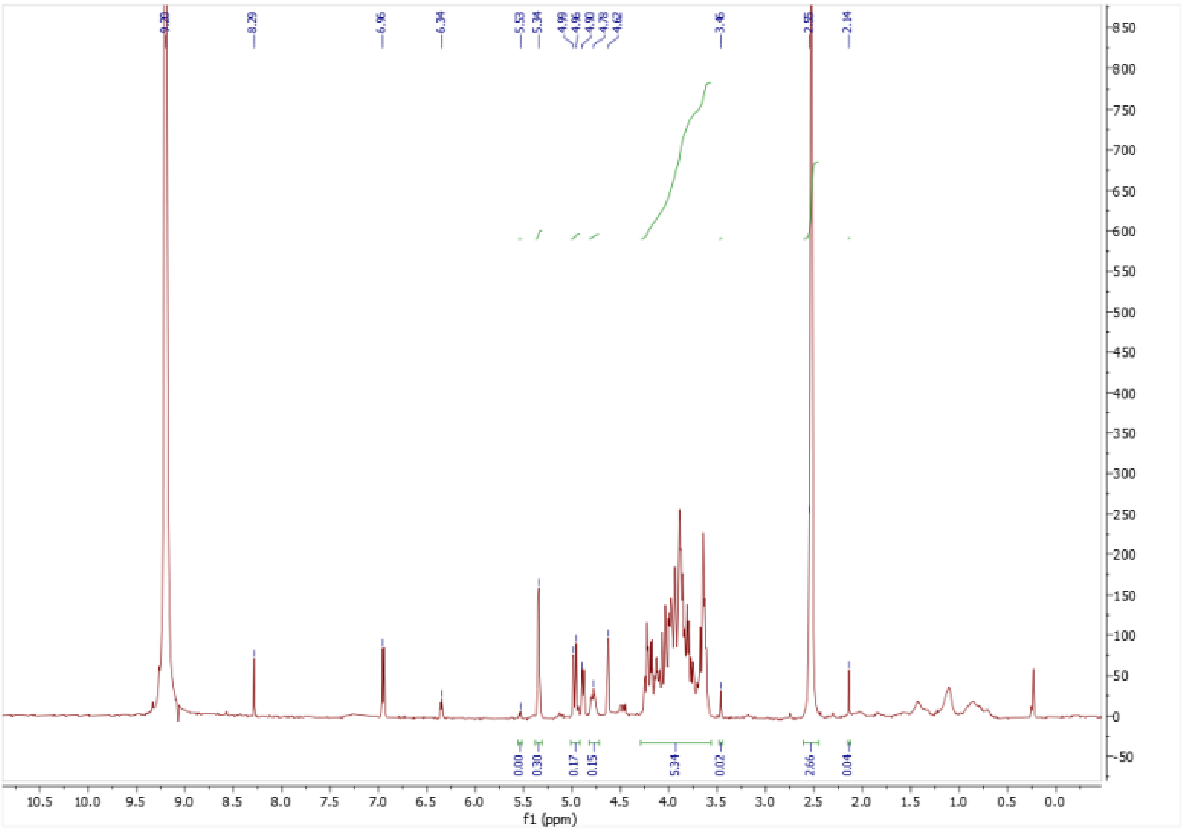

Figure A.4.3.17. ^{1}H-NMR spectrum of chitin pulped with ammonium formate solid salt in DCl 35% in D_2O.

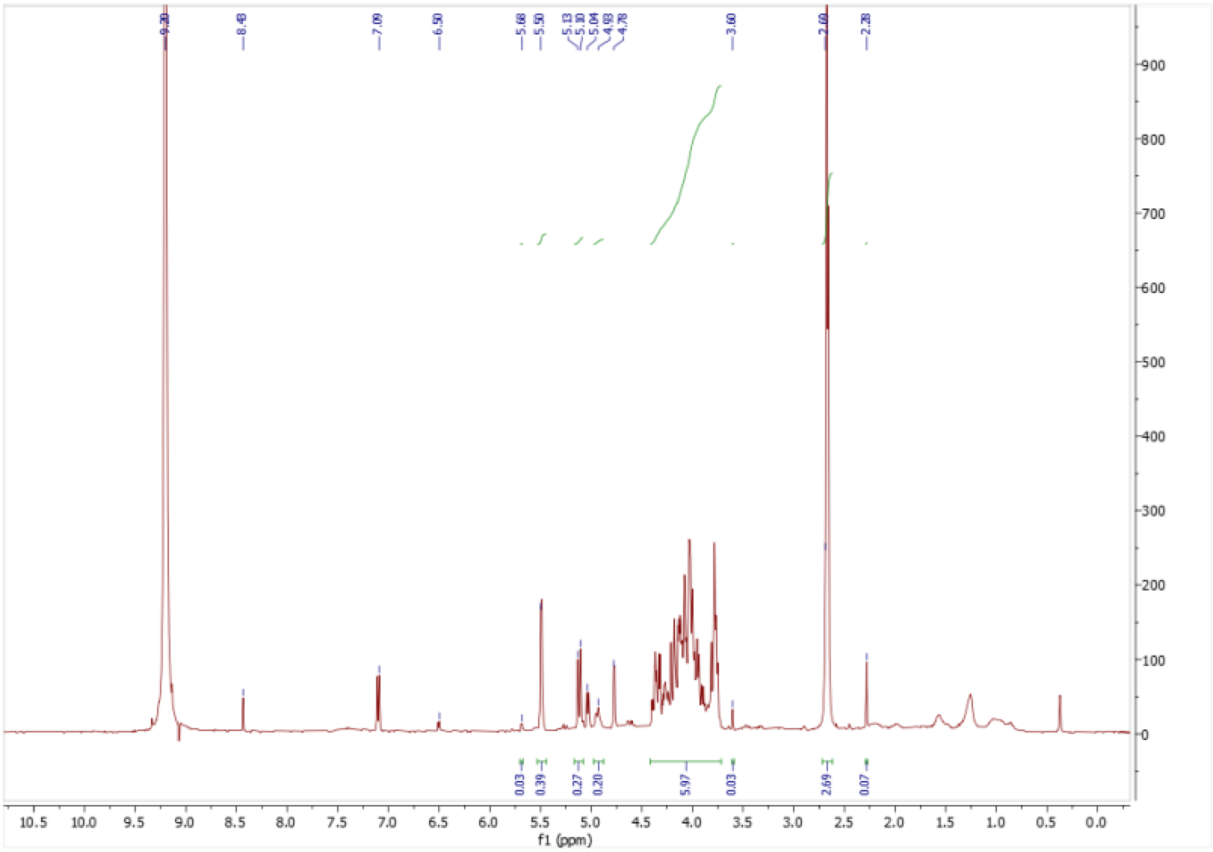

Figure A.4.3.18. ^{1}H-NMR spectrum of chitin pulped with ammonium formate prepared in situ in batch conditions (100°C) by sequential addition of acid prior to base in DCl 35% in D_2O.

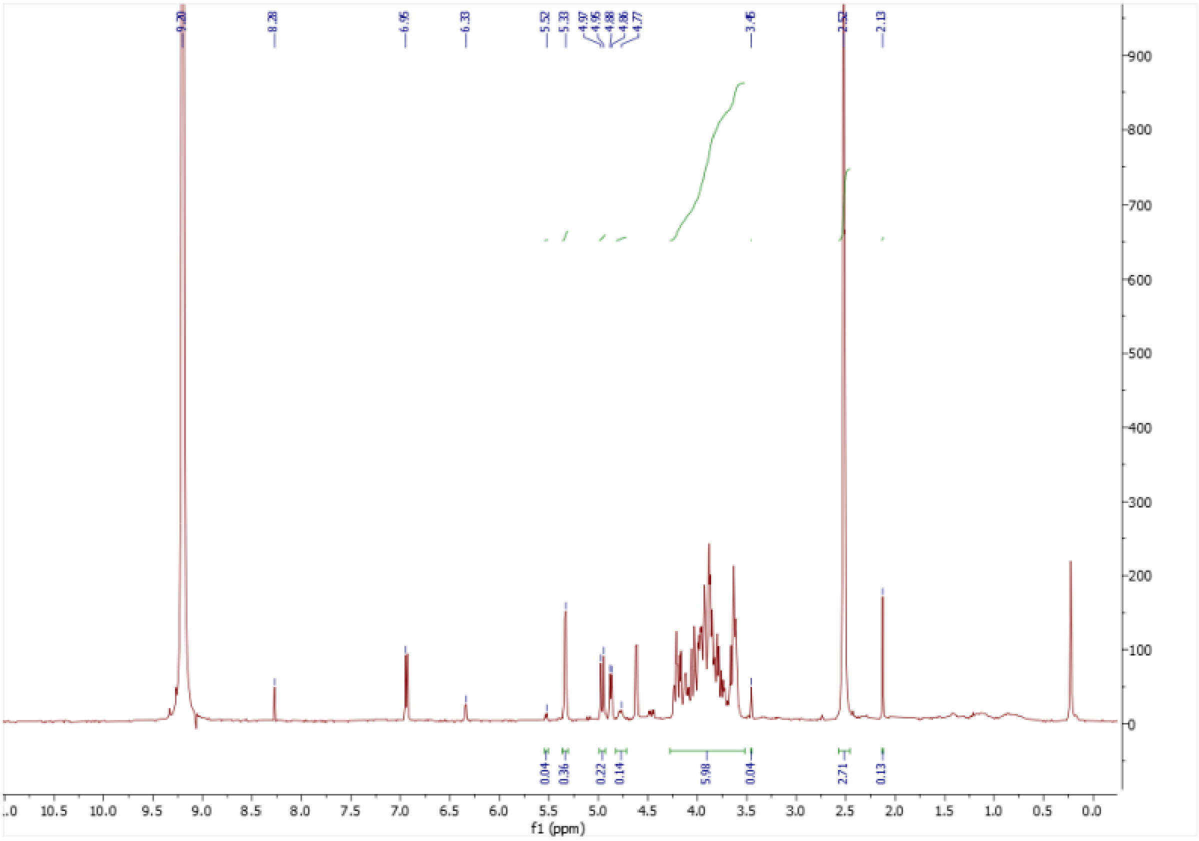

Figure A.4.3.19. ^{1}H-NMR spectrum of chitin pulped with ammonium formate prepared in situ in autoclave (130 °C) by sequential addition of acid prior to base in DCl 35% in D_2O.

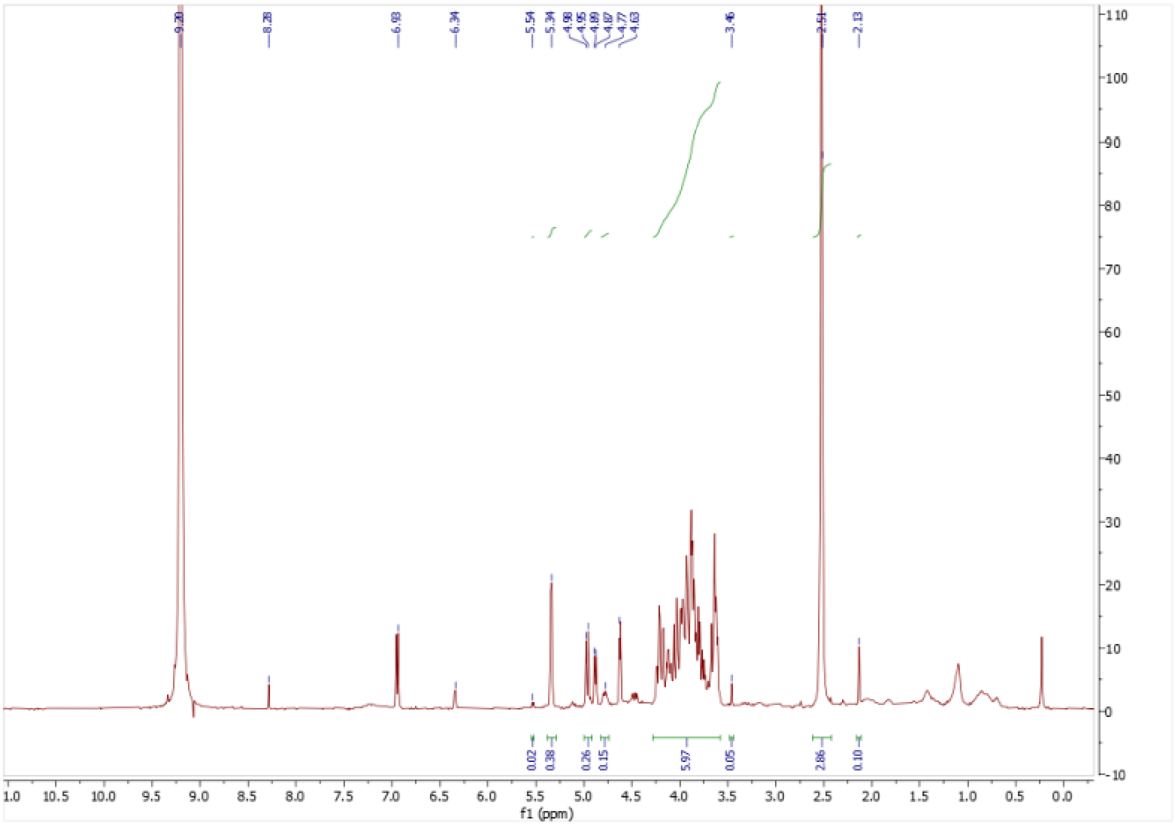

Figure A.4.3.20. ^{1}H-NMR spectrum of chitin pulped with ammonium formate prepared in situ in batch conditions (100°C) by sequential addition of base prior to acid in DCl 35% in D_2O.

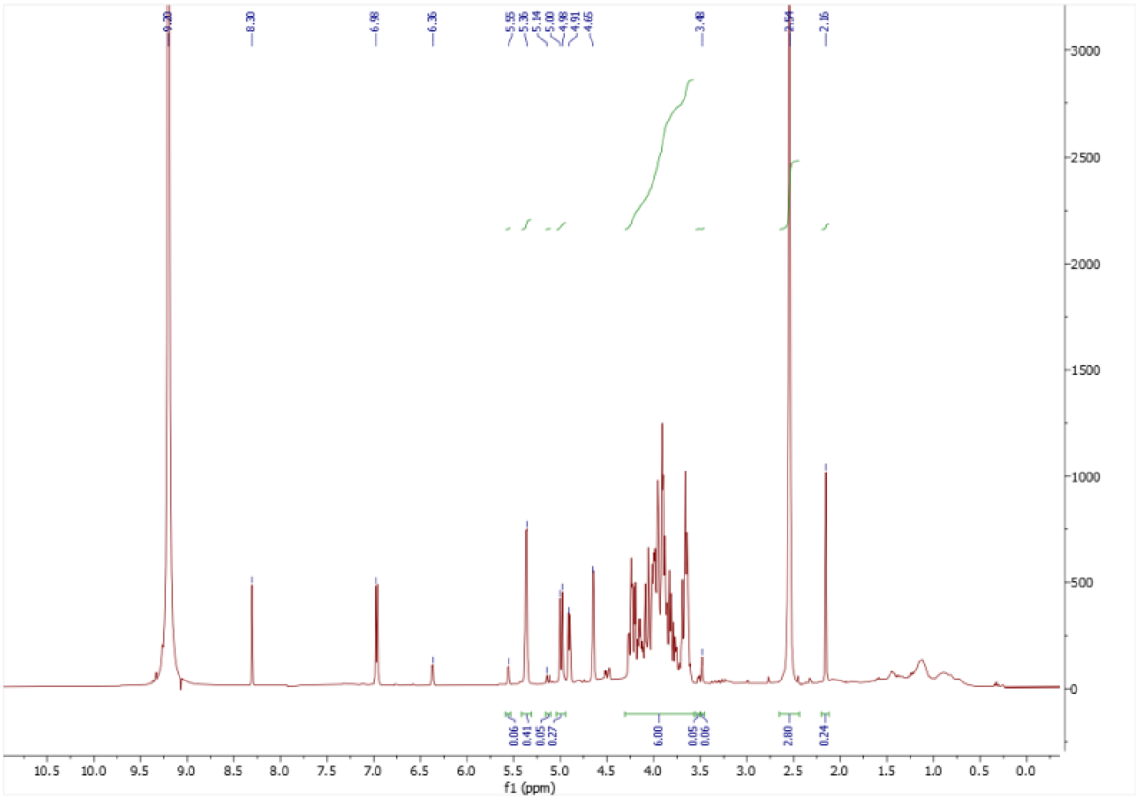

Figure A.4.3.21. ^{1}H-NMR spectrum of chitin pulped with ammonium formate prepared in situ in autoclave (130 °C) by sequential addition of base prior to acid in DCl 35% in D_2O.

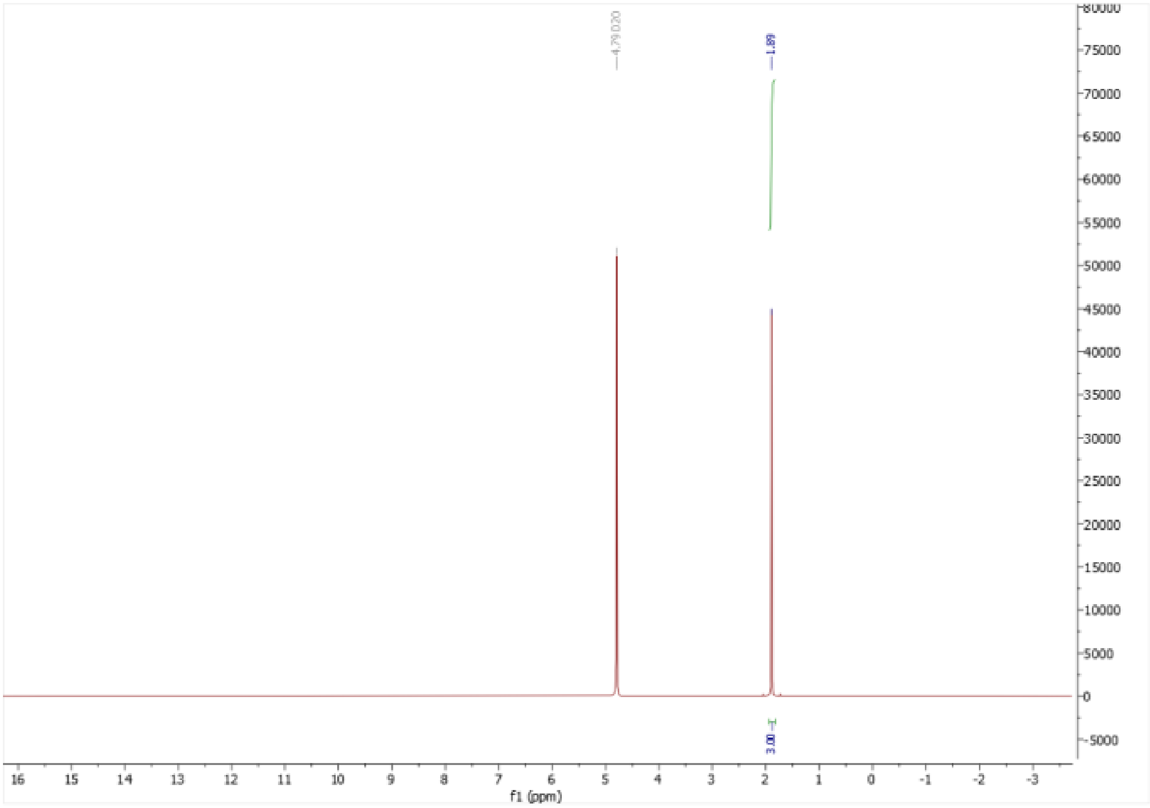

Figure A.4.3.22. ^{1}H-NMR spectrum of hydroxylammonium acetate in D_2O.

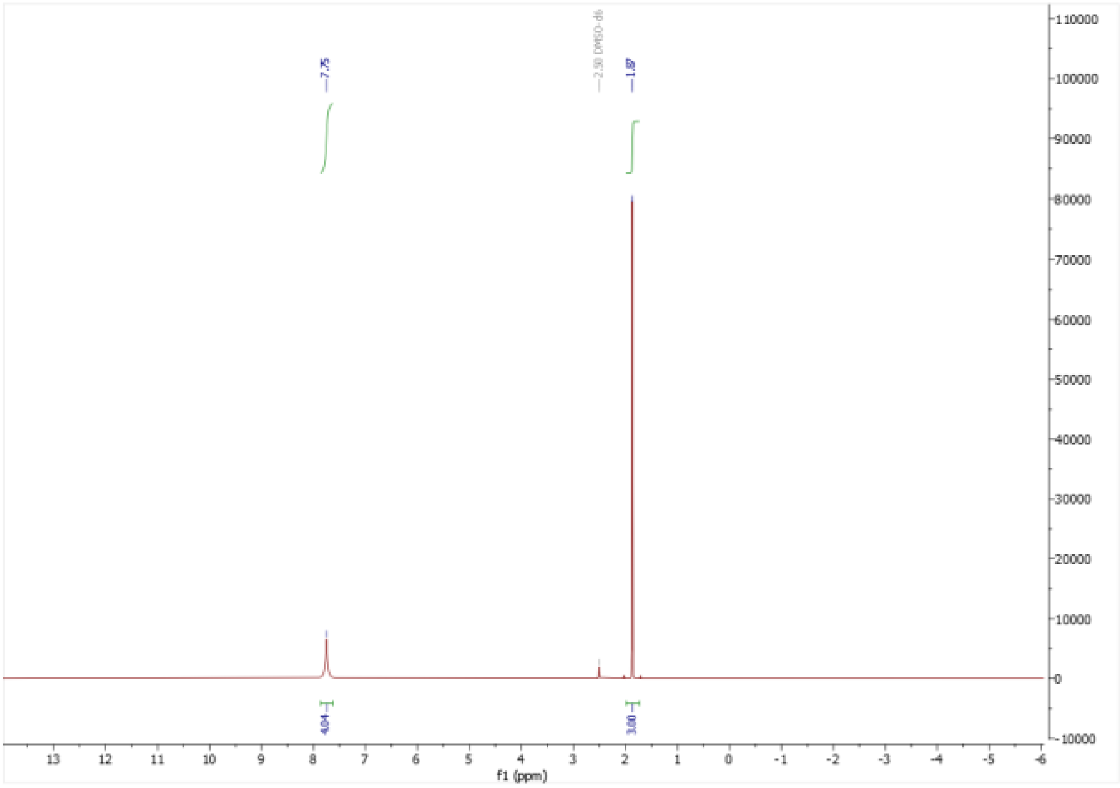

Figure A.4.3.23. ^{1}H-NMR spectrum of hydroxylammonium acetate in DMSO-d_6.

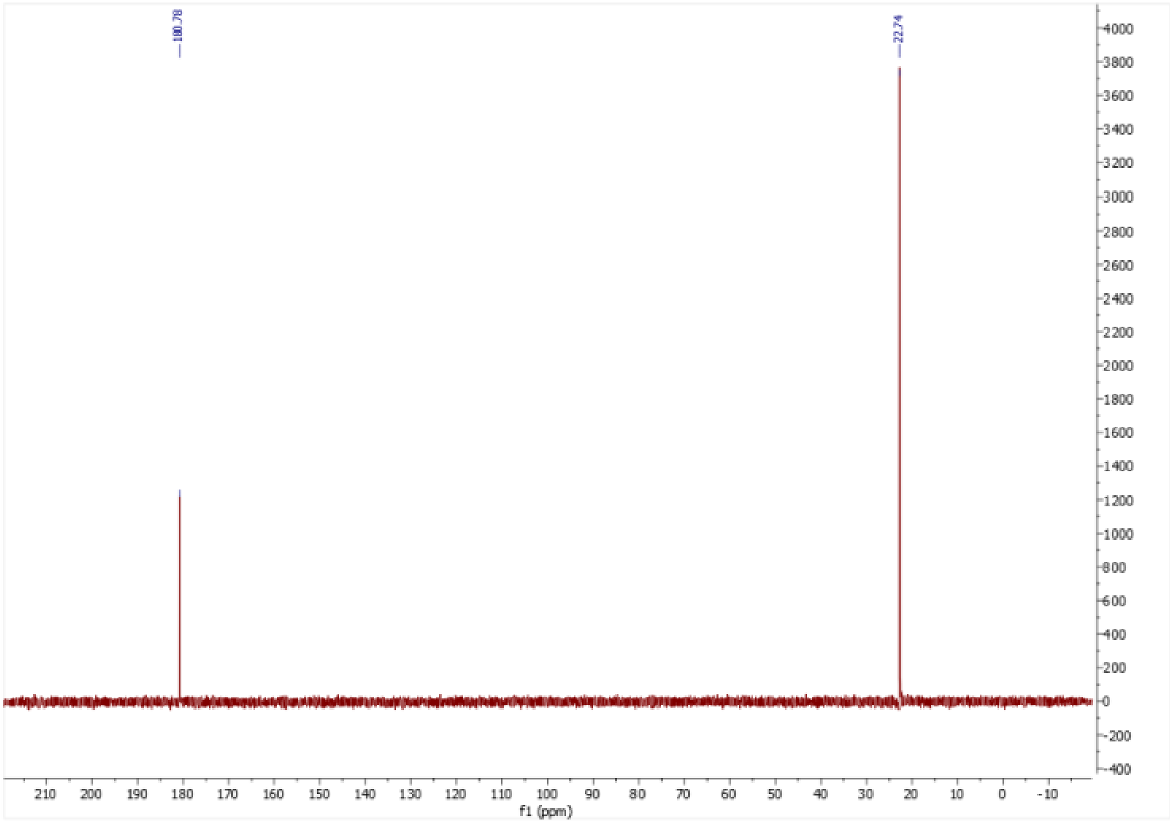

Figure A.4.3.24. ^{13}C-NMR spectrum of hydroxylammonium acetate in D_2O.

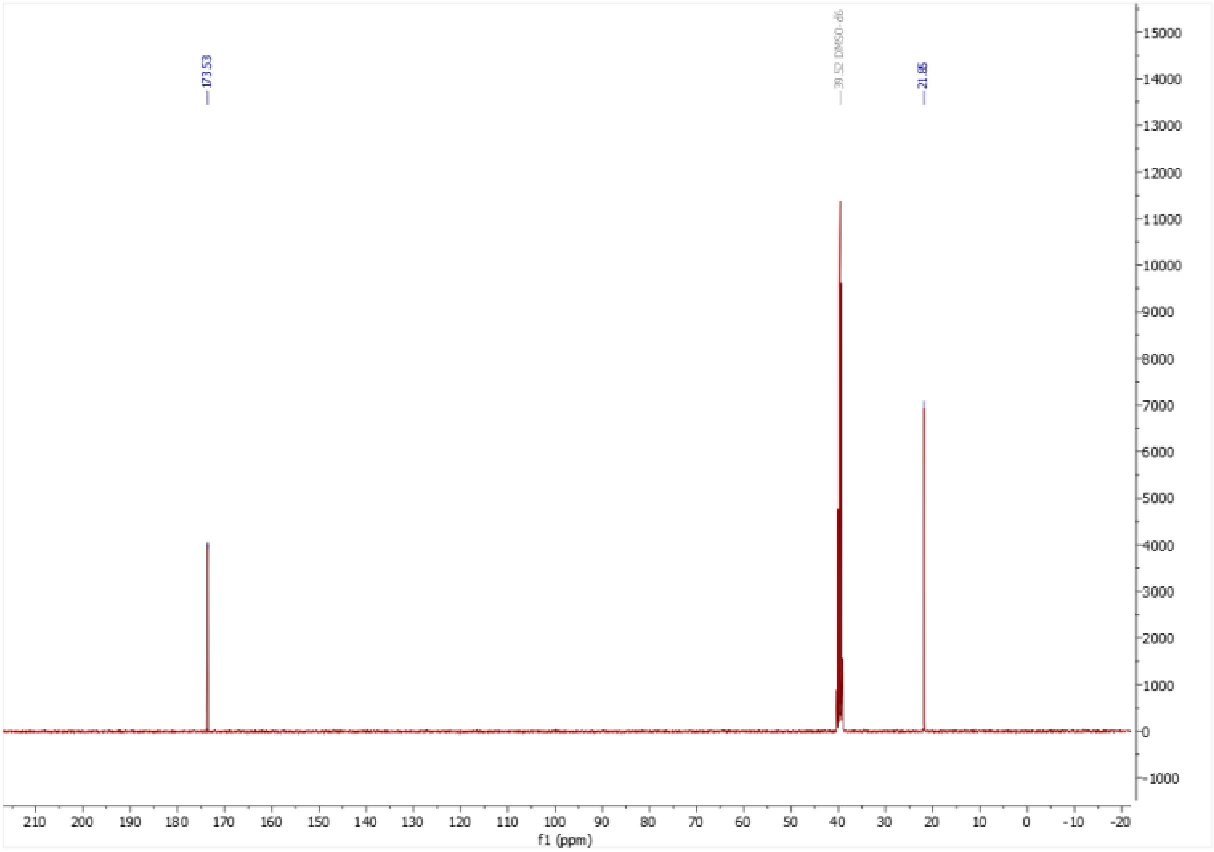

Figure A.4.3.25. ^{13}C-NMR spectrum of hydroxylammonium acetate in DMSO-d_6.

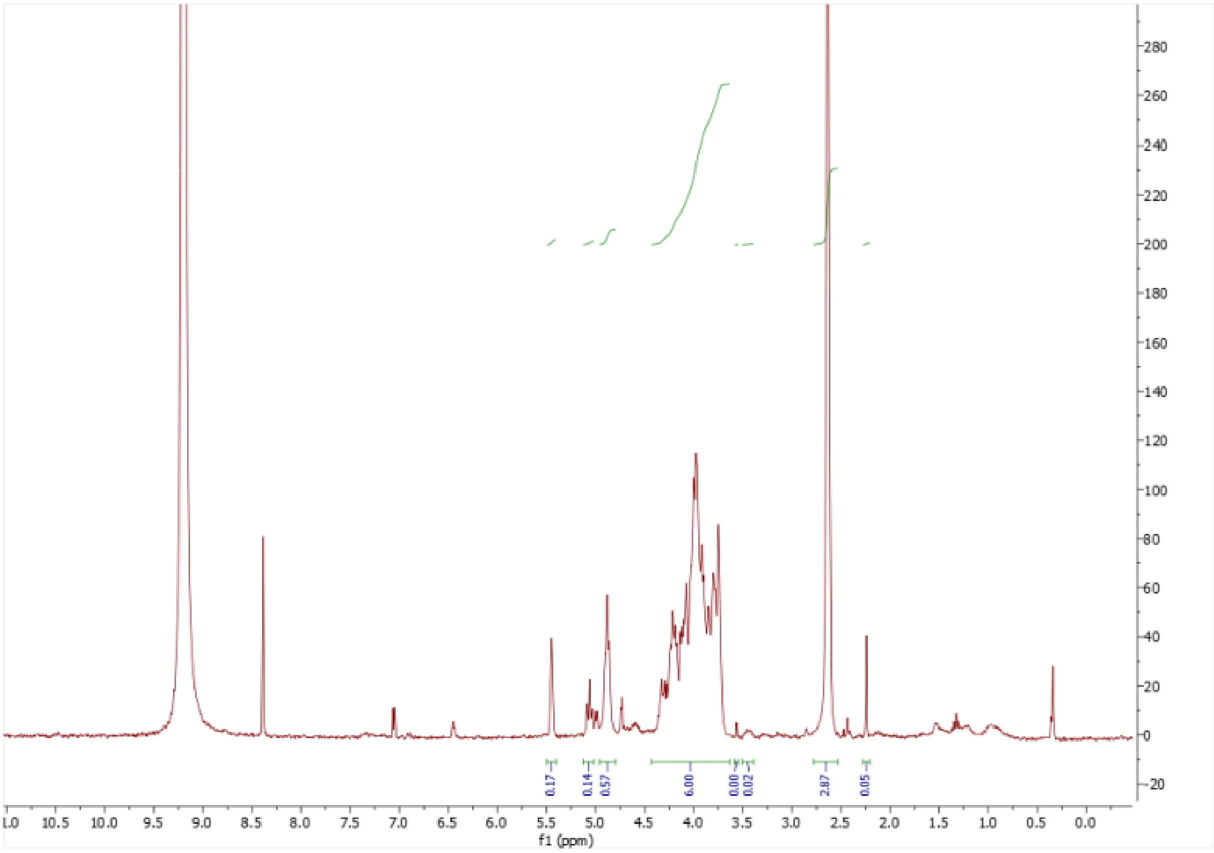

Figure A.4.3.26. ^{1}H-NMR spectrum of chitin pulped with hydroxylammonium acetate solid salt in DCl 35% in D_2O.

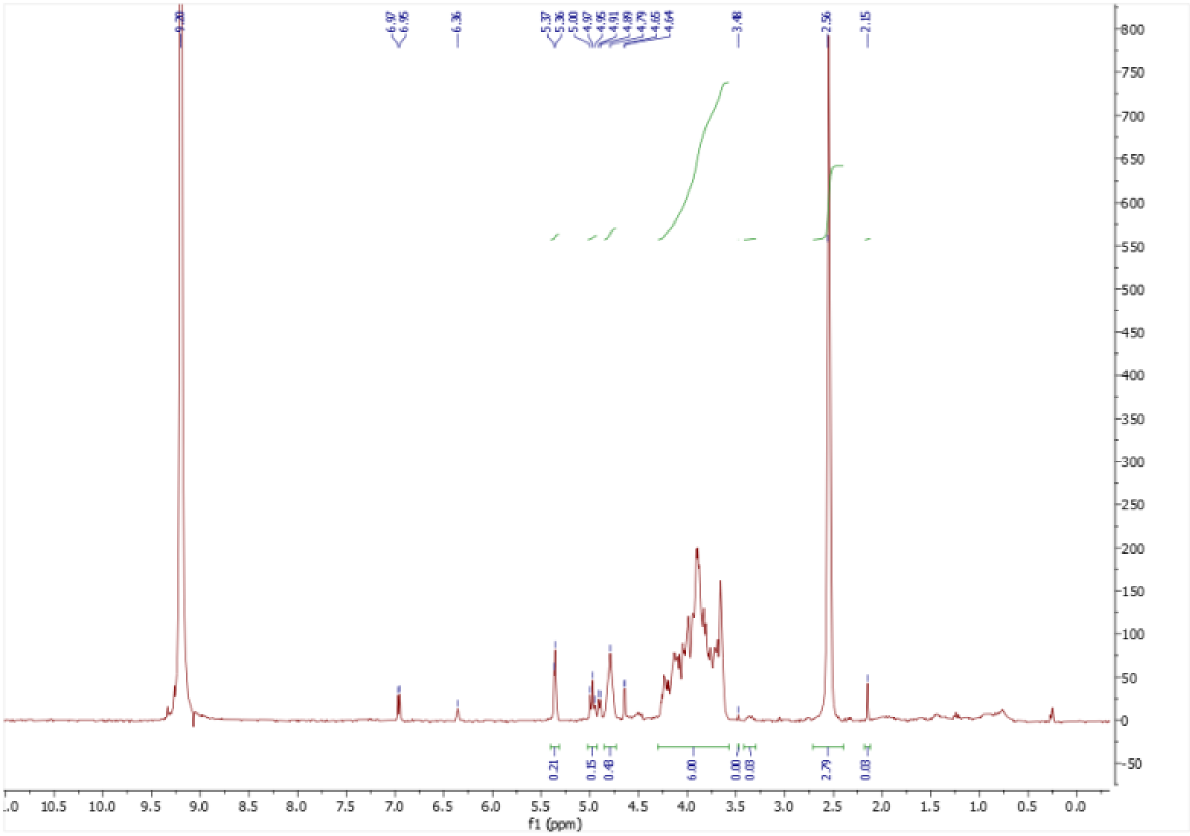

Figure A.4.3.27. ^{1}H-NMR spectrum of chitin pulped with hydroxylammonium acetate prepared in situ in batch conditions (100 °C) by sequential addition of acid prior to base in DCl 35% in D_2O.

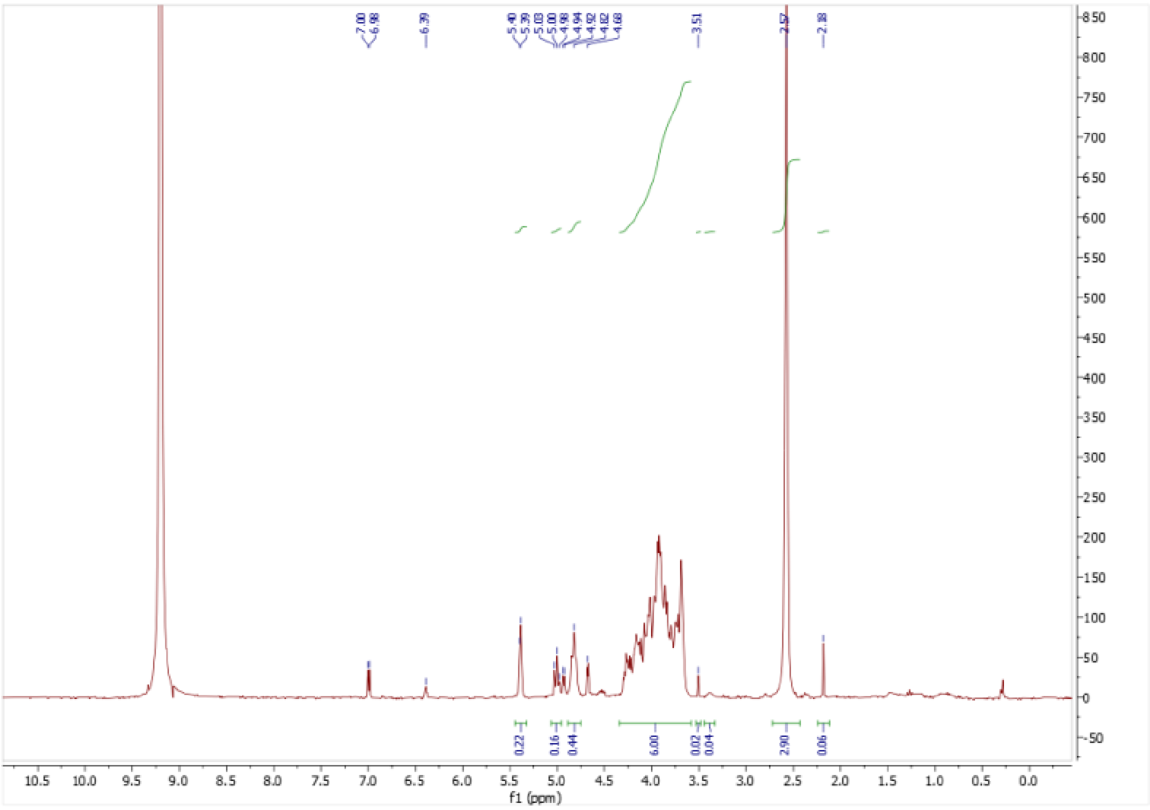

Figure A.4.3.28. ^{1}H-NMR spectrum of chitin pulped with hydroxylammonium acetate prepared in situ in batch conditions (100 °C) by sequential addition of base prior to acid in DCl 35% in D_2O.

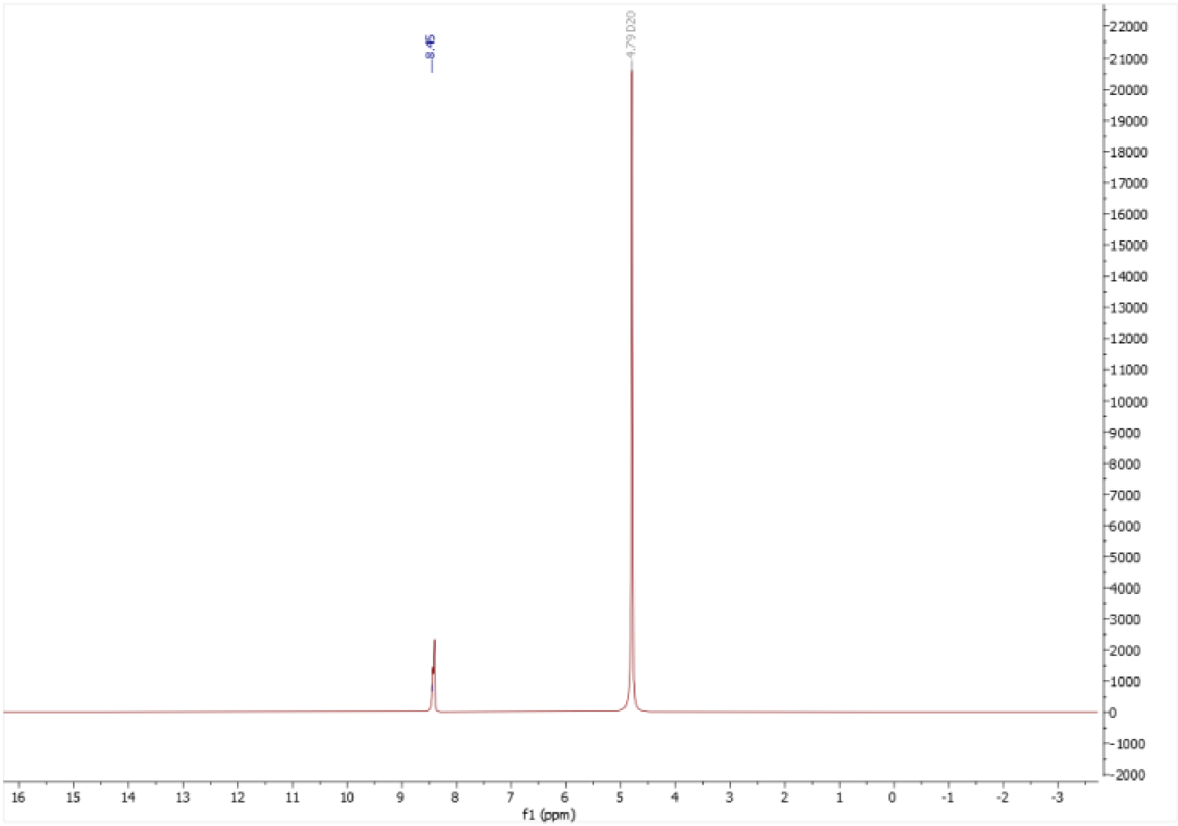

Figure A.4.3.29. ^{1}H-NMR spectrum of hydroxylammonium formate in D_2O.

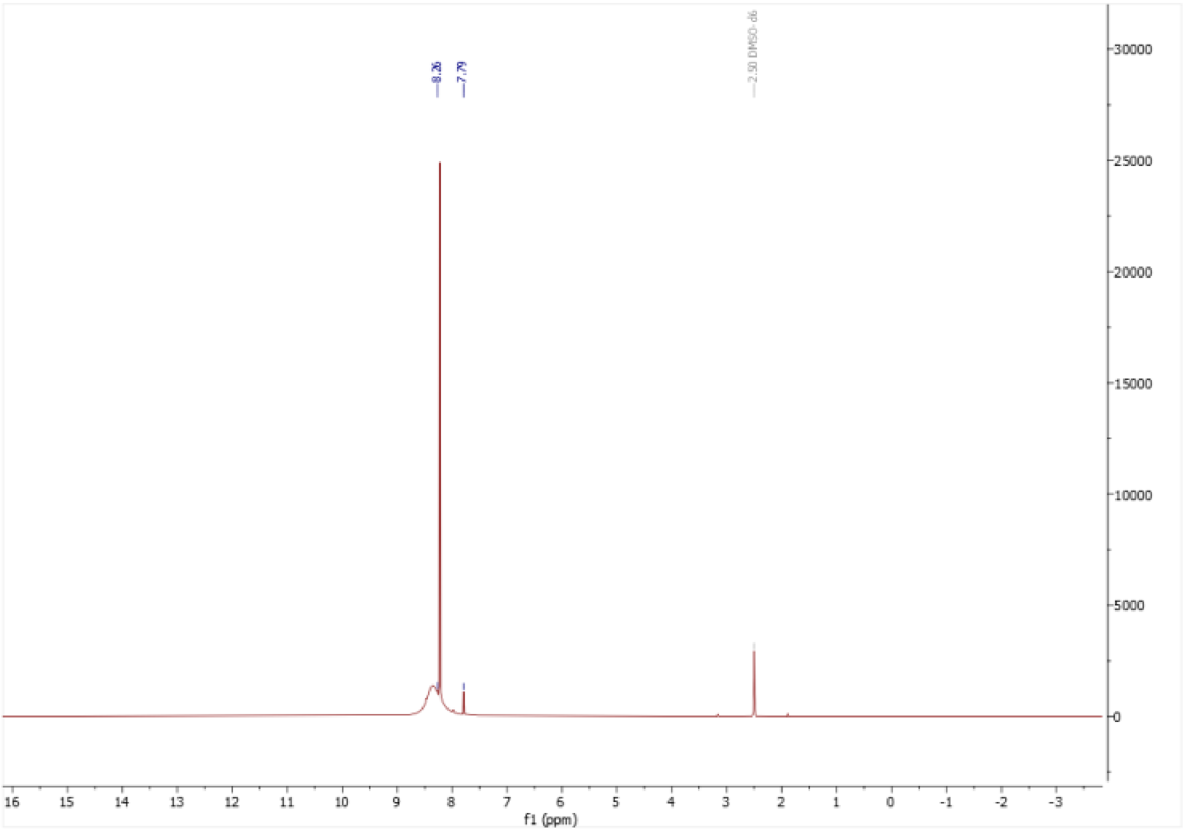

Figure A.4.3.30. ^{1}H-NMR spectrum of hydroxylammonium formate in DMSO-d_6.

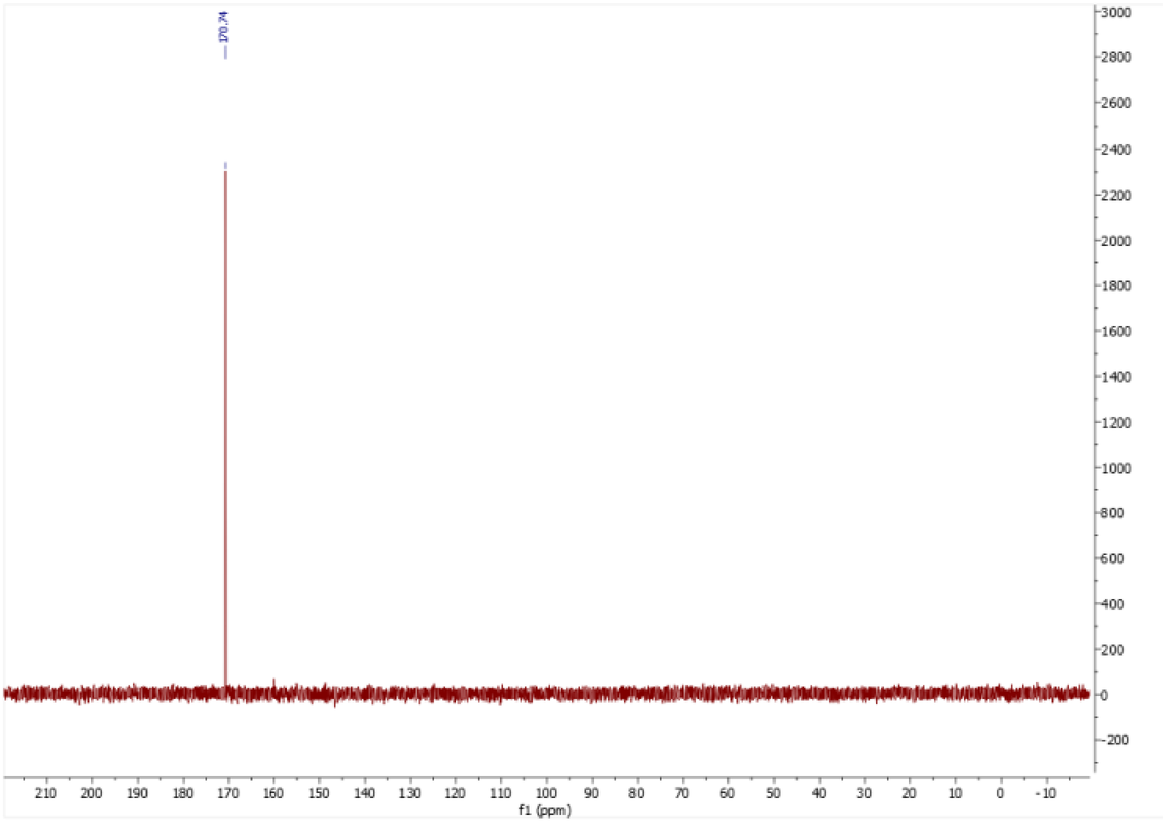

Figure A.4.3.31. ^{13}C-NMR spectrum of hydroxylammonium formate in D_2O.

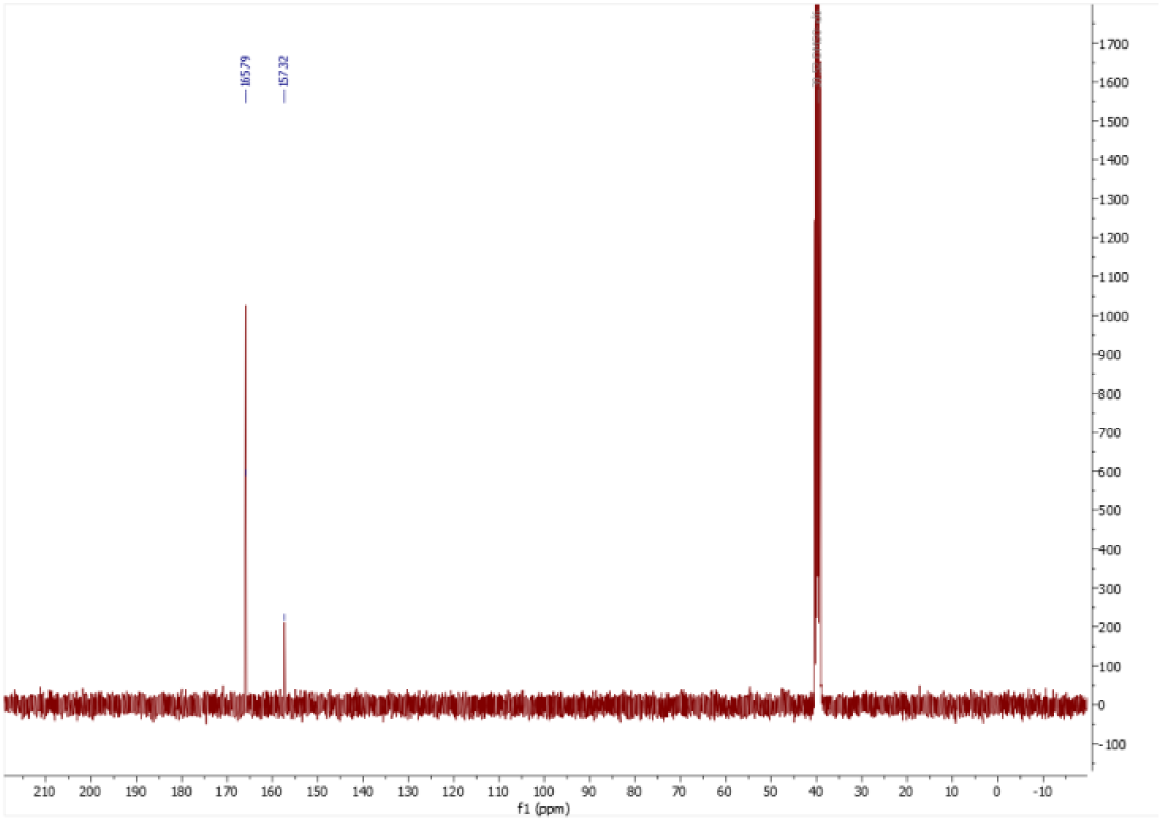

Figure A.4.3.32. ^{13}C-NMR spectrum of hydroxylammonium formate in DMSO-d_6.

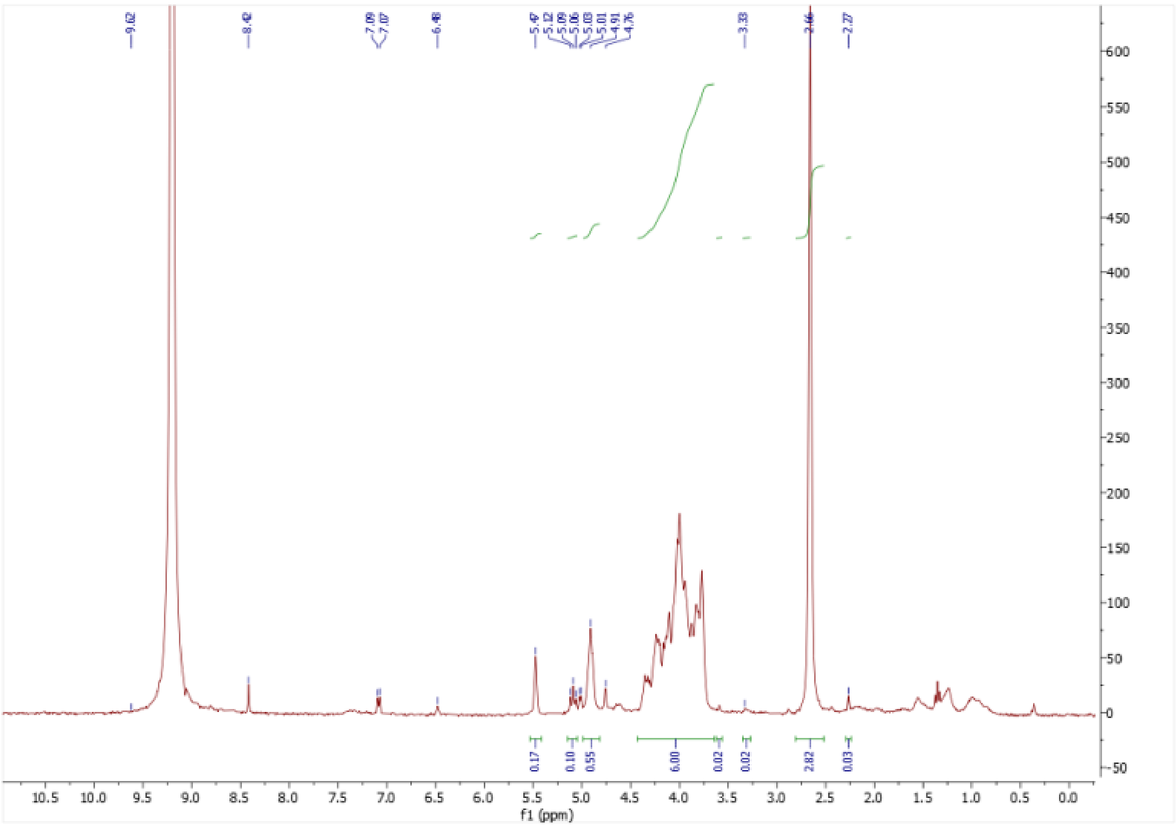

Figure A.4.3.33. ^{1}H-NMR spectrum of chitin pulped with hydroxylammonium formate solid salt in DCl 35% in D_2O.

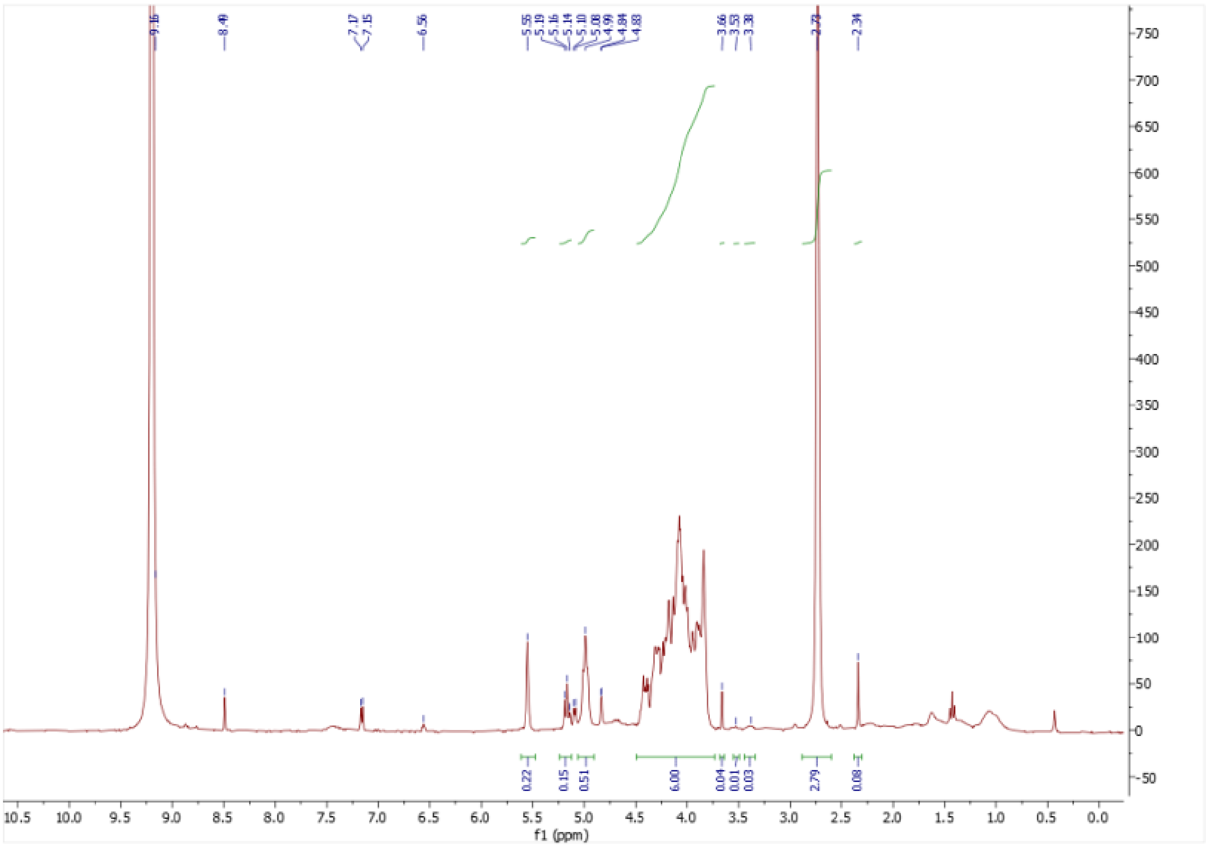

Figure A.4.3.34. ^{1}H-NMR spectrum of chitin pulped with hydroxylammonium formate prepared in situ in batch conditions (100 °C) by sequential addition of acid prior to base in DCl 35% in D_2O.

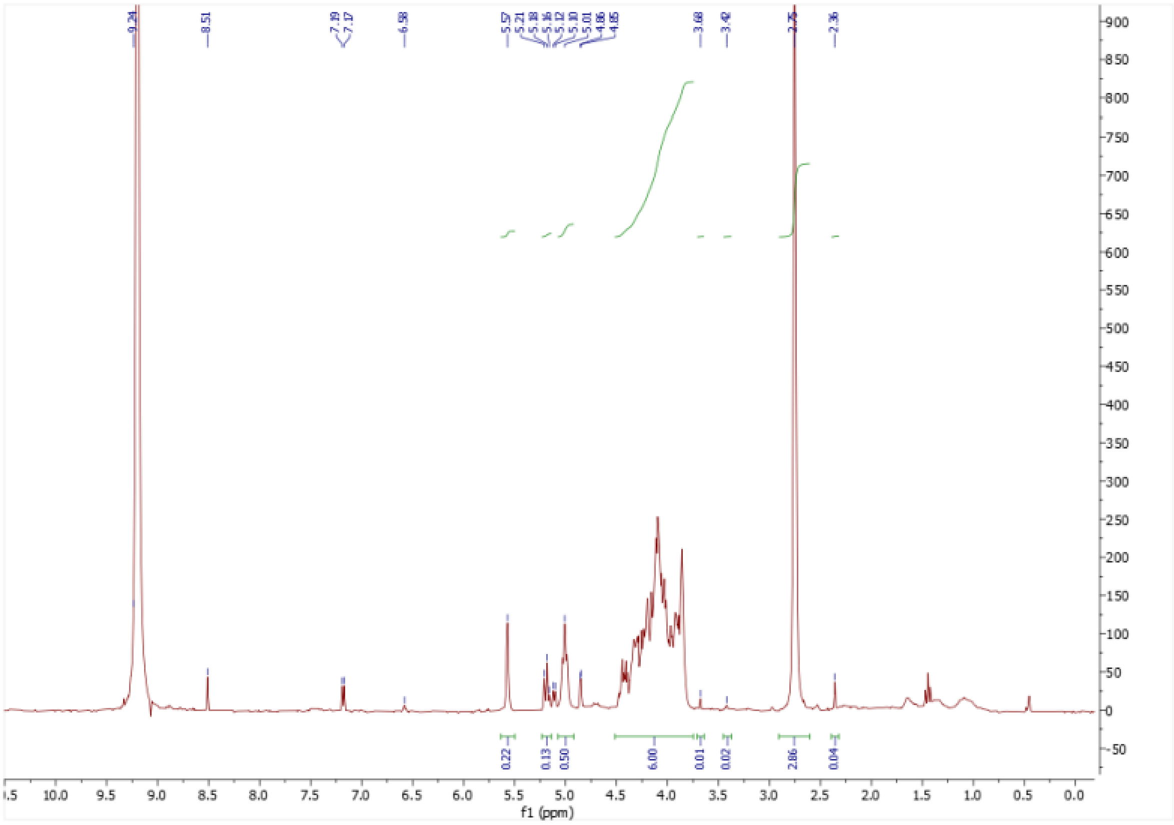

Figure A.4.3.35. ^{1}H-NMR spectrum of chitin pulped with hydroxylammonium formate prepared in situ in batch conditions (100 °C) by sequential addition of base prior to acid in DCl 35% in D_2O.

FT-IT Spectra

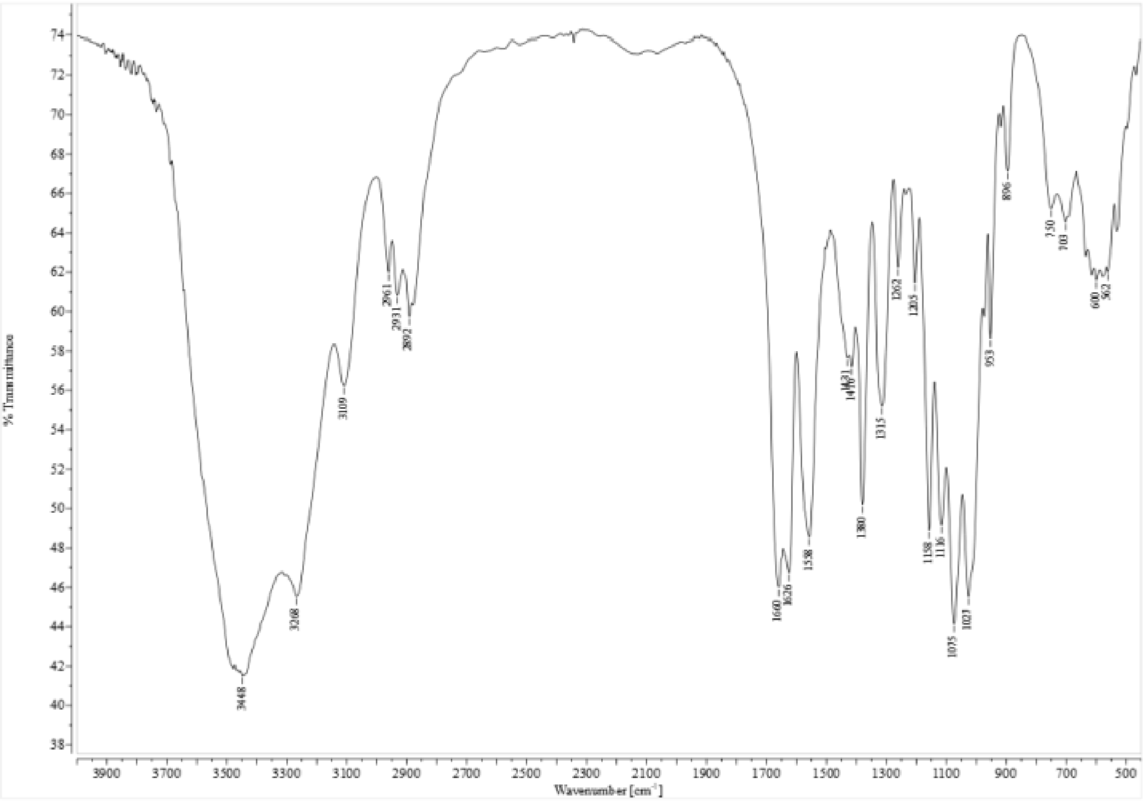

Figure A.4.3.36. FT-IR spectrum of commercial chitin (1 mg) in KBr pellet (100 mg).

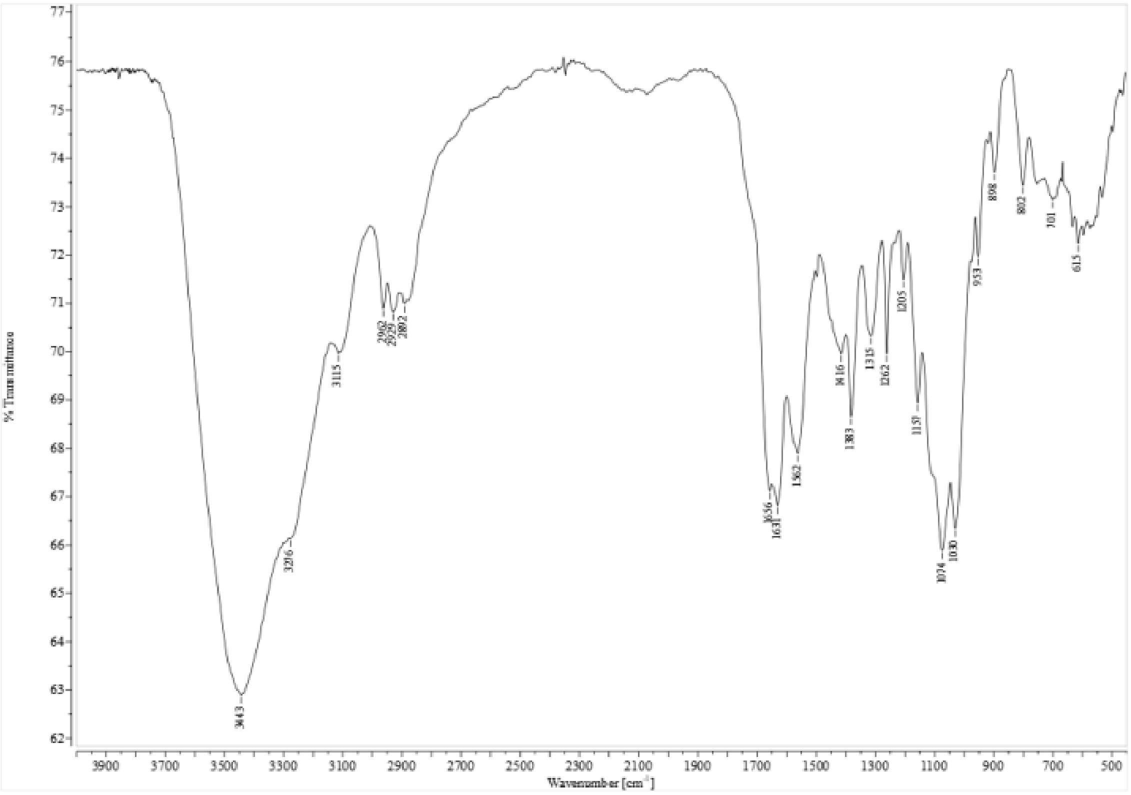

Figure A.4.3.37. FT-IR spectrum of chitin extracted with chemical method (1 mg) in KBr pellet (100 mg).

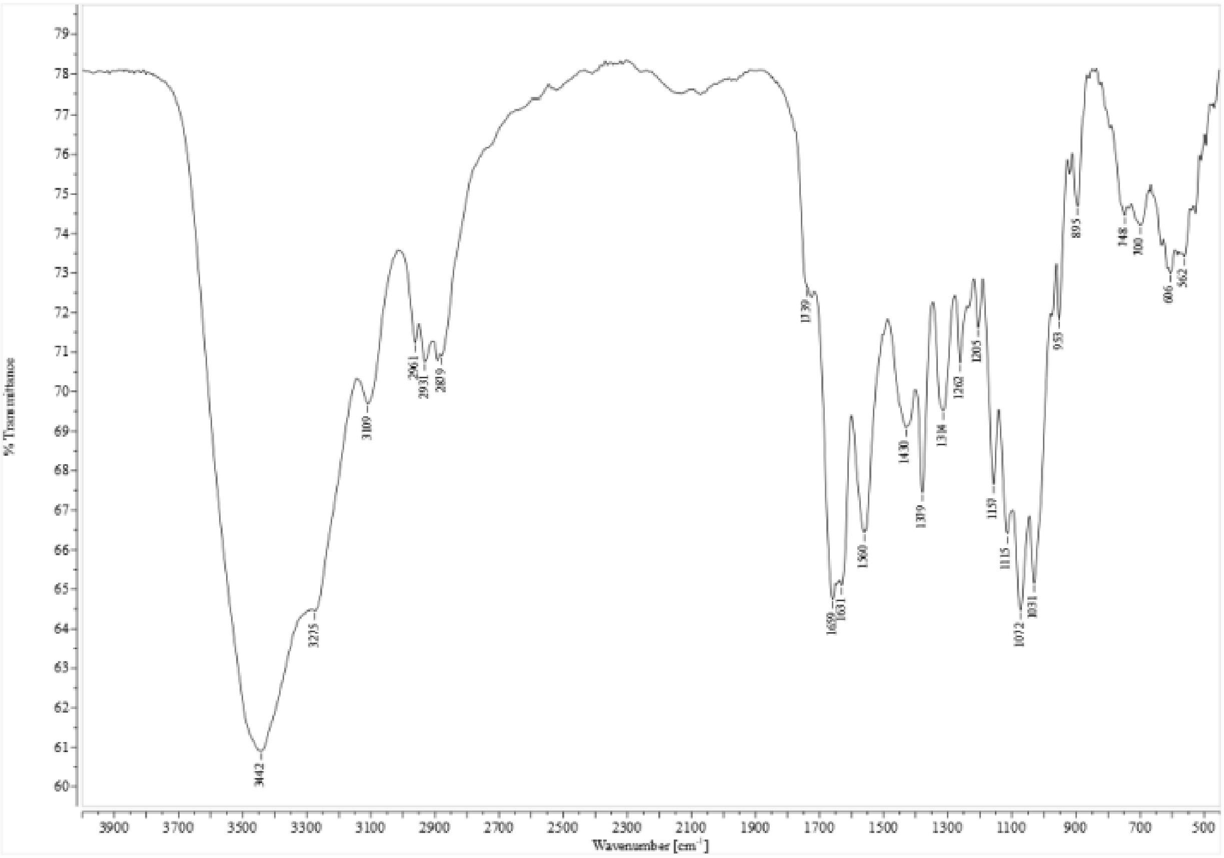

Figure A.4.3.38. FT-IR spectrum of chitin (1 mg) pulped with ammonium acetate solid salt (145 °C) in KBr.

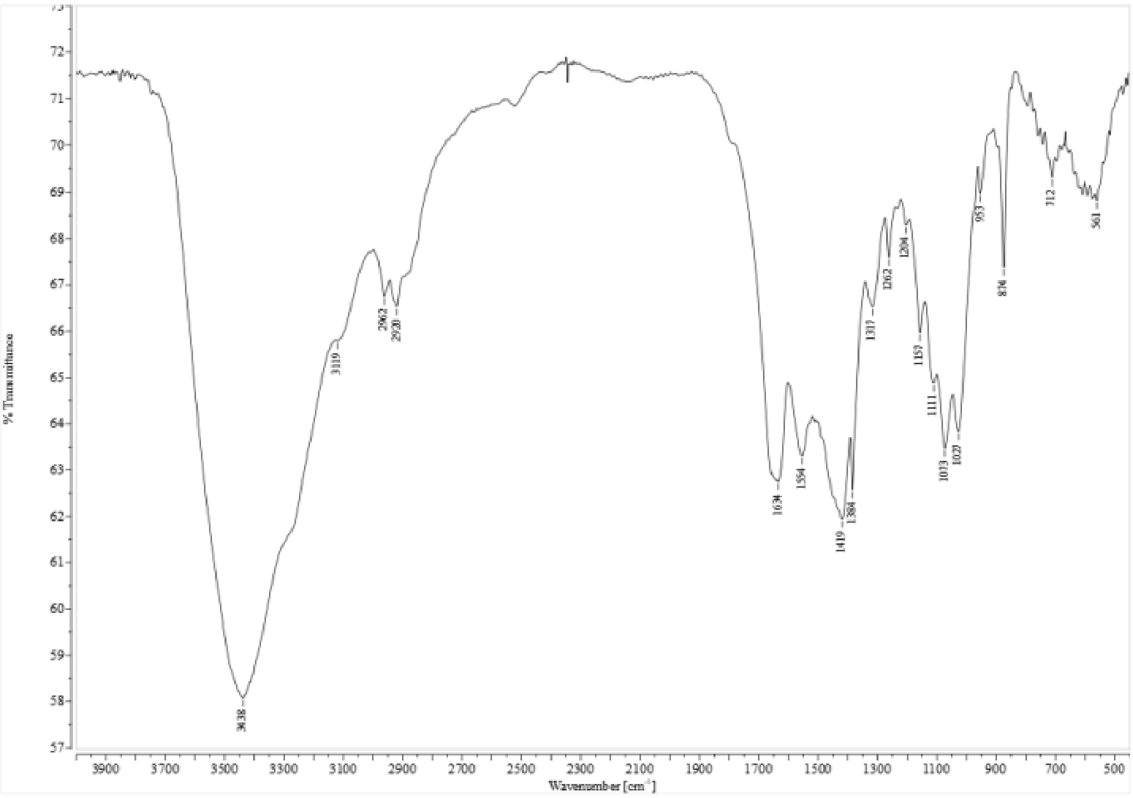

Figure A.4.3.39. FT-IR spectrum of chitin (1 mg) pulped with ammonium acetate prepared in situ in batch conditions (100 °C) by sequential addition of acid prior to base in KBr.

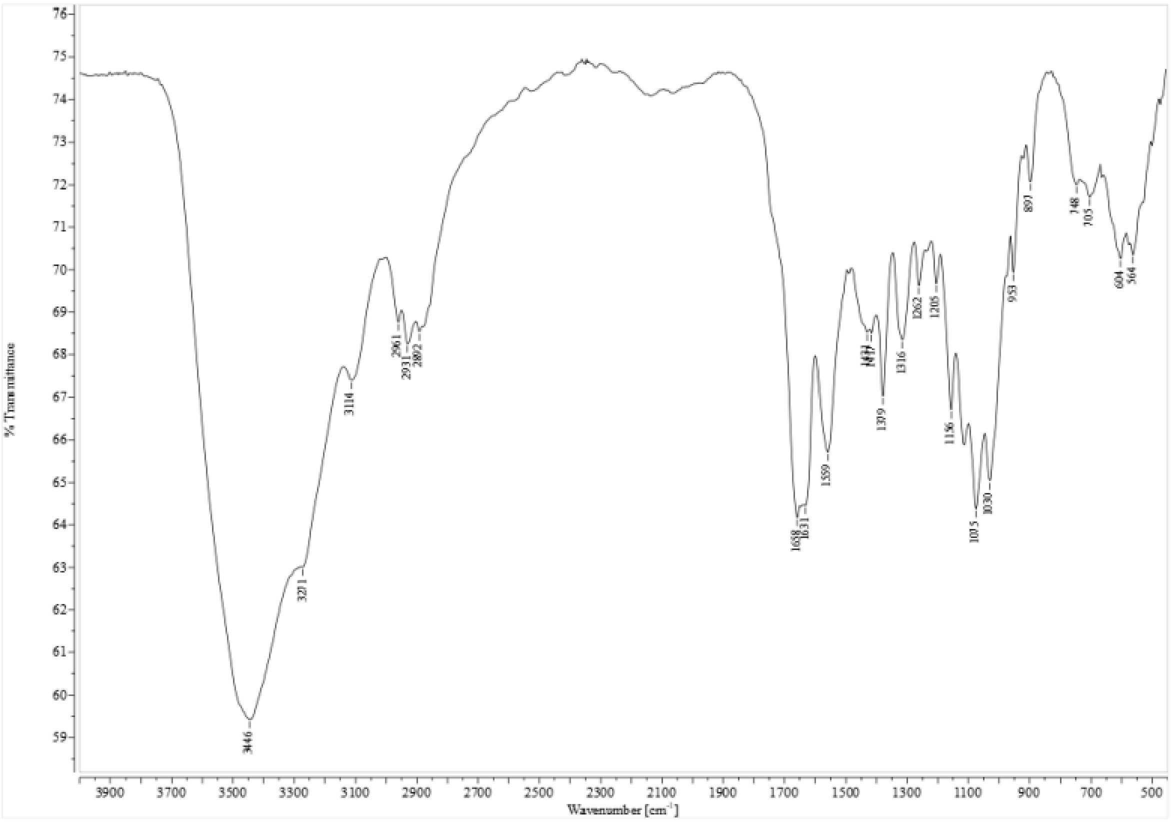

Figure A.4.3.40. FT-IR spectrum of chitin (1 mg) pulped with ammonium acetate prepared in situ in autoclave (145 °C) by sequential addition of acid prior to base in KBr.

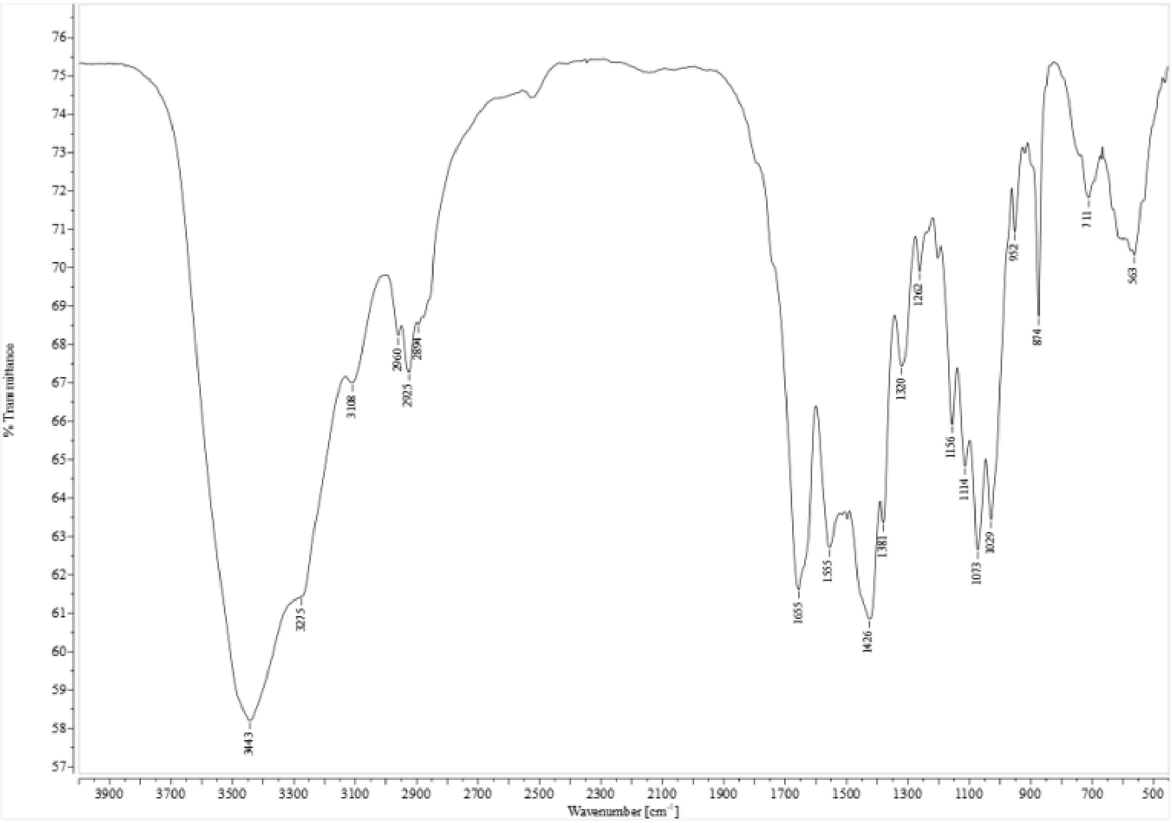

Figure A.4.3.41. FT-IR spectrum of chitin (1 mg) pulped with ammonium acetate prepared in situ in batch conditions (100 °C) by sequential addition of base prior to acid in KBr.

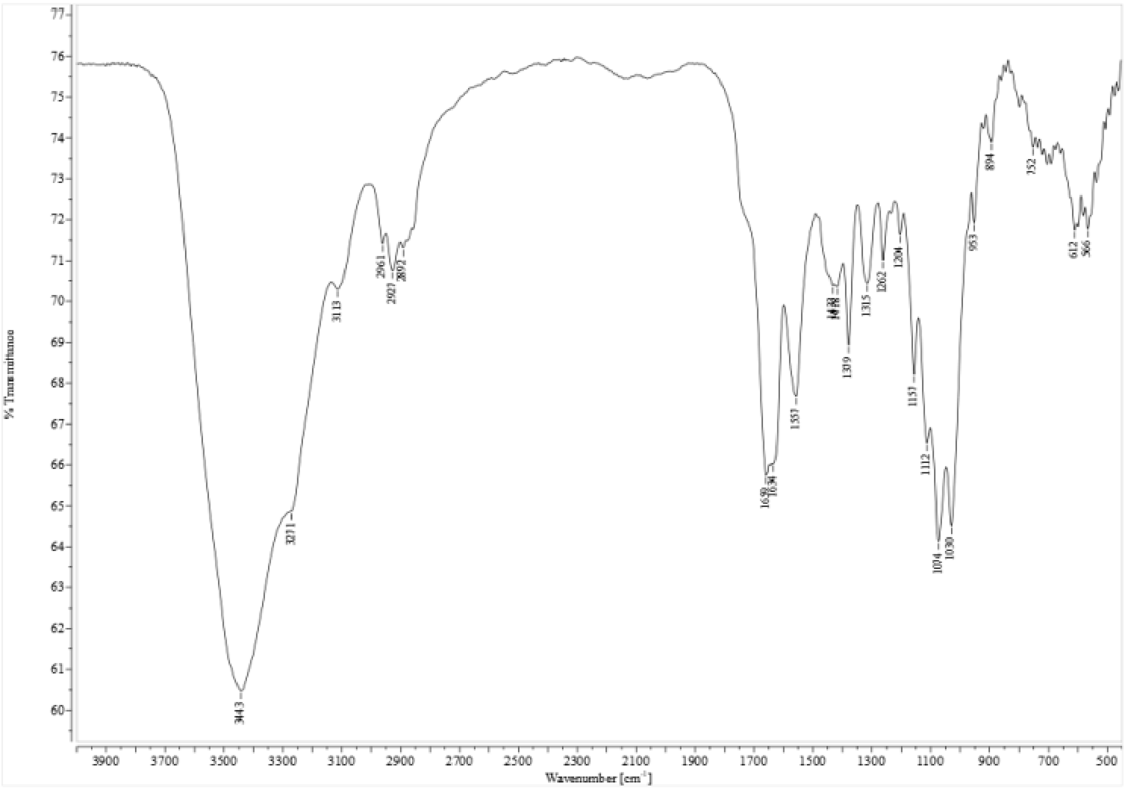

Figure A.4.3.42. FT-IR spectrum of chitin (1 mg) pulped with ammonium acetate prepared in situ in autoclave (145 °C) by sequential addition of base prior to acid in KBr.

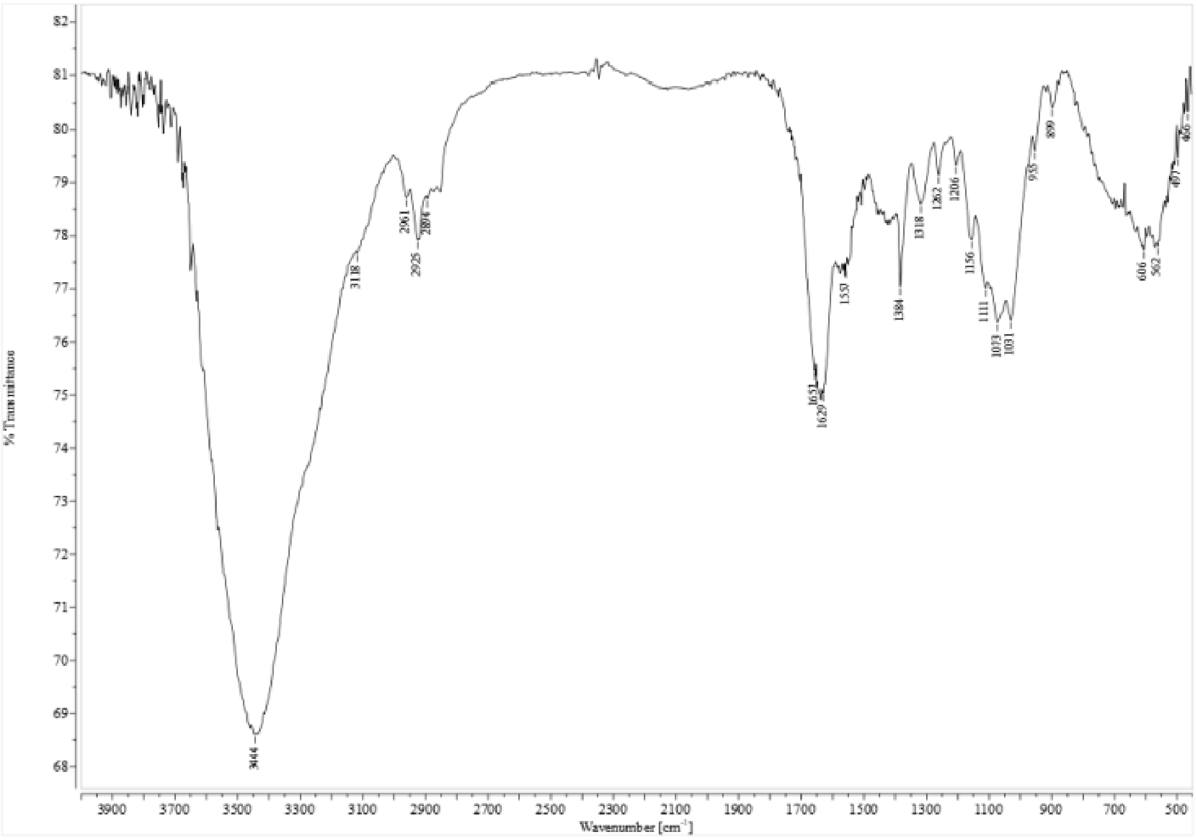

Figure A.4.3.43. FT-IR spectrum of chitin (1 mg) pulped with ammonium formate solid salt (130 °C) in KBr.

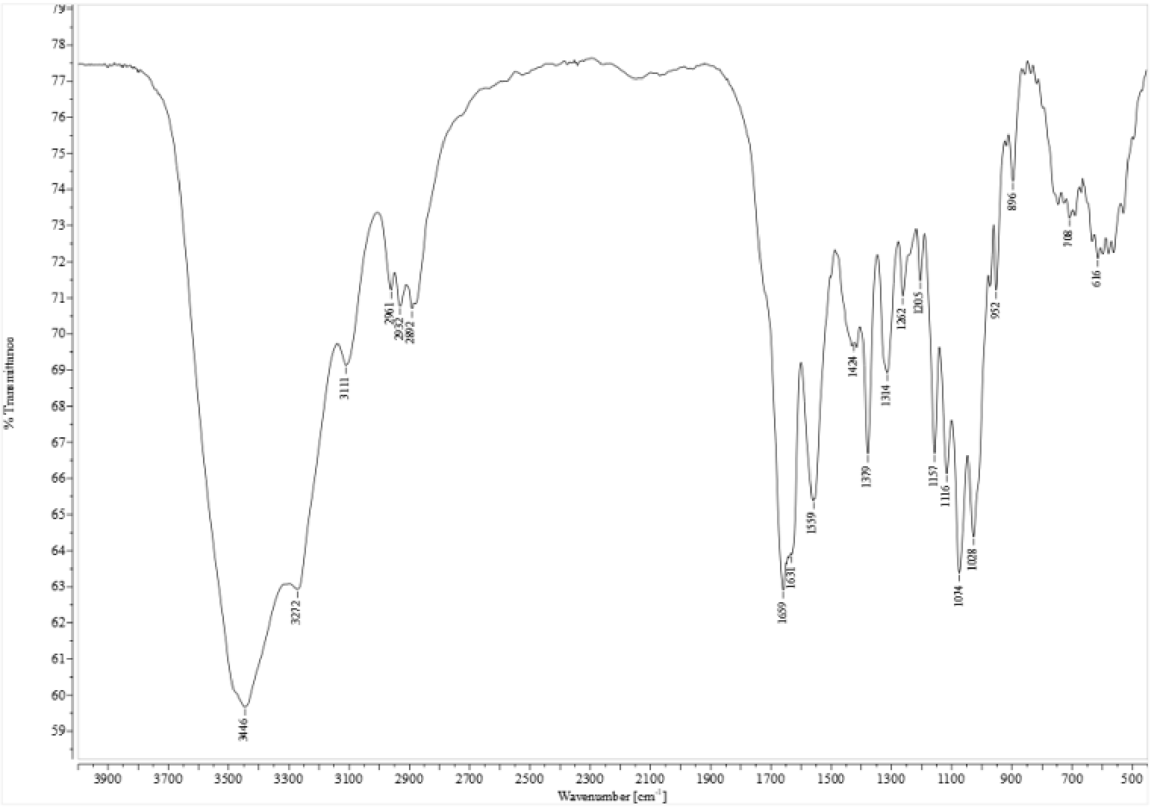

Figure A.4.3.44. FT-IR spectrum of chitin (1 mg) pulped with ammonium formate prepared in situ in batch conditions (100 °C) by sequential addition of acid prior to base in KBr.

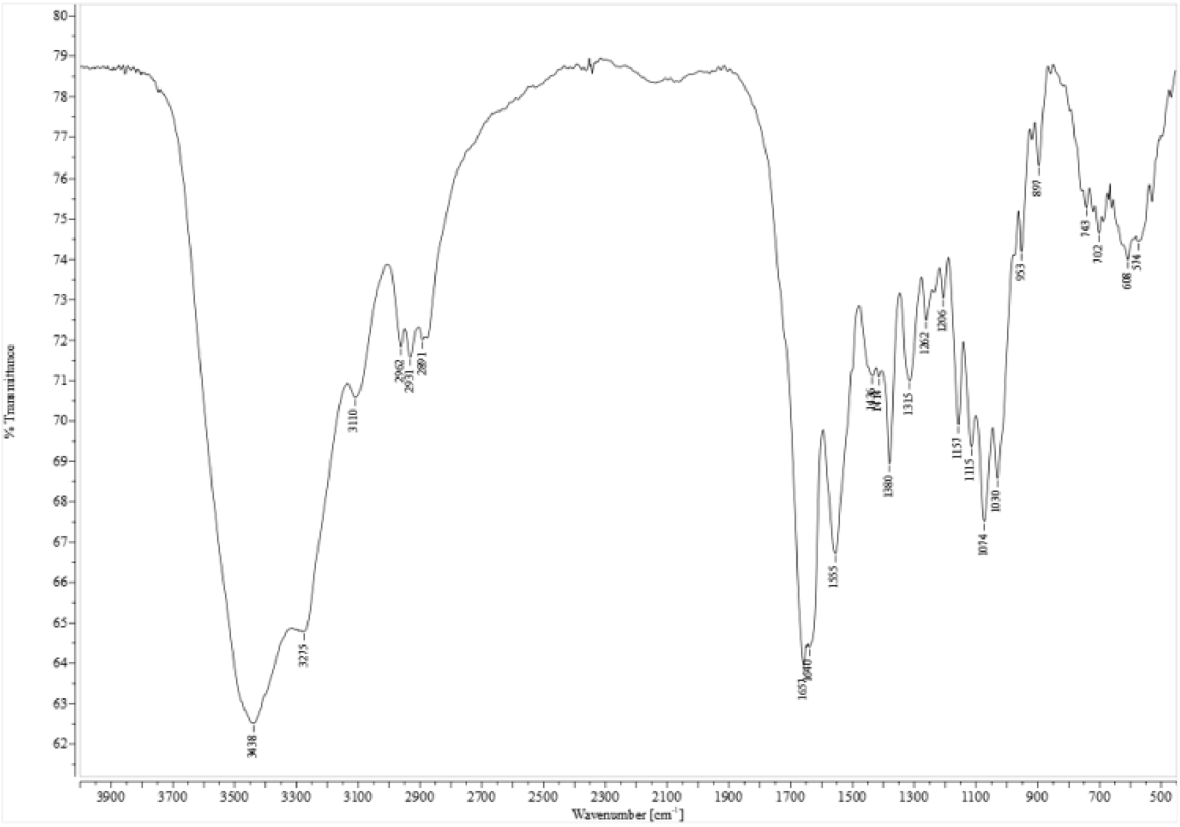

Figure A.4.3.45. FT-IR spectrum of chitin (1 mg) pulped with ammonium formate prepared in situ in autoclave (130°C) by sequential addition of acid prior to base in KBr.

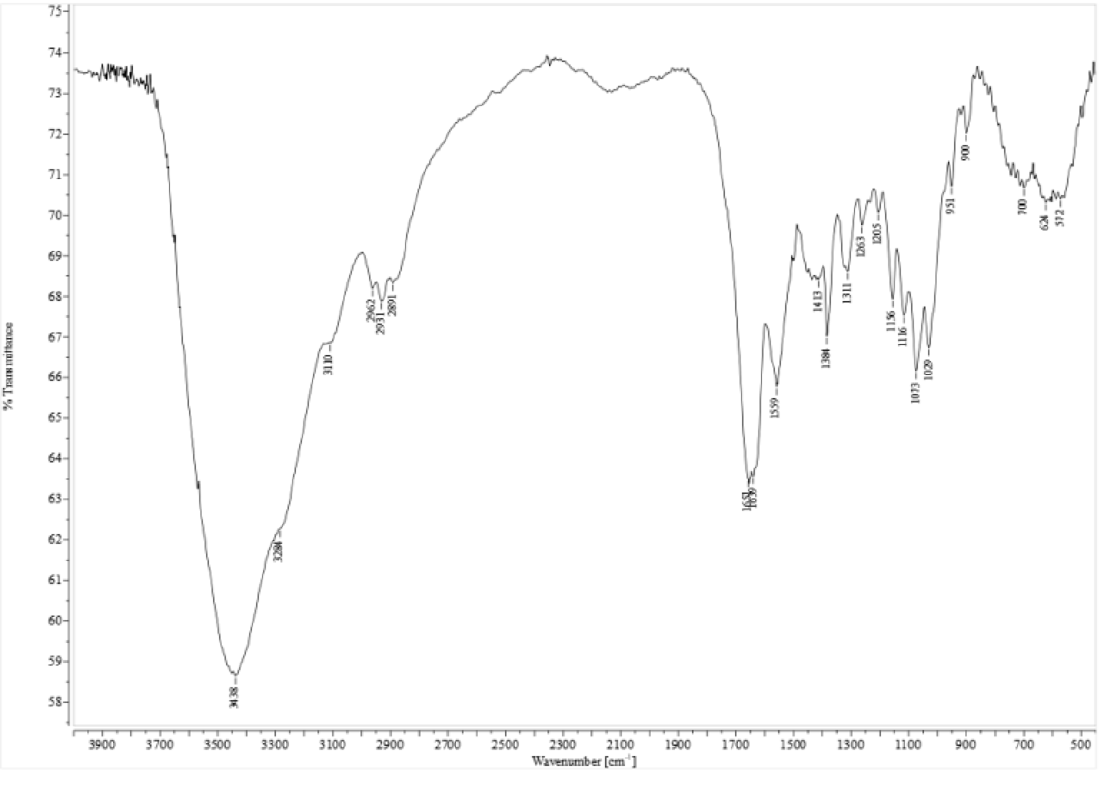

Figure A.4.3.46. FT-IR spectrum of chitin (1 mg) pulped with ammonium formate prepared in situ in batch conditions (100 °C) by sequential addition of base prior to acid in KBr.

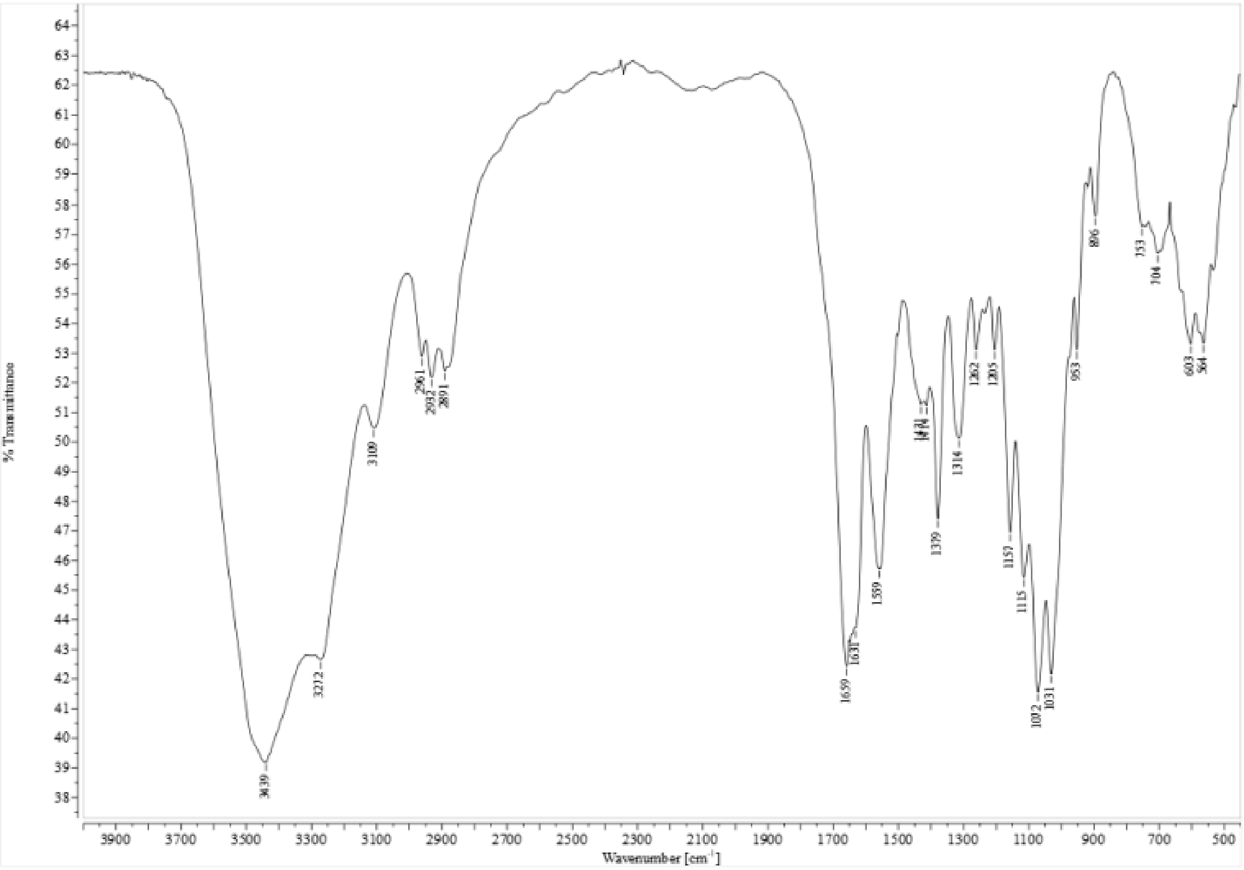

Figure A.4.3.47. FT-IR spectrum of chitin (1 mg) pulped with ammonium formate prepared in situ in autoclave (130°C) by sequential addition of base prior to acid in KBr.

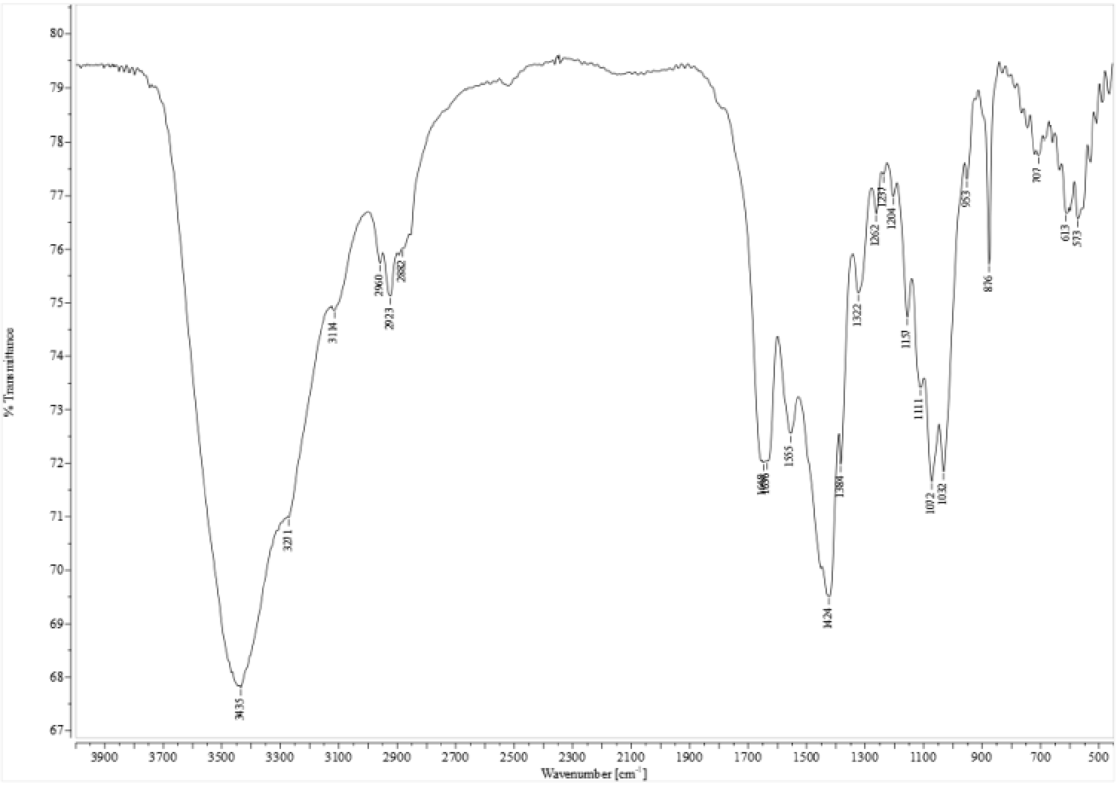

Figure A.4.3.48. FT-IR spectrum of chitin (1 mg) pulped with hydroxylammonium acetate solid salt (100 °C) in KBr.

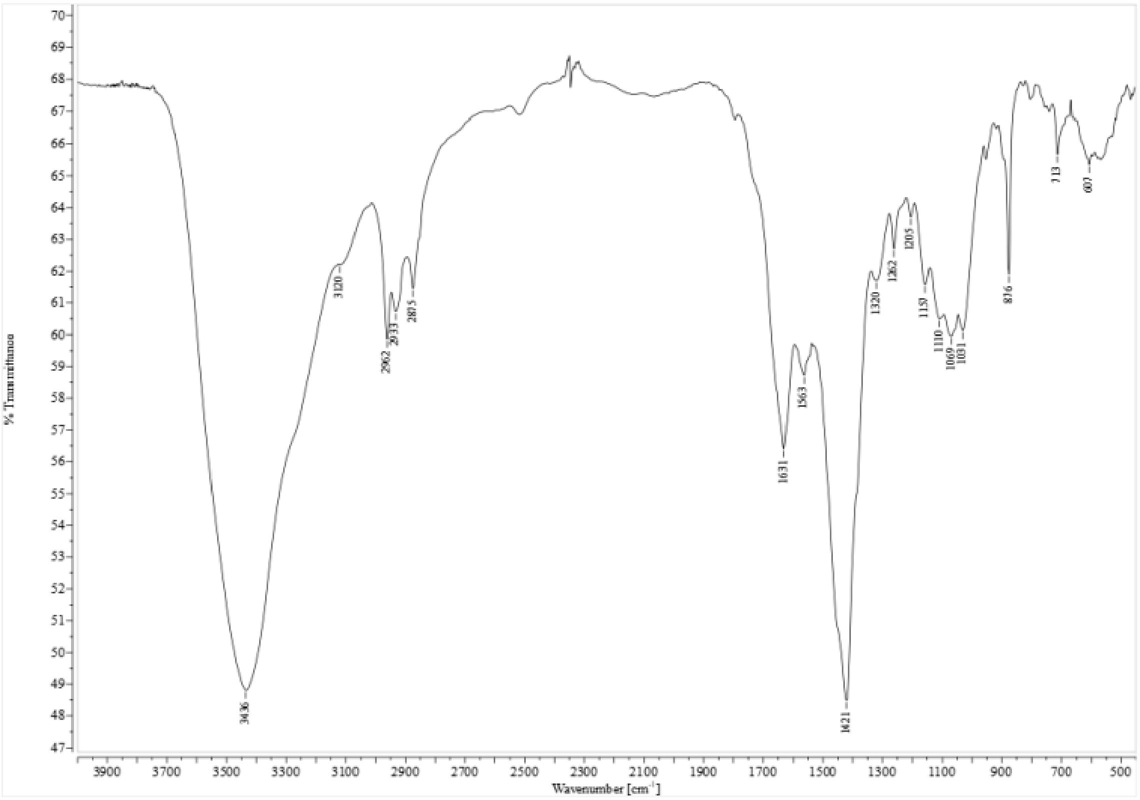

Figure A.4.3.49. FT-IR spectrum of chitin (1 mg) pulped with hydroxylammonium acetate prepared in situ in batch conditions (100 °C) by sequential addition of acid prior to base in KBr.

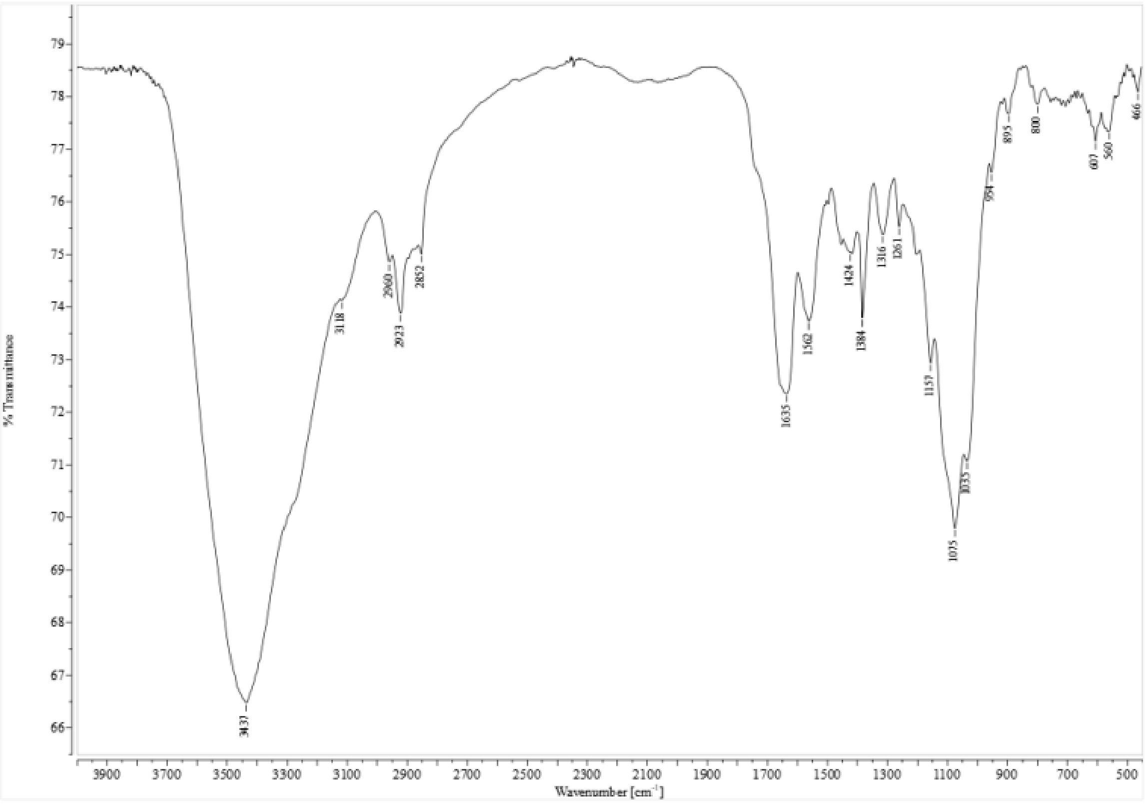

Figure A.4.3.50. FT-IR spectrum of chitin (1 mg) pulped with hydroxylammonium acetate prepared in situ in batch conditions (100 °C) by sequential addition of base prior to acid in KBr.

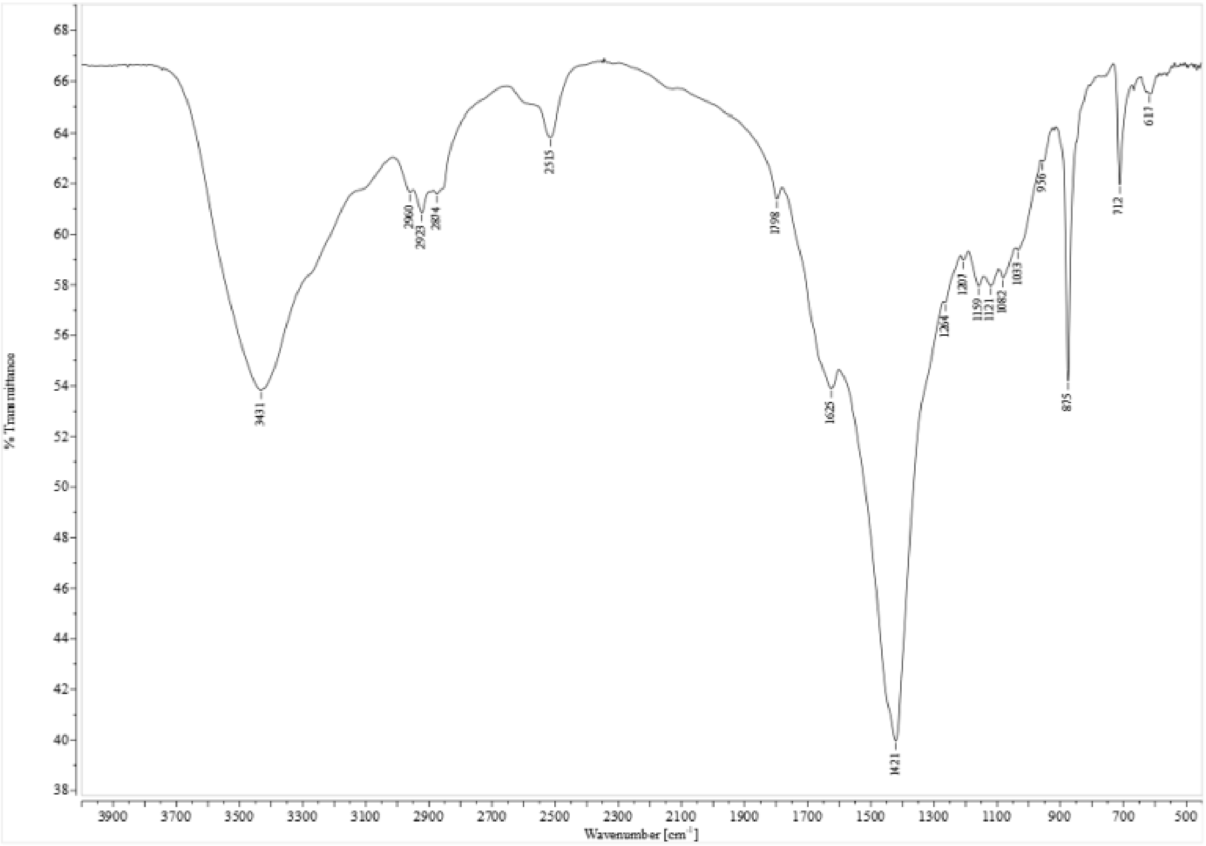

Figure A.4.3.51. FT-IR spectrum of chitin (1 mg) pulped with hydroxylammonium formate solid salt (100 °C) in KBr.

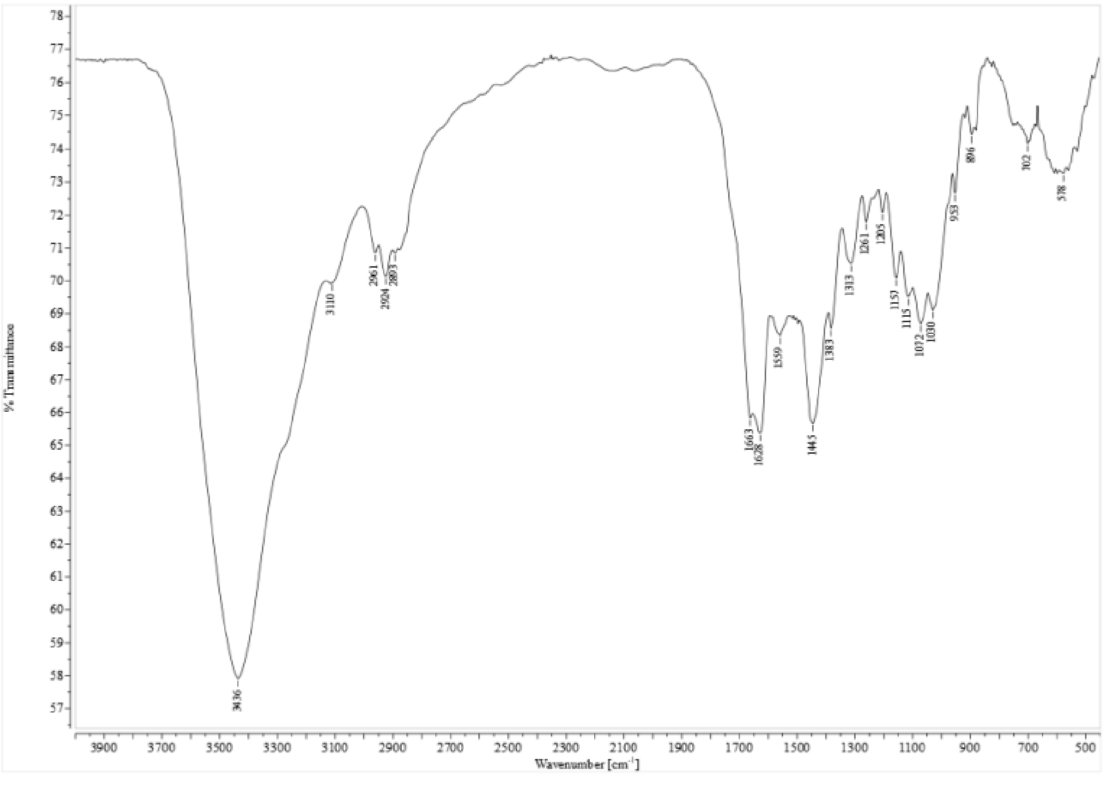

Figure A.4.3.52. FT-IR spectrum of chitin (1 mg) pulped with hydroxylammonium formate prepared in situ in batch conditions (100 °C) by sequential addition of acid prior to base in KBr.

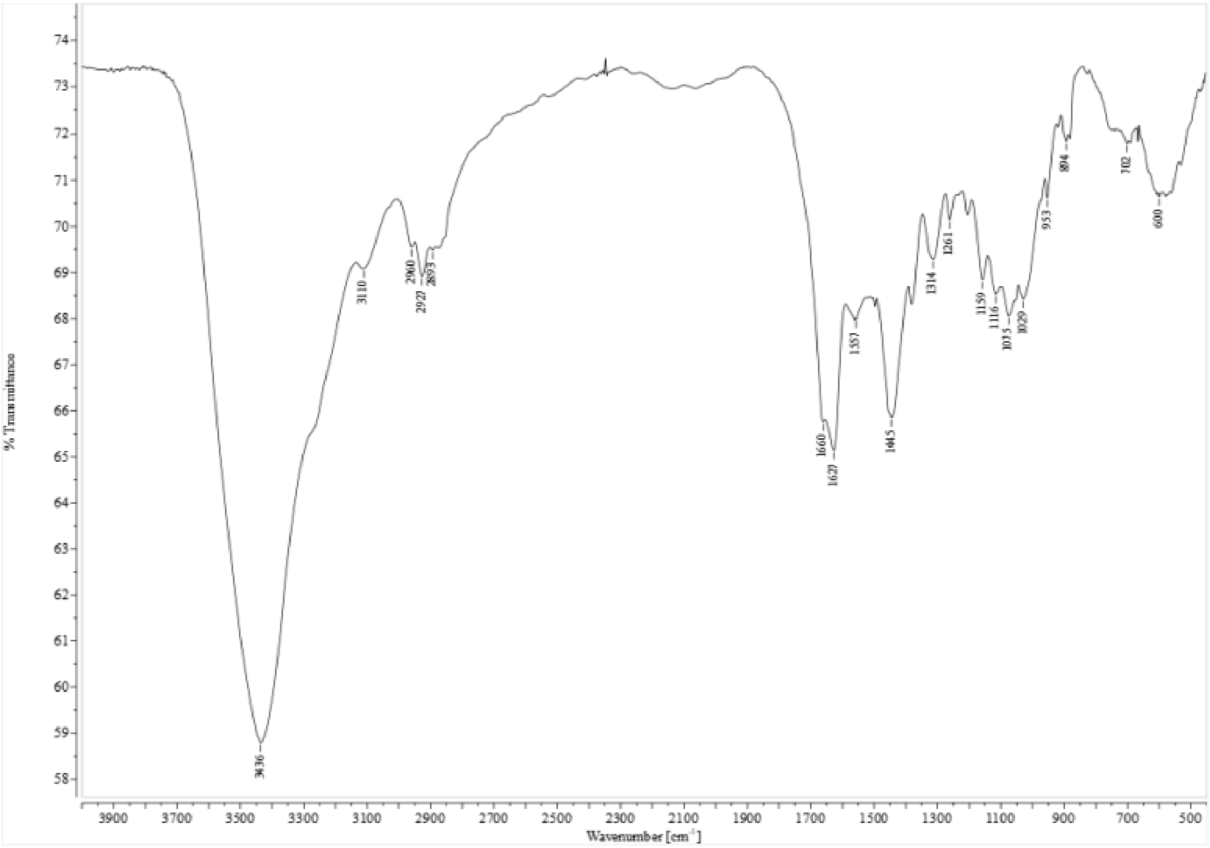

Figure A.4.3.53. FT-IR spectrum of chitin (1 mg) pulped with hydroxylammonium formate prepared in situ in batch conditions (100 °C) by sequential addition of base prior to acid in KBr.

A-5.2 Supercritical CO_2 extraction of natural antibacterials from low-value weeds and agro-waste

NMR Spectra

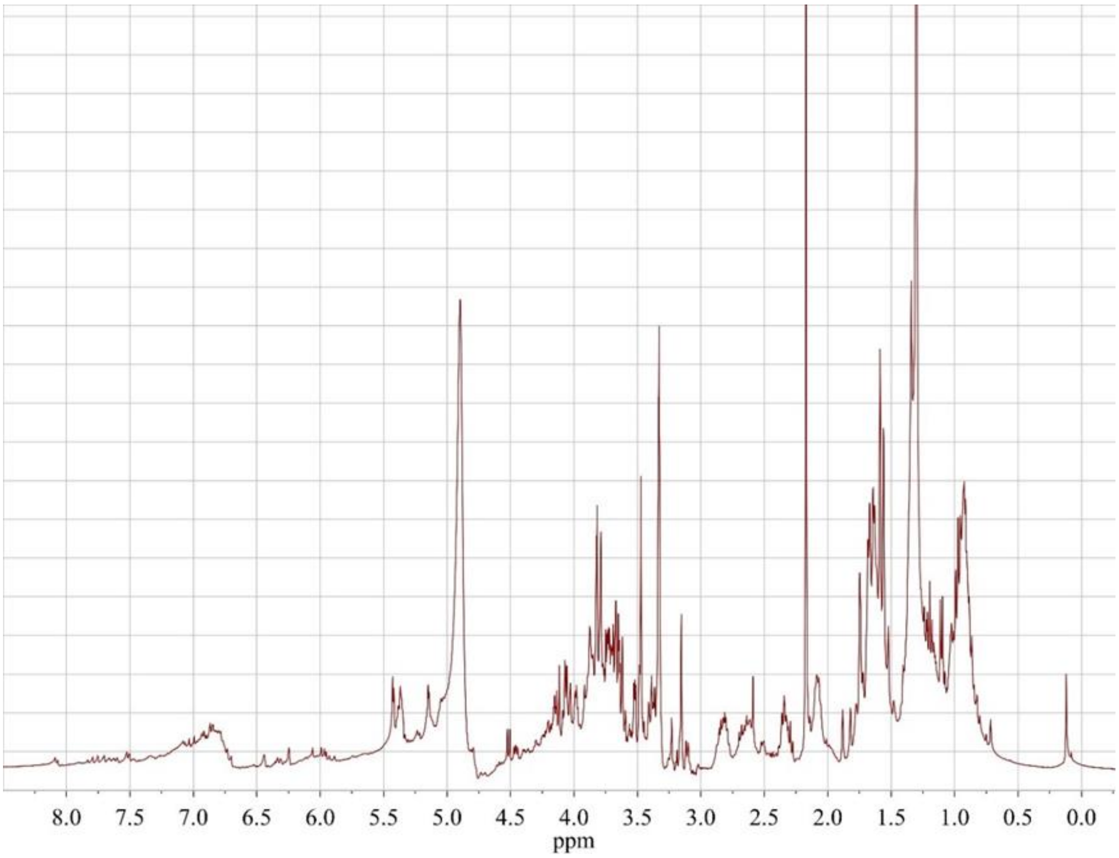

Figure A.5.2.1. $^{13}C\{^1H\}$ NMR spectra of the *Humulus Lupulus* flowers ethanol extract in $(CD_3)_2CO$.

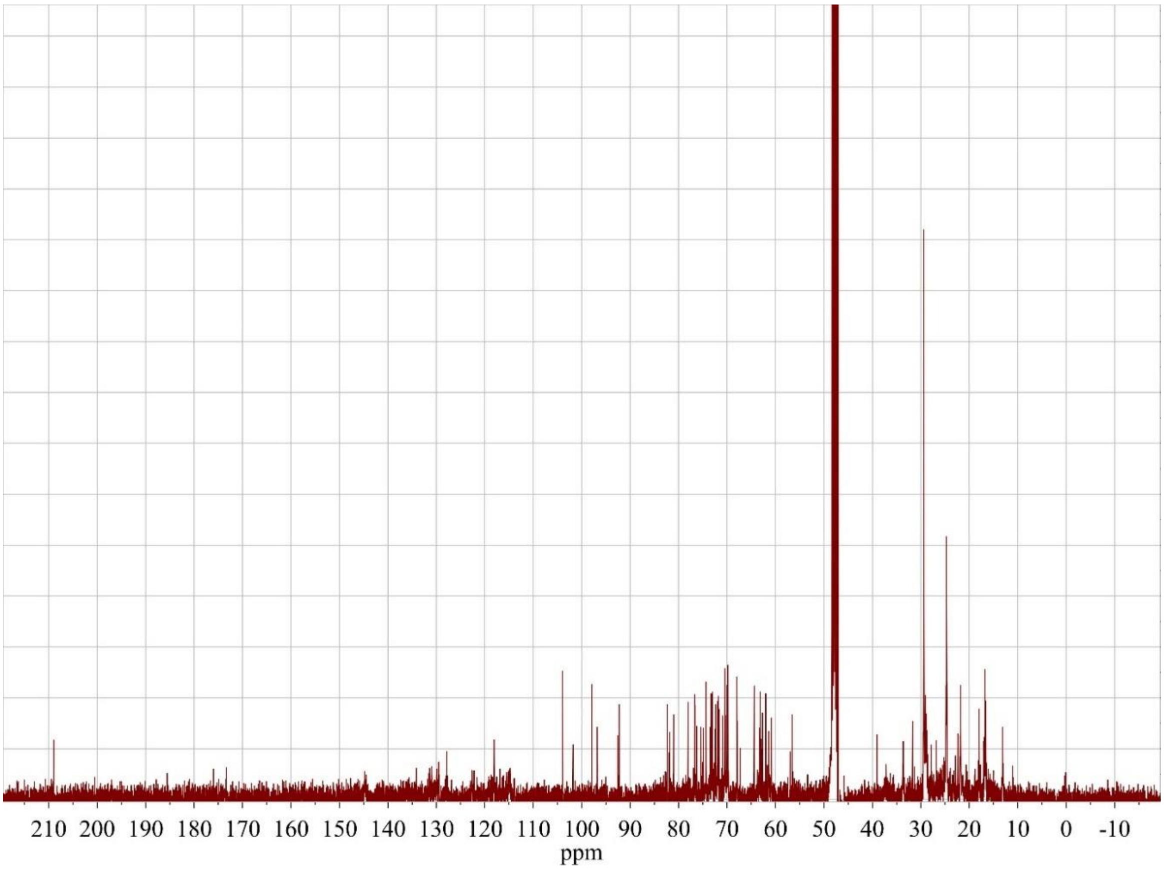

Figure A.5.2.2. $^{13}C\{^{1}H\}$ NMR spectra of the *Humulus Lupulus* flowers ethanol extract in CD_3OD.

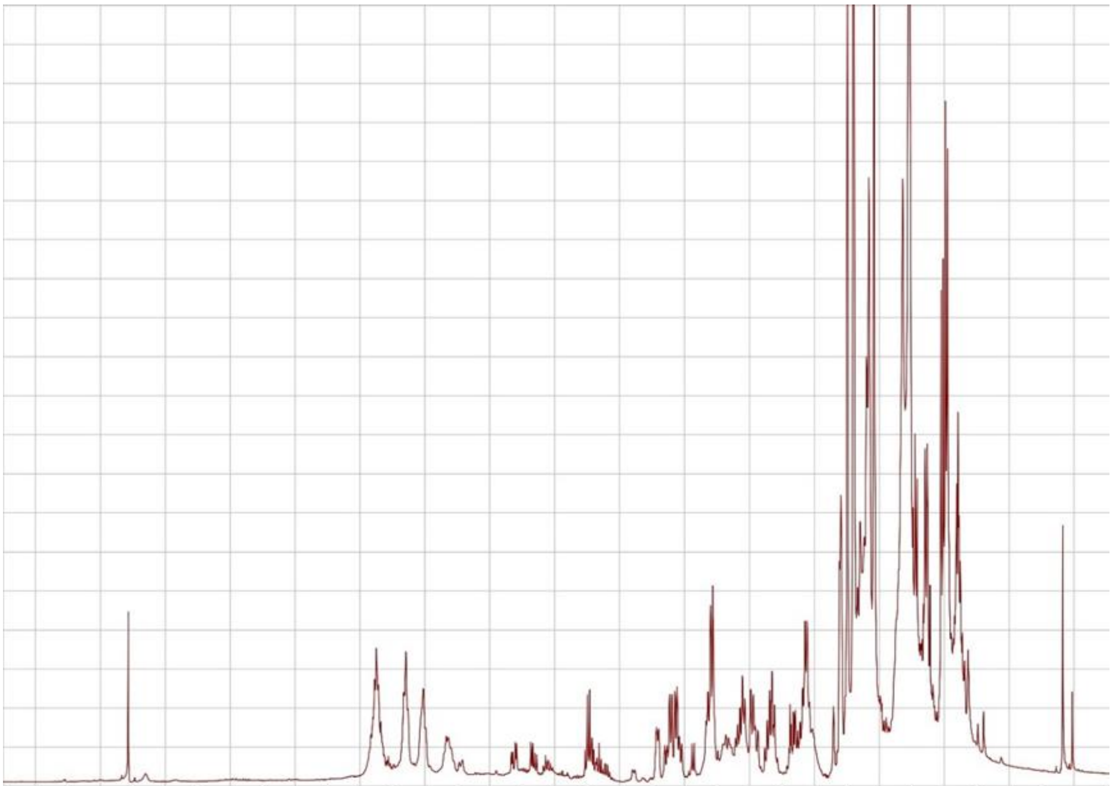

Figure A.5.2.3. ^{1}H NMR spectra of the *Humulus Lupulus* flowers $scCO_2$ extract in $CDCl_3$.

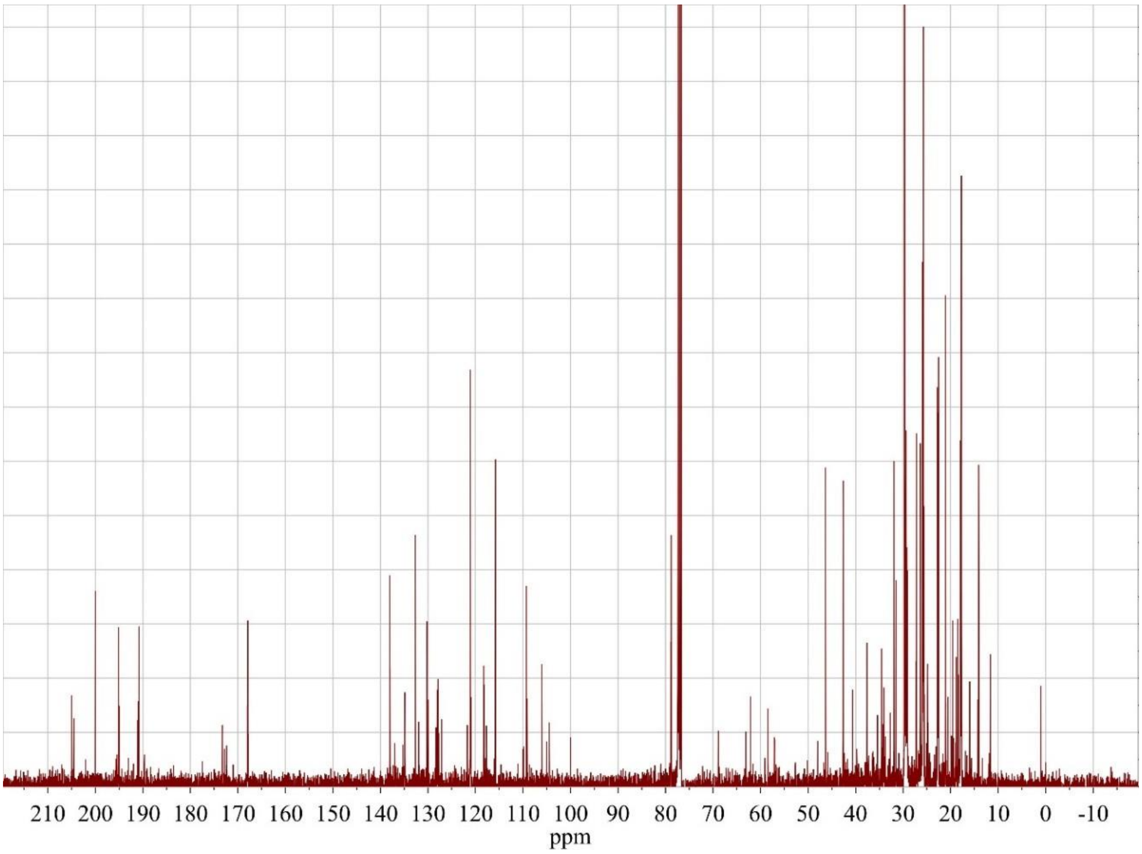

Figure A.5.2.4. $^{13}C\{^{1}H\}$ NMR spectra of the *Humulus Lupulus* flowers $scCO_2$ extract in $CDCl_3$.

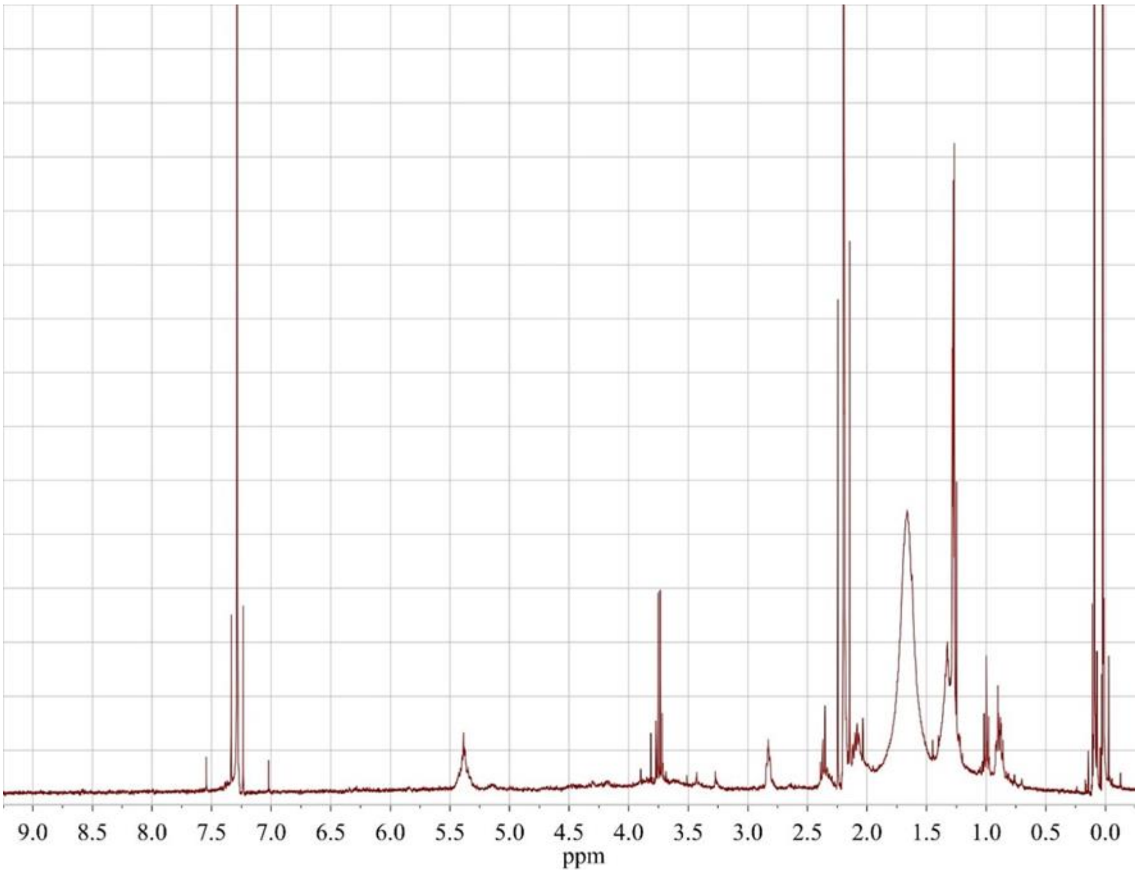

Figure A.5.2.5. ^{1}H NMR spectra of the *Humulus Lupulus* leaves ethanol extract in $CDCl_3$.

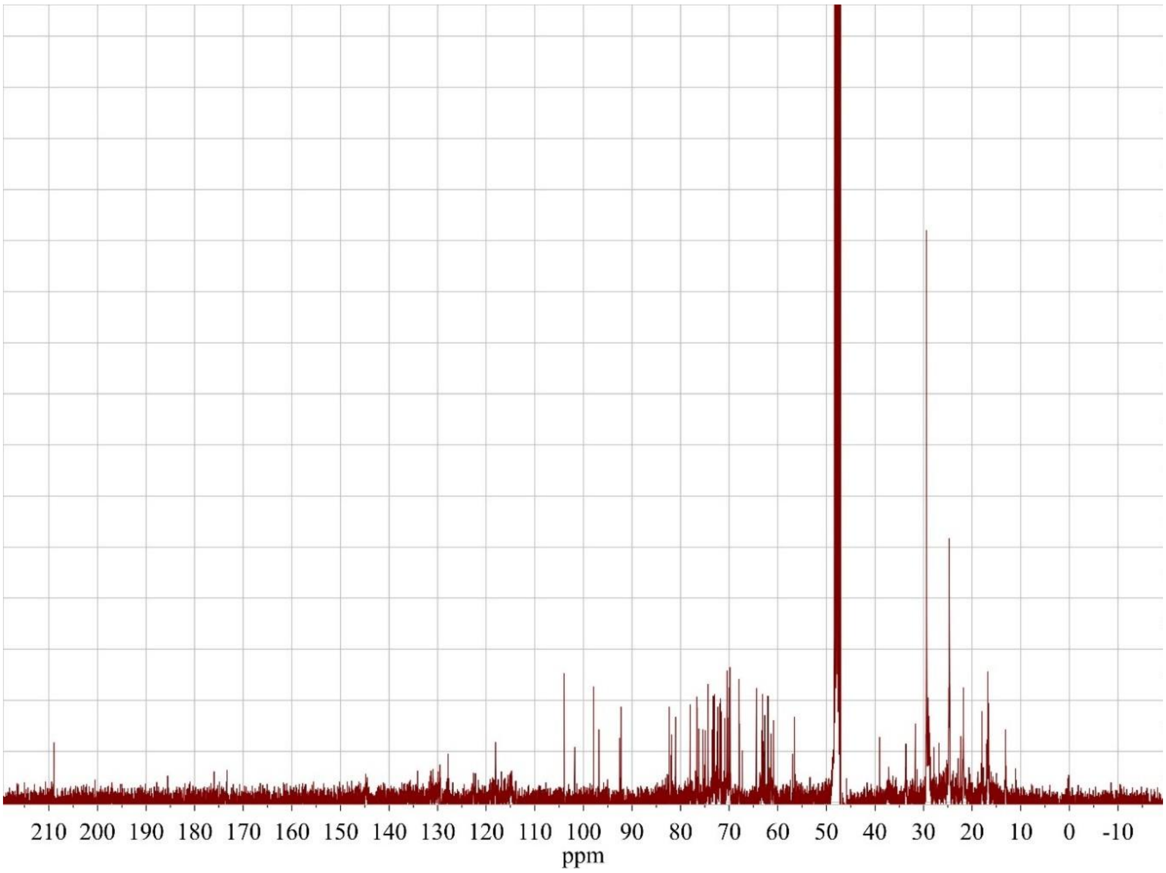

Figure A.5.2.6. $^{13}C\{^1H\}$ NMR spectra of the *Humulus Lupulus* leaves ethanol extract in CD_3OD.

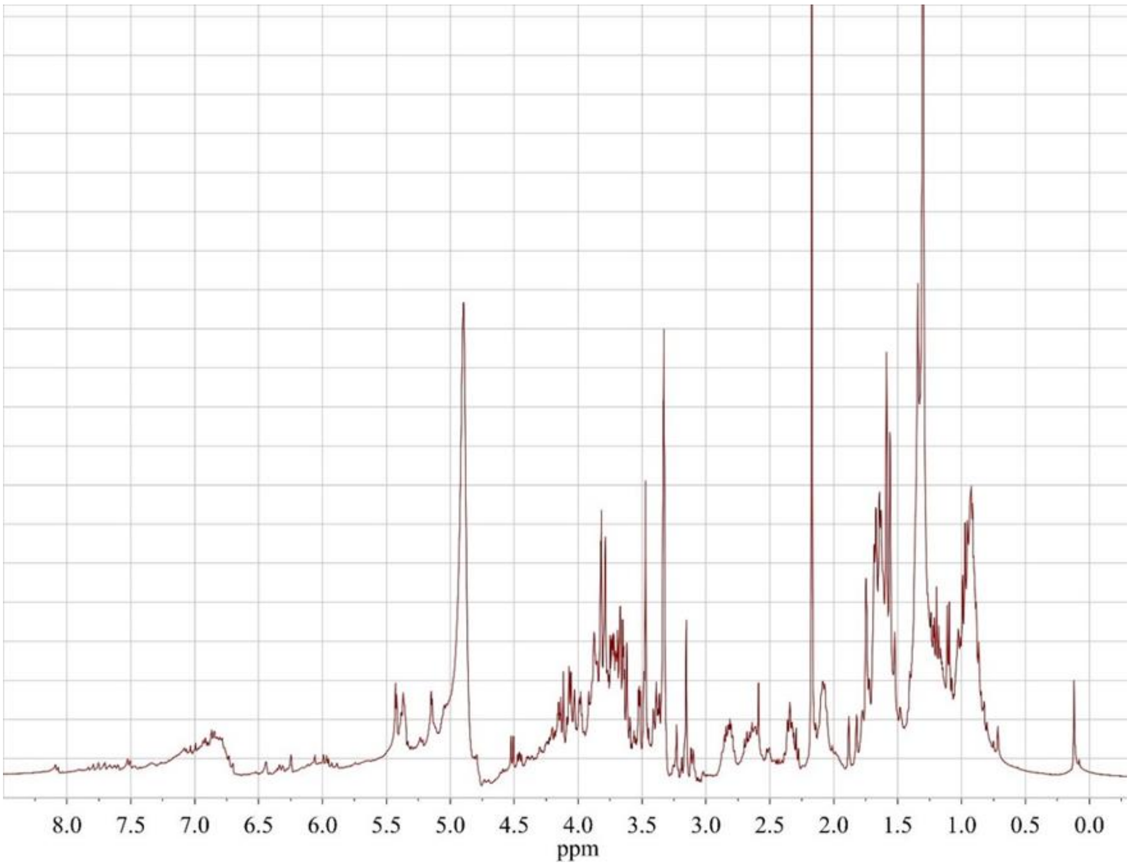

Figure A.5.2.7. ^1H NMR spectra of the *Humulus Lupulus* leaves $scCO_2$ extract in $(CD_3)_2CO$.

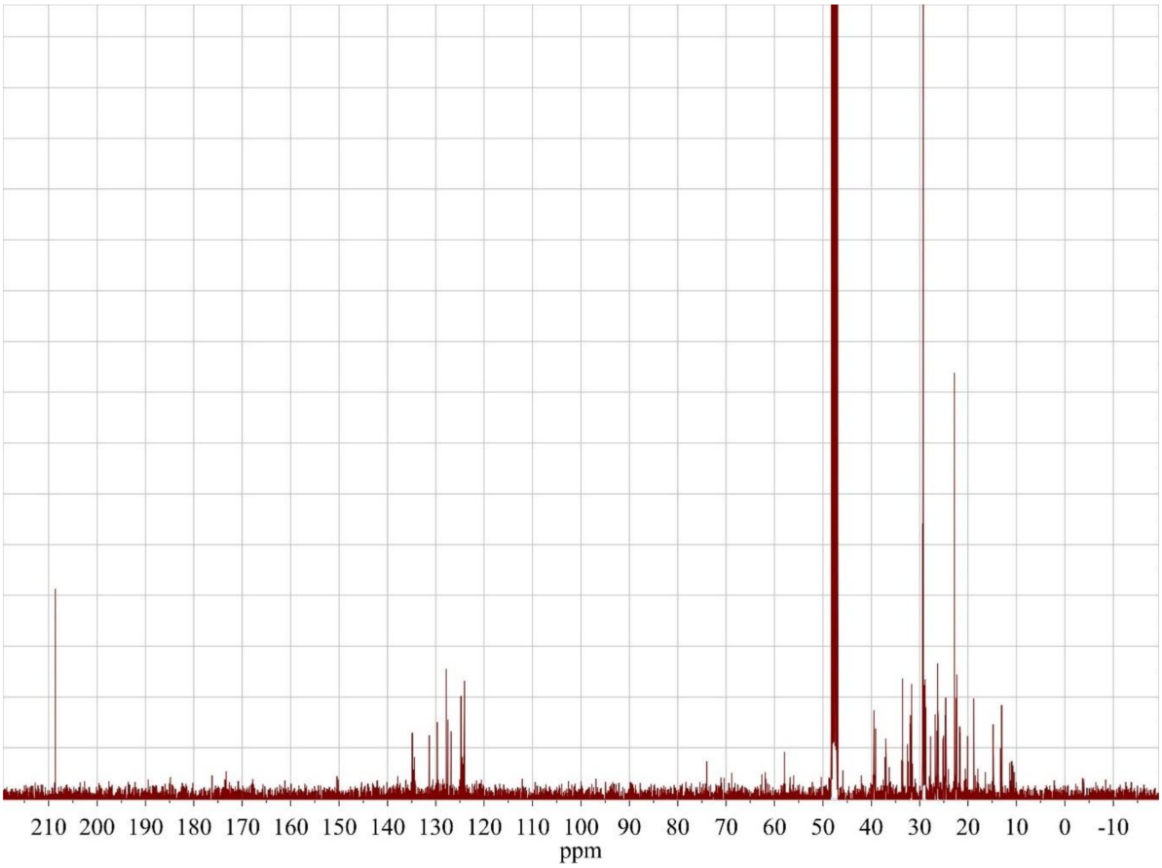

Figure A.5.2.8. $^{13}C\{^1H\}$ NMR spectra of the *Humulus Lupulus* leaves $scCO_2$ extract in CD_3OD.

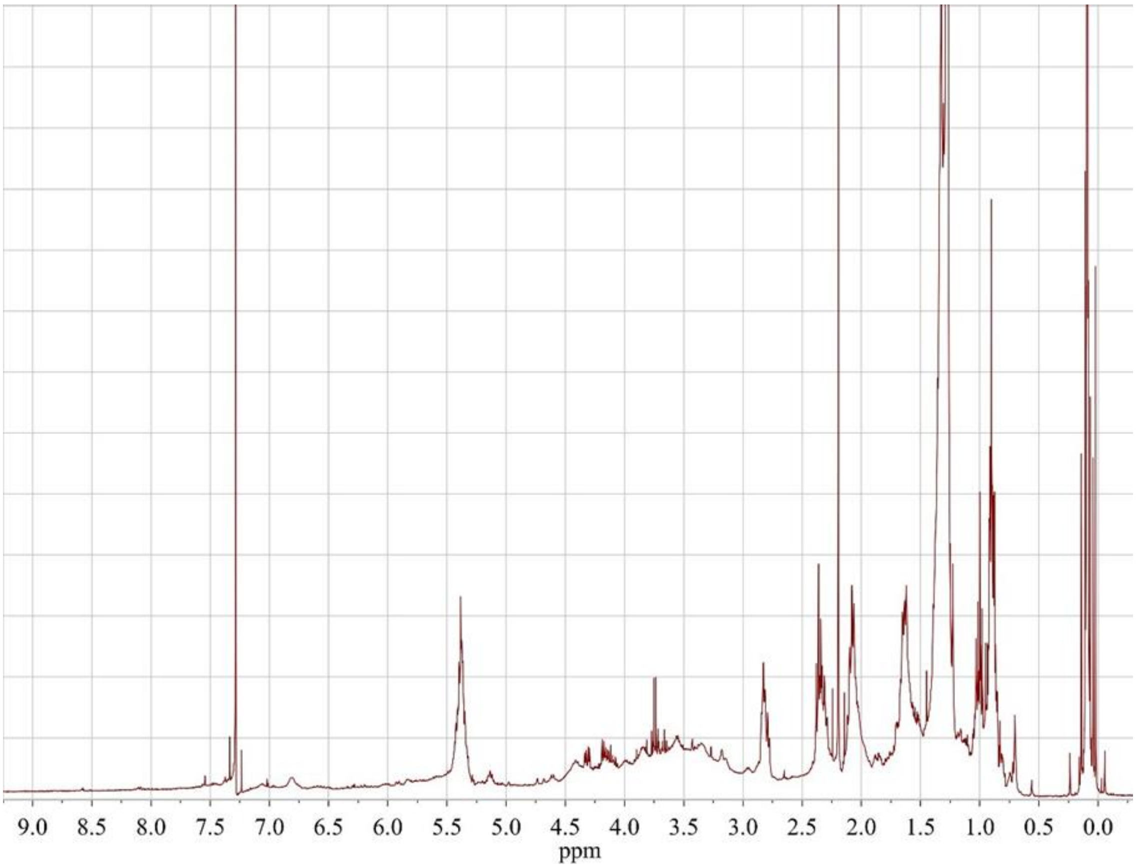

Figure A.5.2.9. ^1H NMR spectra of the *Datura Stramonium* ethanol extract in $CDCl_3$.

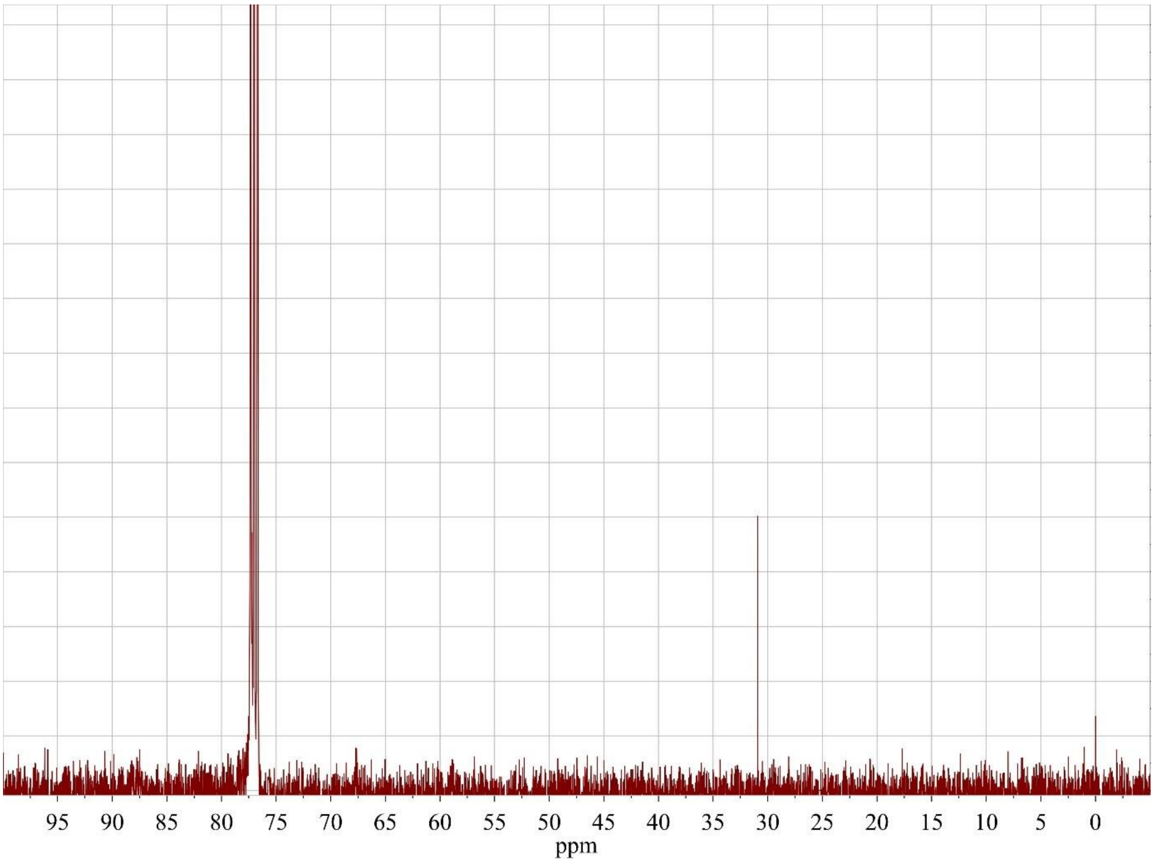

Figure A.5.2.10. $^{13}C\{^1H\}$ NMR spectra of the *Datura Stramonium* ethanol extract in $CDCl_3$.

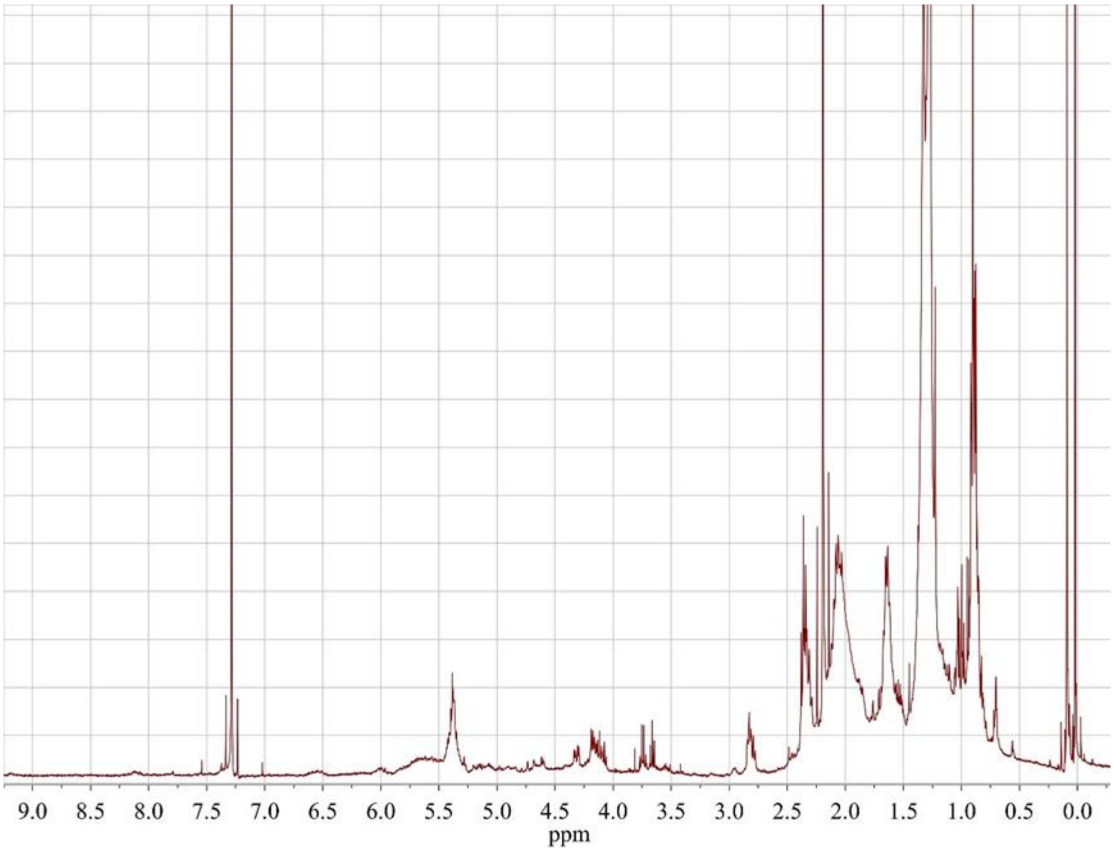

Figure A.5.2.11. ^1H NMR spectra of the *Datura Stramonium* $scCO_2$ extract in $CDCl_3$.

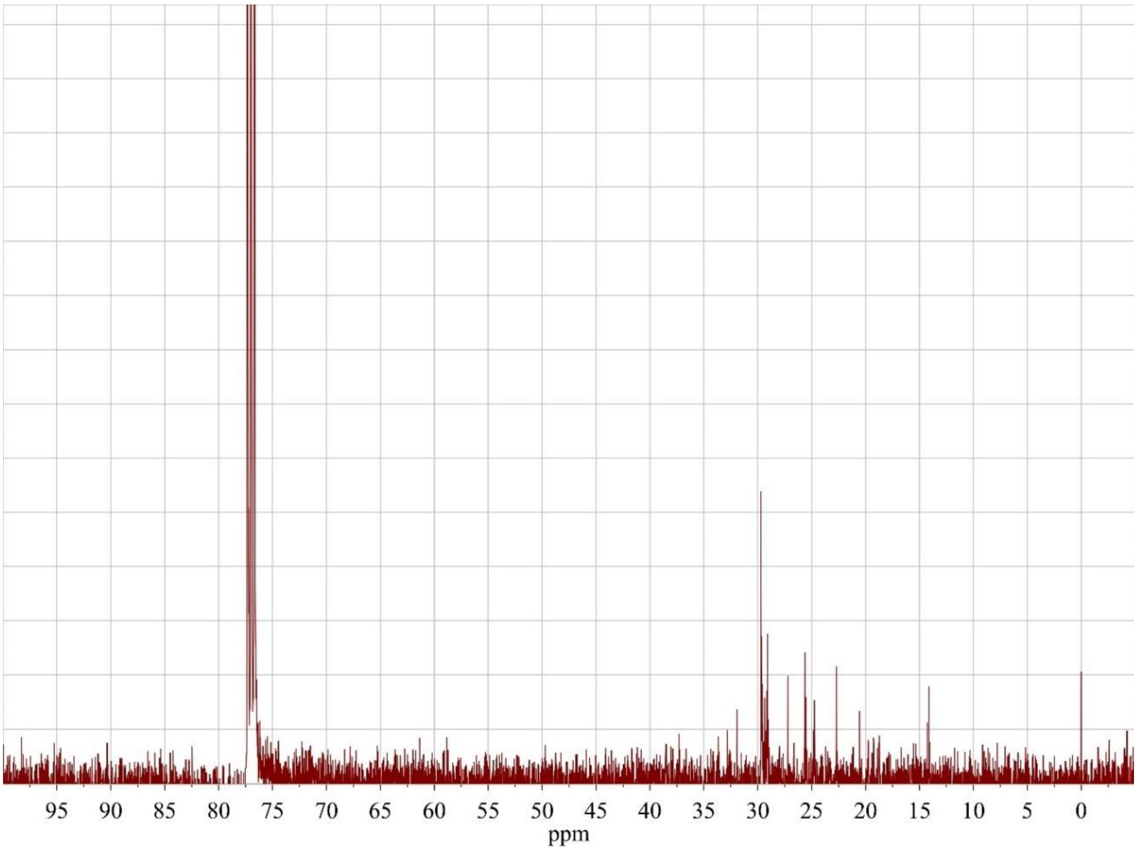

Figure A.5.2.12. $^{13}C\{^1H\}$ NMR spectra of the *Datura Stramonium* $scCO_2$ extract in $CDCl_3$.

A-5.3 Supercritical CO_2 as a green solvent for the circular economy: Extraction of fatty acids from fruit pomace

GC chromatograms

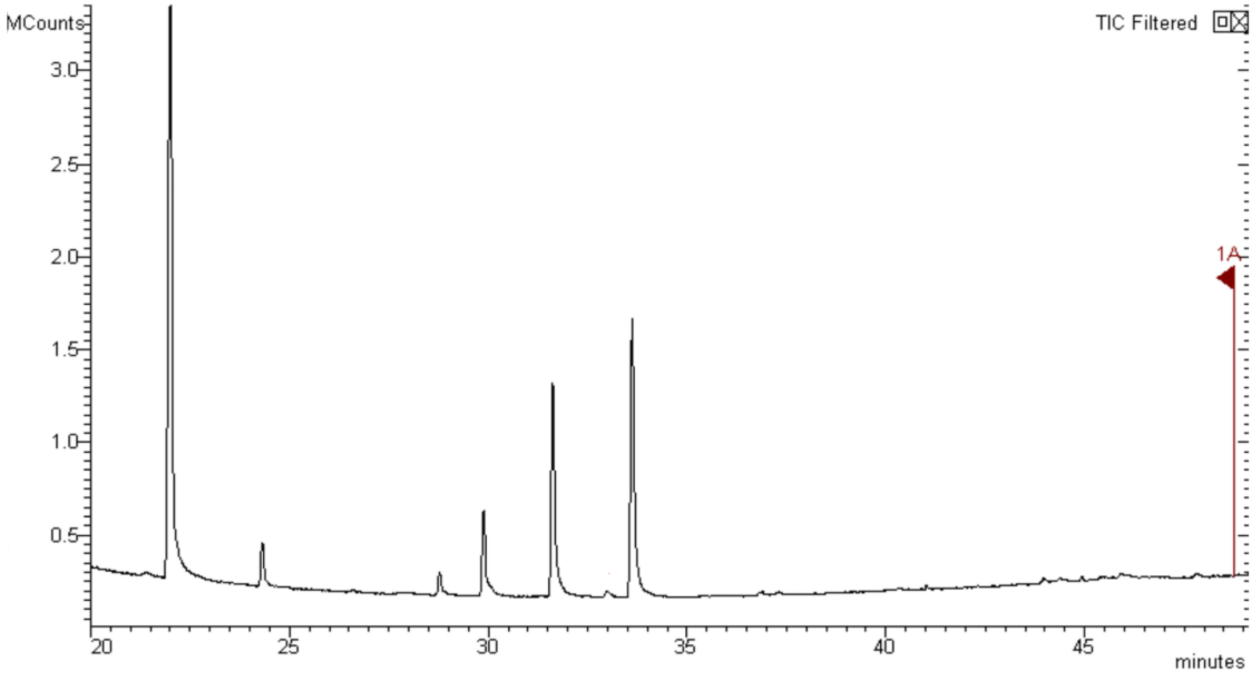

Figure A.5.3.1. GC chromatogram of hexane extract of wild strawberry; peak at 22 minutes is relative to the internal standard methyl pentadecanoate.

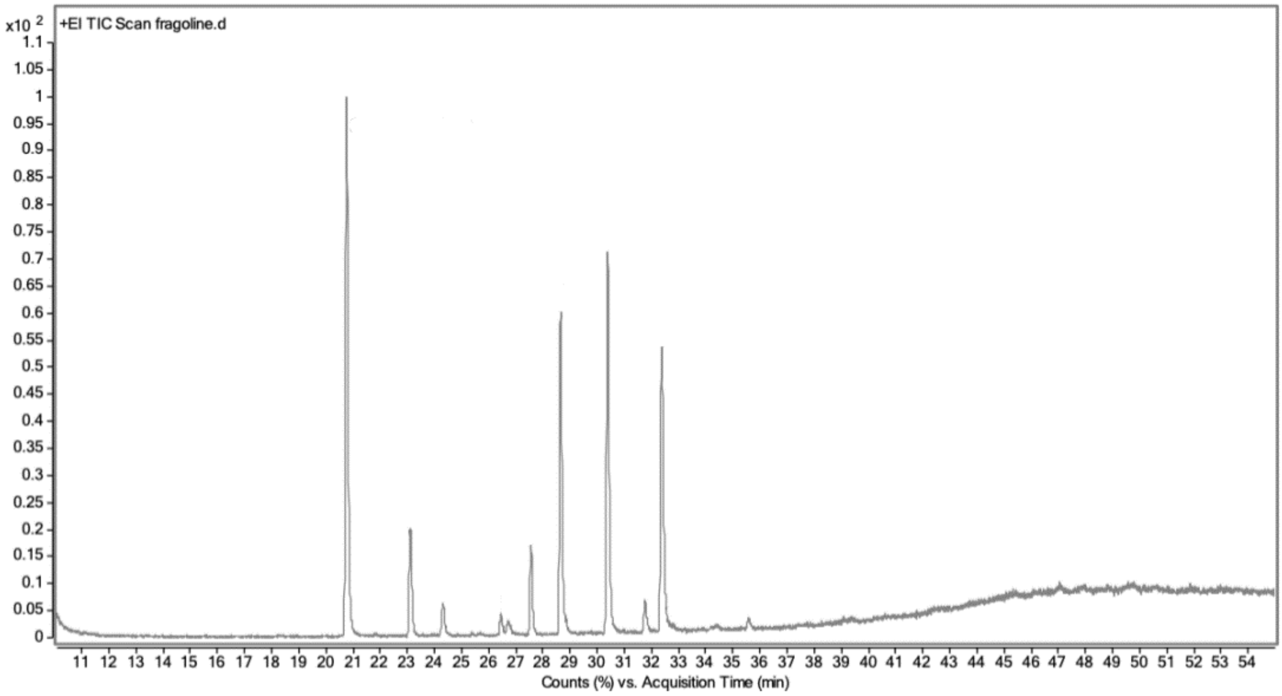

Figure A.5.3.2. GC chromatogram of $scCO_2$ extract of wild strawberry; peak at 21 minutes is relative to the internal standard methyl pentadecanoate.

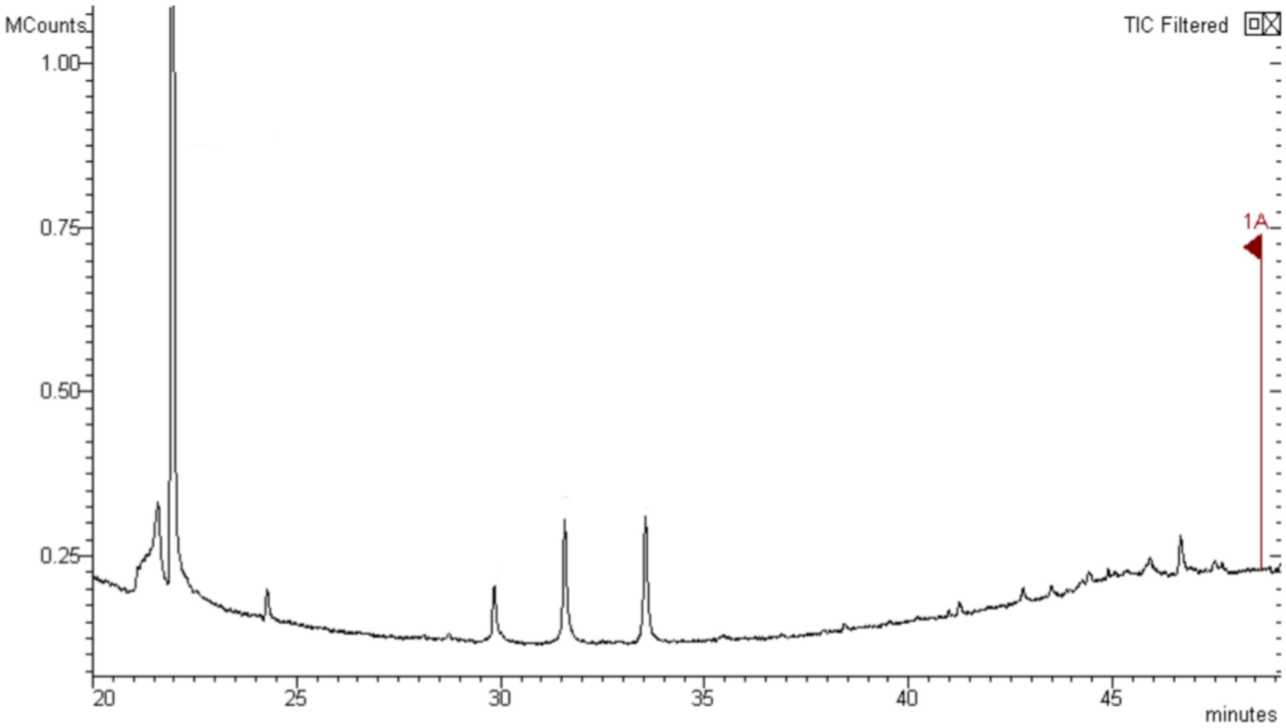

Figure A.5.3.3. GC chromatogram of hexane extract of blueberry; peak at 22 minutes is relative to the internal standard methyl pentadecanoate.

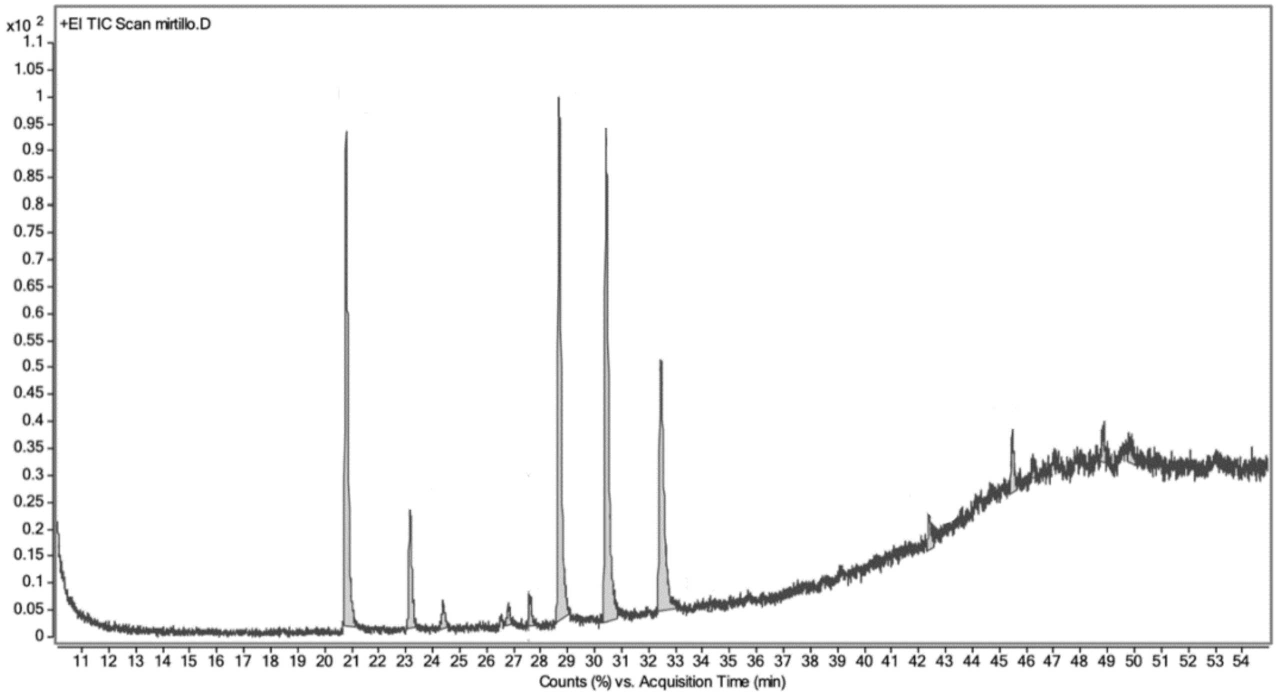

Figure A.5.3.4. GC chromatogram of $scCO_2$ extract of blueberry; peak at 21 minutes is relative to the internal standard methyl pentadecanoate.

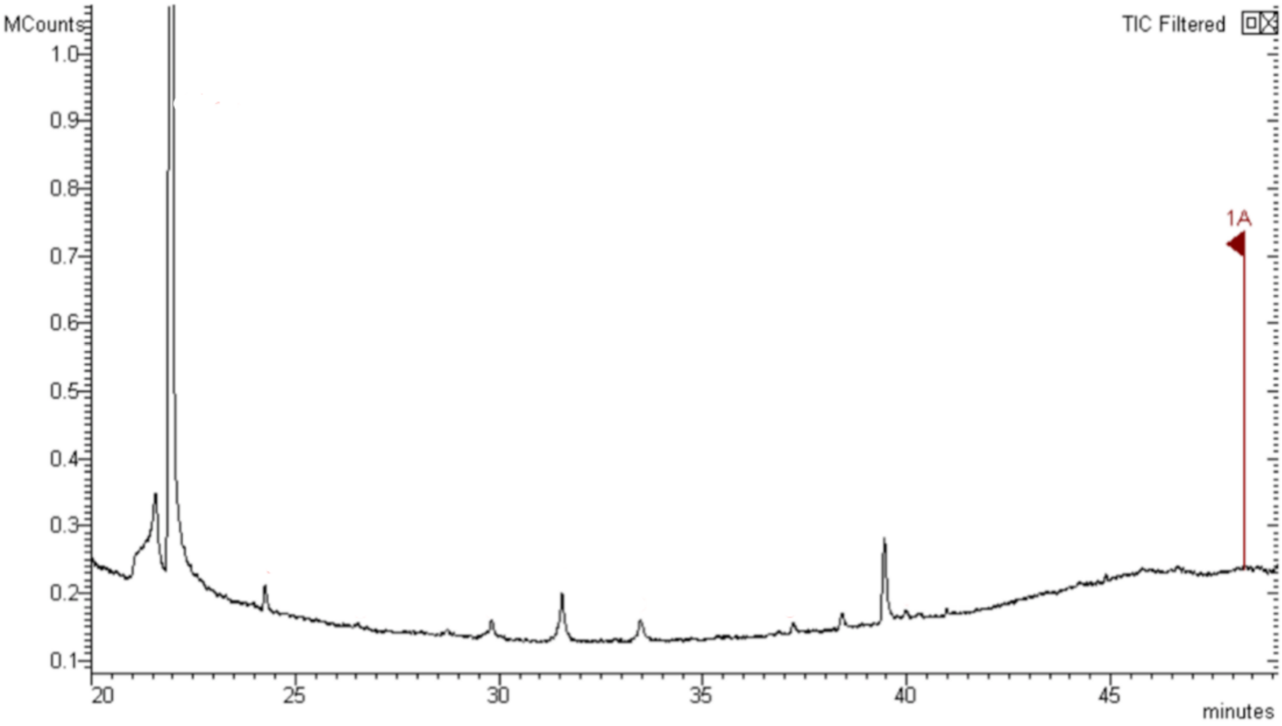

Figure A.5.3.5. GC chromatogram of hexane extract of pomegranate; peak at 22 minutes is relative to the internal standard methyl pentadecanoate.

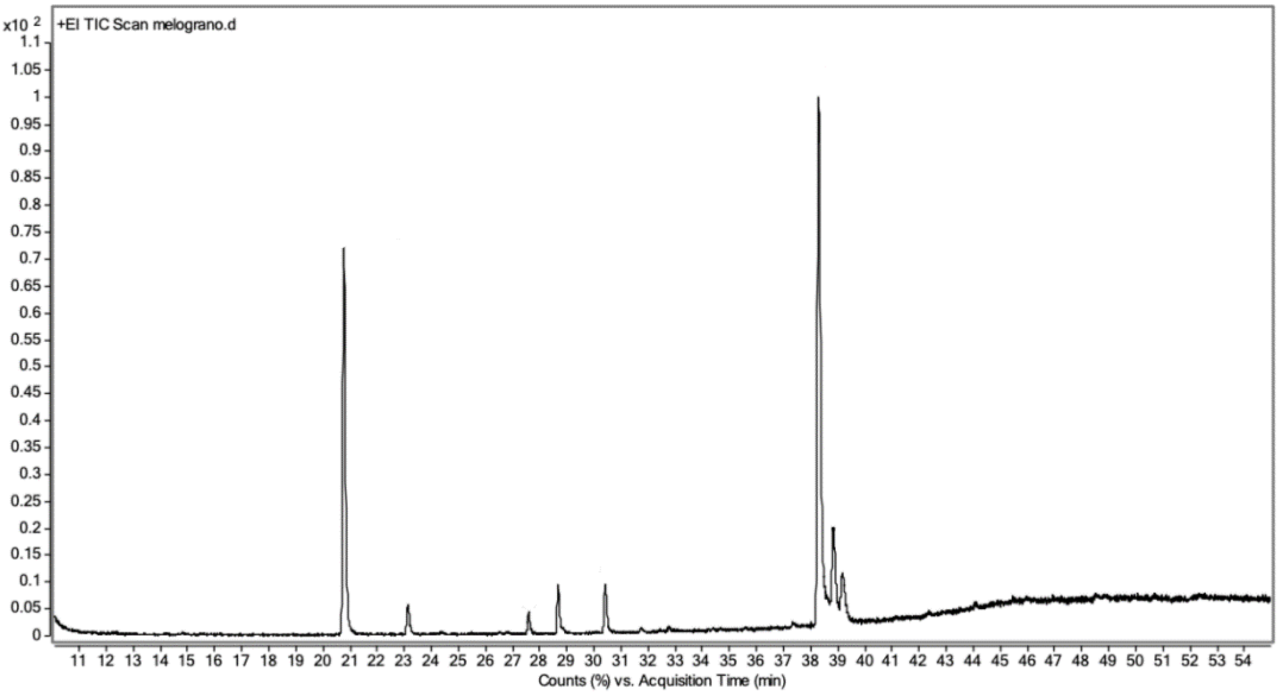

Figure A.5.3.6. GC chromatogram of scCO$_2$ extract of pomegranate; peak at 21 minutes is relative to the internal standard methyl pentadecanoate

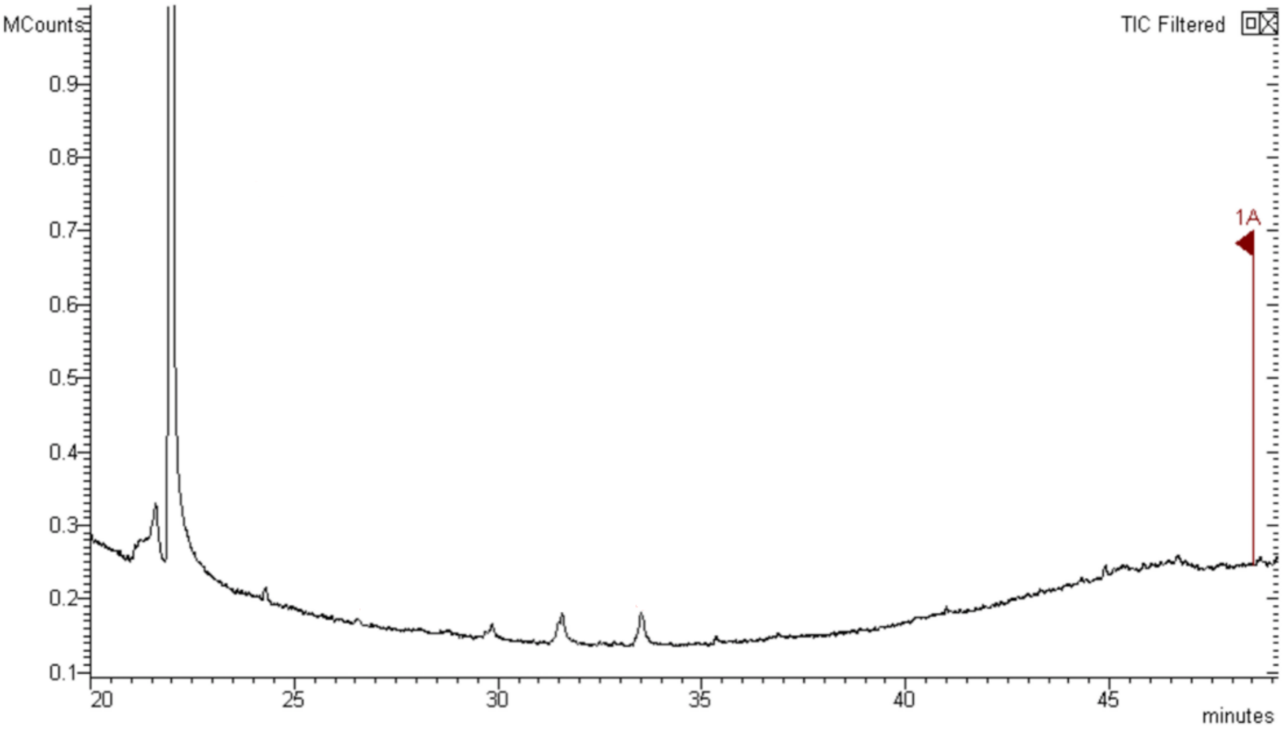

Figure A.5.3.7. GC chromatogram of hexane extract of blackberry; peak at 22 minutes is relative to the internal standard methyl pentadecanoate.

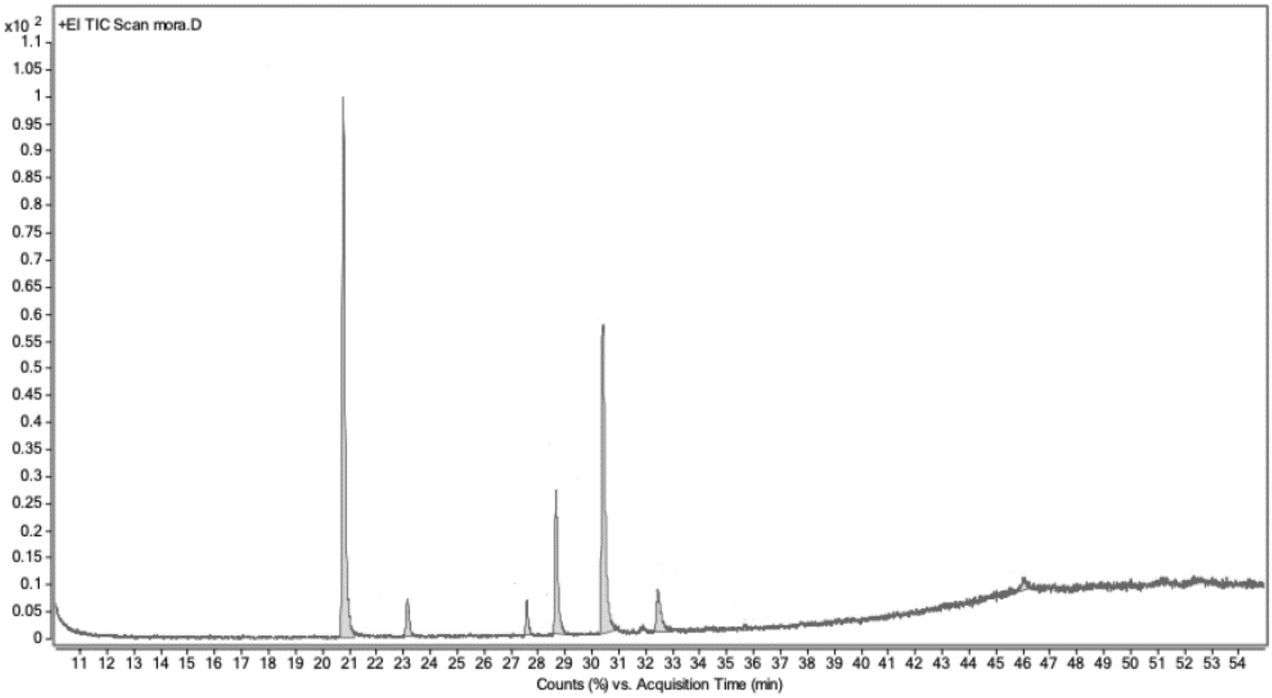

Figure A.5.3.8. GC chromatogram of $scCO_2$ extract of blackberry; peak at 21 minutes is relative to the internal standard methyl pentadecanoate

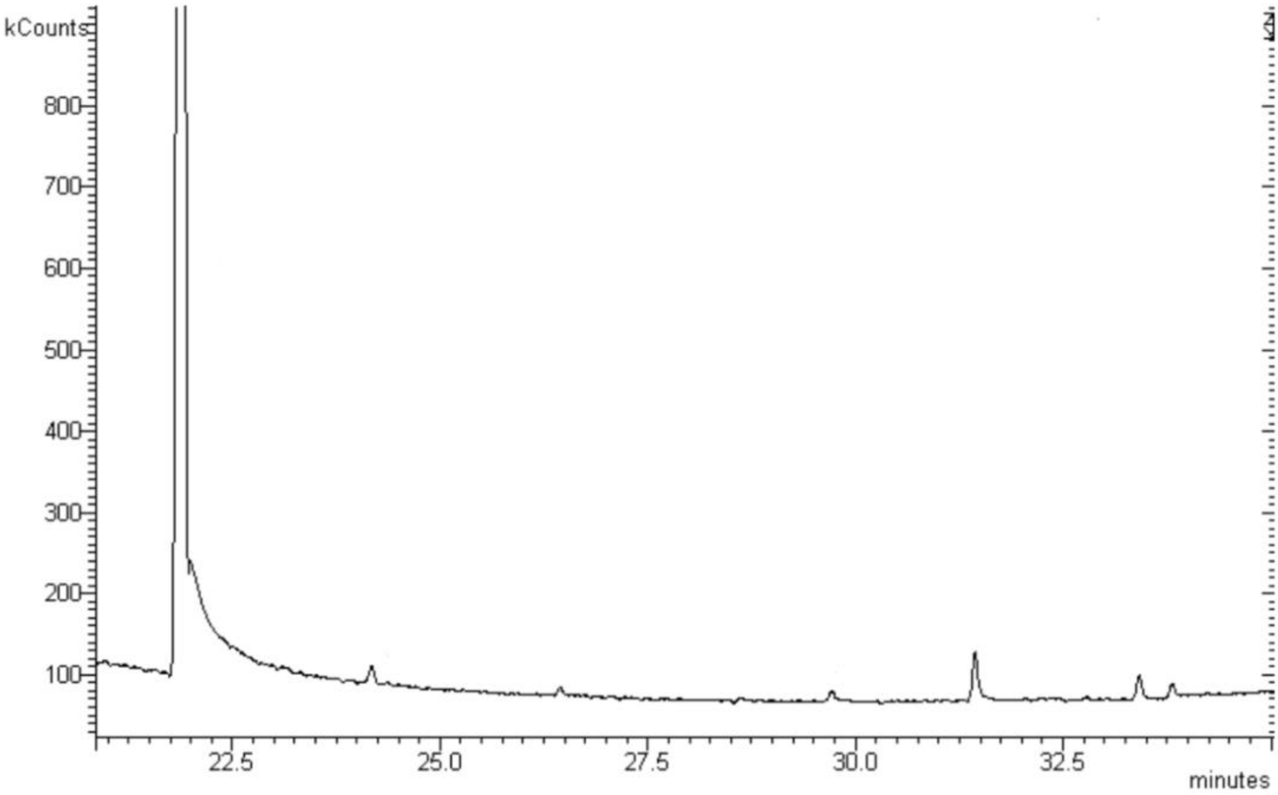

Figure A.5.3.9. GC chromatogram of hexane extract of raspberry; peak at 22 minutes is relative to the internal standard methyl pentadecanoate.

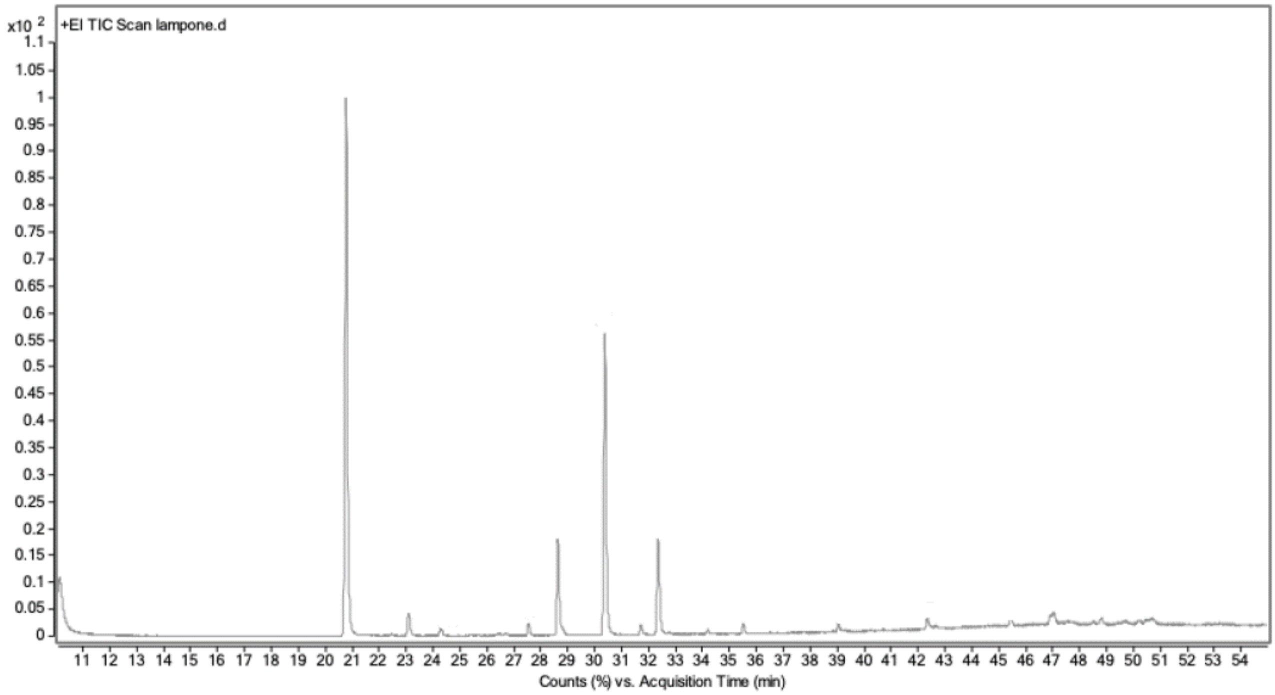

Figure A.5.3.10. GC chromatogram of $scCO_2$ extract of raspberry; peak at 21 minutes is relative to the internal standard methyl pentadecanoate

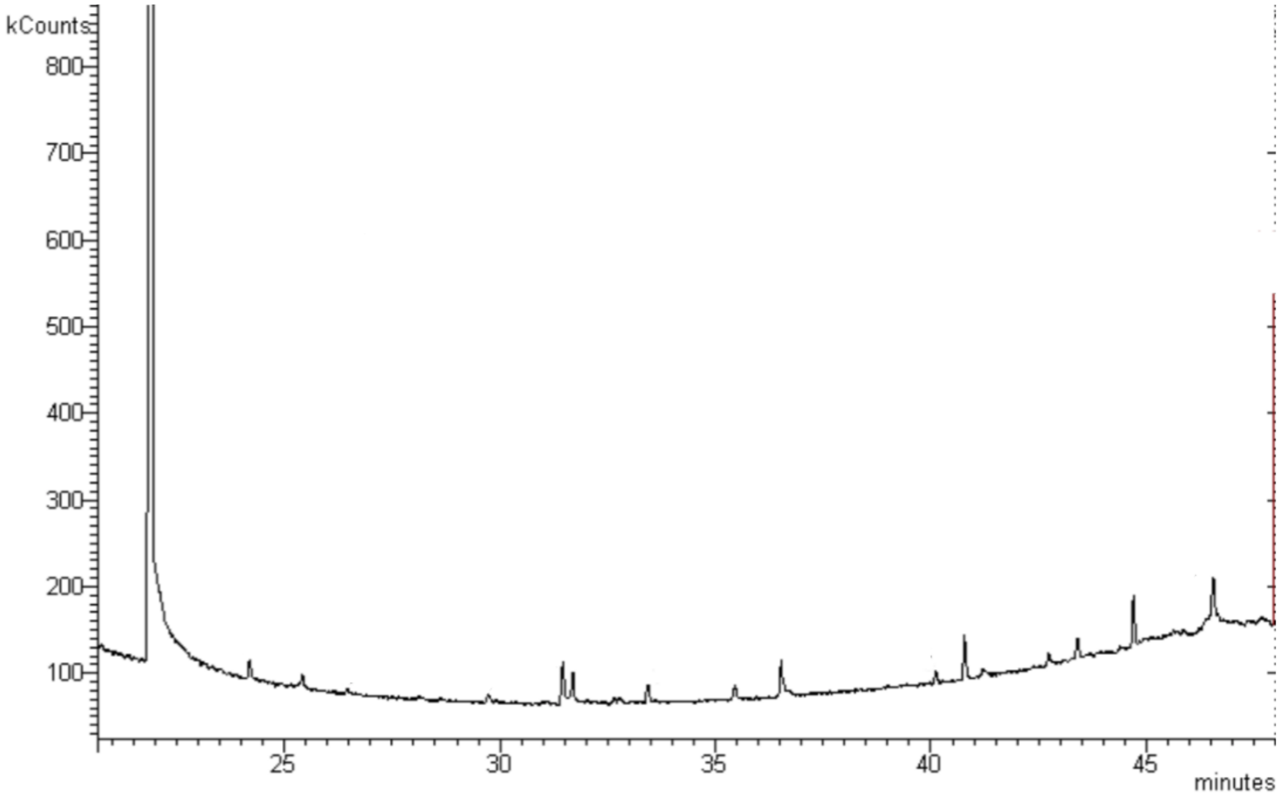

Figure A.5.3.11. GC chromatogram of hexane extract of blackcurrant; peak at 22 minutes is relative to the internal standard methyl pentadecanoate.

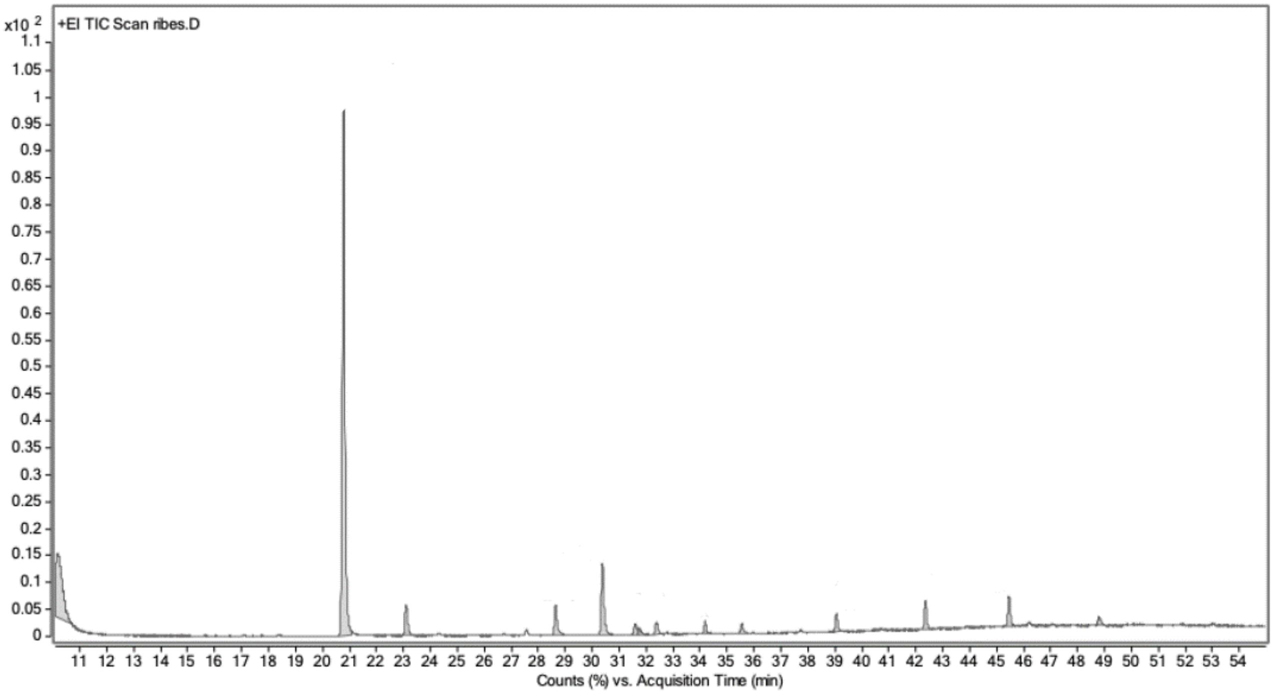

Figure A.5.3.12. GC chromatogram of scCO$_2$ extract of blackcurrant; peak at 21 minutes is relative to the internal standard methyl pentadecanoate

Mass spectra of fatty acids

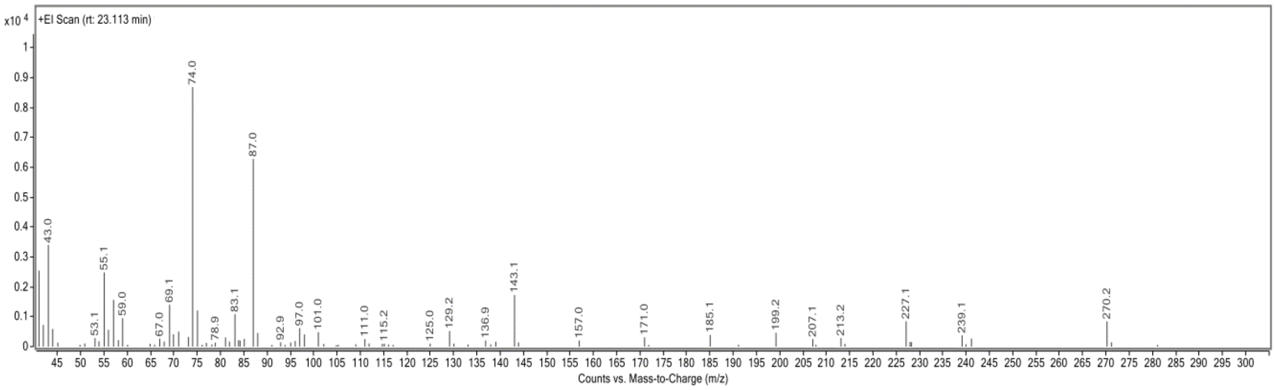

Figure A.5.3.13. Mass spectrum of palmitic acid (**1**).

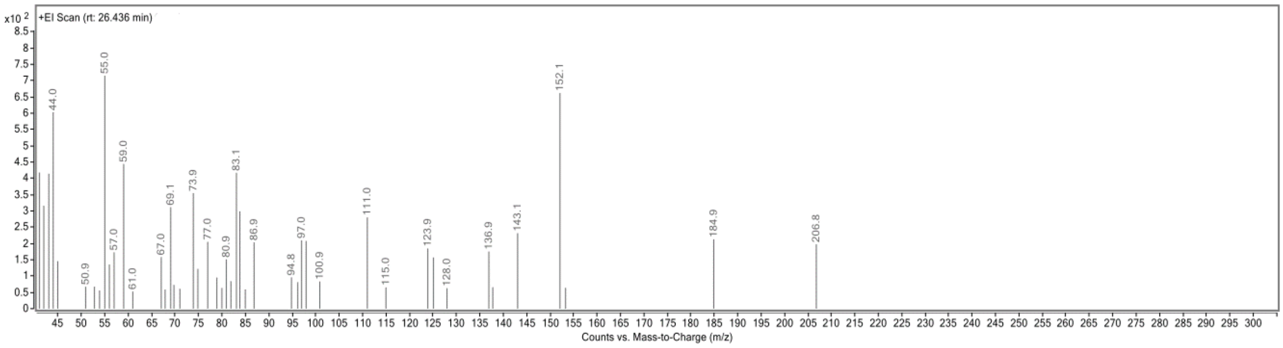

Figure A.5.3.14. Mass spectrum of azelaic acid (**2**).

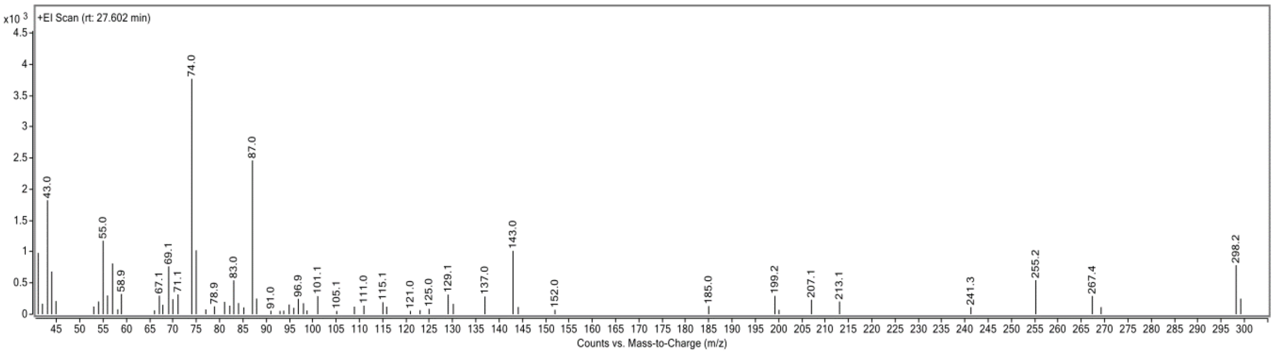

Figure A.5.3.15. Mass spectrum of stearic acid (**3**).

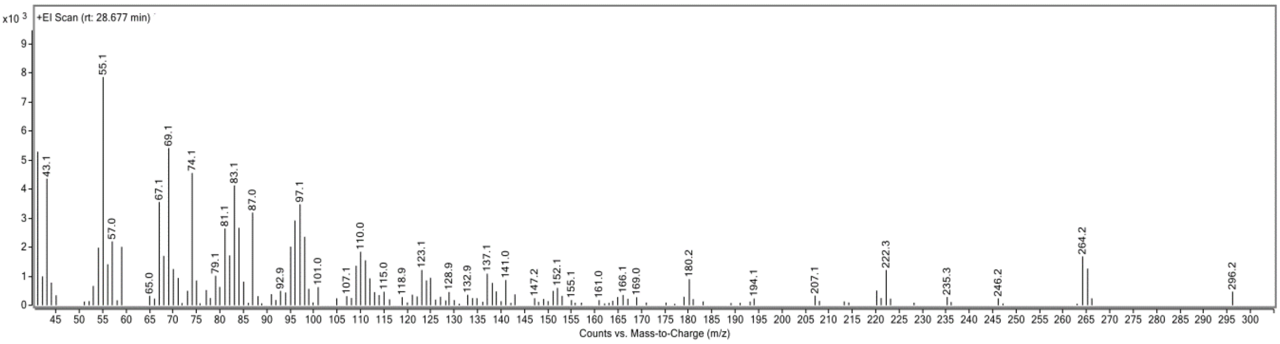

Figure A.5.3.16. Mass spectrum of oleic acid (**4**).

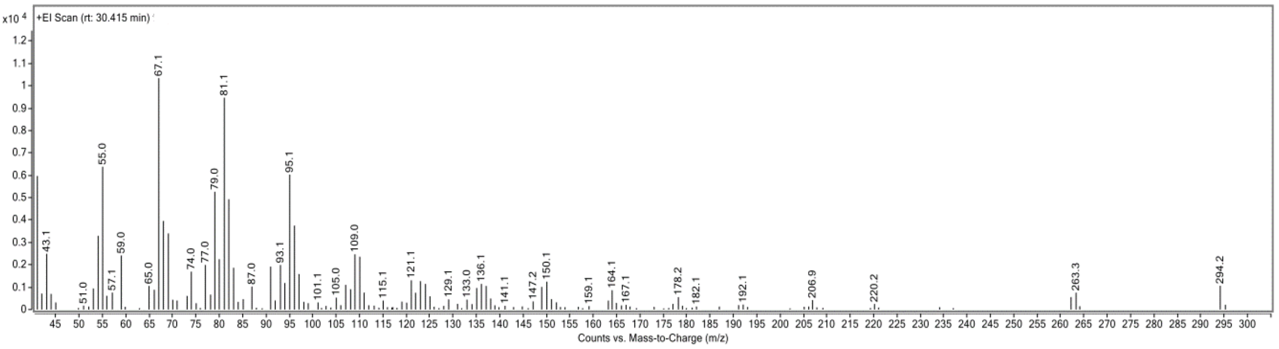

Figure A.5.3.17. Mass spectrum of linoleic acid (**5**).

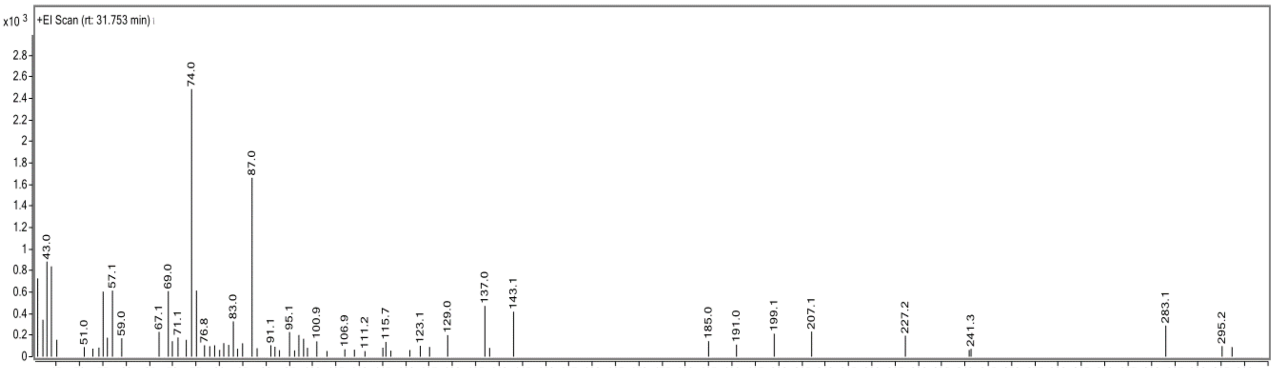

Figure A.5.3.18. Mass spectrum of eicosanoic acid (**6**).

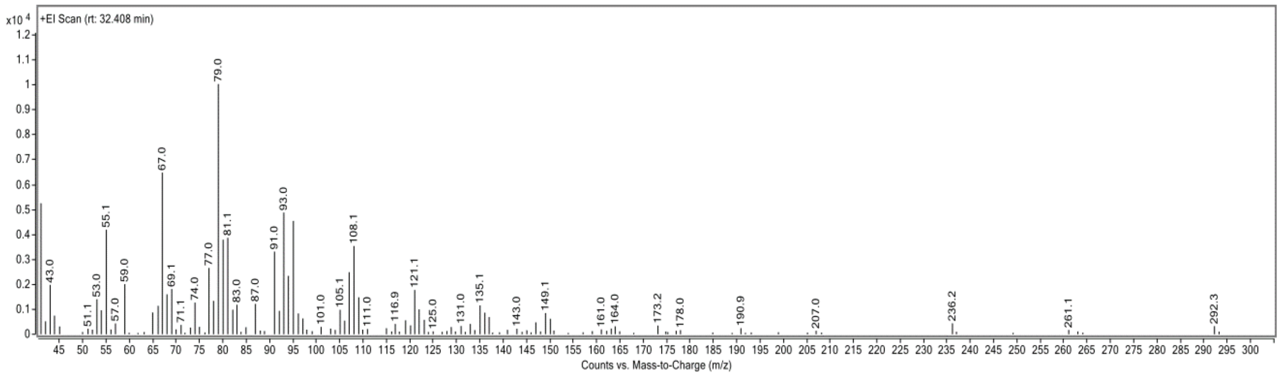

Figure A.5.3.19. Mass spectrum of α-linolenic acid (**7**).

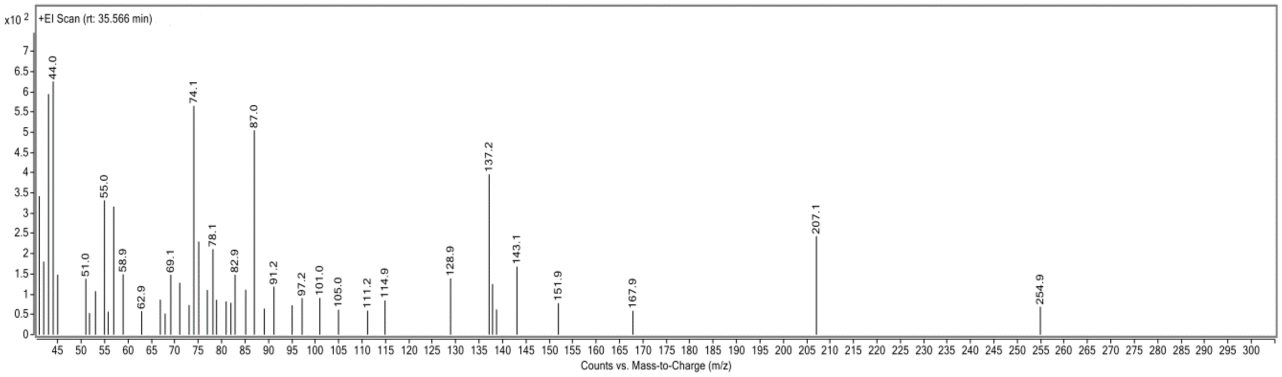

Figure A.5.3.20. Mass spectrum of behenic acid (**8**).

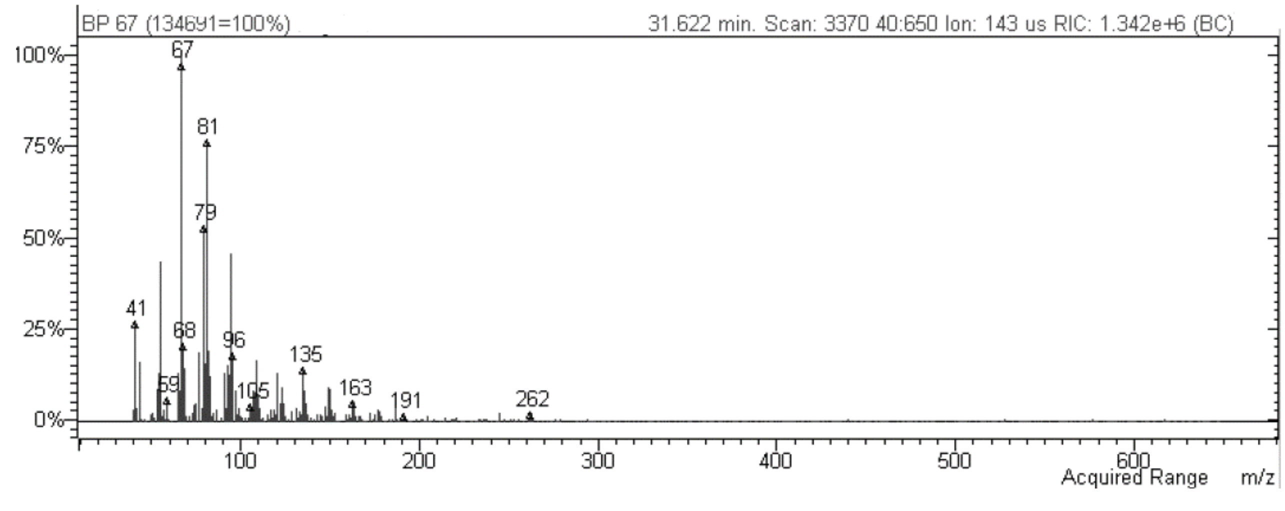

Figure A.5.3.21. Mass spectrum of 9-12 octadecenoic acid (**9**).

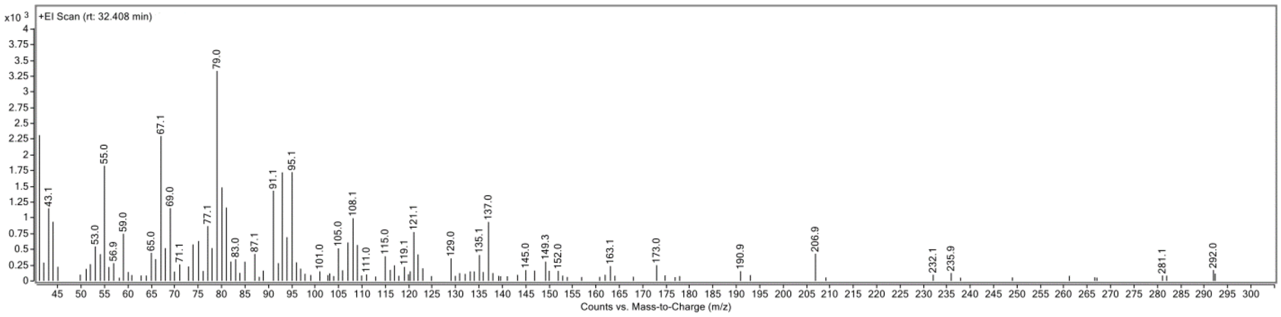

Figure A.5.3.22. Mass spectrum of γ-linolenic acid (**10**).

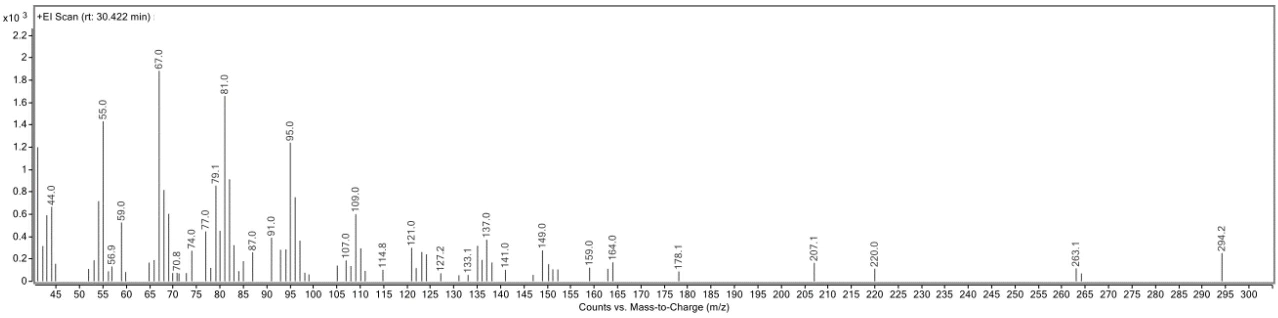

Figure A.5.3.23. Mass spectrum of linolelaidic acid (**11**).

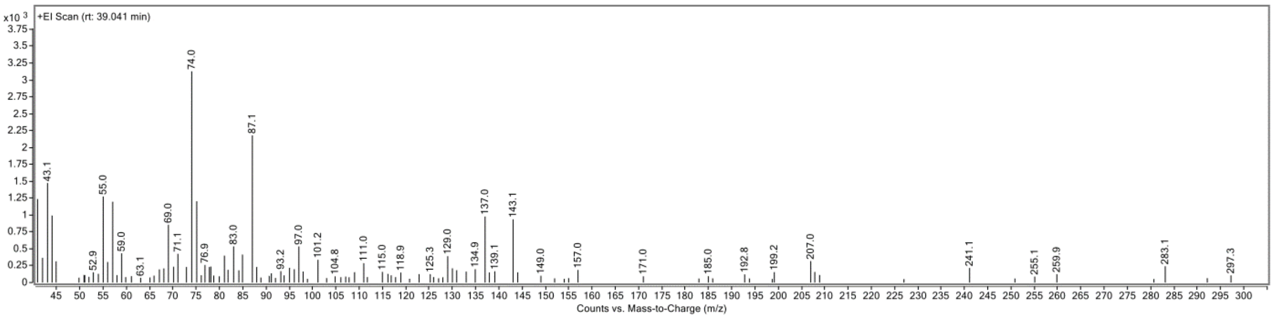

Figure A.5.3.24. Mass spectrum of tetracosanoic acid (**12**).

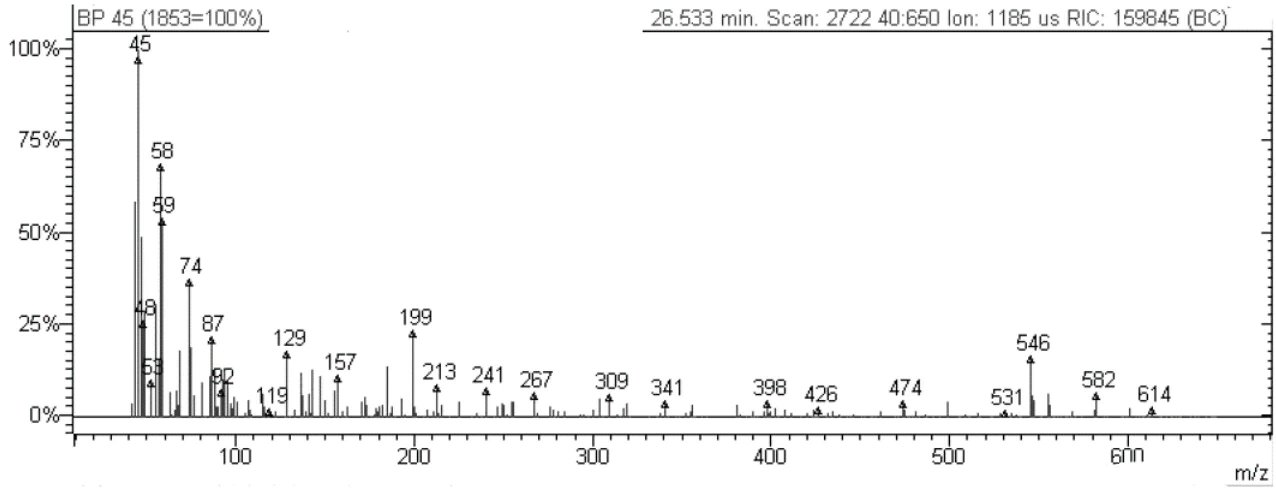

Figure A.5.3.25. Mass spectrum of decanoic acid (**13**).

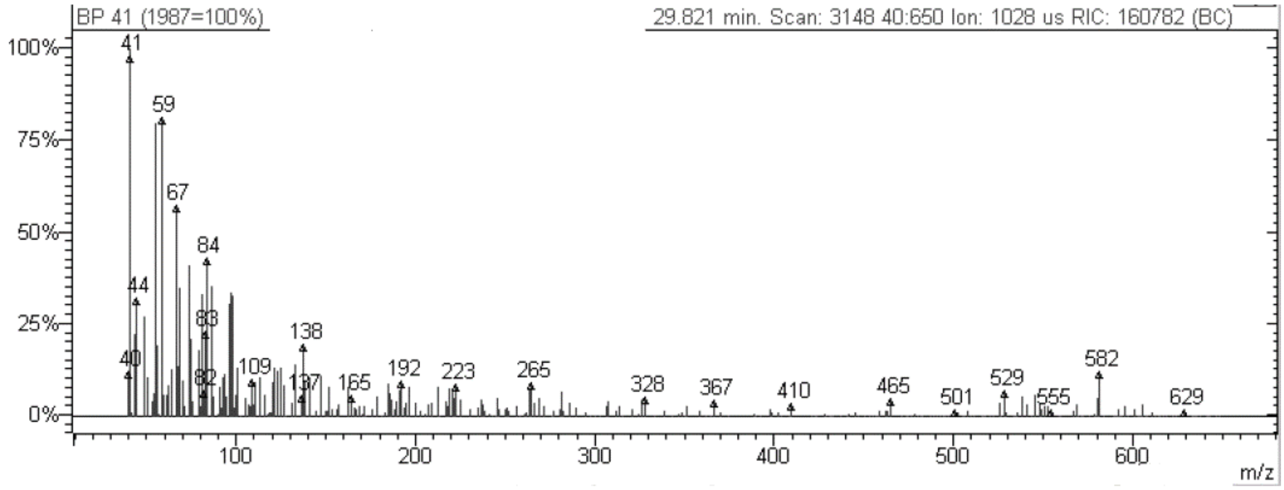

Figure A.5.3.26. Mass spectrum of *trans*-vaccenic acid (**14**).

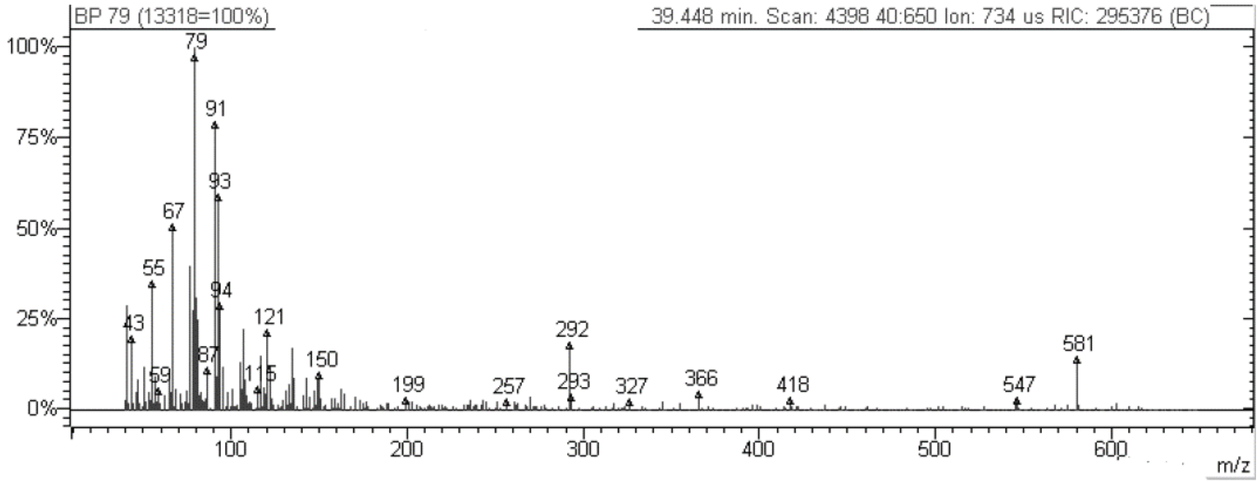

Figure A.5.3.27. Mass spectrum of arachidonic acid (**15**).

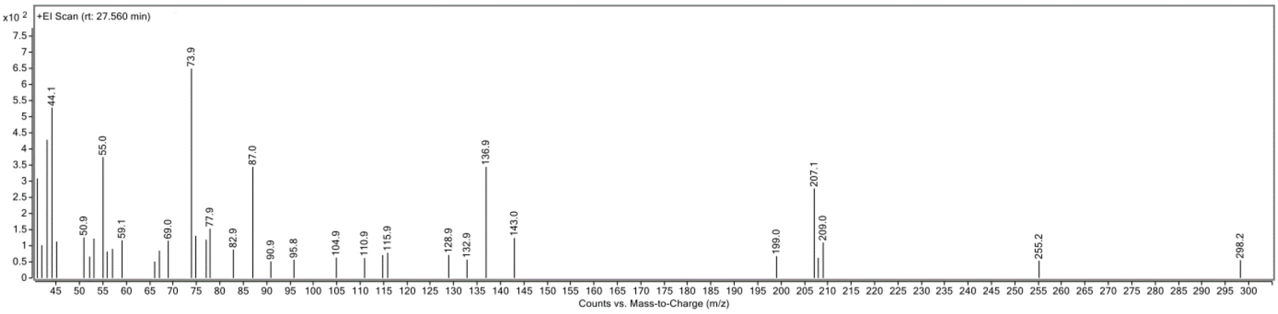

Figure A.5.3.28. Mass spectrum of pentadecanoic acid (**16**).

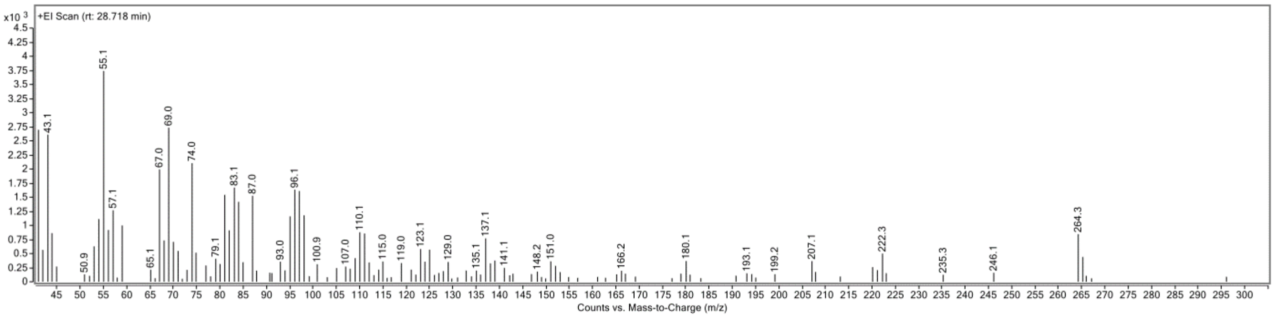

Figure A.5.3.29. Mass spectrum of undecanoic acid (**17**).

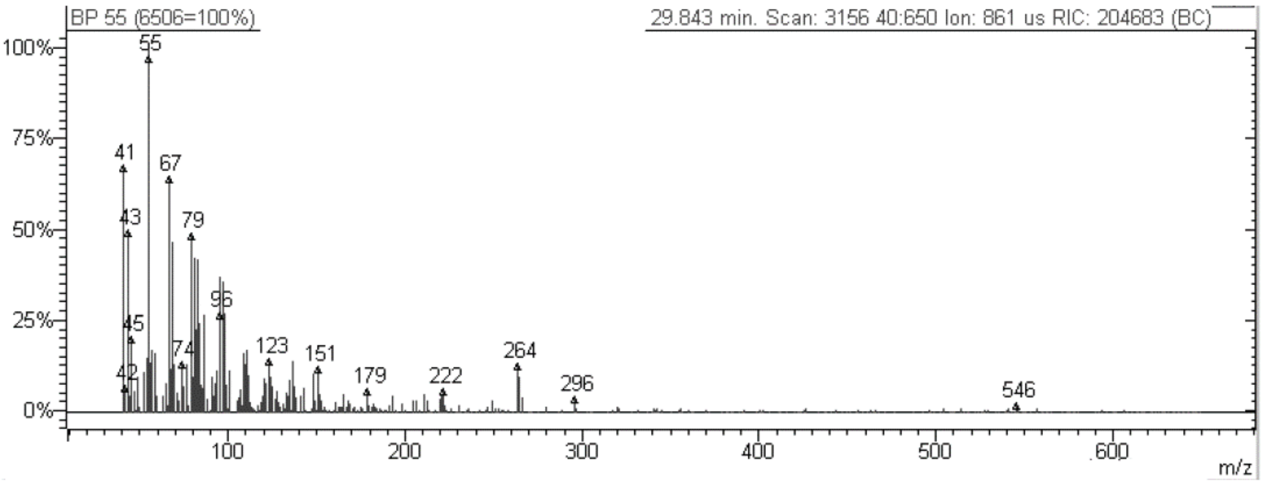

Figure A.5.3.30. Mass spectrum of 10-octadecenoic acid (**18**).

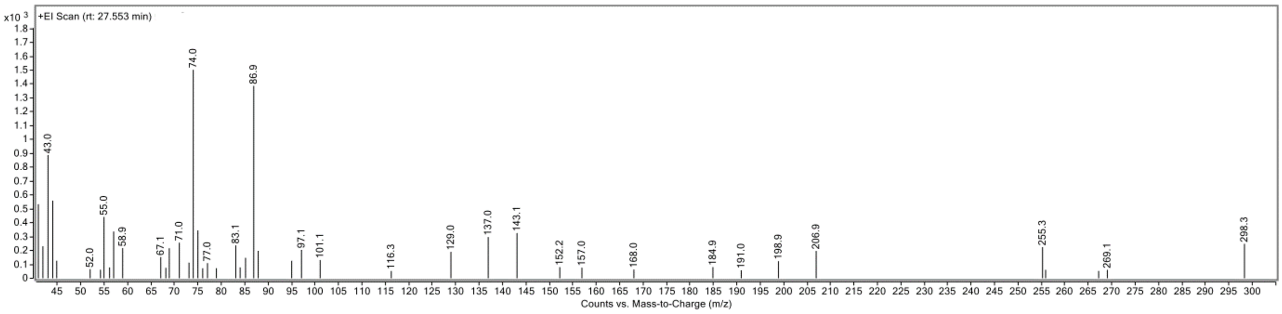

Figure A.5.3.31. Mass spectrum of octadecanoic acid (**19**).

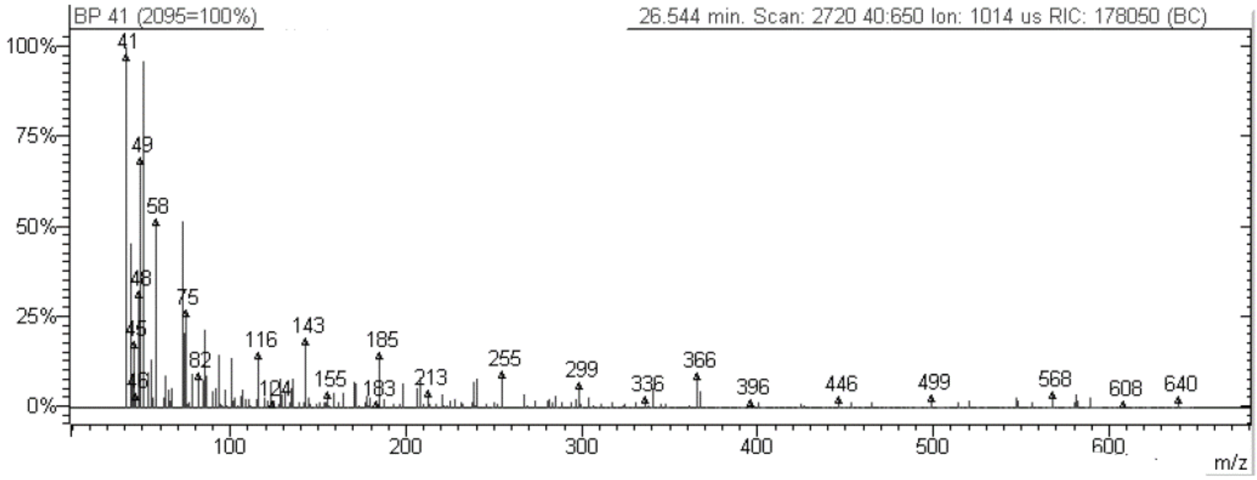

Figure A.5.3.32. Mass spectrum of nonadecanoic acid (**20**).

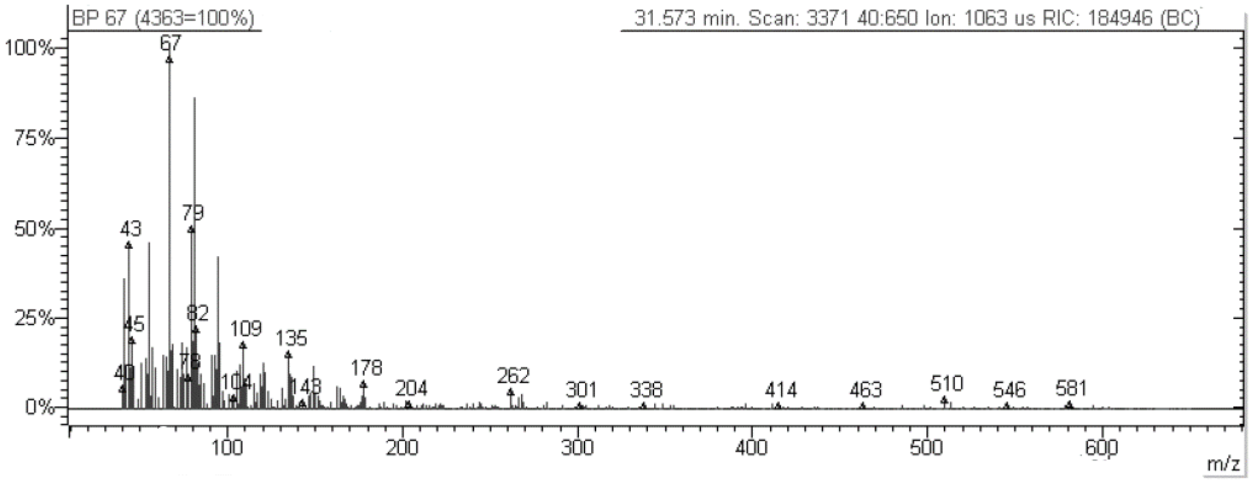

Figure A.5.3.33. Mass spectrum of cyclopropan octanoic acid (**21**).

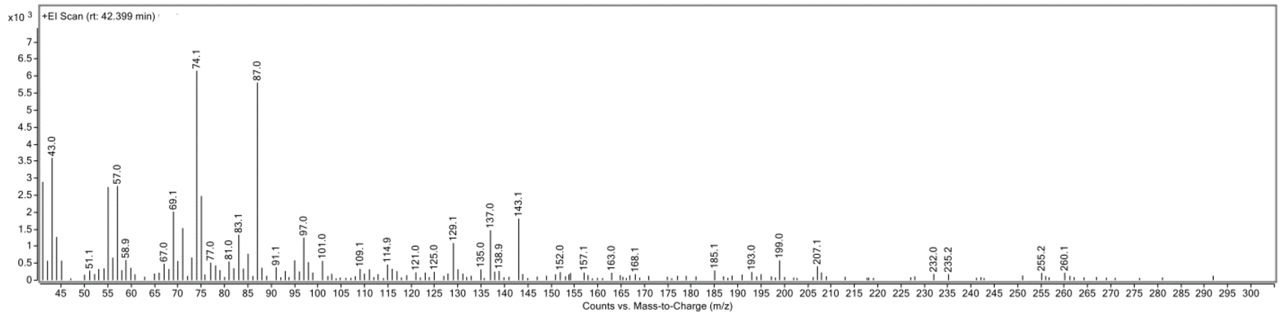

Figure A.5.3.34. Mass spectrum of hexacosanoic acid (**22**).

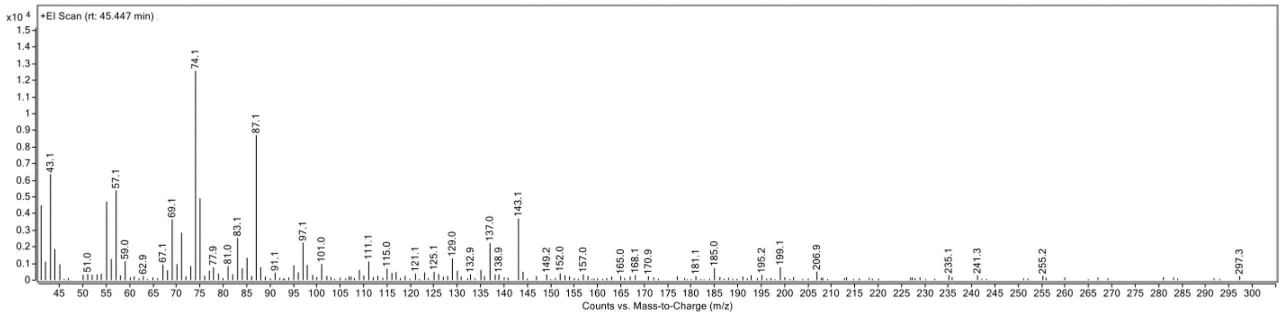

Figure A.5.3.35. Mass spectrum of octacosanoic acid (**23**).

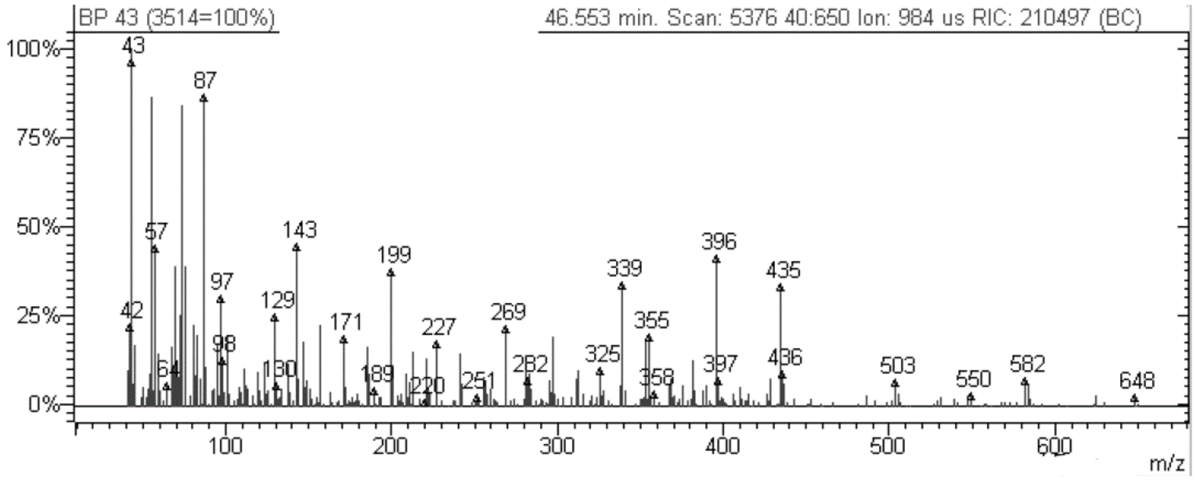

Figure A.5.3.36. Mass spectrum of pentacosanoic acid (**24**).

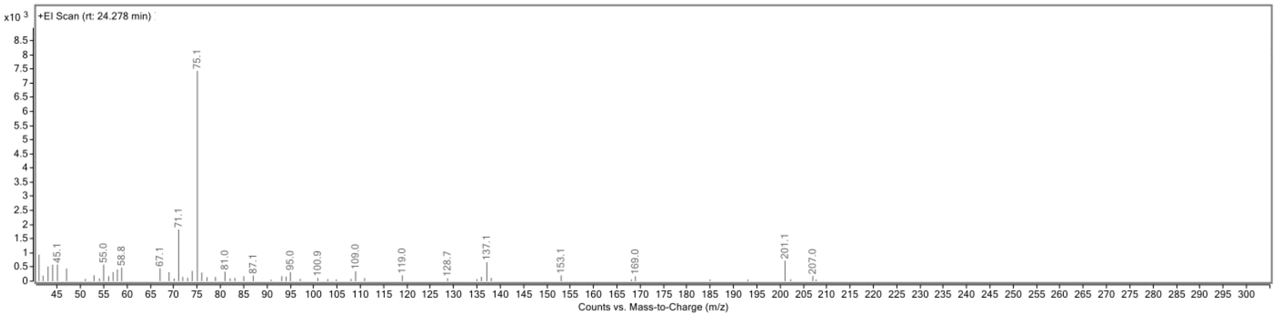

Figure A.5.3.37. Mass spectrum of octanoic acid (**25**).

NMR spectra

For investigation NMR spectra of wild strawberry extracts were conducted using a concentration of 0.01 g/mL in the tube. ^{1}H and$^{13}C\{^{1}H\}$ NMR spectra were collected at 25 °C on a Bruker Ascend 400 operating at 400 MHz for 1H and 100 MHz for 13C. For ^{1}H and $^{13}C\{^{1}H\}$ NMR the chemical shifts (δ) have been reported in parts per million (ppm) relative to the residual non-deuterated solvent as an internal reference and are given in δ values downfield from TMS. ^{1}H NMR spectra are reported in the main text (**Figure 5.3.4**)

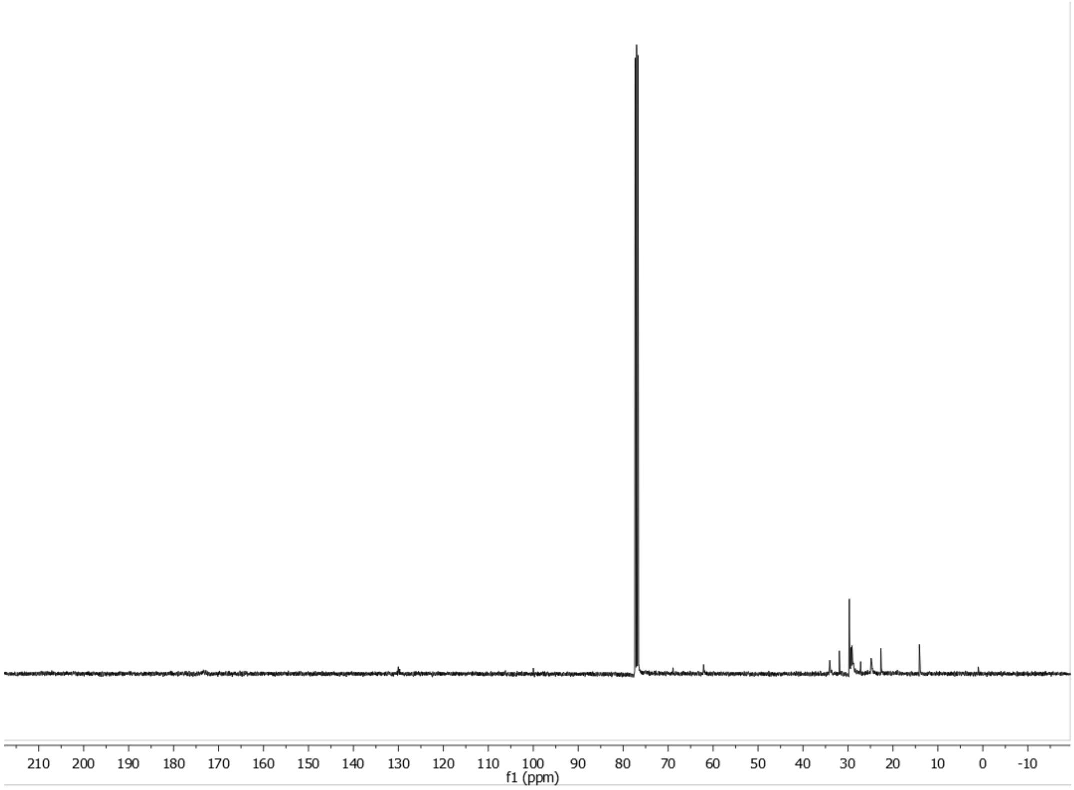

Figure A.5.3.38. ^{13}C NMR spectra of the wild strawberry hexane extract in $CDCl_3$.

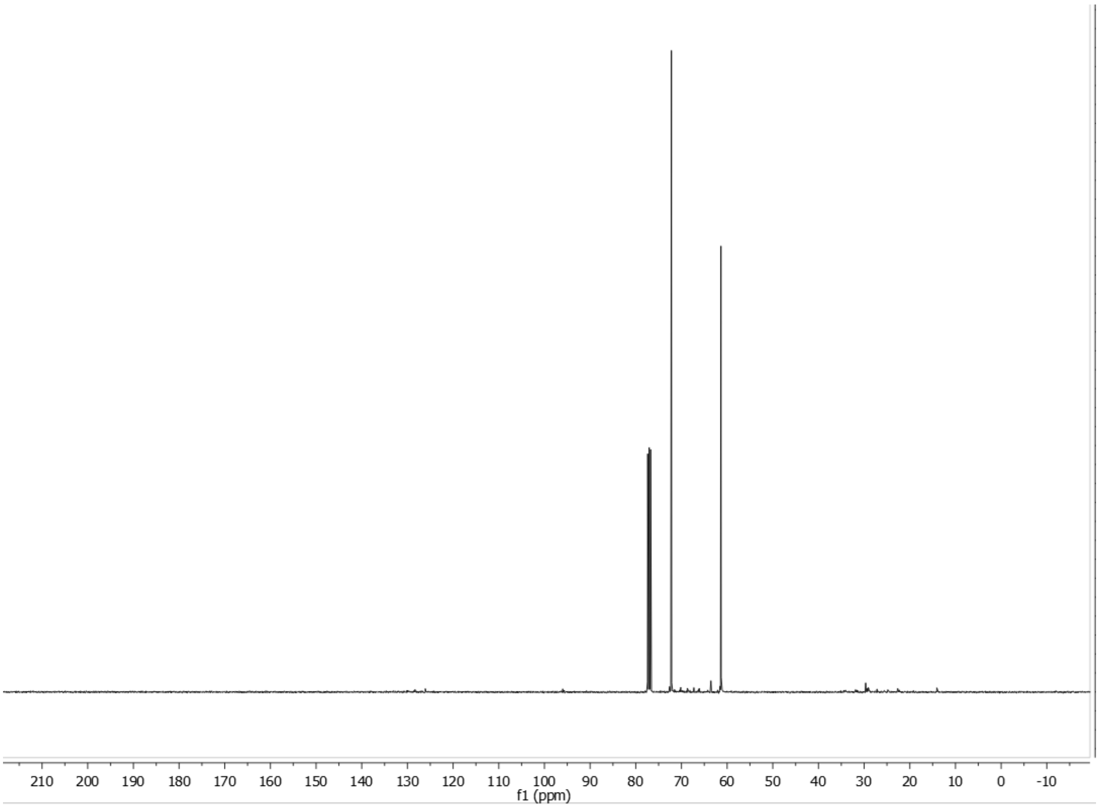

Figure A.5.3.39. ^{13}C NMR spectra of the wild strawberry $scCO_2$ extract in $CDCl_3$.

Bibliography

(1) Doucet, M.; Cho, J. H.; Alina, G.; Attala, Z.; Bakker, J.; Bouwman, W.; Butler, P.; Campbell, K.; Cooper- Benun, T.; Durniak, C. et al. SasView Version 5.0.3 Zenodo (2020, July 4), (Accessed on February 2021). **2021**, *3930098* (1996), 6. https://doi.org/http://doi.org/10.5281/zenodo.http://doi.org/10.5281/zenodo.

(2) Mildner, D. F. R.; Hall, P. L. Small-Angle Scattering from Porous Solids with Fractal Geometry. *J. Phys. D. Appl. Phys.* **1986**, *19* (8), 1535.

(3) Bahrudin, N. N.; Nawi, M. A.; Nawawi, W. I. Enhanced Photocatalytic Decolorization of Methyl Orange Dye and Its Mineralization Pathway by Immobilized TiO 2 /Polyaniline. *Res. Chem. Intermed.* **2019**, *45* (5), 2771–2795. https://doi.org/10.1007/s11164-019-03762-y.

(4) Bahrudin, N. N.; Nawi, M. A. Mechanistic of Photocatalytic Decolorization and Mineralization of Methyl Orange Dye by Immobilized TiO2/Chitosan-Montmorillonite. *J. Water Process Eng.* **2019**, *31* (June). https://doi.org/10.1016/j.jwpe.2019.100843.

(5) Konstantinou, I. K.; Albanis, T. A. TiO2-Assisted Photocatalytic Degradation of Azo Dyes in Aqueous Solution: Kinetic and Mechanistic Investigations: A Review. *Appl. Catal. B Environ.* **2004**, *49* (1), 1–14. https://doi.org/10.1016/j.apcatb.2003.11.010.